

6
AD-A281 578



DOCUMENTATION PAGE

Form Approved
OMB No. 0704-0188

1

Estimate is estimated to average 1 hour per response, including the time for reviewing instructions, searching existing data sources, gathering and reviewing the collection of information. Send comments regarding this burden estimate or any other aspect of this reporting burden, to Washington Headquarters Services, Directorate for Information Operations and Reports, 1215 Jefferson Avenue, and to the Office of Management and Budget, Paperwork Reduction Project (0704-0188), Washington, DC 20503.

2. REPORT DATE June 1994		3. REPORT TYPE AND DATES COVERED Final 5 Mar 93-4 Mar 94	
4. TITLE AND SUBTITLE 1993 Integrated Photonics Research		5. FUNDING NUMBERS DAAH04-93-G-0060	
6. AUTHOR(S) Yaron Silberberg (principal investigator)		8. PERFORMING ORGANIZATION REPORT NUMBER	
7. PERFORMING ORGANIZATION NAME(S) AND ADDRESS(ES) Optical Society of America Washington, DC 20036-2571			
9. SPONSORING/MONITORING AGENCY NAME(S) AND ADDRESS(ES) U.S. Army Research Office P.O. Box 12211 Research Triangle Park, NC 27709-2211		10. SPONSORING/MONITORING AGENCY REPORT NUMBER ARO 31175.1-EL-CF	
11. SUPPLEMENTARY NOTES The views, opinions and/or findings contained in this report are those of the author(s) and should not be construed as an official Department of the Army position, policy, or decision, unless so designated by other documentation.			
12a. DISTRIBUTION/AVAILABILITY STATEMENT Approved for public release; distribution unlimited.		12b. DISTRIBUTION CODE	
13. ABSTRACT (Maximum 200 words) Summaries of papers presented at the Integrated Photonics Research Topical Meeting, March 22-24, 1993, in Palm Springs, California. Sessions include Novel Materials and Devices, Time Domain Methods, Photonic Circuits and Lightwave Reception, III-V Semiconductor Switches and Modulators, Wavelength Selective Components, Optical Waveguide Simulators, Optical Switching, Silica on Silicon, Nonlinear Wave Propagation, Semiconductor Lasers, LiNbO3 and LiTaO3 Devices, Beam Propagation Methods, Photonic Integrated Circuits and Applications, Semiconductor Device Modeling, Waveguide Frequency Conversion, and Spatial and Temporal Solitons.			
14. SUBJECT TERMS Integrated Circuits, Lithium niobates, Photonics, Semiconductors, Switches, Modulators, Optical Devices, Waveguides, Optical Switching, Silicon, Silicon Dioxide, Wave Propagation, Semiconductor Lasers, Solitons		15. NUMBER OF PAGES	
17. SECURITY CLASSIFICATION OF REPORT UNCLASSIFIED		16. PRICE CODE	
18. SECURITY CLASSIFICATION OF THIS PAGE UNCLASSIFIED	19. SECURITY CLASSIFICATION OF ABSTRACT UNCLASSIFIED	20. LIMITATION OF ABSTRACT UL	

DTIC
SELECTE
JUL 12 1994
S B D

ARO 31175.1-EL-CF

INTEGRATED PHOTONICS RESEARCH



Sponsored by
Optical Society of America

Technical Cosponsor
IEEE Lasers and Electro-Optics Society

SEE QUALITY

1993 TECHNICAL DIGEST
SERIES VOLUME 10

MARCH 22-24, 1993
PALM SPRINGS,
CALIFORNIA

540
94-21051





Integrated Photonics Research

*Summaries of papers presented at the
Integrated Photonics Research
Topical Meeting*

March 22-24, 1993
Palm Springs, California

1993 Technical Digest Series
Volume 10

CONFERENCE EDITION

Sponsored by
Optical Society of America

Technical Cosponsor
IEEE/Lasers and Electro-Optics Society

Optical Society of America
2010 Massachusetts Avenue, NW
Washington, DC 20036-1023

94 7 11 055

Articles in this publication may be cited in other publications. In order to facilitate access to the original publication source, the following form for the citation is suggested:

Name of Author(s), "Title of Paper," in Integrated Photonics Research Technical Digest, 1993
(Optical Society of America, Washington, D.C., 1993), Vol. 10, pp. xx-xx.

ISBN Number

Conference Edition	1-55752-295-2
Postconference Edition	1-55752-296-0
(Note: Postconference Edition includes postdeadline papers.)	
1993 Technical Digest Series	1-55752-317-7

Library of Congress Catalog Card Number

Conference Edition	92-62838
Postconference Edition	92-62837

Copyright © 1993, Optical Society of America

Individual readers of this digest and libraries acting for them are permitted to make fair use of the material in it, such as to copy an article for use in teaching or research, without payment of fee, provided that such copies are not sold. Copying for sale is subject to payment of copying fees. The code 1-55752-317-7/93/\$2.00 gives the per-article copying fee for each copy of the article made beyond the free copying permitted under Sections 107 and 108 of the U.S. Copyright Law. The fee should be paid through the Copyright Clearance Center, Inc., 21 Congress Street, Salem, MA 01970.

Permission is granted to quote excerpts from articles in this digest in scientific works with the customary acknowledgment of the source, including the author's name and the name of the digest, page, year, and name of the Society. Reproduction of figures and tables is likewise permitted in other articles and books provided that the same information is printed with them and notification is given to the Optical Society of America. Republication or systematic or multiple reproduction of any material in this digest is permitted only under license from the Optical Society of America; in addition, the Optical Society may require that permission also be obtained from one of the authors. Address inquiries and notices to Director of Publications, Optical Society of America, 2010 Massachusetts Avenue, NW, Washington, DC 20036-1023. In the case of articles whose authors are employees of the United States Government or its contractors or grantees, the Optical Society of America recognizes the right of the United States Government to retain a nonexclusive, royalty-free license to use the author's copyrighted article for United States Government purposes.

Printed in U.S.A.

Accession For	
NTIS GRA&I	<input checked="" type="checkbox"/>
DTIC TAB	<input type="checkbox"/>
Unannounced	<input type="checkbox"/>
Justification _____	
By _____	
Distribution/ _____	
Availability Codes	
Dist	Avail and/or
A-1	Special

CONTENTS

Agenda of Sessions	v
IMA Plenary Session	1
IMB Poster Preview	9
IMC Novel Materials and Devices	81
IMD Time Domain Methods	107
IME Photonic Circuits and Lightwave Reception	141
ITuA III-V Semiconductor Switches and Modulators	167
ITuB Wavelength-Selective Components	197
ITuC Optical Waveguide Simulators	219
ITuD Optical Switching: Materials and Devices	251
ITuE Silica on Silicon 1	279
ITuF Nonlinear Wave Propagation	297
ITuG Semiconductor Lasers	317
ITuH LiNbO₃ and LiTaO₃ Devices	347
ITuI Beam Propagation Methods	371
IWA Photonic Integrated Circuits and Applications	405
IWB Semiconductor Device Modeling 1	431
IWC Waveguide Frequency Conversion	461
IWD Silica on Silicon 2	479
IWE Semiconductor Device Modeling 2	497
IWF Spatial and Temporal Solitons	515
Key to Authors and Presiders	539

INTEGRATED PHOTONICS RESEARCH TECHNICAL PROGRAM COMMITTEE

Raymond J. Hawkins, *Conference Chair, Lawrence Livermore National Laboratory*
Stephen R. Forrest, *Program Chair, Princeton University*
Yaron Silberberg, *Program Chair, Bellcore*

SUBCOMMITTEE 1: Active and Semiconductor Devices

Kam Lau, *Subcommittee Chair, University of California, Berkeley*
Joe Campbell, *University of Texas*
Robert J. Deri, *Bellcore*
Connie Chang-Hasnain, *Stanford University*
K. Kobayashi, *NEC Corporation, Japan*
Tom Koch, *AT&T Bell Laboratories*
Lars Thylen, *Fiber Optics Research Center, Sweden*
Peter Zory, *University of Florida*
Jane Zucker, *AT&T Bell Laboratories*

SUBCOMMITTEE 2: Nonlinear Guided Wave Devices

Martin Fejer, *Subcommittee Chair, Stanford University*
Allan Boardman, *University of Salford, United Kingdom*
Michael Cada, *Technical University of Nova Scotia, Canada*
Dominique Delacourt, *Thomson CSF, France*
Charles Ironside, *University of Glasgow, United Kingdom*
Mohammed Islam, *University of Michigan*
Garo Khanarian, *Celanese Research Company*
Hiroshi Nishihara, *Osaka University, Japan*

SUBCOMMITTEE 3: Modeling, Numerical Simulation, and Theory

Anand Gopinath, *Subcommittee Chair, University of Minnesota*
G. Agrawal, *University of Rochester*
S. Burks, *University of Wales College Cardiff, United Kingdom*
N. Dagli, *University of California, Santa Barbara*
D. Lenstra, *Free University, Netherlands*
R. Pregla, *Fern University, Germany*
S. Seld, *NTT Opto-electronics Laboratory, Japan*
A. Shimizu, *University of Tokyo, Japan*
H. Winful, *University of Michigan*
D. Yevick, *Queens University, Canada*

SUBCOMMITTEE 4: Waveguide Devices

Steven Korotky, *Subcommittee Chair, AT&T Bell Laboratories*
David Haas, *Hoechst Celanese*
Charles Henry, *AT&T Bell Laboratories*
Masao Kawachi, *NTT Opto-electronics Laboratories, Japan*
Keiro Komatsu, *NEC Corporation, Japan*
Gustaaf Mohlmann, *AKZO Research Laboratories Arnhem, Netherlands*
Michel Papuchon, *Thompson CSF LCF, France*
David Smith, *Bellcore*
Ger-Lam Yip, *McGill University, Canada*
Alfredo Yi-Yan, *Bellcore*

INTEGRATED PHOTONICS RESEARCH 1993 ADVISORY COMMITTEE

William K. Burns, *Chair, U.S. Naval Research Laboratory*
Raymond J. Hawkins, *Lawrence Livermore National Laboratory*
W. S. C. Chang, *University of California, San Diego*
Larry A. Coldren, *University of California, Santa Barbara*
G. I. Stegeman, *University of Central Florida*
W. J. Tomlinson, *Bellcore*

AGENDA OF SESSIONS

Monday, March 22, 1993

MESQUITE A	MESQUITE B	MESQUITE C/D
8:30 am–11:15 am IMA Plenary Session		
10:00 am–10:30 am COFFEE BREAK		
10:30 am–11:15 am IMA (Continued)		
11:15 am–12:15 pm IMB Poster Preview		
12:15 pm–1:30 pm LUNCH (on your own)		
1:30 pm–3:15 pm IMC Novel Materials & Devices	1:30 pm–3:45 pm IMD Time Domain Methods	1:30 pm–3:30 pm IME Photonic Circuits and Lightwave Reception
3:30 pm–5:00 pm IPR POSTER SESSION		

AGENDA OF SESSIONS—Continued

Tuesday, March 23, 1993

MESQUITE A	MESQUITE B	MESQUITE C/D
8:30 am–10:30 am ITuA III-V Semiconductor Switches and Modulators	8:30 am–10:15 am ITuB Wavelength-Selective Components	8:30 am–10:15 am ITuC Optical Waveguide Simulators
10:30 am–11:00 am COFFEE BREAK		
11:00 am–12:30 pm ITuD Optical Switching Materials and Devices	11:00 am–12:30 pm ITuE Silica on Silicon: 1	11:00 am–12:30 pm ITuF Nonlinear Wave Propagation
12:30 pm–1:30 pm LUNCH (on your own)		
1:30 pm–3:30 pm ITuG Semiconductor Lasers	1:30 pm–3:30 pm ITuH LiNbO ₃ and LiTaO ₃ Devices	1:30 pm–3:30 pm ITuI Beam Propagation Methods
3:30 pm–4:00 pm COFFEE BREAK		
4:00 pm POSTDEADLINE PAPER SESSION		
6:00 pm–7:30 pm CONFERENCE RECEPTION		

AGENDA OF SESSIONS—Continued

Wednesday, March 24, 1993

MESQUITE A	MESQUITE B	MESQUITE C/D
8:30 am–10:30 am IWA Photonic Integrated Circuits and Applications	8:30 am–10:30 am IWB Semiconductor Device Modeling: 1	8:30 am–10:15 am IWC Waveguide Frequency Conversion
10:30 am–11:00 am COFFEE BREAK		
12:15 pm WD Silica on Silicon: 2	11:00 am–12:30 pm WE Semiconductor Device Modeling: 2	11:00 am WF Spatial and Temporal Solitons

Monday, November 15, 2010

Plenary Session

IMA 8:30am-11:15am
Mesquite A/B

Raymond J. Hawkins, *Presider*
Lawrence Livermore National Laboratory

TDM Soliton Transmission and Storage

H. A. Haus

Department of Electrical Engineering and
Computer Science and Research Laboratory
of Electronics

Massachusetts Institute of Technology

Cambridge, MA 02139

(617) 253-2585

The trans-Atlantic cable to be laid in 1995 will not use solitons. Instead, it will use a dispersion shifted fiber, with zero dispersion at and near the 1.5μ wavelength of the Erbium amplifier. The transmission will be "linear," at 1.5μ , suppressing effects of the nonlinearity of the fiber by staggering slightly positive and slightly negative dispersive fiber segments. This design was chosen, rather than the repeaterless soliton transmission proposed by Hasegawa^[1], and experimentally demonstrated by Mollenauer^[2], because of an effect characteristic of amplified solitons, the so called Gordon-Haus effect^[3]. This effect is due to the shift of the soliton carrier frequency experienced when a soliton is amplified by an amplifier with spontaneous emission noise. The carrier frequency performs a random walk. Even though the "steps" are small, the cumulative effect of travel over long distances shifts the timing of the solitons, leading to errors. Transmission over trans-Atlantic distances is not prevented by this effect. However, the effect increases with increasing power and sets an upper limit to the signal power. A lower limit on the signal power is set by the standard ratio of signal power to noise power, the S/N ratio. The window of permissible power, for a given bit-error rate, is too narrow to assure long term reliability.

This was the situation when plans for the 1995 trans-Atlantic cable were made. In 1991 it was discovered, both at MIT and at AT&T Bell Laboratories, that the Gordon-

Haus effect can be reduced by judicious placement of a filter with every amplifier in the chain^[4,5]. The filters tend to control the carrier frequency of the solitons and thus reduce their random walk. The filters can be of the Fabry-Perot type, allowing several wavelength channels to pass through, with each maximum of filter transmission set at the channel center frequency. In this way it is possible to wavelength multiplex the transmission, whereas the "linear" design can accommodate only one wavelength channel. Solitons of different frequencies can pass through each other and fully recover their shape and spectrum after the "collision." Thus, ideally, there is no crosstalk in spite of the nonlinearity. It is very likely that the transoceanic cables after 1995 will use solitons for transmission. This will foster technological developments in the generation, transmission and switching of solitons.

The bit-rate for transoceanic transmission is limited to about 10 Gbit. The reason for this is that the amplifier spacing must be shorter than a soliton "period" in order to prevent soliton instabilities. At constant power, the period is inversely proportional to the bit-rate squared. Long-distance terrestrial communications will, most likely, follow the transoceanic model, in part because of the same bit-rate limitation, in part to take advantage of the technology developments for transoceanic communications. In this context, one may imagine a scenario in which the local area TDM bit-rate grows beyond the 10 Gbit limit. If local areas are to be interconnected, the problem then is to transmit "bursts" of high bit-rates over wavelength multiplexed channels of lower bit-rates. The transmission can be done, in principle, by demultiplexing and modulation of individual-channel transmitters.

The reception problem is more complicated and calls for the development of novel optical devices. The demultiplexed messages arrive at different times, with pulses adapted to the low transmission bit-rate. The pulses have to be recompressed and variable delays have to be introduced. Finally, an optical storage with high speed access has to be developed. The talk will touch on some possible realizations of such devices, and will give some details on the optical storage ring^[6]. The optical storage ring has gain to compensate for the loss. It resembles a modelocked laser, with some obvious differences. In a modelocked laser, a pulse can be maintained forever however "zeros," gaps between pulses, cannot. We have

shown^[6] that a combination of active modulation, that spreads the spectrum of the noise, and filters, that absorb the spread spectrum, can maintain zeros indefinitely.

The switching in and out of the storage ring could be accomplished by several types of optical switches. It is hoped that the talk will stimulate work on components necessary to accomplish the task of reception of demultiplexed signals. It goes without saying that most of these components are generic and would find use in other applications.

This work was supported in part by National Science Foundation Grant 9012787-ECS.

References

- [1] A. Hasegawa, "Numerical study of optical soliton transmission amplified periodically by the stimulated Raman process," *Appl. Opt.* **23**, 3302 (1984).
- [2] L. F. Mollenauer, B. M. Nyman, M. J. Neubelt, G. Raybon, and S. Evangelides, "Demonstration of soliton transmission at 2.4 Gbit/s over 12,000 km," *Electron. Lett.* **27**, 178 (1991).
- [3] J. P. Gordon and H. A. Haus, "Random walk of coherently amplified solitons in optical fiber transmission," *Opt. Lett.* **11**, 665 (1986).
- [4] A. Mecozzi, J. D. Moores, H. A. Haus, and Y. Lai, "Soliton transmission control," *Opt. Lett.* **16**, 1841 (1991).
- [5] Y. Kodama and A. Hasegawa, "Generation of asymptotically stable optical solitons and suppression of the Gordon-Haus effect," *Opt. Lett.* **17**, 31 (1992).
- [6] H. A. Haus and A. Mecozzi, "Long-term storage of a bit-stream of solitons," *Opt. Lett.* **17**, 1500 (1992).

Optoelectronic and Photonic Integrated Circuits

Martin A. Pollack
AT&T Bell Laboratories
Crawford Hill Laboratory (PO Box 400)
Holmdel, New Jersey 07733
1-908-888-7233

INTRODUCTION

Monolithic integrated circuits containing both semiconductor optical and electronic elements should provide improved performance and functionality compared with their hybrid circuit counterparts. They also have the potential for higher reliability and lower cost. The early realization of these same advantages has driven the incredibly successful development of all-electronic ICs.

However, despite more than a decade of research, most of today's experimental optoelectronic integrated circuits (OEICs) still combine only simple electronic functions with a very limited number of optical devices. In recent years, the potential advantages of integrating greater numbers of semiconductor optical components has become recognized. Such integration can greatly simplify packaging, thus significantly impacting system costs. The term photonic integrated circuit (PIC) has come into use to describe these monolithic circuits, which consist of several photonic/guided-wave optical components, both active and passive, and possibly a small number of electronic devices.

APPLICATIONS

The potential applications of OEICs and PICs extend from very large to very small lightwave system dimensions. Long-haul trunk transmission terminals require the high levels of performance and reliability expected with circuit integration. Higher volume, short distance systems, such as telephone distribution plant, cable TV, and local data networks, demand both high performance and low cost. Optical interconnections between racks, boards, or even chips are future applications for which high reliability and low cost are paramount. Photonic switching, routing, signal processing (logic), and computing are technologies which may only become practical with the increased functionality of OEICs and PICs.

The performance improvements possible with OEICs compared with hybrid circuits will be achieved principally through the reduction of electrical parasitics. This will lead to higher speed lightwave transmitters and lower noise, wide bandwidth receiver circuits. Much work already has been focussed on integrated detector-preamplifier circuits for InP-based long-wavelength (1.3-1.55 μ m) photoreceiver front-ends. Far more advanced integration has been reported for GaAs-based OEICs.

Examples of the increased functionality now possible through the monolithic integration of photonic components into PICs include balanced photoreceivers for long-wavelength coherent systems, laser-amplifier and low-chirp laser-modulator combinations, waveguide multiplexers and demultiplexers, and lasers or modulators with integrated electronic driver circuitry. Laser and receiver arrays for multi-wavelength systems, as well as switch matrix technology, also fall into the category of photonic integrated circuits. In addition to combining discrete devices onto a monolithic chip, increased functionality can also be brought about by combining multiple functions into a single device, as with the SEED and VSTEP technologies.

TECHNOLOGICAL CHALLENGES

Many challenges must be overcome before OEICs and PICs can fully achieve their anticipated potential. Their performance levels now often approach those of hybrids, but predicted higher performance has rarely been realized. So far, most of the research on OEICs and PICs has been concerned with the integration of existing discrete devices. A major thrust of future integration must be in the direction of novel device elements and new combinations.

Higher reliability and lower costs should come about through the reduced component count, reduced circuit size, and simplified packaging possible with monolithic integration. However, the potential of lower costs is not even close to being realized, mainly because of small circuit yields. Concerns over costs and packaging have led many to consider alternatives to OEICs and PICs which involve hybrid integration in the form of flip-chip bonding of discrete components, or the use of silicon "optical bench" or "waferboard" technology.

The past few years have seen rapid growth in OEIC and PIC research, and in the materials and processing technology base required to support it. To those working in this exciting field, it is a matter of faith that OEICs and PICs one day will be the essential elements needed to fully utilize the potential of photonics.

**Current Status of Nonlinear Materials and
Their Application to Waveguide Devices**

**George I. Stegeman
CREOL, Un. Central Florida
12424 Research Parkway, Orlando, FL 32826
407-658-3915**

It was recognized in the early days of nonlinear optics that waveguides provide the optimum beam confinement and long propagation distances needed for efficient nonlinear interactions. This led first to the demonstration of guided wave versions of plane wave nonlinear optical phenomena (e.g. doublers), and later to effects either unique to guided waves (e.g. modulational instabilities) or to phenomena for which the right conditions could only be met in waveguides (e.g. solitons). Over the years this has led to the demonstration of various devices such as efficient doublers for the blue and all-optical switching, logic and demultiplexing. Furthermore, new materials which will lower the device operating powers are continuously being reported.

For example, one of the recent achievements has been the development of waveguide doublers for the blue. Mw of blue are now possible with 100 mw IR inputs. The key has been the development of quasi-phase-matching structures in KTP and lithium niobate, two "old" materials revitalized for nonlinear optics by new processing technologies. At the same time, new molecules are being developed which in poled polymer structures have the potential for much higher conversion efficiencies. On the other hand, the explanation of second harmonic generation in glass fibers has proven to be an interesting materials problem.

In the area of third order effects, there have been many waveguide-specific developments. For example, temporal solitons which are easily excited in fibers can be used for long distance communications, or all-optical switching without pulse distortion. All-optical switching, logic gates, signal demultiplexing have been demonstrated in two-dimensional waveguides. New fibers with nonlinearities larger by 10^2 - 10^4 than $\chi^{(3)}$, and new approaches to producing even larger effective third order nonlinearities have been reported and will be discussed.

These are a few of the examples of the recent developments in nonlinear materials and waveguide phenomena which will be discussed in this talk.



Poster Preview

IMB 11:15am-12:12pm
Mesquite A/B

Stephen Ross Forrest, *Presider*
Princeton University

Yaron Silberberg, *Presider*
Bellcore

Measurement and Calculation of Carrier-Induced Changes of Refractive Index and Absorption in GaInAsP Near the Band Edge

Osamu HANAIZUMI, Hiroyuki TAKEMOTO, Manabu IZUMIKAWA,
Keisuke KUWAHARA, and Shojiro KAWAKAMI

Research Institute of Electrical Communication, Tohoku University
2-1-1 Katahira, Aoba-ku, Sendai 980, Japan
Phone : +81-22-227-6200 (ext.3160), Fax : +81-22-268-9496

The carrier-induced refractive index change of a InV heterojunction is very large[1]. It is produced by bandfilling, band-gap shrinkage, and plasma dispersion. Optical switches utilizing this large index change have already been demonstrated[2,3]. At the photon energies near E_g , however, measurement is difficult due to absorption, so that the experimental verification has not been completely done[4] and the design of the carrier-induced optical devices is still difficult.

Recently, we have proposed a method to measure the complex refractive index change near the band edge using a small interference-ellipsometry bridge and presented several results of measurement of refractive index change Δn [5]. In this paper, we measure the changes of both refractive index and absorption[6] at a higher injection level than before and compare with theories.

Fig.1 schematically shows the structure of the sample. The epitaxial layers were grown by MOCVD. The probe light traverses the sample perpendicularly to the surface and the absorption of the active layer is small even for $\lambda < \lambda_g$. In order to avoid the absorption in the regions other than the active layer, the cap layer is made of InP.

The setup for measuring the complex refractive index changes is shown in Fig.2. The light source is the wavelength-tunable pulse laser system (Quanta-Ray, DCR-2A), with 5nsec width and 10pps repetition frequency. The injected current is rectangular pulses with 1 μ sec width and 10pps repetition frequency (the duty ratio is 10^{-5}) and temperature rise of the active layer is negligible. The optical pulses are synchronized with current pulses by the delay line(SMF2). Part of the light beam is branched by the PBS and the reference signal for compensating the perturbation of the polarization and the power is obtained. The main beam is then led to the microbridge, where the calcite plate 1 and 2 have the same optical path lengths and operate as a splitter and combiner, respectively. The separation width of two beams is 1mm. The extraordinary beam passes through the carrier injection area and is combined with the ordinary beam passed through the dummy electrode by the calcite plate 2. We derived Δn and $2\Delta\alpha$ from the change of the polarization state of the combined beam.

The direction of the rotation of an elliptically polarized light, hence the sign of Δn , cannot be determined from the shape of the ellipse. So that another measurement is necessary. We determine it for every wavelength and every injection level from the change of the polarization ellipse caused by heating a glass plate with a known sign of $\partial n / \partial T (> 0)$ inserted to the same optical path with the sample.

An example of the measurement of the polarization state changed by carrier injection is shown in Fig.3. The power of light passed through the carrier injection area is shown by the y coordinate. In this element, the phase is delayed by the refractive index reduction and the amplitude decreases by the absorption increase. We derived the complex refractive index change by the least-square fitting.

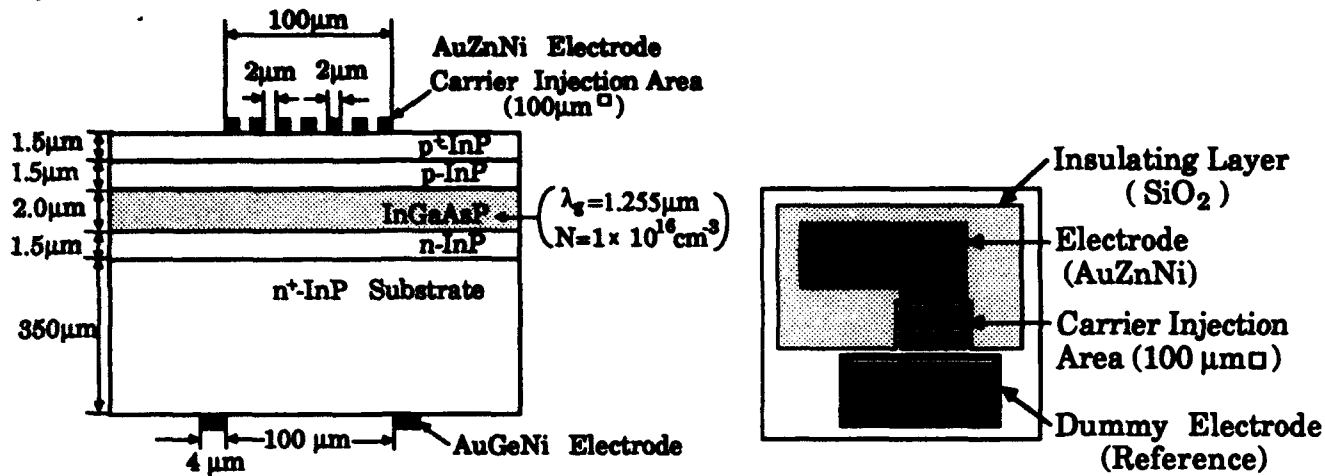
We show measured Δn and $2\Delta\alpha$ in Fig.4(a) and (b), respectively. The carrier density was estimated from the measured decay time of spontaneous emission[7] in another sample of the same lot. We can measure the value of Δn very precisely, so that the measurement of Δn become possible even if the injection level is relatively low. In the vicinity of λ_g , Δn has a negative peak at the shorter wavelength region and has a positive peak at the longer wavelength region. At sufficiently longer wavelengths, Δn has negative values characterized mainly by plasma dispersion. The wavelength dependence of Δn shifts to longer wavelengths by increasing injection. $2\Delta\alpha$ is observed to have a positive peak near λ_g .

Different theories or theoretical models predict different values of complex refractive index changes by carrier injection. We also show the calculated values using the model of Ref.[8] in Fig.5, for example. Calculated Δn has a negative peak much larger than the measured one. $2\Delta\alpha$ has a positive peak slightly larger than the measured one near λ_g . The wavelength dependence of the calculated values is roughly similar to that of measurement.

In conclusion, we have measured Δn and $2\Delta\alpha$ of carrier-injected GaInAsP using a small interference-ellipsometry bridge at the photon energies near E_g , especially $E > E_g$, and compared to previous theories.

References and Comments

- [1]J. Manning, R. Olshansky, and C. B. Su, IEEE J. Quantum Electron., QE-19, 1525 (1983)
- [2]O. Mikami and H. Nakagome, Electron. Lett., 20, 228(1984)
- [3]K. Ishida, H. Nakamura, H. Inoue, and H. Matsumura, IOOC'85, 357(1985)
- [4]U. Keller, S.K.Diamond, B. A. Auld, and D. M. Bloom, Appl. Phys. Lett., 53, 388(1988)
- [5]O. Hanaizumi, H.Takemoto, K. Kuwahara, and S. Kawakami, 4th Optoelectronics Conference, OEC'92, 17C3-4 (1992)
- [6] We define α as an absorption coefficient of amplitude, so that the change of the absorption of power is expressed as $2\Delta\alpha$
- [7]O.Hanaizumi, H.Takemoto, K.Kuwahara, and S. Kawakami, IEICE Tech. Rep., OQE92-98, 1(1992)
- [8]B. R. Bennett, R. A. Soref, and J. A. Del Alamo, IEEE J. Quantum Electron., QE-26, 113(1990)



(a) Cross section of the sample. The light beam diffuses after passing through the p-electrode and has an uniform distribution in the active layer. The space of the grating of the n-electrode is sufficiently wide and the light beam passes through without scattering. The current diffuses from the p-electrode with narrow space and has an uniform distribution in the active layer.

(b) The pattern of the p-electrode. The current is injected from the $100\mu\text{m} \times 100\mu\text{m}$ grating electrode through the window of the SiO_2 insulating layer. In the microbridge, the extraordinary beam passes through the injection area and the ordinary one passes through the dummy electrode in order to coincide the power with the extraordinary one.

Fig.1. Schematic structure of the sample.

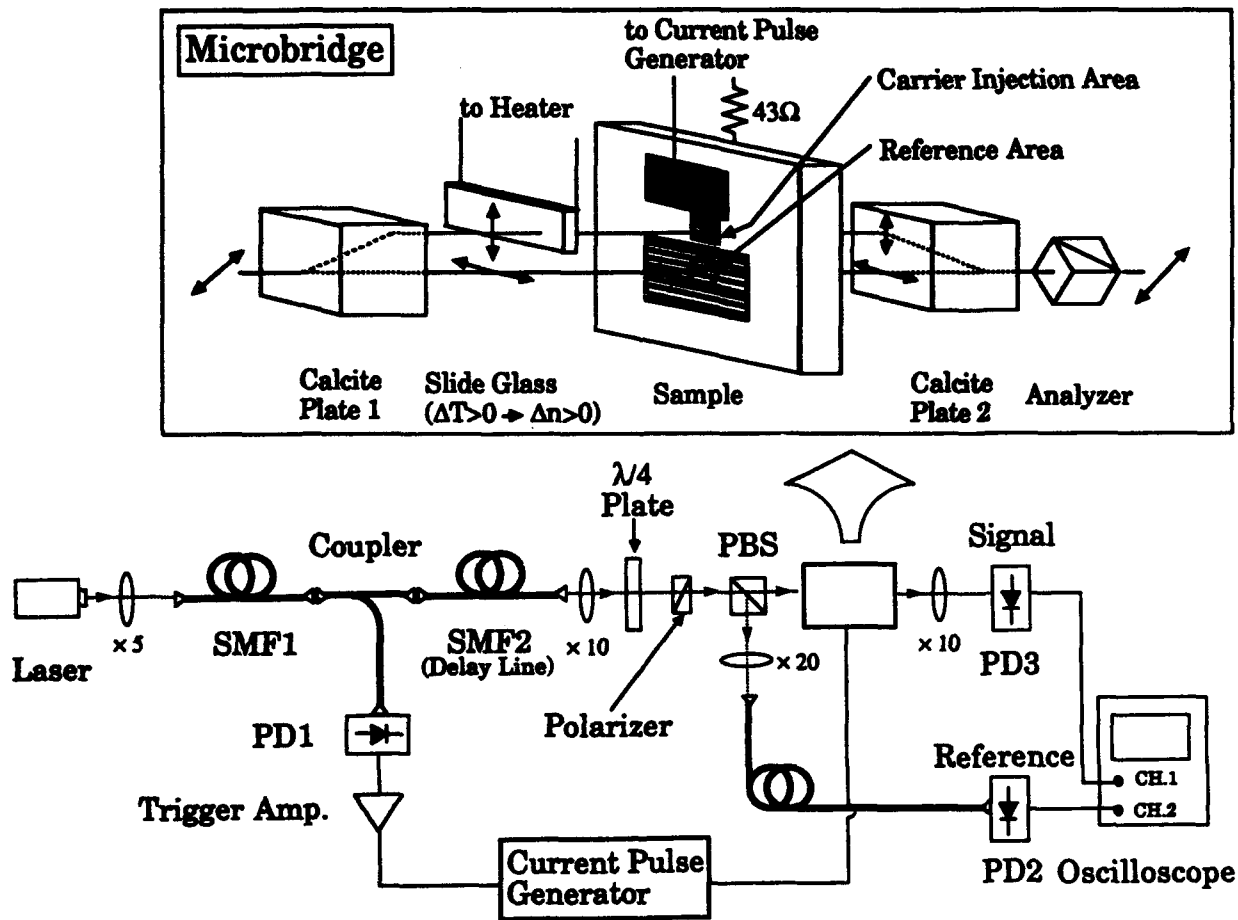


Fig.2. Setup for measuring the complex refractive index change.

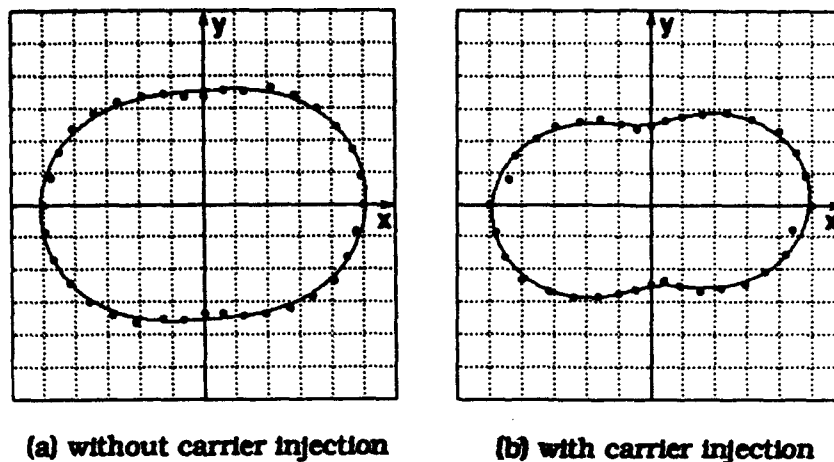


Fig.3. Observed states of polarization by carrier injection (injection level : $3.7 \times 10^{17} \text{ cm}^{-3}$, $\lambda=1.24\mu\text{m}$). The y element is the beam passed through the injection region and the x element is that passed through the dummy electrode. " o " is the power we measured by rotating the analyzer, and the solid line is the calculated value by the least-square fitting. We derived the complex refractive index change from the change of the fitted parameters.

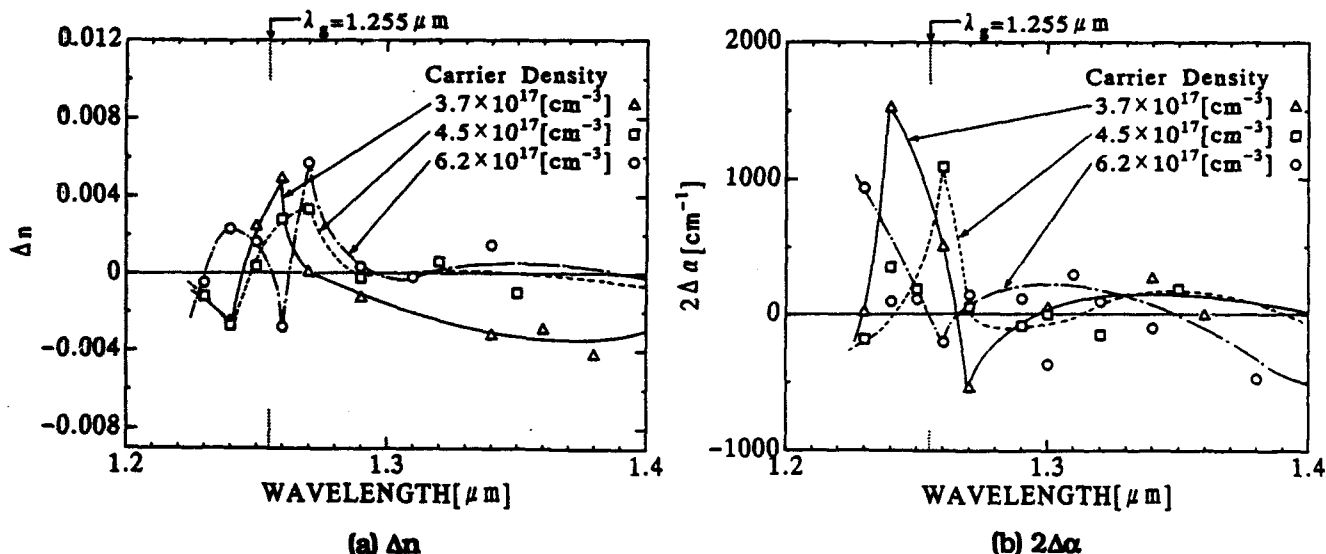


Fig.4. Measured complex refractive index changes.

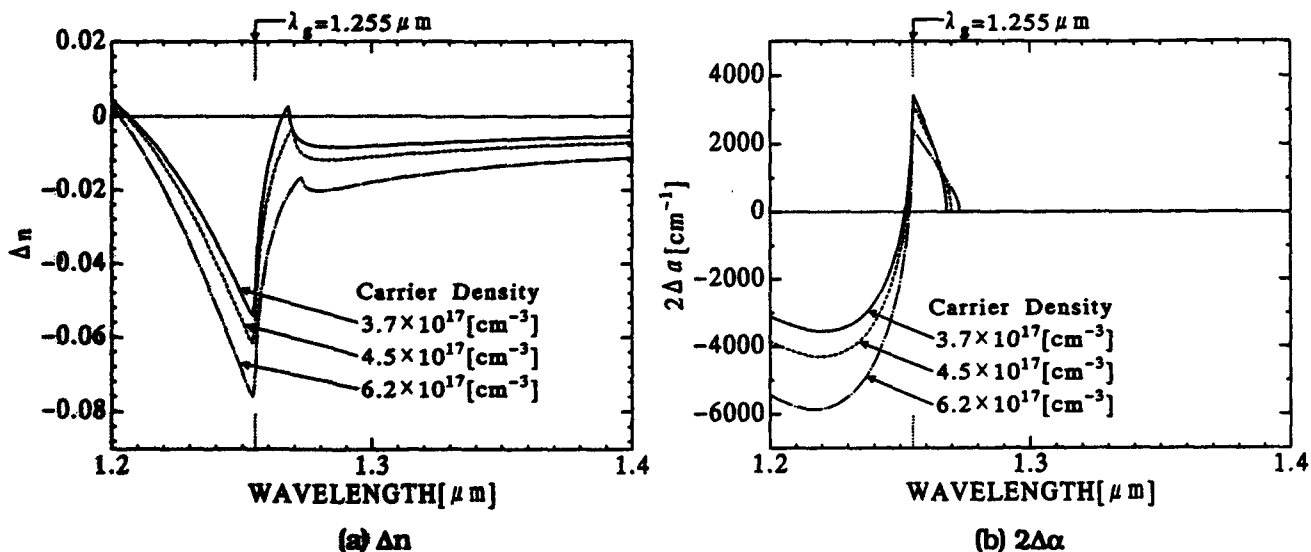


Fig.5. Calculated complex refractive index changes.

A COMPACT INTEGRATED-OPTICAL SWITCH BASED ON DYNAMIC FREE CARRIER GRATINGS IN GAAS

Lewis B. Aronson¹ and Lambertus Hesselink²

1) Hewlett-Packard Labs, Bldg 26M, Palo Alto Ca. 94303

2) Department of Electrical Engineering, Stanford University, Stanford Ca. 94305

Introduction and Background

Future optical communication and computer interconnect systems will require complex switching networks. Computer applications, in particular, may require monolithic, non-blocking switching networks of at least 100×100 elements. Numerous integrated-optical switch designs have been described and demonstrated with low insertion losses and high switching speeds.¹ To date, however, the highest level of integration achieved is a 16×16 LiNbO₃ switch array on a 60 mm long substrate.² One reason why these switch designs can't be integrated to higher levels is the geometry of the basic device which consists of waveguides running in parallel or crossing at very small angles. This results in a device cell which is very long and thin and thus does not efficiently use substrate area. In addition, the near parallel waveguide geometry usually mandates the use of bends for waveguide separation which further increase overall switch area.

Large angle switches with small interaction lengths are possible using short period *active* grating structures (as distinguished from devices based on detuning a static grating) to couple light between crossing waveguides. While dynamic waveguide gratings have been demonstrated,^{3,4,5} they are either too slow or have large grating period and small crossing angles resulting in switch elements similar in size to more conventional designs.

We report a new type of high speed integrated optical switch based on electrically controlled free-carrier gratings in semiconductors. The refractive index change associated with the free carriers in these grating structures diffracts light between crossing waveguides. Fig. 1 shows the overall layout of the active grating and the layout of a full crossbar switch array. There is no need for the waveguides to cross at right angles as shown, and in fact other large crossing angles are shown to be useful for polarization insensitive switches. We believe that this switch principle has the potential for monolithic integration of 100×100 element arrays.

Device Implementations

We have considered three semiconductor structures to control free carriers (and thus the refractive index) in the sub-micron grating pattern required for large angle switching. The first structure, which we have fabricated and tested, is a low efficiency demonstration design which can be built without epitaxial regrowth. A schematic of this device is shown in Fig. 2 and represents the A-A' cross-section in Fig 1. A lightly doped *n*-type GaAs/AlGaAs waveguide is used. At the intersections, a grating of heavily doped *n*-type material is formed using ion implantation. The presence of free carriers results in an index grating which couples light between the guides. When a reverse bias is applied via a Schottky electrode, the free carriers are depleted and the coupling is switched off. Modeling of the efficiency of this switch, which we report in an upcoming paper,⁶ indicates diffraction efficiencies ranging from $2.7 - 11.0 \times 10^{-4}$ for 100 μm guides, depending on which published estimate of the free carrier index changes is used.

We have considered, but not yet fabricated, two designs which involve epitaxial regrowth in their fabrication. By using regrowth in the device fabrication, we have the flexibility to place the free carrier grating at the point of maximum optical field resulting in higher diffraction efficiencies.

Fig. 3 shows the first regrowth design which is based on the depletion of an implanted heavily doped p-n grating in a lightly doped p-n waveguide. Modeling of the efficiency of this switch indicates diffraction efficiencies of 0.02 for 100 μm wide waveguides. The limitations on the diffraction efficiency of depletion mode designs are a result of the limit on the number of carrier which can be depleted before the breakdown field is reached.

Figure 4 shows the second regrowth design based on carrier injection through a periodic structure. In this case, the grating is formed by implanting a reverse p-n junction which becomes depleted during forward bias allowing current to flow only in the unimplanted regions. By using injection, the breakdown field limitations are eliminated. If we assume a grating region 0.1 μm thick with an injected free carrier density of $3 \times 10^{18} \text{ cm}^{-3}$, we calculate a diffraction efficiency as high as 40%. This corresponds to an insertion loss of less than 10 dB if 6 dB coupling and propagation losses are assumed.

Fabrication

A Schottky based depletion mode device was fabricated for use at a wavelength of 1.55 μm . The waveguide layers for the device are grown by molecular beam epitaxy (MBE) on an n+ GaAs substrate ($n=10^{18} \text{ cm}^{-3}$). A 2.5 μm cladding layer of $\text{Al}_{0.7}\text{Ga}_{0.3}\text{As}$ is followed by a 0.4 μm GaAs guiding layer (both layers with $n = 3 \times 10^{16} \text{ cm}^{-3}$). Ridge waveguides are lithographically defined and etched to a depth of 0.2 μm . An SiO_2 layer is deposited and patterned to define the active switch area at the waveguide intersections.

Holographically patterned photoresist is used for the ion implantation mask. An analysis of the tradeoff between implantation depth and lateral straggle yields an optimum implantation energy of 100 KeV for a silicon implant, requiring a photoresist mask at least 0.4 μm thick. For this device, Bragg matching dictates a grating period of 0.35 μm . To achieve the required high aspect ratio, a technique developed by Anderson⁷ is employed. A thin (0.15 μm) absorbing layer (Brewer Scientific OmniLayerTM) is spun on the substrate followed by a 0.4 μm layer of photoresist. This is exposed using an argon ion laser. After development, a ridge structure about 0.15 μm deep remains. A layer of silicon (250 \AA) is shadow evaporated at a 50° angle to coat the tops of the grating ridges. This layer serves as a mask for a low pressure oxygen reactive ion etch which deepens the gratings to the substrate (depth = 0.55 μm).

Using this mask, silicon was implanted at 90 KeV with a dose of $8 \times 10^{12} \text{ cm}^{-2}$. Following an activation anneal, another SiO_2 layer is deposited and patterned to provide electrode isolation. At this stage, the wafers are thinned and a backside ohmic contact (Au/Ge/Ni/Au) is evaporated and annealed (450°C, 10 sec). A liftoff process is used to define the Schottky electrodes which consist of sputtered Indium-Tin-Oxide (ITO) followed by a thin layer of gold for reduced electrode resistance. ITO, a transparent conductor, is chosen as a Schottky electrode because it induces less optical loss than a metal electrode. To suppress unwanted etalon effects, the input and undiffracted output facets were anti-reflection coated. The final device consists of six guides in each direction with widths ranging from 25 - 800 μm and switch elements at the 6 symmetric intersections on a 1 \times 1.5 cm chip.

Experimental Results

An Er^+ fiber laser, tunable from 1.525 to 1.580 μm , was used as an optical source for diffraction efficiency measurements. The output of the laser is focused by a cylindrical lens and an objective onto the input waveguide facet to allow efficient coupling to the lowest order modes of the input guide. This is important since the angular selectivity of the grating allows efficient

coupling only between the fundamental modes for a grating formed at 45° to the waveguides. The transmitted and diffracted outputs are focused by objectives onto Ge detectors. The drive signal for these tests is from +1 to -1 Volt. The modulated diffracted signal is measured using a lock-in amplifier. Static diffraction is measured from the DC output of the detector.

The maximum TM to TM dynamic and static diffraction efficiencies are shown in Fig. 5 as a function of device size. Dynamic diffraction efficiency is observed in all of the devices except for the $50 \mu\text{m}$ switch which shows ohmic rather than rectifying behavior. As expected, the diffraction efficiency scales as device area (straight line in plot). The fall-off for the largest devices is believed to be due to progressively poorer coupling into the lowest order modes of the waveguide. The maximum dynamic diffraction efficiency for the $100 \times 100 \mu\text{m}$ device is seen to be 1.0×10^{-4} which occurred at a wavelength of $1.534 \mu\text{m}$. This value is a factor of 2 to 8 below theoretical predictions for this device which we attribute to incomplete activation of the implant.⁶

Fig 5. also shows the presence of a large static diffraction efficiency. This would lead to unacceptable crosstalk in a practical switch. We don't believe this static coupling is fundamental to our design but is rather a process related artifact such as a surface corrugation or unannealed implant damage which can be eliminated in future versions. The demonstration device, however, exhibits all of the important features of the device design. The wavelength dependence of the static diffraction efficiency for the various polarization cases is shown in Fig. 6. We have fit the data assuming the presence of a surface related static grating, a small rotation error (0.56°) in the grating angle, and the presence of launched power both the fundamental and third order lateral mode and achieved very good agreement with our results.⁶

Conclusions

We have demonstrated a new type of integrated optical switch based on dynamic free carrier gratings. The measured diffraction efficiency is found to be close to predicted values. The performance of the demonstrated switch along with several proposed variations is shown in Table 1. The device in the last column uses a non-orthogonal intersection and offers high diffraction efficiency and polarization independent performance. These switch designs offer the possibility of integrating arrays of 100×100 elements on a single substrate with reasonable insertion loss and high switching speed. We believe that such a switch array could have important implications for computer based optical interconnects.

TABLE I
COMPARISON OF KEY SPECIFICATIONS OF VARIOUS SWITCH DESIGNS

	Schottky (Demonstrated)	P-N Depletion (90° crossing)	P-N Injection (90° crossing)	P-N Injection (28° crossing)
Device Size	$100 \times 100 \mu\text{m}$	$100 \times 100 \mu\text{m}$	$100 \times 100 \mu\text{m}$	$50 \times 50 \mu\text{m}^{[d]}$
η_{max} (TM Input)	1.0×10^{-4}	1.9×10^{-2}	3.8×10^{-1}	4.2×10^{-1}
η_{max} (TE Input) [a]	5.0×10^{-5}	5.2×10^{-6}	0.0	4.2×10^{-1}
$\Delta\lambda$ Bandwidth	18 nm	6 nm	6 nm	42 nm
Switching Speed	28 MHz [b]	1.4 GHz	300 MHz [c]	300 MHz [c]

[a] With device designed for maximum TM response.

[b] Estimated from electrode capacitance ($\sim 700 \text{ pF}$) and 50Ω input resistance.

[c] Higher speeds may be possible with bipolar structures.

[d] Intersection not square, area is approximately $5300 \mu\text{m}^2$.

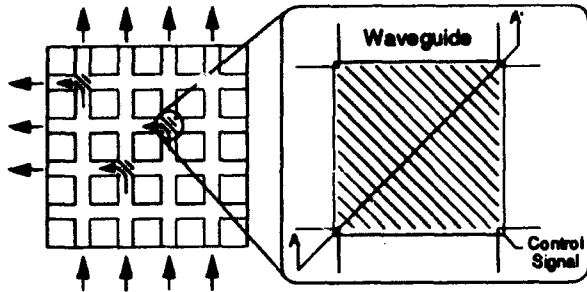


Fig. 1. Illustration of the basic switch and array geometry showing use in a crossbar architecture.

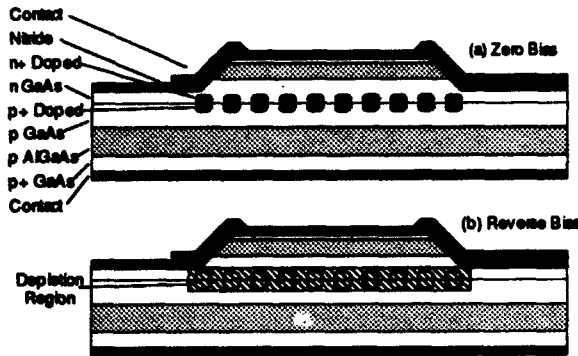


Fig. 3. Regrowth based p-n junction depletion mode switch under zero and reverse bias.

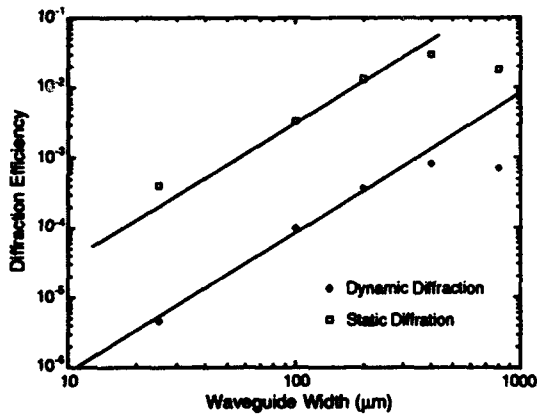


Fig. 5. Measured TM-TM peak dynamic and static diffraction efficiency vs. device size.

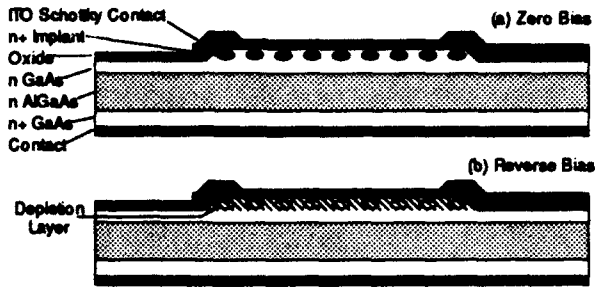


Fig. 2. Non-regrowth demonstration device (Fig. 1 A-A') with no applied bias (a). Device with grating depleted under reverse bias (b).

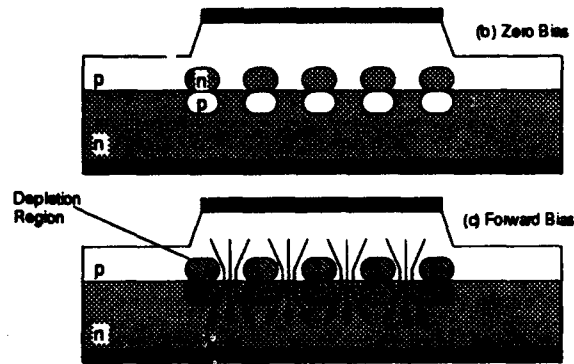


Fig. 4. P-n junction injection mode switch under zero and forward bias.

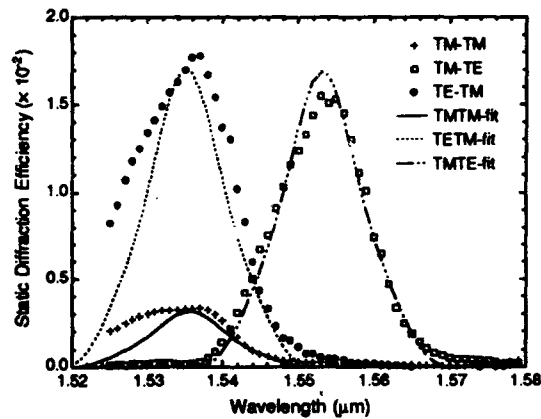


Fig. 6. Measured static diffraction efficiency vs. wavelength with theoretical fit.⁶

References

- 1 R. C. Alferness, IEEE J. Sel. Comm. 6, 1117 (1988).
- 2 P.J. Duthie, M.J. Wale, I Bennion, Electron. Lett. 27, 14 (1991).
- 3 L. B. Aronson and L. Hesselink, Opt. Lett., vol. 15, pp. 30-32, 1990.
- 4 E. M. Strzelecki, J. Chen, and F. Lin, Opt. Lett., vol. 15, pp. 1482-1484, 1990.
- 5 X. Cheng, and C. S. Tsai, J. Lightwave Technol., vol. 6, pp. 809-817, 1988.
- 6 L. B. Aronson, L. Hesselink, Paper on diffraction efficiency analysis in preparation.
- 7 E. H. Anderson, C. M. Horowitz and H. I. Smith, Appl. Phys. Lett. 43, 874 (1983).

High-Sensitivity InGaAs Photoreceiver Arrays in GaAs Waveguide*

T. Q. Vu and C. S. Tsai
Department of Electrical and Computer Engineering and
Institute for Surface and Interface Science
University of California, Irvine
Irvine, CA 92717

Integration of optoelectronic devices in a common waveguide substrate will result in superior device modules for applications in optical communication systems operating in the 1.3 - 1.5 μm wavelength region because of the significant improvements in speed, noise performance, and reliability via reduction of parasitic reactances associated with hybrid interface of individual devices. Arrays of photoreceivers are also needed for systems such as optical cross-point switches for telecommunications,^[1] and analog switching applications such as CATV or for optical interconnects between very large scale integrated circuits.^[2] A number of InP-based single-element waveguide photodetectors^[3] have been reported in recent years. Reports of their GaAs counterparts have been scarce.^[4,5] Furthermore, arrays of waveguide photoreceivers are yet to be realized in GaAs. In this paper we report the realization of a 45-element photoreceiver array in a GaAs waveguide for use at 1.3 μm optical wavelength. The photoreceiver array that utilizes InGaAs photoconductors and passive load resistors has demonstrated important advantages such as large gain-bandwidth product, high degree of compactness, and simple processing requirements. The total active area of the photoreceiver arrays was as small as $0.45 \times 0.25 \text{ mm}^2$. A unique feature of these photodetector and photoreceiver is their very high gain (or sensitivity) at frequency up to 1 MHz which also makes the photoreceiver array an ideal candidate for integration with guided-wave acoustooptic signal processors^[6] in which the integration of more than a few tens of photodetectors with switching bandwidths in the order of 3 MHz on a single integrated circuits has thus far presented difficult problems due to thermal and chip area considerations.^[7]

The optical waveguide used to fabricate the photoreceiver array consists of 1.1 μm GaAs layer on 2.0 μm $\text{Ga}_{0.85}\text{Al}_{0.15}\text{As}$ layer grown by MOCVD on top of a semi-insulating (SI)-GaAs substrate. An absorbing layer 0.3 μm thick with the indium concentration graded from 0 to 53% and followed by a 0.2 μm thick InGaAs layer with 53% indium concentration was subsequently grown by MBE. The absorption coefficient (α) of the InGaAs layer was measured at 1.3 μm to be 460 cm^{-1} (0.2 dB/ μm) by transmission characterization of light through the samples with and without the InGaAs layer. This data suggest that a photodetector as short as 50 μm in the InGaAs layer would absorb 90% of the guided light. Note that this length is only one half of the shortest detector reported^[5] heretofore.

The transimpedance amplification of a photoconductor can be realized by simply connecting in series the photodetector with a matching load resistor of the same resistance value

* This work was supported in part by the UC MICRO project, Amerasia Technology, Inc., and Statek Corp.

for maximum power detection. It is most convenient to use the same photodetector structure for the load resistance by ensuring that no light can reach it. We have realized a 45-element waveguide photoreceiver array using the structure with resistive load. The architecture of photoreceiver array is shown in Fig. 1. The fabrication process involved requires five masks, two metalizations, and two dielectric depositions. The photodetector and the load resistor each consists of $7.5 \times 50 \mu\text{m}^2$ InGaAs mesa and $150 \mu\text{m}$ separation between the two. The $2.5 \mu\text{m}$ wide metal contacts lie on top of the InGaAs mesa with $2.5 \mu\text{m}$ separation between the anode and cathode contacts. The center to center separation between adjacent photoreceiver elements was set at $10 \mu\text{m}$, thus the smallest dimension involved was $2.5 \mu\text{m}$.

Measurements of the photoreceiver array were carried out by both normal incidence and waveguiding using the $1.3 \mu\text{m}$ laser light. The normal incidence measurements have allowed us to calibrate the photovoltage response with the optical power absorbed. Note that the metal 2 layer was designed such that it blocked all the light from reaching the load resistors to ensure that the resistor would be purely passive. Figure 2 shows the photovoltage response of one photoreceiver element with the light incidence from the waveguide. A power dependency of the photovoltage over optical power with a slope of 0.72 on the log-log plot at low optical power was measured. At optical power higher than 300 nW , the slope of the curve was lowered to 0.39. The saturation effect of the photoreceiver as shown in Fig.2 was not observed in our earlier work on photodetector array^[4] due to of the lack of laser source of higher power. Figure 2 shows a dynamic range of more than 35 dB at 1 KHz modulation frequency and a photoresponse as high as 45 to 480 V/mw at $1\mu\text{W}$ to 1nW optical power, respectively. The frequency dependence of the photoresponse at the optical power of $1.0 \mu\text{W}$ is plotted in Fig.3. The frequency response of the photoreceiver is seen to follow approximately an ideal low-pass filter with -20 dB/decade in the slope of the high frequency roll-off, and the photovoltage response at 1GHz is extrapolated to be as high as 45 and 480 V/watt at $1\mu\text{W}$ and 1nW optical power, respectively.

The response of the photoreceiver array was rather uniform, namely, with less than 12.% variation across the whole 45 elements. The electrical cross-talk between the detector elements was measured to be lower than -40 dB by injecting a small-signal current source at one receiver element and measuring the signal output from the other receiver elements. Further amplification of the output signal from the photoreceiver array can be accomplished by using external or monolithically integrated operational amplifier circuits. The detailed fabrication procedures and measured performances of the photoreceiver array will be presented.

REFERENCES

- 1) Y. Liu, S. R. Forrest, G. L. Tangonan, R. A. Jullens, R. Y. Loo, V. L. Jones, D. Persechini, J. L. Pikulski, and M. M. Johnson, "Very-high-bandwidth $\text{In}_{0.53}\text{Ga}_{0.47}\text{As}$ p-i-n detector array," *IEEE Photonic Tech. Lett.* 3, 931(1991).
- 2) M. Kobayashi, M. Yamada, Y. Yamada, A. Mimemo, and H. Terui, "Guided wave optical chip-to-chip interconnections," *Electron. Lett.* 23, 143(1987).
- 3) S Chandrasekhar, J. C. Cambell, A. G. Dentai, and G. J. Qua, "Monolithic integrated waveguide photodetector," *Electron. Lett.* 23, 501(1987); R. Trommer, "Monolithic InGaAs photodiode array illuminated through an integrated waveguide," *Electron. Lett.* 21, 382(1985); P. Cinguino, F. Genova, C. Rigo, C. Cacciatore, and A. Stano, "Monolithic integrated

InGaAs/InP ridge waveguide photodiodes for 1.55 μ m operation grown by molecular beam epitaxy," *Appl. Phys. Lett.* **50**, 1515(1987).

4) T. Q. Vu, C. S. Tsai, and Y. C. Kao, "Integration of curved hybrid waveguide lens and photodetector array in a GaAs waveguide," *Appl. Opt.* **31**, 5246(1992).

5) C. Jagannath, A. Silletti, A.N.M.M. Choudhury, B. Elman, and P. Melman, "1.3 μ m monolithically integrated waveguide-interdigitated metal-semiconductor-metal photodetector on a GaAs substrate," *Appl. Phys. Lett.* **56**, 1892(1990).; F. Mallecot, J. F. Vinchant, M. Razeghi, D. Vandermoere, J. P. Vilcot, and D. Decoster, "Monolithic integration of a short-length GaInAs photoconductor with a GaAs/GaAlAs optical waveguide on a GaAs semi-insulating substrate," *Appl. Phys. Lett.* **53**, 2522(1988).

6) See, for example:

(a) *Guided-Wave Acousto-Optics - Interaction, Devices and Applications*, ed. by C. S. Tsai, Springer Series in Electronics and Photonics 23, Springer-Verlag Berlin-Heidelberg, 1990.

(b) Y. Abdelrazek, C.S. Tsai, and T.Q. Vu, "An integrated optic rf spectrum analyzer in a ZnO-GaAs-AlGaAs waveguide," *IEEE J. Lightwave Tech.* **LT-8**, 1833(1990)

7) R. J. Inkol, W. D. Washkurak, and S. G. Chamberlain, "A photodetector array for acousto-optic signal processors," *Can. J. Phys.* **67**, 400(1989).

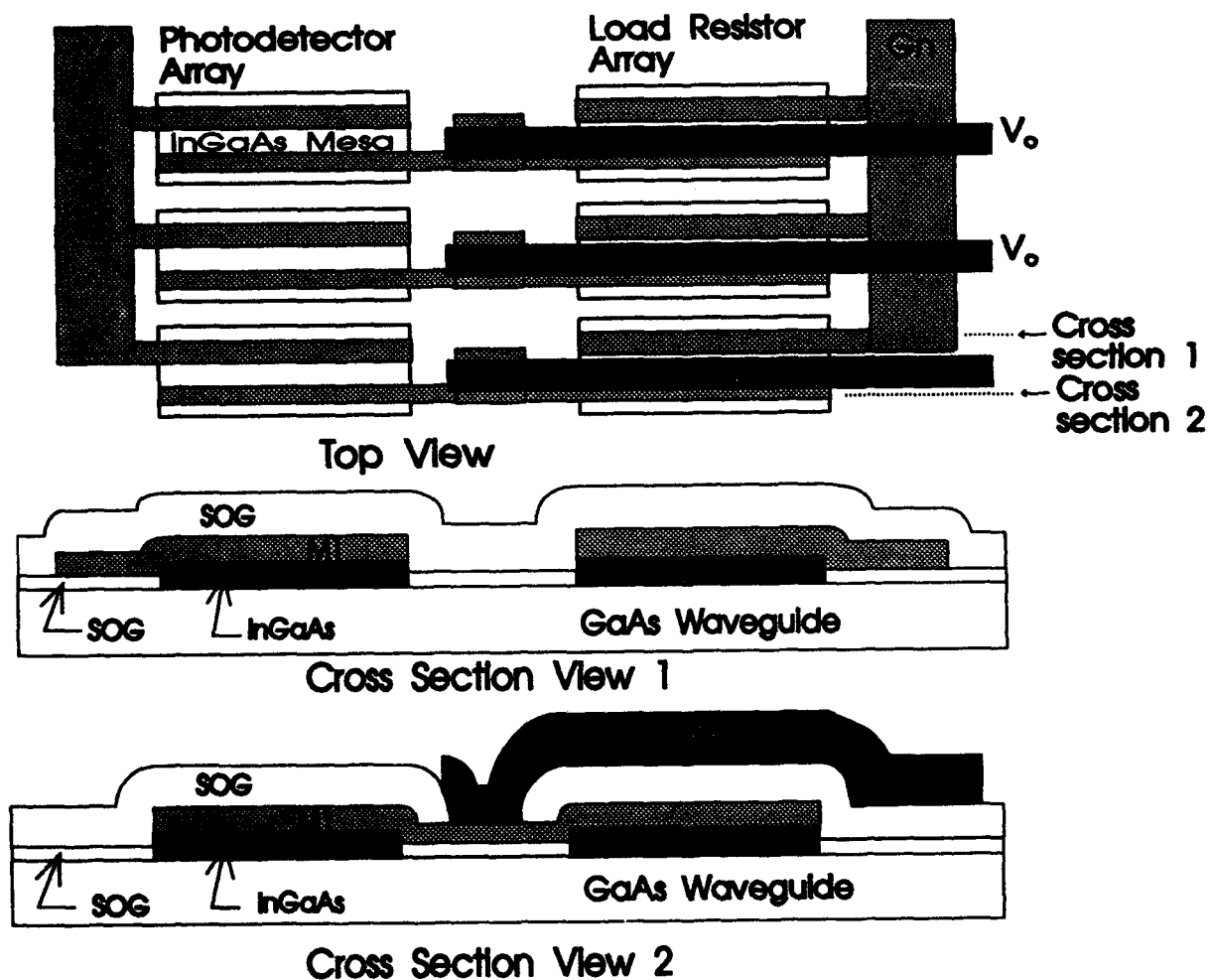


Fig.1 Architecture of Photoreceiver Array

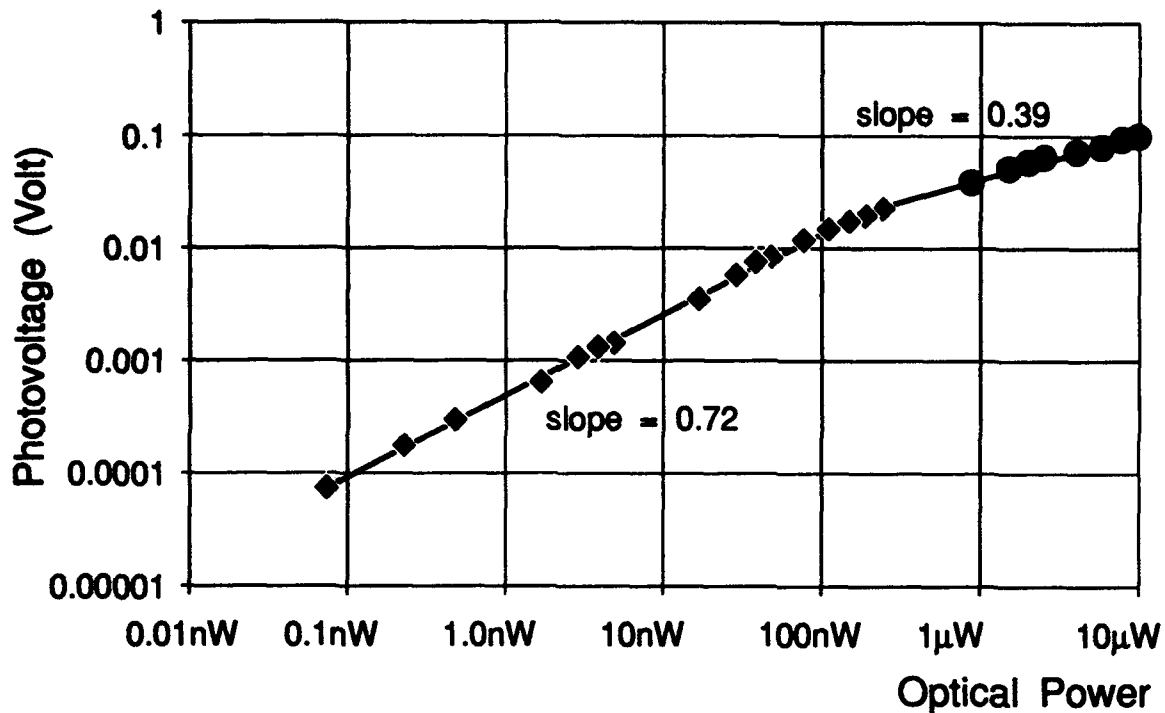


Fig.2 Photovoltage Response of Photoreceiver Element at 1.0 KHz Modulation Frequency

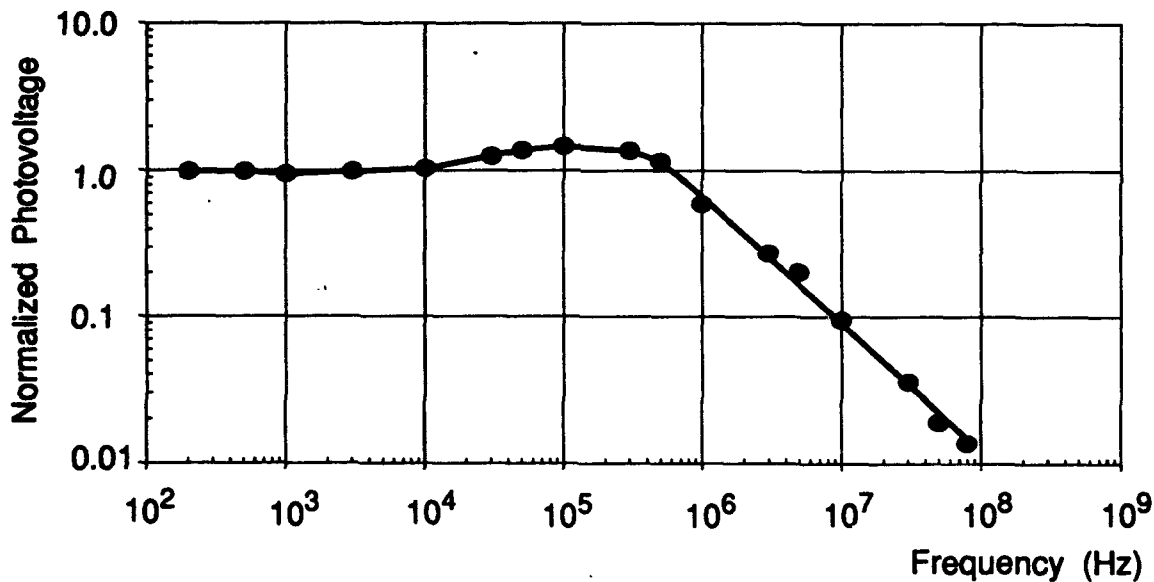


Fig.3 Frequency Photoresponse to Sinusoidal-Wave Modulated Light of The Photoreceiver Array

Low Threshold 45° Folded Cavity Surface Emitting Lasers for OEIC's

N. C. Frateschi and P. Daniel Dapkus
National Center for Integrated Photonic Technology
Department of Electrical Engineering
University of Southern California
Los Angeles, CA 90089-0483
Phone (213) 740-4414, Fax (213) 740-8684

S. S. Ou, J. J. Yang and M. Jansen
TRW, Research Center, Space and Technology Group
One Space Park
Redondo Beach, CA 90278

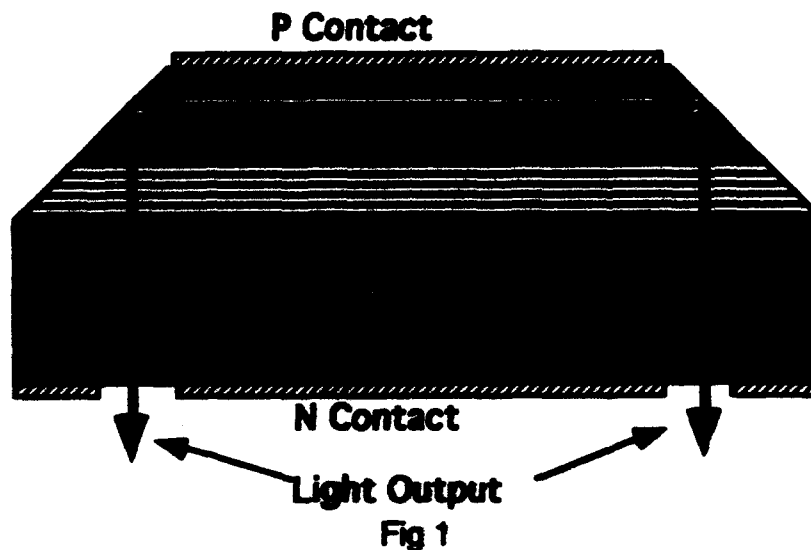
Surface emitting lasers are important elements in optoelectronic integrated circuits and in smart pixel arrays. In these applications, low threshold and high wall plug efficiency are desired since high density packing of such devices is desired. Conventional vertical cavity lasers have been demonstrated that exhibit threshold current below 1 mA. However, stringent growth and processing requirements, maximum output power limitations, and low wall plug efficiency are serious limitations of these devices. Furthermore, the device concept is not easily used in either long or short wavelength lasers where high index of refraction difference dielectric layers are not easily integrated into the cavity.

In this paper, we discuss the design and fabrication of surface emitting lasers based upon an alternate fabrication approach. The device concept is based on a conventional edge emitting geometry into which 45° mirrors are etched to deflect the light perpendicular to the cavity. Integration of high reflectivity cavity mirrors is thus accomplished by deflecting the light to Bragg reflectors incorporated into the epitaxial structure as shown in Fig. 1. In this way an integrated cavity structure is formed in which many of the constraints of vertical cavity device are relaxed. The need for exceedingly high reflectance mirrors is reduced because the gain path is increased. This also reduces the severe constraints on layer thickness control to achieve phase matching at the correct wavelength. Finally, since lower reflectance mirrors and a lower Q cavity can be used, losses in the mirrors due to doping are also reduced. All of these factors improve the producibility and characteristics of the lasers.

The key issue in the design of a high performance laser becomes the coupling between the Bragg mirrors and the waveguide mode and the quality of the 45° reflector. We describe in this talk the performance of, as yet unoptimized AlGaAs/GaAs/InGaAs surface emitting, folded cavity lasers emitting at 0.99 μm . These devices incorporate the Bragg reflector into the epitaxial design by growing the reflector on the substrate, etching the resultant substrate/reflector to produce mesas over which GRINSCH QW laser structures are grown by MOCVD using the temperature engineered growth (TEG) technique. 45° mirrors are then etched into the resultant buried heterostructure cavity to form the integrated structure. Arrays of vertical emitting devices have been fabricated with two integrated mirrors that exhibit thresholds as low as 8 mA and CW output

powers of 20 mW for a $3\mu\text{m}$ wide active stripe. An optimized geometry is expected to have thresholds near 1 mA.

The key issue in the optimization of these devices is to improve the coupling between the Bragg mirror and the cavity mode. We will present the results of analysis of the modal properties of Bragg confinement structures that are expected to minimize the coupling losses between the two sets of mirrors and thus lower the efficiency. We will also present the most recent results in our efforts to realize these structures.



Optically-Activated Integrated Optic Directional-Coupler Modulator Using GaAs Ridge Waveguide

Z. Y. Ren, C. S. Tsai, and T. Q. Vu

Department of Electrical and Computer Engineering and Institute for Surface
and Interface Sciences, University of California, Irvine, California 92717

Phone: (714) 856-5144

Fax: (714) 856-4152

Optically-generated free carriers can cause significant changes in the refractive index and the absorption coefficient of semiconductors. Optical switching and modulation that utilize injection of such free carriers were demonstrated previously in Si [1][2] and GaAs[3]. Most recently, an integrated optic Mach-Zehnder interferometer modulator that utilizes such optical activation in GaAs was reported by us[4]. In this paper, we report successful extension of this work toward the construction of an optically-activated integrated optic directional-coupler modulator using GaAs ridge waveguides.

Fig.1 shows the schematic and dimensions of such optically-activated directional-coupler modulator. A single-mode channel waveguide directional coupler was fabricated in a double-epilayer structure with an undoped-GaAs layer at the top. The directional coupler was in the form of a ridge waveguide structure. In order to increase the phase mismatch between the two arms of the directional coupler, one arm was covered with a Cr film. An anti-reflective ZnO film (about 4000 Å thick) was deposited between the GaAs guiding layer and the Cr film to minimize the propagation loss of the signal light.

In the experiment, a signal beam at the wavelength of 1.15 μm was edge-coupled into one arm of the directional coupler. A pin hole aperture was used to pick up, one at a time, the two light spots appearing at the output edge of the directional coupler. The ratio of the output light powers from the two arms was measured to be $P_{01}/P_{02}=36/30=1.20$. Thus, the coupling coefficient of the directional coupler was calculated to be 0.24 mm⁻¹. Subsequently, either a CW He-Ne laser at the wavelength of 0.6328 μm or a CW Argon laser at the wavelength of 0.511 μm, which served as a modulating light beam, was focused upon the interaction region of the directional coupler. Fig.2 shows the resulting modulations in the signal light of the two output ports when the 0.511 μm modulating light beam was shined upon one of the channel

waveguides. It is seen that the changes in the intensity of the two output light are out of phase as expected. Also, as previously observed^[4], the effect of free carrier-induced absorption for the 1.15 μm signal light was found to be much weaker than the free carrier-induced refractive index change in this particular experiment. When the modulating light intensity was increased, the signal light intensity from one arm (P_{01}) was increased, while the signal light intensity from the other arm (P_{02}) was decreased. The highest depth of modulation ($\Delta P_{02}/P_{02}$) in P_{02} was as high as 65% at the modulating light power of 100 W/cm^2 . The corresponding free carrier concentration (δN) and refractive index change (δn) were estimated to be $1.2 \times 10^{17} [\text{cm}^{-3}]$ and 2.8×10^{-4} . For the experiment with the modulating light at 0.6328 μm , the modulation depths in both arms were found to be nearly identical for the modulating light power up to 10 W/cm^2 . Thus, we conclude that the free carrier-induced absorption was too weak to be detected for the range of modulating light intensity used in the second experiment. For the available intensity of modulating light, namely 10 W/cm^2 , the modulation depth was measured to be 6%. The corresponding free carrier concentration (δN) and refractive index change (δn) were estimated to be $2.5 \times 10^{16} [\text{cm}^{-3}]$ and 6.0×10^{-5} , respectively.

In conclusion, we have designed and constructed an integrated optic ridge waveguide structure to study optically-activated directional coupling effect in GaAs. Free carrier-induced refractive index changes was found to be the main cause of this effect. In this paper, the design, fabrication, and measured results of the preliminary device described above are presented. The experimental results for devices of improved design aimed at higher modulation depth and switching speed measurement will also be reported.

References

- [1] P.D. Colbourne and P.E. Jessop, 'Recovery time for a silicon waveguide all-optical switch', *Electron Lett.* **24**, 303 (1988).
- [2] R.Normandin, 'All-optical fiber-optic modulator and logic gate using nonlinear refraction absorption', *Optics Lett.* **11**, 751(1986).
- [3] G.McWright, B.Ross, W.Guthreau, D. Lafaw, M.Lowry, and W.Tindal, 'All-optical modulation in Gallium Arsenide integrated optical waveguides', *SPIE* **1038**, 454 (1989).
- [4] Z.Y. Cheng and C.S. Tsai, 'Optically activated integrated optic Mach-Zehnder interferometer on GaAs', *Appl. Phys. Lett.* **59**, 2222 (1991).

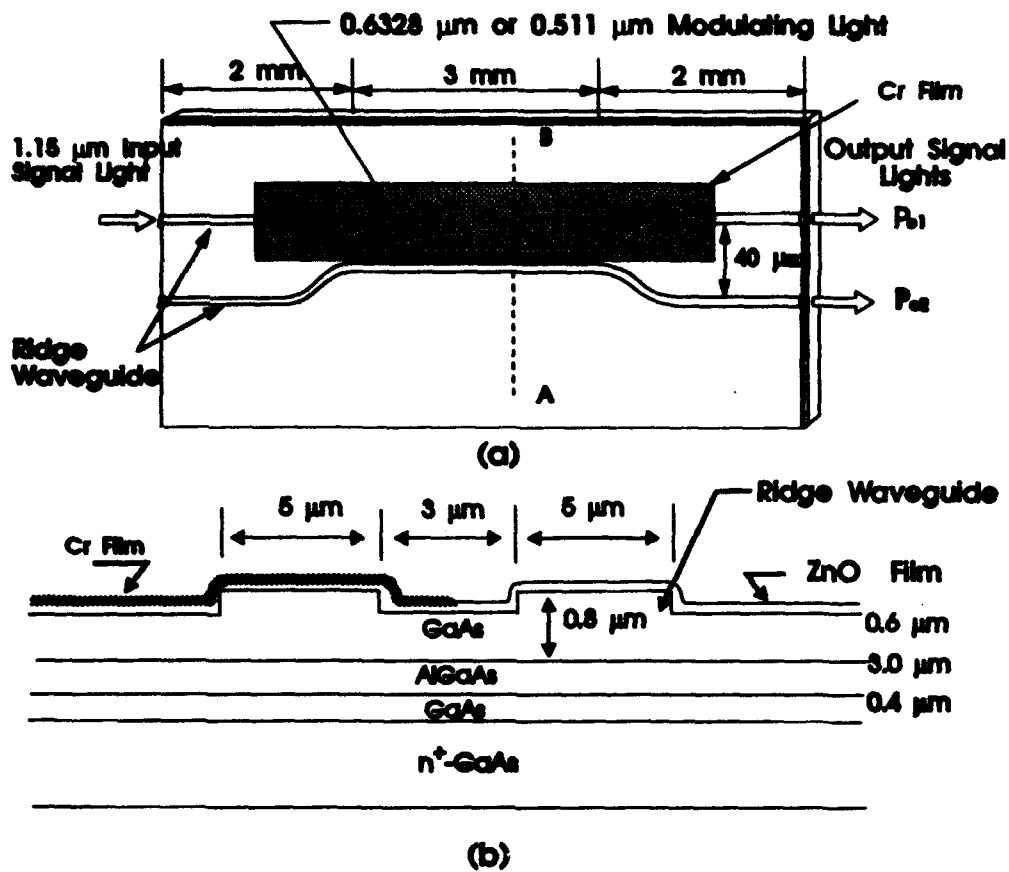


Fig.1 Schematic of the Optically-Activated Directional Coupler Modulator : (a) Top View, and (b) Cross-Sectional View.

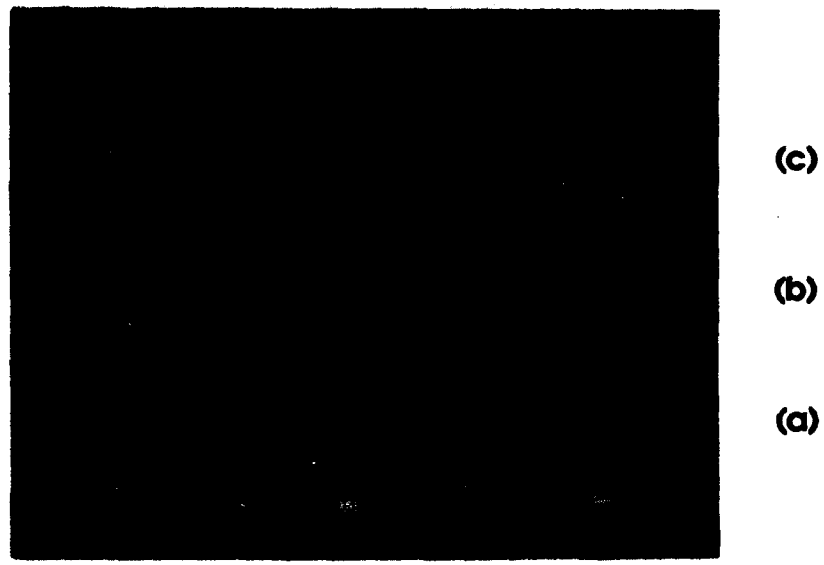


Fig.2 Waveforms of the 1.15 μm Signal Light from Channel P₀₂(Trace a), Channel P₀₁(Trace b), and the 0.511 μm Modulating Light(Trace c).

Carrier Heating Effects on High Frequency Conversion in Semiconductor Laser Devices

G. P. Bava (1) P. Debernardi (2) and M. Tonetti (1),
 (1) Dip. di Elettronica, (2) Cespa-CNR, Politecnico di Torino,
 Corso Duca degli Abruzzi, 24 12129, TORINO, ITALY
 Tel. 011/5644063, Fax 011/5644089

Several papers have recently reported experimental results concerning optical frequency conversion with very large frequency spacing (hundreds of gigahertz) and high efficiency [1,2]. The explanation of such phenomena requires some very fast nonlinearity in the material. Several authors have invoked hot carrier effects to explain ultrafast refractive index dynamics in semiconductor lasers [3, 4, 5].

A model has been developed in order to analyze frequency mixing in semiconductor laser devices under multicarrier injection, by exploiting the nonlinearity due to carrier density and temperature pulsations at the beat frequency. As regards the electron and hole heating, the model includes:

- stimulated and spontaneous recombinations,
- effects of free carrier absorption (through an upper valley in the conduction band, and through a simple plasma model for electrons and holes),
- electron and hole capture in the active layer of the heterostructure,
- carrier cooling by means of thermal coupling with LO-phonons.

The nonlinear behaviour is represented by a contribution to the dielectric constant $\Delta\epsilon_{\Omega}$, oscillating at the beat angular frequency Ω ; it is written as follows:

$$\Delta\epsilon_{\Omega} = M \sum_i E_i^* E_{i+1}$$

where E_i are the electric field of the optical signals. The quantity M is obtained from the contribution $\Delta\epsilon(N, T_e, T_h)$ to the dielectric constant due to the carrier-field interaction that is evaluated from a microscopic model based on the density matrix formalism [6], including the dependence on the carrier density N and the electron and hole effective temperatures T_e and T_h . The connection between M and $\Delta\epsilon_\Omega$ is as follows:

$$\Delta\epsilon_\Omega = M \sum_i E_i^* E_{i+1} = \frac{\partial\Delta\epsilon}{\partial N} N_\Omega + \frac{\partial\Delta\epsilon}{\partial T_e} T_{\Omega,e} + \frac{\partial\Delta\epsilon}{\partial T_h} T_{\Omega,h}$$

since $\sum_i E_i^* E_{i+1}$ appears as a common factor (at least at the first order of perturbation) both in N_Ω and $T_{\Omega,e}$, $T_{\Omega,h}$; these are, respectively, the components of N, T_e, T_h fluctuating at the angular beat frequency Ω .

An example of the behaviour of $\Delta\epsilon_\Omega$ as a function of frequency spacing is shown in Fig. 1 for a quaternary alloy InGaAsP, for a typical choice of the parameters involved in the model. Both the global result and the separate contributions of carrier density and electron and hole temperature fluctuations are reported. It appears clearly that for small frequency spacing, carrier fluctuations represent, as well known, the dominant effect. At increasing Ω the less efficient, but faster carrier heating phenomena, become more and more important.

The preceding material model has been introduced in a coupled mode formalism in order to study frequency mixing in a guided wave device. The model applies to both travelling wave amplifiers and Fabry-Perot or Distributed Feedback oscillators, depending on the boundary conditions. In the first case the problem of intermodulation distortion appears [1], while the second is concerned with frequency conversion, the same device operating as pump and frequency converter [2].

A computer code has been implemented for the numerical integration of the coupled mode equations in devices of different types and using different materials (GaAlAs, InGaAsP). An example of results concerning a travelling wave amplifier, for the same working condition of Fig. 1 is shown in Figs 2 and 3, where the behaviour of the structure with an input constituted of two equal lines is shown. The output powers associated to the two central lines (f2 and f3) and the two adjacent lines (f1 and f4) generated by the non-linear interaction are represented as a function of the frequency spacing between f2 and f3. Fig.2 is concerned with the region of large frequency spacing (>10 GHz), where the carrier temperature effects are dominant [1], while in Fig.3 the low frequency range (<10 GHz) is shown. These results agree satisfactorily with those of the literature in the region of small beat frequency (<10 GHz) [7]; in the case of highly nondegenerate four wave mixing, the results show a behaviour very similar to the experimental data found in [1, 2].

This work was performed with support of Progetto Finalizzato Telecomunicazioni and Progetto Strategico Reti di Comunicazioni All-Optical (Italian CNR), Camera di Commercio (Torino) and Ministry of the University and of Scientific and Technological Research (40% activity).

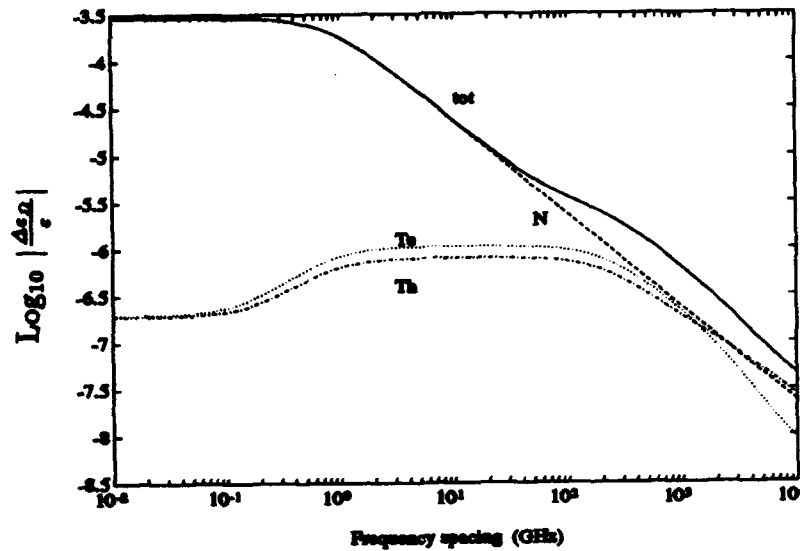


Figure 1: Frequency response of $\Delta\epsilon_n/\epsilon$ for $\sum_{i=1}^4 E_i^* E_{i+1}$ corresponding to a power density of $1 \text{ mW}/\mu\text{m}^2$. It has been computed for a quaternary material, carrier density $N = 3 \cdot 10^{18} \text{ cm}^{-3}$, $\lambda = 1.568 \mu\text{m}$.

References

- [1] L. F. Tiemeijer, *App. Phys. Lett.*, 59, 1991, p. 499
- [2] S. Murata, A. Tomita, J. Shimizu, A. Suzuki, *IEEE Trans. Phot. Tech. Lett.*, 3, 1991, p. 1021
- [3] A. P. DeFonzo, B. Gomatam, *Appl. Phys. Lett.*, 56, 1990, p. 611
- [4] B. Gomatam, A. P. DeFonzo, *IEEE J. QE*, 26, 1990, p. 1689
- [5] C. T. Hultgren, E. P. Hippen, *Appl. Phys. Lett.*, 59, 1991, p. 635
- [6] M. Asada, A. Kameyama and Y. Suematsu, *IEEE J. QE*, 20, 1984, p. 754
- [7] T. Mukai, T. Saitoh, *Sixteen ICQE*, Tokyo, 1988, paper WD-1.

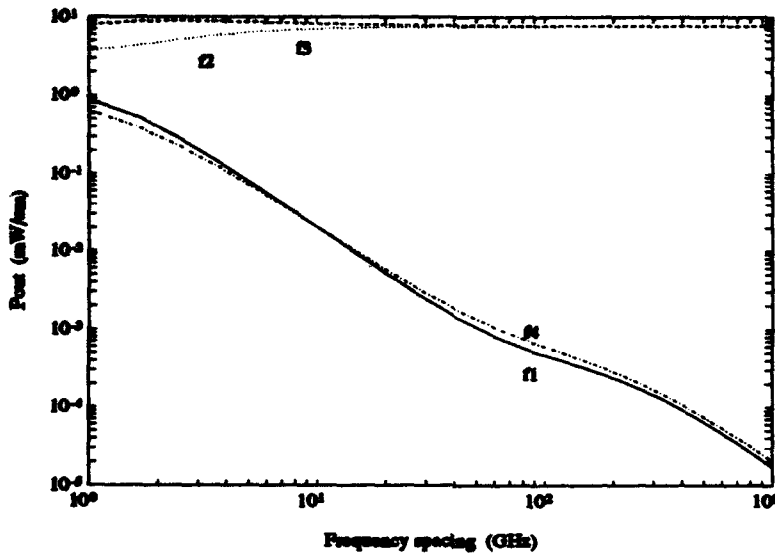


Figure 2: Output powers in a travelling wave amplifier in a quaternary structure (planar waveguide). The two input lines (f2 and f3) have equal powers of $66 \text{ mW}/\mu\text{m}$, the device length is $500 \mu\text{m}$, carrier density is $2.0 \cdot 10^{18} \text{ cm}^{-3}$, which corresponds to a linear gain of 30 dB.

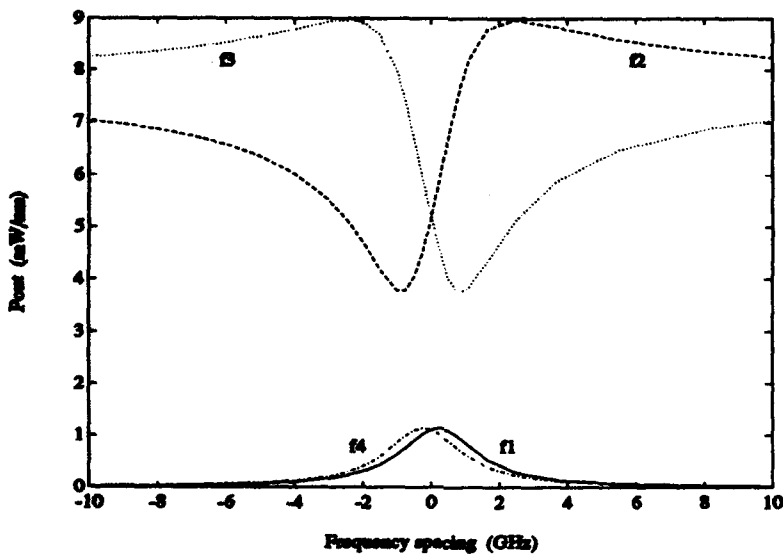


Figure 3: Same as Fig.2.

SINGLE - BEAM FORMATION OF HOLOGRAPHIC DIFFRACTIVE
GRATINGS WITH ARBITRARY PERIODS AT PHOTOREFRACTIVE
PARAMETRIC INTERACTION IN PLANAR WAVEGUIDES ON
LITHIUM NIOBATE

V. Shandarov, S. Shandarov

Institute of Automatic Control Systems and Radioelectronics
40 Lenin Avenue, TOMSK 634050, Russia,

Phone: 007-(3822)-496278, Fax: 007-(3822)-496495.

Optical waves of different kinds, particularly waveguide, radiated and leaky modes can exist in anisotropic optical waveguides. It allows to realize in similar waveguides some nonlinear four - wave processes, where several waves of different kinds can take part. Recently the parametric photorefractive interaction of leaky and radiated modes in $\text{LiNbO}_3:\text{Ti}:\text{Fe}$ waveguide was observed, where the holographic gratings with periods depending on the crystal optical anisotropy appeared at the single input light beam [1,2]. It is of great interest to use this effect for formation of holographic dynamic or stationary gratings with arbitrary periods, which can be used as passive or operating elements in integrated - optical devices. Several results demonstrating such possibility are presented in this report.

1. Conditions of experiments.

Optical waveguides were formed on substrates of Y - cut LiNbO_3 by the serial diffusion of titanium and iron in the air atmosphere. For different substrates an angle between the optical axis of the crystal and the optical wave propagation direction in waveguides was changed from 20° up to 70° . An extraordinarily polarized light beam of a He - Ne laser was

reflected from the waveguide surface inside the substrate and went out it trough the polished lateral side. The parametric scattering pictures and the intensity distribution between output ordinary, extraordinary and generated parametric beams were studied visually on the screen and with a photocamera or photoreceiver outside the substrate.

2. Experimental results.

It is well known that the four - wave interactions are observed at the satisfaction of the following condition:

$$2\bar{k}_1 - \bar{k}_2 - \bar{k}_3 = 0, \quad (1)$$

where \bar{k}_1 - wave vectors of interacting waves. In our case \bar{k}_1 is the projection of an extraordinary beam wave vector on the waveguide surface, \bar{k}_2 , \bar{k}_3 - wave vectors of leaky waves generated in waveguide due to the parametric interaction process (Fig. 1).

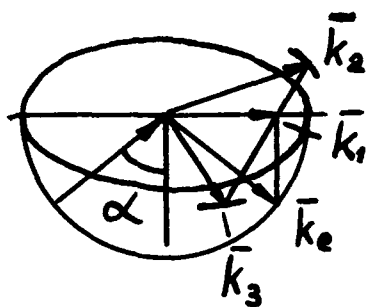


Fig. 1.

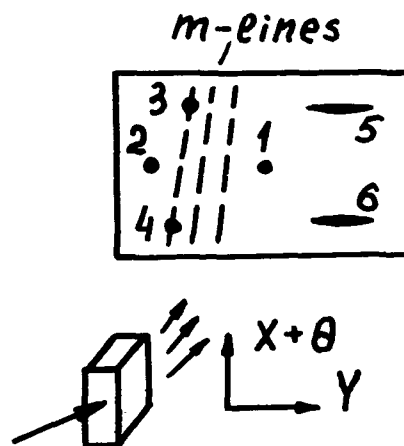


Fig. 2. The intensity distribution picture on the screen.

In experiments the appearance and development of parametric maxima, corresponding to the highest TE - leaky

modes, with propagation directions corresponding to the condition (1) satisfaction, were observed. The instance of an entire picture of the light intensity distribution on the screen is presented on the fig.2. Here the spots 1,2 correspond to the reflected extraordinary and appearing at its reflection an ordinary light beams. The spots 3,4 correspond to the energy of parametrically generated leaky waves radiated from the waveguide as ordinarily polarised light beams. Some part of their energy is radiated from the waveguide edge giving the maxima 5,6. At the laser beam power of about 10 mW and for its aperture of 1 mm the development of parametrical processes took about 10 - 15 minutes. The time dependences of parametric maxima intensity for the different waveguide samples, light beam incidence angles and the inciding light intensity were studied. Because the Fe average concentration for the highest waveguide modes was not very large, the storage time of parametrically generated gratings made up some days. It should be noted, that the relative intensity of such maxima could obtain up to 10% of the input extraordinary light beam intensity.

The next interpretation of this effect is proposed. An interference of inciding and reflected extraordinary waves may be considered as propagation in waveguide region of an extraordinary inhomogeneous wave with the propagation constant $\beta = k_0 n_e \cdot \sin(\alpha)$, where n_e - the refractive index of an extraordinary wave in the waveguide region; α - an angle of its incidence at the waveguide surface. Because of the inciding wave scattering at the waveguide volume and surface perturbations there are very many weak secondary light waves in waveguide belonging to different waveguide modes and propagating into the wide spatial angle. A photorefractive interaction of inhomogeneous extraordinary and scattered secondary waves of different modes leads to an appearance of

"noisy" photorefractive gratings from which by means of the parametric amplification the gratings corresponding to the condition (1) satisfaction are developed.

In conclusion it should be noted the single - beam formation of periodic structures in photorefractive waveguides promises some advantages for the diffractive waveguide elements creation due to its simplicity and possibilities to form some dynamic as well as stationary elements. The possibility of photorefractive impurity concentration changing allows to provide the different characteristics of such separate elements on the ground of the same substrate due to the local doping of some its area with different impurities or with different conditions of technological processes.

R E F E R E N C E S

1. V.M.Shandarov. Photorefractive parametric interaction of volume and leaky optical waves in planar waveguide on lithium niobate. In: Proc.of Top. Meet. on Photorefractive Materials, Effects and Devices. 1991, USA.
2. A.D.Novikov, S.G.Odoulou, V.M.Shandarov, E.S.Shandarov, S.M.Shandarov. Parametric intermode scattering in planar LiNbO_3 waveguides. J.Opt.Soc.Am. B/Vol.8, No.6/June 1991, pp. 1298 - 1303.

**COMPARISON OF FINITE DIFFERENCE AND SPECTRAL INDEX METHODS
FOR ANALYZING SEMICONDUCTOR WAVEGUIDES INCORPORATING
REGIONS OF OPTICAL LOSS OR GAIN.**

S.V.Burke,
Department of Physics and Astronomy,
University of Wales College of Cardiff,
5 The Parade,
Newport Road,
Cardiff CF2 3YB, UK.

T.M.Benson,R.J.Bozeat,M.A.Matin.
Department of Electrical and Electronic Engineering,
University of Nottingham,
University Park,
Nottingham NG7 2RD, UK.

Semiconductor waveguides are widely used in the field of integrated optics as the basis of active and passive devices. Since no analytical solution to the wave equation is available for rib, ridge or strip loaded structures many modelling techniques have been developed to analyze the guiding properties of these structures. These methods vary considerably in accuracy and ease of application. This paper considers two of these analysis methods, the Finite Difference (FD) Method and the Spectral Index (SI) Method, and notes that both approaches can be extended for use in the complex case ie when the local refractive index of the waveguide cross-section may become complex due to the presence of loss or gain. This gives rise to a complex propagation constant. Complex propagation constants obtained from the FD and SI methods are compared for the first time.

The Finite Difference Method is an accurate, versatile and rigorous numerical approach which has been applied to the study of waveguide structures of arbitrary cross-sectional profile. The original scalar finite difference method has undergone several recent developments. Semi-vectorial finite difference methods find solutions to the wave equation for the dominant electric [1] or magnetic [2] field component of a TE-like or TM-like polarised wave and build the discontinuity of the field component considered into the difference equations. Results compare favourably with benchmark Vector Finite Element results [3] for a range of waveguiding structures. Recently the method of false position [4,5,6] was applied to the FD method to simplify the treatment of the semiconductor-air interface such that no mesh points are required in the air region. This considerably reduces memory requirements and computational time [7]. Further, a new correction formula enables the propagation constants of both TE-like and TM-like modes to be accurately obtained from a single scalar solution [8].

The main features of the semi-analytical Spectral Index Method [5,6] can conveniently be introduced by considering a rib waveguide. The method of false position is used to simplify the semiconductor/air interface and the field set to zero on the repositioned boundary. Separate exact solutions to the governing scalar wave equation are obtained for the regions

in and below the rib. These are matched using a variational boundary condition which leads to a transcendental equation for the propagation constant. For many semiconductor waveguides the refractive index in the region below the rib varies in the vertical direction only. By working in the spectral domain the problem is reduced to a one-dimensional one in this region. This means that the SI Method is considerably faster than a full scale numerical method such as FD. The accuracy of the SI Method has previously been established for rib and ridge waveguides with real refractive indices [5,6] and symmetric and asymmetric couplers [9-11].

Oksanen and Lindell [12] recently noted that the stationary points of the real and imaginary parts of a complex functional coincide. A consequence of this is that both FD and SI Methods can be generalised to the complex case in a straightforward way. In the FD method the local refractive index of each mesh point and the propagation constant are defined as complex quantities. In the SI method each real refractive index is allowed to become complex and this produces a complex transcendental equation for the complex propagation constant with the same form as in the real case.

The complex SI and FD Methods are used to study the scalar mode propagation characteristics of the structures shown in Figures 1 and 2. The structure of Figure 1 represents a semiconductor laser with a thin active region. Figure 3(a),(b) presents the real and imaginary parts of modal index (B/k_0) calculated for this structure, as a function of H , at a wavelength of $1.5 \mu\text{m}$. The real and imaginary parts of the modal indices predicted by the FD and SI Methods are consistent across the whole range of H values used. Results obtained using a complex Effective Index (EI) Method [13] are also given in Figure 3 for comparison. As the thickness H is decreased the effective rib discontinuity is increased and this causes the EI method to become inaccurate. It will be shown in our presentation that this inaccuracy extends to predictions of the laser far field pattern.

In a practical laser structure it is likely that current will be injected from a contact placed over a limited area of the laser surface, say at the top of the rib. This will give a localised region of gain within the active region, the exact nature and extent of which will be determined by the carrier diffusion equations. Whilst the FD method is able to deal with an arbitrary refractive index distribution across the laser cross-section the SI method assumes a layered refractive index distribution in the region under the rib. SI analysis must rely on a perturbation analysis for structures where this is not the case. We will show results in our presentation to show that such a perturbation approach is accurate for most modern laser structures in which index guiding dominates gain guiding [14].

The structure of Figure 2 is a TE/TM mode splitter of current practical interest [15]. This consists of two guides fabricated in close proximity. The guide on the left is clad with a metal layer. The problem resembles that of an asymmetric coupler. When evaluating supermode propagation constants and field profiles the FD difference method usually takes advantage of symmetry conditions so that only half of the waveguide cross-section need be considered. The asymmetric problem cannot be partitioned in such a simple manner and a recent "equipartition" methodology [16] must be adopted. However although this method confirms SI results it requires several single rib calculations to determine supermode propagation

constants and construct the supermode fields. The SI Method is able to find these supermode fields and propagation constants quickly and efficiently and provides a much more practical design tool than the FD Method for this class of problem.

CONCLUSIONS

We compare, for the first time, Finite Difference and Spectral Index analysis of optical waveguides containing regions with optical loss or gain. The two methods produce consistent results for a range of test configurations. In our talk we will demonstrate that the two methods complement each other since each is best suited to a different type of problem. The FD Method is able to deal with arbitrary refractive index profiles directly which makes it ideally suited for laser studies. The SI Method provides a much more practical design tool for the TE/TM mode splitter.

REFERENCES

1. STERN M.S.: IEE Proc. J, 1988, 135, pp 56-63.
2. STERN M.S.: IEE Proc. J, 1988, 135, pp 333-338.
3. RAHMAN B.M.A., DAVIES J.B.: IEEE Trans., MTT-32, 1984, pp 922-928.
4. ADAMS M.J.: "An Introduction to Optical Waveguides", Wiley, 1981.
5. ROBSON P.N., KENDALL P.C. (eds): "Rib Waveguide Theory by the Spectral Index Method" Research Studies Press and Wiley, 1990.
6. McILROY P.W.A., STERN M.S., KENDALL P.C.: IEEE J. Lightwave Technol., 1990, LT-8, pp 113-117.
7. BENSON T.M., KENDALL P.C., MATIN M.A.: Elec.Lett.,1992, 29, pp 1897-1898.
8. BENSON T.M., KENDALL P.C., MATIN M.A., STERN M.S.: IEE Proc. J, 1991, 139, pp 39-41.
9. BURKE S.V.: Elect. Lett., 1989, 25, pp 605-606.
10. BURKE S.V.: IEE Proc. J, 1990, 137, pp 7-10.
11. BURKE S.V.: IEE Proc. J, 1990, 137, pp 289-292.
12. OKSANEN M.I., LINDELL I.V.: IEE Proc. H, 1989, 136, pp 281-288.
13. KNOX R.M., TOULIOS P.P.: Proc. MRI Symp. Submillimeter Waves, (New York), 1970, pp 497-516.
14. AGRAWAL G.P., DUTTA N.K.: "Long Wavelength Semiconductor Lasers" , van Nostrand, 1986.
15. ALBREICHT M., HAMACHER M., HEIDRICH H., HOFFMANN D., NOLTING H-P, WEINERT C.M.:IEEE Phot. Tech Lett., 1990, 2, pp 114-115.
16. BENSON T.M., KENDALL P.C.: To appear in IEE Proc. J, 1992.

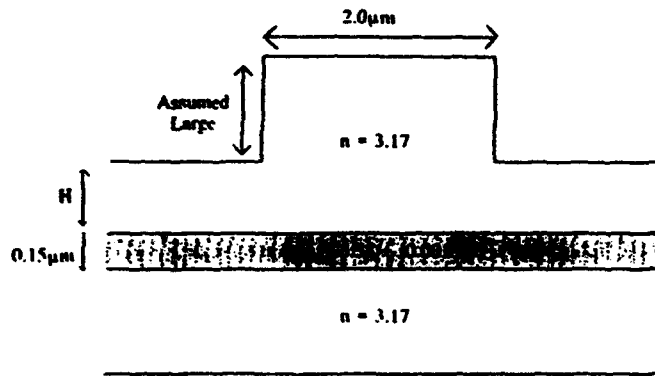


Figure 1. The laser test structure.

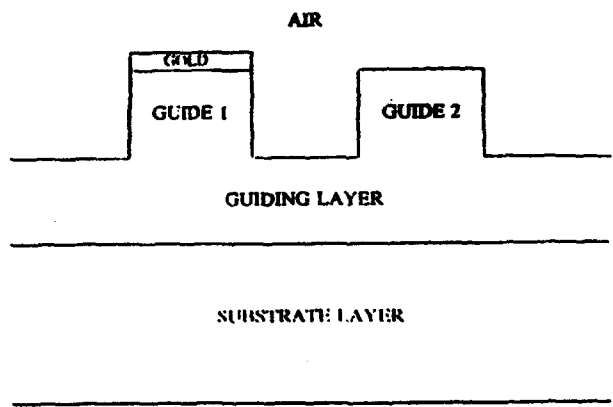


Figure 2. TE/TM mode splitter.

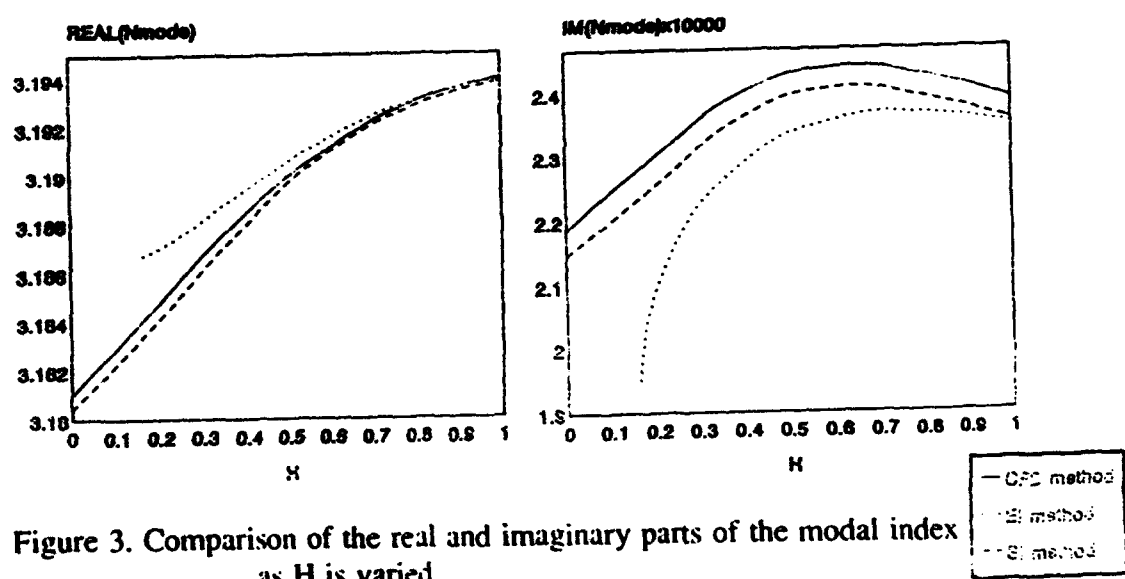


Figure 3. Comparison of the real and imaginary parts of the modal index as H is varied.

The Importance of Including Non-Bound Fields in Eigenmode Expansions

R. E. Smith and S. N. Houde-Walter

The Institute of Optics University of Rochester
Rochester NY, 14627. (716)-275-7629

Many devices have been demonstrated that are not accurately modeled by using only bound eigenmodes. The role of the non-bound fields in these models can go beyond simply representing radiative losses, for example: coherent superposition of radiation modes can produce slowly decaying behavior,[1] radiation modes can be excited and then coupled back into the device,[2] inclusion of radiation modes can be critical for accurate calculations of power in absorbing structures,[3] and radiation modes can influence the calculation of reflection at interfaces. Consequently, there has been an increased interest in eigenmode expansion techniques that include these radiation fields. The two most popular means of appending the radiation field to the bound waveguide mode expansion are the improper "leaky" mode technique[1] and the sampling of the radiation field by means of an imposed boundary (such as a metal wall).[2]

To understand the applicability of "leaky" mode technique consider the structure shown in Fig. 1a. Here a bound mode is used to excite a leaky structure of length L , which in turn excites a third structure supporting a single bound mode. The plot Fig. 1b shows the power transferred from the input mode to the output mode as a function of L . The result predicted by the "leaky" mode and that predicted by metal box technique are seen to be equivalent (better than 0.01%). That the complex leaky solution to the dispersion relation is an accurate representation in this regime can be understood by examining the excitation of the radiation modes as a function of β , the propagation constant. The simple Lorentzian dependence on β reveals the Fourier relationship between the excitation and resulting exponential decay.[4,5]

As an example of a system that is poorly modeled by leaky modes consider the structure in Fig. 2a.[3] When this structure is modeled using only bound modes, power is not conserved across the interface. The plot in Fig. 2b shows the total forward going power as a function of the distance into the detector region. The excitation of the radiation modes is shown in (Fig. 2c). The absence of the Lorentzian form for the excitation suggests that the radiation field would not be modeled well with an exponentially decaying leaky mode. Note that, though in this case power

conservation identified the error introduced by retaining only bound modes in the expansion, power conservation is an inadequate criterion, as is evident if the imaginary part of the index in the absorber layer is taken to be -0.1113 rather than 0.1552 . In this pathological case, although power is conserved across the interface, the fields and the power elsewhere in the waveguide are incorrectly predicted by the bound mode model. In addition to power conservation we suggest a measure of discontinuity of the fields across the interface. For example, discontinuity in the TE electric field might be written as,

$$C_E = \int |E^i + E^r - E^t|^2 dx / \int |E^i|^2 dx, \text{ Eq. 1}$$

where E^i , E^r , and E^t are the incident, reflected and transmitted electric fields respectively. The quantity C_E should be zero. If it becomes significantly larger than zero the expansion must be considered incomplete, or in some other way inaccurate. C_E for the two structures mentioned above can be seen in Table 1. Here the large C_E identifies the error in both structures, whereas power conservation would not.

The two guides shown in Fig. 1a and 2a, represent two regimes. The first is an example of the "tight resonance" regime, characterized by frustrated total internal reflection. In this regime the coherent excitation of radiation modes exhibit a slow exponential decay. Therefore the device is well modeled by using a leaky mode. Further, in this same regime, the slow transverse divergence of the leaky field makes the calculation insensitive to the arbitrary normalization which must be imposed when leaky fields are used. Note that as

Im[n ₂]	Basis	(P _r + P _t)/P _i	C _E
0.1552	Bound	3.5911	2.2805
	Complete	1.003	0.0007
0.1113	Bound	1.002	0.8620
	Complete	1.003	0.0006

Table 1

the resonance becomes tighter, the leaky mode approximation will become more accurate, while the metal box technique becomes more cumbersome, as a progressively larger box is required for accurate sampling. As such, in the tight resonance case the leaky mode approach is preferable since it allows the use of a single mode to represent what would otherwise require many sampled radiation modes. Further, leaky modes do not suffer from the artifactual reflection off of the imposed metal wall.

In the second example radiation modes are important for accurate modeling of device absorption. Here, the weak resonances of modes beyond cutoff are best modeled by using a discrete sampling of the radiation spectrum, such as that obtained by using a metal box. This sampling method is likely to be the more flexible of the two techniques owing to the various

difficulties associated with the divergent, non-orthogonal, leaky modes.

References

1. K. Thyagarajan, S. D. Seshadri, and A.K Ghatak, *J. of Light.Tech.* 9 (1991).
2. H.-P. Nolting,, *IPR Tech. Dig.*10,130(1992).
3. E.C.M Pennings, R.J. Deri, and R.J.Hawkins, *IPR Tech. Dig.* 10,82 (1992).
4. A. W. Snyder and J. D. Love, *Optical Waveguide Theory*, Chapman and Hall(1983).
5. A. K. Ghatak, *Opt. and Quant. Electronics* 17 311 (1985).

Acknowledgments

This work was supported by a National Science Foundation graduate fellowship, the 3M company, and the ARO University Research Initiative.

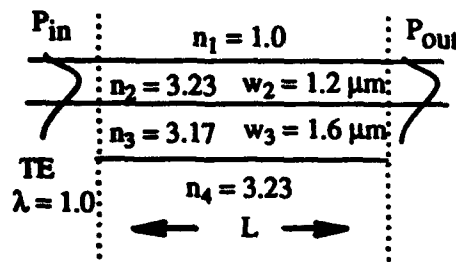


Fig. 1a

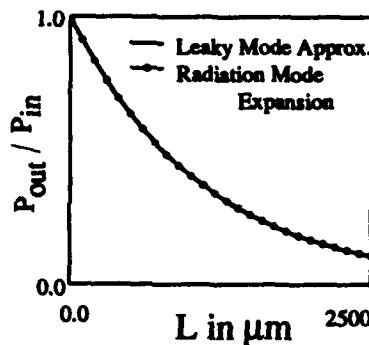


Fig. 1b

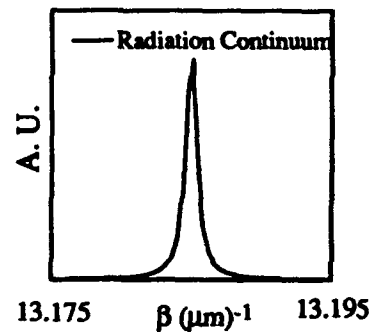


Fig. 1c

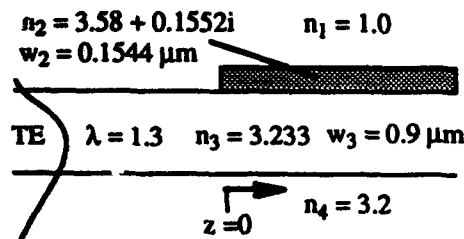


Fig. 2a

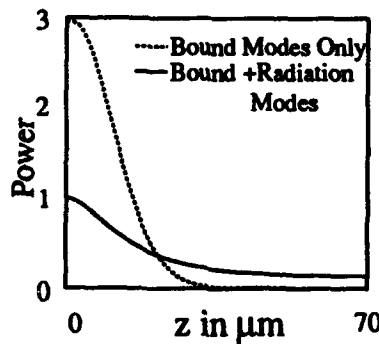


Fig. 2b

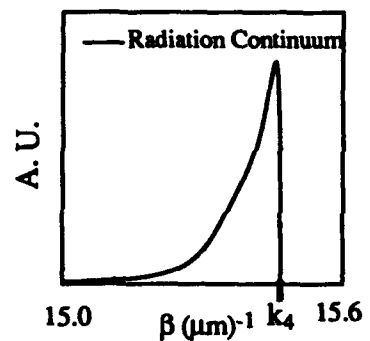


Fig. 2c

The Method of Lines with Improved Special Absorbing Boundary Conditions

Dennis Kremer and Reinhold Pregla

Allgemeine und Theoretische Elektrotechnik

FernUniversität

Postfach 940, D-5800 Hagen, Germany

(Phone: +49 2371 566 255 FAX: +49 2371 51898)

Introduction

In the integrated optics electromagnetic field problems have to be solved with numerical methods, where the structure has to be surrounded by a box of metallic or magnetic walls, whereby box modes can occur and complicate the numerical evaluation. Because these boundaries must not have any influence on the field distribution, the distance between the walls must be chosen very large, especially in case of a structure with a weak confinement. For such a structure the numerical effort is high. In [1] we could demonstrate that these disadvantages can be vanquished by introduction of special absorbing boundary conditions (SABC) in the method of lines (MoL) for the analysis of slab waveguides. Now we will present improved SABC for the analysis of single or coupled channel waveguides and we will elucidate the advantages in relation to the hitherto used Dirichlet and Neumann boundary conditions.

Theory

For the analysis with the MoL [2] we consider a ridge waveguide as demonstrated in Fig. 1. The potentials ψ_e and ψ_h have to fulfill the Helmholtz equation and the Sturm-Liouville equation. In the regions at the top and at the bottom the local wave equations are factorized [3] under utilization of the fact, that the waves are supposed to fulfill the Sommerfeld's radiation condition [4] at the boundary. After discretization of the wave equations and of the boundary conditions we express the potentials ψ_0 and ψ_{N+1} on the boundary through potentials inside the computation window. We obtain the expressions

$$\begin{aligned}\psi_{h,0} &= -a_1\psi_1 + b_1\psi_2 + c_1\psi_3 \\ \psi_{h,N+1} &= -a_b\psi_N + b_b\psi_{N-1} + c_b\psi_{N-2}\end{aligned}$$

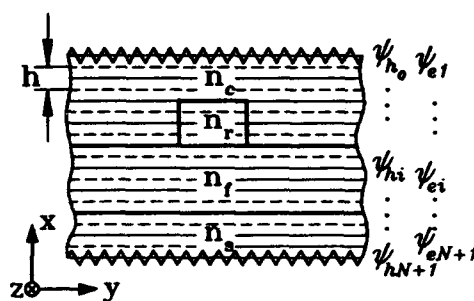


Fig. 1: Computation window

Results

For the example of the weakly guiding rib waveguide, which is shown in Fig. 2, we will exhibit the advantages of the introduction of the SABC opposed to the hitherto used metallic or magnetic walls. The fact that the SABC can be positioned very near to the film is illustrated in Fig. 3 and Fig. 4, where the normalized phase parameter B is presented versus the distance d between the film and the wall in the substrate for the HE_{00} - and EH_{00} - mode. The field distributions in the symmetry plane of the rib waveguide are illustrated in Fig. 5 for the EH_{00} - mode for metallic walls respectively

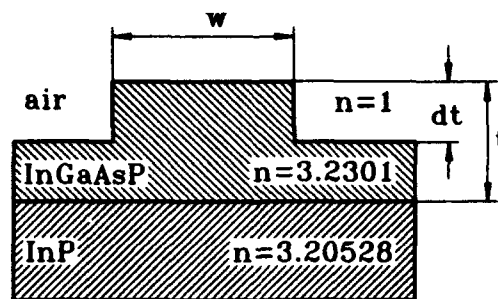


Fig. 2: Rib waveguide with $dt = 0.3\mu\text{m}$, $t = 1.3\mu\text{m}$, $w = 2.0\mu\text{m}$, $\lambda = 1.286\mu\text{m}$

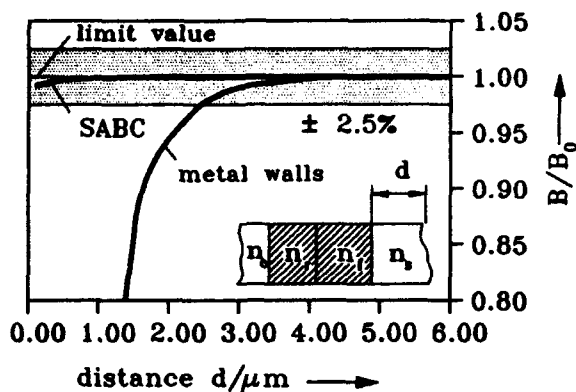


Fig. 3: Convergence behavior of the phase parameter B for the HE_{00} - mode with $B_0 = 0.18006416$
 $B = (n_{eff}^2 - n_s^2)/(n_f^2 - n_s^2)$

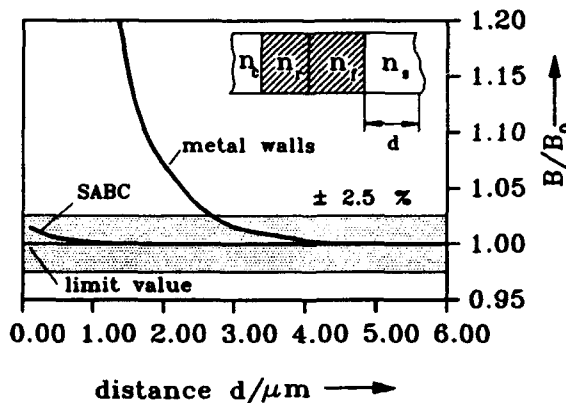


Fig. 4: Convergence behavior of the phase parameter B for the EH_{00} - mode with $B_0 = 0.14628822$

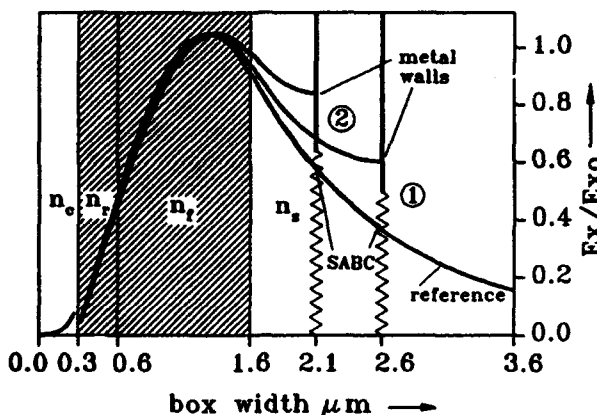


Fig. 5: Normalized x component of the electric field for SABC and metallic walls at the positions 1 and 2

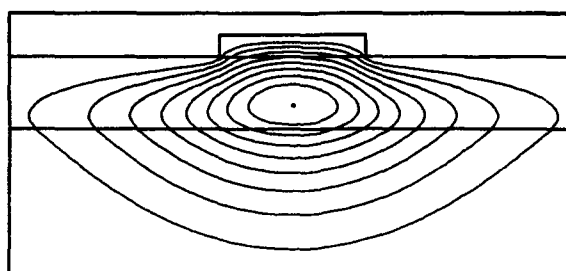


Fig. 6: Reference contour plot of the x component of the electric field for metallic walls for $d = 6\mu\text{m}$.

SABC at the positions 1 and 2. Here we can see that for SABC already at the position 2, where the SABC is very close to the film, the field distribution agrees very good with the reference distribution, whereas for the metallic walls the disturbance is substantial at the

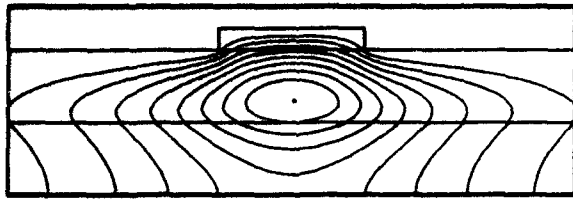


Fig. 7: Contour plot of the x component of the electric field for metallic walls for $d = 1 \mu\text{m}$.

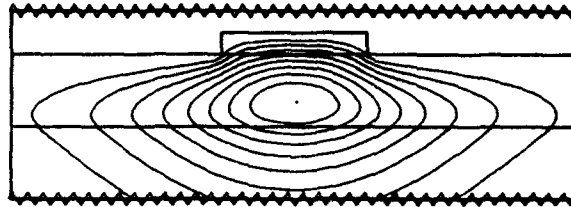


Fig. 8: Contour plot of the x component of the electric field for SABC for $d = 1 \mu\text{m}$.

position 2. Only for very far distances between the metallic wall and the film the deviation from the reference distribution will be smaller. Adequate strong disturbances of the field distributions will be obtained by using magnetic walls. The reference distribution was obtained by using a metal wall in a distance of $d = 6 \mu\text{m}$ from the film. Fig. 6 shows the contour plot of the field distribution for the reference case. Fig. 7 and Fig. 8 illustrate the contour plots for the wall position 2 for metallic walls respectively SABC for the distance $d = 1 \mu\text{m}$. Fig. 7 clearly shows that the field distribution is strongly disturbed by the metallic wall, whereas in case of the SABC in Fig. 8 the field distribution is identical with the reference distribution in Fig. 6.

Conclusion

The introduction of the special absorbing boundary conditions in the method of lines is very advantageous because the SABC can be placed closer to the guiding structure, whereby the discretized area and the corresponding matrices become smaller. With the SABC we simulate an infinite computation window at the place where they are introduced and box modes, which complicate the numerical evaluation, don't occur.

These advantages can be favourable utilized for the analysis of optical structures with metal. At the conference, first results from the analysis of an optical TE/TM mode splitter with the MoL and SABC will be presented.

References

- [1] R. Pregla and D. Kremer, "Method of Lines with Special Absorbing Boundary Conditions - Analysis of Weakly Guiding Optical Structures", *IEEE Microwave and Guided Wave Lett.*, Vol. 2, No. 6, pp. 239-241, June 1992.
- [2] R. Pregla and W. Pascher, "The Method of Lines," in T. Itoh, (editor), *Numerical Techniques for Microwave and Millimeter Wave Passive Structures*, pp. 381-446, J. Wiley Publ., New York, 1989.
- [3] T. G. Moore, J. G. Blaschak, A. Taflove, G. A. Kriegsmann, "Theory and Application of Radiation Boundary Operators", *IEEE Trans. Antennas Propagat.*, AP-36, pp. 1797-1812, Dec. 1988.
- [4] A. Sommerfeld, *Partial Differential Equations in Physics*. Academic Press, New York, 1967.
- [5] U. Rogge and R. Pregla, "Method of Lines for the Analysis of Strip-Loaded Optical Waveguides", *J. Opt. Soc. Am. B*, 8, pp. 459-463, 1991.

Novel Kind of Waveguide Modes in Anisotropic Structures

L. Torner, C. Ojeda and C. Santos
Polytechnic University of Catalonia
Department of Signal Theory and Communications
P.O. Box 30002, 08080 Barcelona, Spain
Fax: (34) 3 4017232
Tel: (34) 3 4016527

Our goal in this paper is to point out that ultrathin optical films bounded by low-loss birefringent materials allow an additional type of guided waves that has not been noticed early. For illustrative purposes, we pay attention here to a film of thickness D of an isotropic material with refractive index n_f , surrounded by an isotropic material with refractive index n_c and a positive birefringent crystal, whose ordinary and extraordinary refractive indices are n_{os} and n_{es} . The optical axis of the crystal is assumed to lie on the guide plane, forming an angle θ with the waveguide axis, which corresponds to off-axis propagation in an X or Y -cut sample. With the exception of on-axis propagation configurations, waves guided by such an structure are of the hybrid type, with the six field components.

Integrated optical technology typically employs materials for which $n_{es} > n_{os} > n_c$. Nevertheless, our aim here is to point out that when the involved materials verify $n_{es} > n_c > n_{os}$, the resulting structures allow existence of guided waves for waveguide parameters below usual cutoff. Above cutoff these waves become the well-known hybrid guided modes [1], and for $D/\lambda \rightarrow 0$, with λ being the wavelength of the used radiation,

they become the surface waves guided by the interface between the dielectric materials forming the substrate and the cover, which have been pointed out by Dyakonov [2].

The effective index N of the allowed stationary guided modes is obtained as roots of the eigenvalue equation verifying $N > n_c$, $N > n_{os}$ and $N > n_{es}(\theta)$, with $n_{es}(\theta)$ being the refractive index for the extraordinary wave propagating in an unbounded crystal. When $n_{es} > n_{os} > n_c$, guided propagation requires $N > n_{es}(\theta)$, hence existence of guided modes is governed by the extraordinary-cutoff for radiation to the substrate. Usual waveguide modes fulfill this requirement, but there is a cutoff thickness (in units of λ) for the guided waves to be allowed. In the case $n_{es} > n_c > n_{os}$, guided solutions occur above both the extraordinary-cutoff to the substrate and the usual cutoff for radiation to the cover, thus guided propagation requires $N > n_{es}(\theta)$ and $N > n_c$. The point is that such kind of guided waves exist for any value of the ratio D/λ , provided that a suitable orientation of the crystal optical axis is taken. This is true even for $D/\lambda = 0$, then the waves being guided by the cover-substrate dielectric interface.

Figure 1 shows the allowed values of the optical axis orientation for the guided waves to exist, as a function of the ratio D/λ . In our calculations we take the parameters of a glass film ($n \simeq 1.57$), deposited over a crystal quartz substrate ($n_o \simeq 1.544$, $n_e \simeq 1.553$), with a low-alkali, lime-alumina borosilicate ($n \simeq 1.548$) forming the cover, operating at $\lambda = 589.3$ nm. At $D/\lambda = 0$, the allowed angular interval is nearly centered at θ_0 , which is the orientation verifying $n_{es}(\theta_0) = n_c$. This interval is extremely narrow, $\Delta\theta \equiv \theta_{c2} - \theta_{c1} \simeq 2^\circ \times 10^{-3}$, although it increases fast with D/λ . As D/λ grows, $\theta_{c1} \rightarrow 0^\circ$ and $\theta_{c2} \rightarrow 90^\circ$, with the limiting values being reached at the cutoff point of the TE_0 wave taking place at these symmetric orientations. In Figure 2 we have plotted the effective index of the allowed hybrid guided wave as a function of the optical axis orientation, for a waveguide with $D/\lambda = 0.2$. Dashes indicate the cutoff lines $N = n_c$ and $N = n_{es}(\theta)$.

References

- [1] A. Knoesen, T. K. Gaylord and M. G. Moharam, "Hybrid Guided Modes in Uniaxial Dielectric Planar Waveguides," *J. Lightwave Technol.*, vol. LT-6, pp. 1083-1104, 1988.
- [2] M. I. D'yakonov, "New Type of Electromagnetic Wave Propagating at an Interface," *Sov. Phys. JETP*, vol. 67, pp. 714-716, 1988.

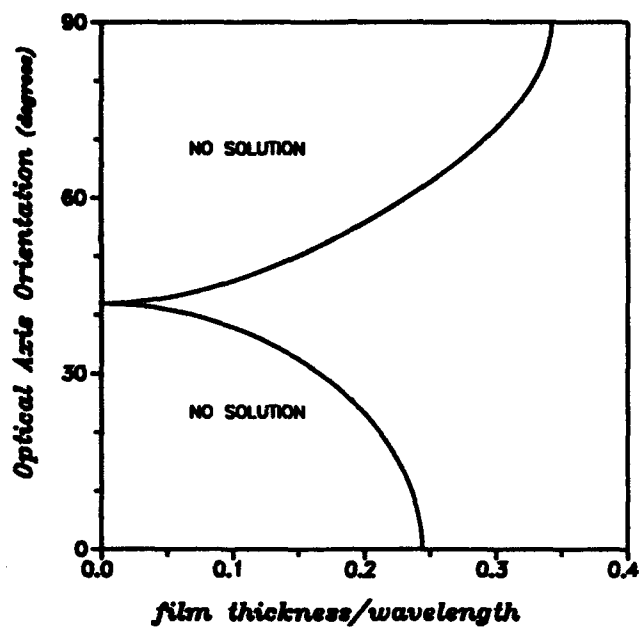


Figure 1: Allowed optical axis orientations for guided waves to exist.

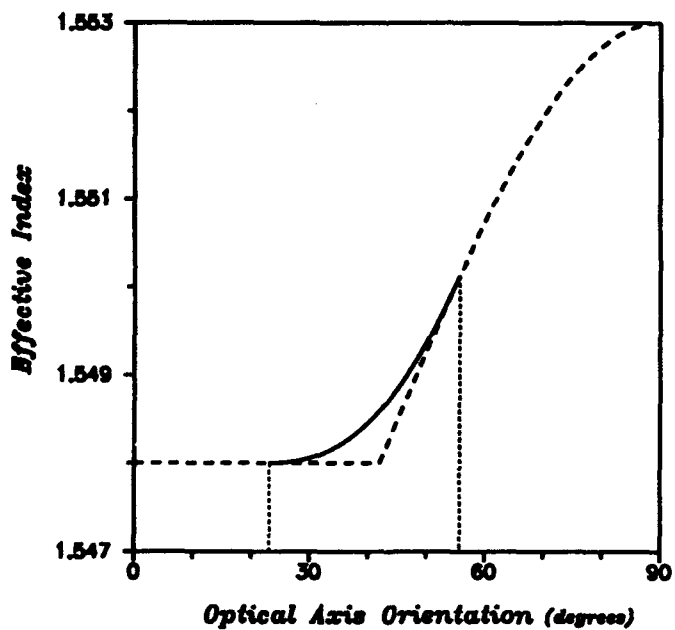


Figure 2: Effective index as a function of the optical axis orientation.

Stable long-distance pulse propagation in nonlinear optical fibers using periodically-spaced parametric amplifiers

J. Nathan Kutz and William L. Kath

Engineering Sciences and Applied Mathematics

Ruo-Ding Li and Prem Kumar

Electrical Engineering and Computer Science

McCormick School of Engineering and Applied Science

Northwestern University, 2145 Sheridan Rd., Evanston, IL 60208-3125

Phone: (708) 491-5585 Fax: (708) 491-2178

Parametric amplifiers have been proposed [1] as an alternative to lumped erbium-doped amplifiers for long-distance optical pulse propagation in fibers. While filtering techniques [2] have been demonstrated to suppress the bit-rate limitation caused by the Gordon-Haus jitter [3] — the random walk of solitons caused by spontaneous emission noise of the erbium amplifiers, or by initial fluctuations in the soliton parameters — a chain of lumped parametric amplifiers should have higher possible bit-rates because no such amplifier noise is present [1].

Here, we present a theoretical analysis of pulse evolution in a nonlinear optical fiber where loss is balanced by a chain of periodically-spaced phase-matched, degenerate parametric amplifiers. Such a system can be shown to be governed by the equation

$$\frac{\partial q}{\partial Z} = \frac{i}{2} \frac{\partial^2 q}{\partial T^2} + i|q|^2 q + \frac{1}{\epsilon} h\left(\frac{Z}{\epsilon}\right) q + \frac{1}{\epsilon} f\left(\frac{Z}{\epsilon}\right) q^*, \quad (1)$$

where $h(Z/\epsilon)$ and $f(Z/\epsilon)$ model both the uniform loss in the fiber and the optical phase-sensitive gain of the lumped parametric amplifiers. Furthermore, the amplifiers are modelled as periodically spaced delta functions in which the pump pulses are assumed to be much wider than the signal pulses and undepleted. As in the case of erbium-doped amplifiers [4], the length Z in equation (1) has been scaled on a typical soliton period Z_0 (e.g., 500 km for erbium amplifiers [5]); the amplifier spacing Z_l is assumed to be much shorter than this

length (e.g., 33 km [2]). Mathematically, we set $Z_l/Z_0 = \epsilon l$ where $\epsilon \ll 1$ and l is an $O(1)$ quantity.

We perform a multiple scale expansion in the fast length scale $\zeta = Z/\epsilon$, the soliton period Z , and the slow length scale $\xi = \epsilon Z$. This expansion is similar in spirit to the Lie transform method for the guiding-center soliton [4]. After a few amplifiers, the pulse locks onto and follows the phase of the amplifiers, i.e., $q = R(Z, \xi, T)e^{i\phi(Z)/2}$ (while the phase in quadrature to that of the amplifier decays exponentially with distance). Solvability conditions show that $\frac{\partial R}{\partial Z} = 0$; therefore, *unlike erbium-doped amplifiers* [4], *no evolution occurs on the scale of the soliton period Z_0* . In this case, evolution $R(\xi, T)$ occurs on the longer length scale ξ (e.g., 7500 km if the soliton period and amplifier spacing are as indicated above) due to amplification in one quadrature and attenuation in the other.

Higher order solvability gives the evolution equation

$$\begin{aligned} \frac{2}{l} \tanh(\Gamma l) \frac{\partial R}{\partial \xi} + \frac{1}{4} \frac{\partial^4 R}{\partial T^4} - \frac{\kappa}{2} \frac{\partial^2 R}{\partial T^2} + \left(\frac{\kappa^2}{4} + \Gamma_2 \right) R \\ - \beta_1 \kappa R^3 + \beta_2 R^5 + \beta_3 R \left(\frac{\partial R}{\partial T} \right)^2 + \beta_4 R^2 \frac{\partial^2 R}{\partial T^2} = 0, \end{aligned} \quad (2)$$

where $\phi(Z) \equiv \kappa Z$, the β_i 's depend on the parameters Γ and l , and Γ_2 is an $O(\epsilon^2)$ deviation from an exact balance between amplification and decay. As a preliminary investigation of pulse stability, we examine the above equation for small amplifier spacing l . Although this is perhaps somewhat unrealistic physically, it is mathematically convenient since simple solutions of (2) are known in closed form in this limit. We therefore expand $\Gamma_2 = \gamma_1 l + \gamma_2 l^2 + \dots$ and $R = R_0 + l R_1 + \dots$, collecting terms with equal powers of l to determine stability. The leading order steady-state problem has a hyperbolic secant solution of the form $R_0 = A \operatorname{sech} AT$ where $A = \kappa^2$. This agrees with what is expected physically as the amplifier spacing l approaches zero.

Second-order perturbation theory shows that $\gamma_1 = 0$ and that there is a critical value of the parameter γ_2 ($\gamma_c = -1.48A^4\Gamma^2$), above which pulse solutions are stable. Numerical analysis is in progress to determine the full range of stability for the nonlinear evolution equation. This preliminary analysis, however, strongly indicates that this equation will have stable, steady-state pulse solutions (in an appropriate parameter range), and that within the stability regime, initial pulses will *decay exponentially onto the stable solution* in an entirely local manner due to the diffusive nature of the envelope equation; this is in contrast with the stability of erbium-doped amplifier systems where steady-state soliton pulses are reached via the shedding of dispersive radiation.

This work was supported in part by the AFOSR, DARPA, NSF and ONR.

References

- [1] H. Yuen, *Opt. Lett.* **17** 73 (1992).
- [2] Y. Kodama and A. Hasegawa, *Opt. Lett.*, **17** 31 (1992); D. Marcuse, *Opt. Lett.*, **17** 34 (1992); L. F. Mollenauer *et al.*, *Electronic Letts.*, **28** 792 (1992).
- [3] J. P. Gordon and H. A. Haus, *Opt. Lett.*, **11** 665 (1986).
- [4] A. Hasegawa and Y. Kodama, *Opt. Lett.*, **15** 1443 (1990); *Phys. Rev. Lett.*, **66** 161 (1991).
- [5] L. F. Mollenauer, S. G. Evangelides and H. A. Haus, *J. Lightwave Tech.*, **9** 194 (1991).

**INVESTIGATION OF SINGLE-MODE STRUCTURES IN
HETEROSTRUCTURE AlGaAs/GaAs RIDGE WAVEGUIDES**

M. Nisa Khan and Anand Gopinath

**Department of Electrical Engineering
University of Minnesota
200 Union Street, SE
Minneapolis, MN 55455
(612) 625-3049**

Accurate single-mode waveguide geometry is determined for heterostructure ridge waveguides in AlGaAs/GaAs using a semivectorial finite difference technique. The results are compared with the effective index method.

Ridge waveguides are widely used in integrated optics and optoelectronic devices for their two-dimensional (2-D) mode confinement and simplicity of fabrication. For most applications, ridge waveguides are required to operate as single-mode guides and hence there is current interest in different modeling techniques to accurately design single-mode structures. Unlike circular waveguides with radial symmetry, for example optical fibers, where a single V parameter is sufficient to determine single-mode design, the effective cross-sectional waveguiding area of a ridge guide is usually asymmetrical about the lateral direction resulting in asymmetric modal field distributions about this direction. Thus, determination of accurate single-mode ridge waveguide geometry is not straight forward and requires the solution of the 2-D wave equation satisfying the boundary conditions.

In this paper, we use a semivectorial finite difference method (SFDM) to show that for a 3-layer double heterostructure ridge guide with a ridge width not too large compared to the wavelength of operation, operates initially as a multimode guide for small ridge heights. The guide becomes single-mode for a range of larger ridge heights, and then becomes multimode again with further increases in the ridge height, before becoming cutoff.

M. W. Austin [1] observed a similar behavior in 2-layer rib guides using the variational technique. He also demonstrated experimentally that the number of modes in such guides decreases with increasing rib height, and at some point the structures become single-mode and then cutoff with further increases in the rib height. In contrast, the waveguide in our investigation has both upper and lower cladding, and therefore, the optical confinement is able to increase within the ridge even when it is etched slightly beyond the guide layer. Hence, as the etch depth is increased beyond the single-mode range, the guide becomes multimode again before becoming cutoff. We also show that although the effective index method has been shown to produce modal refractive indices in good agreement with those from other more accurate methods, it fails to predict this single/multimode behavior of ridge guides.

The AlGaAs/GaAs ridge waveguide geometry which we investigate at $0.83 \mu\text{m}$ wavelength, is illustrated in Fig. 1. Such structures are often used in waveguide devices such as phase modulators, couplers, and interferometers to achieve high-speed and high modulation efficiency characteristics [2, 3]. The epitaxial layer design was optimized to achieve low loss at this wavelength and a propagation loss of only 1.0 dB/cm was measured for single-mode waveguides fabricated on gas-source MBE-grown wafers, despite the high aluminum concentration in the layers.

The SFDM technique, employing the closed boundary condition, is used to solve the guided modes and their field distributions in the ridge waveguide for various ridge heights H , and widths W . In this boundary condition approximation, the optical field is set to zero at the outer boundary of the finite difference grid box, which introduces a small error since the array size is large compared to the ridge width. A 22×22 array is used with x and y grid spacings of 0.20 and $0.16 \mu\text{m}$ respectively. The modal effective indices only decrease by ~ 0.0005 when the array size is increased to 44×44 with x and y grid spacings of 0.1 and $0.08 \mu\text{m}$ respectively. The single-mode ridge width, $W_s = 2.4 \mu\text{m}$, is first determined by analyzing structures of different ridge widths at the etch depth

of 1.44 μm . This depth is chosen to achieve appreciable confinement within the ridge itself by partially etching the guide layer.

In order to determine the range of etch depth for which the structure in Fig.1 is single-mode, H is varied from 0.16 to 1.92 μm in increments of 0.16 μm , keeping W fixed at 2.4 μm . A ridge waveguide structure with a small ridge height has a large effective cross-sectional waveguiding area that spreads out of the ridge in the lateral direction which can allow for several modes to propagate. As the ridge height is increased, the effective cross-sectional area gets smaller and becomes concentrated only under the ridge, allowing propagation of only the lowest order mode. If the ridge height is increased further by etching beyond the guide layer into the lower cladding, higher order modes are again allowed to propagate because confinement within the ridge becomes very strong. This behavior is observed from the SFDM calculations which is shown in Table I.

Table I: Modal Effective Indices of TE Modes Calculated Using SFDM

Ridge Height (μm)	$n_{\text{eff}0}$	$n_{\text{eff}1}$	$n_{\text{eff}2}$	$n_{\text{eff}3}$
0.16	3.433305270	3.428166166	3.421782336	-
0.32	3.433305274	3.428166172	3.421782336	-
0.48	3.433305286	3.428166190	3.421782336	-
0.64	3.433305326	3.428166255	3.421782341	-
0.80	3.433431055	3.429025538	3.424652759	3.419919928
0.96	3.433308903	3.428177538	3.421795846	-
1.12	3.432754158	3.426061451	3.418559717	-
1.28	3.432287881	3.423973807	-	-
1.44	3.431961705	3.422402783	-	-
1.60	3.427051201	-	-	-
1.76	3.431687575	3.421106434	-	-
1.92	3.431657687	3.420968863	-	-

These calculations indicate that the ridge structure is single-mode approximately in the range, $1.44 \mu\text{m} < H < 1.76 \mu\text{m}$. As H is increased beyond 1.60 μm , the ridge waveguide again becomes multimode due to higher mode confinement. The modal field distribution of the fundamental mode of the single-mode structure at $H = 1.60 \mu\text{m}$, is shown in Fig. 2. The field distributions for $H = 1.92 \mu\text{m}$, supporting two modes are shown in Figs. 3(a) and 3(b). If H becomes very large, the waveguide will eventually become cutoff because much of the optical energy will then be radiated in the etched region.

The effective index method (EIM), however, does not show this behavior because it is not valid for guides with strong mode confinement, or those near cut-off [4]. The EIM calculations suggest that the structure in Fig. 1 is single-mode upto $H = 0.8 \mu\text{m}$, supports two modes in the range $0.8 \mu\text{m} < H \leq 1.28 \mu\text{m}$, and supports three modes at $H = 1.44 \mu\text{m}$, becoming cutoff beyond $H > 1.44 \mu\text{m}$. The modal effective indices are in good

agreement with those from the finite difference method only in the range $0.8 \mu\text{m} \leq H \leq 1.28 \mu\text{m}$. As seen from the finite difference results, this is not the single-mode range for the structure in Fig. 1, and hence the effective index method does not appear to be useful for designing single-mode heterostructure ridge waveguides.

In conclusion, we have carried out an investigation on the number of guided modes supported in typical 3-layer heterostructure ridge waveguides, and determined the accurate single-mode ridge waveguide geometry. We have shown using the SFDM, that in a double heterostructure ridge waveguide of fixed width and layer structure, the guide is initially multimode for small ridge heights, single-mode in a small range of larger ridge heights, and multimode again when the ridge height is further increased. Similar behavior was observed in 2-layer rib guides by Austin [1]. From the comparison of the SFDM and EIM results, we conclude that the effective index method is not suitable for determining accurate single-mode ridge waveguide geometry.

References

1. M. W. Austin, *IEEE J. of Lightwave Technology*, Vol. LT-2, No. 5, October 1984.
2. S. S. Lee, R. V. Ramaswamy, and V. S. Sundaram, *IEEE J. of Quantum Electronics*, Vol. 27, No. 3, March 1991.
3. R. G. Walker, *IEEE J. of Quantum Electronics*, Vol. 27, No. 3, March 1991.
4. R. M. Knox and P. P. Toullos, *Microwave Res. Ins. Symp. Ser.*, Vol. 20, p. 497, 1970.

Figures

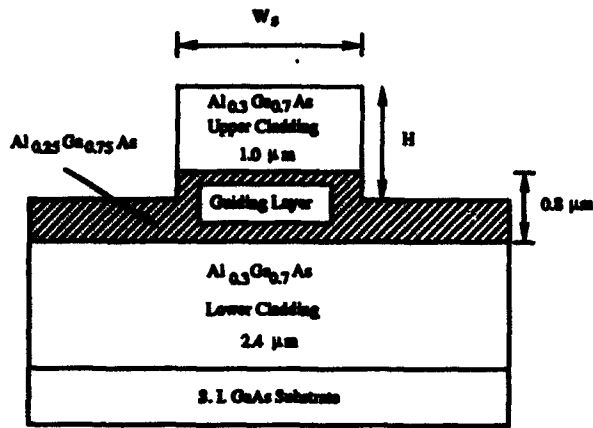


Fig.1. Cross section of ridge waveguide used in the single-mode structure investigation.

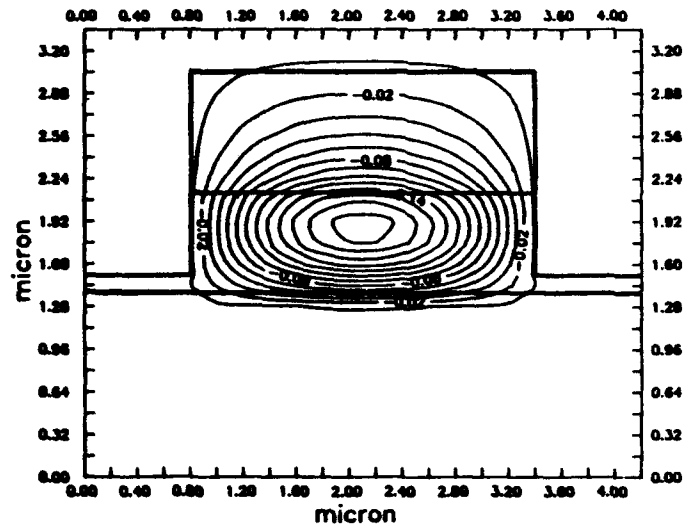


Fig.2. SFDM field calculation of 0th order mode for $H = 1.60 \mu\text{m}$ in Fig.1.

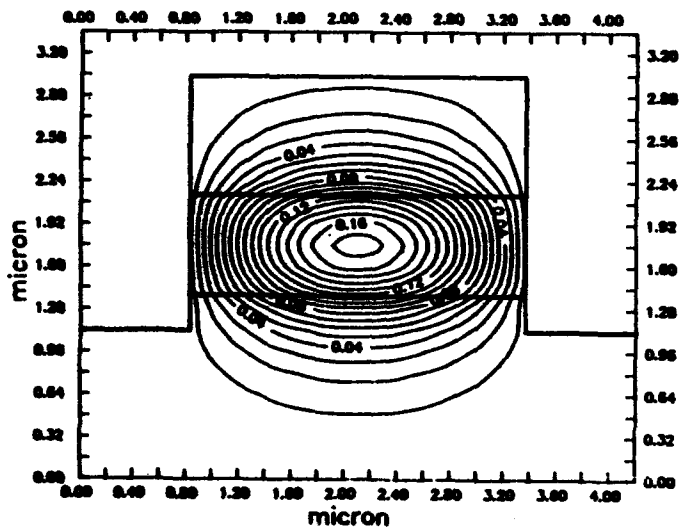


Fig.3(a). SFDM field calculation of 0th order mode for $H = 1.92 \mu\text{m}$ in Fig.1.

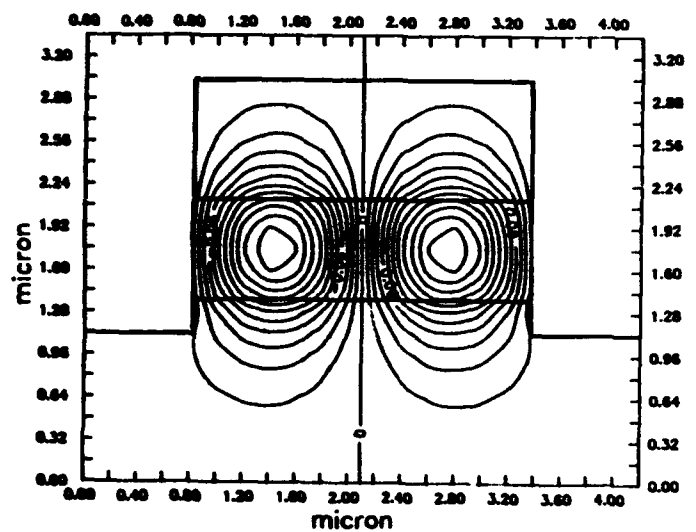


Fig.3(b) SFDM field calculation of 1st order mode, $H = 1.92 \mu\text{m}$ in Fig.1.

Does the Nonlinear Schroedinger Equation Correctly Describe Beam Propagation?

N.N. Akhmediev and A. Ankiewicz

Optical Sciences Center, Institute of Advanced Studies,
Australian National University, Canberra, A.C.T. 2601, Australia
Telephone: (06) 249-0191

The effect of self-trapping and self-focusing of light beams in nonlinear media was predicted in the early 1960s [1,2]. The evolution of light beams in self-focusing media has always been described by the nonli-near Schroedinger equation (NLSE) ever since the very first works devoted to this question [3,4]. It takes the diffraction and nonlinearity into account in a simple way, and describes the field evolution with high accuracy, unless time dependence and dispersion are involved [5]. Thus, the NLSE is a convenient approximation; it provides the possibili-ty of using a powerful tool such as the inverse scattering method [6] for its investigation. In fact, a variety of exact solutions can be obtained for the 1-D NLSE using even simpler approaches [7]. This equation, with variable coefficients adjusted for a layered medium, has been used widely for describing nonlinear wave propagation in optical waveguides and interfaces [8]. It is also important to note that many fast and convenient calculation methods have been developed [9] for numerical simulations of solutions of the NLSE.

Unfortunately, this equation has limitations which have not been discussed before, and which are connected with the approximation of slowly-varying envelope. As can be seen in what follows, some physical implications of this equation can even be misleading and turn out to be at odds with the general theory of wave propagation. Moreover, the NLSE has an infinite number of conserved quantities [6], but none of them has a clear physical interpretation-at least for the problem of beam propagation. The question arises: is approximation by the NLSE good enough to describe nonlinear guided wave phenomena in their full complexity?

We show here that the NLSE is a good approximation unless stationary (in longitudinal direction) solutions (like self-trapping [2] and stationary nonlinear guided waves [8]) or solutions close to them are considered. If the beam has any longitudinal variation during propagation, as happens in most cases of interest, then the equation should be completed by an additional term describing longitudinal field oscillations. This additional term allows us to present a clear physical interpretation of the conserved quantities involved.

We start from the scalar wave equation for a two-dimensional field $E(x,z)$ in a medium [10]:

$$E_{zz} + E_{xx} - \frac{\epsilon(x,|E|)}{c^2} E_{tt} = 0 \quad (1)$$

where subscripts indicate derivatives, E is y -component of optical field, and $\epsilon(x,|E|)$ is the intensity-dependent dielectric permittivity where $\epsilon(x,|E|) = \epsilon_1(x) + \alpha(x)|E|^2$. Here $\epsilon_1(x)$ is the linear part of the transverse profile of the dielectric permittivity of the layered medium, and $\alpha(x)$ is the transverse profile of the nonlinear susceptibility. The field, which also has x and z components of the related magnetic field H , is assumed to be stationary (in time) and monochromatic $E = \psi(x,z) \exp(-i\omega t)$. For convenience we normalize the coordinates x, z using the freespace wavenumber $k = \omega/c$:

$$\psi_{zz} + \psi_{xx} + \epsilon(x) \psi + \alpha(x)|\psi|^2 \psi = 0 \quad (2)$$

We seek a solution of Eq.(2) of the form:

$$\psi(x,z) = B(x,z)e^{i\phi(z)} \quad (3)$$

We assume that the envelope function $B(x,z)$ is slowly varying, and that all fast oscillations are included via the phase function $\phi(z)$. Usually, in the approximation of slowly varying amplitude, we set $\phi(z) = \beta z + \phi_0$, with $\beta = \text{const}$. In this case, if this approximation is used for numerical simulations, then fast oscillations are implicitly included in the function $B(x,z)$. However, the second derivative of this function is then not small, and cannot be dropped completely.

Of course, there is some degree of arbitrariness in extracting the fast oscillatory part from the function $B(x,z)$. This is especially so if the beam divides into two during propagation. In this instance it is more convenient in numerical simulations to keep β constant, as is usually done. On the other hand, the correct separation produces physically important consequences, as we now show.

We suppose that we have only one beam as a solution of Eq.(1), so the function $|B(x,z)|$ has only one maximum at any fixed z and that it approaches zero at $x = \text{infinity}$. Substituting Eq.(3) into Eq.(2) we obtain:

$$B_{zz} + B_{xx} + 2i\phi_z B_z + i\phi_{zz} B - \phi_z^2 B + \epsilon_1(x)B + \alpha(x)|B|^2 B = 0 \quad (4)$$

The term B_{zz} can be omitted from Eq.(4), as is usual in the slowly-varying amplitude approximation. However, this can only be done if $B(x,z)$ does not include any fast field oscillations in the z direction. With our assumption, the rapidly oscillating part of the solution is included via the function $\phi(z)$ in such a way that the function $B(x,z)$ maintains constant phase - at least at the center of the beam where $|B(x,z)|$ has its maximum. If the beam center is located at $x=0$, for example, then we can define the function $\phi(z)$ such a way that

$$\arg[B(x=0,z)] = \text{const} \quad (5)$$

where $B(0,z)$ has been written as $|B(0,z)| \exp[i \arg B(0,z)]$. This in turn means that the ratio of imaginary to real part of $B(0,z)$, i.e. $\text{Im}(B(0,z))/\text{Re}(B(0,z))$, remains constant.

We should remember that these oscillations can appear in a solution as z changes, even if we have $\beta = \text{const}$ at $z=0$. This will happen if the boundary condition $B(x, z=0) = f(x)$ does not coincide exactly with the solution of Eq.(4) which does not depend on z at all. If we include oscillations along z into the exponential factor of Eq.(3), and apply (5), then we must still retain the influence of this oscillatory part in the term with second derivative φ_{zz} from Eq.(4).

Let us define the function $\tilde{\beta}$ as:

$$\tilde{\beta}(z) = \varphi_z \quad (6)$$

This is the instantaneous propagation constant at a given cross section z . Now we can write Eq.(4) in the form:

$$2i\tilde{\beta}B_z + i\tilde{\beta}_z B + B_{xx} - \tilde{\beta}^2 B + \varepsilon_l(x)B + \alpha(x)|B|^2 B = 0 \quad (7)$$

In the case of constant $\tilde{\beta}$, this equation obviously coincides with the standard NLSE for studying the propagation of nonlinear guided waves. The second term in Eq.(7), which can be of the same order as the first one, makes it different from the usual NLSE.

Now let us turn to physical differences which appear when we take this term into account. Consider, for example, the invariants of Eq.(7). By multiplying Eq.(7) by B^* , taking the complex conjugate of this expression, and subtracting and integrating, we obtain:

$$\frac{d}{dz} (\tilde{\beta}I) = 0 \quad (8)$$

where I is the energy invariant for the standard NLSE:

$$I = \int_{-\infty}^{\infty} |B(x, z)|^2 dx \quad (9)$$

We can see now that the product $\tilde{\beta}I$, rather than just I , is the conserved quantity during propagation:

$$\tilde{\beta}(z) I(z) = \text{const.} \quad (10)$$

This product $S_z = \tilde{\beta}I$ is proportional to the integrated energy flow [11] in the z direction, i.e. to the z -component of Poynting vector $\mathbf{S} = \mathbf{E} \times \mathbf{H}$ integrated over the cross section. It can also be called 'power' [11] or 'power flow' [12] crossing a given surface $z = \text{const}$. This is the result which we would expect physically, because in the general theory of wave propagation, the energy flow is the quantity which has to be conserved in media without gain or loss. However, in the standard approximation by NLSE, this conservation law is incomplete, and only the 'energy integral' I is conserved, as rapid oscillations are neglected when the term B_{zz} is dropped. Of course, in the case of constant β , the energy invariant I itself is conserved. This can happen only for stationary solutions of Eq.(2). But in that case it is a trivial result, as the

function $B(x)$ itself then does not depend on z , and so neither will any integral of it.

Let us now consider the second quantity conserved in case of NLSE, namely, the Hamiltonian. By multiplying Eq.(7) by dB^*/dz , taking the complex conjugate of this expression, and adding and integrating over x , we obtain:

$$i \int_{-\infty}^{\infty} dx \tilde{\beta}_z (B_z B^* - B_z^* B) - 2 \int_{-\infty}^{\infty} dx \tilde{\beta} \tilde{\beta}_z |B|^2 + \frac{d}{dz} \int_{-\infty}^{\infty} dx \left[|B_x|^2 + (\tilde{\beta}^2 - \epsilon_1) |B|^2 - \frac{\alpha}{2} |B|^4 \right] = 0 \quad (11)$$

The sum of integrals in (11) is proportional to the energy density of the optical field integrated over x per unit z . The first two terms are the part of the energy density connected with the x component of the magnetic field (H_x^2). These two integrals becomes zero when $\beta = \text{const.}$ in the standard NLSE approximation. In this case the third integral is conserved along z . If $\tilde{\beta}_z$ is nonzero, then the whole expression (11) cannot be represented in the form of a conservation law. The consequence is that the Hamiltonian (the third integral in (11)) is no longer conserved.

In conclusion, we have shown that the standard approximation, which uses the NLSE and is employed in the analysis of nonlinear self-focusing and self-guiding, should be completed with an additional term which takes into account the variation of the propagation constant along the propagation direction.

REFERENCES :

1. G.A.Askar'yan, Sov.Phys.JETP,15, 1088 (1962).
2. R.Y.Chiao, E.Garmire, C.H.Townes. PRL,13,479 (1964).
3. P.L.Kelley, PRL, 15, 1005 (1965).
4. V.E.Zakharov, V.V.Sobolev, V.S.Synakh, Sov.Phys.JETP 33,77(1971).
5. V.E.Zakharov, A.M.Rubenchik, Zh.Eksp.Teor.Fiz. 65, 997 (1973). [Sov. Phys.JETP 38, 494 (1973)].
6. V.E.Zakharov, A.B.Shabat, Sov. Phys. JETP 34, 62 (1972).
7. N.N.Akhmediev, V.M.Eleonskii, N.E.Kulagin, Theor.Math.Phys., 72, 809-818 (1987) [Teor.Mat.Fiz.(USSR), 72, 183 (1987)];
8. C.T.Seaton, G.I.Stegeman, H.G.Winful, Opt.Eng., 24, 593 (1985).
9. T.R.Taha, M.J.Ablowitz, J.Comp.Phys., 55, 203 (1984).
10. M.Born and E.Wolf. Principles of Optics. Pergamon Press, 1980.
11. A.W.Snyder and J.D.Love, Optical waveguide theory. Chapman and Hall, 1983.
12. H.A.Haus. Waves and fields in optoelectronics. Prentice-Hall, Englewood Cliffs, 1984.

Characteristics of Dielectric-clad Directional Couplers for Improved Edge Coupling to Hybrid Detectors

P.C. Noutsios, G.L. Yip

Guided Wave Optics Laboratory

McGill University, Department of Electrical Engineering

3480 University, Montreal, Quebec, Canada H3A 2A7

and

J. Albert

Dept. of Optical Communications Technology

Communications Research Center

Ottawa, Ontario, Canada K2H 8S2

Active components on glass and lithium niobate substrates have been fabricated by combining passive waveguides with an overlay of grafted semiconductor material for optical detection applications¹. To improve the overall coupling from an optical fiber to the detector, a vertical directional coupler that transfers power from a buried waveguide (with a minimal insertion loss) to a surface waveguide was recently proposed and demonstrated using a field-assisted K^+ -ion exchange in glass². Though this scheme works well for vertical coupling of light to the detector, its efficiency is impaired by the presence of a thin layer of low index amorphous material at the semiconductor/waveguide bonding interface³. An effective way to avoid this problem is to use edge coupling to the detector which can be achieved by cladding the waveguide/detector structure with a dielectric thin film of refractive index higher than that of the waveguide⁴. Here, we report preliminary results on the fabrication and measurement of a vertical directional coupler that is clad with a sputtered Corning 7059 glass thin film to take advantage of this edge coupling scheme. In addition, we compare the experimental to the theoretical results obtained using a finite-difference vector beam propagation method⁵ (FD-VBPM).

The dielectric-clad vertical coupler, comprised of two parallel slab waveguides (see Fig. 1), was fabricated by a three-step electric field-assisted K^+ -ion exchange in soda-lime glass². The single-mode buried guide 2 was made by a two-step exchange, using an applied field of 20 V/mm and exchange time $t_1 = 15$ sec in the first step, and 100 V/mm in the second step

with exchange time t_2 varying from 2 to 3 min. The single-mode surface guide 1 was made by a one-step exchange with 20 V/mm and $t_3 = 5$ sec at a constant temperature of 385°C. These fabrication conditions provide for longer coupling lengths (340 – 380 μm) than our previous results² (200 – 280 μm). The cladding layer is formed by plasma sputtering with a Corning 7059 glass target under the conditions of 12 psi Ar/O₂ (4:1 mixture) gas pressure and 20 W rf power. The refractive index, n_c , and film thickness, t , are measured by prism coupling and a surface profilometer, respectively.

The TE and TM effective indices of the even (N_{even}) and odd (N_{odd}) mode m-lines were measured by prism-coupling at $\lambda = 0.633$ μm with an error of $\pm 2 \times 10^{-4}$. The coupling length L_c can be deduced from the mode-index measurements. The relative intensities (power ratios) of the normal modes are measured with an IR vidicon and oscilloscope. An input lens was used to excite both modes simultaneously yielding a streak of periodic dots, representing power transfer². In addition, we determine the coupler's potassium concentration profile directly using an electron microprobe. Prior to measurement, the surface of the (unclad) coupler is tapered by careful polishing to expose the varying potassium concentration with depth (x) using an angle-lapping technique with a taper angle of about 2°. The measured concentration profile, shown in Fig. 2, shows the surface and buried waveguides of the coupler with a large overlap between them.

For the coupler fabricated with $t_2 = 2$ min. and dielectric-clad with $n_c = 1.545 \pm 8 \times 10^{-4}$ and $t = 0.13 \pm 0.04$ μm , the measured coupling lengths for both TE and TM modes are almost identical to those of the unclad coupler, within experimental error. The coupling length is also determined theoretically with the FD-VBPM for varying cladding thickness, as shown in Fig. 3. Modelled results predict an increase in the coupling length with the cladding thickness, as expected, since the peak of the field is being pulled up toward the waveguide-cladding interface, as shown in Fig. 4, thus providing for an improved edge coupling to the detector. For thickness values below 0.1 μm , there is negligible change in the coupling length which is in agreement with the measured sample ($t = 0.13$ μm). Further experiments with thicker cladding layers and more accurate modelling are being pursued with results to be presented at the meeting.

REFERENCES

1. A. Yi-Yan, W.K. Chan, T.J. Gmitter, L.T. Florez, J.L. Jackel, E. Yablonovitch, R. Bhat and J.P. Harbison, 'Grafted *GaAs* detectors on lithium niobate and glass optical waveguides', *IEEE Photonics Technol. Lett.*, 1, pp. 379-380, 1989
2. P.C. Noutsios, G.L. Yip and J. Albert, 'Novel vertical directional coupler made by field-assisted ion-exchanged slab waveguides in glass', *Elect. Lett.*, 28, pp. 1340-1342, 1992
3. W.K. Chan, A. Yi-Yan, T.J. Gmitter, L.T. Florez, J.L. Jackel, D.M. Hwang, E. Yablonovitch, R. Bhat and J.P. Harbison, 'Optical coupling of *GaAs* photodetectors integrated with lithium niobate waveguides', *IEEE Photonics Technol. Lett.*, 2, pp. 194-196, 1989
4. W.K. Chan, A. Yi-Yan, T.J. Gmitter, L.T. Florez, N. Andreadakis and C.K. Nguyen, 'Channel glass waveguide detectors with grafted *GaAs* film in embedded configuration', *Elect. Lett.*, 27, pp. 410-412, 1991
5. W.P. Huang, C.L. Xu, S.T. Chu and S.K. Chaudhuri, 'A vector beam propagation method for guide-wave optics', *IEEE Photonics Technol. Lett.*, 3, pp. 910-913, 1991

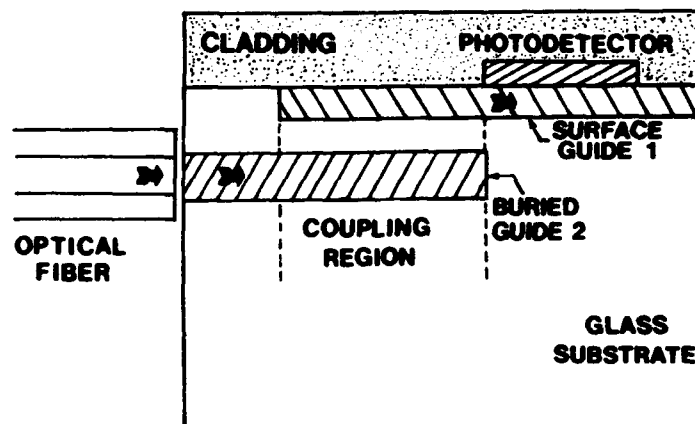


Fig. 1 Dielectric-clad vertical directional coupler used in waveguide-detector geometry

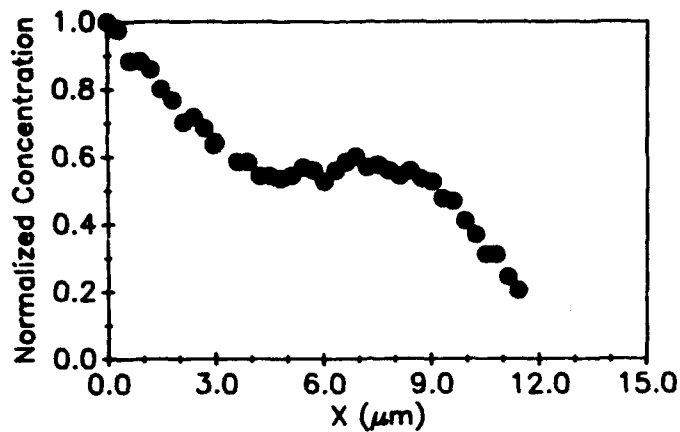


Fig. 2 Scaled electron microprobe concentration profile for the graded-index coupler

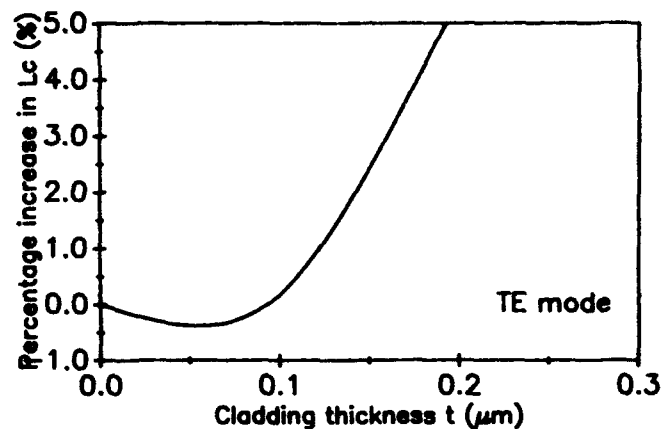


Fig. 3 Percent increase in coupling length with cladding thickness (TE mode)

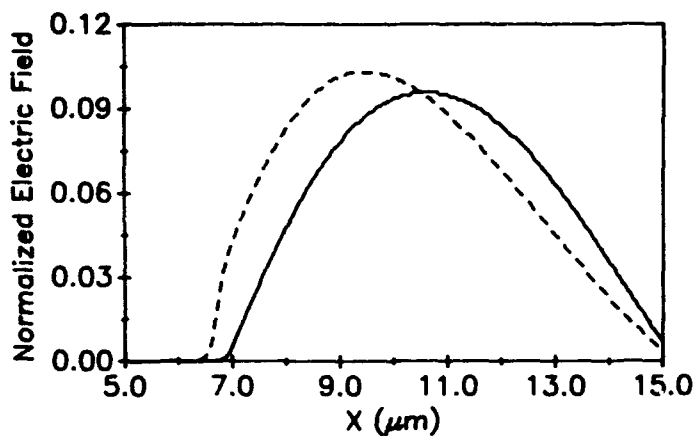


Fig. 4 Normalized electric field distribution for the $t = 0.3 \mu\text{m}$ clad (dashed line) and unclad (solid line) coupler ($x = 7.0 \mu\text{m}$ is the detector-waveguide interface)

Tunable Waveguide Dye Laser with Second-Order Distributed Bragg Reflectors

H.Inuzuka

Advanced Technology Research Center,
Mitsubishi Heavy Industries, Ltd.
1-8-1 Sachiura, Kanazawa-ku, Yokohama, 236, JAPAN
Phone +81-45-771-1255, Fax +81-45-771-1505

Waveguides doped gain active medium offer possible means of incorporating light sources and amplifiers into integrated optical circuits for communications and sensor applications. In particular, the mediums that with wide gain bandwidth such as dye and Ti doped saphier are attractive for wavelength tuning. Dye is one of considerable mediums for the gain medium because there are many applicable materials from UV to near IR wavelength range, and they can be easily doped into organic and inorganic glass thin films. There are several reports for tunable operation of waveguide dye lasers with distributed feed back (DFB) using etched periodical grouves or interference fringes of two pump beam on a waveguide [1-4]. These lasers are, however, difficult to obtain stabilized single mode operation in comparison with distributed Bragg reflector (DBR) lasers especially in pulsed pumping. In this paper, we report successful single mode operation of a waveguide dye laser with second-order DBRs in pulsed pumping and its wavelength tunability.

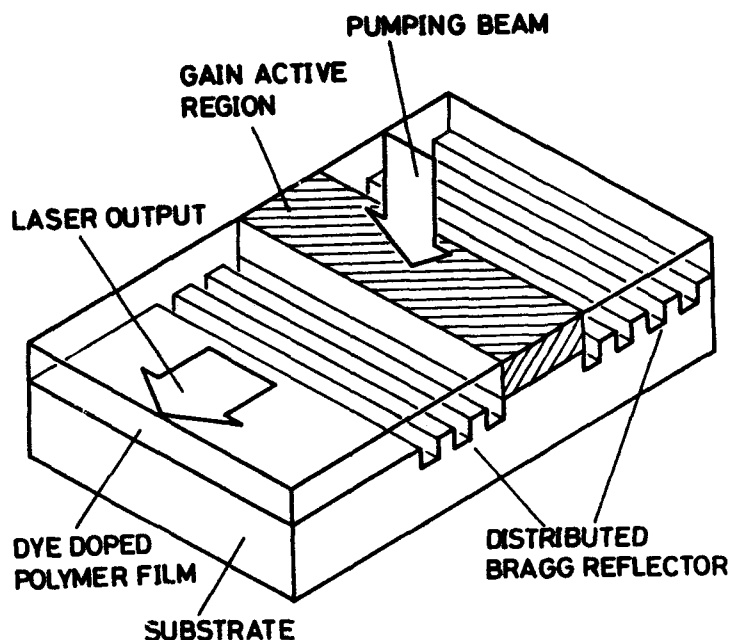


Fig. 1 Fundamental structure of the DBR dye laser

The fundamental structure of the laser is shown in Fig.1. We determined parameters of the DBR laser to obtain a single mode operation around 620nm for the fundamental TE mode. A dye (Kiton-Red 620) doped polymethylmethacrylate (PMMA) film ($n_f=1.49$) and quartz ($n_s=1.46$) were used as guiding layer and substrate respectively. In the film of 1.2 μm thickness (effective index of the waveguide was 1.48), the period of DBRs was determined to be 419nm because of the second-order Bragg condition. The lengths of two DBRs were determined to be 0.8mm, and 0.5mm respectively, and 0.1 μm . These DBRs were designed to have 100% and 99.3% reflection ratio of guided power in 0.5nm bandwidth. In this case, we did not take into account of first-order radiation loss of the DBRs pointed out and analyzed by Streifer et al.[5] so far. Thus, in order to produce longitudinal single mode operation, we determined the required separation of the DBRs (cavity length) to be 0.28mm.

We created the laser as follows. First, we fabricated the DBRs on the quartz surface using holographic exporsuring and reactive ion etching techniques. The SEM photograph of the grating is shown in Fig 2. Then, the laser was completed by coating the dye doped PMMA film on the substrate with a dipping method. This laser structure enables us to refresh the dye repeatedly with simply removing the film with a solvent.

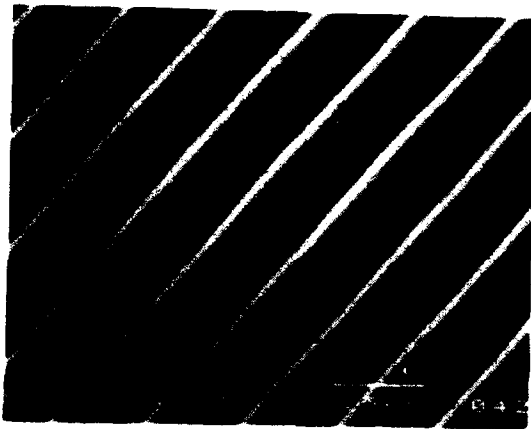


Fig.2 SEM photograph of the grating

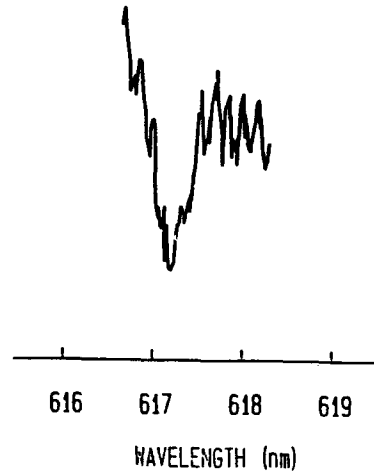


Fig.3 Characteristic of DBR cavity

We investigated characteristics of the second-order DBR cavity by measuring transparency and radiation of the first order reflection using cw dye laser and prism coupling method. As shown in Fig. 3, band eliminated characteristic within 0.5nm bandwidth of the DBR cavity was observed. At the eliminated wavelength, we observed reflected streak. We also observed weak radiation from the DBR due to first order diffraction through all wavelength.

By pumping the dye in the cavity with 532nm laserbeam(2nd-harmonic of Q-switched Nd:YAG laser) that was focused on the cavity from the direction normal to the surface of film, we observed guided laser output through a rutile prism output coupler. The absorbed pump power exceeded 21W in the film. The laser output power versus absorbed pump power is shown in Fig.4. The guided mode was TE fundamental mode for a polarization in the pump beam parallel to the groove of the DBRs. As shown in Fig.5(a), we estimated that the laser operates in single mode at 618.6nm wavelength with 0.07nm linewidth by observing the spectrum of the lightwave. The linewidth was obtained from a coherence length of 5.38mm measured by Michelson interferometer. From a pulsed waveform (Fig.5(b)) with 23ns width and 4ns period of modulation due to pump source characteristics, we believe that the laser is applicable for signals with higher than repetition rate 230MHz. After pumping around 9,000 pulses, the output power decayed to a half.

Linear tuning of the lasing wavelength is possible by changing the cavity length and period of the DBRs in a same ratio. Therefore we changed these parameters by compressing the quartz substrate with a piezo actuator. Linear tuning characteristic was obtained as shown in Fig. 6. The linearity was due to the elastic modulus of quartz and small size of cavity. In this case, break down pressure of the quartz is a limitation of tuning.

In conclusion, we have described the characteristics of a tunable second-order DBR dye laser using a waveguide of the Kiton-Red 620 dye doped PMMA film on a quartz substrate. The laser can generate a guided wave of 618.6nm in a single mode, and can tune the lasing wavelength in the range of 0.1nm.

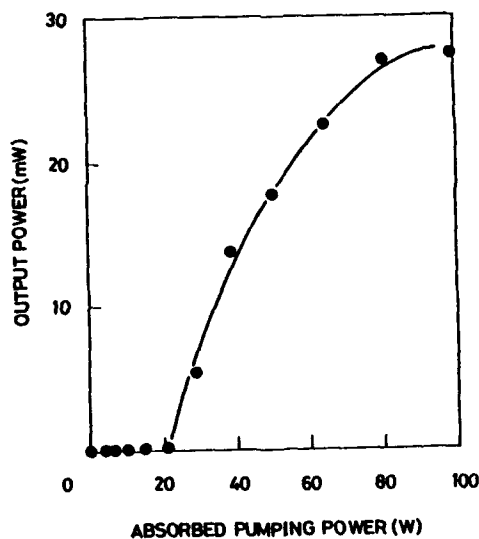


Fig.4 Laser output power versus absorbedpump power

REFERENCES

- [1] H. Kogelnik and C. V. Shank, *Appl.Phys.Lett.* 18,152(1971)
- [2] S. Sriram, Howard E. Jackson and J. T. Boyd, *Appl.Phys.Lett.* 36,721(1980)
- [3] V. M. Arutunyan, A. V. Karmenyan and T. E. Meliksetyan, *Opt.Commun.*, 49,195(1984)
- [4] M.Sugii, O. Sugihara, M. Ando and K. Sasaki, *Jap.J.Appl.Phys.*, 25,1373(1986)
- [5] W. Streifer, D. R. Scifers and R. D. Burnham, *IEEE J.Quantum Electron.*, QE-13,134(1977)

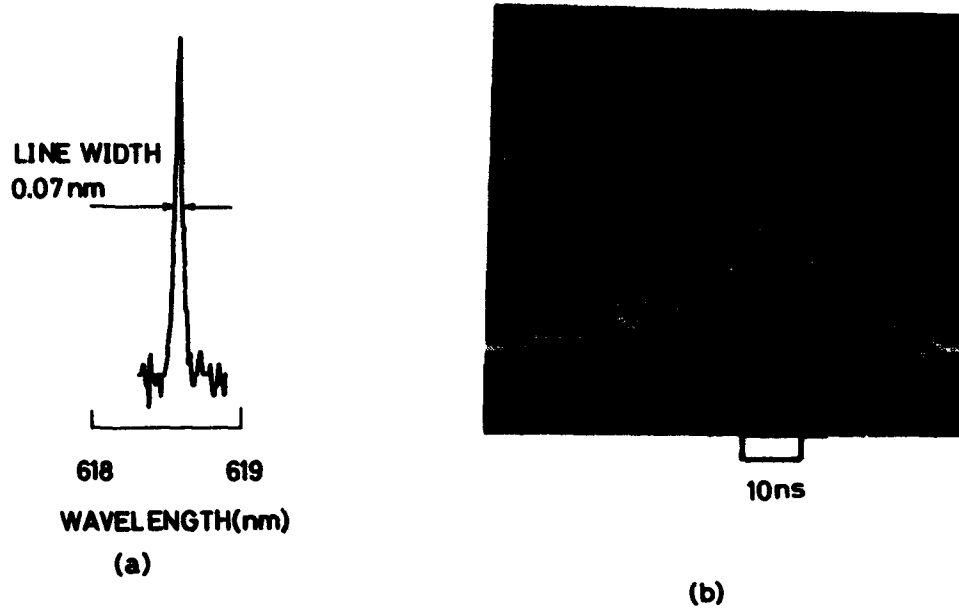


Fig.5 Output spectrum and pulse waveform of the laser
(a)spectrum,(b)pulse waveform

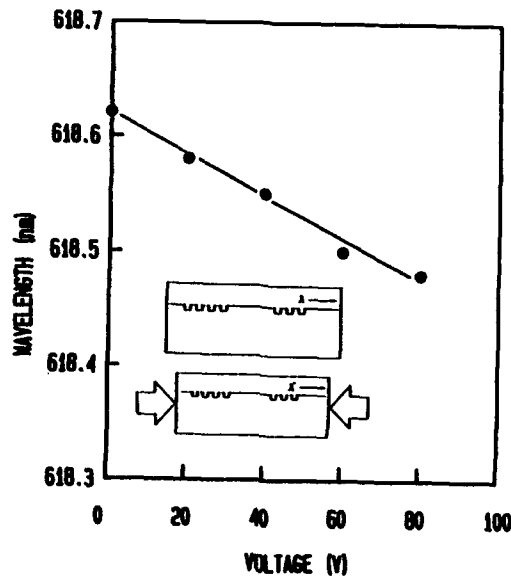


Fig.6 Tuning characteristic of DBR dye laser

Polymeric reflection modulators for free space optical interconnects

J. D. Richards and A. Knoesen

Department of Electrical Engineering and Computer Science
University of California, Davis
Davis, CA 95616
(916) 752-8023

1. Introduction

A reflection-mode spatial light modulator (RSLM) with a high bandwidth, a large contrast ratio, and low power consumption will have great potential for use in free space optical interconnects. Reflection-mode devices modulate the intensity of the reflected light and could possibly be used to optically interconnect internal nodes of a transmitting chip to internal nodes of a receiving chip. Existing electro-optic materials do not allow for a RSLM with all of the above characteristics. As a result of material limitations, current RSLM designs must incorporate performance tradeoffs. The performance of Fabry-Perot (FP), surface plasmon (SP), and long range surface plasmon (LRSP) thin film nonlinear polymeric reflection modulators are analyzed here.

2. Motivation

Nonlinear polymers are a desirable material for the electro-optic dielectric layer in a RSLM because the nonlinear polarization is primarily electronic in nature. This fact, combined with a low dielectric constant, can produce a RSLM with a bandwidth in the gigahertz range and low electrical drive power. Other electro-optic materials most often used in spatial light modulators (SLMs) include: liquid crystals [1], PLZT [2], and multiple quantum wells (MQW) [3]. Liquid crystal SLMs exhibit high contrast ratios but are slow because the molecules must rotate to physically align with the applied electric field. Si/PLZT SLMs have a bandwidth limited by the high capacitance of the structure due to the large relative dielectric constant (e.g., $\epsilon_r=5700$) of PLZT. MQW SLMs are based upon quantum confined electro-absorption effects and have been the subject of recent interest. These MQW structure are grown with well established molecular-beam epitaxy or metallo-

organic chemical vapor deposition techniques, which require fabrication steps significantly more complex than the polymeric structures investigated here. Another alternative is optical interconnect architectures that incorporate vertical-cavity surface-emitting lasers [4]. This approach could be very promising if the large electrical drive powers could be reduced.

Using an organic polymer in a RSLM has several advantages over the other electro-optic materials mentioned. First of all, polymers are suitable for monolithic optoelectronic integration. Fabrication of polymer structures is straightforward because the polymer can be spun-cast onto substrates. Since most integrated circuits are silicon based, it is important that the processing of the polymer is compatible with silicon processing techniques. Secondly, orientational order can be achieved in the polymer film by techniques such as poling, Langmuir-Blodgett, and self-assembly. In the case of poling, a large electric field is applied across the thin polymer film, which is at an elevated temperature. A noncentrosymmetric film with ∞ -mm symmetry is produced. Poling can produce nonlinear polymer films with linear electro-optic coefficients approaching 100 pm/V. It should be noted that the use of nonlinear polymers in optical devices is an emerging field. As refinements are made in material synthesis and orientational techniques, it is expected that the linear electro-optic coefficients will continue to increase.

3. Polymeric Modulator Performance

The FP structure consists of a thin gold layer, a nonlinear polymer layer, and a thick gold electrode. Our group demonstrated experimentally the feasibility of FP reflection-mode polymeric modulators for optical interconnects, as well as a technique for material characterization [5, 6]. The SP structure consists of a high index prism, a thin gold layer, a nonlinear polymer layer, and a thick gold electrode. In surface plasmon structures, the high index prism is required to excite surface plasmons via the method of attenuated total reflection. SP modulators using liquid crystals [1] have been fabricated. The LRSP modulator structure is the same as the SP structure except for a dielectric coupling gap located between the high index prism and the thin gold layer. LRSP modulators using electro-optic crystals [7] have been proposed but not implemented. In this paper, we will present experimental evidence of a polymeric electro-optic LRSP modulator.

Theoretical reflectance and modulation response for the FP, SP, and LRSP modulators have been numerically analyzed with a theory that accounts for layered media, modified for the anisotropy of the nonlinear polymer film. The definition for modulation used here:

$$m = \frac{R_{\max} - R_{\min}}{R_{\max} + R_{\min}}$$

is consistent with the standard used in communication theory. The magnitude of the maximum modulation for the three typical modulator structures is plotted versus $r_{33}V$ in Figure 1.

4. Discussion

The modulation of the LRSP modulator is approximately three times larger than the FP modulator and eight times larger than the SP modulator. From Figure 1, it is clear that the modulation depends upon the quantity $r_{33}V$. If these reflection modulators were used to optically interconnect internal nodes of a transmitting chip to internal nodes of a receiving chip, it is likely that the voltage on these nodes will switch between 0 and 5 volts. If a polymer with $r_{33} \approx 100$ pm/V is developed, the modulation produced by all three structures could be detected with simple detection techniques. In terms of fabrication and implementation complexity, the FP modulator is the most attractive of the three structures since it does not require the use of a high index prism. However, if $r_{33} < 30$ pm/V, the LRSP modulator becomes a more attractive structure because the sharp resonance in the LRSP reflectance curve provides the largest modulation.

References

- [1] E. M. Yeatman and M. E. Caldwell, "Spatial light modulation using surface plasmon resonance," *Appl. Phys. Lett.*, vol. 55, pp. 613-615, Aug. 14, 1989.
- [2] S. H. Lee, S. C. Esener, M. A. Title, and T. J. Drabik, "Two-dimensional silicon/PLZT spatial light modulators: design considerations and technology," *Opt. Eng.*, vol. 25, pp. 250-260, Feb. 1986.
- [3] R.-H. Yan, R. J. Simes, and L. A. Coldren, "Surface-normal electroabsorption reflection modulators using asymmetric Fabry-Perot structures," *IEEE J. Quantum Electron.*, vol. 27, pp. 1922-1931, July 1991.

- [4] C. J. Chang-Hasnain, J. P. Harbison, C.-E. Zah, M. W. Maeda, L. T. Florez, N. G. Stoffel, and T.-P. Lee, "Multiple wavelength tunable surface-emitting laser arrays," *IEEE J. Quantum Electron.*, vol. 27, pp. 1368-1376, June 1991.
- [5] C. A. Eldering, S. T. Kowel, M. A. Mortazavi, and P. F. Brinkley, "Electrooptic polymer materials and devices for global optical interconnects," *Appl. Opt.*, vol. 29, pp. 1142-1149, Mar. 10, 1989.
- [6] D. Yankelevich, A. Knoesen, and C. A. Eldering, 'Reflection-mode polymeric interference modulators', *SPIE*, vol. 1560, pp. 406-415, 1991.
- [7] J. S. Schildkraut, "Long-range surface plasmon electrooptic modulator", *Appl. Opt.*, vol. 27, pp. 4587-4590, Nov. 1, 1988.

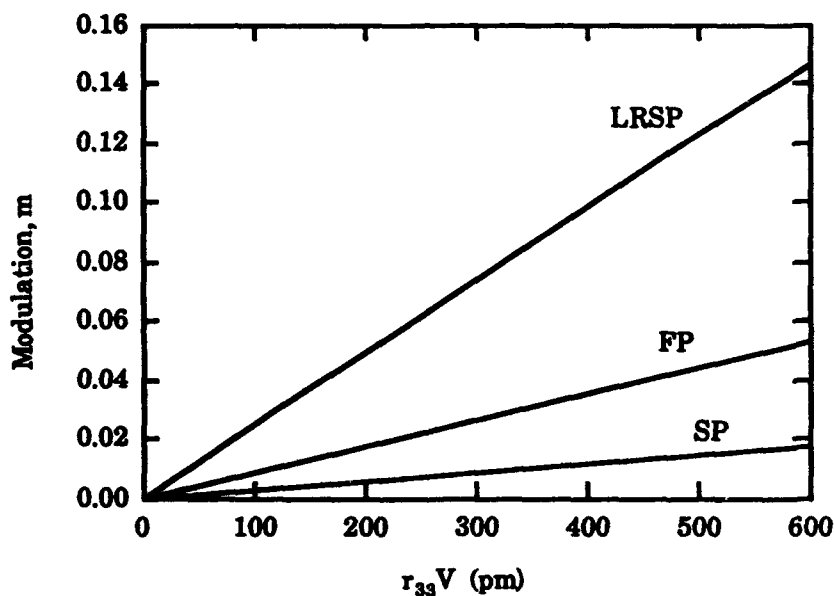


Figure 1 - Theoretical modulation comparison of Fabry-Perot (FP), surface plasmon (SP), and long range surface plasmon (LRSP) polymeric reflection modulators. The FP structure consists of a thin gold layer 48 nm thick, a nonlinear polymer layer 2000 nm thick, and a thick gold electrode. The SP structure consists of a high index prism, a thin gold layer 48 nm thick, a nonlinear polymer layer 1000 nm thick, and a thick gold electrode. The LRSP structure consists of a high index prism, a dielectric coupling gap 650 nm thick, a thin gold layer 20 nm thick, a nonlinear polymer layer 1000 nm thick, and a thick gold electrode. The refractive indices used are $n_{Au} = 0.217 + 3.425i$ for the gold, $n_{np} = 1.52$ for the nonlinear polymer, $n_{prism} = 1.72$ for the prism, and $n_{dielectric} = 1.52$ for the dielectric coupling gap.

**BPM DESIGN OF A WIDENED X-BRANCH DEMULTIPLEXER
IN A GLASS SUBSTRATE BY K⁺ ION EXCHANGE
FOR $\lambda = 1.31 \mu\text{m}$ AND $\lambda = 1.55 \mu\text{m}$**

GAR LAM YIP and LOIC J-M BABIN
Department of Electrical Engineering
3480 University Street
Montreal, P.Q., Canada H3A 2A7

Since first proposed as a total internal reflection (TIR) device in 1978 [1], X-branch waveguide devices have been studied extensively [2]. Their characteristics in terms of the extinction ratio, insertion loss, device dimension prove to be very attractive. The widened X branch (Fig 1) offers the additional advantage of a simpler fabrication process, as there is only one step involved in the ion-exchange. However, in the commonest two mode interference operation region, the requirements on the design parameters of a widened X-branch type demultiplexer are tight, when one wants to achieve wavelength demultiplexing [3], specially in a device made in a glass substrate, which allows little possibilities of an electrooptic adjustment. To find the best point for demultiplexing one can use, the following parameter R [4]:

$$R = \Delta\beta_c(\lambda = 1.31 \mu\text{m}) / \Delta\beta_c(\lambda = 1.55 \mu\text{m}) \quad (1)$$

$$R = (2m\pi - 2\phi_t) / ((2m-1)\pi - 2\phi_t) \quad (2)$$

Where $\Delta\beta_c$ is the difference of the propagation constants between the even and odd mode in the central region. It depends strongly on the width w and the diffusion time used for the ion exchange t_d . $2\phi'$ is the phase angle difference between these two modes in the tapered regions. $2\phi_t$ depends very weakly on t_d and w , but strongly on the branching angle α . Demultiplexing operation is obtained when both equations (1) and (2) are satisfied. For a given w and α , there is only a discrete set of the number m of coupling length l_c , diffusion times t_d and lengths L ($L = (2m\pi - \phi_t) / \Delta\beta_c$) to yield solutions.

Numerically, we used both the effective index method (EIM) plus the Yajima's method (YM) [5] and the EIM plus 2D FD-BPM [6]. When using the EIM we applied a Runge-Kutta scheme [7] for calculating the effective index in the depth direction, and the Yajima for calculating ϕ_t . In a first approximation, for the purpose of a simple comparison between the two methods, we did not take into account side diffusion effects in our modeling of the index profile. We considered only the TE modes for which accurate data are available for the index values at 1.31 and 1.55 μm [8]. From Table 1, we can see that the results from the two methods agree well. The small numerical discrepancies are most likely due to the fact that the BPM takes into account the radiation modes excited along the structure whereas the YM does not.

The appearance of radiation modes associated with a large branching angle or poor confinement of the modes, as revealed by the BPM, does not just simply increase the scattering losses of the structure but also reduces channel isolation as some radiated power is coupled back into the guided modes in both branches (see Table 2).

The best design results using the BPM are shown Fig 2 a,b.

The first problem to solve when one wants to design an X branch, taking into account side diffusion effects, is to find an accurate model for the effective index profile in the transverse direction. Around the merging point of the tapered regions we cannot simply add up the index profile functions of the two separate waveguides to find the index profile of the whole structure [9]. Assuming an erf type function for the channel index profile

including side diffusion, we used like Feit [10], the following normalized model for the transverse effective index:

$$N_{\text{eff}}(x) = (N(x+s/2) + N(x-s/2) - N(\infty)) \cdot N(0) / \max(N_{\text{eff}}(x))_x$$

$$\text{with } N(x) = N(\infty) + \{ \frac{1}{2} (N(0) - N(\infty)) (\text{erf}((x+w/2)/D_x) - \text{erf}((x-w/2)/D_x)) / 2\text{erf}(w/2D_x) \}$$

$N(\infty), N(0)$ are respectively the effective indices calculated in the depth direction for $x=\infty, 0$, D_x is the diffusion constant in the transverse direction ($D_x=D_y=D$ as the glass is assumed isotropic). (see Fig 3).

Considering this model, the values of the design parameters are dramatically changed in comparison to the approach neglecting side diffusion. First of all the diffusion time must be slightly smaller if we want to stay in a pure two mode interference operation region (see Fig 4). Moreover, R is significantly changed (see Fig 5) even though the propagation constants calculated by both models stay close. Variations in ϕ_i (calculated by BPM) are small. This leads to a very different design. It is not surprising: discrepancies as small as 0.0005 in the propagation constants are not negligible in terms of the phase delay when the average length of the device ($L=3000 \mu\text{m}$) is considered.

In conclusion, we have examined the performance characteristics of a widened X-branch demultiplexer made by K^+ ion exchange in a soda-lime glass substrate, employing the EIM and a 2D-FD-BPM scheme. In the case of step index boundaries for the channel guide, the new scheme has been tested against the YM with good agreement. We shall present the optimized device performance figures for this demultiplexer with the inclusion of side diffusion effects. Fabrication of the device using the optimized design data is also being planned.

References:

- [1] C.S. Tsai, B. Kim and F.R. El-Akkhari, IEEE J. of Quantum Electronics, July 1978, pp.513-516
- [2] A. Neyer, SPIE Proceedings, Vol 993, Sept. 1988, pp.68-75
- [3] Y. Chung, J.C. Yi, S.H. Kim and S.S. Choi, IEEE J. of Lightwave Technology, May 1989, pp.766-776
- [4] H.C. Chieng and R. Ramaswamy, IEEE J. of Quantum Electronics, March 1991, pp.567-574
- [5] H. Yajima, Proc. Symp. Optical and Acoustical Microelectronics, April 1988, pp.552-563
- [6] W.P. Huang, C. Xu, S.T. Chu and S.K. Chaudhuri, IEEE J. of Lightwave Technology, March 1992, pp.295-304
- [7] G.L. Yip and J. Ahmew, J. of China Institute of Telecom., Jan. 1985, pp.21-33
- [8] G.L. Yip, K. Kishioka, F.X. Chiang and J.Y. Chen, SPIE Proceedings Vol 1583, Sept. 1991, pp.14-18
- [9] G.L. Yip and J. Albert, IEEE J. of Lightwave Technology, April 1988, pp.552-563
- [10] M.D. Feit and J.A. Fleck, IEEE J. of Quantum Electronics, Nov. 1985, pp.1799-1804

	EIM+YM		EIM+BPM		Extinction ratio (dB) ($10 \log(P_4/P_3)$)		Radiation Loss (dB) ($10 \log(1-P_3-P_4)$)	
	t_0 (mn)	L(μ m)	t_0 (mn)	L(μ m)	$\lambda = 1.31\mu\text{m}$ $\lambda = 1.55\mu\text{m}$		$\lambda = 1.31\mu\text{m}$ $\lambda = 1.55\mu\text{m}$	
$\alpha = 1.2, w = 6.4\mu\text{m}, m = 4$	267	3960	272	3860	23	-24	-7	-13
$\alpha = 1, w = 6.3\mu\text{m}, m = 4$	256	3660	256	3600	35	-27	-13	-15
$\alpha = 0.5, w = 6.4\mu\text{m}, m = 6$	294	5490	288	5450	43	-33	-15	-19

Table 1 : Comparison between EIM and FD-BPM

P_4 = Normalized output Power in branch 4
 P_3 = Normalized output Power in branch 3

Table 2: Extinction ratio vs branching angle

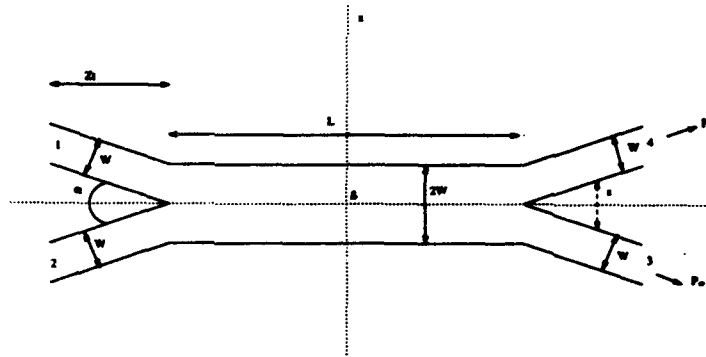


Fig 1: Widened X-Branch demultiplexer

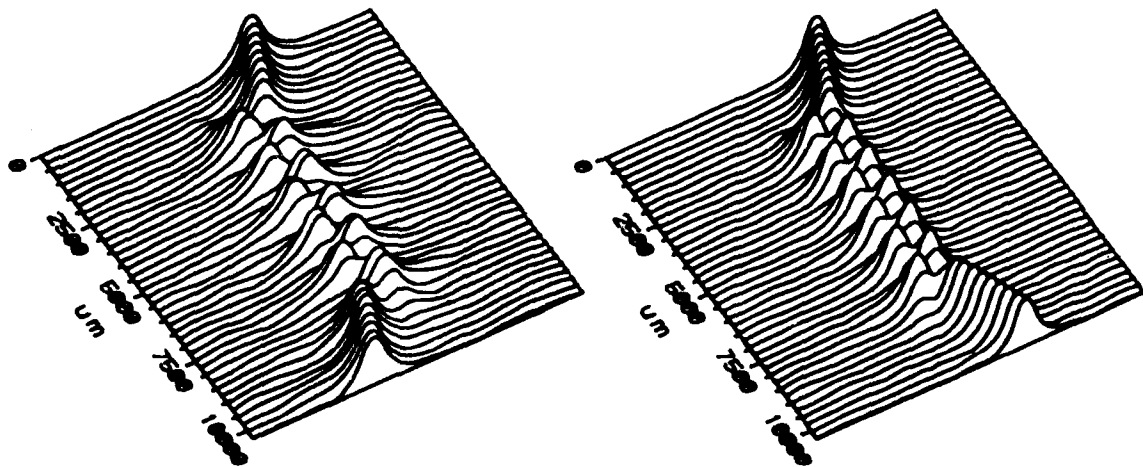


Fig 2: a,b BPM results with $\alpha = 0.5^\circ, w = 6.4 \mu\text{m}, t_0 = 272$ minutes at $1.31\mu\text{m}$ (a) and $1.55\mu\text{m}$ (b)

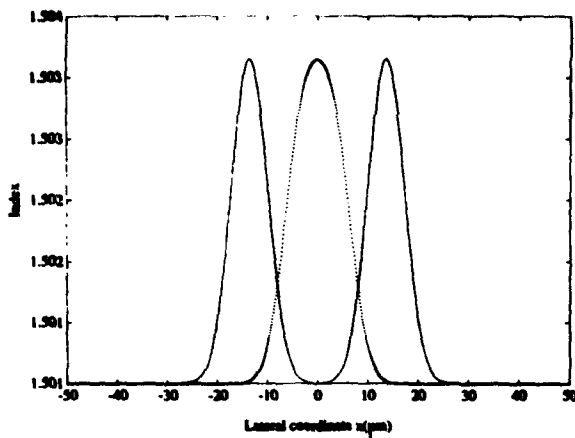


Fig 3: $N_{eff}(x)$, effective index profile in the transverse direction
 $w = 6.4 \mu m$, $t_d = 280$ minutes (ie $N(0) = 1.50365$)
 for $\lambda = 1.31 \mu m$ (ie $N(\infty) = 1.5010$)

— $s = 32 \mu m$
 $s = 0 \mu m$

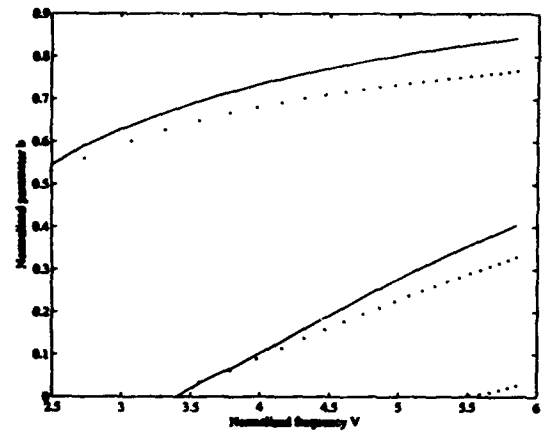


Fig 4: Normalized parameters V versus b

$$V = k_0 w \sqrt{(\beta/k_0)^2 - N(0)^2}$$

$$b = ((\beta/k_0)^2 - N(\infty)^2) / (N(0)^2 - N(\infty)^2)$$

.... with side diffusion
 — without side diffusion

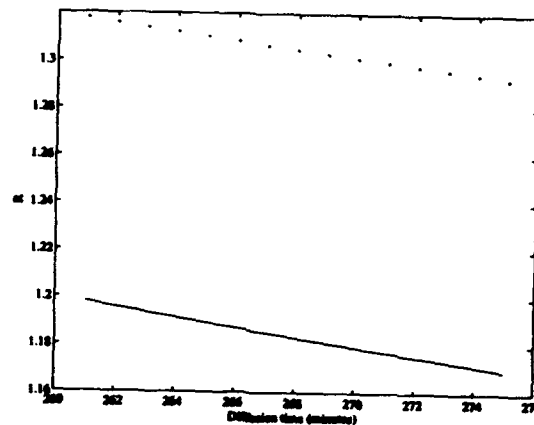


Fig 5: $R = \Delta\beta_c(1.31 \mu m) / \Delta\beta_c(1.55 \mu m)$ vs diffusion time (minutes)

($w = 6.4 \mu m$)

.... with side diffusion
 — without side diffusion

Micromachined optical bench for a surface plasmon sensor

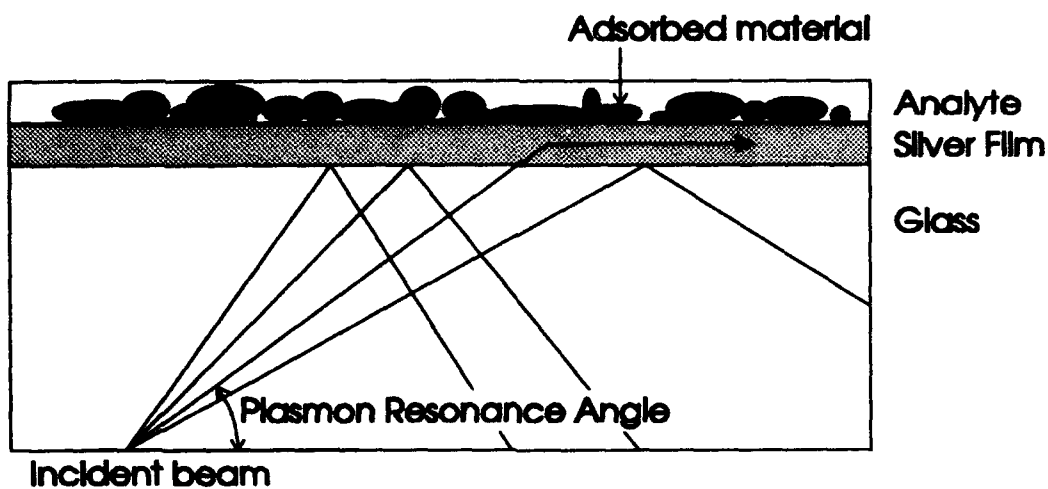
R. Garabedian, C. Gonzales, J. Richards
A. Knoesen, R.L. Smith, R. Spencer, S. Collins
Department of Electrical & Computer Engineering
University of California, Davis
Davis, California, 95616
(916) 752-8023

- **Introduction:**

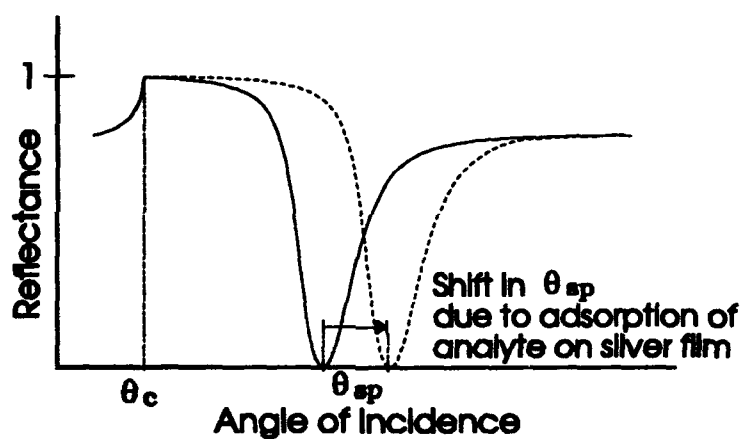
Surface plasmon sensors are used in chemical, gas, and bio-sensing applications. Detection is based on changes in the permittivity of thin interfacial layers^{1,2}. Most surface plasmon detection configurations require expensive optical equipment and a stable optical bench. Thus, surface plasmon sensors have for the most part remained in laboratory environments. The sensors employ a beam of transverse magnetic (TM) polarized light incident through a substrate onto a thin metal film, e.g. Ag or Au. The metal film is chemically sensitized, and exposed to an analyte (see Figure 1.) Above the critical angle, θ_c , the light is totally reflected from the substrate-metal interface, except at a distinct angle of incidence where a surface plasmon mode is generated. At the surface plasmon angle, θ_{sp} , the reflectance reaches a minimum. θ_{sp} is very sensitive to dielectric changes in close proximity to the metal-analyte interface. If the film is sensitized to selectively bind a prescribed chemical, X, a change in permittivity will occur resulting in a shift in θ_{sp} , which can be used to obtain a quantitative measure of the chemical activity of X in the analyte. The basic configuration is shown in Figure 1. All surface plasmon sensors require four basic elements: a source of TM polarized light; a method of coupling this light to a thin metal film through glass so as to achieve incidence angles above the critical angle of reflection; a means of providing a range of incidence angles; and a detector to measure the reflectance as a function of the angle of incidence.

- **System design**

A surface plasmon sensing microsystem is implemented using silicon micromachining and hybrid microelectronics technologies. The system integrates optical, mechanical and electronic elements in a hybrid package, roughly $1 \times 2.5 \text{ cm}^2$.



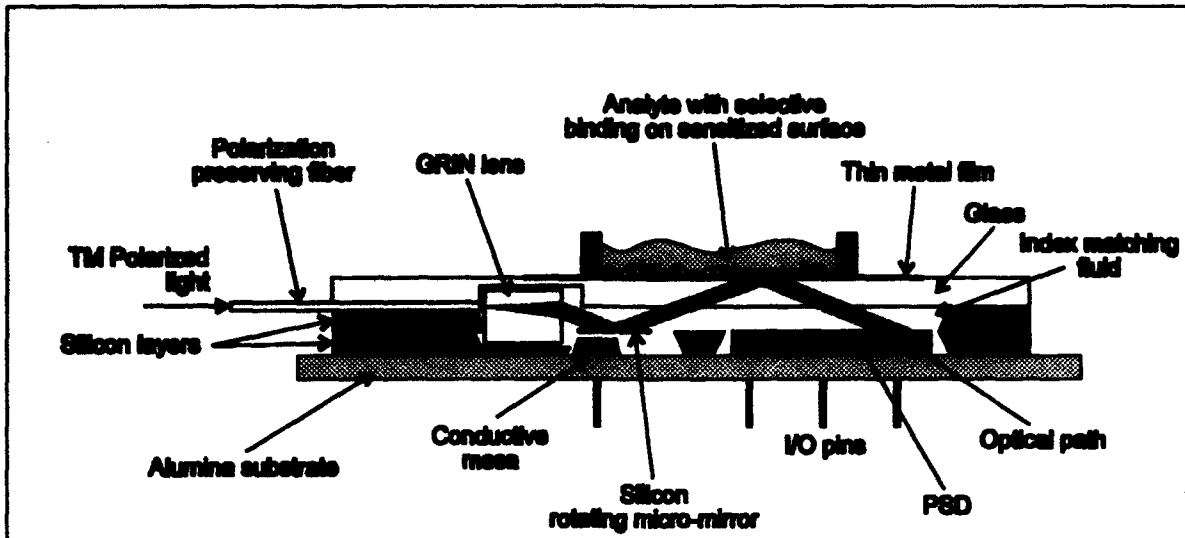
(a) Basic configuration of the surface plasmon sensor



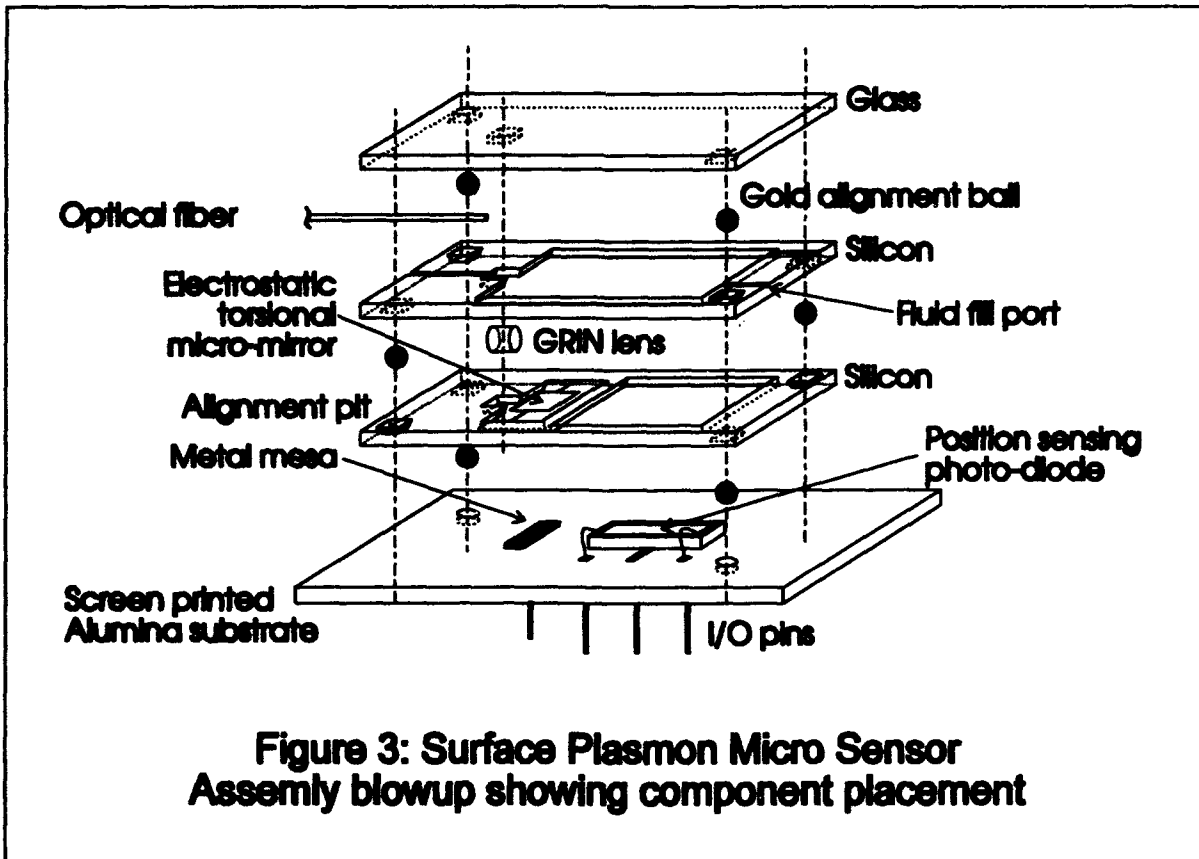
(b) Reflectance vs. incidence angle curve showing θ_{sp} above the critical angle

Figure 1: Surface Plasmon Resonance sensor principle

The complete sensor package is shown in Figure 2. Critical elements include the polarization preserving single mode fiber, collimating lens, a rotating micro mirror, index matching fluid, and precision component-to-component alignment. Figure 3 depicts a blowup of the system components and assembly.



**Figure 2: The Surface Plasmon Sensing Microsystem:
Functional schematic of the miniature optical bench**



**Figure 3: Surface Plasmon Micro Sensor
Assembly blowup showing component placement**

The sensor design employs a variety of materials and fabrication techniques including a laser drilled alumina substrate with printed thick film conductors, two anisotropically etched silicon layers which contain the micro-mirror and lens-to-fiber alignment structure, a position sensitive photo diode, and a machined glass layer. The four layers are joined using several bonding techniques, with the layers positively registered to one another by 0.5 mm metal balls and matching alignment pits. The sandwich of four layers forms a sealed cavity. This cavity is filled with index matching fluid allowing light coupling into the glass layer above the critical angle.

The fiber/lens alignment is accomplished with matched anisotropically etched v-grooves in a single silicon layer. The structure is defined photolithographically, yielding extremely close tolerances. The fiber is intentionally offset from the lens center in order to produce a collimated beam which exits the lens at a small angle toward the mirror plate. The micro mirror is a 2.5mm square plate, suspended by two center torsional silicon tethers. A voltage applied between the mirror and the mesa structure below causes an electrostatic attraction which rotates the mirror about the axis of the tether and scans the light beam toward the metal film. Index matching fluid in the sensor cavity allows light to enter the glass at angles above the critical angle without a prism or grating. Finally, the position sensing photo diode (PSD) simultaneously measures the position and the intensity of the reflected optical beam. The angle of incidence at the metal film is geometrically related to the spot position on the PSD, and can be calculated off-board. In operation, the incident angle is scanned by rotating the micro-mirror. Position and intensity data are collected during the scan, and are transformed to yield reflectance as a function of incidence angle. A base-line scan can be performed before the sensitized film is exposed to analyte. After exposure to analyte, any bound material on the metal surface will result in a shift of the reflectance minimum, indicating the presence of the chemical to which the surface was sensitized.

- Conclusion

The microfabricated surface plasmon sensor is a hybrid device that integrates optical, mechanical, and electronic components. Elements which are common to numerous electro-optical systems are integrated, demonstrating the feasibility of a miniature micromachined optical bench. System miniaturization is achieved with elements including a single mode optic fiber and collimating lens, a scanning rotating micro mirror, index fluid coupling, multi-substrate bonding, and positive component to component alignment.

References:

- ¹ C. Nylander, B. Liedberg, and T. Lind, "Gas detection by means of surface plasmon resonance," *Sensors and Actuators*, vol. 3, pp. 79-88, 1982
- ² B. Liedberg, C. Nylander, and I. Lundstrom, "Surface plasmon resonance for gas detection and biosensing," *Sensors and Actuators*, vol. 4, pp. 299-304, 1983



Novel Materials and Devices

IMC 1:30pm-3:15pm
Mesquite A

Hermann A. Haus, *Presider*
Massachusetts Institute of Technology

Recent Developments in Polymeric Devices

Winfried H.G.Horsthuis, Jean-Luc P.Heldeman, Marcel M.Klein Koerkamp,
Benno H.M.Hams

Alzo Research Laboratories Arnhem, Corporate Research
and

Gustaaf R.Möhimann
Alzo Electronic Products bv.

P.O.Box 9300, 6800 SB Arnhem, The Netherlands
phone: +31 85 662753; fax: +31 85 662669

1. Introduction

In contrast with the limited variety in inorganic electro-optic crystals, an infinite series of different electro-optic polymeric materials can be formed, since these polymers may consist of arbitrarily combinations of, usually organic, building blocks. The chemical synthesist has a large freedom in his or her choice of these building blocks, the way how they are interconnected and the total number of building blocks forming a macromolecule or polymer chain.

This property results in the possibility to individually tune several key characteristics of the material by changing just parts of the macromolecule. This advantage has become more and more attractive since computer automated molecular design has become a mature field. Presently, researchers can first calculate the properties of a novel molecular design, before the tedious process of the chemical synthesis commences. This has resulted in a much more efficient effort in the development of new polymeric materials, such as in the field of nonlinear optical polymers.

2. Materials development

The basic requirements of polymers for integrated optics applications can be well defined [1], and chemical engineers need to translate these properties into materials characteristics. The most critical issues are: low optical losses in the near-infrared, high nonlinear coefficients and a high thermal stability.

2.1 Low loss

Losses in polymers have two major sources: intrinsic losses due to optical absorption, and extrinsic losses due to scattering at imperfections. The first are dominant in most polymer waveguide systems reported thusfar. Two different effects can be distinguished, absorption caused by the long wavelength tail of electronic transitions, and the absorptions caused by vibrational overtones in the infrared. To reduce the first contribution, nonlinear moieties in electro-optic polymers should have absorption maxima far away from the wavelength for its intended use. Most systems (DANS, diazo-dyes) have a λ_{max} between 350 and 500 nm, which will cause no excess losses in the wavelength region between 1 and 1.55 μm . However, the vibrational overtones do cause significant losses in this wavelength region. Especially hydrogen bonds, such as O-H and C-H, exhibit significant absorptions. These can be eliminated by chemical modifications of the materials. Substitution of the hydrogen atoms by heavier species results in a red shift of the overtone absorptions, leaving a highly transparent window. This has been demonstrated in several polymer materials [2].

2.2 High electro-optic coefficients

The net electro-optic effect in (poled) polymers is based on the first order hyperpolarizability (β) of the active moieties and the poling induced polar order. Molecular modelling has been used to calculate the β of many molecules. These molecules consist of electron donating and electron accepting groups connected with a π -electron system. Well known examples of high- β molecules are substituted stilbenes ($300 \cdot 10^{30}$ esu) and diazo-dyes. Molecules with much higher β 's have been realized [3], but the use of these elongated molecules is presently hindered by their adverse effects on other key properties of the polymers, such as a good processability.

2.3 Thermal Stability

Poled polymers depend on the (thermal) stability of the polar order of the active molecules. The polar order is induced at elevated temperatures, but will also relax to a certain extent at higher temperatures. In solid solutions, where the active groups are dissolved in the polymer, the rotation of these groups is hindered only by the size and shape of the group in comparison to the free volume in the polymer. A major improvement is achieved with a covalent attachment of these groups to the polymer backbone, either in the mainchain or as pendant groups, the so-called sidechain polymers. If the polymer forms a network by crosslinks between backbones or via the sidechains, an even higher stability might be obtained. However, crosslinking should then be performed during or after poling, which implies a significant complication in the realization process of devices. Moreover, linear polymers with very high softening points (T_g) are available, which can lead to electro-optic polymers with a long term stability in excess of 150°C.

3. Polymer device processing

Polymers are in general attractive materials for mass production methods. A broad range of processing technologies has been established, including thin film processes such as spincoating, spraying, casting or extrusion. Integrated optic devices require a polymeric multilayer with stringent tolerances in thickness and homogeneity. Such layers can routinely be obtained using spincoat techniques, which results in a thickness tolerance of better than 2% (40 nm for 2 μ m thick films). Once a high quality multilayer has been deposited, channel waveguides can be realized with a variety of techniques. Examples are local poling [4], wet or dry etching of (inverted-) ridges, photopolymerization [5], photobleaching [6] etc. Especially the photoinitiated processes result in smooth channels with low scattering losses, and a flat topography, facilitating high resolution lithography on top of the waveguide system.

The waveguides are subsequently poled, using either a corona discharge (usually in case of crosslinkable systems) or a two-electrode system. When prepared under appropriate clean room conditions, very strong poling fields can be achieved, in excess of 200 V/ μ m. These field strengths result in electro-optic coefficients r_{33} in the range of 40 pm/V for side chain polymers including DANS or DR1 moieties. With a T_g of 140°C of the polymer, the polar order is maintained for several days at temperatures around 100°C [7]. A further increase of T_g can result in acceptable stabilities over long periods of time.

A final key issue in device processing is the interfacing with fibers, or in other words, the pigtailling of these devices. Apart from the development of a pigtailling *technology*, the mode sizes of fiber and device should match perfectly. This implies that both the refractive index contrasts and the core thicknesses of fiber and polymer waveguide should be identical. This can easily be achieved in polymers, since refractive indices can be tuned by slight chemical modifications, and layer thicknesses are well under control. However, the required relatively thick layers have disadvantages as well. First, the switching voltage in electro-optic devices depends linearly on the field strength in the active polymers, which is inversely proportional to the total layer thickness. Secondly, the low index contrast has adverse effects on the minimum radii of curvature of channel guides, resulting in an increase in device length, hence an increase in optical losses. These conflicting requirements in modesizes requires a case-to-case analysis to determine the optimal solution for each device developed. For complicated cascaded designs, such as $n \times n$ switching matrices, the use of thin high contrast layers could be more attractive, despite the increase of pigtailling complexity by adding extra optical components to compensate for the mode mismatch between fiber and device.

4. Current status of polymeric devices

Typical results of present efforts in polymeric devices come close to the performance of competing technologies (i.e. LiNbO₃) (switching voltages, extinction coefficients), or even show an increased level of performance (speed). Optical losses and stability need further improvements, but these are considered to be demonstrated within 1 or 2 years from now.

The results achieved can be described in terms of general device performance, or as a set of separate materials characteristics. The following examples indicate the current status along both lines.

4.1 Electro-optic modulators and switches

Mach-Zehnder interferometers have been extensively studied mainly because the relative simplicity of the waveguide design, and the straightforward performance analysis. It has been demonstrated that high quality modulators can be realized, with low switching voltages (< 5V) and high extinction

coefficients (>20 dB) [7]. More complicated designs have demonstrated the high speed operation of polymers [8], where the speed is limited by electrode design, instrumentation and electrical termination rather than materials properties, in contrast to LiNbO_3 .

Space switches are more difficult to design, especially in the case where detailed insight in the mode profiles of waveguides is missing. Locally poled and bleached waveguides have complicated mode profiles, deviating from the simple step index or diffusion profiles. Until recently, results were often based on non-optimized designs, showing the basic potential of these devices rather than the limits. Nevertheless, space switches with acceptable switching voltages and extinction ratios have been reported [7].

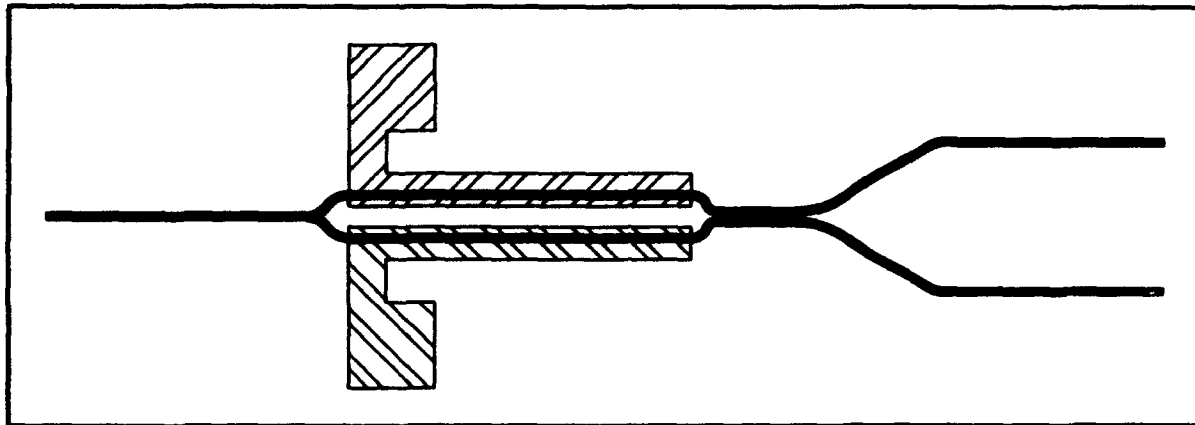


Fig.1. Basic design of polymer electro-optic 1x2 switch.
channel width: $4 \mu\text{m}$, gap: $7 \mu\text{m}$; MZ-length: 21 mm, DC-length: 2.3 mm

Using design rules for bleached polymers, Akzo now have realized electro-optic 1x2 space switches with very good performances. The basic design is depicted in Figure 1, simulations were based on a bleaching induced lateral refractive index contrast of 0.005.

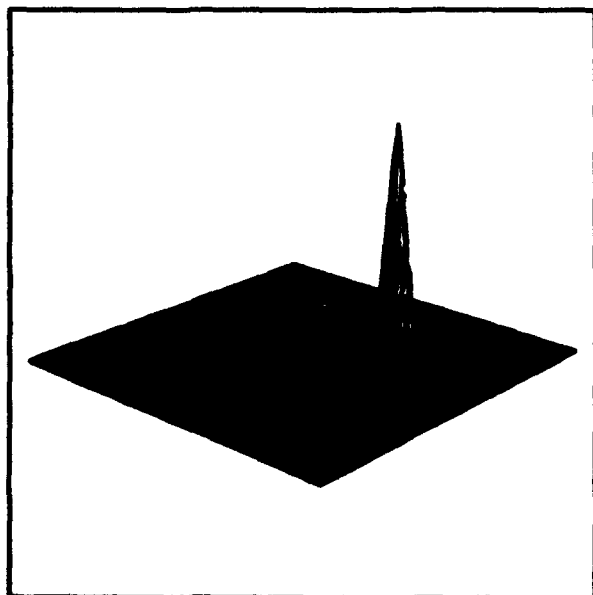


Figure 1a. Camera output of switch: 0 V

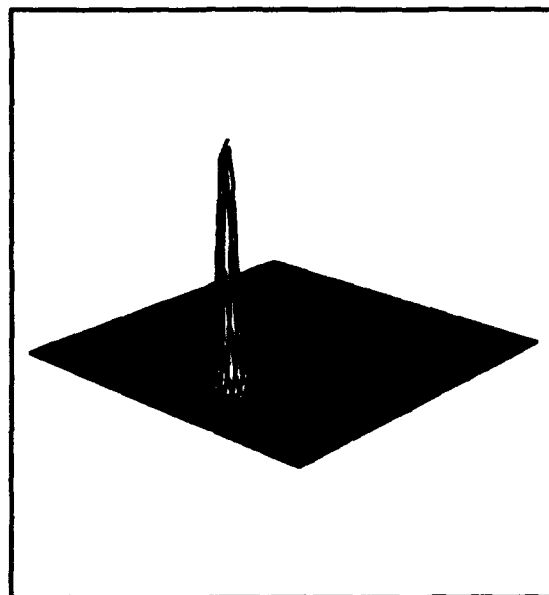


Figure 1b. Camera output of switch: 8 V

Figures 2a and b show the two output states of the 1x2 spatial switch with 0 and 8.5 V drive voltage. Extinction coefficients well over 20 dB are observed, with a driving voltage of 8.5 V for the 21 mm long electrode. This result demonstrates that high quality devices can be realized if the design is optimized for the polymer processing used. As mentioned before, thermal stability, insertion losses and DC-drift observations require further materials and processing improvements for the development of market acceptable devices.

4.2 Thermo-optic switches and modulators

This category of devices can find applications in areas where speed is not of prime importance, such as distributive and protective switches in networks. Thermo-optic devices are based on the $\Delta n/\Delta T$ effect of the polymers, where a heated polymer section will exhibit a decreased refractive index. This effect allows efficient designs, since the change in refractive index can be very high. Digital optical switches have been demonstrated with extinctions well above 20 dB, and switching powers in the order of 100 mW [9]. Thermal stability of these devices is less of a problem, since no polar order is required, reducing the thermal stability issue to a mechanical and chemical integrity. Present polymers (crosslinked or linear) can be used at temperatures above 100°C. Main improvement in this field will be the reduction of insertion losses, the optimization of the mode match with fibers and decreased (intrinsic) optical losses.

5. Conclusions

The field of polymeric integrated optic devices shows a rapid progress. Electro-optic devices can routinely be realized with standardized processes, resulting in devices which show a level of performance close to competing technologies. Present R&D is strongly focused on the reduction of optical losses, the improvement of thermal stability and the efficiency of the pigtailling process. The first attempts to arrive at intrinsically low loss electro-optic polymers show the validity of theoretical predictions with respect to chemical modifications. Polymer chemistry provides the necessary tools to obtain nearly perfect mode matching to fibers, however, a careful analysis of the optimization of the total device performance is required, balancing mode matching with other characteristics.

6. References

- [1] R.Lytel, "Applications of electro-optic polymers to integrated optics", SPIE Proceedings, 1216, (1990), pp 30-39.
- [2] S.Imamura, R.Yoshimura, T.Izawa, "Polymer Channel waveguides with low loss at 1.3 μm ", Electronics Letters, 27, (1991), pp 1342-1343.
- [3] R.A.Huljts, G.L.J.Hesselink, "Length dependence of the second order polarizability in conjugated organic molecules", Chem.Phys.Letters, 156, (1989), pp 209-212.
- [4] J.I.Thackara, G.F.Lipscomb, M.A.Stiller, A.J.Ticknor, R.Lytel, "Poled electro optic waveguide formation in thin-film organic media", Appl.Phys.Lett., 52, (1988), pp 1031-1033.
- [5] P.R.Ashley, T.A.Tumolillo, "Channel waveguides in electro-optic polymers using a photopolymer cladding technique", Appl.Phys.Lett., 58, (1991), pp 884-886.
- [6] M.B.J.Diemeer, F.M.M.Suyten, E.S.Trommel, A.McDonach, J.M.Copeland, L.W.Jenneskens, W.H.G.Horsthuis, "Photoinduced channel waveguide formation in nonlinear optical polymers", Electr.Lett., 26, 1990, pp 379-380.
- [7] G.R.Möhlmann, W.H.G.Horsthuis, B.H.M.Hams, "Nonlinear polymers and devices", SPIE Proceedings, 1512, 1991, pp 34-39.
- [8] D.G.Girton, S.L.Kwiatkowski, G.F.Lipscomb, R.S.Lytel, "20 GHz electro-optic polymer Mach-Zehnder modulator", Appl.Phys.Lett., 58, (1991), pp 1730-1732.
- [9] W.H.G.Horsthuis, F.C.J.M.van Veggel, B.H.M.Hams, C.P.J.M.van der Vorst, J.L.P.Heideman, H.W.Mertens, M.van Rheede, "Photonic polymers in passive and active waveguide devices", SPIE Proceedings, 1775, (1992).

Demonstration of a Polymeric Registered Multilevel Mach-Zehnder Intensity Modulator Array

Thomas A. Tumolillo, Jr.

National Research Council Research Associate, Tel: (205) 876-1902, Fax (205) 876-4759
and

Paul R. Ashley

Weapons Sciences Directorate, RD & E Center, AMSMI-RD-WS-CM, U.S. Army Missile
Command, Redstone Arsenal, AL 35898-5248, Tel: (205) 876-7484, Fax (205) 876-4759

There has been considerable progress made in the demonstration of guided wave devices which use electro-optic polymers as the active layer [1,2,3,4,5,6]. Recently a multilevel polymer waveguide system with an intensity modulator in the top level has been reported [7]. Reported here is a demonstration of a registered multilevel Mach-Zehnder intensity modulator array, including two independent modulator levels vertically aligned. This demonstration establishes the feasibility of using polymer materials to fabricate multilevel active structures not possible in other materials such as LiNbO_3 .

Figure 1 illustrates in detail a cross sectional end face view of the device showing the relative scale all the layers, which include ten distinct spin coated layers. Two arms of one Mach-Zehnder electro optic intensity modulator are shown in the figure. There are twenty modulators in the device, with ten in each level. The two levels of modulators are identical and separated by a high resistivity electrical buffer layer as well as a separate ground plane. Shown in Figure 2 is an illustration of the multilevel modulator array emphasizing the most important layers of the device. The device utilizes a push-pull electrode configuration and the waveguides as well as electrodes are registered to the glass substrate using the gold benchmarks.

The waveguides used in this device were fabricated by a non-contact projection printing technique which images the waveguide pattern into a UV curing cladding layer (Norland 61). Fabrication details of this technique have been previously reported [8].

The glass substrate was coated with 2500 Å of gold and then patterned with photoresist to form the lower ground plane and alignment marks for level to level registration of waveguide patterns as well as electrodes. Pattern placement is within 0.5 μm . The substrate is first spin coated with a 3.5 μm lower buffer layer (NOA 61) and fully cured by UV exposure (450 mw-min/cm²). Relief of the polymer in the electrode pad areas is accomplished by shadow mask during UV curing at each layer. Next the sensitized NOA 61 is spin coated, patterned by UV exposure, and developed. The patterned layer is then coated with the active polymer material (2 μm thick). The electro-optic polymer used in the device was DOW Chemical TP7 (a thermoplastic polymer). This polymer has a T_g of 138°C; typical electro-optic coefficient for TP7 is $r_{33} = 10 \text{ pm/V}$ at a wavelength of 1.3 μm when poled at a field strength 70 V/ μm . The polymer is then baked under vacuum at the T_g temperature for 2 hours to remove residual solvent. The sample is then overcoated with a 3.5 μm upper cladding layer of NOA 61, given a 5 minute UV soft cure (76 mw-min/cm²) followed by a 3 hour bake to fully cure the cladding layer. Next a 2500 Å thick layer of gold is deposited by electron beam evaporation. The gold is patterned into the the poling/switching electrodes using standard photolithographic and chemical etching techniques. The electrodes are 7.5 mm long and complete the fabrication of the first level modulator. Next a 8 μm thick electrical buffer layer as shown in Figure 1 is spun on. The buffer used was a thermoset polymer, DOW Chemical OL2. This buffer layer is thermally cured for 2 1/2 hours at 180°C. The material was chosen to have a resistivity much

greater than that of the NOA 61, near the poling temperature of 140° C as well as throughout the operating temperature range. All the fabrication steps just described are then repeated to form the second level modulator. The second level is accurately registered to the first level during the patterning exposure step using the ground plane alignment marks. The final step in fabrication is the application of a 4 μm overcoat layer for electrical protection against dielectric breakdown and mechanical protection during cutting and polishing.

Shown in Figure 3 is a photograph of the polished end face of the device. Note that the two vertically aligned waveguide levels and electrical buffer layer are distinguishable. The resistivity of the TP7 active polymer, NOA 61 Cladding, and OL2 materials were all measured as a function of temperature and these results are summarized in Table 1. From this table the resistivity of the TP7 and NOA 61 are seen to be within a factor of two at both the poling temp of 140° C, and at the operating temperature (25° C). The resistivities were measured using electrical fields of 70 $\text{V}/\mu\text{m}$ and 5 $\text{V}/\mu\text{m}$ at the corresponding poling and operating temperature respectively to account for the field dependant differences in resistivity. The resistivity of the OL2 is higher than the other materials by well over a factor of 10 at both temperatures. These resistivities ensure that the device poles and operates efficiently, by dropping most of the field across the polymer, while the high resistivity of the electrical buffer layer serves to effectively isolate the lower level from the ground plane of the upper device.

The device was tested at a wavelength of 1.3 μm with TM polarized light using end fire coupling. Shown in Figure 4 is the output of a two by two group of vertically stacked waveguide end faces. The mode size is nearly circular with dimensions of 3.3 μm wide by 2.7 μm deep. The waveguide separation between adjacent devices is 50 μm and the vertical separation between devices is 21 μm . Both modulator levels were poled at 70 $\text{V}/\mu\text{m}$ at 140° C using device electrode poling [9]. V_{π} was measured to be 25 V. Optical cross talk measured between the levels by exciting a modulator in one level and measuring the optical output in the corresponding waveguide of the other level was found to be less than -60 dB (instrument limited). Electrical cross talk between modulator levels was measured by applying a voltage to a modulator on one level while monitoring the output of a corresponding modulator on the other level and found to be less than -51 dB (instrument limited). This large degree of electrical isolation illustrates the effectiveness of the isolation ground plane between modulator levels. Total insertion loss of a 2 cm long device was measured to be 6.6 dB, with 0.44 dB of this loss estimated to be due to mode overlap and reflection losses at the input.

In conclusion we have demonstrated a new polymeric multilevel Mach-Zehnder modulator array. Results indicate that good electro-optical performance and electrical isolation between levels can be achieved by a design using specific polymer materials which optimize resistivity. Accurate registration has been demonstrated between the levels making possible two-dimensional device structures and level to level interactions.

REFERENCES

1. Ashley, P. R., and T. A. Tumolillo, Jr., *Appl. Phys. Lett.*, 58, 884 (1991).
2. Ashley, P. R., and T. A. Tumolillo, Jr., *Integrated Photonics Research, OSA Tech. Dig. Series*, 8, 87 (1991).
3. Haas, D. R., and H. T. Man, *Integrated Photonics Research, OSA Tech. Deg. Series*, 8, 133 (1991).
4. Teng, C. C., *Appl. Phys. Lett.*, 60, 1538 (1992).

5. Mohlmann, G. R., W. H. G. Horsthuis, J. W. Mertens, M. B. J. Diemeer, F. M. M. Suyten, B. Hendriksen, C. Duchet, P. Fabre, C. Brot, J. M. Copeland, J. R. Mellor, E. Van Tomme, P. Van Daele, and R. Beats, *Proc. SPIE*, 1560, 426 (1991).
6. Van Eck, T. E., A. J. Ticknor, R. S. Lytel, and G. F. Lipscomb, *Appl. Phys. Lett.*, 58, 1558 (1991).
7. Girton, D. G., R. Lytel, and G. F. Lipscomb, *OSA Annual Meeting*, TuA3, 49 (1992).
8. Tumolillo, Jr. T. A., and P. R. Ashley, *Proc. SPIE*, 1559, 65 (1991).
9. Tumolillo, Jr. T. A., and P. R. Ashley, *IEEE Photonics Tech. Lett.*, 4, 142 (1992).

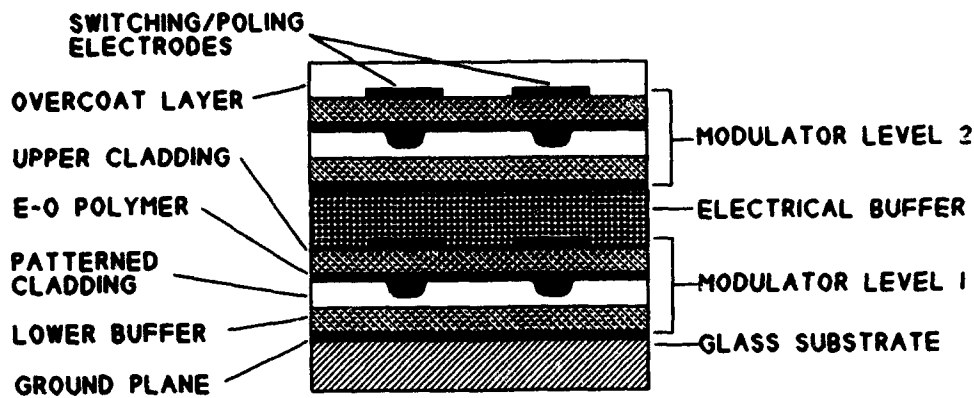


Figure 1. Cross sectional diagram of the multilevel modulator array.

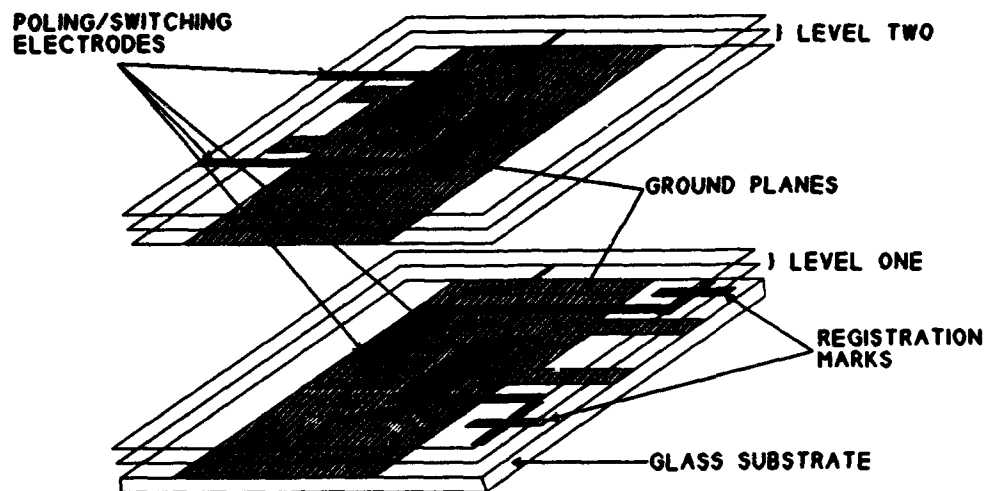
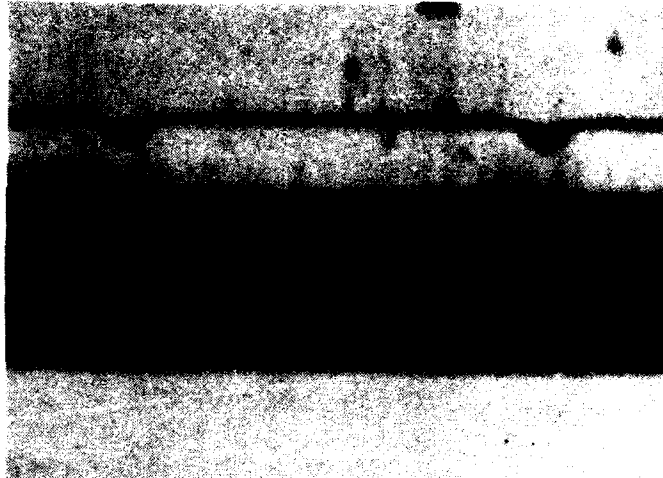


Figure 2. Exploded view of multilevel modulator design.

Figure 3. Polished end face of multilevel waveguide showing four channels. Spacing between waveguides is 50 μm .



Temperature Poling Field	25° C 5 V/ μm	140° C 70 V/ μm
NOA 61	$6.0 \times 10^{15} \Omega\text{-cm}$	$6.5 \times 10^{12} \Omega\text{-cm}$
TP7	$3.3 \times 10^{15} \Omega\text{-cm}$	$4.0 \times 10^{12} \Omega\text{-cm}$
OL2	$1.0 \times 10^{17} \Omega\text{-cm}$	$2.1 \times 10^{14} \Omega\text{-cm}$

Table 1

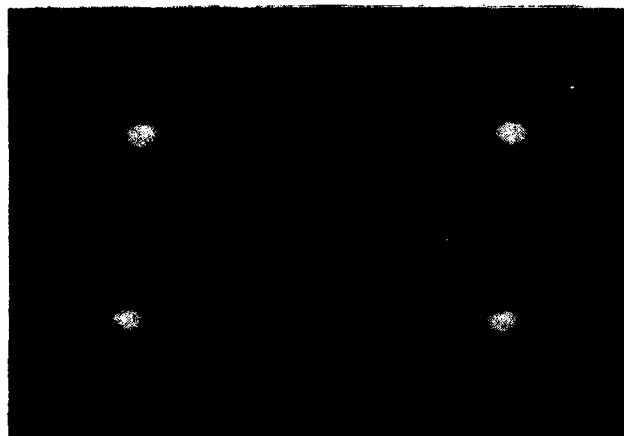


Figure 4. Optical output of four single mode waveguides in the array.

Compact Thin-Film Waveguide Isolator

M. Levy, I. Ilic, R. Scarmozzino, and R.M. Osgood, Jr.
Columbia University Microelectronics Sciences Laboratory
New York, NY 10027
Phone: (212) 854-8980
FAX: (212) 932-9421

R. Wolfe
AT&T Bell Laboratories
Murray Hill, New Jersey 07974

C.J. Gutierrez,* and G.A. Prinz
Naval Research Laboratory
Washington, D.C. 20375

Introduction

There is a persistent need for a compact optical isolator in optical packaging and integrated optical circuits. Current isolator technology is limited by the requirement for bulk magnets to induce Faraday rotation in YIG or Bi-YIG crystals. A thin-film magnet would allow a considerable reduction in size relative to current designs, and, more important, it would also open up the possibility for fully integrating optical isolators on a single wafer.

Within the last decade there have been significant advances in thin-film magnets.^{1,2} The availability of metallic films, which could serve as miniature permanent magnets, opens up the possibility of fabricating very compact magneto-optic structures. In addition, recent advances in Bi-YIG film technology have made it possible to fabricate ridge-waveguide Faraday-rotation isolators with isolation ratios of -35 dB.³

In this paper we demonstrate for the first time that these new technologies can be used to make a thin-film-magnet optical isolator. The basic structure of this device consists of a magnetic film on top of a Bi-YIG waveguide, separated by an appropriate buffering material

(Fig. 1a). Alternatively, the film may be placed on the sides of the waveguide ridge (Fig. 1b). Our tests use epitaxial iron-cobalt films, but the results are applicable to other magnetic films.

Device Fabrication

The 1.5- μm -thick iron-cobalt alloy films used in our experiments are single-crystal films (30% iron, 70% cobalt), grown by molecular beam epitaxy on (110) GaAs substrates. Hysteresis studies of these films show a flat rectangular response and a coercivity of about 50 Oersted, with a remanent $4\pi M$ of about 21,000 Oersted.⁴ The waveguides used in these experiments were triple-layer Bi-YIG films³ designed to support single TE and TM modes. The films were grown by standard liquid phase epitaxy on (111)-oriented gadolinium-gallium-garnet substrates and were subjected to annealing procedures to ensure near-planar magnetization anisotropy of the upper layers. The linear birefringence was reduced to zero at a wavelength near 1.5 μm by etch-tuning the thickness of the top surface.^{3,5} Ridge waveguide patterns were then etched into the surface, parallel to one of the easy axes of magnetization of the Bi-YIG sample. The Faraday rotation in the Bi-YIG films was measured to be 127°/cm at a wavelength of 1.55 μm . The sample was therefore cut to a length of 3.55 mm to provide 45° of rotation, and the edges were optically polished.

Experimental Results

A fully-magnetized 4 mm iron-cobalt alloy film, together with its GaAs substrate, was placed film-side down on top of the Bi-YIG sample, its magnetization parallel to the waveguiding ridges. The iron-cobalt film was found to induce a large Faraday rotation of 30-45°, indicating that 80-100% of the length of the Bi-YIG was saturated.

In order to measure an effective isolation ratio for our device, the iron-cobalt piece was placed with its direction of magnetization parallel to the length of the waveguide ridge, and the analyzer was set at the extinction angle for this geometry. After measuring the power transmitted through the analyzer, the iron-cobalt film was rotated 180° so that its magnetization was oriented antiparallel to the original direction of magnetization, and the transmitted power was measured again. Following R. Wolfe *et al.*,³ the ratio of the detected intensities for the two magnetization directions was taken as the isolation ratio for the ridge waveguide isolator. The value obtained was 120 to 1, corresponding to an isolation ratio of -21 dB.

Conclusion

In summary, we have demonstrated the first compact thin-film-magnet magneto-optic waveguide isolator using iron-cobalt and Bi-YIG thin film technologies. The device exhibits an isolation ratio of -21 dB. Further work is underway to explore the feasibility of a fully integrated structure, possibly using direct metal-film deposition.

The authors would like to acknowledge the support of DARPA/AFOSR, NCIPT, and ARO (M.L., I.I., R.S., and R.M.O., Jr.) as well as ONR (C.J.G. and G.A.P.) and the NRC/NRL Postdoctoral Associate program (C.J.G.).

References

1. Gary A. Prinz, *Science* **250**, 1092 (1990).
2. C.J. Gutierrez, J.J. Krebs and G.A. Prinz, *Appl. Phys. Lett.*, November 1992.
3. R. Wolfe, R.A. Lieberman, V.J. Fratello, R.E. Scotti, and N. Kopylov, *Appl. Phys. Lett.* **56**, 426 (1990).
4. M. McGlashan-Powell, R. Wolfe, J.F. Dillon, Jr., and V.J. Fratello, *J. Appl. Phys.* **66**, 3342 (1989).
5. R. Wolfe, V.J. Fratello, and M. McGlashan-Powell, *J. Appl. Phys.* **63**, 3099 (1988)

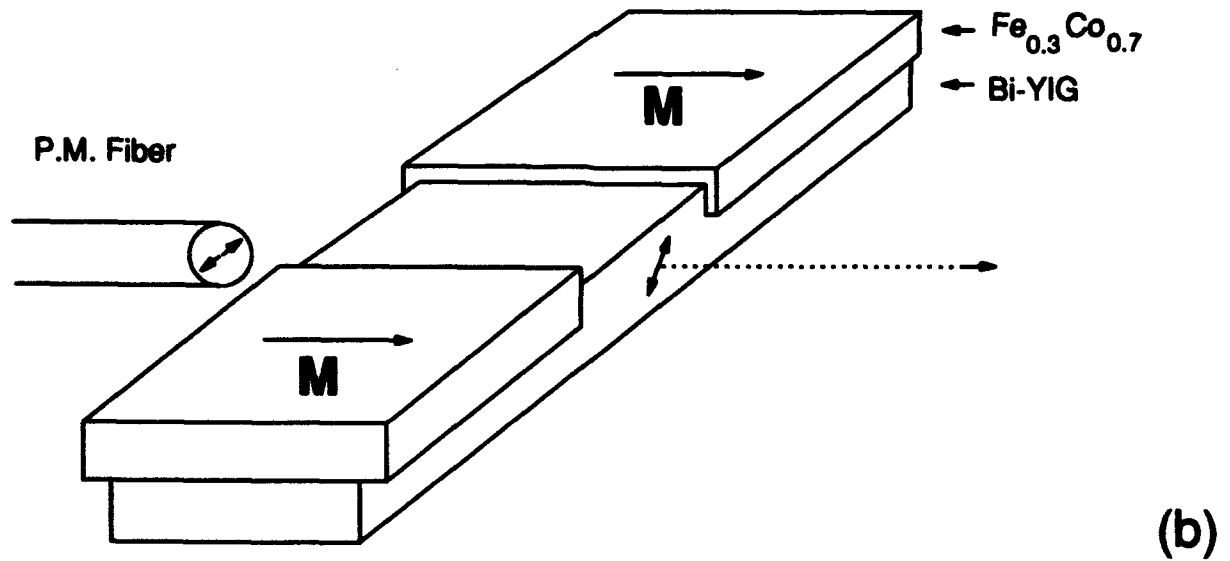
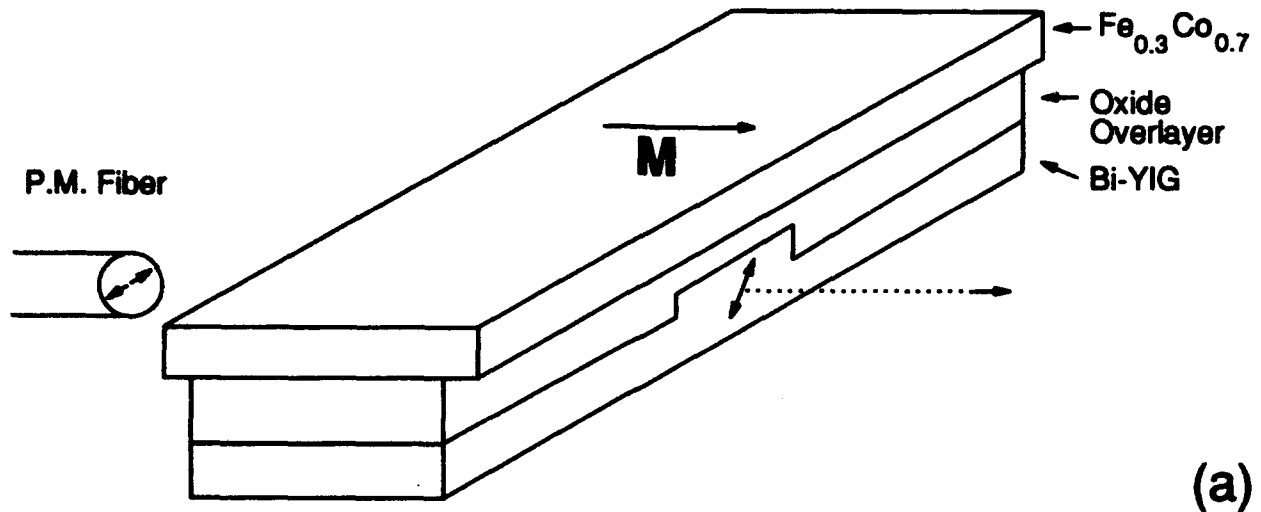


Figure 1. Illustration of thin-film-magnet magneto-optic isolator. Figure 1(a) shows placement on top of the waveguide and Fig. 1(b) shows lateral placement.

Low Loss Laminated Polarization Splitters

T. Sato, K. Shiraishi*, T. Sasaki, and S. Kawakami

Research Institute of Electrical Communication, Tohoku University

2-1-1 Katahira, Aoba-ku,

Sendai 980, Japan

Phone and Fax: +81 22 221 3572

*Faculty of Engineering, Utsunomiya University

2753 Ishii-machi, Utsunomiya 321, Japan

Phone and Fax: +81 286 62 6884

A laminated polarization splitter (LPS) [1] is a building block for a number of ultrasmall fiber-integrated optical devices. Figure 1 schematically shows the structure and performance of an LPS, consisting of alternately laminated dielectric materials with a high refractive index and a low index. Thicknesses of two kinds of layers are the same, and the period is sufficiently small compared to the wavelength λ . The optical properties of an LPS are the same as those of uniaxial crystal because of form-birefringence and the principal axis of the multilayer structure is perpendicular to the layers [2]. The projected light beam splits into an ordinary wave E_o polarized in the y direction and an extraordinary wave E_e polarized in the x direction. This paper discusses the fabrication of high-performance, low-loss a-Si:H/SiO₂ LPS's for 1.55 μ m wavelength region.

To start with, we present a specific example of application and show a typical structure and size. A polarization-independent fiber-integrated isolator [3], shown in Fig. 2, is proposed and demonstrated. Spatial walk-off polarizers are used for splitting an optical beam into two orthogonally polarized beams. In the ultimate configuration of such isolators, LPS's should be used as the spatial walk-off polarizers. Typical values of related parameters are shown in Fig. 2. For this specific example, the calculated diffraction loss of the isolator is 0.55dB [4]. If one wishes to keep the excess insertion loss (absorption or scattering) below 1dB, the attenuation constant of the LPS should be under $\sim 1 \times 10^{-3}$ dB/ μ m. The insertion loss of the previously fabricated LPS ($\sim 8 \times 10^{-3}$ dB/ μ m), however, is much larger than the one ($\sim 5 \times 10^{-4}$ dB/ μ m)

expected from absorption coefficients of the films. The extra loss is caused by scattering loss due to form-imperfection, that is microroughness at boundaries of layers. Reduction of the roughness is essential to obtain LPS's with a low insertion loss.

In our experiments, an rf magnetron sputtering system with the function of bias sputtering, schematically shown in Fig. 3, was used. Use of rf bias sputtering deposition is effective to obtain films having smooth surfaces [5]. A polycrystal silicon and a fused silica target are in the chamber. a-Si:H and SiO₂ alternate layers are fabricated by rotating the substrate electrode. Deposition conditions, summarized in Table 1, were determined so that films have the following optical and mechanical properties,

- (1) low absorption coefficients for a low insertion loss
- (2) high refractive index for a-Si:H and low index for SiO₂ to have a large split angle
- (3) low stresses for mechanical stability.

The stress of films, especially of a-Si:H films, deposited by bias sputtering increases with the power applied to a substrate electrode. In order to obtain LPS's with low stress and a flat surface, SiO₂ films are deposited by bias sputtering and a-Si:H films without. The measured refractive index and absorption coefficient of the a-Si:H films deposited under these conditions are 3.24 and 1×10^{-3} dB/ μ m, respectively, at $\lambda=1.55\mu$ m. Refractive index of the SiO₂ film is estimated to be 1.45.

The layers were deposited on a fused silica substrate $30 \times 30 \text{mm}^2$ and 1.5mm thick. The thickness of each film is 61nm and the total number of laminated layers is 1150. The magnitude of compressive stress of the multilayer structure is 1.8×10^9 dyn/cm², which is small enough for successive mechanical processes.

Figure 4 shows cross-sectional scanning electron microscope (SEM) photographs of the multilayer structure in the vicinity of the surface, where (a) and (b) corresponds to the sample deposited by bias sputtering in this work and one by normal sputtering in our earlier work [1], respectively. From Fig. 4 (a), it is found that each layer has a flat surface and geometrical imperfection disappeared.

The multilayer structure was sliced at $\theta=38^\circ$ (see Fig. 1), and sliced surfaces are polished to a sample thickness of 44 μ m. The measured split

angle is 16.7° at $\lambda=1.55\mu\text{m}$, which is in good agreement with the calculated value from refractive indices of the films.

Both sides of the sample surfaces are antireflection coated with reference to air. Near-field patterns of the output of E_o and E_e are uniform in the part of the LPS. The measured insertion loss excluding reflection loss of E_o and E_e are 0.16dB and 0.17dB, which corresponds to $3.6 \times 10^{-3}\text{dB}/\mu\text{m}$ and $3.9 \times 10^{-3}\text{dB}/\mu\text{m}$, respectively. The attenuation constants are reduced to half from that of a previously fabricated LPS ($\sim 8 \times 10^{-3}\text{dB}/\mu\text{m}$). The new loss figure is not low enough for use in a fiber-integrated isolator of Fig. 2. The present work, however, demonstrates that rf bias sputtering is in the right direction. In addition, the loss figure of this study is sufficiently low for several other applications such as an optical switch using liquid crystals [6]. If a completely flat multilayer structure is obtained, the insertion loss will reduce to the value, $< 5 \times 10^{-4}\text{dB}/\mu\text{m}$, expected from absorption of films.

In conclusion, it is found that rf bias sputtering method is effective to fabricate LPS's with a low scattering loss caused by the microroughness of boundaries between the a-Si:H and SiO_2 layers.

References and Comments

- [1] T. Sato, K. Shiraishi, K. Tsuchida, and S. Kawakami, "Laminated polarization splitter with a large split angle", Appl. Phys. Lett., vol. 61, 30, (1992).
- [2] M. Born and E. Wolf, Principles of Optics (Pergamon, Oxford, 1975), pp. 705-708.
- [3] K. Shiraishi, T. Chuzenji, and S. Kawakami "Polarization-independent in-line optical isolator with lens-free configuration", J. Lightwave Technol., to be published.
- [4] In a recent work, we used rutile polarization splitters. Their split angle is 5.7° , and the total thickness of the two rutile plates is 1.7mm. The diffraction loss of the isolator is 1.8dB.
- [5] T. Mogami, M. Morimoto, H. Okabayashi, and E. Nagasawa, "SiO₂ planarization by two-step rf bias-sputtering", J. Vac. Sci. Technol., B3, pp. 857, (1985).
- [6] O. Hanaizumi, Y. Otera, and S. Kawakami, unpublished work.

Table 1. The deposition conditions

	a-Si:H	SiO ₂
gas	Ar+H ₂ (5%)	Ar+O ₂ (10%)
gas pressure	3.6mTorr	2.0mTorr
substrate temperature	140°C	140°C
distance between electrodes	125mm	125mm

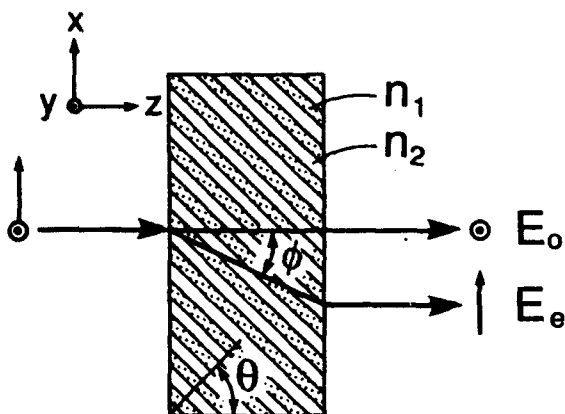


Fig. 1. The structure of a laminated polarization splitter (LPS).

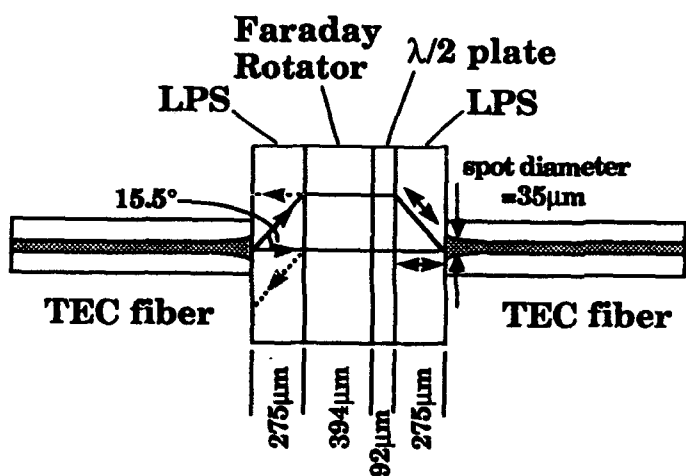


Fig. 2. Schematic illustration of a polarization-independent fiber-integrated isolator.

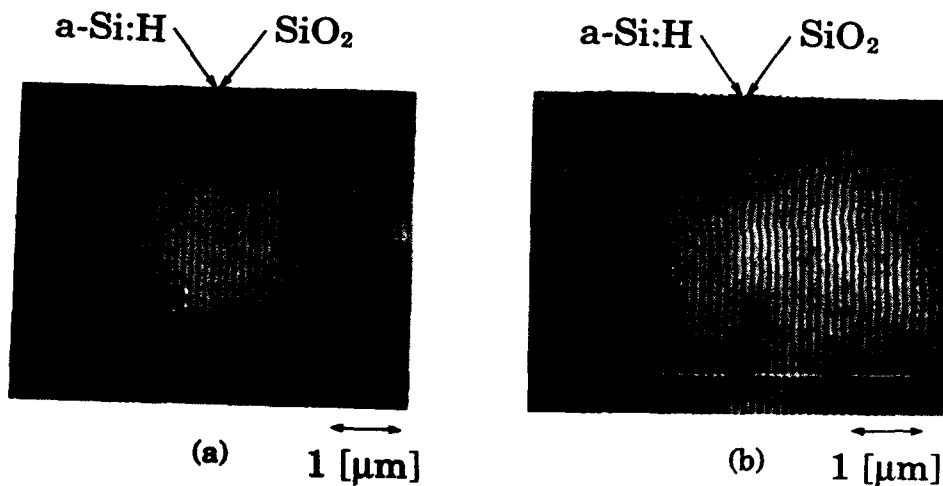


Fig. 4. Cross-sectional SEM photographs of the multilayers deposited by (a) bias rf sputtering and by (b) normal rf sputtering, respectively.

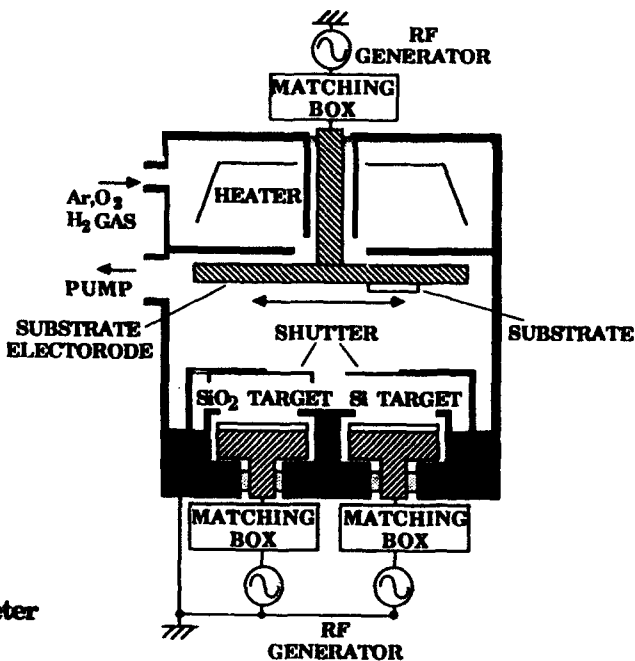


Fig. 3. The rf magnetron sputtering apparatus.

Use of Nematic Liquid Crystal Overlayer Cells to Form Planar Waveguide Mach-Zehnder Interferometer and Deflector

Joseph F. Revelli and Eric T. Prince
Eastman Kodak Company
Corporate Research Laboratories, Building 81
Rochester, New York 14650-2015
 (716)-477-5306

Attempts to take advantage of the large electro-optic effect in waveguides formed directly in liquid crystal (LC) films have met with limited success because of large propagation losses associated with thermal fluctuations of the long-range crystal ordering.¹ Recently, optical waveguide modulators² and switches³ have been formed using nematic LC overlayers on passive waveguides. In both cases, the use of LC overlayer cells on passive waveguides significantly reduced propagation losses due to scattering in the liquid crystal. The reduced propagation losses are a direct result of sampling the LC material only via the evanescent portion of the guided light.

Hu and Whinnery⁴ have analyzed the exact eigenmodes of inhomogeneous, anisotropic structures associated with LC waveguides. It was shown that a simplified three-layer model yielded excellent agreement with the exact results. The simplified model assumes that the three layers are uniaxial but homogeneous, and the effective thickness of each of the two outer boundary layers, ξ , depends on the voltage, V , applied to the LC cell, is given by

$$\xi(V) = t_{LC} \frac{V_C}{\pi V} \quad (1)$$

where t_{LC} is the thickness and V_C is the so-called "critical voltage" of the LC cell. The director, or direction of preferred LC molecular orientation in the middle layer, is maintained along the direction of the applied electric field. In general, V_C depends on both the LC material itself as well as the nature of the alignment layer.⁵

Where light is guided primarily in a passive waveguide with LC cladding, interaction between the light and the LC material is via the evanescent tail. In such a case, it is expected that the detailed nature of the boundary region between the passive waveguide and the LC material would play a major role in determining the change in propagation constant of the guided mode with voltage. In this paper, the simplified three-layer model of Hu and Whinnery is modified in order to analyze the LC-clad passive waveguide. First of all, only the outer boundary region of the overlayer cell immediately adjacent to the passive waveguide is included in the model. Secondly, the boundary region is divided into eight homogeneous and uniaxial layers of thickness $\xi(V)/8$, such that each layer has a different director angle. The angle that the director makes with the normal to the plane of the waveguide is assumed to vary in steps linearly from the value θ_B at the interface between the

passive waveguide and the LC overlayer cell to $\theta_C(V)$ at the center of the LC cell. As the applied voltage increases from V_C , θ_C decreases from θ_B to 0° . $\xi(V)$ also decreases with applied voltage according to Equation (1). θ_C and V_C are taken to be parameters that are adjusted to fit observed data.

For both the MZ interferometer and the deflector, the measure of performance is related to the number of waves of retardation, N_R , that can be generated for a given applied voltage. N_R is given by

$$N_R(V) = \Delta n_{\text{eff}}(V) \frac{L}{\lambda} \quad (2)$$

where $\Delta n_{\text{eff}}(V)$ is the change in effective index of the LC-clad waveguide as a function of applied voltage, L is the length of the cell, and λ is the wavelength of light in free space.

Figure 1a shows a cross section of the LC-clad waveguide structure. Values for the indexes and thicknesses of layers used in the model for both devices are given in Table I. The buffer layer was a thermal oxide grown on conductive silicon substrates. The silicon oxynitride was deposited by plasma-enhanced chemical vapor deposition, and the tantalum pentoxide was deposited by rf sputtering. SiO_x was evaporated at oblique incidence to form the alignment layers. The top half of the LC cell (not shown in Figure 1a) is an ITO-coated microscope slide with a SiO_x alignment layer. After the two halves of the LC cell were spaced one above the other with mylar spacers, the cell was filled with a nematic LC. Figure 1b shows a plan view of the devices. Note that in the case of the MZ interferometer, a rectangular top electrode patch of length $L = 12$ mm was used, whereas two electrically isolated prism-shaped electrodes of length $L = 19$ mm were used for the deflector. AC voltages (10 Hz to 20 KHz) were applied between the conductive substrate and the ITO upper electrode(s).

TM polarized light was coupled into the passive waveguides using either prism or grating couplers with the light propagating along the alignment direction of the LC molecules. Figures 2a and 2b show plots of N_R for the MZ interferometer at $\lambda = 633$ nm for the $m = 0$ and $m = 1$ modes (Figure 2a) and $\lambda = 830$ nanometers for the $m = 0$ mode (Figure 2b). As can be seen from Figure 2a, 100 waves of retardation was obtained for 50 Vrms for the $m = 1$ mode at $\lambda = 633$ nm. Propagation losses in the LC overlayer region for the $m = 1$ mode at $\lambda = 633$ nm were estimated to be 2 to 4 dB/cm with no voltage applied. Actual data points are shown to compare well with the theory for $\theta_B = 39^\circ$ and $V_C = 1.15$ volts.

Figure 3 shows a deflection angle plotted as a function of Vrms for both theory and data. In this device, $\theta_B = 24^\circ$ and $V_C = 0.3$ volts were used to fit the observed data. Note that the two separate sets of data shown plotted in Figure 3 correspond to the two independent prism-shaped top electrodes (i.e., "prism 1" and "prism 2" in the figure). One top prism electrode was shorted to ground, while the second was energized, followed by interchanging the two electrodes. Interchanging

the electrodes caused the beam to be deflected in opposite directions. The number of resolvable spots N_S should be related to the maximum deflection angle, $\Delta\theta_{MAX}$, according to the relationship

$$N_S = 2 \frac{\Delta\theta_{MAX}}{\delta\theta_{DIF}} \approx 2 \frac{\Delta n_{eff} L}{W_C} \left(\frac{\lambda}{W_B} \right)^{-1} = 2 N_R \frac{W_B}{W_C} \quad (3)$$

where $\delta\theta_{DIF}$ is the diffraction-limited divergence of a beam of diameter W_B and W_C is the width of the prism electrodes. The factor of two arises from the deflection of the beam in two directions by the two prisms. Given a beam width of 3.5 mm and a prism electrode width of 4.76 mm, the number of resolvable spots from Equation (3) and Figure 3 should be approximately 40. The observed number of resolvable spots was closer to 15 for $V_{rms} = 28$ volts. The discrepancy between the expected and observed values of N_S is due to the fact that the divergence of the beam exiting the deflector was broader than the diffraction limit.

1. C. Hu and J. R. Whinnery, J. Opt. Soc. Am. **64**(11), 1424 (Nov. 1974).
2. Okamura, et al., J. Lightwave Technol. **LT-4**(3), 360 (March 1986).
3. Kobayashi, et al., IEEE J. Quantum Electron., **QE-18**(10), 1603 (Oct. 1982).
4. C. Hu and J. R. Whinnery, IEEE J. Quantum Electron., **QE-10**(7), 556 (July 1974).
5. L. M. Blinov, "Electro-Optical and Magneto-Optical Properties of Liquid Crystals," J. Wiley & Sons Ltd., Belfast, 1983, Chapter 4.

Table I

layer	material	index (633 nm)	thickness (μm)
substrate	p+ silicon		
buffer	SiO ₂	1.457	3.0
waveguide (MZ int.)	SiO _{0.8} N _{0.8}	1.79	0.94
waveguide (def.)	Ta ₂ O ₅	2.11	0.32
alignment	SiO _x	2.0	0.005
LC	ZLI-1289	1.692 (n_e)	12.5
	(Merck)	1.514 (n_o)	

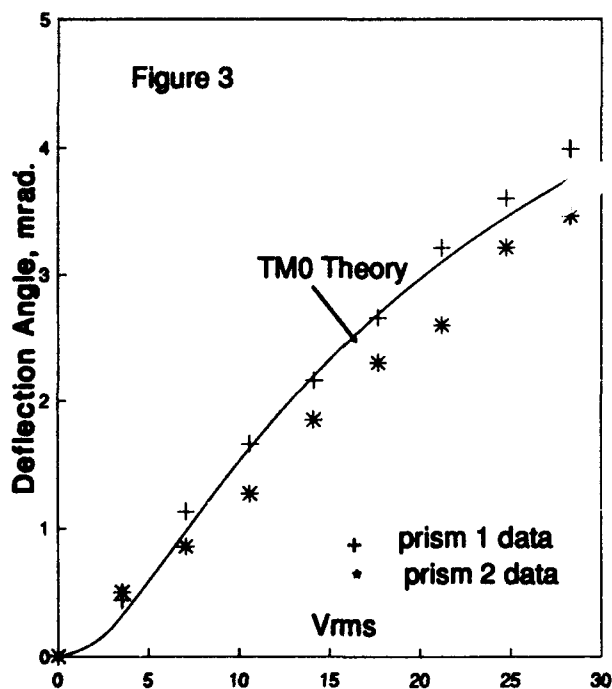
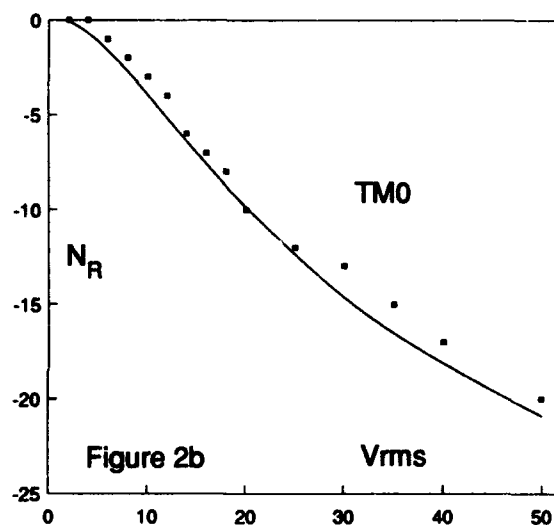
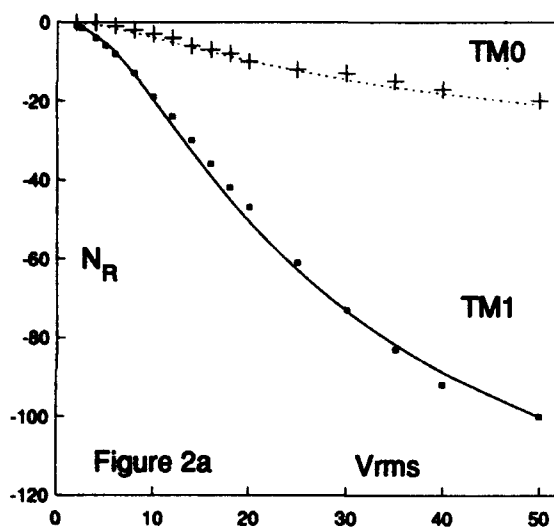
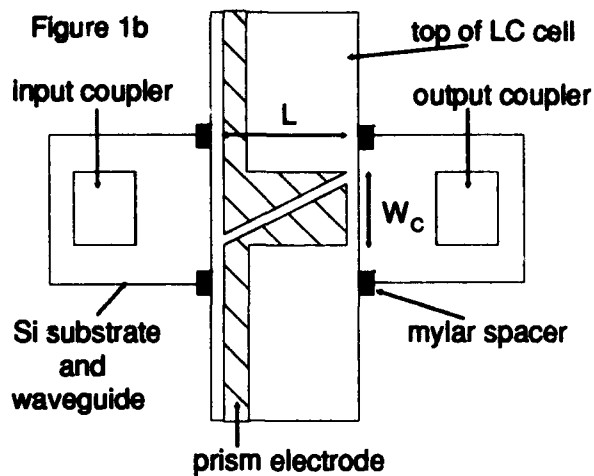
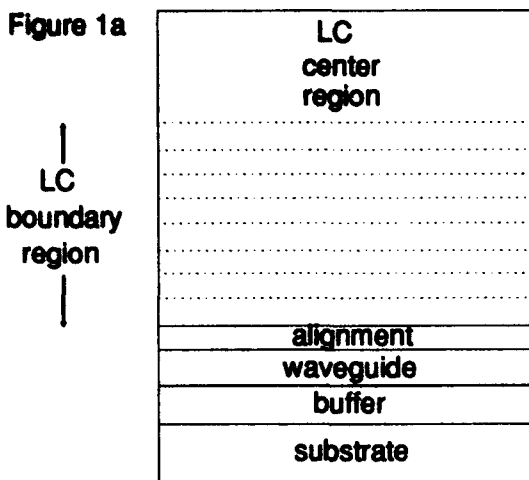


Figure 1. Schematic diagrams of LC-clad passive waveguide: (a) cross section view, and (b) plan view.

Figure 2. Plots of N_R (theory and data) as a function of applied voltage for the phase shifter LC overlayer waveguide device: (a) $m = 1$ and $m = 0$ modes at $\lambda = 633$ nm, and (b) $m = 0$ mode at $\lambda = 830$ nm.

Figure 3. Plot of deflection angle (theory and data) as a function of the applied voltage. Data is shown for both prism 1 and prism 2.

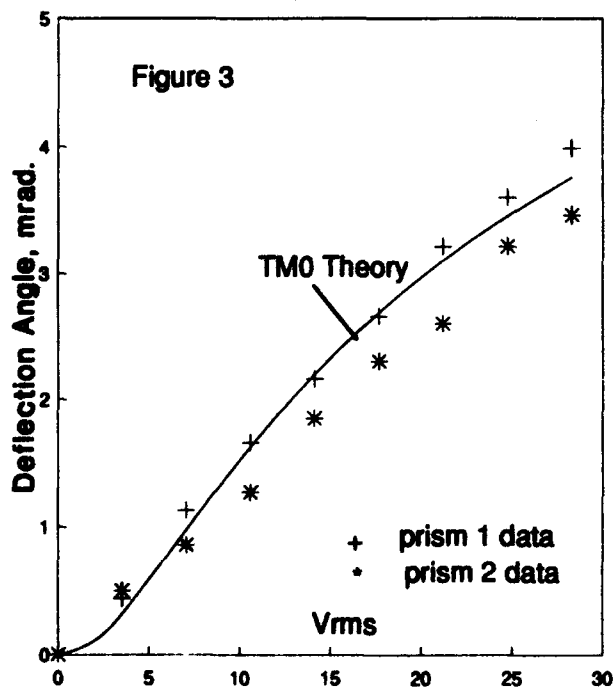
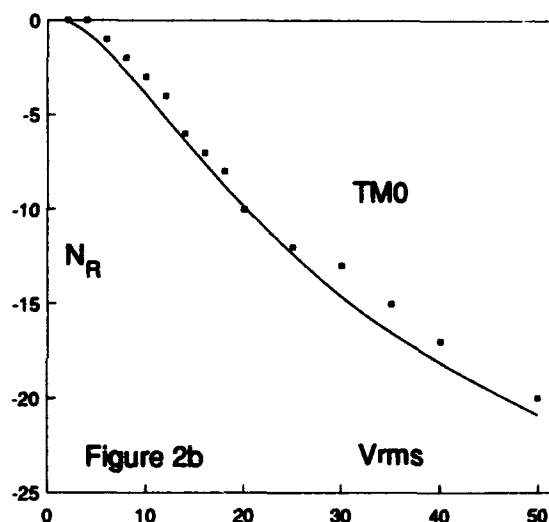
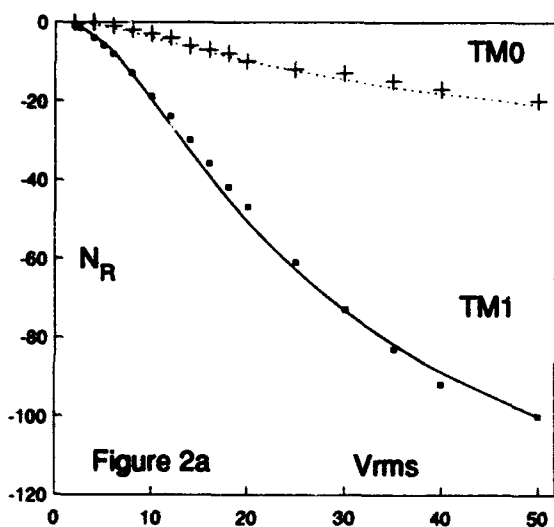
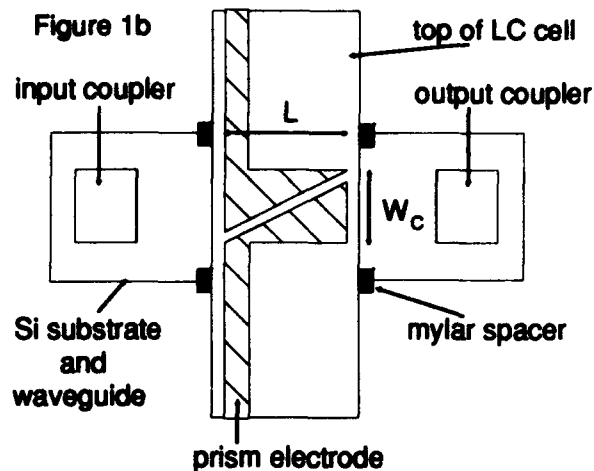
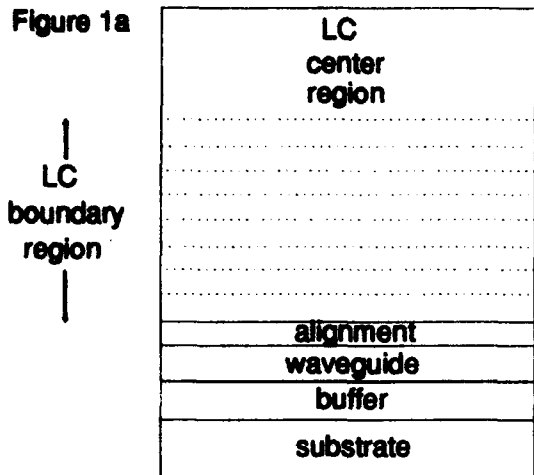


Figure 1. Schematic diagrams of LC-clad passive waveguide: (a) cross section view, and (b) plan view.

Figure 2. Plots of N_R (theory and data) as a function of applied voltage for the phase shifter LC overlayer waveguide device: (a) $m = 1$ and $m = 0$ modes at $\lambda = 633$ nm, and (b) $m = 0$ mode at $\lambda = 830$ nm.

Figure 3. Plot of deflection angle (theory and data) as a function of the applied voltage. Data is shown for both prism 1 and prism 2.

Zero Gap Electron Waveguide Coupler

Mason Thomas, Nadir Dagli, Jonathan Waldman, and Arthur Gossard
Electrical and Computer Engineering Department
University of California
Santa Barbara
CA 93106
Phone (805) 893-4847
Fax (805) 893 3262

We have fabricated and characterized zero gap couplers for electron waves. These couplers behave analogously to integrated optical zero gap couplers. This analogy is due to the wave-like behavior of electrons when they are quantum confined in two dimensions and their phase information is preserved. Such behavior is first observed in electron waveguides [1], [2]. The successful operation of these devices prompted the proposal of other novel devices taking parallel from integrated optics and exploiting the wave nature of electrons [3]. We report here the first successful operation of a novel device using electron waveguides--a zero gap coupler.

The schematic of the zero gap coupler is shown in figure 1. We assume the input and output guides are single moded while the wider waveguide at the center is double moded. An incident electron wave will excite a superposition of the two modes of the central guide. There will not be significant reflections of the incident wave if the transition to the wider guide at the center is accomplished adiabatically using tapers. If the phase of the electrons entering the central region is preserved, the modes of this waveguide acquire a phase difference since they have different subband energies resulting in different velocities for electrons coupled into these modes. Depending on their phase difference at the end of this region, their superposition hence the excitation of the output guides will differ. Thus by controlling the phase difference between the two modes of the central region or the length of this region, electron waves can be coupled to either output guide. Externally this will be observed as current switching.

In the experimental structure required two dimensional quantum confinement is achieved using Schottky gate electrodes on the surface of a two dimensional electron gas sample. Cross sectional profile of this arrangement is shown in Figure 2. Two dimensional electron gas sample is a GaAs/AlGaAs heterostructure which provides quantum confinement along the vertical direction. The electrons are further confined by applying negative voltage to the Schottky gates which depletes electrons from the 2DEG underneath the gates. This way a narrow and short channel, which confines and guides electrons, i.e., an electron waveguide is formed. Furthermore, by changing the magnitude of the gate voltage the degree of lateral confinement can be changed. The changes in the lateral confinement changes the number of modes and their their energy separations. A scanning electron microscope picture of the zero gap structure showing the gates on the surface is shown in figure 3.

The fabricated structures are characterized by measuring the currents coming out of the output waveguides as a function of the voltage applied to the electrodes defining the wider central region. This arrangement is shown in figure 4. Preliminary measurements indicated that waveguiding effects occurred strongly at 0.1Kelvin, but very weakly at 4.2Kelvin. When measured at 0.1K under appropriate bias conditions the coupler exhibited current modulation indicative of proper coupler operation as shown in Figure 5. The coupling was not 100% however, due to the presence of more than two modes in the wider central guide. To verify that current modulation was due to waveguiding effects, the same experiment was performed at successively higher temperatures, where the waveguiding effects were known to decrease. The current modulation also decreased at higher temperatures, verifying that it is due to modal interference.

This is the first time an electron waveguide coupling device has been experimentally demonstrated. The zero gap coupler shows promise for further waveguiding experiments. We would like to acknowledge Rich Muller and Paul Maker of JPL for electron beam lithography and Esther Yuh and Elizabeth Gwinn for help with low temperature measurements. We also acknowledge support from the NSF Science and Technology Center for Quantized Electronic Structures under grant #DMR 91-20007.

[1] B. J. van Wees et al., Phys. Rev. Lett. 60, 848 (1988).

- [2] D. A. Wharam et al., J. Phys. C 21, L209 (1988).
 [3] N. Dagil et al., J. Appl. Phys. 69, 1047 (1991).

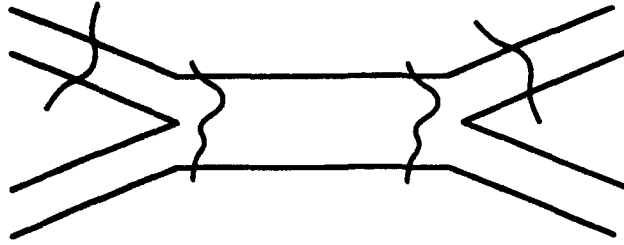


Figure 1. Schematic describing the basic principle of operation. Electron waves in lowest mode of input waveguide excite modes of wider central guide. These modes interfere and excite the modes of the output guides depending on the coupling length and phase difference between the modes of the central guide.

Schottky gates on semiconductor surface

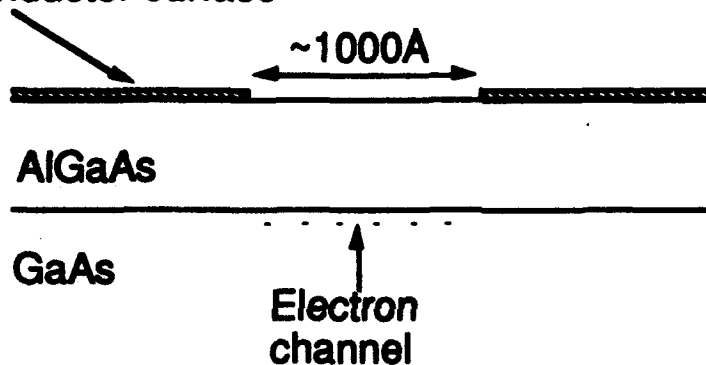


Figure 2. Cross sectional profile of the fabricated waveguides. Electrons are confined at the interface between AlGaAs and GaAs. Reverse bias on Schottky gates provides lateral confinement by depleting electrons underneath the gates.

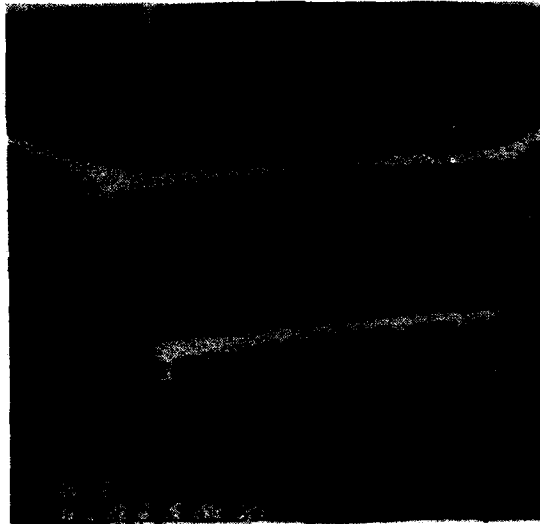


Figure 3. SEM photo of the coupler. Light regions are metal Schottky gates on semiconductor surface (dark). Distance between the side gates is $0.15 \mu\text{m}$, between top and bottom is $0.7 \mu\text{m}$.

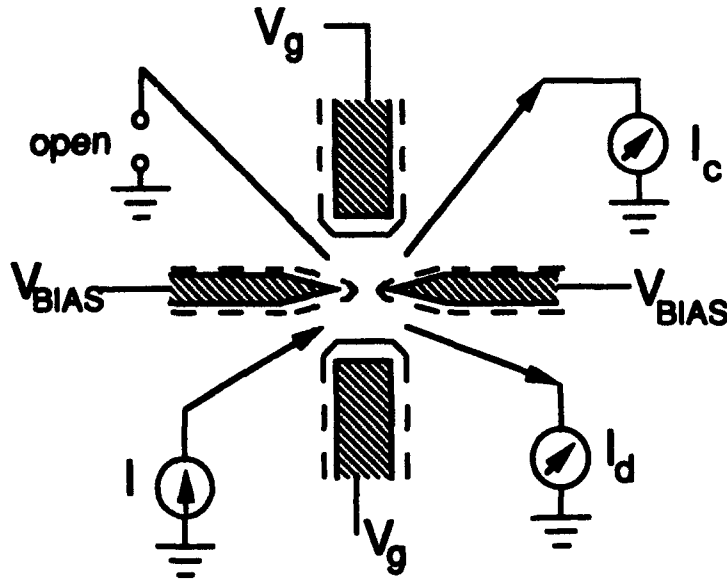


Fig. 4 Bias for measurement. The side gates are biased to create a fixed coupling length. Current is injected in one input guide and the direct (I_d) and coupled (I_c) currents are measured. The top and bottom gate voltages (V_g) are varied to vary the lateral dimensions of the guides and hence the number of modes supported by the guides.

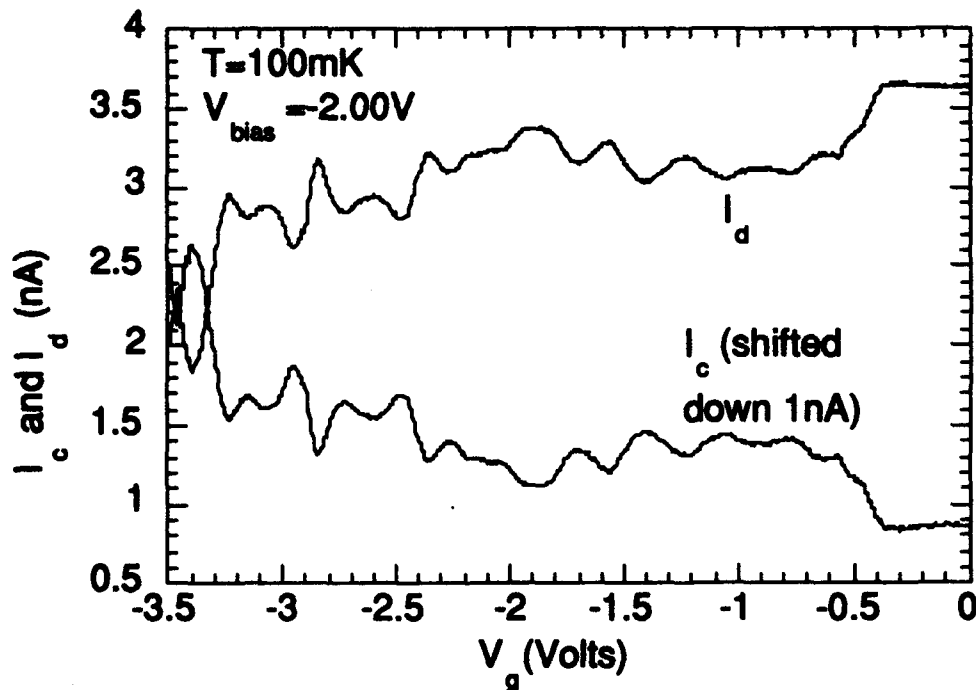


Fig. 5 Coupling Results. I_c and I_d are the coupled and direct currents as shown in fig. 4. Oscillations are seen in these currents as V_g decreases--the input, output and coupling guides support fewer modes--and the oscillations become stronger at larger reverse biases.

Time Domain Methods

IMD 1:30pm-3:45pm
Mesquite B

Reinhold Pregla, *President*
Fem University

Finite-Difference Time-Domain Algorithms in the Analysis and Design of Optical Guided-Wave Devices

S. T. Chu, S. K. Chaudhuri^{}, and W. P. Huang*

**Department of Electrical and Computer Engineering
University of Waterloo
Waterloo, Ontario
Canada, N2L 3G1**

Over the past decade, the finite-difference time-domain (FDTD) method has been established in microwave and millimeter wave research as one of the most versatile and accurate methods, for the analysis of problems involving electromagnetic wave interactions. However, present optical devices contain large electrical lengths which demand vast computational resources for their analysis. This makes the applications of the FDTD method in the optical regime less attractive. This paper discusses a class of optical device analysis where the FDTD method can make a significant impact. Modifications to the full-vector algorithm, such as the semi-vectorial and scalar formulations, are also discussed. These alternate approaches improve the computational efficiency while maintaining the accuracy of the FDTD method.

1. Introduction

The design of optimized integrated-optical (IO) circuits requires a detailed understanding of the various factors that affect the characteristics of their constituent devices. In addition to optimal design, it would be advantages to have accurate methods which can emulate these IO circuits without the expense of fabrication and testing. These methods would also allow the exploration of new device ideas. The CAD tools and simulators have played a critical role in the tremendous advancements in the area of microelectronics. The CAD tools for optical circuit simulation are much less advance than their counterpart in microelectronics. It is obvious that the development of the CAD tools for IO circuits is only in their infant stage and more sophisticated CAD tools are needed in the advancement of IO research.

Generally, an IO circuit consists of two types of geometries which require different approaches for their analysis. First, for the axially uniform geometry, it is necessary to determine its normal mode distribution and the associated propagation constant. Second, for the axially non-uniform geometry, it is necessary to observe the behaviour of the optical signal as it propagates along the structure. In principle, the solution to these problems can be found by solving Maxwell's equations in an appropriate domain subject to the boundary conditions dictated by the geometries.

A number of methods have been developed for uniform structure analysis. The effective index method, the variational method, the weighted-index method, the finite-element method, and the finite-difference method are some of the examples. For non-uniform structures, commonly used approaches are the coupled-mode theory (CMT) and the beam-propagation method (BPM) [1]. The CMT usually considers only the propagation of the two dominant guided modes while neglecting the coupling effects of the radiation modes. The theory is very effective in situations where the radiation is small. The forward propagating radiation fields are accounted for by the BPM, which solves the one-way wave equation in the spatial domain. Although the method assumes the reflection effects are weak and can be neglected, it is a good approximation for many optical structures and is the ideal method for the analysis of adiabatic structures.

A more versatile method which is capable of studying the important effects of polarization, reflection, radiation, dispersion, and non-linearity in a complicated structure is the FDTD method. The method is an important addition to the arsenal of tools for the design of IO circuits, especially, in situations where the limitations of the CMT and BPM have been reached.

2. Full-Wave FDTD Algorithm:

The FDTD algorithm converts the two coupled curl equations in Maxwell's equations of electromagnetic theory into their difference expressions in time and space. A *leap-frog* scheme is used to decouple the curl equations, leading to a sequential algorithm (a propagator in time) for the calculation of the electric and the magnetic fields in the time-domain. This full-wave approach provides flexibility in the analysis of arbitrarily shaped or profiled complex structures that may contain electrically and/or magnetically anisotropic media. The details on the implementation and the operation of the method can be found in [2-3].

The salient feature of the FDTD method is its ability to solve guided-wave problems that contain strong wave interactions and/or cause strong reflections. Problems such as the design of sharp bends and mirrors are of current research interest. To achieve efficient integration, optical signals must be routed sharply within the optical circuit. If these signals can be routed within a few rather than hundreds of wavelengths, valuable chip space can be saved. Another device that is well suited for a FDTD analysis is the distributed feedback (DFB) structure. As the grating structure in the DFB laser becomes a part of the lasing geometry, it is necessary to investigate the wave interactions in these cavities. The FDTD method is ideal in the analysis of small distributed reflections which can add up coherently.

Since the FDTD simulation is performed in the time-domain, the analysis of time-varying media is straight forward. This unique feature makes the method attractive for the analysis of electro-optical or acousto-optical devices. As an example, the modulation characteristics of a travelling wave Mach-Zehnder modulator can be simulated by the FDTD method.

The appeal of the FDTD method can be further enhanced by improving its computational efficiency. In the next section, two alternate approaches based on the scalar limits are presented.

3. Scalar and Semi-Vectorial Wave FDTD Algorithms [4,5]:

Starting with the vector wave equations in a linear and inhomogeneous medium,

$$\mu\epsilon \frac{\partial^2 \vec{E}}{\partial t^2} = \nabla^2 \vec{E} - \nabla \left[\nabla \frac{1}{\epsilon} \cdot \epsilon \vec{E} \right], \quad (1a)$$

$$\mu\epsilon \frac{\partial^2 \vec{H}}{\partial t^2} = \nabla^2 \vec{H} + \nabla \epsilon \times \left[\frac{1}{\epsilon} \cdot \nabla \times \vec{H} \right]. \quad (1b)$$

If the electric field is linearly polarized in the x direction where the dominant field components are E_x and H_y , then both the x component of (1a) and the y component of (1b) can be used to describe the propagation of the field exactly. Under the semivectorial approximation, the interfaces between the different indices are assumed to be parallel to the x and y directions. The terms involving the minor components, which are responsible for the coupling between the dominant component and the remaining minor components, are neglected. The resulting equations are the semi-vectorial wave equations (SVWEs):

$$\mu\epsilon \frac{\partial^2 E_x}{\partial t^2} = \frac{\partial^2 E_x}{\partial y^2} + \frac{\partial^2 E_x}{\partial z^2} + \frac{\partial}{\partial x} \left[\frac{1}{\epsilon} \frac{\partial}{\partial x} \epsilon E_x \right], \quad (2a)$$

and

$$\mu\epsilon \frac{\partial^2 H_y}{\partial t^2} = \frac{\partial^2 H_y}{\partial y^2} + \epsilon \frac{\partial}{\partial x} \left[\frac{1}{\epsilon} \frac{\partial H_y}{\partial x} \right] + \epsilon \frac{\partial}{\partial z} \left[\frac{1}{\epsilon} \frac{\partial H_y}{\partial z} \right]. \quad (2b)$$

For guided-wave optical problems in two dimensions, there is only one dominant field component; these equations are sufficient to describe the propagation behaviours of the optical signal.

In situations where the refractive index changes are small, $\nabla \epsilon \approx 0$, the SVWEs reduce to their scalar forms and the scalar wave equation (SWE) is:

$$\nabla^2 \psi - \frac{n^2}{c^2} \frac{\partial^2 \psi}{\partial t^2} = 0, \quad (3)$$

with ψ representing the dominant field component. For the x polarized wave in this example, ψ can either be E_x or H_y .

In the alternate FDTD algorithms, the SWE and the SVWEs are solved numerically using the finite-difference approach. An explicit time-domain approach similar to the full-wave FDTD algorithm is used to solve the reduced wave equations. In this way, the majority of the above mentioned advantages of the full-wave FDTD analysis are maintained.

The SWE and SVWEs are second order equations with respect to time, in the implementation the field values at the two previous time steps, at $t = n - 1$ and $t = n$, must be known in the calculation of the field value at $t = n + 1$. However, the equations contain only one unknown field component, they require less memory storage than the full wave FDTD algorithm. In comparison with the full wave FDTD algorithm, the memory requirements for the alternate algorithms are reduced to one-thirds for 3-D and to two-thirds for 2-D problems. Similar improvement in computational efficiency is also found.

Comparison between the FDTD and these schemes in terms of accuracy and efficiency in the analysis of 2-D and 3-D geometries will be presented at the conference.

4. References

- [1] for a review of the methods, see ch. 3, 4, and 7 in *Guided-Wave Optoelectronics 2nd ed.* T. Tamir ed., Springer-Verlag, Heidelberg, 1990.
- [2] S. T. Chu and S. K. Chaudhuri, "A finite-difference time-domain method for the design and analysis of guided-wave optical structures," *IEEE/OSA J. Lightwave Technol.*, vol. LT-7, pp. 2033-2038, 1989.
- [3] P. M. Goorjian and A. Talfove, "Direct time integration of Maxwell's equations in non-linear dispersive media for propagation and scattering of femtosecond electromagnetic solitons," *Optics Letters*, 17, pp. 180-181, 1992.
- [4] W. P. Huang, S. T. Chu, A. Goss, and S. K. Chaudhuri, "A scalar finite-difference time-domain approach to guided-wave optics," *IEEE Photon. Technol. Lett.*, vol. 3, pp. 524-526, June 1991.
- [5] W. P. Huang, S. T. Chu, and S. K. Chaudhuri, "A semivectorial finite-difference time-domain method," *IEEE Photon. Technol. Lett.*, vol. 3, pp. 803-806, Sept. 1991.

Acknowledgement

This research was supported by a grant from the Canadian Institute of Telecommunications Research under the NCE program of the Government of Canada.

Time-Domain Finite Element Modeling of 3D Integrated Optical Devices

G. Wojcik, J. Mould Jr., Weidlinger Associates, 4410 El Camino Real, Los Altos, CA 94022 ((415) 949-3010); L.C. West, 4G518, AT&T Bell Labs, Crawfords Corner Rd., Holmdel, NJ 01133 ((908) 949-8715)

Introduction

As integrated optical devices become more sophisticated, so does the experimentation and analysis required to design them. By augmenting conventional experiments with rigorous computer modeling we can lower costs, shorten schedules, and provide faster, more accurate predictions. Discrete modeling codes using finite differences or finite elements are the most general, albeit expensive. Nonetheless, they are competitive today by virtue of simple, robust algorithms and modern workstations that put near-supercomputer capabilities on the desktop.

In support of computer modeling this paper demonstrates the practicality of time-domain finite element codes for simulating 2D and 3D devices on UNIX workstations. We describe EMFlex, a finite element wave solver for large-scale electromagnetic simulations, and apply it to highly confining dielectric waveguides in 3D routing and 2D grating couplers. EMFlex was originally developed for optical lithography and metrology studies^{1,2}, funded in part by the NSF and SEMATECH.

Time-Domain Finite Elements

We seek discrete solutions of Maxwell's equations in heterogeneous dielectric and semiconductor domains. Solving in the frequency-domain couples fields at all points in space and yields large systems of equations. A more practical approach is to integrate Maxwell's equations in the time-domain using finite differences. The equations' fundamental hyperbolicity decouples points separated by Δx if time step Δt is less than $\Delta x/c$, where c is the local speed of light. The discrete problem is then solved locally at each time step—by summing nodal contributions from nearest neighbors and integrating each node independently using a leapfrog scheme. "Lumping" permittivity at the nodes yields further simplification. This approach eliminates the large system of frequency-domain equations and yields a simple, fast algorithm that is well suited to pipelined or parallel computer architectures.

There are two standard methods for spatial discretization of Maxwell's equations, finite differences and finite elements. Finite differences³ are the oldest and the most efficient for structurally simple models. Finite elements are newer and better suited to structurally complex models, but increase the floating point operation count. They also yield simpler (nonstaggered) field sampling and include nonlinear material behavior more readily. The dominance of finite elements in the commercial sector (thermal, structures, fluids, EM) is due to geometric adaptability and modeling ease. Speed turns out to be a secondary issue in most cases.

A critical issue for discrete solvers is grid truncation error caused by spurious reflections at the model's artificial boundaries. Radiation conditions are necessary to reduce this error. In time-domain analysis these are usually local relations among nodal boundary values derived from the paraxial wave equation⁴. However, higher order implementations tend to degrade in 3D vector domains. Also, the local phase velocity is required. A better approach is based on the formalism outlined below.

$$\dot{E}_n = \frac{1}{\epsilon} \frac{\partial(n \cdot H)}{\partial n}, \quad \frac{\partial}{\partial n} = S_n \frac{\partial}{\partial t} \Rightarrow \dot{E}_n = -\text{sign} \left[\frac{\partial E_n}{\partial n} \right] \sqrt{\frac{1}{\epsilon} \left| \frac{\partial E_n}{\partial n} \right|} |n \cdot H|$$

The first equation rewrites the normal component of Maxwell's equation on E (similarly for H). The second is the plane wave jump condition projected onto the

boundary normal, where S_n is the unknown normal component of slowness. Applying this jump condition to the two sides of the first equation and eliminating S_n yields the third equation, giving the time derivative of the normal electric field in terms of its normal derivative and the time derivative of the magnetic field. Tangential conditions may be derived in the conventional fashion, by differencing nodal values for example. The important point is that these boundary conditions do not involve the local speed of light and they perform as well as 4th order paraxial conditions but with less computational overhead. They are unique in that nonlinear material behavior is permitted at the radiating boundary.

In addition to its fundamental wave solving capabilities, a practical code needs various pre- and post-processing options, both quantitative and graphical. For example, pre-processing includes calculating "illumination" conditions representing the optical field incident from outside the model, e.g., plane waves, Gaussian beams, waveguide modes, etc. To make these compatible with the radiation conditions, EMFlex does exact phase velocity matching using dispersion analysis of the discrete equations on the boundary. Post-processing includes automated amplitude and phase extraction from the steady state time-domain solution, scattered field extraction, far-field extrapolation, plane wave decomposition, and other means of characterizing device performance, e.g., modal mixes in a 3D waveguide. In addition, there is a complete graphical display and PostScript capability for interactive plotting of time histories, field snapshots, and movies.

Model Problems

Our interest is integrated optical waveguides with high index of refraction contrast between the guide and surrounding dielectrics. Such high-contrast may allow unprecedented optical component and wiring densities, comparable to electronic integration, with compaction two orders of magnitude smaller than typical integrated optics. Unfortunately, this approach has not received much attention because fabrication of devices for 1 micron light pushes the outer limits of optical lithography. Also, practical analysis of these devices is difficult if not impossible using perturbation, paraxial, and ray theories. This causes us to question design rules and how they reflect limitations of traditional analysis methods.

Initial realization of these devices has been in the mid-IR (10 microns) with Ge waveguides ($n=4.0$) on GaAs ($n=3.27$). A typical waveguide is 1.75 microns high and 3.0 microns wide. The mid-IR region is considered ideal for device development because of fabrication ease, good dimensional control, and relative surface smoothness. Also, many practical nonlinear and electro-optic elements (detectors, modulators, logic, etc.) can be made with intersubband transitions⁵ in the mid-IR. With advances in lithographic resolution, we expect these concepts to be useful in near-IR (1 micron) too, e.g., sizes should scale with wavelength to 0.2-0.3 microns.

Our model problems concern low-loss routing of optical signals through a circuitous waveguide and coupling off-chip beams into on-chip waveguide modes. In particular, we use EMFlex to calculate TM modes in 3D waveguides, propagation through a tight waveguide turn, and scattering from a single tooth in a 2D waveguide. Our eventual objective is to optimize designs for a given set of nominal dimensions and layout constraints. These calculations were done on an IBM RS/6000 Model 350 workstation with 64 megabytes of memory.

Mode shapes are calculated in the time-domain by applying an approximate TM mode to one end face of a long 3D symmetric model with radiation or symmetry conditions on the other faces. The model is 10.5 microns deep, 9 microns wide, and 60 microns long ($71 \times 61 \times 406 = 1.76$ million nodes). Shape of the stable mode that arrives

approximately 12 wavelengths from the illuminated end is then measured. Thus, we use the finite element model as a waveguide filter. These experiments are done for a number of cross-sections and the effective index is calculated to insure that modes are trapped. Leaky modes are also apparent by their gradual amplitude decay. Mode shapes calculated in this manner are illustrated in Figure 1 for a 1.75 x 3.0 micron cross-section. The effective index is 3.33. Waveguide height is the critical dimension in these 3D experiments. For example, a 1.65 x 3.0 micron cross-section is leaky although the 1.65 x ∞ micron case (slab) is not.

To illustrate modeling of waveguide routing we use the above cross-section and model a 7.5 micron radius turn (2.5 wavelengths). The TM mode shape is applied as a boundary condition on the input face with radiation conditions on the other five faces. Snapshots of the field are shown in Figure 2 after the mode has traversed the bend and a few waves have been absorbed at the other face. The model is 15 microns square and 10.5 microns deep ($101 \times 101 \times 71 = 724,000$ nodes).

Our basis for investigating grating couplers is scattering from a single tooth. This is used to design arbitrary output beam profiles. The 2D Ge waveguide is 1.75 microns thick over GaAs. The tooth is 1.5 microns wide and etched into the waveguide from above. The 2D model is 24.4 microns deep and 150 microns long ($138 \times 1001 = 138,000$ nodes). Illumination and boundary conditions are similar to those described above. Results for the fundamental TM mode incident from the left are illustrated in Figure 3. This shows amplitudes of the vertical (top) and horizontal (bottom) electric field components in the neighborhood of a 0.477 micron tooth, and a plot of reflected amplitude coefficient, transmitted amplitude coefficient, and scattered power coefficient for tooth depths from 0. to 1.75 microns (full penetration).

Conclusions

We have shown that workstation-based computer modeling of 3D high-contrast optical devices is practical. There are limitations of course, on problem size and complexity, wavelength versus feature size (subscale roughness), and boundary conditions—but none appear insurmountable. General modeling codes like EMFlex that are tailored to facilitate numerical experimentation will prove valuable to the designer and experimentalist, particularly as desktop computing power increases.

Concerning the high-contrast wafer-scale models described here, it is clear that complete performance information can be obtained in regimes where more classical approximations fail utterly. We know how to fabricate these devices but lack the knowledge to design them. Tailored modeling codes can help develop the necessary knowledge base and facilitate new classes of integrated optical devices.

References

1. G. Wojcik, D. Vaughan, and L. Galbraith, "Calculation of light scatter from structures on silicon surfaces," *SPIE Vol. 774, Lasers in Microlithography* (1987).
2. G. Wojcik, et. al, "Numerical simulation of thick line width measurements by reflected light," *SPIE Vol. 1464, IC Metrology, Inspection & Process Control* (1991).
3. K.S. Yee, "Numerical solution of initial boundary value problems involving Maxwell's equations in isotropic media," *IEEE Trans. Antennas Prop.*, AP-14, pp. 302-307 (1966).
4. B. Engquist, A. Majda, "Absorbing boundary conditions for the numerical simulation of waves," *Math. Comp.*, 31, pp. 629-651 (1977).
5. L.C. West, "Picosecond Integrated Optical Logic," *Computers*, 20, pp. 34-46 (1987).

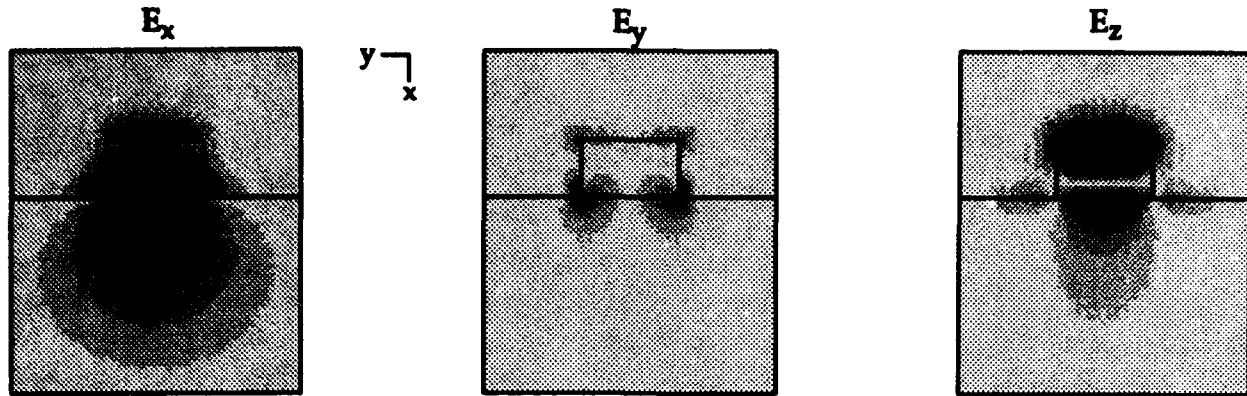


Figure 1. Fundamental TM mode shapes in a 1.75 x 3.0 micron Ge ($n=4.0$) waveguide on GaAs ($n=3.27$). Free-space wavelength is 10 microns and effective index of the mode is 3.33. The smaller E_y and E_z fields are scaled by a factor of 2.0 over E_x .

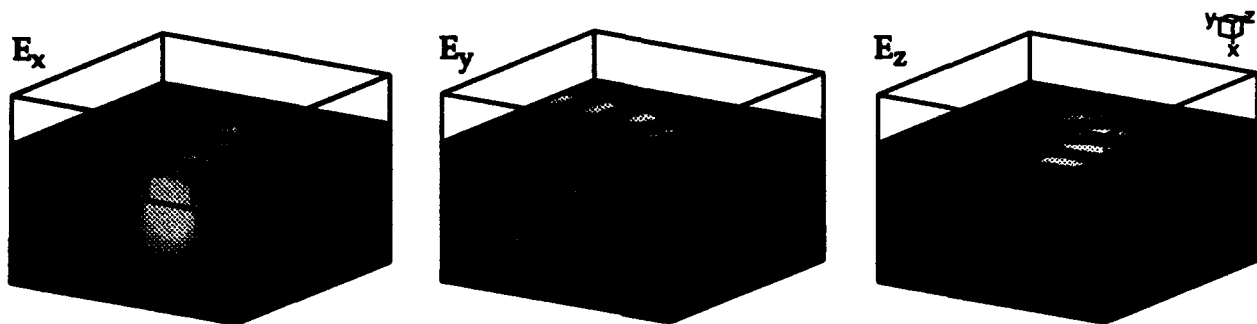


Figure 2. Fundamental TM mode propagation in the waveguide of Figure 1 with a 7.5 micron radius turn. The mode is applied on the left, front face and absorbed on the left, rear face. The smaller E_y and E_z fields are scaled by a factor of 1.6 over E_x .

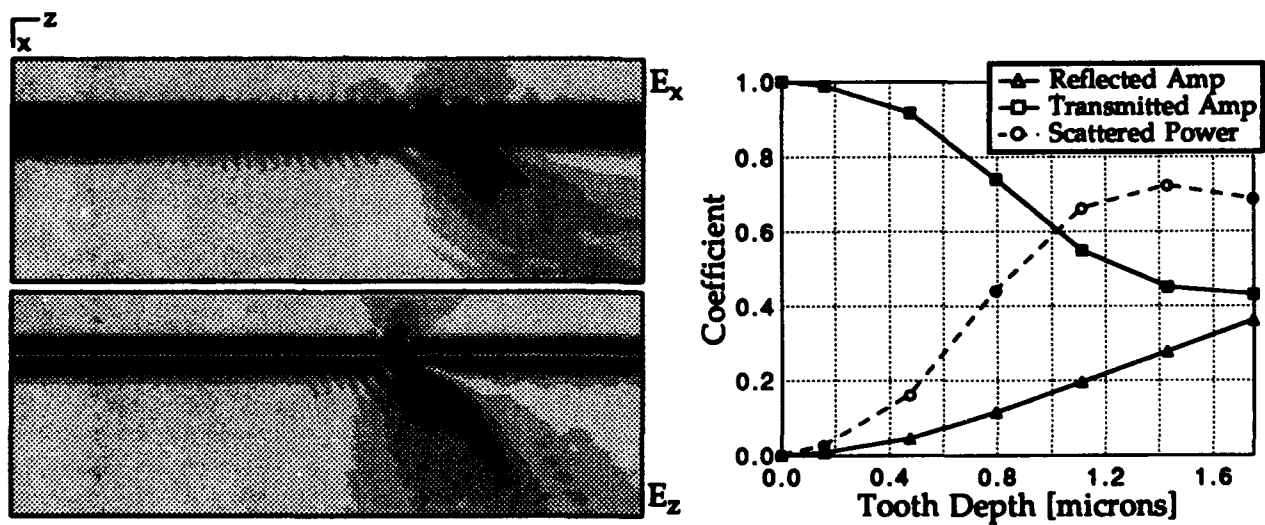


Figure 3. Scattering from a 1.5 micron wide tooth in a 1.75 micron Ge slab waveguide over GaAs. Fields scattered from a 0.477 micron deep tooth are shown on the left. Scattering coefficients as a function of tooth depth are plotted on the right.

Full-Wave Simulation of the Thumbtack Laser²

R.J. Hawkins, N.K. Madsen, J.S. Kallman, M.D. Feit, C.C. Shang, B.W. Shore, and J.F. DeFord
Lawrence Livermore National Laboratory, Livermore CA 94550
 (510) 422-0581

The whispering-gallery mode microdisk - or thumbtack - laser is a novel, strongly confining, microstructure with "potential for the integrability and low-power operation required for large-scale photonic integration"³. It is a thin dielectric ($n \approx 3.5$) cylinder - or disk - on top of a rhomboid post. Analysis of the optical modes of this structure have, to date, consisted of scaling arguments drawn from the theory of whispering-gallery spheres. While this analysis has proved useful in understanding the basic aspects of the operation of this laser, it is limited. We have undertaken a complete electromagnetic analysis⁴ of the thumbtack laser using 2-D, 2.5-D and 3-D Finite-Difference Time-Domain (FDTD) codes which range in complexity from 2-D studies of the mode structure of the disk to a geometrically complete 3-D analysis of the radiation emitted from the laser. The goal of this project is to predict changes in the optical behavior that accompany structural changes in and about the laser described elsewhere in these proceedings⁵, and to guide optimized device design.

To understand the etiology of the experimentally observed $M = 8$ azimuthal whispering-gallery modes, our analysis began with a time-domain study of the mode structure of a cylinder excited by a dipole using TSARLITE⁶. A dielectric cylinder was externally excited by a transient optical dipole oscillating at $\lambda = 1.5 \mu\text{m}$ as shown in Fig. 1. This initial condition evolved into a mode pattern dominated by the experimentally observed $M = 8$ azimuthal whispering-gallery mode shown in Fig. 1. We varied the initial excitation of this system to study the robustness of this mode structure. Excitation of the cylinder with a variety of dipole positions - both inside and outside of the cylinder - demonstrated the robustness of this mode.

Examination of the properties of individual azimuthal modes was carried out using AMOS⁷. This code differs from TSARLITE in that it treats rotationally symmetric problems with arbitrary variation along the axis of symmetry, and has the ability to easily focus on specific azimuthal modes. We have used AMOS to calculate the Q of the disk laser set upon a cylindrical pedestal. In Fig. 2

²This research was performed under the auspices of the U.S. Department of Energy by the Lawrence Livermore National Laboratory under contract W-7405-ENG-48.

³S.L. McCall, A.F.J. Levi, R.E. Slusher, S.J. Pearton, and R.A. Logan, "Whispering-gallery mode microdisk lasers," *Appl. Phys. Lett.* **60**, 289-291 (1992).

⁴Since we are not yet including gain in these simulations we are, effectively, cold-testing these structures.

⁵R.E. Slusher, A.F. J. Levi, S.L. McCall, J.L. Glass, S.J. Pearton, and R.A. Logan, "Output couplers for whispering gallery mode microdisk lasers" this digest.

⁶TSARLITE solves the time-dependent Maxwell's curl equations on a two-dimensional cartesian grid using the standard leap-frog FDTD algorithm with 1st-order radiation boundary conditions.

⁷AMOS computes the temporal evolution of electromagnetic fields in rotationally symmetric simulation volumes by using the FDTD algorithm on fields distributed on a two-dimensional (2D) field grid with radial and axial coordinates, r and z respectively. The projection of the fields in the volume onto the 2D grid is accomplished by expanding the fields in a Fourier series in the cylindrical (azimuthal) coordinate, ϕ . The M th term, or multipole mode, in the series varies as $\exp(iM\phi)$; AMOS is used to solve for the temporal evolution of the M th mode via user specification of M . AMOS allows the fields to vary in a predefined (harmonic) fashion in the ϕ coordinate; it is for this reason that AMOS is called a 2.5D code to distinguish it from a purely 2D code in which the fields do not vary with ϕ . See, J.F. DeFord, G.D. Craig, and R.R. McLeod, "The AMOS wakefield code," *Proc. Conf. on computer codes and the linear accelerator community*, (Los Alamos, NM) 256 (January, 1990); also LLNL UCRL-102731.

we see a portion of a typical power spectrum calculated from the $E_x(t)$ at a point inside the laser. The signal amplitude shows no discernible decrease over the timespan used. However, the resulting spectrum consists of well resolved spectral lines quite adequate for finding line center frequencies and Q values using a lineshape fitting method⁸. This method involves windowing the time signal before Fourier transforming to avoid aliasing errors. It then uses the ratio of amplitudes on either side of a spectral peak to determine real and imaginary parts of the frequency. The first two lines shown in the Fig. 3 have $Q = 207.7$ and $\omega = 1.62 \times 10^{15} \text{ sec}^{-1}$ and $Q = 163.9$ and $\omega = 1.83 \times 10^{15} \text{ sec}^{-1}$. We also find that Q diminishes approximately exponentially with radial mode number.

The thumbtack laser is not rotationally symmetric: it consists of a disk set upon a rhomboid pedestal. The complete electromagnetic treatment of the laser was accomplished using DSI3D⁹, where the full geometric complexity of the microstructure can be represented. The use of a general nonorthogonal mixed-polyhedral unstructured grid permits a variable mesh that can follow closely the geometry of the microstructure, thus allowing for efficient computation. DSI3D has shown a variety of results. In particular, the impact of the pedestal is clearly seen as illustrated in Figs. 3a,b where the intensity in the plane of the disk is shown with and without the pedestal. The pedestal clearly modifies the modal solution and seems to give rise to the preferential directions of light emission observed experimentally¹⁰.

Because the thumbtack laser is small, a complete numerical electromagnetic analysis can be finished in a short amount of time. Indeed, even in DSI3D, this problem is not considered large. Consequently, we have used these tools to begin studying the effect of structural modifications of the disk on the optical structure. Initial results are encouraging. Adding a slight bulge to the disk resulted in an enhanced intensity in the region of the bulge as observed experimentally. Extensive video demonstration of these and other results will be given at the meeting.

Optically confining microstructures with volumes on the order of the cube of the optical wavelength can be studied efficiently using FDTD techniques. This means that a complete full-wave electromagnetic analysis of these structures is indeed possible. The ability to fully characterize such microstructures and to study the impact of structural alterations on optical behavior in a timely manner is a significant development in integrated optical design.

⁸M.D. Feit and J.A. Fleck, Jr., "Spectral approach to optical resonator theory," *Appl. Opt.* **20**, 2843-2851 (1981); M.D. Feit, J.A. Fleck, Jr., and A. Steiger, "Solution of the Schroedinger equation by a spectral method," *J. Comp. Phys.* **47**, 412-433 (1982).

⁹DSI3D uses a discrete surface integral method for solving Maxwell's Equations in the time domain. This method, which allows for the use of general nonorthogonal mixed-polyhedral unstructured grids, is a direct generalization of the canonical staggered-grid finite difference method. Employing mixed polyhedral cells, this method allows more accurate modeling of non-rectangular structures and objects because the traditional "stair-stepped" boundary approximations associated with the orthogonal grid based finite-difference methods can be avoided. See, N.K. Madsen, "Divergence preserving discrete surface integral methods for Maxwell's equations using non-orthogonal unstructured grids," submitted to *J. Comp. Phys.*; also LLNL UCRL-JC-109787

¹⁰ACKNOWLEDGEMENT: We thank R.E. Slusher for discussing his observations of the thumbtack laser with us

FIGURES:

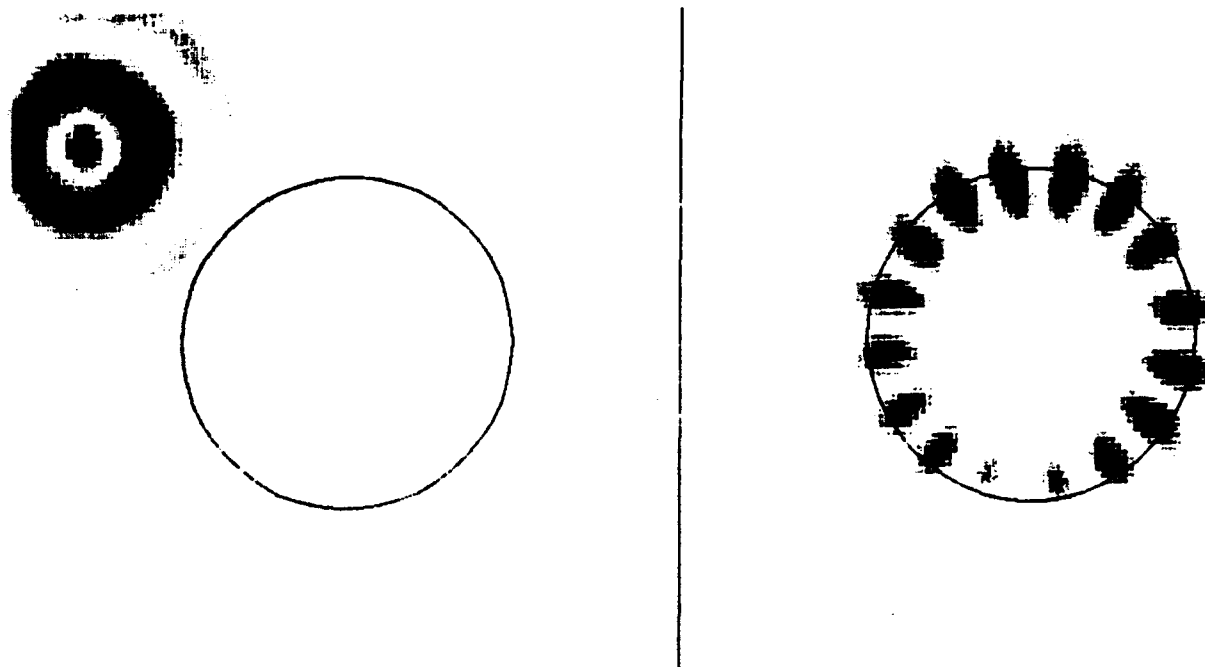


[Figure 1] On the left is an early time slice showing the initial excitation of a dielectric cylinder by a transient dipole. The grey scale follows the intensity of the E_z component of the electric field. On the right is a later time slice in the same simulation. The dipole has now been off for some time, and an $M = 8$ azimuthal whispering-gallery mode is apparent.

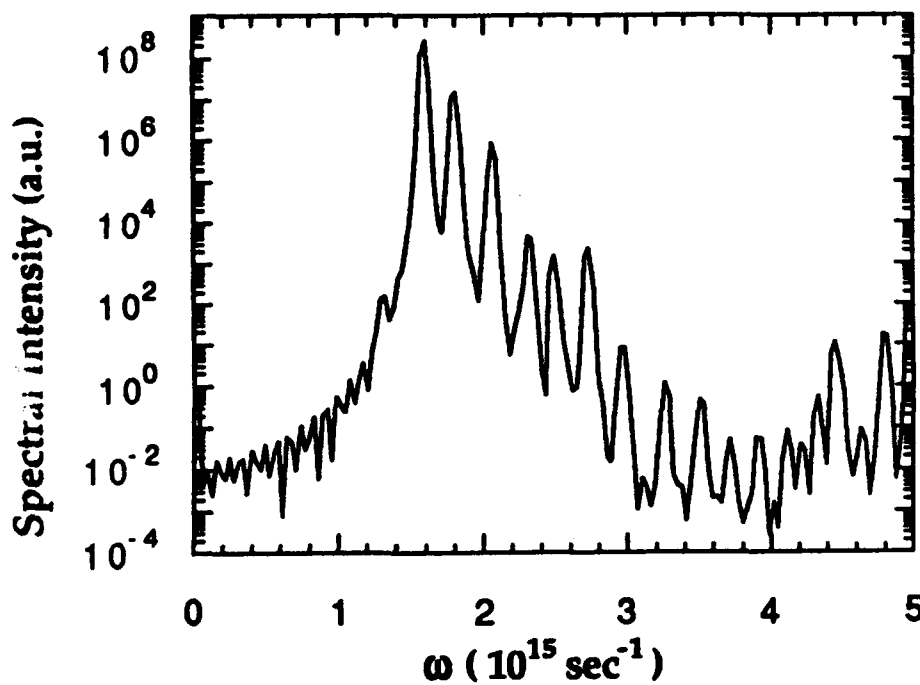


[Figure 2] The modal spectrum for the $M = 8$ modes.

FIGURES:

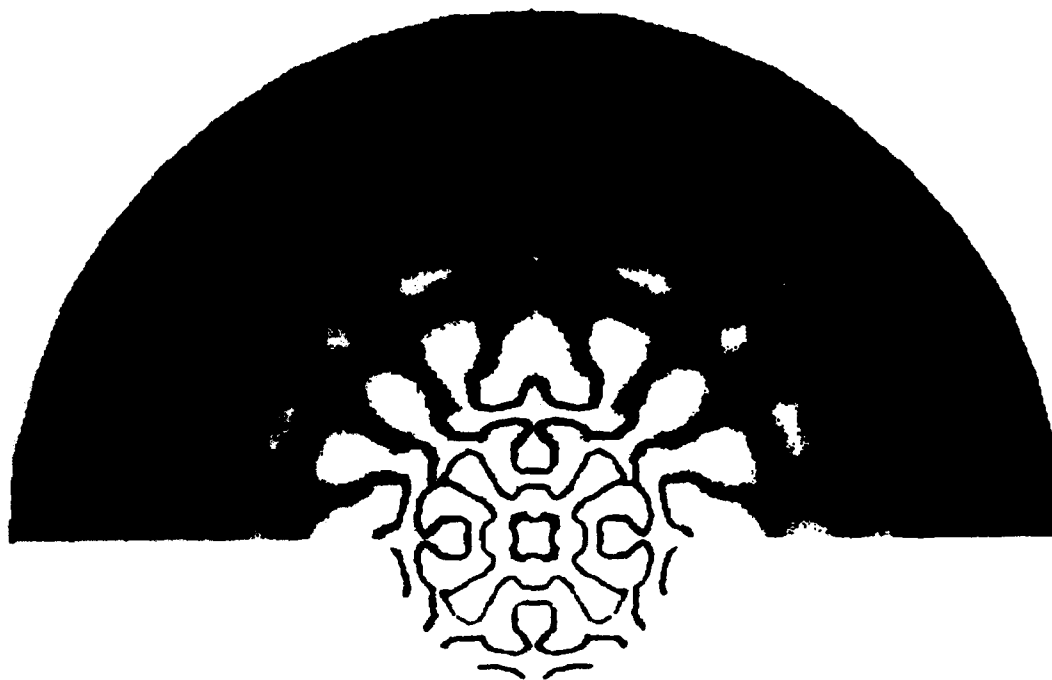


[Figure 3a] The time slice of the mode pattern within the plane of the disk of the thumbtack laser with the refractive index of the pedestal set to 1. The radiation pattern in the lower half of the figure has been removed to show the radius of the disk. The grey scale follows the intensity of the E_z component of the electric field.

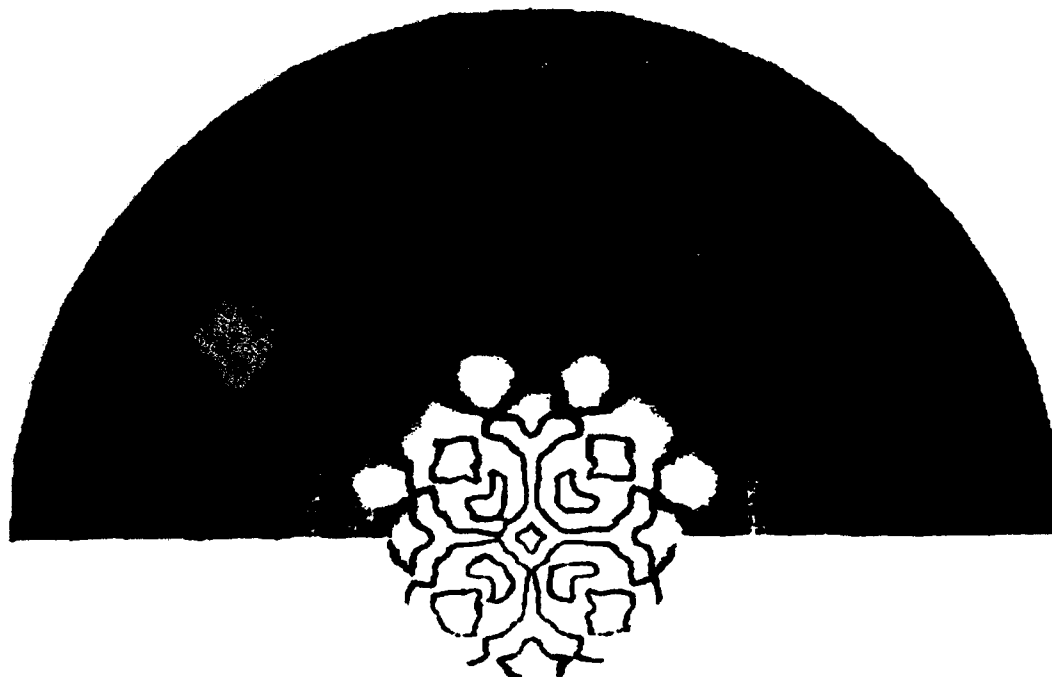


[Figure 3b] The mode pattern contemporaneous to Fig. 3a, but with the rhomboid dielectric post. The radiation pattern in the lower half of the figure has been removed to show the radius of the disk.

Reflection Analysis from the Endface of Optical Waveguides Using the Finite-Difference Time-Domain Method

Junji YAMAUCHI, Takashi ANDO and Hisamatsu NAKANO

College of Engineering, Hosei University
3-7-2, Kajino-cho, Koganei, Tokyo 184, Japan
Tel: 423-87-6190

1. INTRODUCTION

Optical feedback is the major cause in the deterioration of laser signal quality. To suppress reflections from connectors, tilting the endface of the waveguide is beneficial [1][2]. Tilting the endface prevents the coupling of the reflected beam back into the fundamental mode. Considerable effort has also been made in obtaining an antireflective coating for the endfaces of dielectric waveguides [3]-[5]. However, the full-wave analysis of these reflection problems has not appeared to date.

The purpose of this paper is to analyze the reflection problems of optical waveguides using the finite-difference time-domain (FDTD) method [6][7] combined with the absorbing boundary condition [8]. The FDTD method allows us to obtain information on reflected power for both TE and TM polarizations.

2. EFFECTS OF A TILTED ENDFACE

Consideration is first given to the analysis of reflected power from the tilted endface shown in Fig.1. The two-dimensional waveguide to be considered has refractive indices of $N_{CO}=1.515$ and $N_{CL}=1.5$. The adjacent medium on the right is air ($N_A=1$). The width of the waveguide is taken to be $2D=3.0 \mu\text{m}$, and the wavelength is chosen to be $\lambda=1.55 \mu\text{m}$, so that the guided modes supported by the waveguide are the TE_0 and TM_0 modes. The endface is tilted by an angle of θ .

The CW simulation of the TE wave is considered. The $+z$ propagating incident wave is generated on the incident plane located at $z_{inc}=1 \mu\text{m}$. In this excitation scheme, the total field and reflected field regions [7] are located at $z \geq 1 \mu\text{m}$ and $z < 1 \mu\text{m}$, respectively. Since only the $-z$ propagating field generated at the endface exists in the reflected field region, the amount of the reflected power is easily calculated. The increments used for the simulation are $\Delta x=0.05 \mu\text{m}$, $\Delta z=0.025 \mu\text{m}$ and $c\Delta t=0.02 \mu\text{m}$, where c is the velocity of light in free space.

Fig.2 shows the reflected power of the fundamental mode observed after the transient has passed ($ct=20 \mu\text{m}$). For the normal incidence, i.e., $\theta=0^\circ$, the reflected power is calculated to be 4.2%. This value is close to that evaluated by the simple reflection coefficient of a plane wave. It is seen that the reflectivity decreases monotonically as the tilt angle θ is increased. For example, for $\theta=10^\circ$, the reflected power is less than 0.05%. Although the result for the TM wave is not shown, it is similar to the TE one.

Fig.3 shows the $-z$ propagating E_y field observed in the reflected field region. The fundamental mode is found to propagate for the normal incidence

case. In contrast, for $\theta=10^\circ$, the propagating field can be regarded as a radiation mode, so that the reflected power of the guided-mode is suppressed.

Next, we consider the reflection and transmission problems of a mated interconnection shown in Fig.4. A waveguide identical to that in Fig.2 is used for the analysis. Fig.5 shows the reflected and transmitted power of the fundamental mode as a function of the endface separation S . It is found that the reflected power oscillation observed for $\theta=0^\circ$ is greatly suppressed for $\theta=10^\circ$. It should be noted, however, that the transmitted power undergoes oscillation even in the case of $\theta=10^\circ$. This is due to the multiple reflections between the endfaces.

The maximum transmitted power for $\theta=10^\circ$ and $S \approx 0.8 \mu\text{m}$ is almost 100%, since the separation between the endfaces is small. When the separation is large, we must offset the receiving waveguide toward the $+x$ direction to obtain the maximum transfer, due to the refraction at the boundary between the waveguide and the air. In Fig. 5, the effect of the refraction is seen in the fact that the period of the transmitted power oscillation for $\theta=10^\circ$ is longer than that for $\theta=0^\circ$.

3. ANTIREFLECTIVE COATING

Another method of reducing the reflection is to coat the endface with an antireflective dielectric layer, as shown in Fig.6. The following parameters are used for the simulation; $D=0.13 \mu\text{m}$, $N_{\text{CO}}=3.6$, $N_{\text{CL}}=3.24$, $\lambda=0.86 \mu\text{m}$, $\Delta x=\Delta z=0.01 \mu\text{m}$ and $c\Delta t=0.007 \mu\text{m}$. The thickness of the antireflective coating is designated as L . Since the antireflection mechanism of the coating is considered to be impedance matching between the waveguide and the air, the refractive index in the coating is taken to be $N_{\text{AR}}=\sqrt{N_{\text{E}}N_{\text{A}}}$, where N_{E} is the effective index of the waveguide.

Fig.7 shows the reflectivities of the TE_0 and TM_0 modes as a function of the thickness L . For $L=0$, we can compare our results with the analytical results obtained by Vassallo [5]. The reflectivities for the TE_0 and TM_0 modes are 40.8% and 26.8%, respectively, while those in reference [5] are 41.5% and 26.5%. Good agreement is found to exist between both sets of results.

As expected, we can obtain minimum reflection when the thickness L is around $0.25 \lambda/N_{\text{AR}}$. It is interesting to note that the optimum thickness for the TE wave is slightly different from that for the TM wave.

4. CONCLUSIONS

Reflected guided power from the tilted endface has been calculated using the FDTD method. It is shown that the transmitted power in a mated interconnection oscillates as a function of endface separation due to multiple reflections. Waveguides with an antireflective coating are also investigated, and the polarization dependence of the reflected power is revealed.

ACKNOWLEDGMENT

The authors would like to thank Mr. Victor Shkawrytko for his kind assistance in the preparation of the manuscript.

REFERENCES

- [1] R.Rao and J.S.Cook, Electron. Lett., 22, (14), pp.731-732, 1986.
- [2] P.Kaczmarek, R.Baets, G.Franssens and P.E.Lagasse, Electron. Lett., 25, (11), pp.716-717, 1989.
- [3] G.Eisenstein, Bell Syst. Tech. J., 63, (2), pp.357-364, 1984.
- [4] T.Saitoh, T.Mukai and O.Mikami, J. Lightwave Tech., LT-3, (2), pp.288-293, 1985.
- [5] C.Vassallo, J. Opt. Soc. Am. A, 5, (11), pp.1918-1928, 1988.
- [6] K.S.Yee, IEEE Trans. Antennas Propagat., AP-14, (3), pp.302-307, 1966.
- [7] S.T.Chu and S.K.Chaudhuri, IEEE J. Lightwave Tech., LT-7, (12), pp.2033-2038, 1989.
- [8] G.Mur, IEEE Trans. Electromagn. Compat., EMC-23, (4), pp.377-382, 1981.

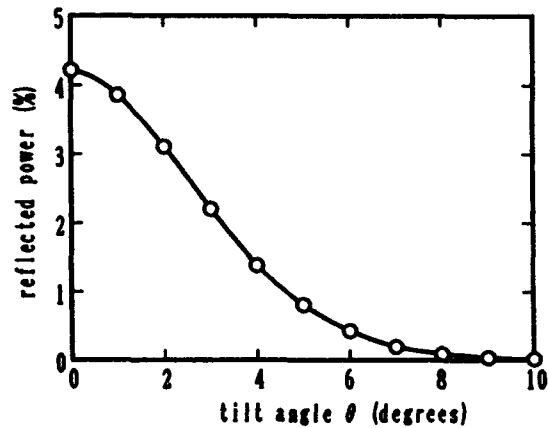
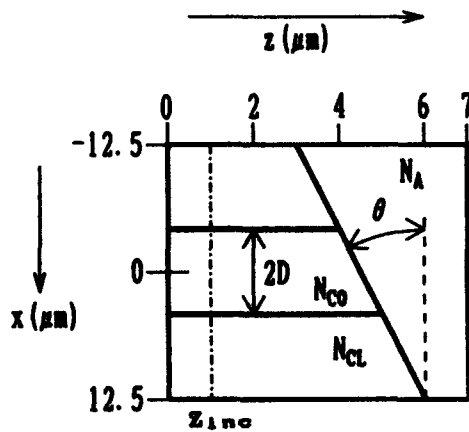


Fig.1 Configuration of tilted endface Fig.2 Reflected guided power

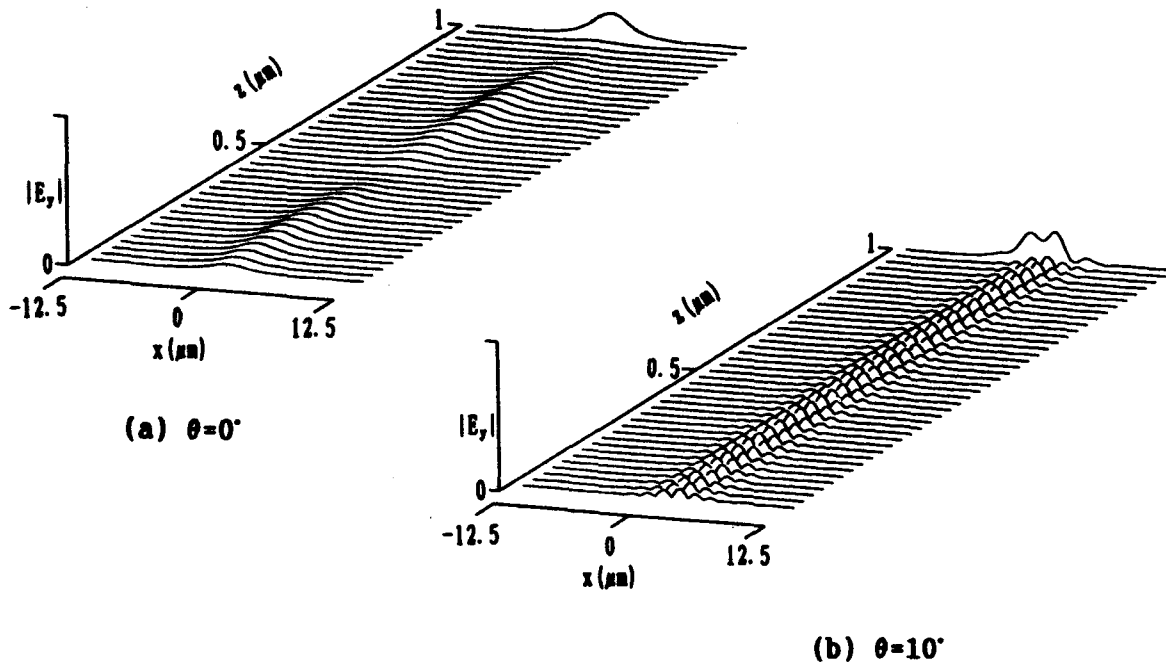


Fig.3 -z propagating E_y field observed in the reflected field region

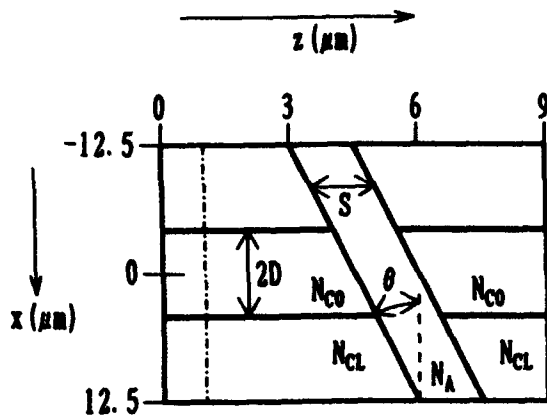


Fig. 4 Configuration of mated interconnection with tilted endface

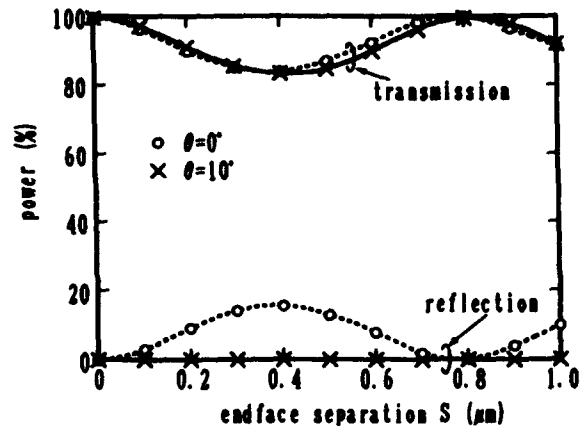


Fig. 5 Reflected and transmitted power as a function of endface separation

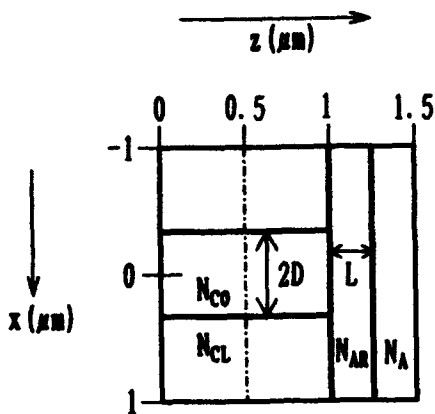


Fig. 6 Configuration of endface with antireflective coating

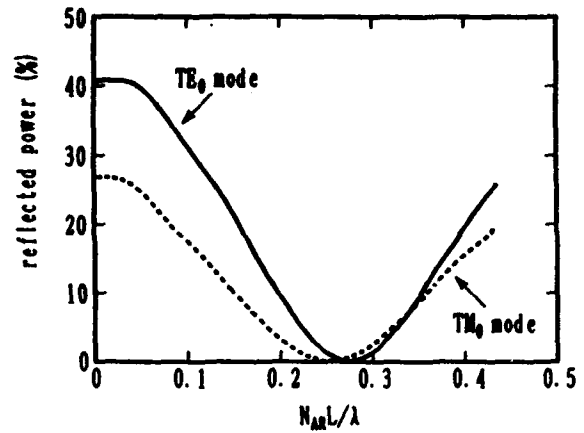


Fig. 7 Reflected power as a function of coating thickness

Direct Time Integration of Maxwell's Equations in 2-D Dielectric Waveguides for Propagation and Scattering of Femtosecond Electromagnetic Solitons

Peter M. Goorjian
Mail Stop 202A-2
NASA-Ames Research Center
Moffett Field, CA 94035
(415) 604-5547

Rose M. Joseph and Allen Taflove
EECS Department
McCormick School of Engineering
Northwestern University
Evanston, Illinois 60208-3118
(708) 491-4127

I. Introduction

Experimentalists have produced all-optical switches capable of 100-fs responses [1]. To adequately model such switches, nonlinear effects in optical materials [2] (both instantaneous and dispersive) must be included. In principle, the behavior of electromagnetic fields in nonlinear dielectrics can be determined by solving Maxwell's equations subject to the assumption that the electric polarization has a nonlinear relation to the electric field. However, until our previous work [3, 4], the resulting nonlinear Maxwell's equations have not been solved directly. Rather, approximations have been made that result in a class of generalized nonlinear Schrodinger equations (GNLSE) [5] that solve only for the *envelope* of the optical pulses.

2-D and 3-D engineered inhomogeneities in nonlinear optical circuits will likely be at distance scales in the order of 0.1 - 10 optical wavelengths, and all assumptions regarding slowly-varying parameters (which ran throughout GNLSE theory) will be unjustified. For such devices, optical wave scattering and diffraction effects relevant to integrated all-optical switches will be difficult or impossible to obtain with GNLSE because its formulation discards the optical carrier. The only way to model such devices is to retain the optical carrier and solve Maxwell's vector-field equations for the material geometry of interest, rigorously enforcing the vector-field boundary conditions and the physics of nonlinear dispersion.

In this paper, we describe first-time solutions of the 2-D vector nonlinear Maxwell's equations for material media having linear and nonlinear instantaneous and Lorentz-dispersive effects in the electric polarization. We use the finite-difference time-domain (FD-TD) method in an extension of our previous work in 1-D [3, 4]. The optical carrier is retained in this approach. The fundamental innovation is the treatment of the linear and nonlinear convolution integrals which describe the dispersion as new dependent variables. By differentiating these convolutions in the time domain, an equivalent system of coupled, nonlinear, second-order ordinary differential equations (ODE's) is derived. These equations together with Maxwell's equations form the system that is solved to determine the electromagnetic fields in nonlinear dispersive media. Backstorage in time is limited to only that needed by the time-integration algorithm for the ODE's (2 time steps), rather than that needed to store the time-history of the kernel functions of the convolutions. Thus, a 2-D nonlinear optics model from Maxwell's equations is now feasible.

II. A New Approach for Modeling Optical Pulse Phenomena in Nonlinear Dispersive Media in Two Dimensions

Consider a 2-D transverse magnetic (TM) problem. Maxwell's equations for the electric and magnetic field intensities, E_z , H_x , and H_y , are given by:

$$\frac{\partial \mu_0 H_x}{\partial t} = -\frac{\partial E_x}{\partial y}, \quad \frac{\partial \mu_0 H_y}{\partial t} = \frac{\partial E_x}{\partial x}, \quad \frac{\partial D_z}{\partial t} = \frac{\partial H_y}{\partial x} - \frac{\partial H_x}{\partial y} \quad (1)$$

We allow for dielectric nonlinearity by assuming that the electric polarization, P_z , consists of a linear part, P_z^L , and a nonlinear part, P_z^{NL} [5]. Then, we have:

$$D_z = \epsilon_0 \epsilon_{\infty} E_z + P_z, \quad P_z = P_z^L + P_z^{NL} \quad (2)$$

P_z^L is given by a convolution of $E_z(x, t)$ and the Lorentz susceptibility function, $\chi^{(1)}$:

$$P_z^L(x, t) = \epsilon_0 \int_{-\infty}^{\infty} \chi^{(1)}(t-t') E_z(x, t') dt', \quad \chi^{(1)}(t) = \left(\frac{\omega_p^2}{v_0} \right) \exp(-\delta t / 2) \sin(v_0 t) \quad (3)$$

Here, $\omega_p^2 = \omega_0^2(\epsilon_s - \epsilon_{\infty})$ and $v_0^2 = \omega_0^2 - \delta^2 / 4$. Further, we assume a dispersive (memory-type) material nonlinearity characterized by the following time convolution for P_z^{NL} [2]:

$$P_z^{NL}(x, t) = \epsilon_0 \chi^{(3)} E_z(x, t) \int_{-\infty}^{\infty} g(t-t') E_z^2(x, t') dt' \quad (4)$$

where $\chi^{(3)}$ is the nonlinear coefficient and $\int_{-\infty}^{\infty} g(t) dt = 1$. Eqn. (4) accounts for phonon interactions and nonresonant electronic effects, as given by

$$g(t) = \alpha \delta(t) + (1-\alpha) g_R(t), \quad g_R(t) = \left(\frac{\tau_1^2 + \tau_2^2}{\tau_1 \tau_2^2} \right) \exp(-t / \tau_2) \sin(t / \tau_1) \quad (5)$$

Here, $\delta(t)$ is the instantaneous delta function that models Kerr nonresonant virtual electronic transitions in the order of about 1 fs or less, and $g_R(t)$ models transient Raman scattering.

We now describe the system of coupled nonlinear ODE's that governs the time evolution of the polarization. Assuming zero values of the electromagnetic field and the kernel functions for $t \leq 0$, define the functions, $F(t)$ and $G(t)$, as respectively the convolutions:

$$F(t) = \epsilon_0 \int_0^t \chi^{(1)}(t-t') E_z(x, t') dt', \quad G(t) = \epsilon_0 \int_0^t g_R(t-t') E_z^2(x, t') dt' \quad (6)$$

Then, by time-differentiating F and G , these functions satisfy the following coupled system:

$$\frac{1}{\omega_0^2} \frac{d^2 F}{dt^2} + \frac{\delta}{\omega_0^2} \frac{dF}{dt} + \left(1 + \frac{\epsilon_s - \epsilon_{\infty}}{\epsilon_{\infty} + \alpha \chi^{(3)} E_z^2} \right) F + \left[\frac{(\epsilon_s - \epsilon_{\infty})(1-\alpha) \chi^{(3)} E_z}{\epsilon_{\infty} + \alpha \chi^{(3)} E_z^2} \right] G = \left(\frac{\epsilon_s - \epsilon_{\infty}}{\epsilon_{\infty} + \alpha \chi^{(3)} E_z^2} \right) D_z \quad (7)$$

$$\frac{1}{\bar{\omega}_0^2} \frac{d^2 G}{dt^2} + \frac{\bar{\delta}}{\bar{\omega}_0^2} \frac{dG}{dt} + \left[1 + \frac{(1-\alpha) \chi^{(3)} E_z^2}{\epsilon_{\infty} + \alpha \chi^{(3)} E_z^2} \right] G + \left(\frac{E_z}{\epsilon_{\infty} + \alpha \chi^{(3)} E_z^2} \right) F = \left(\frac{E_z}{\epsilon_{\infty} + \alpha \chi^{(3)} E_z^2} \right) D_z \quad (8)$$

where $\bar{\delta} = 2 / \tau_2$ and $\bar{\omega}_0^2 = (1 / \tau_1)^2 + (1 / \tau_2)^2$. Eqns. (7) and (8) are first solved simultaneously for F and G at the latest time step by using a second-order accurate finite-difference scheme that operates on data for the current value of D_z and previous values of D_z , E_z , F , and G . Then, the latest value of E_z can be obtained via a Newton's iteration, using the new values of D_z , F , and G :

$$E_z = \frac{D_z - F - (1 - \alpha)\chi^{(3)}E_z G}{\epsilon_0(\epsilon_\infty + \alpha\chi^{(3)}E_z^2)} \quad (9)$$

The system of Eqns. (7) - (9) determines values of E_z and P_z so that Eqn. (2) is satisfied. This procedure, combined with the usual FD-TD realization of Maxwell's equations, Eqn. (1), comprises the complete solution method.

III. Results

The modeling capabilities of this new algorithm are demonstrated by 2-D calculations of propagating and colliding solitons. The calculations are for a propagating pulse with a carrier frequency of $1.37 \cdot 10^{14}$ Hz ($\lambda = 2.19 \mu\text{m}$), and a hyperbolic secant envelope having a characteristic time constant of 14.6 fs. The computational domain for the 2-D dielectric waveguide is $110 \times 5 \mu\text{m}$, with the dielectric waveguide itself $1 \mu\text{m}$ thick and $2 \mu\text{m}$ of air on either side. The first calculation simulates Lorentz-medium linear dispersion alone (Eqn. 4). As Fig. 1 shows, the pulse undergoes predicted [5] pulse lengthening due to dispersive effects.

The second calculation simulates the effects of the full linear (Eqn. 3) and nonlinear (Eqns. 4 and 5) polarizations. As shown in Fig. 2, the propagating pulse now has the features of a soliton with the retention of its length. In addition, detailed plots show a second, low-amplitude, high-frequency, "daughter" pulse forms and moves out ahead of the soliton.

The third calculation simulates the collision of two equal-amplitude, counter-propagating solitons. The results show the solitons interacting during the collisions and then separating without general changes. However, by comparing the carriers of the collided solitons with those of the non-collided solitons, precise carrier phase lags of the collided solitons are measured.

The presentation also includes a color video of these calculations that shows the pulse evolution in time. Also, results will be shown of colliding solitons at angles other than head-on.

IV. Implications

The novel approach discussed here achieves robustness by rigorously enforcing the vector field boundary conditions at all interfaces of dissimilar media in the time scale of the optical carrier, whether or not the media are dispersive or nonlinear. As a result, the new approach is almost completely general. It assumes *nothing* about: (a) the homogeneity or isotropy of the optical medium; (b) the magnitude of the nonlinearity; (c) the nature of the material's $\omega - \beta$ variation; and (d) the shape, duration, and vector nature of the optical pulse(s). By retaining the optical carrier, the new method solves for *fundamental quantities* - the optical electric and magnetic fields in space and time - rather than a nonphysical envelope function. It has the potential to provide an unprecedented 2-D and 3-D modeling capability for millimeter-scale integrated optical circuits having sub- μm engineered inhomogeneities.

References

1. S. R. Friberg, A. M. Weiner, Y. Silberberg, B. G. Sfez, and P. S. Smith, *Optics Letters* **13**, 904-906 (1988).
2. K. Blow and D. Wood, *IEEE J. Quantum Electronics* **25**, 2665-2673 (1989).
3. P. M. Goorjian and A. Taflove, *Optics Letters* **17**, 180-182 (1992).
4. P. M. Goorjian, A. Taflove, R. M. Joseph, and S. C. Hagness, *IEEE J. Quantum Electronics* **28**, 2416-2422 (1992).
5. G. P. Agrawal, *Nonlinear Fiber Optics*. New York: Academic Press (1989).

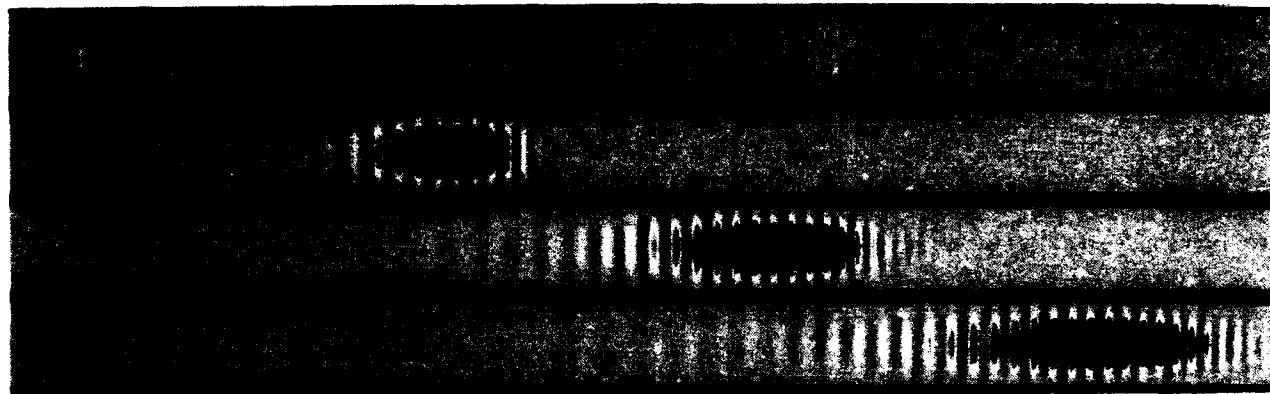


Fig. 1. Electric field of propagating optical carrier pulse with initial hyperbolic secant envelope ($\lambda = 2.19 \mu\text{m}$, $\tau = 14.6 \text{ fs}$) in $1\text{-}\mu\text{m}$ thick linear Lorentz-medium dielectric waveguide.

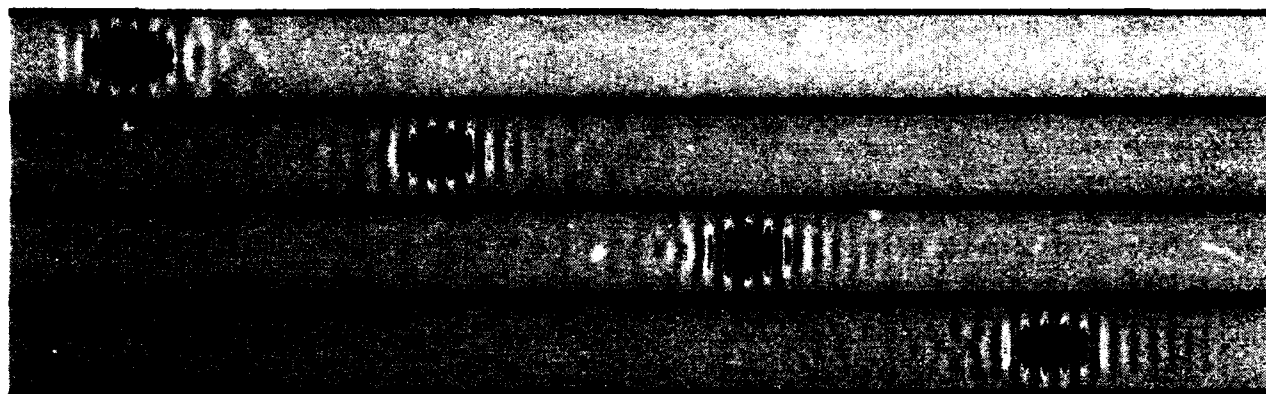


Fig. 2. Electric field of optical soliton carrier pulse corresponding to Fig. 1, including quantum effects such as the Kerr and Raman interactions.

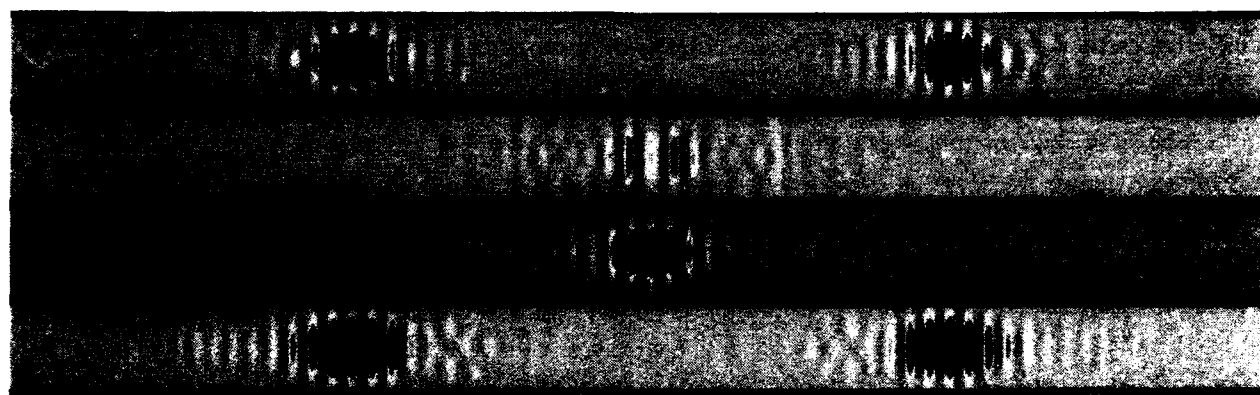


Fig. 3. Electric field of colliding counter-propagating solitons corresponding to Fig. 2 (approaching, destructively interfering, constructively interfering, separating).

Linear-Nonlinear Interfaces: Results from Full-Wave, Vector Maxwell Equation NL-FDTD Simulations

Richard W. Ziolkowski and Justin B. Judkins
 Department of Electrical and Computer Engineering
 The University of Arizona
 Tucson, AZ 85721
 (602) 621-6173

In this paper we discuss the characteristics of the scattering of pulsed Gaussian beams from a variety of linear-nonlinear interfaces. These results are obtained [R. W. Ziolkowski and J. Judkins, "Full-wave vector Maxwell equation modeling of the self-focusing of ultrashort optical pulses in a nonlinear Kerr medium exhibiting a finite response time", to appear in JOSA B, January 1993.] with a multi-dimensional, full-wave, vector Maxwell's equation solution method that models the interaction of ultra-short, pulsed optical beams with a nonlinear Kerr material having a finite response time. This nonlinear finite difference time domain (NL-FDTD) approach combines a nonlinear generalization of a standard, FDTD, full-wave, vector, linear Maxwell's equation solver with a currently used phenomenological time relaxation (Debye) model of a nonlinear Kerr material. In contrast to a number of recently reported numerical solutions of the full-wave, vector, *time-independent* Maxwell's equations and of vector paraxial equations, the FDTD approach is a *time-dependent* analysis which accounts for the complete time evolution of the system with no envelope approximations.

NL-FDTD results for normal, oblique, and grazing incidence nonlinear interface and dielectric slab waveguide problems will be emphasized in this paper. Although these basic geometries are straightforward, the NL-FDTD approach can readily handle more complex, realistic structures. These example *TE* and *TM* nonlinear optics problems will highlight the differences between the scalar and the vector approaches and the effects of the finite response time of the medium. Moreover, by incorporating single-cycle as well as multiple-cycle (envelope) pulses in the analysis, we can completely characterize, for instance, the potential of linear-nonlinear interfaces or linear-nonlinear slab waveguide configurations as all-optical switches for pulses generated with current as well as future laser systems. This case separation also affords us the opportunity to investigate the differences between the scalar envelope and full-wave vector equation models.

The NL-FDTD method is beginning to resolve several basic physics and engineering issues concerning the behavior of the full electromagnetic field during its interaction with linear-nonlinear interfaces. In particular, using the NL-FDTD approach we have (to the best of our knowledge) (1) performed the first complete full wave, vector treatment of *both* the *TM* and *TE* models of an optical diode (linear-nonlinear interface switch); (2) characterized the performance on an optical diode to single-cycle and multiple-cycle pulsed Gaussian beams including the appearance of a nonlinear Goos-Hänchen effect, the stimulation of stable surface modes, and the effects of a finite response time of the Kerr material; (3) shown definitively that the linear-nonlinear interface does not act like an optical diode for a tightly focused, single-cycle pulsed Gaussian beam; and (4) characterized the performance of linear-nonlinear slab waveguides as optical threshold devices. In these analyses we have identified the role of the longitudinal field component and the resulting transverse power flows in the interface scattering-coupling process.

The NL-FDTD method solves numerically Maxwell's equations

$$\partial_t [\mu_0 \vec{H}] = -\nabla \times \vec{E} \quad (1)$$

$$\partial_t [\epsilon_L \vec{E}] = \nabla \times \vec{H} - \partial_t \vec{P}^{NL}, \quad (2)$$

where the nonlinear polarization term $\vec{P}^{NL} = \chi^{NL}(\vec{r}, t, |\vec{E}|^2) \vec{E}$ is specified by solving simultaneously a Debye model for the third order, nonlinear susceptibility χ^{NL} of the Kerr medium:

$$\partial_t \chi^{NL} + \frac{1}{\tau} \chi^{NL} = \frac{1}{\tau} \epsilon_2 |\vec{E}|^2. \quad (3)$$

This approach models the medium as having a finite response time τ . If T represents the pulse width, then by setting $T \gg \tau$, one obtains an instantaneous response model: $\chi^{NL} \approx \epsilon_2 |\vec{E}|^2$, i.e., the medium follows

the pulse. On the other hand, if $T \leq \tau$, then the finite response time effects are maximal and the medium's response significantly lags the pulse. The NL-FDTD approach can treat both extremes. Moreover, the divergence equation associated with this system includes the nonlinear source term: $\nabla \cdot [\epsilon_L \vec{E}] = -\nabla \cdot \vec{P}^{NL}$. In two space dimensions and time with coordinates the (x, z, t) and with the choice of a TM_x polarized wave, the NL-FDTD method solves for the complete time history of each of the components (E_x, E_z, H_y) . The equations for a TE_z polarized wave can be obtained by reciprocity: $\vec{E} \rightarrow \vec{H}$ and $\vec{H} \rightarrow -\vec{E}$, and they lead to the NL-FDTD solution of the components (E_y, H_x, H_z) . The nonlinear source term strongly couples the transverse and longitudinal electric field components in the TM case; the corresponding magnetic field components in the TE case are driven by the transverse electric field component which exhibits the nonlinear growth. Additionally, when the linear-nonlinear interface problem is treated, Maxwell's equations naturally provide the boundary conditions appropriate for this lossy dielectric interface. Thus, the linear-nonlinear interface problem can be handled without imposing any additional constraints on the fields. Moreover, more complex structures can be added to the simulation with little difficulty, giving the NL-FDTD approach a great deal of flexibility. Note that we have taken the linear permittivity to be a constant. We have currently incorporated linear dispersion in the FDTD approach and are studying its effects on the optical diode. Because of the versatility of the FDTD approach, we have been able to "turn-on" the dispersion effects to analyze their impact on the linear-nonlinear interface reflection-transmission processes. The NL-FDTD results to be reported were obtained by carefully designing and testing the numerical grid, material parameters, and the algorithm to insure stability, accuracy, and efficiency.

In all of the interface problems we assumed that the interface was in the far-field of the source. We thus used a single bipolar pulse excitation for the single-cycle cases. This initial pulse was given by the function

$$F(t) = x(1-x^2)^3 H(1-|x|) \quad ; \quad x = \frac{2t}{T} - 1 \quad (4)$$

where $H(x)$ is Heaviside's function. A total pulse width $T = 20.0$ fs corresponds to an effective wavelength of $4.0 \mu\text{m}$. This initial driving function has both first and second time derivatives continuous at its endpoints, thus reducing the numerical noise initially generated in the grid.

For the normal incidence cases we used a $30.0 \mu\text{m} \times 40.0 \mu\text{m}$ rectangular grid with $\Delta z = 0.02 \mu\text{m}$ and $\Delta t = 0.018$ fs resolution. This resolution gives a problem 1500×2000 cells large. The discretizations thus provided an average spatial resolution of $\Delta z = \lambda/160$. The nonlinear medium parameters were set to the value $n_2 = \epsilon_2/(2n_0) = 1.0 \times 10^{-16} (\text{m}^2/\text{V}^2)$, where $n_0 = 1.0$. The initial transverse amplitude waist was taken to be $w_0 = 10.0 \mu\text{m}$. Most of our results were obtained with the nearly instantaneous-regime medium response time of $\tau = 4.0$ fs $= 0.2 T$. Typical results are depicted in Figure 1 in which the waist of the energy of the beam is plotted as a function of its location along the direction of propagation. For low intensity, the beam diffracts as though it were in free space; for high intensity, some portion of the beam reflects and the transmitted beam self-focuses in the Kerr medium. The actual reflection coefficient is substantially below the value anticipated from an equivalent monochromatic beam. This is due primarily to the fact that the pulse does not cause the medium to respond instantly; hence, much of the energy penetrates into the medium before the boundary is sufficiently reflective. The transmitted beam behaves as predicted from previously reported self-focusing beam propagation simulations.

The goal of the oblique incidence cases was to construct a configuration in which the pulsed Gaussian beam is either transmitted or reflected completely from the linear-nonlinear interface. By design, the incident wave is assumed to be beyond critical where the critical angle

$$\theta_{inc} > \theta_{crit} = \sin^{-1} \left(\frac{n_b - \Delta n + n_2 |E_0|^2}{n_b} \right), \quad (5)$$

the index of the linear medium being n_b and the index of the nonlinear medium being $n_b - \Delta n + n_2 |E_0|^2$. The expectation from linear theory is that a monochromatic plane wave will be reflected when it is incident beyond the critical angle and transmitted when it is below that value. Including the nonlinearity, one introduces a control over the critical angle. In particular, the critical angle will disappear at sufficiently high field intensities. This optical diode has been considered as a proto-type all-optical switch. Because the NL-FDTD approach is a complete vector model, it is a good method for modeling the wide range of wave vectors contained in a tightly focused, strongly diffracting beam that scatters from a sharp index step at any angle of incidence considered in this problem.

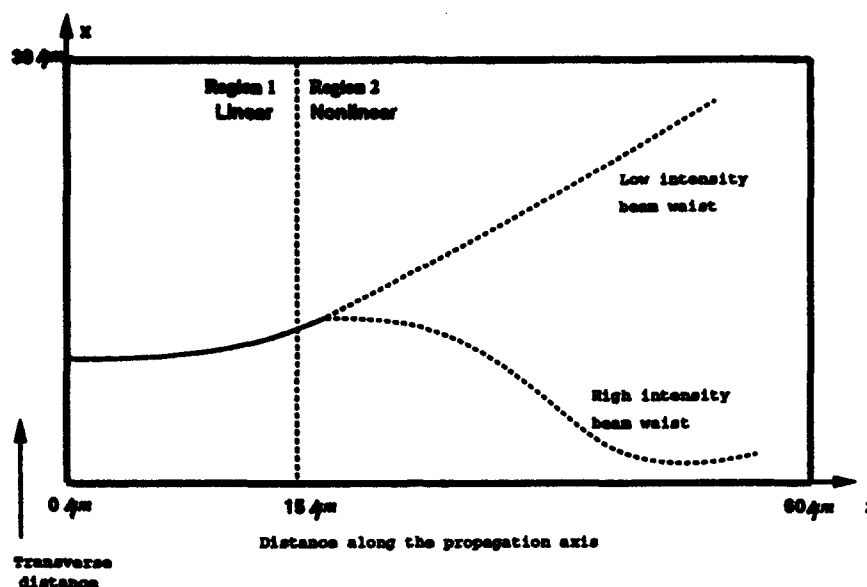


Figure 1. The normal incidence problem is divided into two regions: the incident region which is linear and the transmission region which is nonlinear. The linear index is continuous across the interface so that a low intensity beam will propagate unchanged. As the intensity increases, the pulse experiences some reflection and the transmitted pulse will self-focus if the initial transmitted field amplitude is above threshold.

For the oblique incidence cases considered, we used a $105 \mu\text{m} \times 305 \mu\text{m}$ rectangular grid with $\Delta x = 0.125 \mu\text{m}$ and $\Delta t = 0.018 \text{ fs}$ resolution. The nonlinear medium parameters were set to the same value $n_2 = \epsilon_2 / (2n_0) = 1.0 \times 10^{-18} \text{ (m}^2/\text{V}^2)$, where n_0 is the background index. The initial pulse was given by Eq. (4) but with a pulse width of $T = 30.0 \text{ fs}$, hence, an effective wavelength of $6.0 \mu\text{m}$. The discretizations thus provided an average spatial resolution of $\Delta x = \lambda/48$. The initial waists range from $10 \mu\text{m}$ to $15 \mu\text{m}$. Several medium response times τ were investigated from $\tau = 5.0 T$ to $\tau = 0.05 T$. Most of the cases were run with the parameters $n_0 \equiv n_1 = 1.56$ and $\Delta n = 0.06$, giving $\theta_{\text{crit}} = 74.1^\circ$. A variety of initial field amplitudes and angles of incidence we explored.

We have found that this optical diode may be realizable for plane waves, but it does not appear to be feasible for realistic, pulsed, finite beams. Figure 2 represents the typical results. We have explicitly demonstrated the presence of the nonlinear Goos-Hächen effect as indicated. However, because the tightly focused beam contains such a large variety of wavevectors, a large portion of the incident beam penetrates into the medium, even in the linear case. Our best results to date have only indicated a $\sim 40\%$ reflection coefficient for either the TE or the TM cases. Only when the beam was highly defocused so that it behaved more like a plane wave did we see more substantial reflections. These results indicate that the linear-nonlinear switch will perform poorly as an optical diode in any ultrashort, focused optical system.

With these initial disappointing results for the optical diode, we have switched our attention to optical threshold devices in dielectric waveguides. Figure 3 represents the basic idea. A linear guiding film is sandwiched between a linear cover region and a nonlinear substrate region. The substrate and cover have the same linear attributes. If the intensity of the pulse propagating in the channel is below threshold, the pulse remains confined within the guide. On the other hand, if the pulse amplitude is close to or above threshold, the coupling of the propagating mode to the nonlinearity causes some of the energy to switch out of the guide into the Kerr medium. The energy emitted into the nonlinear substrate is either channeled into a nonlinear surface mode along the film/substrate interface or gets distributed between the surface mode and a self-trapped channel and propagates away from the guide at an angle dependent on the initial pulse intensity. A second guide can then be positioned to capture the energy switched out of the first guide. The waveguiding nature of these configurations appears to overcome the diffraction spreading of the wavevectors that occurs with tightly focused beams in the linear-nonlinear switch geometry. We are currently studying the switching efficiency of these optical threshold waveguide configurations and will report the results of our complete study.

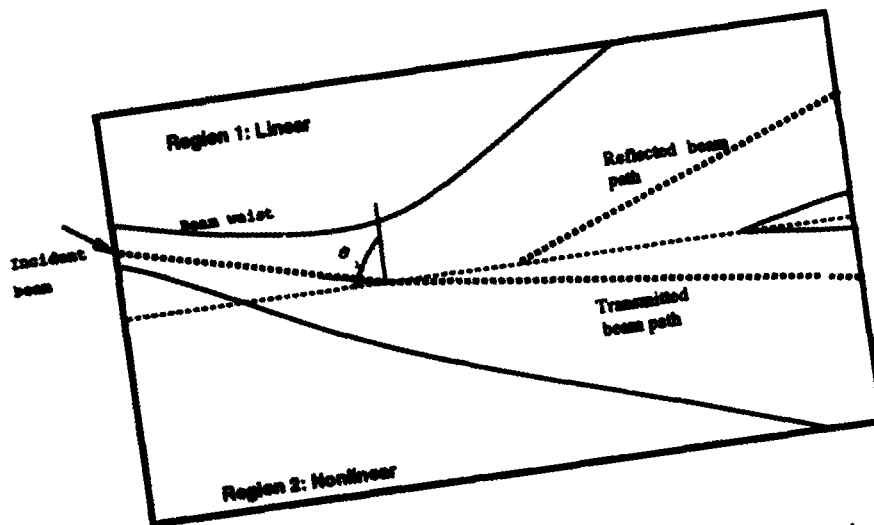


Figure 2. The oblique incidence problem is also divided into the linear and nonlinear regions. There is a small index step between the mediums with the incident medium having a higher index. The index step size is chosen such that the critical angle θ_{crit} is smaller than the incident angle θ_{inc} to create a condition approaching total reflection. The translation of the beam center corresponding to the nonlinear Goos-Hächen effect is depicted. However, for a tightly focused pulsed Gaussian beam, a substantial portion of the beam is transmitted into Region 2 as shown, even for low initial field amplitudes.

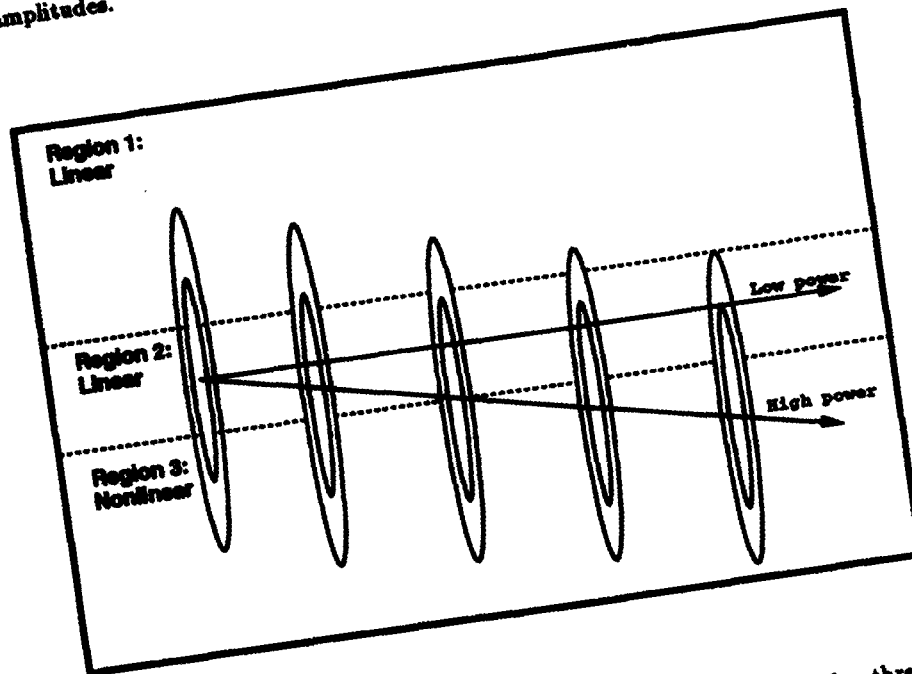


Figure 3. The general configuration for a slab waveguide threshold device includes three regions: a linear substrate sandwiched between a linear and a nonlinear substrate. A pulse (packet) of energy in the lowest order mode is launched from the left into the guide. This packet will either remain in the guide or will be coupled into the nonlinear substrate and form its own guiding channel at an angle that depends on the intensity of the initial pulse.

A Unifying Formulation of Material Dispersion in Finite-Difference Time-Domain Simulations of Optical Problems

Charles Hulse and André Knoesen
 Department of Electrical Engineering and Computer Science
 University of California, Davis
 Davis, CA 95616
 Tel: (916) 752-8023
 E-mail: {hulse,knoesen}@eeecs.ucdavis.edu

I. INTRODUCTION

Methods of solving Maxwell's equations on a discrete grid in space and time show promise in predicting the time-evolution of ultrashort pulse propagation in optical devices [1, 2]. Finite-Difference Time-Domain (FDTD) algorithms developed for microwave problems [3, 4] discretize Maxwell's curl equations and consider the permittivity ϵ and permeability μ of a material to be constant. Over the bandwidth of short optical pulses, the material dispersion cannot be ignored. Recently, various authors [5-11] have attempted to model this dispersion by adding finite-difference approximations of the constitutive equations to the algorithm. Two competing approaches with very different motivations have emerged; comparisons between them have been in the form of lengthy numerical simulations. We formulate the problem of modeling dispersive materials as a filter design problem in signal processing. The formalism of discrete-time linear systems then enables us to examine the difference equation as an approximation to the desired continuous filter, and to equate the design of an optimal filter to the solution of a constrained minimization problem. We show that the previously used methods of approximating dispersion are analogous to the matched and bilinear approximation methods of discrete filter design theory. We compare the exact frequency response of existing discretizations to the desired response for Debye and Lorentzian media.

II. THEORY

Maxwell's Equations relate the spatial derivatives of the electric and magnetic fields, E and H , respectively, to the time derivatives of the electric and magnetic flux densities, D and B . The constitutive equations represent the effects of the material on the radiation; they relate the fluxes and fields through the electric and magnetic polarization response of the medium. In this paper, we consider only the dispersion in permittivity, but the approach can also be applied to a dispersive permeability as well.

In general, the constitutive relation describing the electric response of a material is a convolution

$$D(t) = \int_{-\infty}^t \epsilon(\tau)E(t - \tau)d\tau. \quad (1)$$

As a linear system, equation (1) indicates that the polarization response of a material is a linear time-invariant filter whose input is the electric field and whose output is the electric flux. To construct an appropriate model for FDTD, we start with the general form for a discrete-time linear filter:

$$b_0 D^n + b_1 D^{n-1} + b_2 D^{n-2} + \dots = a_0 \epsilon_0 E^n + a_1 \epsilon_0 E^{n-1} + a_2 \epsilon_0 E^{n-2} + \dots, \quad (2)$$

where n corresponds to the time step. Any realizable approximation of (1) can be cast into this form; the only differences in the various approaches lie in the method used to derive (2) and the specifics of implementation, e.g., the use of intermediate variables. The two general approaches used to discretize the polarization equation are direct integration [5, 6] and differentiation [9]. Direct integration requires first converting the frequency response of the permittivity to a time-domain impulse response, then approximating the convolution integral. A recursive sum simplification (in the manner of [6, 12]) may not be obvious or stable, forcing the storage of the entire time-history of the simulation. Differentiation, on the other hand, is straightforward for a simple dispersive behavior, but may quickly lead to a large number of coupled equations if several resonances are to be considered. Most importantly, neither method is capable of giving a quantitative answer to the all-important question of how well it models the desired response. To answer that question, we appeal to linear systems theory, which is able to examine convolution, integration, and differential equations in a more general setting. By examining these systems in the frequency domain, we may directly observe the frequency response $\tilde{\epsilon}_r$ of a given discrete equation and compare it with the desired frequency response ϵ_r :

$$\epsilon_r(j\omega) \approx \tilde{\epsilon}_r(j\omega) = \frac{a_0 + a_1 \exp(-j\omega\Delta t) + a_2 \exp(-2j\omega\Delta t) + \dots}{b_0 + b_1 \exp(-j\omega\Delta t) + b_2 \exp(-2j\omega\Delta t) + \dots}. \quad (3)$$

We introduce the z -terminology [13] for a delay of Δt ,

$$z^{-1} \equiv \exp(-j\omega\Delta t). \quad (4)$$

Equation (4) allows direct translation of a frequency-dependent permittivity to the "delay" domain with a rational z -polynomial approximation of $j\omega$. Alternatively, equation (4) may be used to formulate the design as a linear minimization problem.

III. COMPARISON TO EXISTING METHODS

Exploiting the linear systems perspective, we recast the work of previous researchers as discrete filters and compare them to $\epsilon_r(j\omega)$. In this form, the nature of the approximation to equation (4) becomes evident.

The recursive convolution approach originally taken by Yee *et al* [12] and subsequently followed by Luebbers *et al* [6, 8, 10, 11] preserves the poles of $\epsilon_r(j\omega)$ exactly. For this reason the analogous approach in linear systems theory is called a matched transform:

$$j\omega + a \approx a \left(\frac{1 - \exp(-a\Delta t)z^{-1}}{1 - \exp(-a\Delta t)} \right). \quad (5)$$

Employing this simple relation, the inverse Fourier transform and approximate integration can be bypassed completely, and one arrives at equation (2) in two steps for an arbitrary frequency function. In comparison to other techniques of approximating (4), the matched transform has the feature that in simple cases it requires minimal operations, and, more importantly, only one delayed variable for each pole. Unfortunately, this method is only accurate near the pole frequencies, i.e., for low frequencies. The simplest example of a matched transform is the backward difference approximation to a derivative.

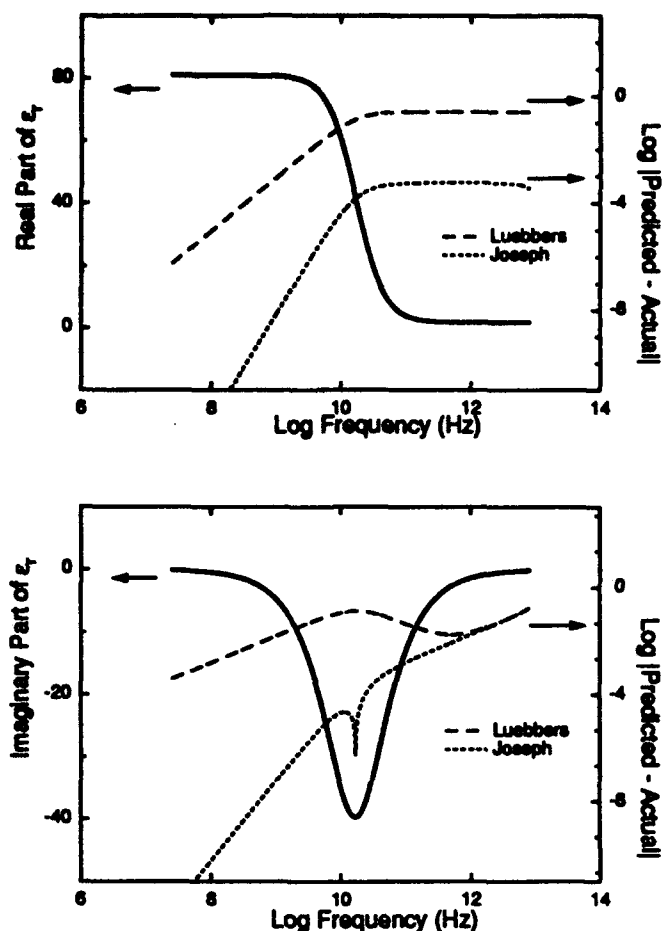


Figure 1: The frequency response of the Debye relaxation (left axis) and the error in the approximation (right axis) of two existing models. Parameters are as given in Ref. [6].

Both the trapezoidal integration technique of Kashiwa and Fukai [5, 7] and the differential equation techniques of Joseph *et al* [9] are analogous to the bilinear transform:

$$j\omega \approx \frac{2}{\Delta t} \left(\frac{z-1}{z+1} \right). \quad (6)$$

It is termed bilinear because a single pole or zero is replaced by a discrete pole-zero pair. Once again, this relation considerably simplifies the process of deriving a differencing scheme for (1). The bilinear transform offers a good approximation to ω over the bandwidth of the simulation, but if implemented directly as in (2), it doubles the memory necessary at each grid point. The simplest bilinear filter is "box scheme" differentiation.

IV. RESULTS

Figure 1 illustrates the insight obtained from linear system theory. It shows a comparison of the exact dispersive response to FDTD models; a comparison made in the context of a digital filter approximation. The exact filter in this case is the Debye polarization model (with parameters given in [6])

$$\epsilon(j\omega) = \epsilon_{\infty} + \frac{\epsilon_s - \epsilon_{\infty}}{1 + j\omega\tau}. \quad (7)$$

Superimposed is the error of the matched (Luebbers) and bilinear (Joseph, Kashiwa) filters. The bilinear transform consistently exhibits several orders of magnitude better accuracy than the matched

transform. Both methods lose accuracy as the frequency approaches cutoff at $f = 1/2\Delta t$.

Similar comparisons have been made with the Lorentzian model of electronic polarization, with similar results.

V. CONCLUSIONS

In this paper, the formalism of linear systems theory was used to compare existing models for common polarization responses of optical materials. This approach to implementation and analysis of frequency-dependent material models in FDTD was shown to be much simpler than existing techniques. Systems techniques can also be used to approximate an arbitrary frequency-dependent response function, or to tailor the frequency response to be highly accurate over a specific bandwidth. Furthermore, this approach can be used to implement specific filters with a tradeoff between economy and numerical sensitivity. In short, the system theory perspective promises to be strengthened and simplify the development and analysis of finite-difference time-domain techniques for modeling optical problems.

REFERENCES

- [1] P. M. Goorjian et al., *IEEE J. Quant. Elect.*, vol. 28, pp. 2416-2422, Oct. 1992.
- [2] S. T. Chu and S. K. Chaudhuri, *IEEE Trans. Microw. Theor. Tech.*, vol. 38, pp. 1755-1760, Nov. 1990.
- [3] K.S. Yee, *IEEE Trans. Ant. Prop.*, vol. AP-14, pp. 302-307, May 1966.
- [4] A. Taflov, *Wave Motion*, vol. 10, pp. 547-582, Dec. 1988.
- [5] T. Kashiwa and I. Fukai, *Microw. and Opt. Tech. Lett.*, vol. 3, pp. 203-205, June 1990.
- [6] R. J. Luebbers et al., *IEEE Trans. Elect. Compat.*, vol. 32, pp. 222-227, Aug. 1990.
- [7] T. Kashiwa and I. Fukai, *Microw. and Opt. Tech. Lett.*, vol. 3, pp. 416-419, Dec. 1990.
- [8] R. J. Luebbers et al., *IEEE Trans. Ant. Prop.*, vol. 39, pp. 29-34, Jan. 1991.
- [9] R. M. Joseph et al., *Opt. Lett.*, vol. 16, pp. 1412-1414, 1991.
- [10] R. Luebbers et al., in *APS Digest*, pp. 1972-1974, July 1992.
- [11] F. Hunsberger et al., in *URSI Digest*, p. 454, July 1992.
- [12] K. S. Yee et al., Preprint UCRL-75007, Lawrence Livermore Laboratory, July 1973.
- [13] R. D. Strum and D. E. Kirk, *First Principles of Discrete Systems and Digital Signal Processing*, Addison-Wesley Publishing Company, Inc., 1988.

Linear electronic dispersion and Finite-Difference Time-Domain calculations: a simple approach²

R.J. Hawkins and J.S. Kallman

Lawrence Livermore National Laboratory, Livermore CA 94550

(510) 422-0581

The Finite-Difference Time-Domain (FDTD) treatment of electromagnetic pulse propagation holds much promise for the complete numerical description of integrated optical device behavior where reflections and/or coherent effects are important. The recent application of FDTD to problems in integrated optics³ has indicated that electronic dispersion must be included to treat realistically the broadband behavior of integrated optical devices. The inclusion of material dispersion (electronic or magnetic) in FDTD calculations has historically been quite limited. The first formulation of broadband dispersion in FDTD was presented in a pioneering paper by Luebbers *et al.*⁴ who demonstrated that if the electronic susceptibility was expanded as a series of exponentials that the treatment of dispersion could be reduced to a recursive update. The incorporation of this update, however, requires a substantial rewriting of the standard electric field update equations. More recently, Lee *et al.*⁵ and Joseph *et al.*⁶ demonstrated a different formulation to the linear problem in which they solve explicitly the equation of motion for the polarizability using finite-differencing. Goorjian and Taflov⁷ have extended this alternative formulation to nonlinear optical propagation. In this paper we follow the general approach of Luebbers *et al.* but exploit a simple causality argument that enables us to write dispersion as a simple recursive *additive* term in the common electric field update equations. This is of particular interest since it will enable the treatment of dispersion in a large number of existing FDTD design codes with minimal computational modification. We then demonstrate the accuracy of our formulation by simulating the reflection of a broadband pulse from an air-water interface.

We begin with a quick review of the Yee formulation⁸ of Maxwell's curl equations since the steps in this derivation will be followed in our development below. In Yee's notation the one dimensional Maxwell's curl equations for a nonpermeable, nondispersive, and isotropic medium

$$\frac{\partial B_z}{\partial t} = -\frac{\partial E_y}{\partial x}, \quad (1)$$

²This research was performed under the auspices of the U.S. Department of Energy by the Lawrence Livermore National Laboratory under contract W-7405-ENG-48.

³S.T. Chu and S.K. Chaudhuri, "A Finite-Difference Time-Domain Method for the Design and Analysis of Guided-Wave Optical Structures", *J. Lightwave Technol.* LT-7, 2033-2038 (1989); S.T. Chu, *Modelling of Guided-Wave Optical Structures by the FDTD Method*, Doctoral Thesis, University of Waterloo (1990); S.T. Chu and S. Chaudhuri, "Combining Modal Analysis and the FDTD Method in the Study of Dielectric Waveguide Problems," *IEEE Trans. Microwave Theory* 38, 1755-1760 (1990).

⁴R. Luebbers, F.P. Hunsberger, K.S. Kunz, R.B. Standler, and M. Schneider, "A frequency dependent Finite-Difference Time-Domain formulation for dispersive materials," *IEEE Trans. Electromagn. Compat.* EMC-32, 222-227 (1990).

⁵C.F. Lee, R.T. Shin, and J.A. Kong, *PIER4 Progress in Electromagnetics Research*, edited by J.A. Kong (Elsevier, New York, 1991), pp. 415-435.

⁶R.M. Joseph, S.C. Hagness, and A. Taflov, "Direct time integration of Maxwell's equations in linear dispersive media with absorption for scattering and propagation of femtosecond electromagnetic pulses," *Opt. Lett.* 16, 1412-1414 (1991).

⁷P.M. Goorjian and A. Taflov, "Direct time integration of Maxwell's equations in nonlinear dispersive media for propagation and scattering of femtosecond electromagnetic solitons," *Opt. Lett.* 17, 1412-1414 (1992).

⁸K.S. Yee, "Numerical solution of initial boundary value problems involving Maxwell's equations in isotropic media," *IEEE Trans. Antennas Propag.* AP-14, 302-307 (1966).

$$\frac{\partial D_y}{\partial t} = -\frac{\partial H_x}{\partial x}, \quad (2)$$

become, with $B_x = \mu H_x$,

$$\frac{H_x^{n+1/2}(i+1/2) - H_x^{n-1/2}(i+1/2)}{\Delta t} = -\frac{E_y^n(i+1) - E_y^n(i)}{\mu \Delta x}, \quad (3)$$

$$\frac{D_y^{n+1}(i) - D_y^n(i)}{\Delta t} = -\frac{H_x^{n+1/2}(i+1/2) - H_x^{n+1/2}(i-1/2)}{\Delta x}, \quad (4)$$

where $E_y^n(i)$ denotes the value of the y -component of the electric field at position $x = i\Delta x$ and time $t = n\Delta t$; the displacement field $D_y^n(i)$ and magnetic field $H_x^n(i)$ being similarly denoted. Using the constitutive relation $D_y(t) = \epsilon_0 E_y(t)$ we can clear D_y from Eq. 4 and obtain the field update equations

$$H_x^{n+1/2}(i+1/2) = H_x^{n-1/2}(i+1/2) - \left(\frac{\Delta t}{\mu \Delta x}\right) [E_y^n(i+1) - E_y^n(i)], \quad (5)$$

$$E_y^{n+1}(i) = E_y^n(i) - \left(\frac{\Delta t}{\epsilon_0 \Delta x}\right) [H_x^{n+1/2}(i+1/2) - H_x^{n+1/2}(i-1/2)]. \quad (6)$$

Equations 5 and 6 are the standard Yee formulation field update equations. We now consider the constitutive equation for linear dispersion

$$D(t) = \epsilon_0 E(t) + \epsilon_0 \int_0^t \chi(t-\tau) E(\tau) d\tau, \quad (7)$$

$$= \epsilon_0 E(t) + \epsilon_0 P(t), \quad (8)$$

where $\chi(t)$ is the linear susceptibility and where we have defined $P(t)$ to be the integral in Eq. 7. Proceeding as we did above we obtain the following modified version of Eq. 6:

$$E_y^{n+1}(i) = E_y^n(i) - \left(\frac{\Delta t}{\epsilon_0 \Delta x}\right) [H_x^{n+1/2}(i+1/2) - H_x^{n+1/2}(i-1/2)] - [P_y^{n+1}(i) - P_y^n(i)]. \quad (9)$$

To evaluate $P_y^{n+1}(i) - P_y^n(i)$ it is useful to return to the continuous representation:

$$P_y(t + \Delta t) = \int_0^t \chi(t + \Delta t - \tau) E_y(\tau) d\tau + \int_t^{t+\Delta t} \chi(t + \Delta t - \tau) E_y(\tau) d\tau. \quad (10)$$

The second integral in Eq. 10 vanishes because (i) $\chi(0) = 0$ ⁹ and (ii) the contribution to the integral at $\tau = t$ is contained in the first integral in Eq. 10 when rectangular quadrature is used. Thus

$$P_y(t + \Delta t) - P_y(t) = \int_0^t [\chi(t + \Delta t - \tau) - \chi(t - \tau)] E_y(\tau) d\tau. \quad (11)$$

This is a particularly useful result because it eliminates the term $E_y(t + \Delta t)$ from the convolution and, thus, makes electronic dispersion an *additive* contribution to the standard Yee formulation. Thus, adding dispersion to an existing FDTD code can now be done by adding a term. This

⁹Electronic susceptibilities are impulse response functions for materials. Causality states that the material cannot respond before the field arrives. The statement $\chi(0) = 0$ simply means that the material responds to the field and that this response is not instantaneous.

contrasts with the formulation of Luebbers *et al.* that required a rewriting of the electric-field update equation.

A simple recursion for Eq. 11 can be obtained by writing the susceptibility as $\chi(t) = \sum_l \alpha_l e^{\beta_l t}$. Substituting this into Eq. 11 and casting the integral as a rectangular quadrature we obtain

$$P_y^{n+1}(i) - P_y^n(i) = \Delta t \sum_l \alpha_l (e^{\beta_l \Delta t} - 1) R_{l,y}^n(i), \quad (12)$$

where,

$$R_{l,y}^n(i) = \sum_{j=0}^n e^{\beta_l(n-j)\Delta t} E_y^j(i). \quad (13)$$

It is a straightforward matter to show that the recursion for $R_{l,y}^n$ is

$$R_{l,y}^n(i) = e^{\beta_l \Delta t} R_{l,y}^{n-1}(i) + E_y^n(i), \quad (14)$$

$$R_{l,y}^0(i) = E_y^0(i). \quad (15)$$

Summing up, we substitute Eq. 13 into Eq. 6 we obtain the following update equation

$$E_y^{n+1}(i) = E_y^n(i) - \left(\frac{\Delta t}{\epsilon_o \Delta x} \right) \left[H_x^{n+1/2}(i+1/2) - H_x^{n+1/2}(i-1/2) \right] - \Delta t \sum_l \alpha_l (e^{\beta_l \Delta t} - 1) R_{l,y}^n(i). \quad (16)$$

Comparing this with Eq. 6 reveals that linear dispersion simply adds a recursive term to the standard Yee equations.

A similar result has been obtained for the case of magnetic dispersion by DeFord *et al.*¹⁰. These results taken together constitute a complete solution to the treatment of dispersion - both electronic and magnetic - in FDTD calculations.

To test this approach we have reproduced the calculation given in the paper of Luebbers *et al.* of the reflection of a 1 kV/cm Gaussian pulse from an air-water interface in 1-dimension.¹¹ The results are shown in Fig. 1 where we compare the results of our formulation to that of Luebbers *et al.*. Using the method discussed by Luebbers *et al.* we have also calculated the reflection coefficient as a function of frequency, and we show the result of this calculation together with the exact result in Fig. 2. The essentially identical results demonstrate the accuracy of our formulation.

In summary, we have demonstrated an alternative formulation of dispersion in the FDTD equations and have shown that our approach reproduces accurately the reflection of a broadband electromagnetic pulse from an air-water interface. Our new formulation has the novel feature that dispersion enters as an additive term and, thus, provides a computationally simple introduction of dispersion into the standard Yee formulation.¹²

¹⁰J.F. DeFord, G.D. Craig, L. Walling, P. Allison, and M. Burns, "Development and application of Dispersive Soft-Ferrite Models for Time-Domain Simulation," (to be published).

¹¹To obtain the coefficients needed for our calculation we fit the Lorentzian form of $\chi(\omega)$ to that used by Luebbers *et al.*: $\chi(\omega) = (\epsilon_s - \epsilon_\infty)/(1 + i\omega t_o)$ where $\epsilon_s = 81$, $\epsilon_\infty = 1.8$, and $t_o = 9.4$ picoseconds. We thus obtained $\omega_o = 135$ GHz, $\gamma = 1000$ GHz, and $m = 6.86 \times 10^{-7}$ GHz⁻¹. The numerical experiment was set up identically to that of Luebbers *et al.*: a problem space of 1000 cells (499 air; 501 water), $\Delta x = 37.5 \mu\text{m}$, and $\Delta t = 0.0625$ picoseconds.

¹²ACKNOWLEDGEMENTS: We thank Dr. John F. Deford of LLNL for his help in this work and for providing a preprint of his work on magnetic dispersion. We also thank Scott Nelson for enlightening discussions and for his help in the calculation of the reflection coefficients.

FIGURES:

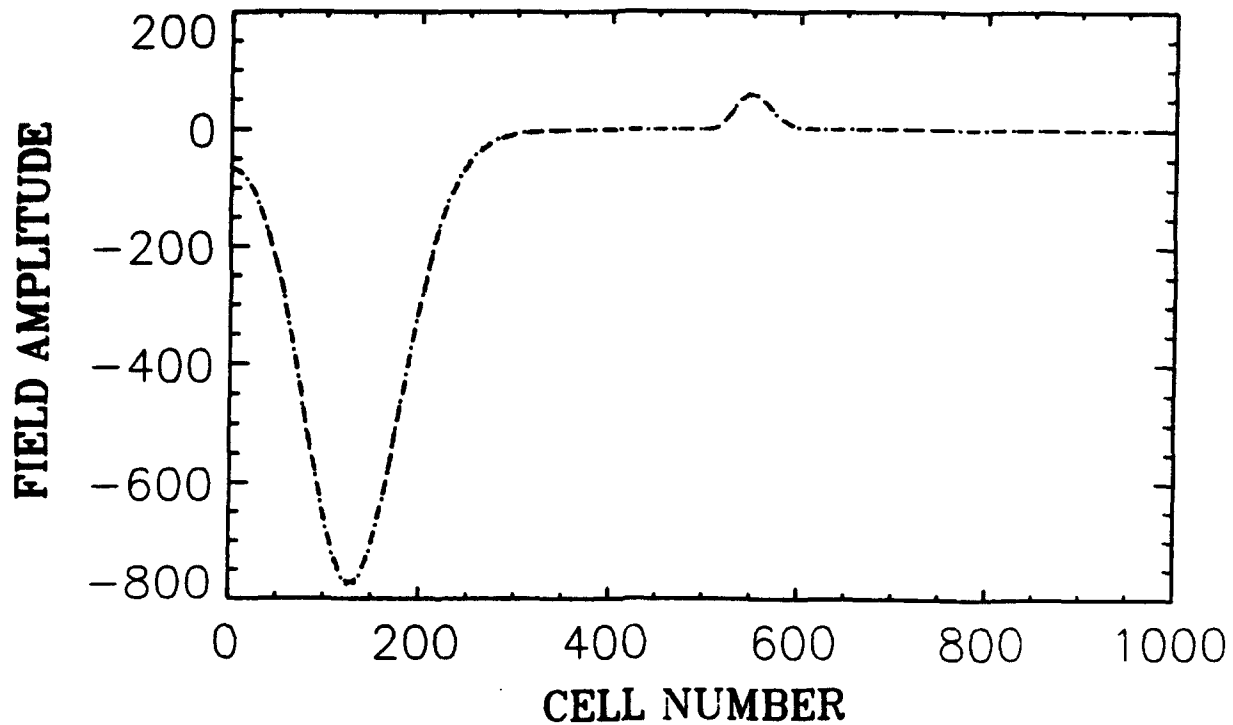


[Figure 1] A comparison of the total electric field after reflection from an air-water interface. The dashed line is the result using the formulation of Luebbers *et al.*. The dotted line is the result of our formulation.

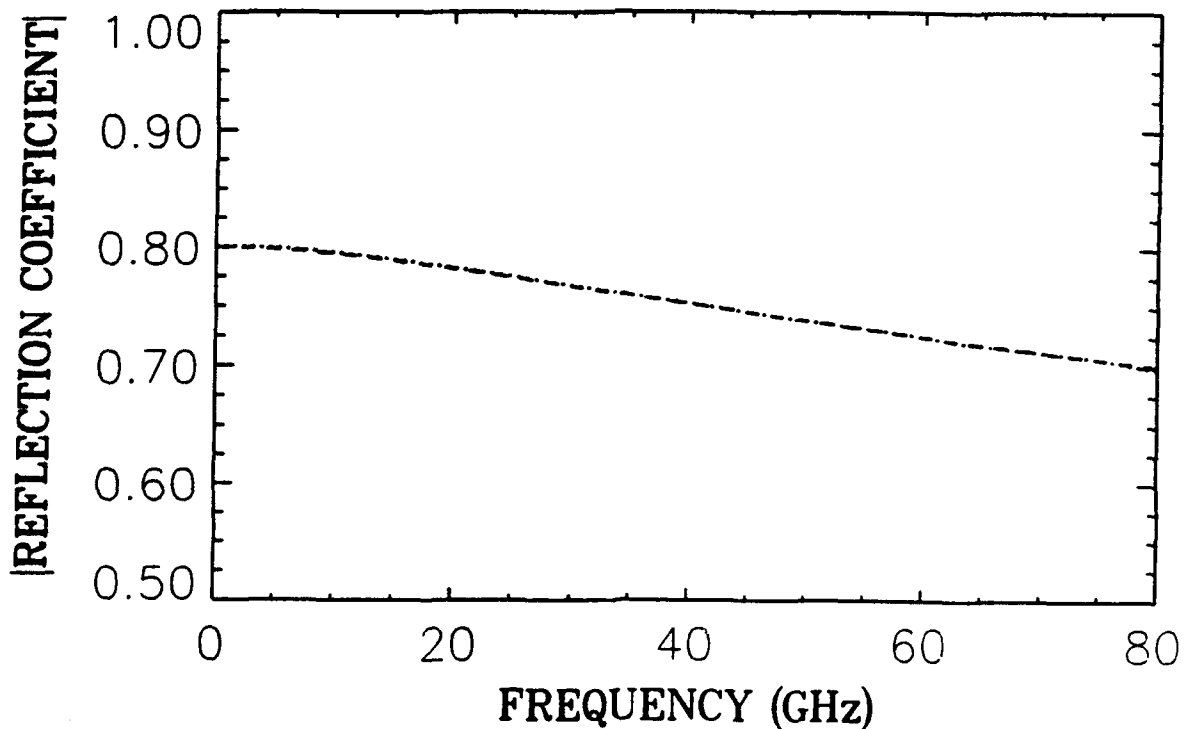


[Figure 2] A comparison of the broadband reflection coefficient. The dashed line is the exact result. The dotted line is the result of our formulation.



Photonic Circuits and Lightwave Reception

IME 1:30pm-3:30pm
Mesquite C/D

Robert J. Deri, *Presider*
Lawrence Livermore National Laboratory

Integrated Optics in the European RACE Program

**Hans Melchior
ETH-Honggerberg
Micro and Optoelectronics HPT
Zurich, Switzerland CH-8093**

Summary not available at time of printing.

A Frequency Reference Photonic Integrated Circuit for WDM with Low Polarization Dependence

J.-M. Verdiell, M. A. Newkirk, T. L. Koch, R. P. Gnall, U. Koren, B. I. Miller, B. Tell
AT&T Bell Laboratories, Crawfords Corner Rd, PO Box 3030, Holmdel, NJ 07733-3030

Photonic Integrated Circuits (PICs) based on InGaAsP are attractive for implementing WDM filters, but achieving absolute wavelength reproducibility on the order of a few Å and low polarization dependence is still an important challenge. We present a frequency referencing PIC implementing 10 narrowly spaced frequency filters with low polarization sensitivity and improved wavelength reproducibility.

The wavelength reproducibility of integrated optical filters that rely on geometrical dimensions of the structure (i.e., corrugation period and strength of a grating, phase-shift locations, relative facet locations and physical length) is limited by the degree of control of the effective index of the waveguide. The latter will vary because of non-uniformities in the quaternary material photoluminescence wavelength and thickness. Moreover, the large index step of typical waveguides on InP materials inevitably introduces an undesirable waveguide birefringence, even in the case of a slab waveguide. Besides improving fabrication tolerances, it is possible to optimize waveguide design with regard to reproducibility and polarization dependence by lowering the index step and enlarging the core size. An elegant way of growing a waveguide core which satisfies this criterion is to use a multi-quantum-well (MQW) [1,2] diluted waveguide, where the core region consists of a few regularly spaced quantum wells separated by a relatively thick binary material barriers. It offers the advantages of acting like a layer with an arbitrary small index step [3] without relying on very tight composition control. A theoretical comparison between a standard slab waveguide (2000Å, $\lambda_{pl}=1.3 \mu\text{m}$ core) and a diluted MQW waveguide (9 pairs of 50 Å wells of $\lambda_{pl}=1.1 \mu\text{m}$ and 1250 Å InP barriers) is summarized in Fig. 1. Note that an impressive 15 fold decrease in polarization sensitivity is expected.

Such a MQW guide as been incorporated in our frequency referencing PIC as depicted in Fig.1. The working principle is as follows: the input light is launched through a 500 μm long rib-loaded waveguide. After reaching the end of the input waveguide, the light freely expands in the slab MQW waveguide, then travels through a 3 mm Bragg grating section, whose corrugations have been etched in a thin quaternary layer on top of the waveguide. An array of 10 MQW detectors samples the light coming out at different angles through the grating. Since each ray traveling at an angle θ within the grating sees a different effective grating pitch, each detector will show a dip in its response curve when the input wavelength λ satisfies:

$$\frac{\lambda - \lambda_0}{\lambda_0} \approx \frac{n_{eff}}{n_{eff \text{ group}}} (\cos \theta - 1) \quad (1)$$

where the Bragg wavelength λ_0 at $\theta = 0$ is determined by the grating pitch $\Lambda = \lambda_0 / 2n_{eff}$. The detector signal thus behaves like an "artificial" absorption line to which a laser

frequency can be locked [4].

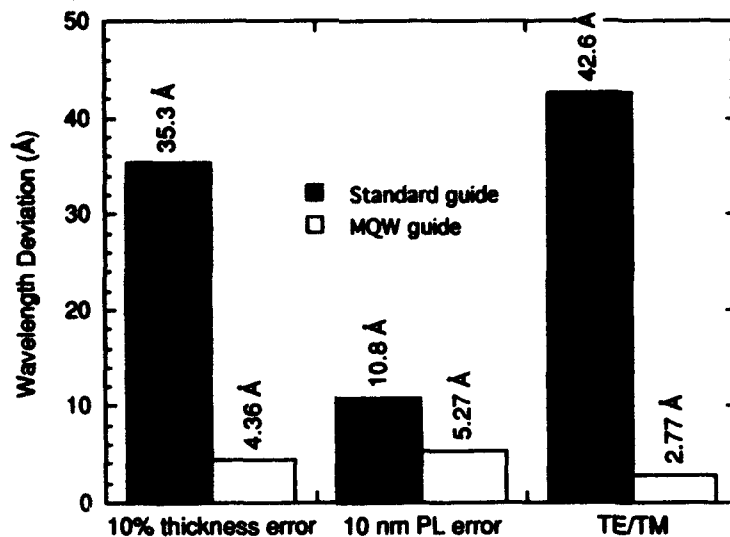


Fig. 1 Wavelength deviation caused by manufacturing errors and polarization for standard and diluted MQW waveguides.

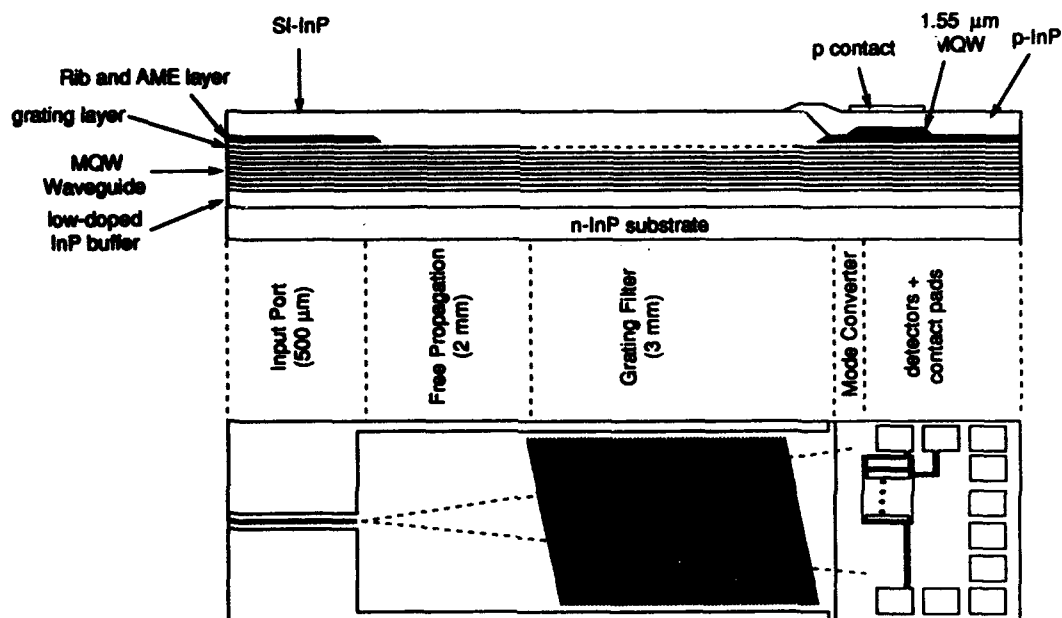


Fig. 2 : Frequency Reference PIC. Top: layer structure, bottom: circuit layout.

We briefly describe the processing sequence of the PIC [5]. The device material was grown using atmospheric pressure MOVPE. The base wafer before processing consists of the MQW waveguide structure previously described, a 135 Å thick InGaAsP layer ($\lambda_{pl} = 1.30 \mu\text{m}$) in which the grating is etched, a 2000 Å thick layer ($\lambda_{pl} = 1.30 \mu\text{m}$) which serves as the rib loading for the input guide and as a mode converter in front of the detectors, a stack of four InGaAs quantum wells separated by InGaAsP barriers ($\lambda_{pl} = 1.30 \mu\text{m}$) which are used for the detectors and absorbers, and finally p-doped InP layers. All the quaternary layers are separated by thin InP etch stops to facilitate processing. The InGaAs

quantum wells were first selectively removed by wet etching in the passive sections, and left to form the absorbers on each side of the chip and in a rectangle delimiting the detector region. Subsequent layers were patterned to form the input guide and the mode converter, then the slightly slanted ($\theta_0=6.5^\circ$) grating was defined by holographic exposure. The upper 1.2 μm thick semi-insulating InP cladding was regrown by MOVPE, then selectively etched away from the detector and contact pad region. p+ doped contact layers were then regrown and etched away from the passive regions. After gold contact formation and patterning, the whole p+ region was ion implanted except for the detectors. A Cr/Au guard ring surrounding each detector and contact pad, not shown on the figure, was then deposited and patterned by lift-off. The total size of the cleaved device was 6.1 mm x 1 mm.

The performance of the device was tested using a Hewlett Packard tunable laser source coupled with a lensed fiber to the PIC. The wavelength channels were exceptionally regularly spaced as shown in Fig. 3. A linear fit with a correlation coefficient $R=0.999$ indicates a 7.2 \AA spacing, only 0.5 \AA from the design goal.

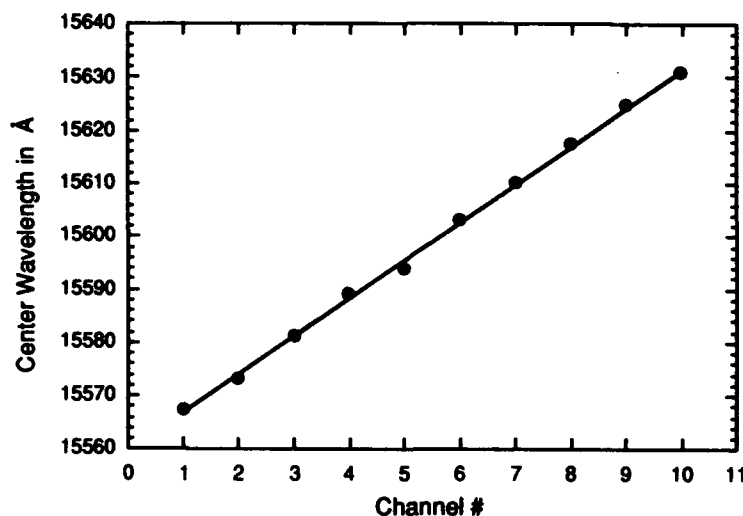


Fig. 3 Center wavelength of the 10 channels.

The response curve of one detector for both TE and TM polarized input is shown in Fig. 4. A narrow dip at 1.5610 μm is obtained. The cause of the apparent "ringing" on the longer wavelength side of the dip, however, is not yet known. All channels displayed similar curves translated in wavelength. One of the detectors (channel 10) showed the largest TE/TM shift of 2 \AA . All other channels had shifts below 1.2 \AA , with an average value of 1 \AA . To the best of our knowledge, this represents the lowest polarization sensitivity ever reported for an InP based PIC.integrated filter.

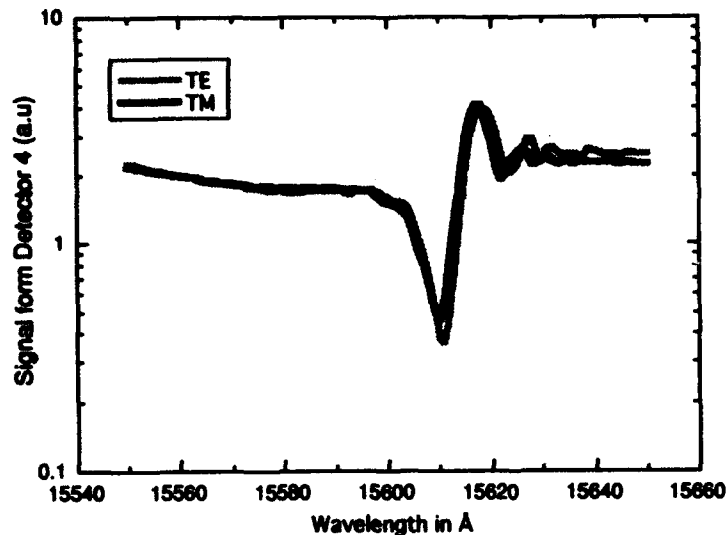


Fig. 4. Detector response for TE and TM light input.

In order to assess the absolute wavelength reproducibility, we measured the first channel center wavelength of 33 devices chosen randomly from two samples measuring about 1 square inch each. These samples were processed separately but came from the same 2 inch diameter base wafer. The standard deviation obtained from these measurements is $\sigma=3.33 \text{ \AA}$, and the total range is 12 \AA . Although this represents quite a good result, we believe that these numbers may still be limited by the unevenness of the grating layer which was partially washed out during regrowth, and not by the uniformity of the MQW guide itself.

In conclusion, we have demonstrated a frequency reference PIC incorporating a diluted MQW waveguide for improved wavelength reproducibility and low polarization dependence. This concept could potentially be applied to other PICs performing functions necessary for WDM, where tight wavelength control and low TE/TM sensitivity is desirable.

- [1] R.J. Deri, E. Kapon, *IEEE Journal of Quantum Electron.*, vol. 27, p. 626, 1991.
- [2] U. Koren, B. I. Miller, T. L. Koch, G. D. Boyd, R. J. Capik, S. E. Soccolich, *Appl. Phys. Lett.*, vol. 49, p. 1602, 1986.
- [3] G.M. Alman, A. Molter, H. Shen, M. Dutta, *IEEE J. of Quantum Electron.*, "Refractive index approximation from linear perturbation theory for planar MQW waveguides", vol. 28, pp 650-657, 1992.
- [4] Y.C. Chung, R.M. Derosier, H.M. Presby, C.A. Burrus, Y. Akai, and M. Masuda, "A $1.5 \mu\text{m}$ laser package frequency locked with a novel miniature discharge lamp", *IEEE Photon. Tech. Lett.*, vol. 3, pp 841-844, 1991.
- [5] T. L.Koch, U. Koren, "Semiconductor lasers for coherent optical fiber communications", *J. of Lightwave. Technol.*, vol.8, pp 274-293, 1990.

Polarization Independent 8x8 Multiplexer on InP

M. Zirngibl, C. H. Joyner, L. W. Stulz, Th. Gaiffe, C. Dragone
 AT&T Bell Laboratories
 Crawford Hill Laboratory
 Holmdel, NJ 07733
 Phone: 908-888-7153

$N \times N$ waveguide grating multiplexers are key components in wavelength division multiplexed (WDM) transmission systems and networks [1]. Recently, we demonstrated a 15×15 InP multiplexer that was comparable in performance to SiO_2 -based devices [2]. One problem with the InP multiplexer was the TM-TE polarization shift of the spectral characteristics. This is not acceptable for many applications where the polarization state of the input signal from a fiber transmission line is random. One can always try to achieve polarization independence by reducing the waveguide birefringence. This approach, however, may be too much of a compromise if one also requires low straight- and bend-loss and reproducibility. Here, we show that the multiplexer can be designed to operate independent of polarization even though the waveguides are birefringent.

The trick is to choose the free spectral range (FSR) so that it equals the TM-TE shift. This means that the grating order for the TM mode is exactly one lower than the TE mode at the same wavelength [3]. The FSR is then given in the frequency and wavelength domains, respectively, by

$$\frac{\text{FSR}(f)}{f} = \frac{\text{FSR}(\lambda)}{\lambda} = \frac{\Delta n}{n}$$

where f is the optical signal frequency, λ the signal wavelength and $\Delta n/n$ the waveguide birefringence. The FSR or optical bandwidth over which the multiplexer can operate is limited by $\Delta n/n$. For our buried-rib waveguide, $\Delta n/n = 3.7 \times 10^{-3}$ [2]. This gives a FSR of about 700 GHz in the $1.5 \mu\text{m}$ window, which is sufficient for many applications. Experiments show that the birefringence is only weakly dependent on the actual waveguide dimensions, and we observed identical TM-TE shifts for multiplexers from several different fabrication runs. Therefore, we think that polarization independent devices are producible.

The multiplexer has 8 input/output ports and 24 grating arms. The path length difference between neighboring grating arms is $133 \mu\text{m}$. This should give us the desired FSR that matches the TM-TE shift of 5.7 nm observed with the previously described 15×15 multiplexer [2]. The total size of the device is $6 \times 9 \text{mm}^2$, with input/output ports spaced by $100 \mu\text{m}$. Otherwise, we followed the same design rules for the bends, epilayer composition and multiplexer layout as described in Refs. [2] and [4]. A tunable laser source was used as a probe signal with 100 MHz step resolution. The light was launched into the device by a lensed fiber. The temperature of the sample was controlled by a Peltier element.

In Figure 2, we display the spectra for all eight output ports for light coupled into port 5. Channels 1 and 8 are the outermost ports. The measurement was done for the TM mode. The insertion loss is calibrated against a straight test waveguide; it does not include fiber-to-waveguide coupling loss. We find a channel spacing of 88.4 GHz (0.71 nm), a channel-to-channel cross-talk of -20 dB and a 3 dB channel-bandwidth of 39 GHz (0.31 nm). The insertion loss is very uniform and below 5 dB for all channels. In Figure 3, we have overlaid TE and TM spectra of output channel 5; the two curves overlap almost completely showing thereby that polarization independence is indeed achieved. By varying the temperature of

the device, we find a tuning coefficient for TE and TM modes of $18.75 \text{ GHz } (1.5\text{\AA})/\text{°C}$. In WDM transmission systems, this tunability could be exploited to align the multiplexer to different signal wavelengths. In WDM networks, one could also imagine using the multiplexer tuning for slow switching between optical channels.

To the best of our knowledge, the only truly polarization insensitive NxN multiplexer has been demonstrated by Takahashi et al [4]. This SiO_2 based device has a $\lambda/2$ plate inserted in the middle of the arrayed waveguide grating. It exhibited very low crosstalk of -30 dB due to the much larger number of grating arms per channel than for our device and device insertion loss of 8.3 dB. A direct comparison of insertion losses should, of course, also take into account fiber-to-waveguide coupling losses which are generally lower for silica devices than for InP devices.

In conclusion, we have demonstrated a polarization insensitive multiplexer on InP which has low crosstalk, low insertion loss and high wavelength resolution. This, together with the potential of tunability, should make this device an attractive component for WDM systems.

REFERENCES

- [1] I. P. Kaminow, "FSK with Direct Detection in Optical Multiple-Access FDM Networks", *IEEE J. Select. Areas Commun.*, Vol. 8, pp. 1005-1014, 1990.
- [2] M. Zirngibl, C. Dragone, C. H. Joyner, "Demonstration of a 15x15 Arrayed Waveguide Multiplexer on InP", to be published in *IEEE Photon. Technol. Letters*.
- [3] M. K. Smit, "Integrated Optics in Silicon-Based Aluminum Oxide", Proetschrift, 1991.
- [4] C. Dragone, "Optimum Planar Bends", to be published.
- [5] H. Takehashi, Y. Hibino and I. Nishi, "Polarization-Insensitive Arrayed-Waveguide Grating Wavelength Multiplexer on Silicon", *Optics Letters*, Vol. 17, pp. 499-501, 1992

FIGURE CAPTIONS

- Figure 1 Schematic layout of the multiplexer.
- Figure 2 Spectral characteristics for all 8 channels for TM polarization; input to channel 5.
- Figure 3 TM and TE spectra of channel 5.
- Figure 4 Temperature tuning of multiplexer spectrum.

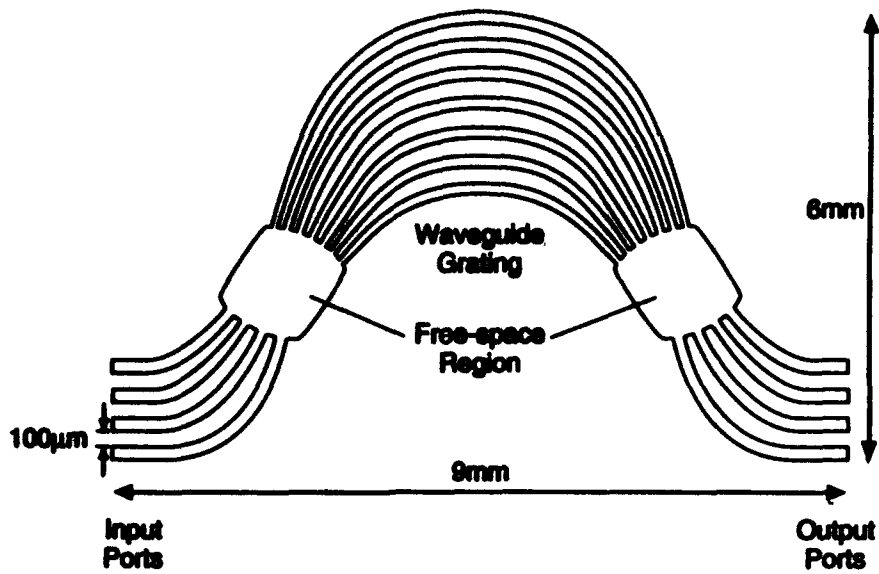


Figure 1

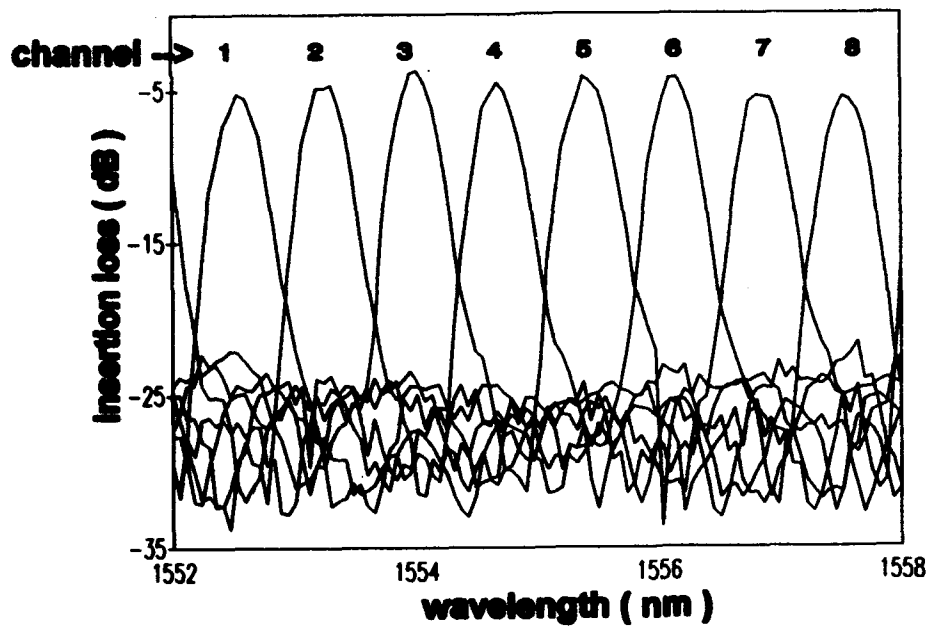


Figure 2

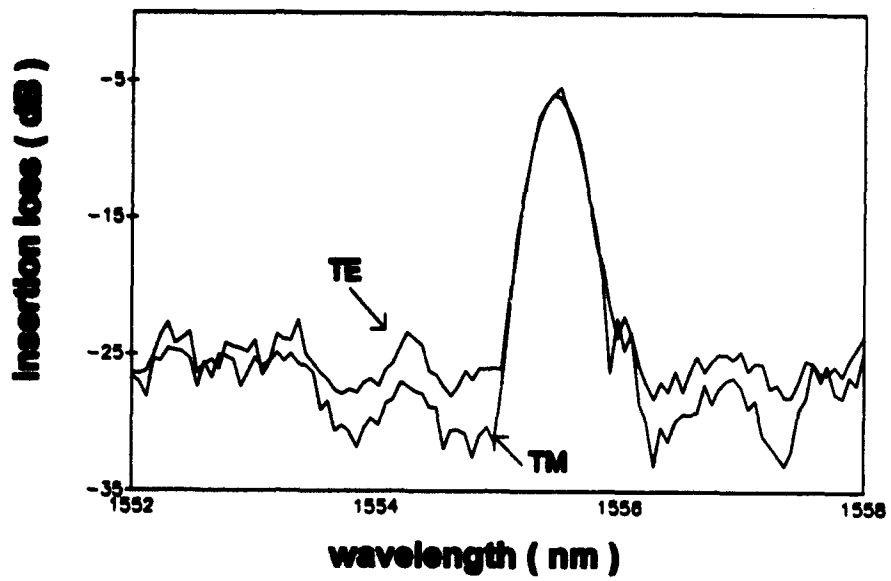


Figure 3

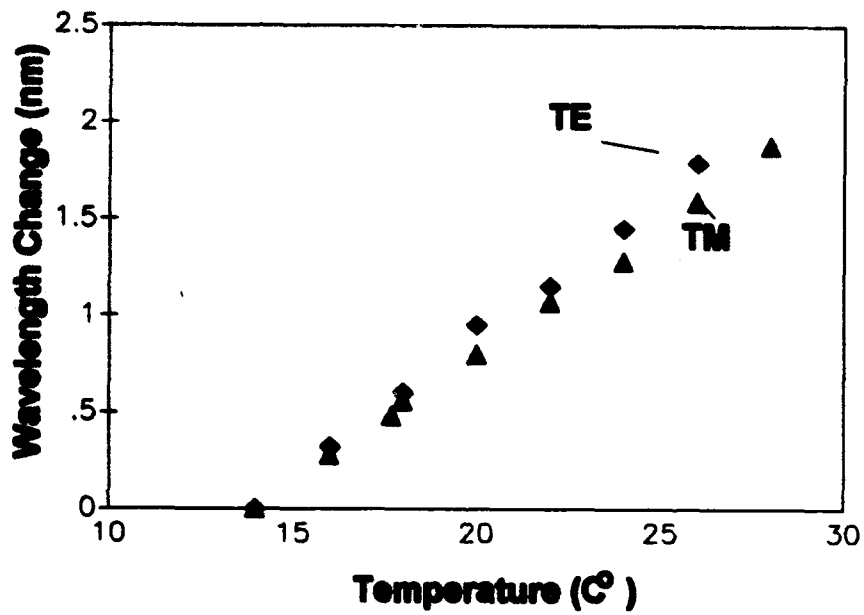


Figure 4

Design and Fabrication of a InP/InGaAsP Multimode Power Splitter

A. Ferreras, F. Rodríguez, E. Gómez-Salas, J.L. de Miguel, F. Hernández-Gil

Telefónica, Investigación y Desarrollo
C/ Emilio Vargas 6. MADRID 28043. SPAIN
Phone: (34-1) 3374683 - Fax: (34-1) 3374212

Introduction

There is an increasing interest in passive optical integrated devices based on multimode interference (MMI), that can produce real one-dimensional self-images by interference of the waveguide modes [1,2,3]. These type of devices include 3 dB couplers [4,5,6,7], passive optical 90° hybrids [11] and power combiners/splitters [8,9,10]. The last ones are usually made by means of Y-Junction or 3 dB coupled based structures. Multimode interference provides shorter and more compact devices than adiabatic ones, and preserve the balanced output characteristics. Recently, a general design method for 1xN MMI power splitters/combiners has been developed [8,9]. We present here more detailed designing formulas and report the first implementation of these devices on InP materials. Results of a fabrication tolerance analysis are also presented.

Design Method

Fig. 1 shows a top view of the multimode interference power splitter. It consists of a rectangular section of width W and length L , an input waveguide centred symmetrically, and four (n in a general case) output guides. The input and output guides have the same width. Fig. 2 shows the evolution of the fundamental mode power of the input guide incoming to the device; it has been calculated by means of a BPM analysis. The input mode is coupled only to the even modes of the rectangular section. These modes propagate with different phase velocities, shaping different power profiles. The propagation constant of these even modes can be approximated by:

$$\beta_m = \frac{2\pi}{\lambda} \sqrt{N^2 - \frac{(2m+1)^2 \lambda^2}{4W_{eff}^2}} = \beta_0 - \frac{(m^2+m)\lambda\pi}{W_{eff}^2 N} \quad (1)$$

where N is the effective index (2D analysis) of the guiding layer, λ vacuum wavelength, $m(0,1,2,..)$ even mode number, and W_{eff} is the modified width of the rectangular section, assuming the mode perfectly confined inside the section. This modified width is slightly greater than the real width, and it has been proved that works better. It is defined by:

$$W_{eff} = \frac{\lambda}{2 \sqrt{N^2 - n_f^2}} \quad (2)$$

where n_f is the effective index of the fundamental mode of the multimode section.

So, all the even modes constructively interfere at a distance along the propagation direction defined by $d = (NW_{\text{eff}}^2 / \lambda)$, where the input image is reproduced. At distances defined by d/n , where n is an arbitrary positive integer number, the modes interfere shaping a pattern with n images equally spaced. Particularly, if we excite with a field distribution defined by the Dirac Function $\delta(x)$ centred at the rectangular section input plane and supposing that there are infinite modes absolutely confined in the multimode section that follow (1), then the field image formed at a distance d/n is defined by the "transference function":

$$H_n(x) = \frac{1}{n} e^{-j\beta_0 \frac{d}{n}} e^{j\pi \frac{n^2-1}{4n}} \sum_{p=-\frac{n-1}{2}}^{\frac{n-1}{2}} e^{-j\pi \frac{p^2}{n}} \delta(x + \frac{p}{n} W) \quad (3)$$

This formula is a very useful design tool, that provides, besides the phase relation between outputs, the correct localization of the output guides that minimizes the insertion losses.

Since the modes are not perfectly confined, there exists a "border aberration"; it consists of a distortion of the lateral lobes at the output planes. There is also another source of potential error because of the finite number of confined modes that can increase the insertion losses. In order to minimize these two error sources it is preferred a highly confined guided structure, as the buried one. It has also small losses, and is compatible with other integrated devices, as lasers or guided photodetectors; so this structure is suitable for photonic integrated circuits.

Fabrication and Measurements

We have designed and fabricated a power combiner/splitter (1x4) on InP technology. Figure 3 shows two micrographs of the input and output of the power splitter, before the last InP regrowth. The cross section structure is shown in Fig. 4. It consists of a layer of InGaAsP (1.3 μm) 0.3 μm high, surrounded by InP. The layers have been grown by MOVPE on an InP, S doped, substrate. The pattern definition has been made by RIE. Afterward a 1.5 μm high InP regrowth has been carried out also by MOVPE. The input and output guides are 2.5 μm wide, (there are two confined modes); the rectangular section has 24 μm width (22 confined modes) and of variable length, around the design length of about 300 μm . The output guides have 6 μm separation between guide centres; and S-bends provide 50 μm separation between output branches at wafer the device output.

Measurements have been performed focusing into the devices the light of a 1.55 μm DFB laser, by means of microscope objective lenses. Figure 5 shows a camera image and a power scan of the output power. The total unbalanced power between lateral and central branches has been tested. These power is the sum of the power carried by the two modes supported by the waveguide; however the second mode has greater attenuation than the fundamental due to the radiation losses at the output S-Bend. Results are shown in Figure 6 with the simulated curve (total power difference). Figure 6 also includes the theoretical difference

between power contained in fundamental modes at output branches, eliminating the second mode power (BPM analysis).

Tolerances

A tolerance analysis, carried out by BPM analysis, has shown that parameters as quaternary composition ($1.3 \pm 0.1 \mu\text{m}$ bandgap), quaternary layer height ($0.3 \pm 0.03 \mu\text{m}$) or light wavelength ($1.55 \pm 0.03 \mu\text{m}$) can vary over a relative wide range without degrading device performance, keeping insertion losses below 0.5 dB and 0.2 dB unbalance between output branches. On the other hand, the photolithography tolerances are critical. The total width of the rectangular section must be controlled with a $0.3 \mu\text{m}$ precision in order to keep the insertion losses below 0.5 dB. Figure 7 shows the output branches insertion losses versus the photolithography error on total width over the designing value of $24 \mu\text{m}$.

Aknowlegments

This work has been partially supported by the RACE project OMAN.

References

- [1] O.Bryngdahl, *J. Opt. Soc. Am.*, Vol.63 No.4 pp.337-9, April 1975
- [2] M.Born and E.Wolf, "Principles of Optics", Pergamon, New York, 1965.
- [3] R.Ulrich and T.Kamiya, *J. Opt. Soc. Am.*, Vol.68 No.5 pp.585-92, May 1978
- [4] L.B.Soldano et al. IPR Conference 1991, New Orleans. TuD Posters Previews.
- [5] E.C.M.Pennings et al. IOOC-ECOC'91. Paris. WE.A7.2
- [6] L.B.Soldano et al. IOOC-ECOC'91. Paris. TU.B5.2
- [7] F.B.Veerman et al. *J. Lighthwave Tech.*, Vol. 10 No. 3, pp. 306-11, March 1992
- [8] A.Ferreras et al. URSI. Torremolinos (Málaga). E4.1. pp. 508-12. Sept. 1992
- [9] J.M.Heaton et al. *Appl. Phys. Lett.*, Vol.61, No. 15, pp. 1754-6. October 1992
- [10] L.B.Soldano et al. ECOC'92. Berlin. WE.B10.5
- [11] E.C.M. Pennings et al. ECOC'92. WE.B10.4

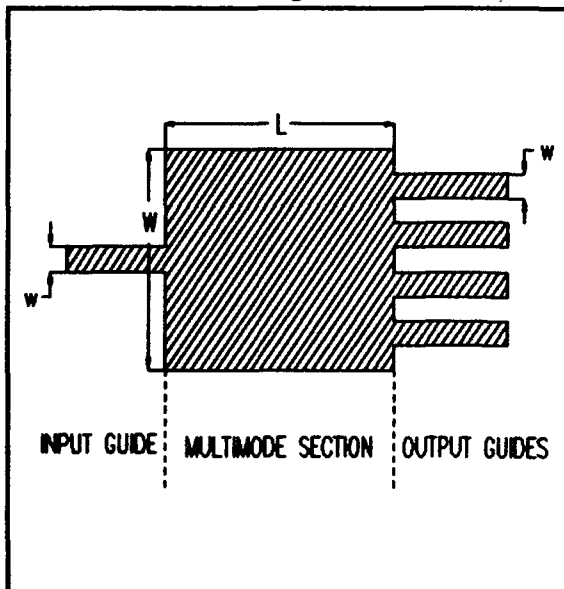


Figure 1. Top view of a multimode interference power splitter (1x4)

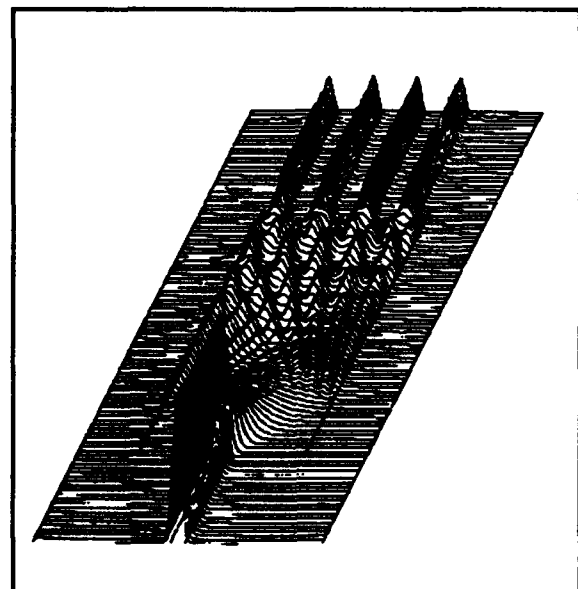


Figure 2. BPM Power Splitter simulation.

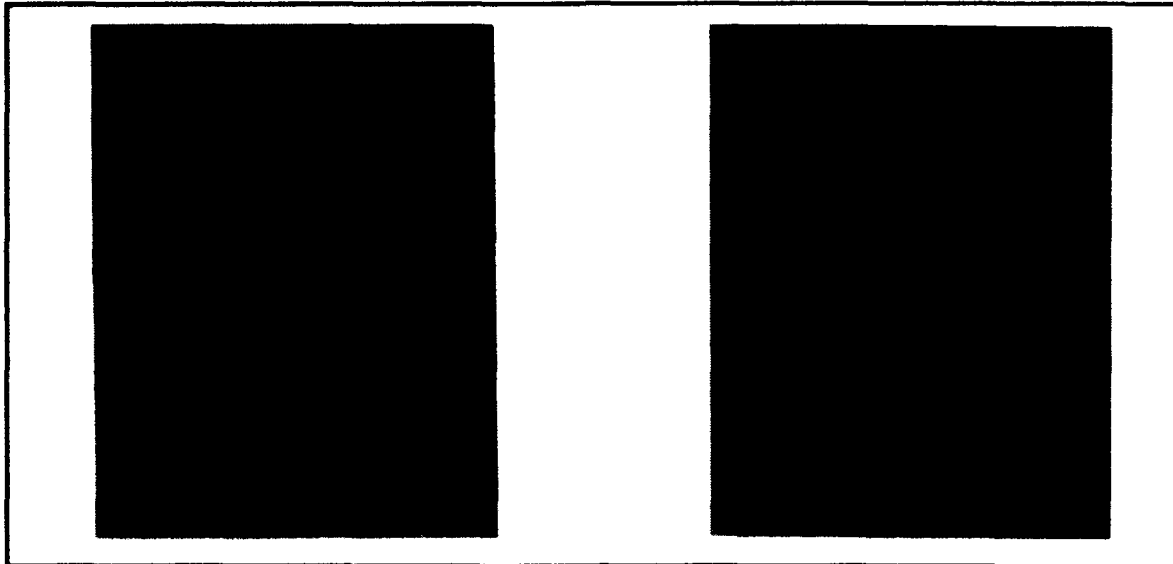


Figure 3. Microscope photographs of two power splitter details. Input zone (left) and output zone (right). The photographs has been taken before the InP regrowth

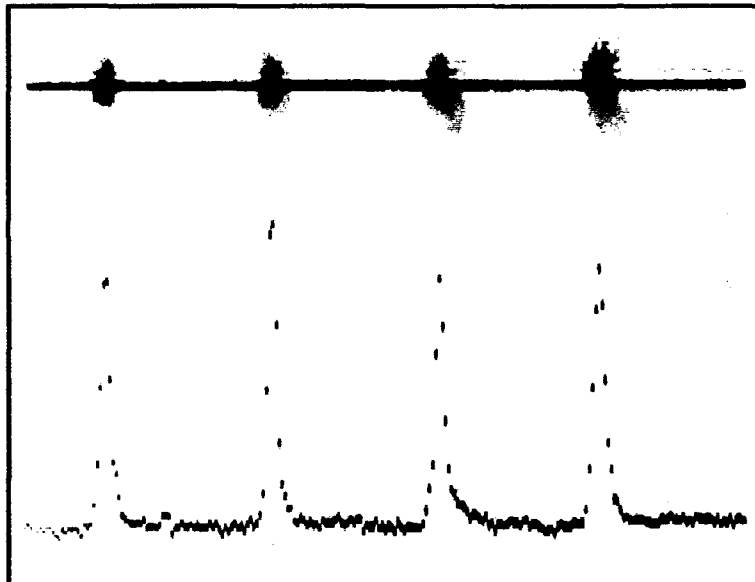


Figure 4. Infrared photograph and line scan of the output power. Negative image shown.

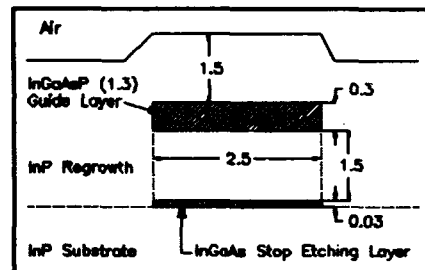


Figure 5. Cross sectional structure dimensions (μm).

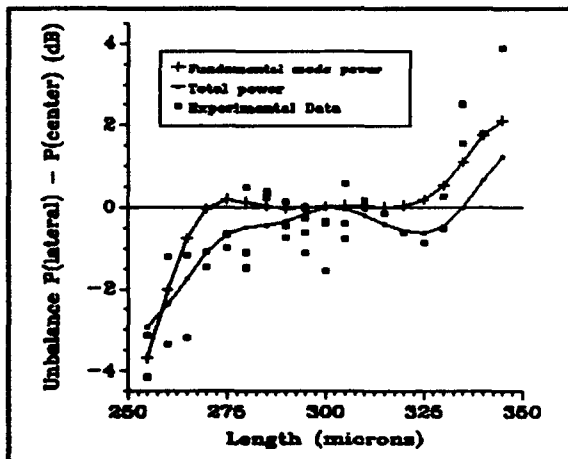


Figure 6. Power unbalance between output branches vs. splitter length.

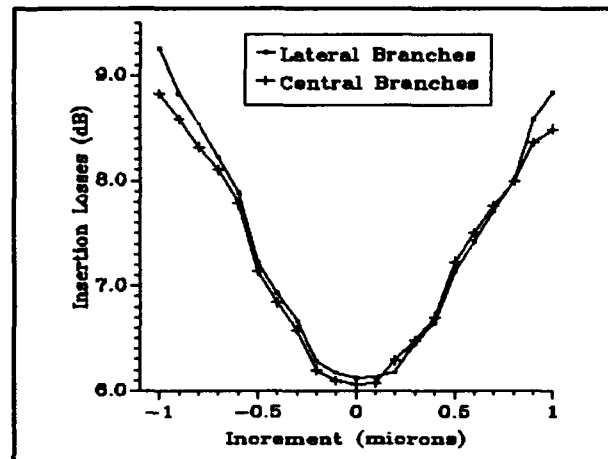


Figure 7. Power splitter losses versus photolithography error.

Near-Infrared Twelve-Channel Wavelength Division Demultiplexer on A Semi-insulating GaAs Substrate

Ray T. Chen
Microelectronics Research Center
University of Texas, Austin
Austin, TX 78712
Tel:512-471-70351.0 Introduction

Wavelength division multiplexing (WDM) and demultiplexing (WDDM) devices have been under intensive research for the past 15 years. Many WDMs and WDDMs that use absorption and/or interference filters [1,2] and diffraction gratings [3-6] have been reported. Wavelength division multiplexing and demultiplexing is a promising technique for both optical communication and sensing systems. Multiplexing an array of signal carriers with different optical frequencies greatly enhances the transmission capacity and the application flexibility of an optical communication system. The dispersion characteristic of the diffraction grating provides an opportunity to employ WD(D)M devices for optical encoders [7,8] to detect both linear and rotational positions. We have developed four-channel visible (543, 594.1, 611.9 and 932.8 nm), five-channel near IR (730, 750, 780, 810 and 840 nm), eight-channel (740, 750, 760, 770, 780, 790, 800, and 810nm) near IR and ten-channel near IR single-mode wavelength division demultiplexers using a graded index (GRIN) polymer waveguide in conjunction with a highly multiplexed waveguide hologram [9,10]. Due to the index tunability of the polymer guide, the reported device can be implemented on high refractive index substrates such as GaAs and Si [11,12,13].

We are reporting for the first time a twelve-channel single-mode waveguide WDDM on a semi-insulating GaAs substrate (Fig.1). The center wavelengths of these channels are located at 830, 840, 850, 860, 870, 880, 890, 900, 910, 920, 930 and 940 nm. To construct a highly multiplexed waveguide hologram, twelve channels in this case, the dispersion of the polymeric material was first determined within the wavelength of interest. The phase-matching condition associated with each grating and the corresponding diffracted beam can be constructed afterwards. Note that the isotropic characteristic of the polymer thin film significantly eases the fabrication of the associated diffraction gratings. Anisotropic diffraction is eliminated in this case.

To precisely control the Bragg diffraction angle θ_j , n_j has to be measured before hologram formation. Coating thickness and dry and wet processing conditions have to be standardized to validate the design process. To fabricate a waveguide hologram with a desired grating spacing, a well-collimated beam is introduced onto the waveguide emulsion containing the hologram [14]. The object and reference beams thus generated require a very short temporal coherence length of the laser beam. The beam size of the collimated beam is much larger than the interaction length (submillimeter), i.e., grating thickness (Figure 1), of the waveguide. As a result, each waveguide hologram is formed by two plane waves. For a perfectly phase-matched, lossless, unslanted transmission grating, the diffraction efficiency can be written as [15]

$$\eta_j = \sin^2 \left(\frac{\pi \Delta n_j d}{\lambda_j \cos \theta_j} \xi \right) \quad (1)$$

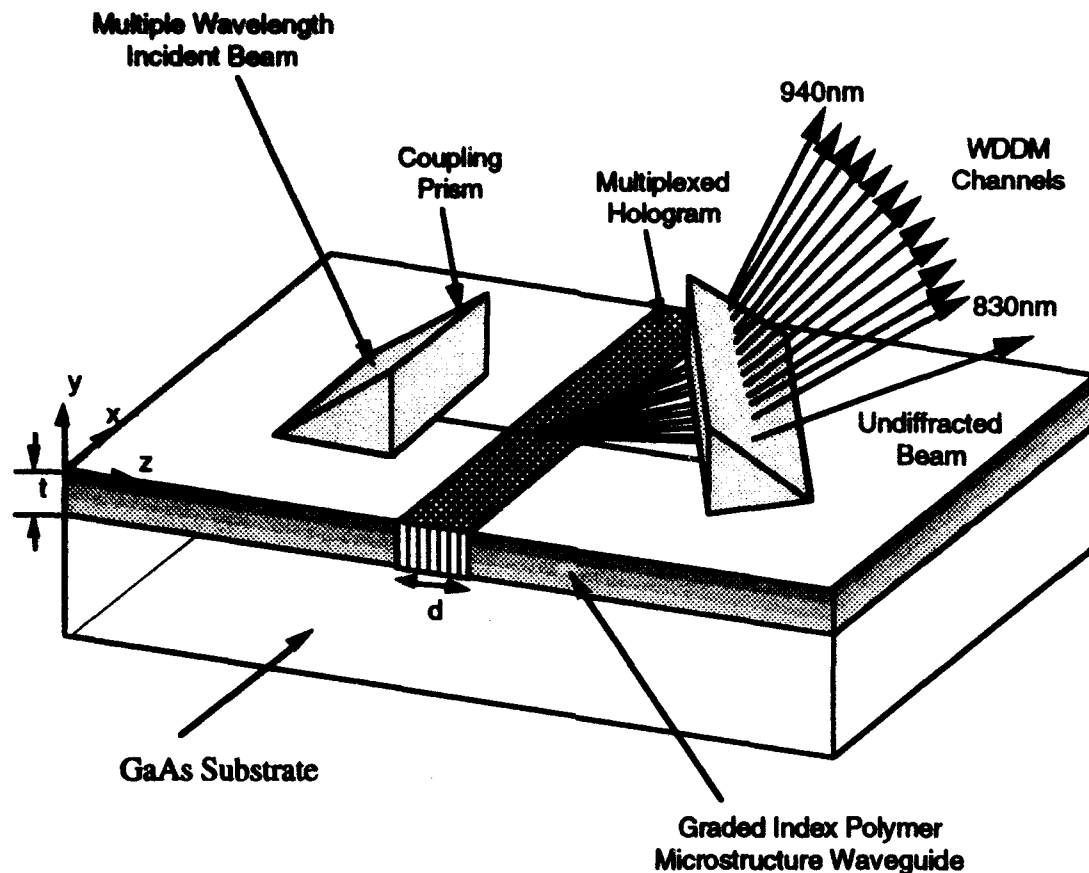


Figure 1
Reconstruction of the waveguide WDDM device using a Ti:Al₂O₃ laser.

where θ_j is the Bragg diffraction angle of the j th signal beam, Δn_j and d are the associated index modulation and the interaction length, respectively, and ξ is a constant which varies between 0 and 1 depending on the polarization of the incident beam [12]. The sinusoidal nature of the device requires precise control of θ_j , Δn_j and d in order to generate a highly multiplexed hologram with uniform fan-out intensity. d is controlled by the lithographic process and Δn is manipulated through exposure dosage and wet and dry processing parameters. To introduce the desired index modulation, the exposure time t_j needed for the j th hologram should satisfy the following equation [15]

$$t_j = \frac{1}{E\beta} \ln \left[-\Delta n_j + \left(\Delta n_{\max} - \sum_{i=1}^{j-1} \Delta n_i \right) \right] / \left[\Delta n_{\max} - \sum_{i=1}^{j-1} \Delta n_i \right] \quad (2)$$

where β is the sensitivity constant for the emulsion, E is the exposure intensity of the laser beam, Δn_i is the index modulation for the i th exposure and Δn_{\max} is the maximum index modulation for the holographic material. Note that the exposure dosage needed to generate a fixed value of index

modulation increases as the number of holograms to be multiplexed increases. This is due to the fixed value of Δn_{\max} and the linear response of the film. Eq. (2) has been experimentally confirmed and further results will be presented in the future.

For the present WDDM device, the gratings were designed to operate at the diffraction angles of 10, 15, 20, 25, 30, 35, 40, 45, 50, 55, 60 and 65 degree to selectively disperse signals at the center wavelengths of 830, 840, 850, 860, 870, 880, 890, 900, 910, 920, 930 and 940 nm, respectively. For each λ_j , the corresponding recording angles were selected to generate a waveguide transmission hologram with the desired grating periodicity and θ_j . Figure 1 shows the reconstruction of the waveguide WDDM device using Ti:Al₂O₃ laser light as the input signal. The interaction length of the multiplexed waveguide hologram is 0.4 mm. The mode dots coupled out of the prism coupler are shown in Figure 2 with the corresponding wavelengths as indicated. The observation of these clean mode dots verified the quality of the polymer waveguide. A propagation loss in the neighborhood of 0.1 dB/cm has been routinely achieved in a Class 100 clean room environment. As was previously reported, the channel density [13] of the WDDM device is a function of Δn_j , d and θ_j . The correlation of these parameters can also be observed in Eq. (1). A higher index modulation and longer interaction length provide us with a narrower FMHW (full width at half maximum) diffraction spreading and, thus, higher channel density.

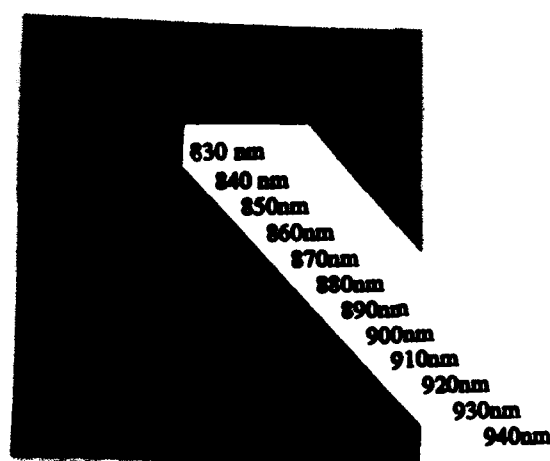


Figure 2

Mode dots from the output prism coupler (Figure 1) of the 12-channel WDDM on GaAs Substrate.

The noise of the fan-out channels of the WDDM device is mainly from the crosstalk of the signals from adjacent channels. An average crosstalk figure of -20.5 dB was measured with diffraction efficiency from 40% to 55% among these output channels. The spectral width of the Ti:Al₂O₃ laser from Spectrophysics was also measured. A -3 dB bandwidth of ~4 nm was found. The results suggest that the WDM devices of better than 4 nm wavelength separation cannot be experimentally realized without significant channel crosstalk. Theoretically, our device structure is capable of operating at a channel-to-channel spacing as small as 1 nm under the current design when a DFB laser diode is employed. The -20.5 dB crosstalk is primarily due to the wavelength spreading of the Ti:Al₂O₃ laser rather than the waveguide device itself.

As far as the throughput intensity is concerned, the 33% diffraction efficiency represents an output power as high as 50 mW. For a communication system involving the reported WDDM device, the system power budget will be determined by laser power, modulation speed, bit error rate and

detector sensitivity. Employing a PIN-FET as the demodulation scheme, theoretically we can utilize a ~0.5 mW semiconductor laser to obtain 1 Gbit/sec communication with a 21.5 dB signal-to-noise ratio. The above power budget assumes 50% diffraction efficiency, 1 dB waveguide propagation loss, 3 dB waveguide coupling loss, 2 dB hologram excess loss, 4 dB fiber propagation loss, 5 dB system power margin and room temperature operation condition with an amplifier noise figure equal to 4. The current design allows us to provide 60-channel multiplexibility with the maximum value of index modulation set at 0.1.

We report, for the first time, a single-mode, GRIN-polymer-based waveguide WDDM device on a semi-insulating GaAs substrate. Twelve-channel WDDM (830, 840, 850, 860, 870, 880, 890, 900, 910, 920, 930 and 940 nm) with channel separation of 5° in space and 10 nm in wavelength has been demonstrated with an average crosstalk figure of -20.5 dB. The spreading of the Ti:Al₂O₃ laser turned out to be the major source of the crosstalk from adjacent channels. Theoretically, WDDM channel spacing as small as 1 nm is plausible under the current design criterion. To understand the effect of finite beam size and interaction length, the diffracted beam spot size was also considered. The variation of beam spot size as a function of diffraction angle and grating interaction length with 100 μ m input beam width is presented here. A diffraction spot whose beam width is larger than that of its output fiber requires the implementation of a waveguide lens array to enhance the coupling efficiency.

The device reported here not only enhances the bandwidth of optical interconnects but also provides us with a new avenue through which dispersion-sensitive optical sensors, such as optical encoders [7], can be realized. The GRIN property of the polymer waveguide allows us to implement the reported device on an array of substrates. Such universality greatly enhances the application scenarios in which the conventional guided wave devices can be used.

References

1. I. Bennion, D. C. Reid, C. J. Rowe, and W. J. Stewart, *Electron. Lett.*, **22**, 341 (1986).
2. W. V. Sorin, P. Zorahedian and S. A. Newton, *IEEE J. Lightwave Tech.*, **LT-5** (9), 1199 (1987).
3. K. Kobayashi and M. Seki, *IEEE J. Quantum Electron.*, **OE-16** (1), 11 (1980).
4. S. Ura, M. Morisawa, T. Suhara, and H. Nishihara, *Appl. Opt.*, **29** (9), 1369 (1990).
5. Y. Fujii, J. Minowa, and Y. Yamada, *IEEE J. Lightwave Technology*, **LT-2** (5), 731 (1984).
6. T. Von Lingelsheim, *IEEE Proc.*, **131** (5), 290 (1984).
7. R. T. Chen, M. R. Wang, G. Sonek, and T. Jansson, *Opt. Eng.*, **30**, 622 (1991).
8. D. W. Seal, Final Report to NASA, Cont. No. NAS3-25345, 1989.
9. M. R. Wang, R. T. Chen, G. Sonek and T. Jansson, *Opt. Lett.*, **15**, 363 (1990).
10. M. R. Wang, G. Sonek, R. T. Chen and T. Jansson, *IEEE Photonics Technology Letters*, **3**, 36 (1991). and R. T. Chen and Huey Lu, "Ten-channel Single-mode Wavelength Division Demultiplexer in near IR, *Proc. SPIE*, Vol.1583-15 (1991).
11. R. T. Chen, W. Phillips, T. Jansson, and D. Pelka, *Opt. Lett.*, **14**, 892 (1989).
12. R. T. Chen, M. R. Wang, and T. Jansson, *Appl. Phys. Lett.*, **56**, 709 (1990).
13. R. T. Chen, *Proc. SPIE*, **1374**, 20 (1990).
14. R. T. Chen, M. R. Wang, F. Lin, and T. Jansson, *Proc. SPIE*, **1213**, 27 (1991).
15. R. T. Chen, M. R. Wang, and T. Jansson, *Appl. Phys. Lett.*, **57**, 2071 (1990).
16. R. T. Chen, H. Lu, and T. Jansson, *Topical Meeting on Gradient-Index Optical Systems, Technical Digest Series*, (Optical Society of America, Washington, DC 1991), PD2-1.
17. R. T. Chen, Final Report to Army Harry Diamond Lab, Cont. No. DAAL02-91-C-0034, 1991.

A Monolithically Integrated Frequency Mixing Photoreceiver

Y. K. Chung

**Department of Electrical Engineering
University of Southern California, Los Angeles, CA 90089-0241**

and

S. R. Forrest

**Department of Electrical Engineering
Princeton University ATC/POEM, Princeton, NJ 08544**

In the standard architecture for optical communications receivers there are typically three basic elements, a photodetector, a pre-amplifier, and a filter. If the signal is frequency multiplexed, there must be an additional mixing stage to separate the different incident optical channels. Sensitivity and gain are most critical for these elements since the signal is weakest and most susceptible to noise at the receiver front end. In commercial receivers, the photodetector and mixer are separate from the pre-amplifier and must be integrated by hybrid techniques. Interconnections between the pre-amplifier and the other components frequently require complex matching networks or interconnection schemes which introduce unwanted noise while reducing reliability. We have designed and tested a high sensitivity p-i-n/JFET, monolithically integrated photoreceiver which incorporates a p-i-n photodiode and a voltage tunable transimpedance preamplifier for 1.3-1.55 μm optical fiber communication. This design allows us to monolithically mix an optical signal with an electrical signal for use in applications such as frequency demultiplexing or coherent detection. Comparison of our results with alternative mixer technology indicates good efficiency with low signal distortion.

A schematic diagram of the setup used to test our mixer/receiver is shown in Figure 1. The photodetector, amplifier, and tunable feedback resistor are monolithically integrated using $\text{In}_{0.53}\text{Ga}_{0.47}\text{As}$ and $\text{In}_{1-x}\text{Ga}_x\text{As}_y\text{P}_{1-y}$ lattice matched to an InP substrate. The amplifier uses an active load common source amplifier front end DC coupled to an output stage. A more detailed description of the integrated receiver has been previously published [1,2]. Equalization of the circuit is accomplished using a single pole passive RC network. The variable feedback

mixing resistor is a narrow gate JFET operated in its linear regime denoted Q_{FB} in Figure 1. Since Q_{FB} is operated as a feedback resistor, the drain-to-source voltage is close to 0 V. In this circuit, the feedback resistance, and therefore the transimpedance of the amplifier, depends on the gate bias voltage of Q_{FB} . The feedback resistance R_F can be expressed as

$$R_F = \frac{L_g}{qN_D\mu Z \left[a - \sqrt{\frac{2\epsilon_s}{qN_D}(V_G + V_{bi})} \right]} \quad (1)$$

where L_g is the gate length, q is the electron charge, N_D is the doping concentration in the channel, μ is the electron mobility in the channel, Z is the gate width, a is the channel thickness, ϵ_s is the dielectric constant of the semiconductor, V_g is the gate bias voltage, and V_{bi} is the p-n junction built-in voltage. For our receiver, $L_g = 25 \mu\text{m}$, $N_D = 8 \times 10^{16} \text{ cm}^{-3}$, $\mu \cong 9 \times 10^3 \text{ cm}^2/\text{V}\cdot\text{s}$, $Z = 5 \mu\text{m}$, $a = 0.2 \mu\text{m}$, $\epsilon_s = 12\epsilon_0$, and $V_{bi} = 0.68 \text{ V}$. From this equation we would expect a nearly linear resistance vs. voltage relation for small gate voltages. Measurement of the feedback resistance for gate voltage values between 0.4 and -0.4 V does reveal a linear resistance dependence of $16.5 \text{ k}\Omega/\text{V}$, as shown in Figure 2. By changing the gate bias of Q_{FB} from 0.4 to -0.4 V, the transimpedance of the amplifier can be varied from approximately 8.7 to $22.5 \text{ k}\Omega$. For an open loop voltage gain $\gg 1$, the transimpedance of the amplifier is approximately equal to R_F . Therefore we can expect linear frequency mixing without unwanted high order intermodulation frequency products. The 2.6:1 contrast ratio available in feedback resistance should also allow for good conversion efficiency for the mixed signals.

The optical signal frequency was set to 900 MHz to test the receiver performance. An electrical input of 700 MHz was applied to the gate of Q_{FB} , with a 100Ω shunt resistance to ground to reduce impedance mismatch. Figure 3a is a plot of the output spectrum of the receiver without the electrical input to Q_{FB} . A -34 dBm peak power is observed at 900 MHz for an input optical power of approximately $10 \mu\text{W}$. In Figure 3b, a 0.0 dBm electrical signal is applied to Q_{FB} creating a new peak of -43 dBm at 200 MHz. A -8 dBm peak is also observed at 700 MHz, corresponding to the frequency of the electrical mixing signal. This "leakage" of the electrical input is due to poor biasing and impedance match to the

gate of Q_{FB} . The FWHM of the frequency peaks are less than 10 kHz and are limited by the FWHM of the oscillator source. For an 800 MHz electrical signal, varying the power of the electrical signal from -10.0 dBm to 0.0 dBm yields signal strengths of -44 dBm to -37 dBm, respectively, for a 100 MHz signal. With respect to the receiver output, this corresponds to a conversion loss of 11 to 4 dB. Taking into account the 24 dB gain of the amplifier, this corresponds to an overall signal gain of 13 to 20 dB. This value compares well with typical conversion gains reported for Schottky barrier diode or dual gate MESFET microwave mixers.

Using a lower frequency electrical mixing signal, higher order frequency products and frequency isolation can be observed. To measure this, the electrical frequency is reduced to 100 kHz and the optical signal frequency is changed to 850 MHz. Second order frequency products are visible at approximately -80 dBm, which is 26 dB lower than the first order sidebands. The FWHM is again 10 kHz limited by the oscillator source. Isolation between peaks 100 kHz apart is greater than 40 dB with power falling off at over 1000 dB/MHz. The sensitivity of our receiver has been calculated from preliminary measured bit error rates to be better than -31.4 dBm for BER 10^{-9} at 500 Mbit/s. These results indicate that there is excellent signal fidelity and low noise in the receiver. This in turn allows close spacing of frequency multiplexed channels without significant crosstalk.

In conclusion, this is the first demonstration of a monolithically integrated photoreceiver and mixer. Although similar results have been achieved with avalanche photodiodes (APDs) by varying the bias voltage [3,4], the conversion loss and mixing linearity of the APD scheme are inferior to those presented here.

The authors thank the Office of Naval Research (Y. S. Park) and the National Center for Integrated Photonic Technology for partial support of this work.

1. D. C. W. Lo, Y. K. Chung, and S. R. Forrest, *IEEE Photon. Tech. Lett.*, PTL-3(8) p. 757, 1991.
2. D. C. W. Lo, J. J. Brown, J. T. Gardner, Y. K. Chung, C. D. Lee, and S. R. Forrest, *IEEE Trans. Electron. Dev.*, ED-37 (11), p. 2292, 1990.
3. M. A. Abuelma'atti, *IEE Proc.*, Vol. 135, Pt. J, No. 2, 183, 1988.
4. A. J. Seeds and B. Lenoir, *IEE Proc.*, Vol. 133, Pt. J, No. 6, p. 353, 1986.

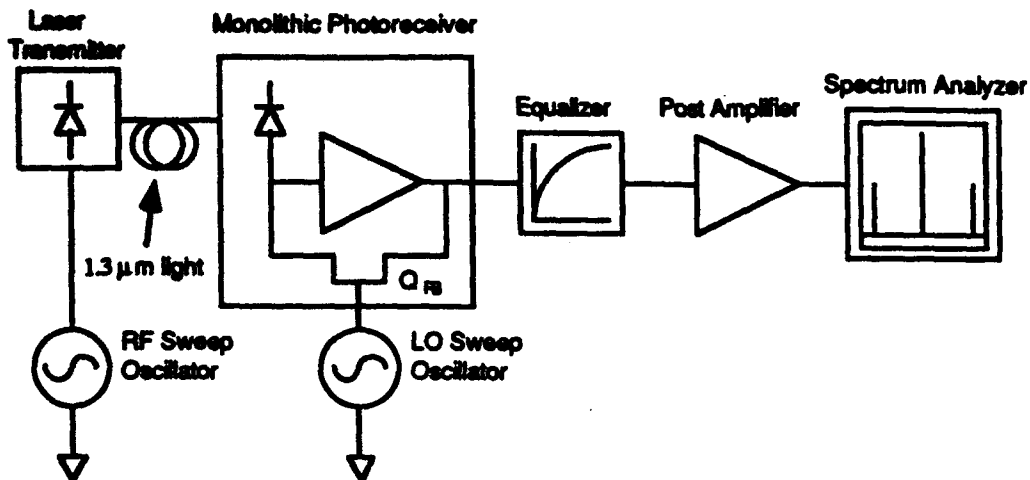


Figure 1. Test setup schematic diagram

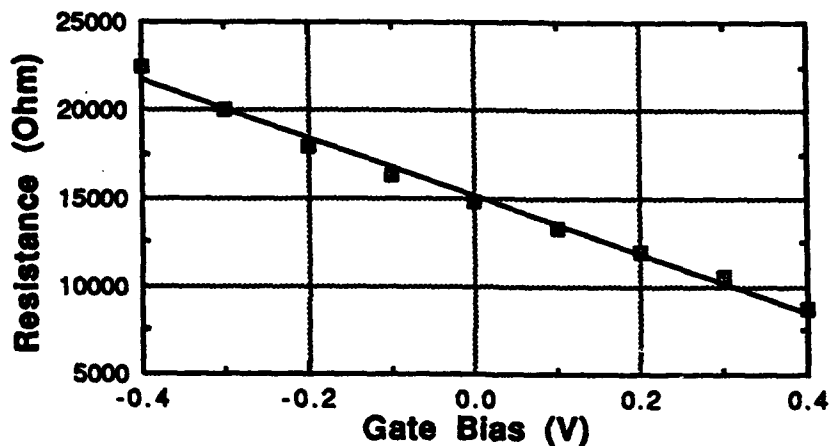


Figure 2. Feedback resistance vs. gate bias voltage (V_G).

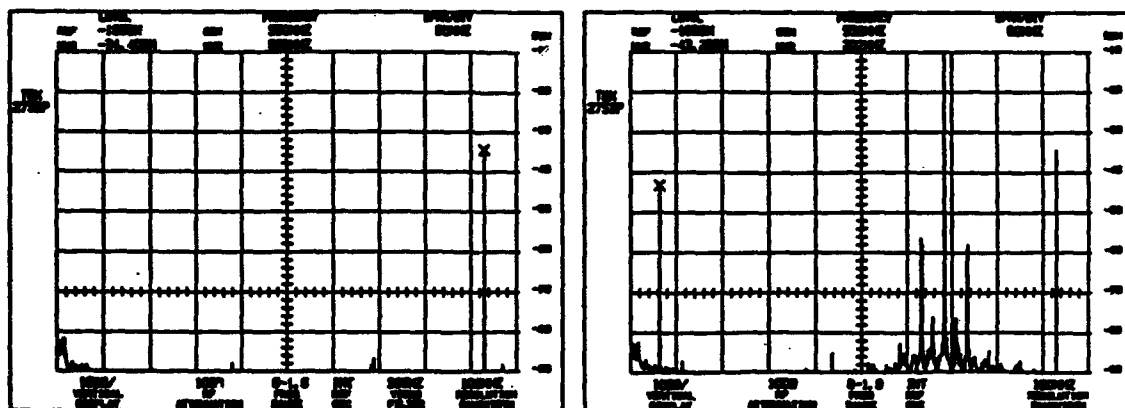


Figure 3a and 3b. Receiver output before and after application of mixing signal.

Silicon Monolithically Integrated Optoelectronic Receiver

Y.-S. He, L. D. Garrett, J. C. Campbell, E. Tuncer, S.I. Javalagi, and D.-L. Kwong

Microelectronics Research Center
Department of Electrical and Computer Engineering
University of Texas, Austin, TX
78712, USA

Lightwave communication has become the technology of choice for long-haul, high-bit-rate transmission[1]. While optical transmission has the benefits of high bandwidth and low signal loss, system design and fabrication are usually relatively expensive. As a result, there is a need to develop low cost components and circuits. To date, optoelectronic circuitry has utilized III-V compound materials. However, Si integrated circuit technology is mature, compact, inexpensive, and has demonstrated high reliability. The speed of Si devices has been improved dramatically by scaling the channel length of Si-MOSFETs into the deep submicron regime[2]-[3]. These characteristics make Si-based integrated circuit technology very attractive for lightwave communications, particularly, for short-haul, low-bit-rate communication systems such as local area networks and domestic services. We report an integrated receiver which consists of a planar Si p-i-n photodiode and a Si-MOSFET preamplifier.

The transimpedance preamplifier was designed, with the aid of the SPICE simulation program, for depletion mode MOSFETs with a gate length of $1\ \mu\text{m}$ and a threshold voltage of -0.1V . Figure 1 shows a circuit diagram of the receiver. The first stage is a common-source FET amplifier, with a gate width of $5\ \mu\text{m}$ for the drive transistor and a gate width of $15\ \mu\text{m}$ for the active load transistor. The gate ratio of the input common-source stage and the series resistor value of the first source-follower stage were adjusted to bias the feedback loop for zero dc feedback current while providing adequate open-loop voltage gain. For the second and third stage source-followers FETs 3 through 6 have a gate width of $100\ \mu\text{m}$. The final source-follower stage was designed for impedance matching to a $50\ \Omega$ load.

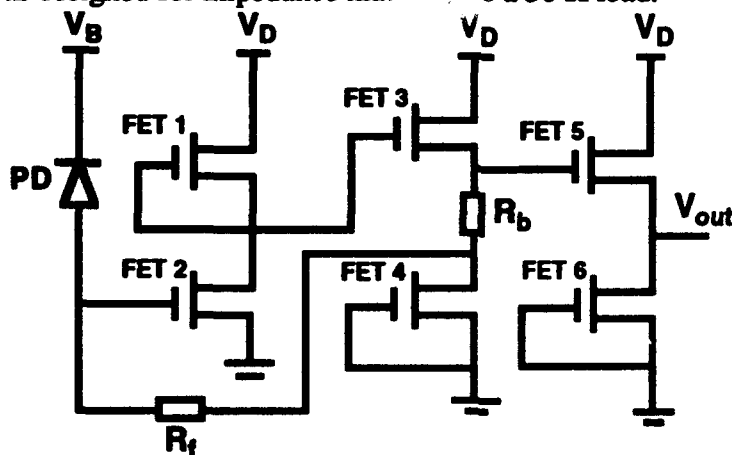


Figure 1. Circuit diagram of the Si MOSFET-based OEIC receiver.

The feedback resistor and the bias resistor have resistances of approximately $1\text{k}\Omega$. Three different photodiode diameters (20, 50, and $100\ \mu\text{m}$) were employed.

The fabrication of the integrated lightwave receiver was carried out on high-resistivity ($60\ \Omega\text{cm}$), p-type Si substrates. High substrate resistivity helps to suppress the parasitic effect of the pad capacitance at high frequency. The circuit was fabricated using a seven layer photolithographic process. In the first step, an n^- well was formed to isolate the photodiode from the substrate by a P diffusion at $850\ ^\circ\text{C}$ for 10 mins and a drive-in step at $1050\ ^\circ\text{C}$ for 400 mins. This produced an n^- well approximately $2\ \mu\text{m}$ deep with an impurity concentration of $10^{16}\ \text{cm}^{-3}$. Isolation of the MOSFETs was accomplished with a standard LOCOS oxide isolation technique. The gate oxide was thermally grown at $850\ ^\circ\text{C}$ in dry oxygen for 60 mins followed by annealing in a nitrogen atmosphere at $950\ ^\circ\text{C}$ for 60 mins. The resulting thickness of the gate oxide was $90\ \text{\AA}$. Thereafter, $4000\ \text{\AA}$ of heavily-doped polysilicon was deposited to form the gate. A $1000\ \text{\AA}$ -thick spacer layer was then deposited by CVD. The source and drain regions of the MOSFETs and the n^+ regions of the photodiodes were formed by a P diffusion at $900\ ^\circ\text{C}$ for 15min. The p^+ region of the photodiode was created by B implantation at a dose of $4 \times 10^{15}\ \text{cm}^{-2}$ and an energy of $50\ \text{keV}$ through a $1500\ \text{\AA}\ \text{SiO}_2$ mask layer. This yielded a surface doping of $2 \times 10^{20}\ \text{cm}^{-3}$ and formed a good ohmic contact.

The discrete FETs exhibited an external transconductance of $177\ \text{mS/mm}$. The gate leakage current was found to be less than $1\ \text{pA}$. This low value for the gate-leakage current helps suppress circuit noise [4]. The dark current of the Si photodiode was $5\ \text{nA}$ at $3\ \text{V}$ and the breakdown voltage was $6.7\ \text{V}$. The external quantum efficiency of the photodiode was approximately 70% without an AR coating at $\lambda = 700\ \text{nm}$.

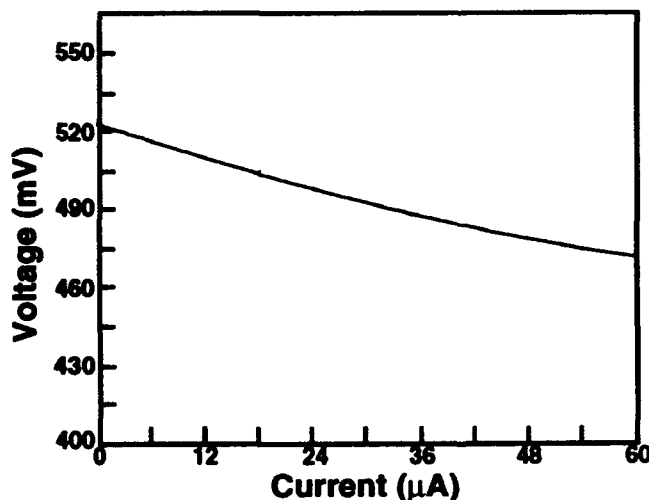


Figure 2. Closed-loop transfer characteristic of the transimpedance amplifier at $V_D = 4\text{V}$. The slope indicates the transimpedance of the circuit.

The open-loop dc voltage gain of the first amplifier stage is measured to be 8.9 with $V_D=4$ V. This is sufficient to achieve a closed-loop transimpedance of about 90% of the value of the feedback resistor. Figure 2 shows the transfer characteristics of the amplifier circuit measured at $V_D=4$ V. The transimpedance, Z_T , as given by the slope of the curve, is approximately 900Ω , and the curve is found to be nearly linear up to $60 \mu\text{A}$.

The frequency response of the discrete MOSFETs was measured in the common-source configuration using an HP 8510 network analyzer with Cascade Microtech $150 \mu\text{m}$ ground-signal-ground coplanar waveguide probes. Drain to source and gate to source biases of 3V and 2V were used, respectively. On-wafer s-parameter measurements, corrected for bonding pad parasitics, yielded a short circuit current gain cutoff frequency of $f_T = 4.5$ GHz, as shown in figure 3. The frequency response of the circuit, also obtained from s-parameter measurements, shows that the 3dB bandwidth of the circuit is approximately 320 MHz. Further improvement in the performance of the preamplifier could be achieved by reducing the gate length as well as the gate resistance. The use of a self-align silicide process should reduce the gate resistance as well as the source and drain resistance significantly. Another approach for improving the performance of the circuit would be to utilize a SiGe MODFET design. It has recently been demonstrated by König et al. that higher transconductance can be achieved with this type of structure[5].

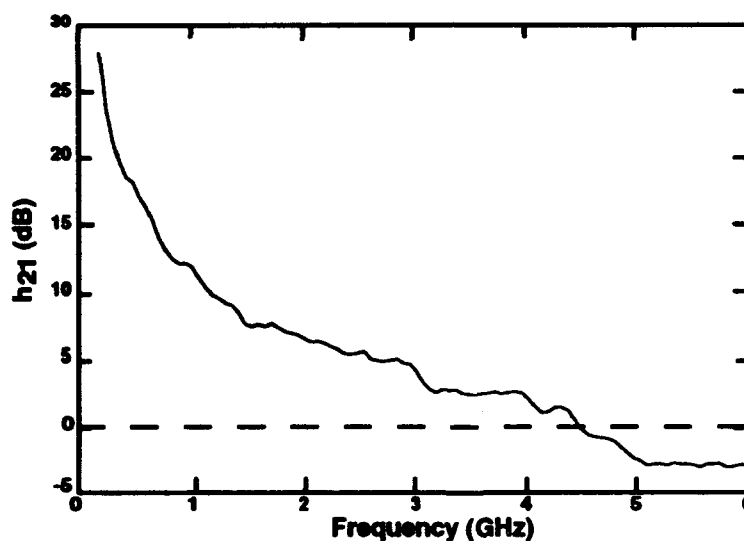


Figure 3. Current gain h_{21} versus frequency for the discrete Si MOSFET, showing f_T of 4.5GHz for $V_{GS}=2$, $V_{DS}=3$. Gate length and width are $1\mu\text{m}$ and $40\mu\text{m}$, respectively.

The noise current of the receiver was calculated using:

$$\langle i^2 \rangle_c = \langle i^2 \rangle_T + 2qI_d I_2 B$$


where, $\langle i^2 \rangle_T$ is the equivalent amplifier input noise current [6], I_d is the dark current of the photodiode, and I_2 is normalized noise-bandwidth intergal. The receiver total capacitance is 1.4 pF, the intrinsic transconductance of the MOSFET is 5.83 ms, and I_d is 5 nA. Assuming a load resistor sufficiently large that its noise can be neglected, we have calculated that $\langle i^2 \rangle_c = 8.95 \times 10^{-19} \text{ A}^2$ at 750 Mbit/s. At this bit rate, the receiver sensitivity should be within 3dB of that of a GaAs MESFET circuit.

In conclusion, we have fabricated the first fully monolithic Si MOSFET lightwave receiver. The receiver consists of a planar Si p-i-n photodiode and a Si-MOSFET preamplifier. The Si p-i-n showed an external quantum efficiency of 70% at a wavelength of 700 nm. The transimpedance was 900 Ω and the 3dB bandwidth of the preamplifier was found to be 320 MHz.

This work was supported by the Office of Naval Research (Contract # 26-0679-73XX) and a grant from the National Science Foundation (Grant # 26-1000-56XX).

REFERENCES

1. Li, T., IEEE J. Sel Area Comm. SAC-1, 1983, pp356-372
2. Yan, R.-H., Lee, K. F., Jeon, D. Y., Kim, Y. O., Park, B.G., Pinto, M. R., Rfferty, C. S., Tennant, D. M., Westerwick, E. H., Chin, G. M., Morris, M. D., Early, E., Mulgrew, P., Mansfield, W. M., Watta, R. K., Voshchenkov, A. M., Bokor, J., Swartz, R. G., and Ourmazd, A., IEEE Electron Device Lett., 1992, vol. 13, NO.5, pp256-258
3. Raynaud, C., Cautier, J., Guegan, G., Lerme, M., Playze, E., and Dambrine, G., IEEE Electron Device Lett., 1991, vol. 12, NO.12, pp667-669
4. Ogawa, K., Owen, B., and Boll, H. J., Bell Syst. Tech. J.1983, 62, pp1181-1188
5. Konig, O., Boers, A. J., Schaffler, F., and Kasper, E., Electron. Lett., 1992, 28, pp160-162
6. Smith, R. G., and Personick, S. D. 'Receiver design for optical fiber communication systems,' In " Topics in Applied Physics." (H. Kressel, ed.), 1982, 39, pp89-160, Springer-Verlag, Berlin



III-V Semiconductor Switches and Modulators

ITuA 8:30am-10:30am
Mesquite A

Joseph Charles Campbell, *Presider*
University of Texas at Austin

Switch Arrays Based on Semiconductor Laser Amplifiers

Mats Gustavsson⁽¹⁾ and Mats Janson⁽²⁾

⁽¹⁾Fiber Optics Research Center
Ericsson Telecom AB, S-126 25 Stockholm, Sweden

⁽²⁾Opto and Microwave Electronics Division
Ericsson Components AB, S-164 81 Kista, Sweden

INTRODUCTION

A near term application of photonic switch arrays appears to be in the broadband telecommunications transport network as optical cross-connects in a transparent optical layer of the network. Fig. 1 schematically illustrates such a system where photonic switch arrays can be used for protection switching and network reconfiguration whereas the digital cross-connects are used for, e.g., routing in digital transmission hierarchies and for regeneration of optical signals [1]. Prerequisites for the employment of switch arrays in such systems are introduction of high (≥ 10 Gb/s) bitrate communications, such that the photonics layer in the system complements electronic systems in a meaningful way, as well as adequate performance of the switch arrays.

LiNbO₃ switch arrays have been extensively used for systems experiments [1]. Their losses are a major problem, which, in principle, can be overcome with optical amplifiers. However, switch arrays based on integrated semiconductor laser amplifiers appear to offer superior performance in (physical and port) size, functionality and cost. One approach to such switch arrays is to use gated amplifier switches of the tree architecture. Advantages of such gate arrays are simple structure (one structure, the amplifier, is used for switching, amplification, and monitoring), equal power in point-to-point and multipoint operation as well as being a strictly nonblocking architecture. A disadvantage is the loss incurred in the power splitters in a point-to-point connection: $L(\text{dB})=6 \cdot \text{ld}(N)$, where the switch size is $N \times N$ and ld is the base 2 logarithm. This type of loss does not occur in switches which spatially switch the signal at each switch point. When the switch array is operated in a broadcast mode, these losses are reduced to $L(\text{dB})=3 \cdot \text{ld}(N)$ as compared to switch arrays using spatial switch points. The speed of rearrangement is limited to around 1 GHz, unlikely to be a limitation in most applications.

LASER AMPLIFIER GATE SWITCH ARRAYS

Fabry-Perot and travelling wave semiconductor laser amplifiers are suitable for use as ON/OFF switches owing to their large extinction ratio and nanosecond switching time [2], [3]; travelling wave devices provide a large optical bandwidth, high saturation output power, and stable operation and are preferred in high bitrate multicarrier systems. More complex photonic switching functions are feasible using a number of these ON/OFF switches interconnected by optical waveguides [2]. Early demonstrations of space switch matrices based on semiconductor optical gate switches include a switch comprising a hybrid-integrated indium phosphide laser diode gate in a 4×4 silica waveguide structure [4] and monolithic InGaAsP/InP 2×2 laser diode matrix switches [5], [6]. Recently, several low loss hybrid-integrated as well as monolithic space switches and switches with gain have been presented, with port size up to 4×4 and 1×16 , see, e.g., [7]-[16].

The photograph in fig. 1 shows a gate switch array developed by Ericsson, which will be discussed in the following. The switch architecture is a strictly nonblocking tree structure comprising passive waveguides for signal transport, passive Y-branches for power splitting and combining, and integrated amplifiers for gating, amplification and monitoring. Each of the $N=4$ inputs is connectable with each output by a passive binary tree splitter of $\text{ld}(N)$ levels at the input and a passive binary tree combiner of $\text{ld}(N)$ levels at the output which form an active connection region with N^2 waveguides connecting the splitter with the combiner; this region is used to control the switch state by gating the signals with integrated amplifiers. A switch array of this type will thus need at least N^2 integrated amplifier gates; in addition, to keep the signal level high throughout the switch, one or more stages of booster amplifiers can be included (in this case two booster stages are included). To minimise the coupling loss between plane cut fibres and the chip, the passive waveguides at the input and at the output have been provided with linear tapers.

Integration of passive and active (amplifier) waveguides is a main problem in the development of compact monolithic switch arrays. The structure should exhibit high coupling efficiency and low reflectivity at

the passive-active waveguide interface, and low polarisation dependence; the active waveguide should be low noise (at least the input amplifier), have a large extinction ratio and short switch time (at least the gate), and provide high saturation output power (at least the output amplifier). Further, the passive interconnecting waveguides should be low loss and allow small bend radii. A butt-joint integration approach (with regrown passive waveguides) provides flexibility in the separate optimisation of the passive and different active sections of the switch structure; however, another, more reproducible, butt coupling approach as described in the following has been used. The switches are fabricated in the InGaAsP/InP material system, and the fabrication process [10] is based on metal-organic vapour-phase epitaxy (MOVPE) and reactive ion etching (RIE) to form the waveguide mesa; selective wet chemical etching is used to define the active sections in the direction of light propagation. Regrowth is performed in two steps by MOVPE: firstly, iron doped semi-insulating (SI) and n doped current blocking layers are selectively grown over the wafer, and secondly, the contact layers are grown. To laterally isolate the active sections from each other, the contact layers outside the contacts are removed by RIE. Schematic waveguide cross sections are depicted in fig. 2. Antireflective coatings are applied to the cleaved chips to reduce the optical feedback and for improved coupling efficiency. Length and width of the 4x4 switch array chips are approximately 7 mm and 3 mm, respectively.

The fabricated switches operate at wavelengths around 1.55 μm ; an example of switch characteristics at a signal wavelength of 1.543 μm for a 4x4 gate switch array is shown in fig. 3; as can be seen, net optical signal gain can be provided between fibres; also, the extinction ratio is high, typically 40 to 50 dB. In this type of gate switch arrays, contributions to spatial crosstalk include incomplete signal absorption in the amplifier gates in their OFF-states, crosstalk in waveguide crossings, and scattered light in the chip. A signal in a point-to-point connection contributes to crosstalk for other signal channels directed to the three other output ports. The design and fabrication process allow typical crosstalk levels less than -40 dB.

Amplifier saturation output power and requirements on error rate performance limit the size of amplifier based space switches and systems with such switches. A number of analyses on switch and system properties and size limitations have been published, see, e.g., [17]-[21]; large ($\gg 8 \times 8$) strictly non-blocking switches are predicted to be feasible. Considering available substrate area and fabrication yield, space switches larger than 8x8 are probably best realised by employing a hybrid-integration technique using monolithic 8x8 or smaller switches in a SiO₂/Si or polymer passive waveguide pattern.

CONCLUDING DISCUSSION

When contrasting the systems requirements on switch arrays with data for the gate amplifier switch arrays, these clearly represent an interesting option. It should, however, be noted that other alternatives, such as digital switch arrays [22], combined with laser amplifiers and/or erbium doped fibre amplifiers, overcome the inherent power splitting loss problems, at the expense of a more complex switch element structure, the excess loss of which has to be significantly lower than 3 dB. Interesting alternatives are also monolithic switch arrays which combine the use of optical switches, such as directional couplers or digital optical switches, as switch points with integrated laser amplifiers; the integrated amplifiers can be used to improve crosstalk performance of the switch arrays, and for monitoring, loss compensation and power equalisation.

In summary, it appears that the switch arrays described here can be developed to sizes required for systems applications ($\geq 8 \times 8$), and that, in general, switch arrays with integrated optical amplifiers will bring the photonic network significantly closer.

ACKNOWLEDGEMENTS

The authors wish to thank their colleagues at Ericsson who have contributed to this work, particularly Wim van Berlo, Bo Lagerström, Lena Lundgren, Ann-Caroline Mörner, Peter Ojala, Michael Rask, Björn Stoltz, Jan Söderström, and Lars Thylén who now is with the Royal Institute of Technology. This work was in part performed within the RACE 1033 (OSCAR) project and within the RACE 2028 (MWTN) project.

REFERENCES

- [1] S. Johansson: 'Transparent optical multicarrier networks', Proc. 18th European Conf. on Optical Communication, pp. 781-786, 1992.
- [2] M. Ikeda: 'Laser diode switch', Electron. Lett., vol. 17, pp. 899-900, 1981.

- [3] M. Ikeda: 'Optical properties for an antireflection-coated LD optical switch', *Electron. Lett.*, vol. 19, pp. 826-828, 1983.
- [4] M. Kobayashi, A. Himeno, H. Terui: 'Guided-wave optical gate matrix switch', *Proc. IOOC-ECOC '85*, post-deadline paper, pp. 73-76, 1985.
- [5] M. Ikeda: 'Proposal of laser diode integrated-optical matrix switches', *Trans. IECE Japan*, vol. E 69, pp. 1072-1074, 1986.
- [6] M. Ikeda, O. Ohguchi, K. Yoshino: 'Monolithic LD optical matrix switches', *Proc. 13th European Conf. on Optical Communication*, pp. 227-230, 1987.
- [7] S. Oku, K. Yoshino, M. Ikeda: 'Design and performance of monolithic LD optical matrix switches', *Proc. Photonic Switching*, pp. 98-100, 1990.
- [8] I. H. White, J. J. S. Watts, J. E. Carroll, C. J. Armistead, D. J. Moule, J. A. Champelovier: 'InGaAsP 400×200 μm active crosspoint switch operating at 1.5 μm using novel reflective Y-coupler components', *Electron. Lett.*, vol. 26, pp. 617-618, 1990.
- [9] H. Terui, T. Kominato, M. Kobayashi: 'Lossless 1×4 laser diode optical gate switch', *J. Lightwave Technol.*, vol. 9, pp. 1518-1522, 1991.
- [10] M. Janson, L. Lundgren, A.-C. Mörner, M. Rask, B. Stoltz, M. Gustavsson, L. Thylén: 'Monolithically integrated 2×2 InGaAsP/InP laser amplifier gate switch arrays', *Electron. Lett.*, vol. 28, pp. 776-778, 1992.
- [11] J. Singh, I. D. Henning, P. S. Mudhar, M. A. Fisher, S. Perrin, D. A. H. Mace, M. J. Adams: 'A novel twin-ridge-waveguide optical amplifier switch', *IEEE Phot. Technol. Lett.*, vol. 4, pp. 173-176, 1992.
- [12] J. D. Burton, P. J. Fiddymment, M. J. Robertson, P. Sully: 'Low loss monolithic 2×2 laser amplifier gate switch matrix', *Proc. 13th IEEE International Semiconductor Laser Conf.*, pp. 128-129, 1992.
- [13] M. G. Young, U. Koren, B. I. Miller, M. A. Newkirk, M. Chien, M. Zirngibl, C. Dragone, B. Glance, T. L. Koch, B. Tell, K. Brown-Goebeler, G. Raybon: 'A 1×16 photonic switch operating at 1.55 micron wavelength based on optical amplifiers and a passive optical splitter', *OSA Proc. Optical Amplifiers and their Applications*, post-deadline paper, pp. 33-37, 1992.
- [14] M. Gustavsson, B. Lagerström, L. Thylén, M. Janson, L. Lundgren, A.-C. Mörner, M. Rask, B. Stoltz: 'Monolithically integrated 4×4 InGaAsP/InP laser amplifier gate switch arrays', *OSA Proc. Optical Amplifiers and their Applications*, post-deadline paper, pp. 38-42, 1992.
- [15] D. A. O. Davies, P. S. Mudhar, M. A. Fisher, D. A. H. Mace, M. J. Adams: 'Integrated lossless 1 to 4 optical splitter/combiner operating at 1.55 μm ', *OSA Proc. Optical Amplifiers and their Applications*, post-deadline paper, pp. 43-46, 1992.
- [16] D. K. Probst, L. G. Perryman, B. C. Johnson, R. J. Blackwell, J. A. Priest, C. L. Balestra: 'Demonstration of an integrated, active 4×4 photonic crossbar', *IEEE Phot. Technol. Lett.*, vol. 4, pp. 1139-1141, 1992.
- [17] J. D. Evankow, R. A. Thompson: 'Photonic switching modules designed with laser diode amplifiers', *IEEE J. Selected Areas in Commun.*, vol. 6, pp. 1087-1095, 1988.
- [18] M. Ikeda: 'Maximum number of connectable laser diode optical switch (LDSW) systems', *Opt. Quantum Electron.*, vol. 20, pp. 515-524, 1988.
- [19] M. Gustavsson and L. Thylén: 'Switch matrix with semiconductor laser amplifier gate switches: A performance analysis', *OSA Proc. 2nd Topical Meeting on Photonic Switching*, pp. 180-182, 1989.
- [20] R. F. Kalman, L. G. Kazovsky, J. W. Goodman: 'Space division switches based on semiconductor optical amplifiers', *IEEE Phot. Technol. Lett.*, vol. 4, pp. 1048-1051, 1992.
- [21] E. Berglind and L. Gillner: 'A simple method for noise analysis of a chain of linearised optical two-ports', *OSA Proc. Optical Amplifiers and their Applications*, pp. 131-134, 1992.
- [22] J. F. Vinchant, M. Renaud, A. Goutelle, J. L. Peyre, P. Jarry, M. Erman, P. Svensson, L. Thylén: 'First polarisation insensitive 4×4 switch matrix on InP with digital optical switches', *Proc. 18th European Conf. on Optical Communication*, pp. 341-344, 1992.

FIGURE CAPTIONS

Fig. 1. Schematic illustration of a transport network with OXC/DXC nodes; the photograph shows a 4×4 semiconductor laser amplifier gate switch array which can be used as a central part of the OXC in an OXC/DXC node [1].

Fig. 2. Schematic passive and active waveguide cross sections for a switch array of the type shown in fig. 1.

Fig. 3. Example of switch characteristics: Switch characteristics of four of the sixteen transmission paths in a 4×4 gate switch array of the type shown in fig. 1. The input and output booster amplifiers are biased at 50 mA each.

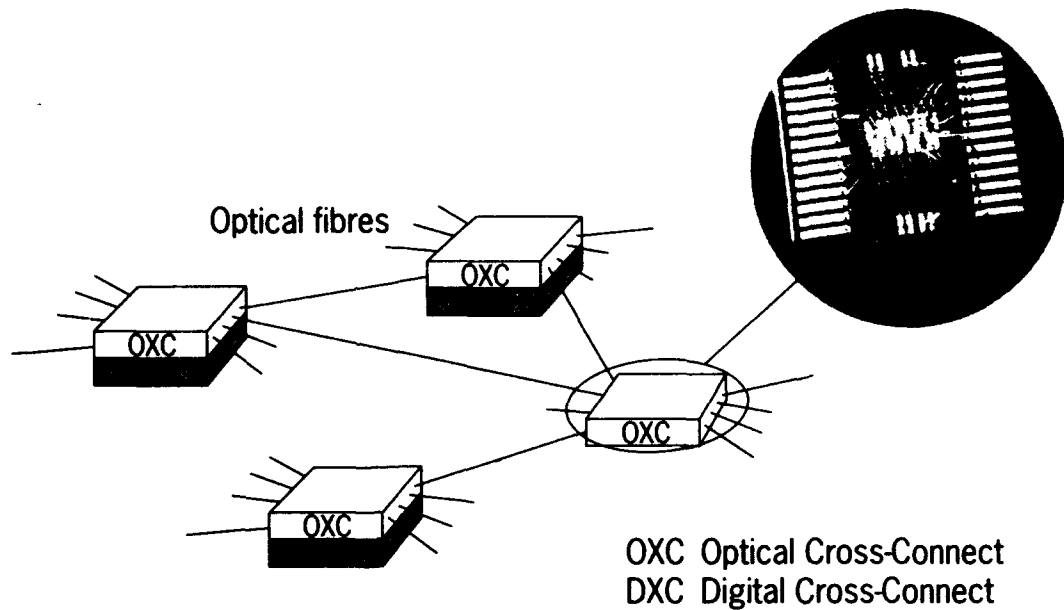


Fig. 1

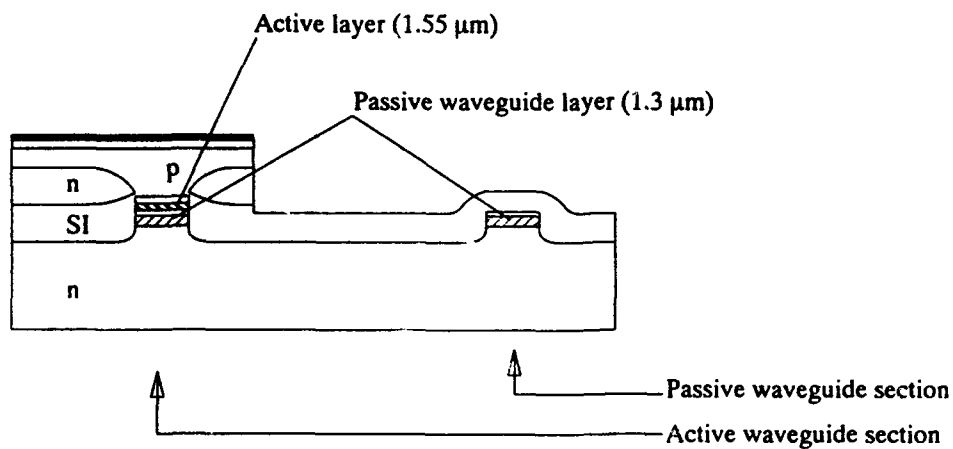


Fig. 2

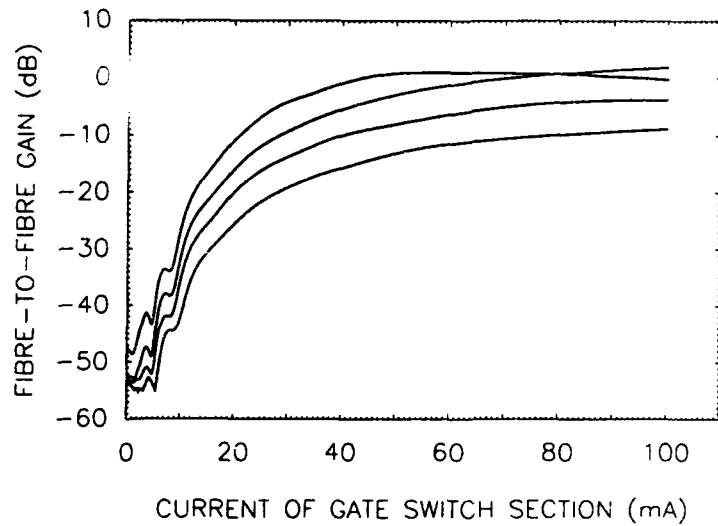


Fig. 3

Extremely Low Loss 4X4 GaAs/AlGaAs Optical Matrix Switch

K. Hamamoto, S. Sugou, K. Komatsu and M. Kitamura
Opto-Electronics Research Laboratories, NEC Corporation
34 Miyukigaoka, Tsukuba city, Ibaraki 305, Japan
Phone:+298(50)1534 Fax:+298(50)1106

1. Introduction

An optical matrix switch is one of key components for photonic switching systems. So far, several kinds of switch element have been investigated.⁽¹⁾⁻⁽⁵⁾ Among them, the GaAs/AlGaAs electro-optic directional coupler (EODC) switch has several advantages including (1) the low electric power consumption and fast switching speed inherent to electro-optic effect, and (2) low absorption loss in the long wavelength region of 1.3 - 1.5 μm .

We previously reported the development of a 4X4 optical matrix switch using GaAs/AlGaAs EODC switches with uniform device characteristics.⁽²⁾ Its total waveguide loss was over 10 dB, however, which was higher than the expected value. A total waveguide loss of about 1 dB was calculated for the matrix switch, assuming 0.5 dB/cm absorption loss.

In this paper, we present an extremely low loss 4X4 GaAs/AlGaAs optical matrix switch. The total waveguide loss has been drastically reduced to 1.6 dB. This drastic reduction was achieved by layer structure optimization, crystal quality improvement, and plasma damage reduction.

2. Loss reduction approaches

A schematic diagram of the 4X4 GaAs/AlGaAs optical matrix switch is shown in Fig. 1. It is designed with a simplified tree architecture similar to the one used for the above switch.⁽²⁾ This device is 17 mm long and 1.4 mm wide. The waveguide width is 2 μm . The waveguide spacing and length in the EODC region are 2 μm and 3 mm respectively. The waveguide bend radius is 4 mm.

The total waveguide loss includes radiation loss, intersecting loss, absorption loss, and excess loss (damaged etch surface, scattering, etc.). As radiation loss and intersecting loss have been already reduced to under 0.5 dB,⁽²⁾ we made efforts to reduce absorption loss and excess loss using the following three methods.

(1) Reduction of free carrier absorption by layer structure modification: The layer structure used is shown in Fig. 1(a) in comparison with the conventional layer structure in Fig. 1(b). In the conventional structure, an i-GaAs guiding layer was stacked directly on top of an n-AlGaAs cladding layer. The high

free-carrier absorption loss was mainly due to the n-cladding layer. In order to reduce this free-carrier absorption, a lower i-AlGaAs cladding layer (0.2 μm thick) is inserted between the n-AlGaAs cladding layer and the i-GaAs guiding layer, as shown in Fig. 2(a). The reduction in free-carrier absorption is calculated to be 4.3 dB.

(2) Reduction of excess loss by 2-step RIBE technique: Waveguide fabrication for GaAs/AlGaAs matrix switches has conventionally been performed using reactive ion beam etching (RIBE)⁽⁶⁾ with Cl_2 gas. There has been concern that the plasma damage caused by high energy ions may increase propagation loss. In order to avoid plasma damage, the 2-step RIBE technique was newly introduced. In this technique, high-energy ion etching, which gives a moderately high etching rate, is carried out as the first step. Then low-energy ion etching,⁽⁷⁾ which removes only the damaged etch surface, follows as the second step. Acceleration voltage values were 400 V and 30 V for the first- and second-step etching, respectively. The estimation of excess loss using this method is 1.2 dB, revealed by the difference in propagation loss between waveguides fabricated by high-energy RIBE alone, and by 2-step RIBE.

(3) Reduction of excess loss by crystal quality improvement: Excess loss is also influenced by the crystal quality of epitaxial layers. The oval defect density in particular, peculiar to molecular beam epitaxy (MBE) grown layers, should be decreased. In this experiment, gas source molecular beam epitaxy (GS-MBE) system with low-defect cells⁽⁸⁾ was employed for crystal growth. The density of oval defects was 100 cm^{-2} , which is ten times smaller than that using the conventional MBE system. Based on this, the rate of occurrence of oval defects in a 4X4 matrix switch is 0.3 particle/chip.

3. Results and discussion

A 4X4 optical matrix switch was fabricated by 2-step RIBE on a wafer grown by GS-MBE, using the above loss-reduction approaches. The matrix switch characteristics were measured by coupling 1.3- μm wavelength TE polarized light.

Total waveguide loss inside a matrix switch, excluding coupling loss and reflection loss, was 1.6 dB. In comparison to the 10.6 dB loss of the 4X4 matrix switch reported previously,⁽²⁾ a drastic loss reduction of 9 dB was accomplished. The reduction in the free-carrier absorption loss by layer structure modification, was calculated to be 4.3 dB. This value agrees well with the measured loss difference for waveguides with and without a second i-AlGaAs cladding layer below the GaAs guiding layer. The decrease in excess loss due to plasma damage reduction was

estimated to be 1.2 dB. The remaining 3.5 dB are attributed to the lessened number of oval defects. This loss reduction analysis is summarized in Fig. 3.

Typical switching characteristics of an EODC switch element are shown in Fig. 4. Under alternating $\Delta\beta$ operation, the \otimes -state and \ominus -state were obtained at 12 V and 25.5 V, respectively. The switching voltages only increased 3 V compared with those of previously reported,⁽²⁾ mainly due to the fact that the grown layers are thicker than those of the designed rather than the insertion of a lower i-AlGaAs cladding layer between an n-cladding layer and an i-GaAs layer.

4. Conclusion

We have developed an extremely low loss 4X4 GaAs/AlGaAs optical matrix switch. The total waveguide loss was 1.6 dB, which makes the devices suitable for optical switching systems.

References

- (1) K. Hamamoto, et. al., Electron. Lett., 28 (1992) 441
- (2) K. Komatsu, et. al., J. Lightwave Technol., LT-9 (1991) 871
- (3) M. Gustavsson, et. al., OAA PD9 (1992) 38
- (4) T. Kirihara, et. al., Photonic Switching 14D-6 (1990)
- (5) S. Oku, et. al., Photonic Switching 13-7 (1990)
- (6) H. Takeuchi, et. al., Electron. Lett., 23 (1986) 1241
- (7) Y. Ide, et. al., Inst. Phys. Conf., 7 (1990) 495
- (8) T. Sonoda, et. al., J. Cryst. Grow., 95 (1989) 317

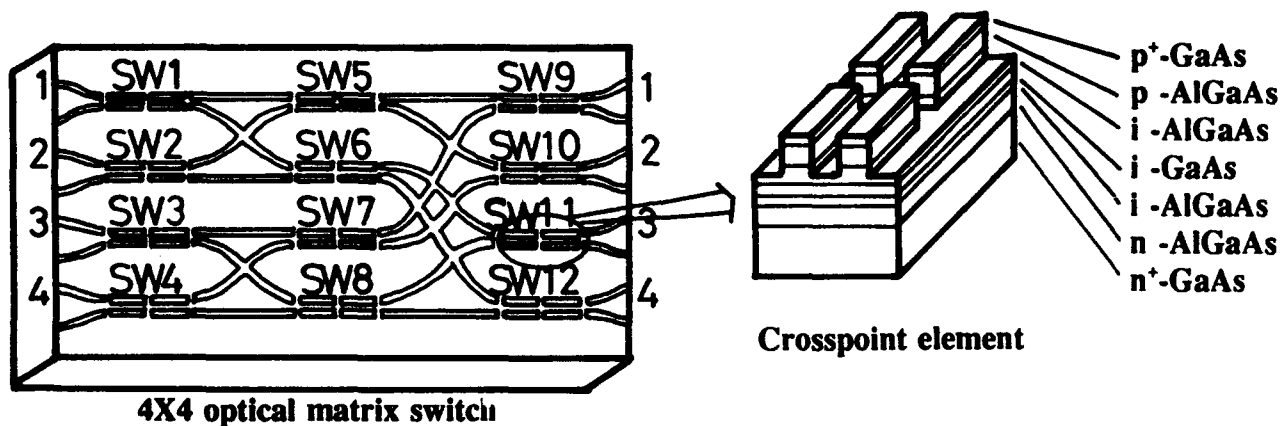


Fig. 1. 4X4 GaAs/AlGaAs optical matrix switch.

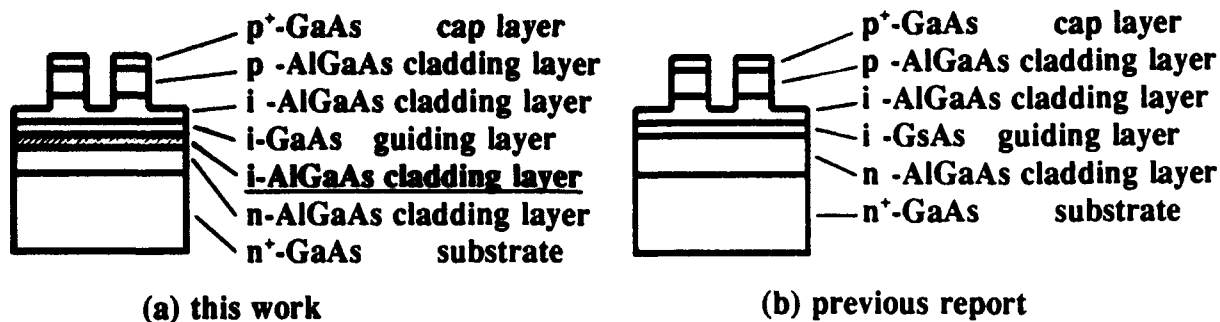


Fig. 2. Layer structure modification.

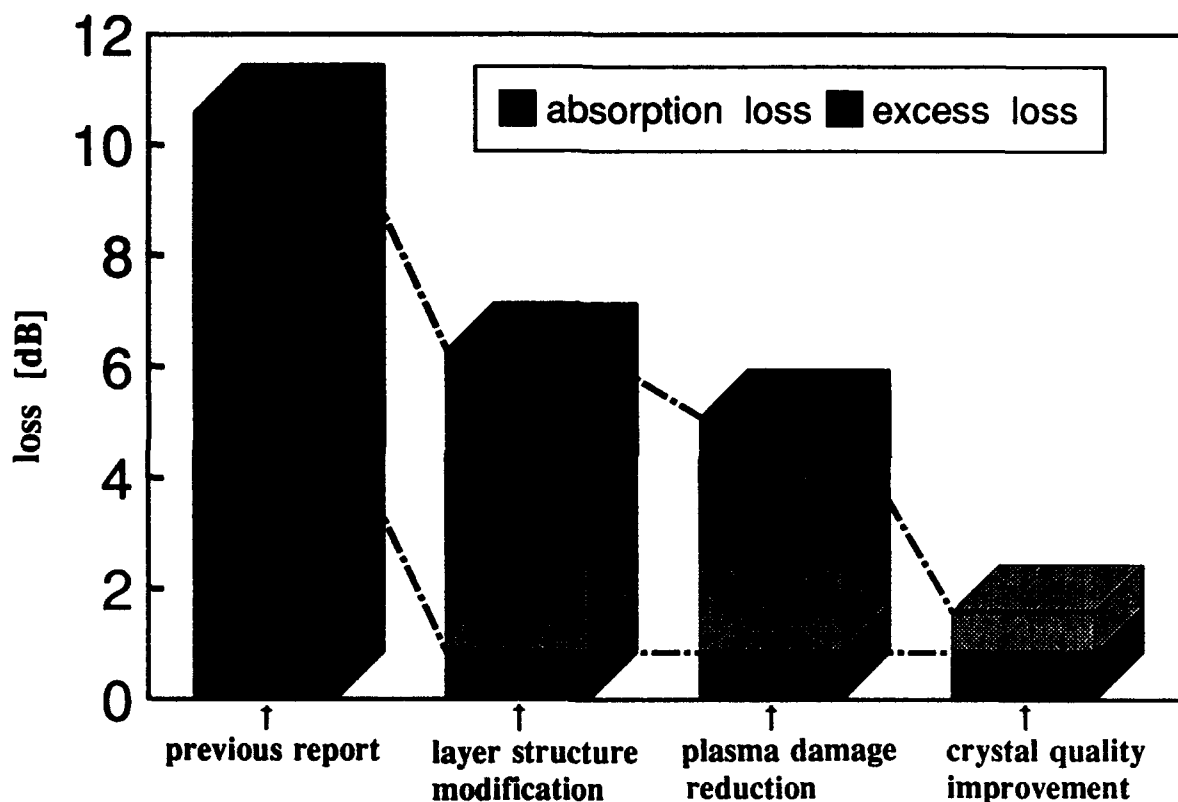


Fig. 3. Loss analysis.

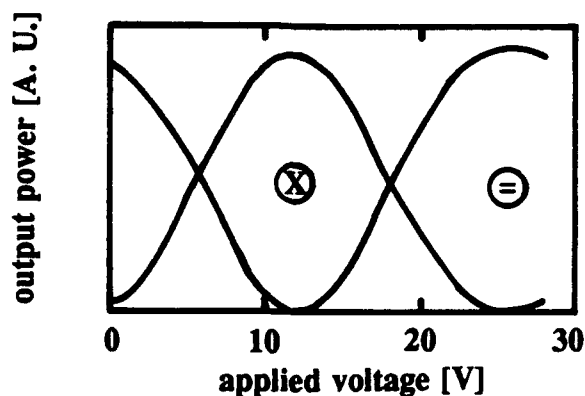


Fig. 4. Typical switching characteristics.

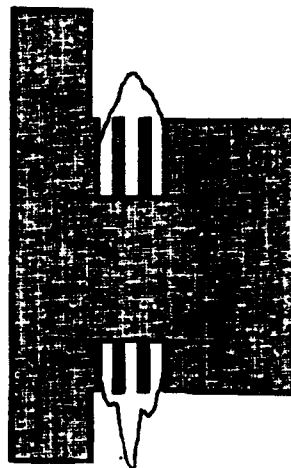
Y-Branch Electro-Optic Waveguide Switch at 1.55 μm using Chopped Quantum Well Electron Transfer Structure

Yi Chen, J. E. Zucker, T. Y. Chang, N. J. Sauer, B. Tell, K. Brown-Goebeler
Room 4F 311

AT&T Bell Laboratories, Holmdel NJ USA 07733
908 949 6137

Y-branch electro-optic waveguide switches based on modal evolution¹ (rather than modal interference) have received wide attention for their wavelength- and polarization-insensitive properties. Semiconductor Y-branch switches^{2,3} usually employ current injection since large refractive index changes are required. Compared to current injection, electrooptic switches possess the advantages of high speed and low power dissipation. However, most voltage-controlled y-branches suffer high drive voltage requirements due to weak electrooptic effects. Recently a waveguide structure has been demonstrated that produces large electrooptic phase shifts with high-speed (> 10 Gbps) capability⁴. Interferometric waveguide modulators⁵ based on the InGaAs / InAlAs / InGaAlAs Barrier, Reservoir, and Quantum Well Electron Transfer Structure (BRAQWETS) have employed 70 \AA InGaAs quantum wells for electrorefraction at 1.58 μm . In order to shift the wavelength of operation to the gain bandwidth of Er-doped fibre amplifiers, we here employ the chopped quantum well (CQW) concept. Three 6 \AA thick InGaAlAs "spikes" are inserted in the 70 \AA InGaAs well to yield the energy band diagram shown in Fig.1. (Also shown are the InAlAs barrier on the left of the CQW and the InGaAlAs electron reservoir on the right). This technique allows three or more effective InGaAlAs compositions to be grown in a molecular beam epitaxial system with only two Al source cells. Using the tunneling resonance method, we calculate that insertion of the InGaAlAs spikes results in a significant blue-shift of the ground state $n=1$ heavy hole exciton transition, from 1.51 μm to 1.40 μm at flat-band. However, the spikes are thin enough to allow easy tunnelling of electrons and holes as shown in Fig.1. The electron and hole wavefunctions are relatively smooth, reflecting a potential well layer with an average bandgap between that of .74 eV InGaAs and 1.06 eV InGaAlAs.

Fig.1 Band diagram for a chopped quantum well that contains three 6 \AA InGaAlAs spikes inside a 70 \AA InGaAs quantum well. At left, the InAlAs barrier; at right, a reservoir layer composed of 1.06 eV bandgap InGaAlAs. Electron and heavy-hole wavefunctions (calculated by tunneling resonance) average over the chopped potential.



A BRAQWETS n-i-n waveguide was grown with an active core composed of twelve CQWs as detailed above, each accompanied by a 250 Å p-doped InAlAs barrier and a 200 Å n-doped InGaAlAs reservoir. Fig.2 shows the normal-incidence electroabsorption spectrum of this sample. As predicted, the bandedge appears near 1.4 μm. Moreover, the spectra show the same characteristic features as in unchopped BRAQWETS. At applied voltage $V < 0$, absorption at long wavelength increases as the ground state exciton red shifts, while $V > 0$ produces bandfilling and decreasing exciton absorption.

For wavelengths near 1.55 μm, the change in absorption is minimal and we can expect refractive index change $\Delta n < 0$ from bandfilling and $\Delta n > 0$ from the red-shift. This ability to produce both positive and negative Δn is a significant advantage of the BRAQWETS for y-branch switches which operate by directing light to the higher index waveguide port. In contrast to current injection switches, where only $\Delta n < 0$ is produced, both sides of a BRAQWETS y-branch can be actively controlled.

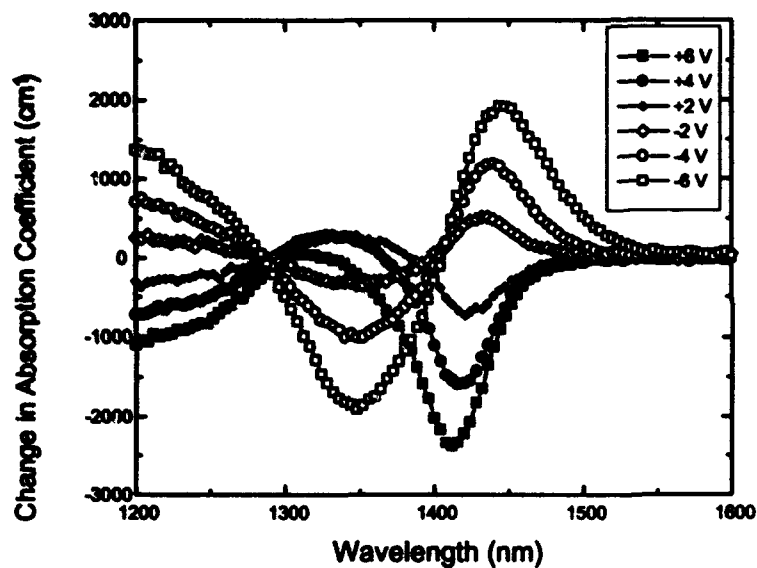


Fig.2 Normal incidence electroabsorption spectrum from chopped BRAQWETS waveguide sample. Positive applied voltage causes electrons to transfer from reservoir layers into the quantum wells, causing bandfilling and a bleaching of exciton absorption. Negative applied voltage empties the well and increases the field across it, causing red shift of the exciton absorption.

We wet-etched rib waveguide y-branches, shown schematically in Fig.3, from the 12-period CQW BRAQWETS wafer. The active region of the switch where voltage is applied is 500 μm long, with a standard 1.5 mm total cleaved length. (Complete switches can be cleaved much shorter, ~ 600 μm). The y-branch angle is 15 mrad. Electrical isolation between the two sides of the switch is provided by a two step ion implant into a narrow central region of the waveguide.

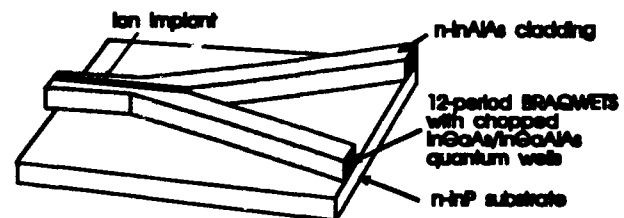


Fig. 3 Schematic of BRAQWETS y-branch switch.

Fig.4 shows the measured switching characteristics as a function of voltage applied to a single side. At 0 V, we have 50:50 split, as designed. For positive applied voltage, the output light is directed away from the active port and for negative applied voltage, light exits from the active port. This behavior is consistent with the BRAQWETS electrooptic properties mentioned above, with $V > 0$ producing $\Delta n < 0$ and vice-versa. The switching characteristics are remarkably consistent for the wavelength range measured, between 1.50 and 1.59 μm .

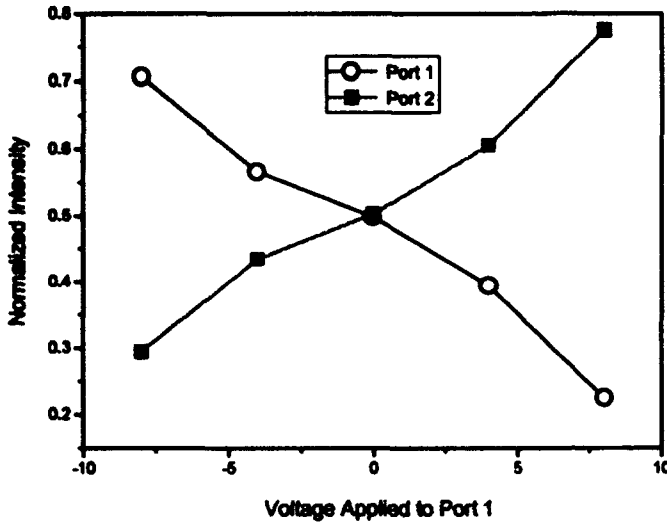


Fig. 4 Measured relative output power as a function of drive voltage to a single side of the BRAQWETS y-branch switch.

Fig. 5 shows the calculated switch performance as a function of refractive index change for single-arm drive operation. This beam-propagation-method result indicates that the maximum refractive index change we are producing in the waveguide with single-arm drive is $\sim 6 \times 10^{-4}$. With dual-arm drive (or with the larger refractive index change we have obtained in other BRAQWETS samples⁵) we calculate that we will obtain > 10 dB crosstalk.

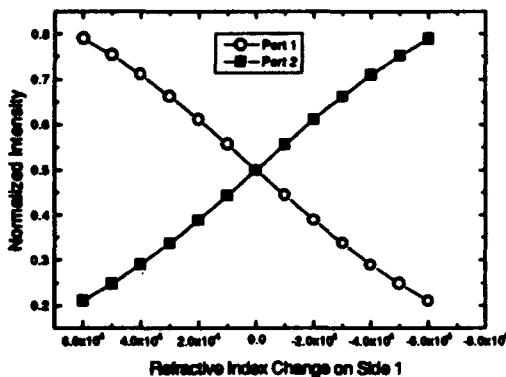


Fig.5 BPM simulation of switch response as a function of voltage-induced refractive index change.

In conclusion, we have demonstrated the first Y-branch switch based on quantum well electron transfer waveguides. This material system provides both positive and negative refractive index change with high-speed capability. We have successfully employed the chopped quantum well concept to shift the wavelength of operation to the 1.55 μm wavelength range. The measured switching characteristics are in excellent agreement with calculated performance.

REFERENCES

- ¹ W. K. Burns, A. B. Lee and A. F. Milton, "Active branching waveguide modulator," *Appl. Phys. Lett.* 29, pp. 790-792 (1976).
- ² H. Yanagawa, K. Ueki, and Y. Kamata, "Polarization- and wavelength-insensitive guided-wave optical switch with semiconductor Y junction," *J. Lightwave Technol.* 8, pp.1192-1197 (1990).
- ³ J. A. Cavailles, M. Renaud, J. F. Vinchant, M. Erman, P. Svensson, and L. Thylen, "First digital optical switch based on InP/InGaAsP double heterostructure waveguides," *Electron. Lett.* 27, pp. 699-700 (1991).
- ⁴ J. E. Zucker, J. L. Marshall, T. Y. Chang, N. J. Sauer, C. A. Burrus, and J. C. Centanni, "15 GHz Bandwidth Quantum Well Electron Transfer Intensity Modulator at 1.55 μm ," *Electron. Lett.* 1992.
- ⁵ J. E. Zucker, K. L. Jones, T. Y. Chang, N. Sauer, B. Tell, K. Brown-Goebeler, M. Wegener, and D. S. Chemla, "Compact Low-Voltage InGaAs/InAlAs Multiple Quantum Well Waveguide Interferometers," *Electron. Lett.* 26, pp. 2029-2030 (1990).

Compact GaAs/AlGaAs Waveguide Optical Switch with Adjustable Y-Junction

T. C. Huang, G. J. Simonis, M. Stead, R. P. Leavitt, J. Bradshaw, and J. Pham

Army Research Laboratory, AMSRL-EP-EE

2800 Powder Mill Road, Adelphi, MD 20783

Tel: (301) 394-2042

A compact GaAs/AlGaAs optical switch with a y-junction structure in which the two output arms can be individually turned on or turned off electrically is demonstrated here for the first time. This initial experimental result shows that switching operation has been achieved with a crosstalk of less than -12 dB for a device with a transition length of less than $400 \mu\text{m}$ at $1.06\text{-}\mu\text{m}$ wavelength.

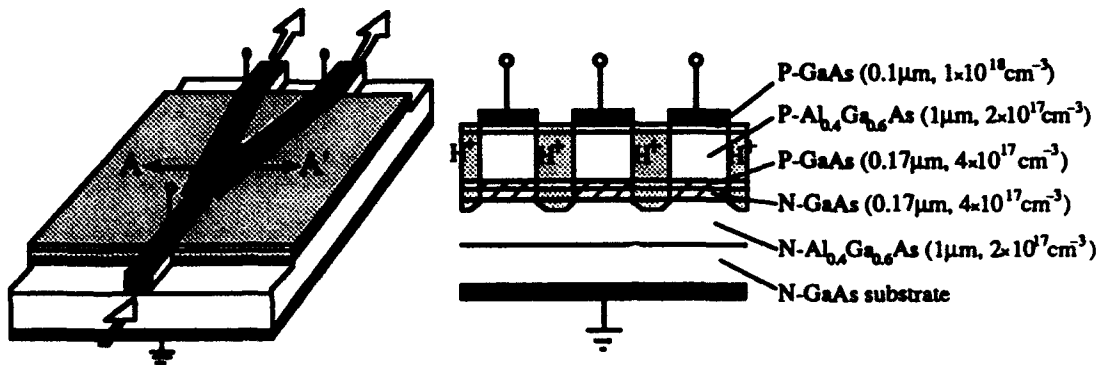


Fig. 1(a) Schematic diagram of the y-branch switch. The guide width is $4 \mu\text{m}$; the gap size between the input and output guides is $1 \mu\text{m}$.

Fig. 1(b) Cross section through points A-A' of Fig. 1(a). The guide layer is a $0.34\text{-}\mu\text{m}$ -thick GaAs layer with a pn junction at the center.

A schematic view of the optical switch is shown in Fig. 1(a). The device structure consists of three voltage-adjustable field-induced waveguides (FIGs). The operational principle of the switch is based on the special property of the FIGs, i.e., that the waveguides can be turned on and turned off electrically [1]. As shown in Fig. 1(a), at the center of the y-junction, the transition section of the switch consists of three arrow-shaped FIGs overlapped in the propagation direction. The specially shaped y-junction of two output guides has

adjacent channels close to the input waveguide, with narrow proton implanted gap separations. This provides the smooth waveguide transition section as well as electrical isolation. With this waveguide electrode configuration plus the unique property of the FIGs, this device structure allows us to switch the input light from one output guide to another. When a DC reverse bias is applied to the input waveguide, and reverse biases are applied to either of the two arms of the y-junction, the propagation path depends on which output arm is turned on. Thus, the switching operation between the two output waveguides can be realized by changing the reverse bias applied to the output arms of the y-junction.

Optical switches were designed and fabricated based on the device concept described above. A cross-sectional view of the y-junction is shown in Fig. 1(b). Devices were fabricated from GaAs/AlGaAs heterostructures grown on a [100]-oriented n-type GaAs substrate by molecular beam epitaxy (MBE). The angle between the two output arms is 3° . The separation of the two output guides is $20\ \mu\text{m}$, and the length of the output guides is $400\ \mu\text{m}$. Multiple-energy proton implantation is carried out using the thick plating Au layer as the implantation mask. The electrical isolation gap between the guides is less than $1\ \mu\text{m}$ wide.

Switching properties were investigated at $1.06\text{-}\mu\text{m}$ wavelength. Incident light was end-fire coupled into the input end facet of the device as a DC bias was applied to the input guide. The light beams exiting from the output facets were recorded by a detector and infrared camera. As a DC reverse bias was applied to the input guide with no bias on either output arm of the y-junction, there was only a very small amount of light out of the output guides; this was due to scattering and weak guiding in the side guides from the built-in junction voltage. However, when reverse biases were applied to the output guides, the near-field patterns of the output guides indicated well-confined single-mode operation of the switch. In addition, as reverse biases were applied to the output guides alternately, switching performance was achieved between the two guides.

Fig. 2 shows the measured output light intensity (normalized to the maximum output as a reference point) as a function of the reverse bias applied alternately to the left and right

guides, with a -9 V DC bias applied to the input guide. When the reverse bias to the left (right) guide changes from $+1$ to -9 V with no bias to the right (left) guide, the output light intensity increases from the left (right) guide, and the output light intensity is almost unchanged from the right (left) guide. Extinction ratios larger than 12 dB have been achieved for both guides as the reverse bias changes from $+1$ to -9 V. Thus, the crosstalk between the two output guides is less than -12 dB. It is also found that the outputs from the left and right guides are quite symmetric under the same bias condition, due to the symmetric structure of the switch.

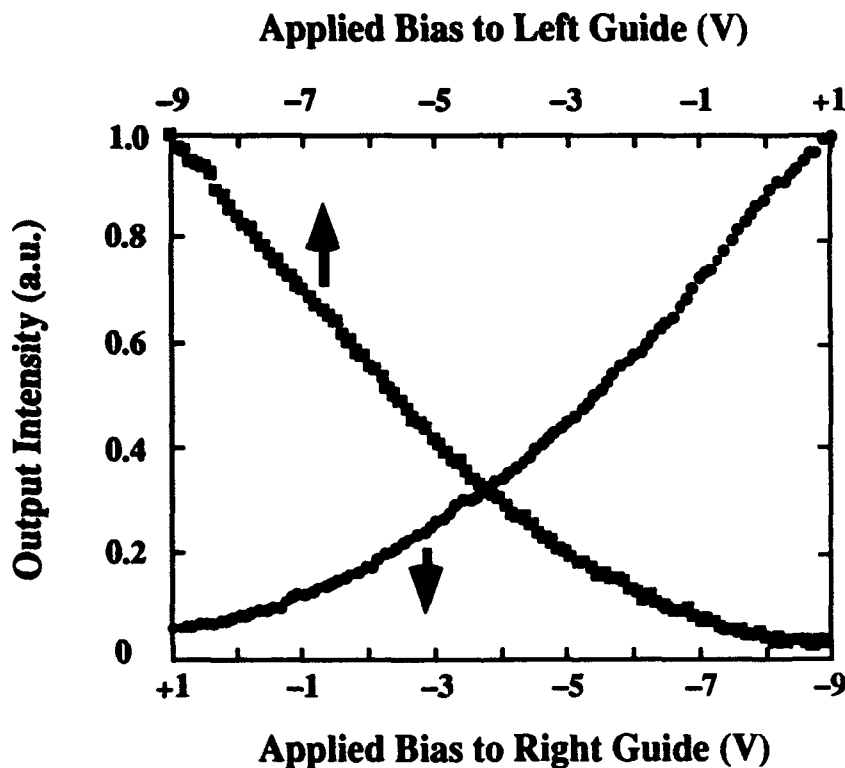


Fig. 2 Normalized output light intensity as a function of the applied reverse biases to the left (square) and right (dot) guides, when a -9 V DC bias was applied to the input guide. The extinction ratios for both left and right guides are larger than 12 dB. The crosstalk of the switch is therefore less than -12 dB.

The propagation loss of this device at the maximum optical switching is 8.5 dB. A large part of this loss comes from the mismatch between the FIG regions and the spatial filter

sections. This loss can be eliminated in the integrated optics or optical fiber coupling since spatial filtering is not necessary in those cases. The proton implantation damage also caused about 2 dB loss in this experiment; it could be reduced to less than 0.4 dB by more carefully optimizing the annealing process as reported previously [1].

Unlike the reflection-type and mode-coupling-type switches, which involve optical mode coupling between the input and output ends [2, 3], the switching operation for this device is smoothly transferring the incident light to the output guide. Therefore, this device structure should reduce the mode transition loss within the device, as well as providing good preservation of the light mode quality. Another attractive feature of the switch is that devices with small size can be achieved. In large-scale monolithic integrated opto-electronics, it is very important to minimize the switch length in order to make many devices on a single wafer, reduce the insertion loss, and increase the switching speed. The transition section of this switch involves only a short distance; therefore, a small size device is predictable. Also, since it uses non-resonant refractive-index-change effects, this optical switch can operate over a broad wavelength range.

In conclusion, we have demonstrated a novel optical switch structure. The fabrication processes and the initial experimental results have been reported. A switching operation has been observed with reverse bias applied to the two arms of the y-branch alternately. A crosstalk of less than -12 dB has been achieved with an active length of less than 400 μm at 1.06- μm wavelength. This device structure should provide some superior characteristics such as large extinction ratios, small device size, low insertion losses, large optical bandwidth, light mode quality preservation, and relaxed fabrication and operation tolerances.

References:

- [1] T. C. Huang, Y. Chung, N. Dagli, and L. A. Coldren, to be published in *IEEE J. Quantum Electron.*
- [2] J. Nayyer, Y. Suematsu, and K. Shimomura, *J. Lightwave Technol.*, 6, no. 6, p. 1146, June 1988.
- [3] W. M. Gibbons and D. Sarid, *Appl. Phys. Lett.*, 51, no. 6, p. 403, August 1987.

DIRECTIONAL COUPLER ELECTROOPTIC MODULATOR IN AlGaAs/GaAs WITH LOW VOLTAGE-LENGTH PRODUCT

M. Nisa Khan, Wei Yang, and Anand Gopinath

Dept. of Elec. Eng., University of Minnesota, 200 Union St., SE, Minneapolis, MN 55455

Electrooptic III-V directional couplers have been demonstrated both in multiple quantum well (MQW) and bulk systems [1]-[4]. The results indicate that the MQW devices exploiting the quantum-confined Stark effect and other quadratic electrooptic effects have much shorter device lengths as well as lower voltage-length (VL) products than those of the bulk devices. However, MQW devices are wavelength and temperature dependent, and have high propagation losses ($\sim 20\text{-}40$ dB/cm) [2]. The linear electrooptic bulk waveguide devices, employing the Pockels effect away from the bandgap, are fairly insensitive to wavelength and temperature changes and are able to exhibit low loss. In this paper, we present a directional coupler electrooptic modulator in epitaxially-grown bulk AlGaAs/GaAs, for which we have experimentally achieved a voltage-length product of only 7.0 V-mm, and a propagation loss of 3.4 dB/cm at 0.83 μm wavelength.

The geometry of our directional coupler modulator is shown in Fig. 1. The coupler interaction length L was designed to be one coupling length and the optical power output was taken only from the adjacent grounded guide with respect to the input guide as shown in this figure. At 0V bias, the input guide, most of the power transfers to the coupled guide. When bias is applied to the input guide with respect to the ground plane on the adjacent etched mesa, output light intensity is reduced. The device dimensions are shown in the cross-section schematic in Fig. 2(a). The coupler was differentially-etched so that the gap etch-depth was shallower than that of the outer sides. This design allowed us to reduce the coupling length by nearly a factor of 3 and to achieve a higher overlap efficiency between the optical and electrical fields.

The device was fabricated from AlGaAs waveguide heterostructures grown on a [100] oriented semiinsulating GaAs substrate by gas-source molecular beam epitaxy (MBE). The waveguide layers were unintentionally doped to the background p-doping level of $\sim 1 \times 10^{15}$ cm $^{-3}$. The differentially-etched structure was formed by a two-step RIE process where SiO $_2$ and photoresist masked the first etch, and a second photoresist layer protected the gap for the second deeper etch at the outer sides of the coupler. The electrodes on the coupler were Schottky contacts formed by evaporation and lift-off of 300Å/1200Å of Ti/Au. Air-bridges were fabricated to make connections from the narrow electrodes on ridge guides to the probe pads. Forward and reverse breakdown voltages for the ridges were 15 V and 35 V at 1 μA leakage respectively. The scanning electron micrograph of the cross-section of the device is shown in Fig. 2(b).

Modulation characteristics were determined by applying a bias to the two back-to-back Schottky contacts on the input guide and its adjacent mesa plane, while the contacts on the coupled guide and its adjacent mesa were both grounded. In order to achieve a large electric field in the input guide which is nominally p-type, the depletion region was increased with a positive bias to this guide with respect to the adjacent contacts. Intensity modulation with voltage variation was monitored via an infrared camera and simultaneously measured by dividing the output beam with pellicle beamsplitter and using a Si-photodetector with a narrow vertical slit to prevent detection of light from the input channel. Intensity modulation of approximately 13 dB was measured at only 2V. Modulated intensity as a function of voltage for the coupler is shown in Fig. 3.

Optical loss in single ridge waveguides, fabricated alongside the modulator, was measured using the Fabry-Perot resonance technique. The propagation losses in the waveguides with and without electrodes were approximately 2.8 and 3.4 dB/cm

respectively. The propagation loss is not dominated by intrinsic absorption of the AlGaAs layers, but rather by the sidewall roughness created from the RIE process, as loss of only 1.0 dB/cm was measured for the shallower wet-etched waveguides on the same material. This is also confirmed by higher losses for the narrower ridge guides alongside the modulator. Our low propagation loss and low current (~ 100 nA at 2 V) injection from the Schottky diode I-V measurements indicate that the index change from Franz-Keldysh and thermal effects are very small.

Accurate calculation of the VL product for a modulator structure such as ours, has not yet been found in the literature. Therefore, we compare our experimentally determined result with the following well-known simplified formula for an electrooptic modulator with only two planar electrodes [5]

$$VL = \frac{p \lambda G}{n^3 r_{41} \Gamma} \quad (1)$$

where p , according to coupled-mode equations, is $\sqrt{3}$ for directional couplers, n is the average refractive index, r_{41} is the electrooptic coefficient, λ is the operating wavelength, G is the gap between the electrodes, and Γ is the overlap integral between the applied electric field and the optical modes. We have calculated an overlap integral of 0.93 from the 2-D optical and electrical field distributions numerically determined using the semivectorial finite difference method [6]. Our modulator electrode structure, consisting narrow electrodes on top of the waveguides, and ground electrodes at a different level, all separated by spacings on the order of 1-2 μm , increases the electric field in the optical waveguiding region considerably. Furthermore, due to the height difference between the electrode on the input guide and the adjacent ground electrode on the etched mesa, increases the vertical electric field component utilized for the electrooptic phase change. Thus, the VL product for our modulator is expected to decrease from that given by Eq.(1) by several factors. We have experimentally determined that our modulator VL product is approximately a factor of 3 lower than that obtained from Eq.(1).

In conclusion, we have fabricated a low optical loss directional coupler optical modulator with a measured voltage-length product of only 7.0 V-mm at 0.83 μm wavelength. We have significantly reduced the VL product for the electrooptic modulator utilizing the Pockels effect by using an efficient electrode configuration and the differential-etch design. Such an intensity modulator/switch is attractive because of its low absorption loss in long wavelength regions, wide bandwidth, and low electric power consumption. To our knowledge, this VL product is the lowest reported for an epitaxially-grown bulk electrooptic modulator in AlGaAs/GaAs material system.

References

1. B. P. Keyworth, M. Cada, J. M. Glinski, A. J. Springthorpe, C. Rolland, and K. O. Hill, *Electronics Letters*, **26**, 24, (1990).
2. J. E. Zucker, K. L. Jones, M. G. Young, B. I. Miller, and U. Koren, *Appl. Phys. Lett.*, **55**, 22, (1989).
3. K. Komatsu, K. Hamamoto, M. Sugimoto, A. Ajisawa, Y. Kohaga, and A. Suzuki, *J. Lightwave Tech.*, , LT-9, (1991), pp. 871-878.
4. T. Ushikubo, I. Asabayashi, A. Hashimoto, and T. Ishida, *J. Lightwave Tech.*, LT-8, No. 2, (1990).
5. R. C. Alferness, *IEEE Trans. Microwave Theory and Tech.*, **30**, 8, (1982).
6. M. Khan, A. Gopinath, J. P. G. Bristow, and J. P. Donnelly, "Technique for Velocity-Matched Traveling-Wave Electrooptic Modulator in AlGaAs/GaAs," to be published in *IEEE Trans. Microwave Theory and Tech.*, February, 1993.

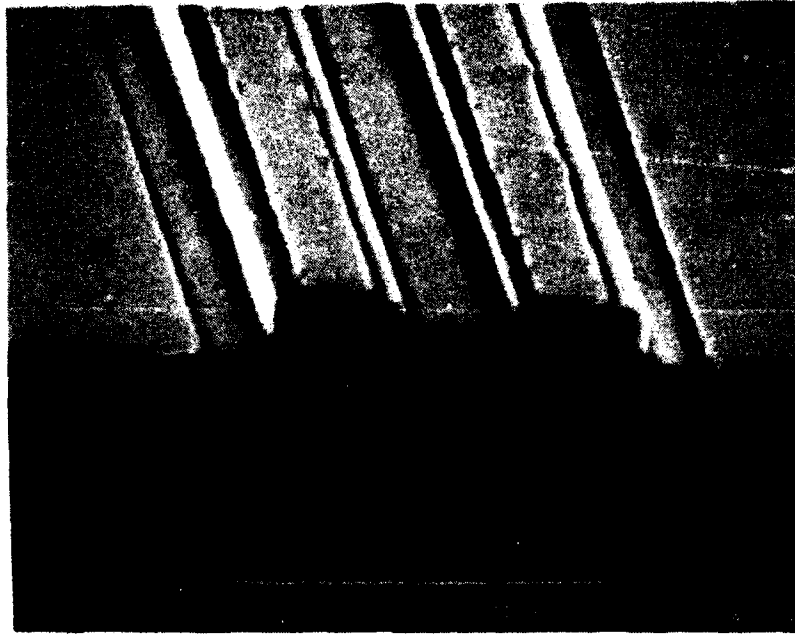


Fig. 2(b) SEM photograph of the coupler cross-section showing the different etch depths for the gap and outer sides, and the electrode configuration.

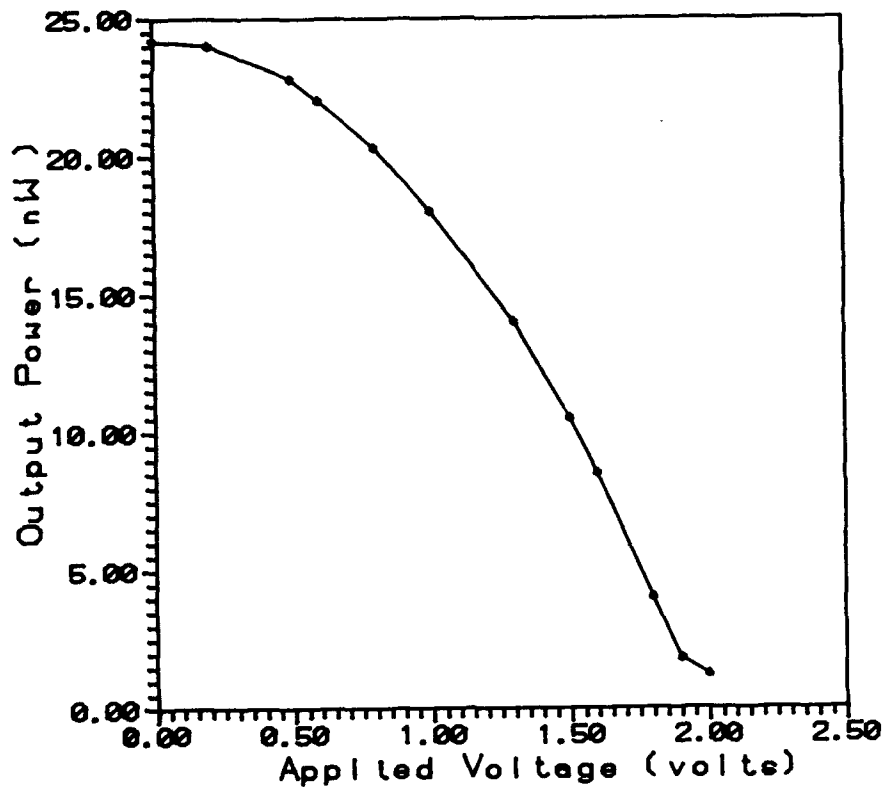


Fig. 3. Experimental data of the modulated light intensity as a function of applied voltage for the directional coupler.

Figures

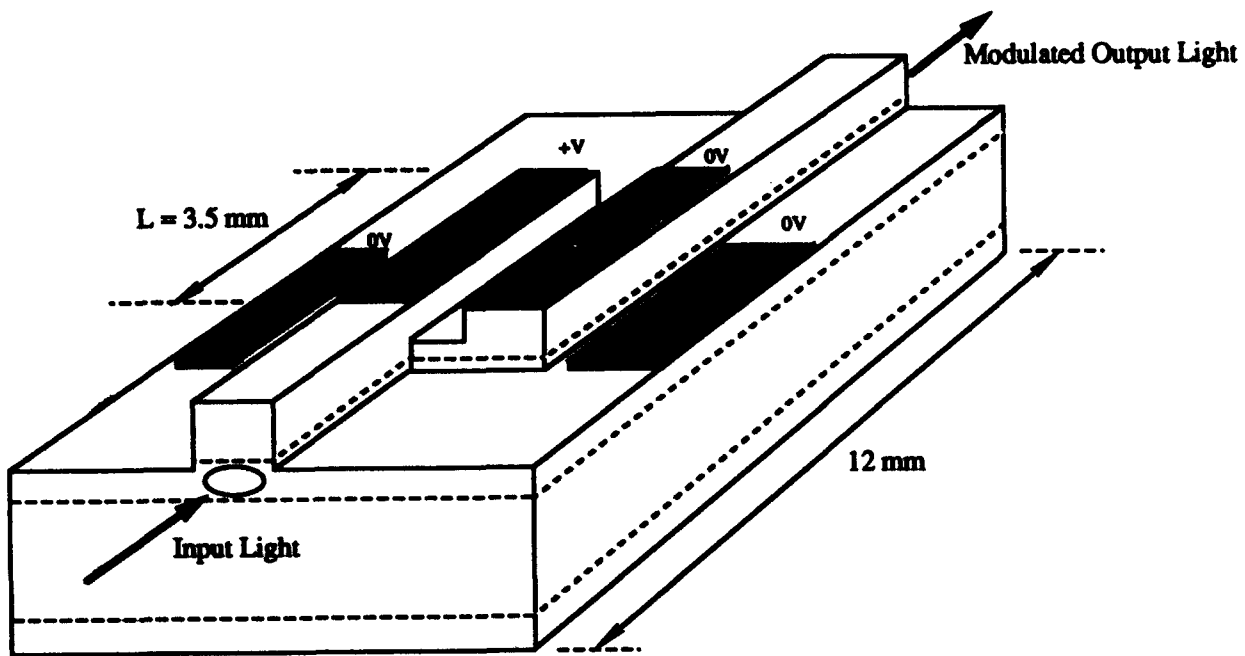


Fig.1. Schematic of ridge directional coupler modulator showing input and output guides.

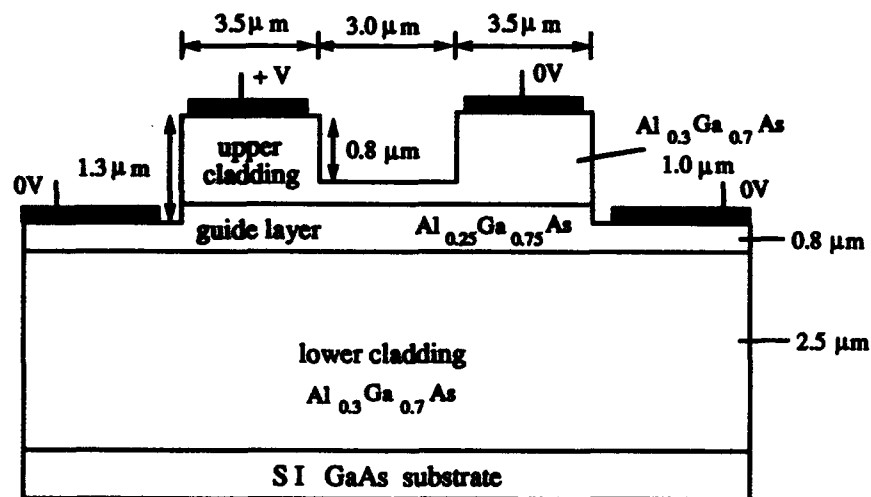


Fig.2(a) Cross-section of the differentially-etched coupler showing the layer design. Gap etch depth < Outer etch depth is shown.

Monolithic Integration of 1.3- μm Photodetectors and Waveguide Modulators on GaAs

D. E. Bossi, R. W. Ade, R. P. Basilica, and R. N. Sacks

United Technologies Research Center
East Hartford, Connecticut 06108
(203) 727-7297

Optoelectronic transceivers are critical components for many high-performance lightwave communication systems. In the case of a 1.3- μm analog fiber-optic link employing external modulation of a cw optical source, a transceiver module consists of an integrated-optic modulator, a photodetector, and transmit/receive electronic control circuitry. GaAs is a promising substrate material for pursuing *monolithic* optoelectronic transceiver integration because of its mature electronics technology and its ability to support high-performance 1.3- μm electro-optic waveguide modulators and photodetectors [1,2]. Toward this end, monolithic integration of GaAs waveguide modulators with MESFET drive electronics has already been demonstrated [3]; however, photodetector integration with active waveguide devices has not been previously reported. This paper reports for the first time the integration of an optical waveguide modulator and a 1.3- μm photodetector on a common GaAs substrate, thereby demonstrating the feasibility of monolithic optoelectronic transceiver integration.

A schematic cross-section of the monolithically integrated GaAs/AlGaAs Mach-Zehnder modulator and InGaAs metal-semiconductor-metal (MSM) photodetector is shown in Fig. 1. A single molecular beam epitaxy (MBE) growth sequence is used to produce the epitaxial layer structure of Fig. 1 on a (100) n^+ -GaAs substrate. The lower part of the structure consists of GaAs and $\text{Al}_{0.1}\text{Ga}_{0.9}\text{As}$ layers, which are used to form the double heterostructure waveguide. Lattice-mismatched buffer and detector layers (0.5- μm -thick $\text{In}_{0.2}\text{Ga}_{0.8}\text{As}$ and 0.75- μm -thick $\text{In}_{0.4}\text{Ga}_{0.6}\text{As}$, respectively) are grown on top of the waveguide structure. Finally, a 600-Å cap layer graded from $\text{In}_{0.4}\text{Ga}_{0.6}\text{As}$ to $\text{In}_{0.4}\text{Al}_{0.6}\text{As}$ is used to enhance the MSM Schottky barrier height.

The optical modulator described in this paper utilizes the linear electro-optic effect in the intrinsic region of a reverse-biased p-i-n diode. Following photodetector mesa etching, the vertical p-i-n diodes that serve as the waveguide active regions are produced by localized Be implantation and an 850 °C activation anneal. Ti/Pt/Au electrodes are patterned by liftoff to form the modulator and detector contacts, and backside metallization provides contact to the n-type terminal of the modulator. Wet chemical etching in 8 H_2SO_4 : 1 H_2O_2 : 1 H_2O is used to define the 7- μm -wide single-mode strip-loaded waveguides that form the Mach-Zehnder interferometer.

The optical transfer characteristic of the integrated Mach-Zehnder modulator with 8-mm active electrodes is shown in Fig. 2. The half-wave voltage for this device is 6.7 V at $\lambda = 1.3 \mu\text{m}$, in agreement with calculations based on the linear electro-optic effect. The 2.3-cm-long device exhibits <5-dB on-chip optical loss and a contrast ratio greater than 25 dB. As shown in Fig. 3, the 3-dB bandwidth for this lumped-element modulator is 1.5 GHz, limited by electrode capacitance. By utilizing a traveling-wave electrode geometry, the bandwidth of similar modulators on an n^+ substrate has been extended to >5 GHz [4]. The performance characteristics of modulators with on-chip InGaAs photodetectors were identical to those of discrete GaAs/AlGaAs Mach-Zehnder devices.

The concept for our photodetector structure builds upon the previous work of Rogers *et al.* [5]. Thick, deliberately lattice mismatched layers of InGaAs are grown on GaAs to force the dislocations that are generated to be confined within a relatively thin region at the interface. In addition, the present structure utilizes a graded cap layer that is lattice matched to the underlying

detector layer, thereby avoiding the generation of dislocations at the wafer surface. Details of the MBE growth of the detector structure are reported elsewhere [6].

Interdigitated MSM photodetectors with 1- μm fingers and spacing were fabricated on the integrated modulator/detector sample. These devices exhibit $\sim 1\text{-}\mu\text{A}$ dark current at a bias voltage of 10 V and breakdown voltages between 20 and 30 V. Under frontside illumination from a single-mode optical fiber, the detectors exhibit a responsivity of 0.2 A/W at 10-V bias. When corrected for finger shadowing and surface reflection, this corresponds to an internal quantum efficiency of 55%, as expected for a 0.75- μm -thick $\text{In}_{0.4}\text{Ga}_{0.6}\text{As}$ absorption layer. As InGaAs-on-GaAs photodetectors, these devices can also be back-illuminated for enhanced detector responsivity. The frequency response of the fiber-illuminated photodetector, shown in Fig. 4, was measured using a lightwave component analyzer at a dc optical power level of 365 μW . The detector's rf optical responsivity (0.2 A/W) is identical to its low-frequency value. The 3.7-GHz detector bandwidth shown in Fig.4 is limited by the $150 \times 150 \mu\text{m}^2$ bond pad-to- n^+ backplane capacitance.

In summary, we report the first monolithic integration of 1.3- μm photodetectors and optical waveguide modulators on a common GaAs substrate. In conjunction with the previously demonstrated integration of modulators with MESFET electronics, this result represents the enabling device technology for realizing a monolithic 1.3- μm GaAs optoelectronic transceiver. Additionally, the present integrated structure is compatible with an efficient GaAs waveguide-to-photodetector coupling technique [7], which may provide enhanced 1.3- μm transceiver functionality.

The authors would like to acknowledge D. W. Eichler for assistance with the MBE growth.

References

- [1] R. G. Walker, "High-speed III-V semiconductor intensity modulators," *IEEE J. Quantum Electron.*, vol. QE-27, pp. 654-667, 1991.
- [2] W. Ng, A. Narayanan, R. Hayes, and D. Yap, "High-efficiency waveguide-integrated 1.3 μm InGaAs/GaAs MSM detector as an optical delay line switch for microwave phased arrays," in *Integrated Photonics Research*, vol. 10, OSA Technical Digest Series, (Optical Society of America, Washington, DC, 1992), pp. 118-119.
- [3] R. W. Ade, D. E. Bossi, R. P. Basilica, and J. M. Berak, "Monolithic integration of GaAs-waveguide optical intensity modulator with MESFET drive electronics," *Electron. Lett.*, vol. 28, pp. 702-703, 1992.
- [4] S. Y. Wang and S. H. Lin, "High-speed III-V electro-optic waveguide modulators at $\lambda = 1.3 \mu\text{m}$," *J. Lightwave Technol.*, vol. LT-6, pp. 758-771, 1988.
- [5] D. L. Rogers, J. M. Woodall, G. D. Pettit, and D. McInturff, "High-speed 1.3 μm GaInAs detectors fabricated on GaAs substrates," *IEEE Electron. Device Lett.*, vol. EDL-9, pp. 515-517, 1988.
- [6] R. N. Sacks, R. W. Ade, D. E. Bossi, R. P. Basilica, and D. W. Eichler, "High-speed $\lambda = 1.3 \mu\text{m}$ metal-semiconductor-metal photodetectors on GaAs," to appear in *J. Vac. Sci. Technol. B*, 1993.
- [7] D. E. Bossi, R. W. Ade, R. P. Basilica, and J. M. Berak, "Regrowth-free waveguide-integrated photodetector with efficient total-internal-reflection coupling," to appear in *IEEE Photon. Technol. Lett.*, 1993.

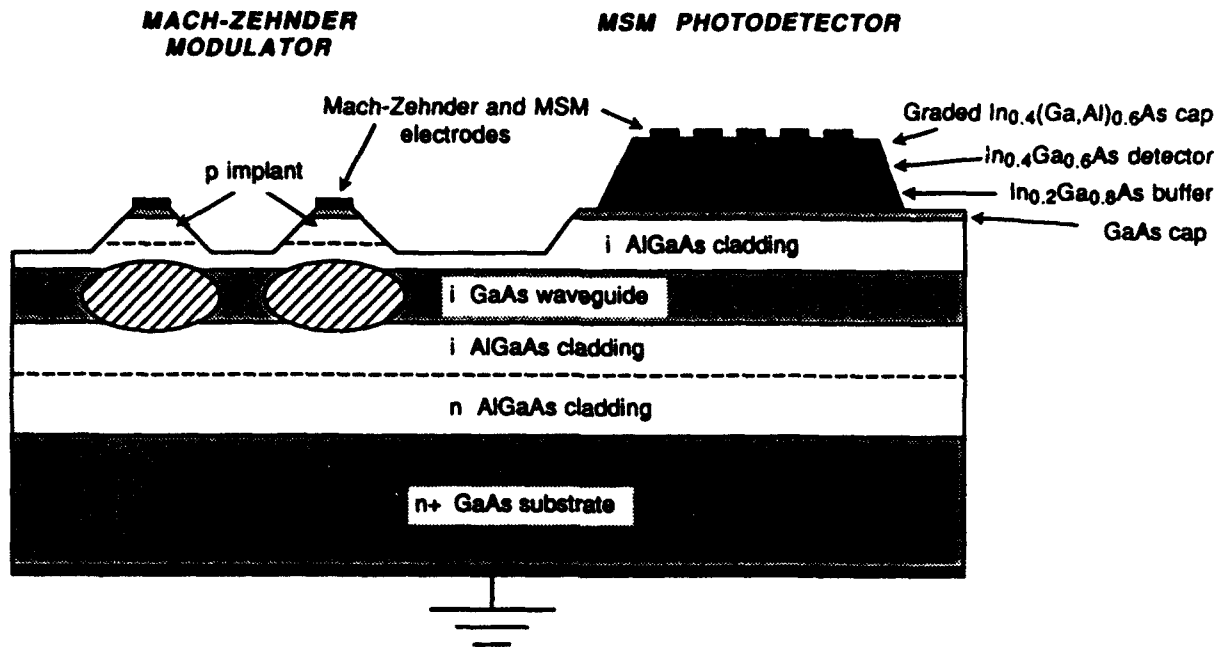


Fig. 1 Schematic cross-section of monolithically integrated GaAs/AlGaAs Mach-Zehnder modulator and interdigitated InGaAs MSM photodetector operating at $\lambda = 1.3 \mu\text{m}$.

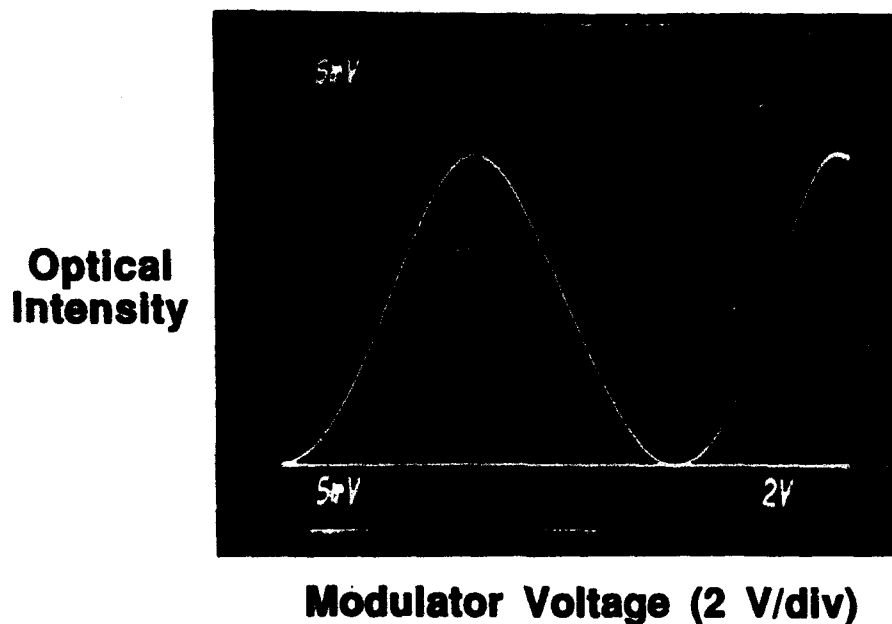


Fig. 2 Optical transfer characteristic of integrated Mach-Zehnder modulator with 8-mm-long electrodes, exhibiting 6.7-V half-wave voltage and >25-dB contrast ratio at $\lambda = 1.3 \mu\text{m}$.

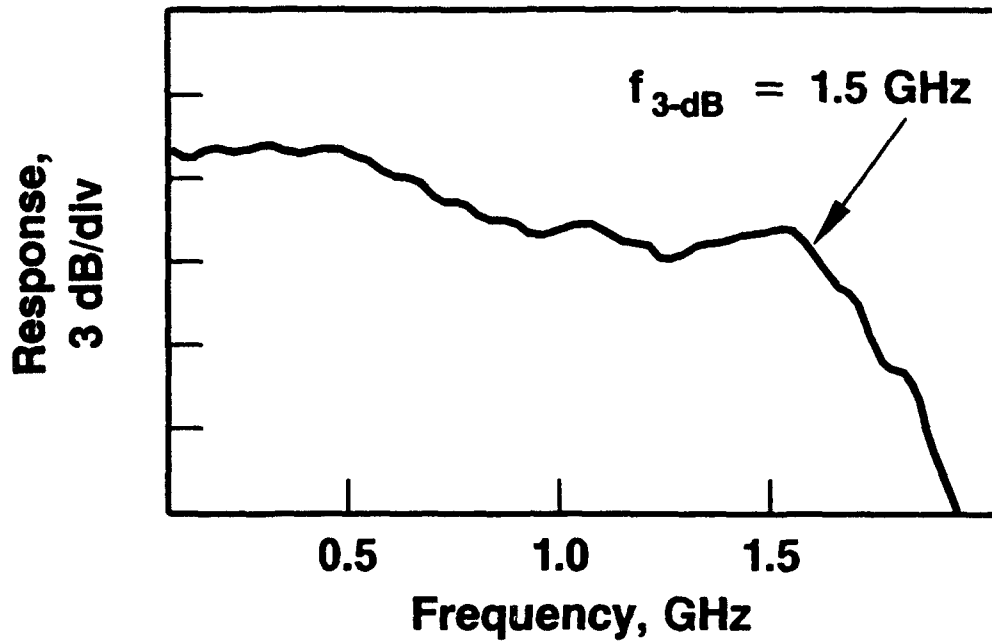


Fig. 3 Microwave response of integrated Mach-Zehnder modulator with 8-mm lumped-element electrodes.

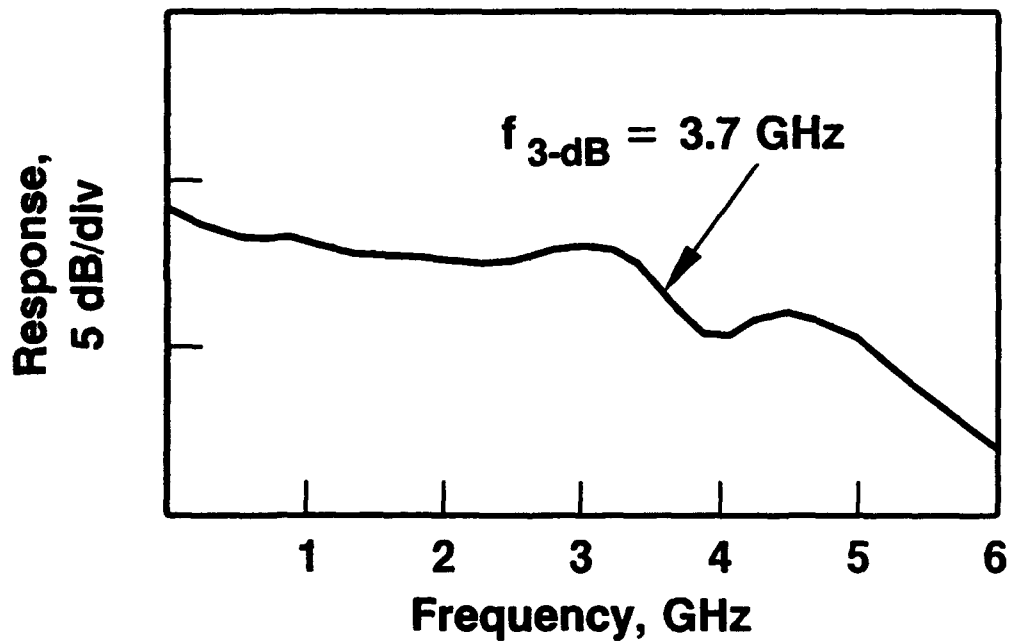


Fig. 4 Microwave response of 1.3- μm InGaAs-on-GaAs MSM photodetector with on-chip GaAs/AlGaAs electro-optic waveguide modulator.

Digital and Analog Low Power Opto-electronic and Opto-optical Elements Based on n-i-p-i Doping Superlattices

P. Kiesel⁺, K.H. Gulden⁺⁺, A. Höfler⁺, B. Knüpfer⁺, M. Kneissl⁺,
P. Riel⁺, X. Wu^{*}, J.S. Smith^{*} and G.H. Döhler⁺

⁺Institut für Technische Physik, Universität Erlangen-Nürnberg
Erwin-Rommel-Str. 1, W-8520 Erlangen, FRG
Phone: +49-9131-857603, Fax: +49-9131-857293

^{*}Electronics Research Laboratory, University of California,
Berkeley CA 94720, USA

The required performance characteristics for photonic devices are quite diverse, depending on their specific tasks. In most of the applications for optical information processing, however, high speed, low power dissipation, high switching contrast, and gain are necessary. Detectors and electro-optical modulators represent, apart from light emitters the key components as interface between optical and electrical information processing. During the past few years all-optical components which avoid the (explicite) use of electronics have found increasing attention. So far S-SEEDs are considered as the most promising components for all-optical information processing [1].

In this paper we present the first realization of a new concept based on n-i-p-i doping superlattices [2] which - as we believe - is highly suitable for many applications in the field of opto-electronic and all-optical digital and analog information processing.

Some time ago we demonstrated the prototype of a new 3-terminal photo-conductive device [3]. This device can be operated either as a sensitive and fast detector or as a threshold or bistable opto-electronic switch with high gain. In the detector mode its response is linear up to a saturation value and the gain can be adjusted via an external (input) series resistance. For the switch mode it is advantageous to replace the series resistance by a photo diode fabricated from the same layer structure as the 3-terminal device. Depending on the design of this structure and on the wavelength of the light, bistable or threshold switching is possible. The switching *energies* are determined by the capacitances of these two components which can be in the low fF range. In the sub-GHz range the internal carrier drift and diffusion times [4] do not limit the speed of these devices. The switching *times* τ_s depend therefore on the ratio of capacitance and pulse *power* P_{in} .

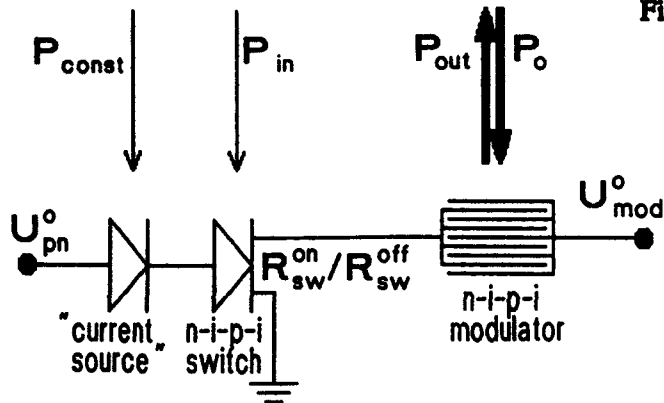


Fig. 1: Schematic picture showing a smart pixel for all optical switching. The n-i-p-i switch is a 3-terminal device with photoconductive gain providing amplified photocurrents for operating the modulator with very low optical input power P_{in} . The switching power depends on the optical power P_{const} incident on the "current source" diode.

In a combination of this detector/switch with an electro-optical modulator - in our present case a n-i-p-i Franz-Keldysh modulator - the latter can be operated with unusually low optical input power due to the large photoconductive gain and with high speed due to the low resistance of the switch in the "on"-state which allows for short RC response times (see Fig.1).

In the all-optical *switch* mode these "smart pixels" combine all the virtues of S-SEEDs with additional advantages. First there is direct opto-optical gain instead of sequential gain. Second the optical and electrical power dissipation is much lower [2]. Further there is much better thermal stability, since we use Franz-Keldysh type modulators which exhibit a much broader wavelength response spectrum compared to MQW-SEEDs. Moreover the switches and modulators can be optimized individually. This way one avoids the inevitable compromises imposed by the partly opposing requirements on the double purpose multiple quantum well p-i-n components used in the SEED approach. It should be pointed out that - like the SEED concept - our approach allows for extensions to build more complex functional units.

If our 3-terminal device is operated in the detector mode the smart pixel can be used for many all-optical analog information processing tasks. These may range from linear amplification to soft or sharp highly nonlinear input/output relations to be used in neural networks operating at particularly low optical and electrical power levels.

The function of the detector or switch is based on the light induced increase of conductance of the n-layers in n-i-p-i structures which in the dark state are nearly depleted (in the detector mode) or fully depleted (in the switching mode) by a reverse bias applied in series with an external load resistor (replacing the left photodiode in the circuit shown in Fig. 1) [3]. In our present investigation we used a p-i-n structure whose n-layer was thin enough to represent a n-channel which can be depleted [5]. By spatially separating a relatively large absorption area and a small detection area both, the capacitance (in this case <30fF) and

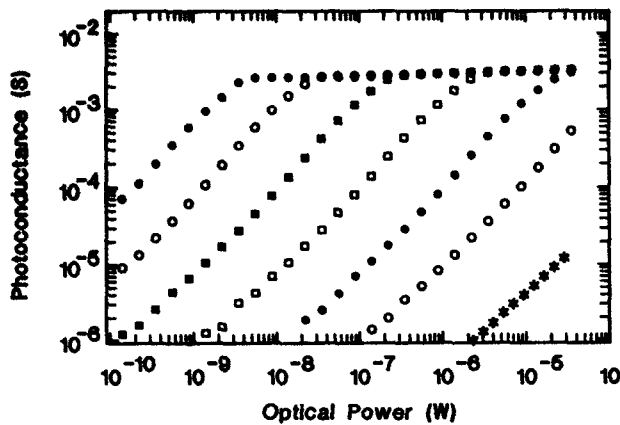


Fig. 2: Double logarithmic plot of photoconductance vs. optical power for different values of the load resistor $R_L = 10^4, 10^3, 10^2, 10^1, 1,$ and 10^{-1} M Ω (from left to right). The p-n photocurrent is indicated by ***. For 1 Volt applied between the two n-contacts the gain corresponds to the ratio of conductance value / p-n photocurrent value.

the transit time between the two n-contacts can be minimized. Fig. 2 shows the (nearly linear) photoconductance vs. optical power curves for different values of the load resistor. The photoconductive gain at $R_{pn} = 10$ G Ω is $> 10^6$.

In Fig. 3 we present an example for bistable opto-electronic switching. In this case the negative photo current characteristic of the left photodiode, resulting from the Franz-Keldysh absorption above the bandgap, is responsible for the bistability. Because of the very low dark currents of our switch and photo diode (< 1 pA) bistability occurs at optical power < 500 pW. The on/off ratio and the opto-electronic gain exceed 10^6 .

In Fig. 4 we show results for a smart pixel composed of the switch of Fig. 3 and a selectively contacted n-i-p-i modulator grown with the epitaxial shadow mask technique [6]. The optical gain between input and output signals largely exceeds 10^5 . The contrast ratio is 4.6

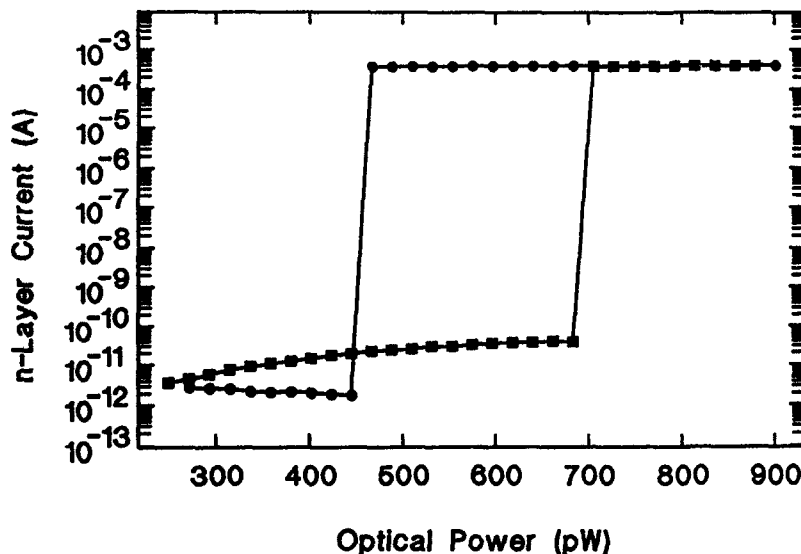


Fig. 3: Bistable opto-electronic switching with a gain $> 10^6$ at < 500 pW

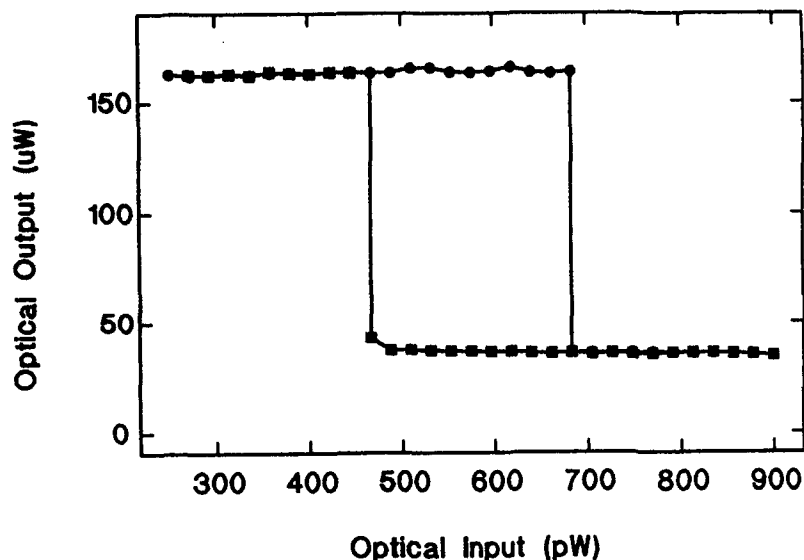


Fig. 4: *Bistable all - optical switching with an optical gain of 3×10^5 observed in a smart pixel containing the bistable switch used for Fig. 3*

These first results have been obtained on devices which have not yet been optimized at all. They are, however already quite encouraging. The observed optical holding power of less than 1 nW required for maintaining the bistable state implies the possibility of operating a memory array consisting of $10^3 \times 10^3$ elements at optical power < 1 mW. Using typical modulator leakage currents we estimate an electrical power dissipation of 50 mW for this example. Finally we would like to point out that the monolithical integration of the two kind of components to 2-D arrays should pose no fundamental problems.

References:

- [1] A.L. Lentine, H.S. Hinton, D.A.B. Miller, J.E. Henry, J.E. Cunningham, and L.M.F. Chirovsky, *IEEE J. Quantum Electron.* **25**, 1928-1936 (1989)
- [2] G.H. Döhler, P. Kiesel, H. Lin, P. Riel, K. Ebeling, and J.N. Miller, *SPIE Proceedings* **1283**, 103-117 (1990)
- [3] P. Kiesel, P. Riel, H. Lin, N. Linder, J.F. Miller and G.H. Döhler, *Superlattices and Microstructures* **6**, 363 (1989)
- [4] K.H. Gulden, H. Lin, P. Kiesel, P. Riel, K.J. Ebeling, and G.H. Döhler, *Phys. Rev. Lett.* **66**, 373-376 (1991)
- [5] P. Riel, P. Kiesel, M. Ennes, Th. Gabler, M. Kneissl, G. Böhm, G. Tränkle, G. Weimann, K.H. Gulden, X.X. Wu, J.S. Smith, and G.H. Döhler, *SPIE Proceedings* **1675**, 242-254 (1992)
- [6] X. Wu, K.H. Gulden, M. Thomas, G.H. Döhler, J.R. Whinnery, and J.S. Smith, to be published in *Proceedings of the 7th international conference on molecular beam epitaxy*, Schwäbisch Gmünd, Germany 1992

Friday, March 25, 1993

Wavelength-Selective Components

ITuB 8:30am-10:15am
Mesquite B

David Arthur Smith, *President*
Bellcore

Wavelength Multiplexing using Waveguide Arrays

**C. Dragone
AT&T Bell Laboratories
HOH R 213, P.O. Box 400
Holmdel, NJ 07733**

Summary not available at time of printing.

Sub-Angstrom Planar Channel-Dropping Filters

M. Levy, L. Eldada, R. Scarmozzino, and R.M. Osgood, Jr.
Columbia University Microelectronics Sciences Laboratory
New York, NY 10027
Phone: (212) 854-8980
FAX: (212) 932-9421

P. S. D. Lin
Bellcore, 331 Newman Springs Rd.
Red Bank, N.J. 07701

F. Tong
IBM T.J. Watson Research Center
Yorktown Heights, NY 10598

Introduction

The increased interest in dense wavelength division multiplexing for optical broadcast networks has generated a need for sub-Angstrom bandwidth optical filters which can be used to extract a single wavelength signal from a multiple wavelength optical bus. Recently, a novel design for narrow-band channel-dropping filters (CDF) has been proposed by H.A. Haus.¹ These filters use waveguide couplers combined with quarter-wave shifted DFB resonators, and are capable of selecting channels significantly narrower than 1 Å bandwidth, by appropriate choice of the coupling parameters in the device. In this paper we demonstrate the fabrication and operation of such a device for the first time.

Device Fabrication and Principle of Operation

The device was fabricated on a GaAs/AlGaAs slab waveguide heterostructure. The waveguide coupler and other waveguide components were produced using a technique we have developed for prototyping integrated optical devices by maskless laser etching of GaAs;² once

tested, these components can be made by more conventional planar processing. The grating was patterned in photoresist using e-beam writing and etched using chemically assisted ion beam etching. A diagram of the device is shown in Fig. 1.

The device can, in principle, produce resonant coupling of 50% of the light to the receiver arm in an extremely narrow wavelength region, while allowing the remaining wavelength signals to pass unperturbed through the transmission bus. This narrow bandwidth results from the high Q of the resonant DFB cavity, and can be controlled by adjusting cavity losses through the inter-waveguide coupling between the bus and the resonator, the position of the quarter-wave step and the magnitude of the grating coupling constant.

Experimental Results

The measured response in the receiver arm is shown in Fig. 2. The most important feature of the response is the pronounced narrow peak at about $1.5518 \mu\text{m}$, which exhibits a FWHM bandwidth of 0.8 \AA and a power transfer of about 30%. This peak is entirely repeatable and reproducible from scan to scan for all of several devices fabricated. The peak position is in good agreement with the expected resonant wavelength of $1.5508 \mu\text{m}$, and the power transfer is also in the predicted range. Further, it was found that this peak was accompanied by a corresponding decrease in the power observed in the transmission bus. The bandwidth is in the expected sub-Angstrom range. The high frequency variations present throughout the entire signal are due to Fabry-Perot resonances from the end facets of the device, and are observable when looking at the transmission of a simple straight waveguide. This is shown in the inset to Fig. 2. These high frequency variations would be eliminated in a practical device through the use of antireflection coatings on the waveguide facets.

Conclusion

In summary, we have fabricated the first channel-dropping filter of the type proposed in [1], and have demonstrated the basic principle of operation. The results show resonant transfer of power near the expected wavelength and within the expected range of efficiency and bandwidth for our designs. Further work is underway to improve the performance of the device.

The authors would like to acknowledge the support of the Defense Advanced Research Projects Agency / Air Force Office of Scientific Research, the National Center for Integrated Photonic Technology, and the Army Research Office.

References

1. H.A. Haus and Y. Lai, "Narrow-Band Optical Channel-Dropping Filter," *J. Lightwave Tech.* **10**, 57 (1992).
2. L. Eldada, M.N. Ruberto, R. Scarmozzino, M. Levy, and R.M. Osgood, Jr., "Laser-Fabricated Low-Loss Single-Mode Waveguiding Devices in GaAs," *J. Lightwave Tech.* **10**(11) (1992).

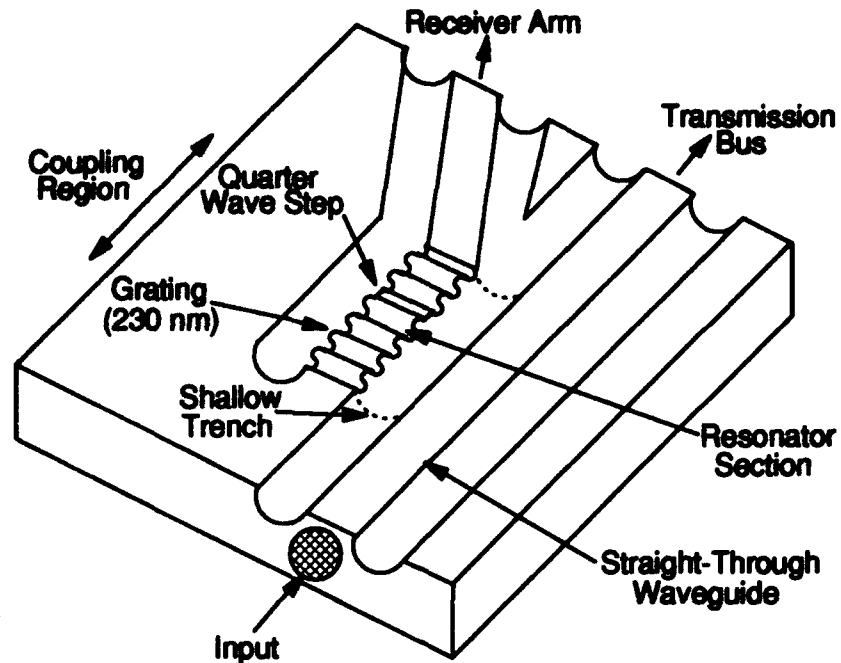


Figure 1. Schematic diagram of the channel-dropping filter demonstrated here.

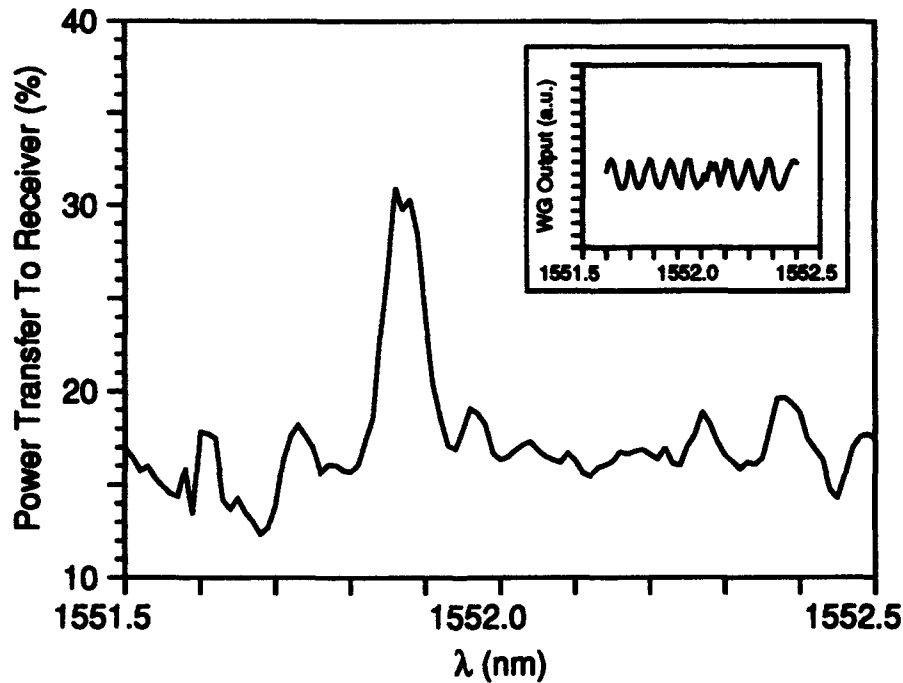


Figure 2. Measured response of the CDF shown in Fig. 1, demonstrating a pronounced narrow resonant peak. The high-frequency variations are Fabry-Perot peaks, as demonstrated in the inset which shows the response of a simple straight waveguide.

Design Model for Low Crosstalk Acousto-Optic Tunable Filters

Antonio d'Alessandro, D. A. Smith, J. E. Baran and J. J. Johnson

Rm 3X-201, Bellcore, 331 Newman Springs Rd, Red Bank, NJ, 07701, tel. (908) 758 3011

Introduction. One of the major issues in designing Acousto-optic tunable filters (AOTF) for optical networks remains the reduction of interchannel crosstalk, one significant source of which is the sidelobes in the typical sinc-squared transmission passband of the device. Interchannel crosstalk reduction can be achieved by sidelobe suppression, as has been experimentally demonstrated using two different techniques: (i) employing apodization of the acousto-optic interaction strength by means of acoustic wave couplers [1]; or (ii) by using focused surface acoustic waves [2].

AOTF's employ the interaction between sound and light in a birefringent medium to provide, on resonance, narrow band optical filters and switches for wavelength division multiplexed (WDM) systems. These devices, using lithium niobate as acousto-optic medium, are capable of a broad tuning range (about 300 nm in the region of 1.5 μm), narrow passbands (on the order of 10 \AA) and require only few milliwatts of radio frequency power to select a single optical channel in the integrated optic versions [3]. Furthermore, AOTF's are unique among optical filters in their ability to provide simultaneous and independent filtering of many optical channels. These features make AOTF as unique "traffic light" to rule the traffic of optical signals in dense (WDM) communications systems.

In this paper we present a simple theoretical model describing the fine structure of the AOTF passband. Our model is a generalization of coupled mode theory [4] to describe local variations in acousto-optic coupling strength, waveguide effective index and variations in acoustic velocity. The two main purposes of this model are: (i) to simulate and understand transmission passbands of real acousto-optic filters; and (ii) to design a contoured acousto-optic interaction strength along the device which results in sidelobe suppressed AOTF's.

Theory. The AOTF acts as a polarization converter by means diffraction of light by a grating created by a traveling surface acoustic wave across a birefringent medium. The model of large-angle Bragg diffraction can describe the acousto-optic interaction by using the mathematical formalism of collinear coupled mode theory [4]. Let us consider the filter configuration of Fig. 1, where infrared light propagates through a Ti-indiffused waveguide in a x -cut/ y -propagating lithium niobate crystal. Acoustic waves, generated by interdigital transducers, propagate collinearly with the optical beam. The polarization evolution of propagating light, at wavelength λ , is described by coupled mode theory, indicating with E_1 the amplitude of electric field of input light, with longitudinal propagation constant β_1 , and E_2 the amplitude of the electric field, with longitudinal propagation constant β_2 , diffracted after the interaction with a surface acoustic wave, with a period Λ , along the interaction length:

$$\frac{d E_1}{dy} = -j \frac{\beta_1}{|\beta_1|} \kappa_{12} E_2 e^{j\Delta\beta y}, \quad \frac{d E_2}{dy} = -j \frac{\beta_2}{|\beta_2|} \kappa_{12}^* E_1 e^{-j\Delta\beta y} \quad (1)$$

where $\Delta\beta = \beta_1 - \beta_2 - 2\pi/\Lambda$ is the mismatch or detuning between sound and light and κ_{12} is the acousto-optic coupling coefficient. The general solutions, by integrating (1) between 0 and y , can be expressed as, $E(y) = M(\kappa, \delta, y)E(0)$ in terms of polarization transformation matrix $M(\kappa, \delta, y)$ of the Jones vector $E(y)$ after a propagating distance y .

$$\begin{pmatrix} E_1(y) \\ E_2(y) \end{pmatrix} = \frac{1}{\mu} \begin{pmatrix} e^{\delta y} (\mu \cos \mu y - \delta \sin \mu y) & -i\kappa e^{\delta y} \sin \mu y \\ -i\kappa e^{-\delta y} \sin \mu y & e^{\delta y} (\mu \cos \mu y + \delta \sin \mu y) \end{pmatrix} \begin{pmatrix} E_1(0) \\ E_2(0) \end{pmatrix} \quad (2)$$

where the detuning is $\delta = \Delta\beta/2$ and $\mu^2 = \kappa^2 + \delta^2$. E_1 and E_2 usually correspond to light beams with orthogonal states of polarization, the TE and TM modes.

The key to simulate birefringence nonuniformities of real devices and coupling strength variation along the device, is to model the overall acousto-optic interaction as a sequence of interaction regions, each with a local coupling coefficient κ_j and detuning parameter δ_j as shown in Fig. 1. Then the overall polarization transformation through an interaction length L is described by a product of matrices:

$$E(L) = \prod_j M(\kappa_j, \delta_j, y_j) E(0) \quad (3)$$

According to the particle picture of the acousto-optic interaction the matching condition happens when the difference between the momenta of incident and diffracted light beams or photons, $2\pi\Delta n/\lambda$, is compensated by the momentum of the acoustic wave or phonon $2\pi/\Lambda$, i.e. $\Delta\beta = \delta = 0$.

Fig. 2a shows the plot of the transmission function in dB versus the detuning δ/π related to the variation of the optical wavelength and fixed acoustic wave for an ideal device. The plot represents a sinc-squared function with the maximum of transmission on resonance ($\delta=0$). In this case, both birefringence and coupling coefficient are uniform along the device. The transmission function is symmetric about the maximum with secondary maxima (sidelobes), whose intensity is about -10 dB.

Simulation of sidelobe asymmetry. The matching condition can also be written as $\Lambda = L_b$, where $L_b = \lambda/\Delta n$ is the polarization beat length. The typical asymmetry of sidelobes, observed in most devices has been demonstrated experimentally to be related to nonuniformity of effective birefringence along the acousto-optic interaction region [5][6].

Fig. 2b shows simulation in sidelobe asymmetry obtained by introducing a parabolic variation (decreasing) of effective birefringence away from the center of the interaction region. In this case an additional detuning δ' has been taken into account such that $\delta' L = -16\pi(y-L/2)^2/L^2$. Our model predicts that only even order variations of birefringence introduce asymmetry, odd order variations broaden the passband and enhance the sidelobes while preserving their symmetry.

Index variations in real devices can arise from many sources. For titanium-indiffused optical waveguides in LiNbO_3 , Δn changes with variations in titanium stripe width or metal thickness or by in diffusion temperature along the sample. This implies that optical waveguide width can be contoured to control sidelobe suppression on one side of passband spectrum.

According to this result, it is certainly possible to build a two stage acousto-optic filter with suppressed sidelobes by countouring the waveguide of each stage, such that one stage has sidelobe suppression in the short wavelength side of the passband, while the other stage has sidelobe suppression on the long wavelength side [6].

Simulation of sidelobe suppressed filters. Sidelobe suppression by cascaded filters, as described above [6], cannot reduce the most serious source of interchannel crosstalk in the multiwavelength operation of the AOTF: coherent crosstalk [7]. Specifically, in a one stage filter, a single optical beam can be selected by two different acoustic frequencies one of the which is in resonance with the input optical wavelength, while the other frequency is mismatched but in resonance with the first sidelobe of the transmission function for that wavelength. In this case, the optical signal will reach the output with components at different optical frequencies, because of the different frequency shifts induced by the two acoustic RF frequencies [8]. The different frequency components will interfere and will constitute an error source in data transmission. The solution of coherent crosstalk is to reduce sidelobes in a single stage. The source of sidelobes, simply stated, is the abrupt onset and cutoff of the acousto-optic interaction, whose Fourier transform is represented in the filter transmission function as a sinc-squared response. By tapering the interaction strength, the high frequencies components (sidelobes) can be reduced. This tapering can be achieved in a number of ways, including the creation of a raised-cosine SAW intensity by embedding the active optical waveguide in one arm of a SAW waveguide directional coupler, as shown in Fig. 2c. The result is a coupling coefficient profile $\kappa(y) = \kappa_0 \sin(\pi y/L)$, with the predicted sidelobe suppression plotted in the same figure. Experiments confirm the predicted degree of sidelobe suppression [1].

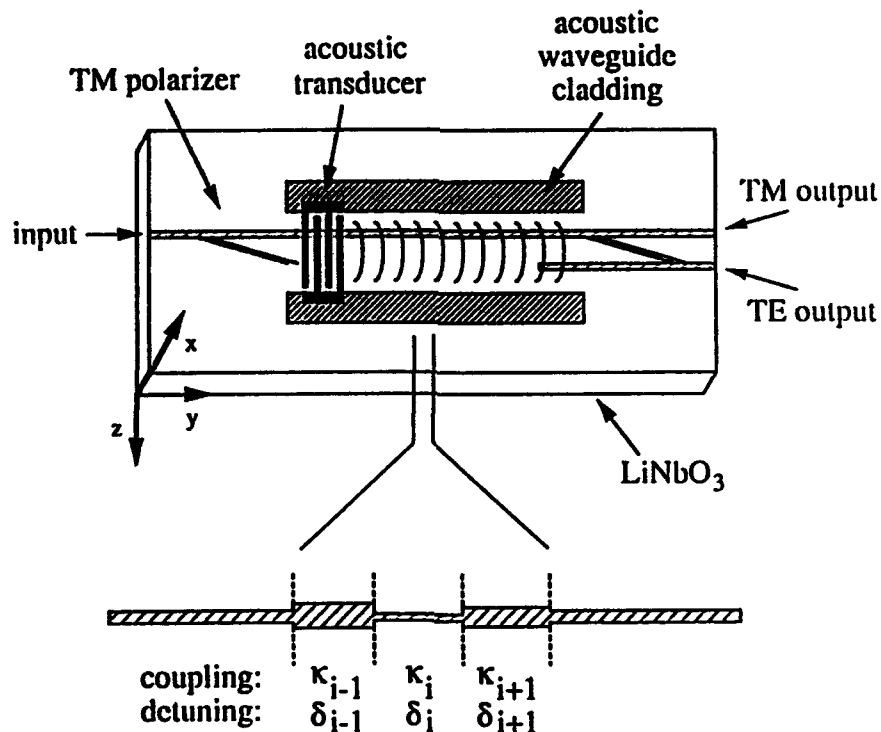


Fig. 1. Scheme of a collinear AOTF and local acousto-optic interaction regions.

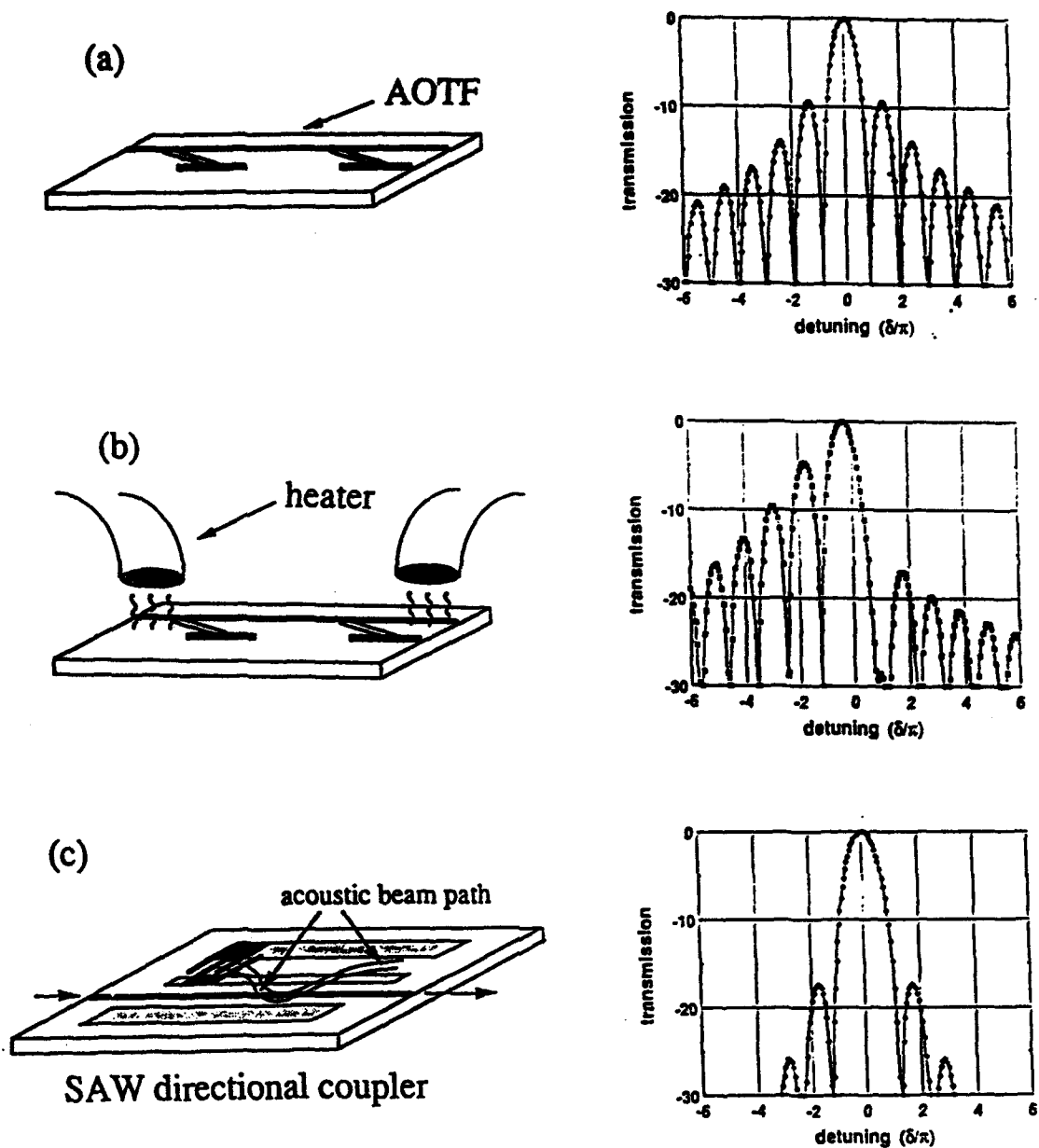


Fig.2. Three AOTF situations (left) and the corresponding calculated sidelobe structure (right): (a) ideal filter, (b) filter with an induced variation of birefringence, (c) apodized filter for sidelobe suppression.

- [1] D. A. Smith and J. J. Johnson, *Appl. Phys. Lett.* **61**, 1025 (1992)
- [2] A. Kar-Roy and C. S. Tsai, *IEEE Photon. Technol. Lett.* **4**, 1132 (1992)
- [3] D. A. Smith and J. J. Johnson, *IEEE Photon. Technol. Lett.* **3**, 923 (1991)
- [4] A. Yariv and P. Yeh, *Optical Waves in Crystals* (Wiley, New York, 1984), p. 349
- [5] D. A. Smith, A. d'Alessandro, J. E. Baran and H. Hermann, *Appl. Phys. Lett.*, to be published
- [6] W. R. Trutna, Jr. D. W. Dolfi and C. A. Flory, *Opt. Lett.*, to be published
- [7] M. M. Choy, K. W. Cheung, D. A. Smith, J. E. Baran, *IEEE Photon. Technol. Lett.* **1**, 171 (1989)
- [8] R. W. Dixon, *IEEE J. Quantum Electron.*, **QE-3**, 2 (1967).

Integrated Acousto-Optic Tunable Filters Using Bidirectional Surface Acoustic Waves

Arjun Kar-Roy and Chen S. Tsai

Department of Electrical and Computer Engineering
and Institute of Surface and Interface Science,
University of California, Irvine, CA 92717.
Tel : (714) 856-5144; Fax : (714) 856-4152

Integrated acousto-optic tunable filter (IAOTF) technology, with applications to narrowband wavelength division multiplexed (WDM) systems, has reached some maturity [1]. Recent progresses in IAOTFs include the realization of low drive power [2] and low sidelobe level [3-5] devices. However, all the IAOTFs reported heretofore have the surface acoustic wave (SAW) generating interdigital transducer (IDT) located at one end of the filter interaction length. This results in longer switching times as the SAW has to traverse the entire interaction length of the filter. In this paper, we present a new IAOTF configuration using bidirectional SAWs which reduces the filter switching time by a factor of two while retaining all the desirable characteristics of the conventional IAOTFs. Application of this filter configuration to high-speed self-heterodyne optical communication systems will also be reported.

Fig. 1 shows the architecture of the proposed IAOTF using bidirectional SAWs in which the IDT is placed in the middle of the interaction length. The SAW generated propagates a distance equal to half the total interaction length in both directions before being terminated by SAW absorbers. This arrangement results in a reduction of the switching (access) time of the IAOTF, i.e., the propagation time of the SAW along the interaction length, by a factor of two in comparison to the conventional IAOTFs [1]. Such an architecture effectively uses the SAW in either direction and significantly reduces the effect of SAW attenuation for narrow optical bandwidth filters having long interaction lengths. The attenuation of the SAW results in higher RF drive power requirements as well as degradation of sidelobe levels [6]. It is to be noted that the desirable features of the IAOTFs such as

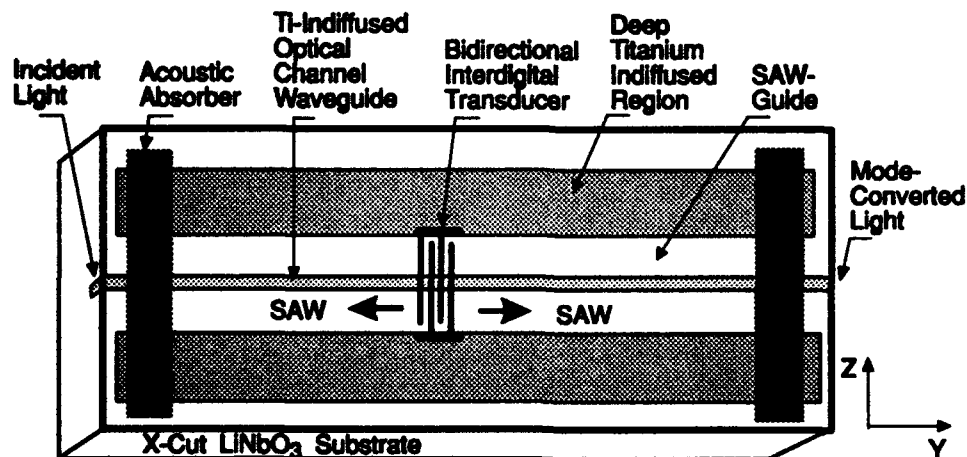


Fig. 1: Schematic diagram of the integrated acousto-optic tunable filter using bidirectional surface acoustic waves.

broad optical wavelength tunability, low RF drive power requirements and narrow filter bandwidths are retained in this configuration. Furthermore, unlike the conventional IAOTF configurations in which the mode-converted light undergoes either a Doppler frequency upshift or downshift, the mode-converted light in the proposed filter configuration consists of both upshifted and downshifted components. For instance, if the input light in Fig. 1 is TM-polarized, the mode-converted light will undergo a Doppler frequency downshift (equal to acoustic frequency for mode-conversion f_a) in the first half of the interaction length due to the counter-propagating direction of the SAW. However, a Doppler frequency upshift will result in the second half of the interaction length due to the reversal of propagation direction of the other SAW. Simultaneous existence of upshifted and downshifted components has also facilitated experiment on optical self-heterodyne detection.

The IAOTF of Fig. 1 using bidirectional SAWs was fabricated on a X-cut, Y-propagating LiNbO₃ substrate, 17mm in length. Titanium-indiffused single-mode optical channel waveguide at the wavelength of 1.31 μ m was formed by using a strip of Ti film, 650 Å in thickness and 6.5 μ m in width, and indiffusion at 1020°C for 15hrs in a flow of dry oxygen. Titanium indiffused barriers for the single-mode SAW-guide of 100 μ m aperture [7] were formed by using strips of Ti film, 1500 Å in thickness and 300 μ m in width, and indiffusion at 1020°C for 37hrs in a flow of dry oxygen. The edges of the substrate were subsequently polished to facilitate edge-coupling of the light beams. The IDT with the acoustic center frequency of 214 MHz was designed for the IAOTF to operate at the optical wavelength of 1.31 μ m [4]. The IDT had a periodicity of 17.6 μ m, an aperture of 95 μ m and 20 finger electrode pairs, and was

tilted by five degrees from the Y-axis to offset the acoustic walkoff for X-Y LiNbO₃. Electric black tapes were used to absorb the SAWs in both ends of the interaction length.

In the experiment, a microscope objective was used for edge coupling of the input light beam obtained from a laser diode at a fixed optical wavelength of 1.31 μ m. A second microscope objective followed by an analyzer was used to image the outgoing mode-converted light beam onto an InGaAs photodetector. The filter response of the IAOTF was obtained by scanning the acoustic frequency at the fixed optical wavelength. Peak mode-conversion was observed at the drive frequency of 212.8MHz. The measured -3dB acoustic bandwidth of 0.35MHz corresponds to an optical bandwidth of 2.15nm for the interaction length of 15.5mm. Fig. 2 shows the measured mode-conversion efficiency versus RF drive power. A maximum mode-conversion efficiency over 90% at an RF drive power as low as 265mW was measured. Fig. 3 shows the oscilloscope trace of the mode -converted light obtained

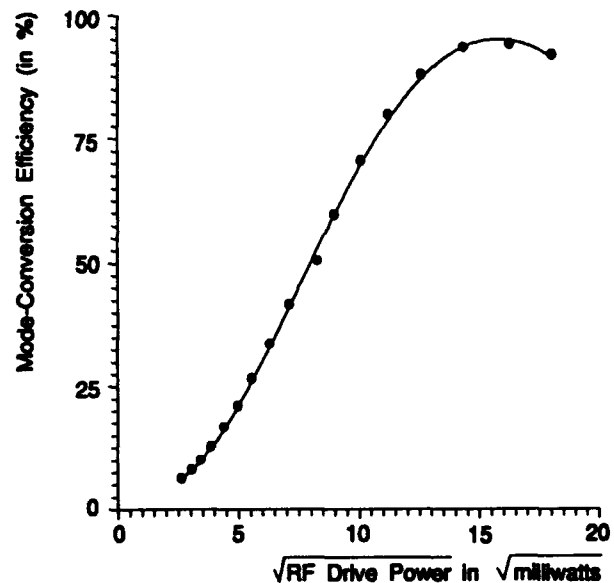


Fig. 2: Measured mode-conversion efficiency versus RF drive power.



Fig. 3 : Oscilloscope traces for rise time measurement. The top trace shows the modulation pulse used to generate the pulsed RF drive signal. The bottom trace shows the resulting mode-converted optical signal waveform (horizontal scale = $2\mu\text{s}/\text{div}$).

from the photodetector when a pulsed RF signal, $6.0\mu\text{sec}$ in width, was applied to the IDT for rise time measurements. The rise time of the IAOTF (10% to 90% of the on-off signal intensity) was measured to be $1.48\mu\text{sec}$, in good agreement with the theoretical prediction.

The co-existence of the Doppler frequency upshifted and downshifted components of the mode-converted light was verified by self-heterodyne detection. In this measurement scheme, self-heterodyning between the frequency upshifted and downshifted components of the mode-converted light results in an intermediate frequency (IF) component equal to twice the RF drive frequency. Fig. 4 shows the double-Doppler frequency shifted IF self-heterodyne spectral component at the frequency of 425.6MHz . The single Doppler frequency-shifted spectral component was completely suppressed when the analyzer was set parallel to the polarization direction of the mode-converted light (Fig. 4a), but appeared as expected when the analyzer was rotated by a small angle (Fig. 4b). It should be noted that

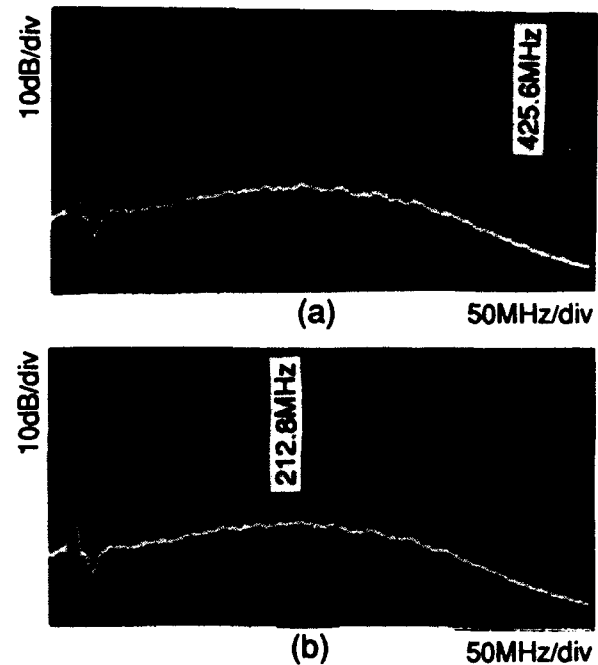


Fig. 4 : Self-heterodyne output spectra of the IAOTF module using bidirectional SAWs showing the double-Doppler frequency shifted component at 425.6MHz with the (a) analyzer parallel to the polarization direction of the mode-converted light, and (b) analyzer deviating slightly from the condition of (a).

the magnitude of the spectral component at 425.6MHz was suppressed by -19dB with respect to the 212.8MHz component as the photodetector used had a base bandwidth of 300MHz only.

In summary, we have proposed the first IAOTF configuration using bidirectional SAWs. Experiments have clearly demonstrated the reduction of switching time by a factor of two and the improvement in RF drive power efficiency. This configuration is better suited than the conventional IAOTFs of long interaction length due to its faster switching speed. Reduced SAW propagation losses potentially results in lower RF drive power requirements and prevents sidelobe level degradation. Potential applications of the resultant IAOTF module to self-heterodyne optical communication systems,

utilizing the coexisting frequency upshifted and downshifted components, will also be presented.

References

1. See, for example, D. A. Smith, J. E. Baran, J. J. Johnson and K. W. Cheung, "Integrated-optic acoustically tunable filters for WDM networks," *IEEE J. Sel. Areas Commun.*, vol. 8, 1151-1159, 1990.
2. D. A. Smith and J. J. Johnson, "Low drive-power integrated acousto-optic filter on X-cut Y-propagating LiNbO₃," *IEEE Photon. Technol. Lett.*, vol. 3, 923-925, 1991.
3. Y. Yamamoto, C. S. Tsai, and K. Esteghamat, "Guided-wave acousto-optic tunable filters using simple coupling weighting technique" Proc. 1990 IEEE Ultrasonics Symposium (IEEE, New York, 1990), 605-608 (IEEE Cat. No. : 90CH2938-9).
4. A. Kar-Roy and C. S. Tsai, "Low-sidelobe weighted-coupled integrated acoustooptic tunable filter using focused surface acoustic waves," *IEEE Photon. Technol. Lett.*, vol. 4, 1132-1135, 1992.
5. D. A. Smith and J. J. Johnson, "Sidelobe suppression in an acousto-optic filter with a raised-cosine interaction strength," *Appl. Phys. Lett.*, vol. 61, 1025-1027, 1992.
6. A. Kar-Roy and C. S. Tsai, "Integrated acousto-optic tunable filters with weighted-coupling," To be published.
7. J. Frangen, H. Herman, R. Ricken, H. Seibert, W. Sohler and E. Strake, "Integrated optical acoustically tunable wavelength filter," *Electron. Lett.*, vol. 25, 1583-1584, 1989.

Laser-Beam Periodic-Dot Writing For Fabrication of Ti:LiNbO₃ Waveguide Wavelength Filters

M. Haruna, T. Kato, K. Yasuda and H. Nishihara
Department of Electronics, Faculty of Engineering, Osaka University
2-1 Yamada-Oka, Suita, Osaka 565, Japan

Laser-beam (LB) writing is a useful technology for patterning of channel waveguides in photoresist coated on a substrate, as already reported by some researchers [1-3]. In particular, the authors developed the practical LB writing system which consisted of a closed-loop-controlled X-Y translation stage, a focusing optics of the 442-nm He-Cd laser and a LB intensity control circuit [3]. In this system, 3-to-8- μm wide channel waveguides can be formed automatically over an area of $10 \times 10 \text{ cm}^2$ with an accuracy of nearly 0.1 μm . Very precise waveguide patterning is thus possible because of extremely smooth movement of the X-Y stage whose translation speed fluctuation $\delta v/v$ is less than 10^{-4} , as will be discussed below; therefore, when the focused LB is switched on/off regularly under a constant-speed movement of the stage, dots should be aligned with a uniform period in photoresist. In this paper, we demonstrate such a new LB periodic-dot writing used to form interdigital electrodes required for TE-TM mode conversion in Ti:LiNbO₃ waveguide wavelength filters.

The basic system configuration is shown in Fig. 1 where the stage is driven at a constant speed v . A pulse generator is triggered by a counter/comparator in synchronization with the stage movement, and the output pulse voltage of the generator is fed into an AOM to switch the laser beam at a repetition frequency f . Periodic-dot patterns are then formed in photoresist coated on a substrate, as shown in Fig. 1, where the period $\Lambda = v/f$. In a commercially available pulse generator, the frequency fluctuation δf is $\pm 0.01 \text{ Hz}$ around $f = 100 \text{ Hz}$. It, therefore, is expected that the period is controlled with an accuracy of the order of nanometer when $v \sim 1 \text{ mm/s}$. The dot size and spacing are also adjustable by the focused LB spot size, a pulse voltage and its duty cycle T_2/T_1 . In the test patterning, 10-mm long periodic dots were made repeatedly in 1- μm thick photoresist, shifting the starting point, where $v = 1.23 \text{ mm/s}$, $f = 125.01 \text{ Hz}$ ($\pm 0.01 \text{ Hz}$) and $\Lambda = 9.839 \mu\text{m}$. The LB periodic-dot writing was followed by lift-off of Ti sputtered film, resulting in the dot pattern of Fig. 2. It was then found that the period fluctuation $\delta \Lambda$ was less than 4 nm by dividing a dot array of Fig. 2 into segments having 100 dots and measuring the segment length. This result indicates that the translation speed fluctuation $\delta v/v$ of the stage is sufficiently less than 10^{-4} because $\delta \Lambda$ is mainly caused by the frequency fluctuation of the generator.

The LB periodic-dot writing was used to form interdigital electrodes required for

TE-TM mode conversion in the Ti:LiNbO₃ waveguide wavelength filter whose structure is illustrated in Fig. 3 [4,5]. The electrode period Λ satisfies the phase matching condition of $\Lambda = \lambda_c / \Delta N$ where λ_c is the center wavelength of the filter and $\Delta N (=N_{TM} - N_{TE})$ is the modal birefringence. It, however, is generally difficult to evaluate precisely ΔN at a certain wavelength. In design of an actual filter, ΔN was approximated by the index difference Δn of ordinary and extraordinary waves in bulk LiNbO₃ [6]; and thereby, Λ was easily calculated to be 10.154 μ m when λ_c was given as 805nm. The pulse frequency $2f (=2v/\Lambda)$ of the generator became 242.27Hz when $v=1.23$ mm/s, because a main portion of the interdigital electrodes was formed by repeating the LB dot writing with the period of $\Lambda/2$, shifting the starting point by a dot radius, as shown in Fig. 3. The electrode patterning was also performed in photoresist coated on Ti-LiNbO₃ after alignment of the scanning direction of the focused LB spot along a 3.7 μ m wide channel waveguide. The writing time for the whole electrode was nearly 6min. Finally, the electrode was made by lift off of Ti film, as shown in Fig. 4. The fabricated filter was characterized by use of a tunable Ti-sapphire laser as a light source. The measured filter characteristic is shown in Fig. 5. A complete mode conversion was attained with a drive voltage of 7.5V at the center wavelength λ_c of 802.9 nm. λ_c was apart only by 2.1nm from the given value of 805nm even though ΔN was approximated by the birefringence of bulk LiNbO₃ in the filter design. The filter bandwidth (FWHM) was also 1.1nm which coincided with the theoretically predicted value [5]. The experimental results described here indicates that the LB periodic-dot writing can define precisely the interdigital electrodes with a uniform period according to the design parameters.

Subsequently, in order to confirm controllability of the electrode period Λ by the LB periodic-dot writing, eight filters with 5-mm long interdigital electrodes were integrated on a LiNbO₃ substrate, as shown in Fig. 6. The center-wavelength spacing $\Delta\lambda_c$ between adjacent filters was 5.4nm which corresponded to the electrode-period difference $\Delta\Lambda$ of 80nm. The interdigital electrodes for each filter were formed by changing the pulse frequency f in the same manner as mentioned above, where the frequency change $\Delta f=0.88$ to 0.96Hz. In the fabricated device, variation of the measured center wavelength λ_c with the electrode period fitted well a straight line, as shown in Fig. 7. If Δf is around 0.1Hz in the LB periodic-dot writing, it should be fully possible to integrate the filters with a center-wavelength spacing of nearly 1nm.

In conclusion, we have demonstrated the LB periodic-dot writing in which dot patterns of a nearly 10 μ m period is formed with a period fluctuation of <4nm. This new LB writing technique has been successfully applied to define 5-mm long interdigital electrodes of Ti:LiNbO₃ waveguide wavelength filters. The filter bandwidth is 1.1nm at $\lambda_c \sim 0.8\mu$ m which is in good agreement with the theoretical value. The electrode period is also controllable with an accuracy of the order of 10nm, indicating that the filters with the center-wavelength spacing of >1nm are

integrated on a LiNbO₃. Moreover, it should be possible to fabricate a filter having the interdigital electrode of >15mm which exhibits the FWHM of a few Å.

References

1. R.A. Becker, B.I. Sopori and W.S.C. Chang: Appl. Opt. 17, p.1069 (1978).
2. K.E. Wilson, C.T. Mueller and E.M. Garmire: IEEE Trans. Hybrid & Manufacturing Technol. CHMT-5, p.202 (1982).
3. M. Haruna, S. Yoshida, H. Toda and H. Nishihara: Appl. Opt. 26, p.4587 (1987).
4. R.C. Alferness and L.L. Buhl: Opt. Lett. 5, p.473 (1980).
5. F. Heismann and R.C. Alferness: IEEE J. Quantum Electron. QE-24, p.83 (1988).
6. C.J.G. Kirkby: "Properties of Lithium Niobate", INSPEC, The Institution of Electrical Engineers, London and New York, p.131 (1989).

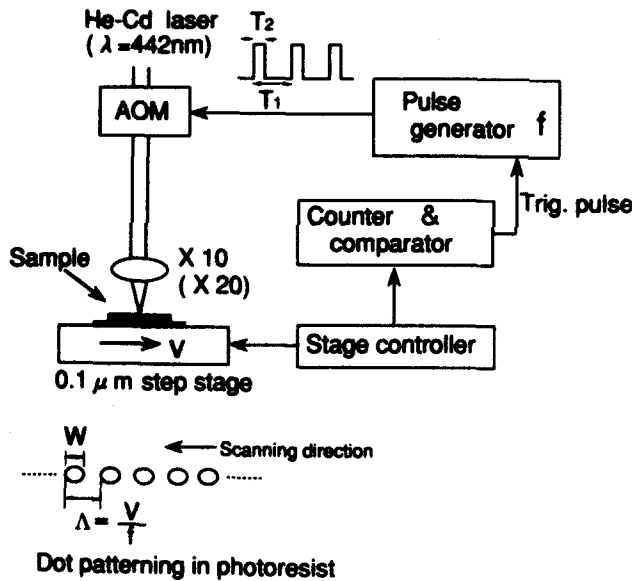


Fig. 1 Brief system configuration of the LB periodic-dot writing.

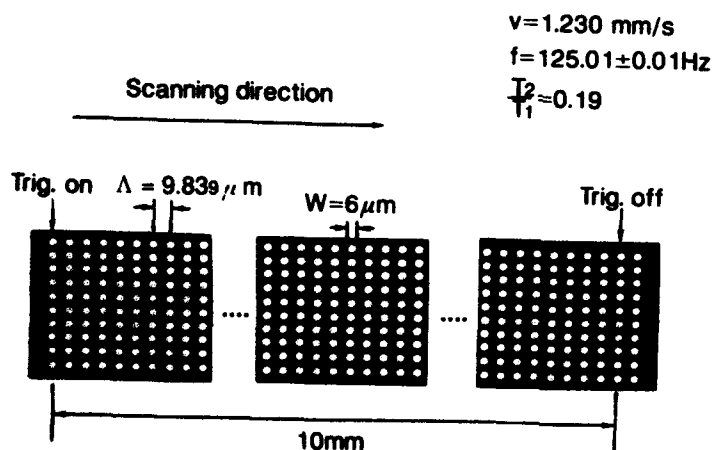


Fig. 2 Dot patterning with a uniform period.

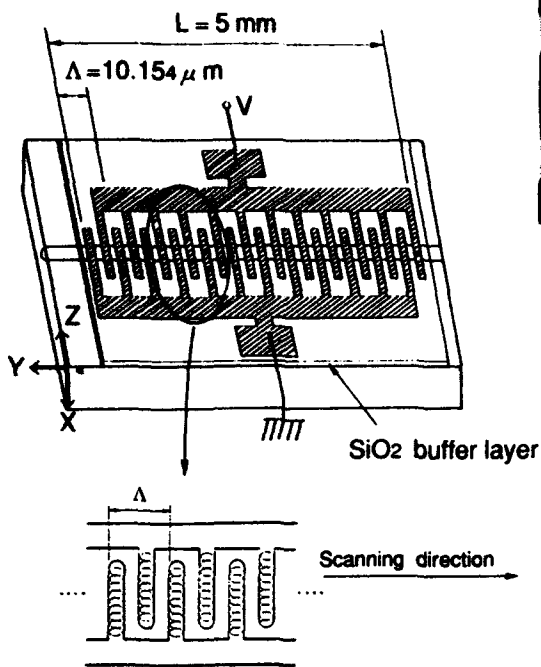


Fig. 3 Electrode structure of Ti:LiNbO₃ waveguide wavelength filters.

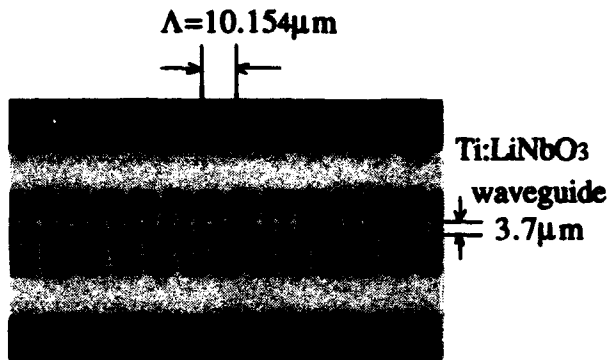


Fig. 4 LB written interdigital electrodes.

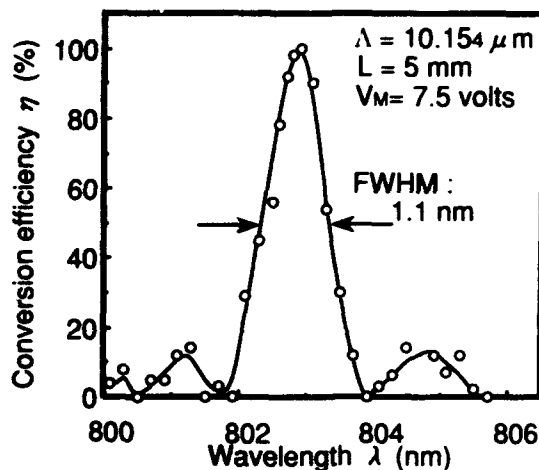


Fig. 5 Measured characteristic of the fabricated filter.

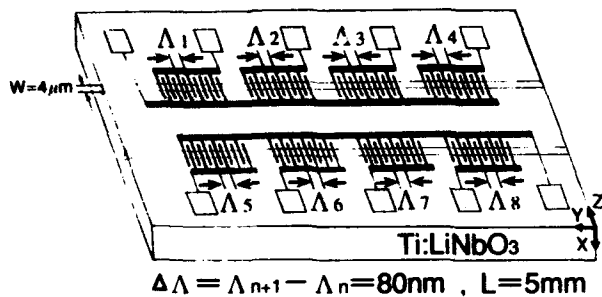


Fig. 6 Integration of the filters where the electrode period is different by 80nm for each filter.

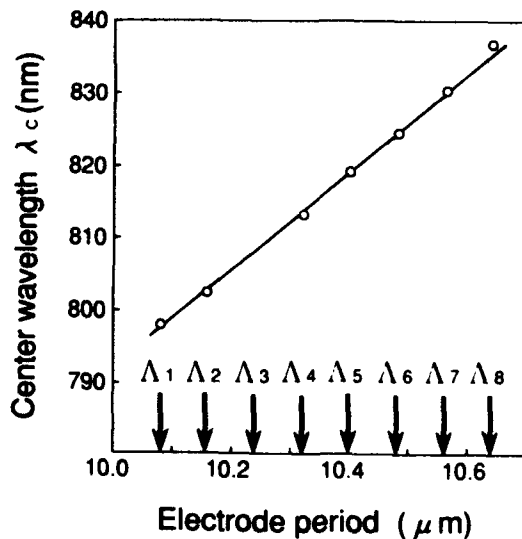


Fig. 7 Measured center wavelength λ_c vs. the electrode period Δ.

A NEW SCHEME FOR WIDEBAND ELECTRONICALLY OPTIC TUNABLE FREQUENCY SHIFTING USING MAGNETOOPTIC BRAGG DIFFRACTION

Y. Pu and C.S. Tsai

**Department of Electrical and Computer Engineering
and**

Institute for Surface and Interface Sciences

University of California at Irvine

Irvine, CA 92717

Phone #:(714)856-5144

Fax #:(714)856-4152

Integrated optic frequency shifters which provide wideband electronically tunable frequency shift and output light propagating at a fixed angle, irrespective of the amount of frequency shift, are highly desirable [1,2]. In this paper, a new optical frequency shifting scheme which utilizes noncollinear guided-wave magneto-optic (MO) Bragg diffraction by magnetostatic forward volume waves (MSFVW) in yttrium iron garnet-gadolinium gallium garnet (YIG-GGG) -based optical waveguide structure [3] (Fig.1) is presented. The constancy of output angle of the frequency-shifted light is facilitated by maintaining a constant wave number for the MSFVW using a dual-tuning mechanism which involves synchronous tuning between the carrier frequency of the RF driving signal (and thus the MSFVW) and the bias magnetic field (Fig.2). In so doing the spatial scan of the frequency-shifted light beam resulting from the tuning of the RF driving frequency is exactly compensated by that resulting from the synchronous tuning of the bias magnetic field. As a result, the Bragg-diffracted light propagates at a constant output angle, irrespective of the RF driving frequency, and thus enables a very large bandwidth to be achieved. Wideband electronically tuned frequency shifting at various carrier frequency ranges (2-12 GHz) was accomplished using a MO Bragg cell in a bismuth-doped YIG/GGG waveguide substrate, $6 \times 10 \text{ mm}^2$ in size, inserted in a compact magnet housing which consists of a pair of

permanent magnets and a pair of current-carrying coil. A specially designed electronic synchronizer was used to convert the reference voltage from an X-band microwave oscillator, which was linearly proportional to its output frequency, into a current to drive the pair of coils and facilitated the synchronous tuning between the bias magnetic field and the carrier frequency. Tunable bandwidths of 1.61 and 2.35 GHz have been accomplished at the center carrier frequencies of 6.035 and 11.025 GHz, respectively. The maximum deviations of the output angle of the frequency-shifted light measured at the two center carrier frequencies are 3.5×10^{-4} and 2.0×10^{-4} radians, which are well within the tolerance limitation for efficient edge-coupling with a single-mode optical fiber. Linear dynamic ranges of 33.7 and 31.0 dB were obtained at the two center frequencies, respectively. The corresponding MO diffraction efficiencies were 8.5% and 7.9% at input RF drive power of 30 dBm. The tuning speed of the device, as determined by the response time of the current-carrying coils, was measured to be 10 μ s. With improvement in the designs of the synchronizer circuitry and the coils, the tunable bandwidth can be readily increased by a factor of 2 to 4, and the tuning speed improved by a factor of 10.

REFERENCE

- [1]C.S. Tsai and Z.Y. Cheng, "Novel Guided-Wave Acoustooptic Frequency Shifter Scheme Using Bragg Diffractions In Cascade," *Appl. Phys. Lett.*, **54**, 24 (1989)
- [2]Z.Y. Cheng and C.S. Tsai, "A Baseband Integrated Acoustooptic Frequency Shifter," *Appl. Phys. Lett.*, **60**, 12 (1992)
- [3]C.S. Tsai and D. Young, "Magnetostatic-Forward-Volume-Wave-Based Guided-Wave Magneto-optic Bragg Cells and Applications to Communications and Signal Processing," *IEEE Trans. Microwave Theory and Technol.* **MTT-38**, 560 (1990)

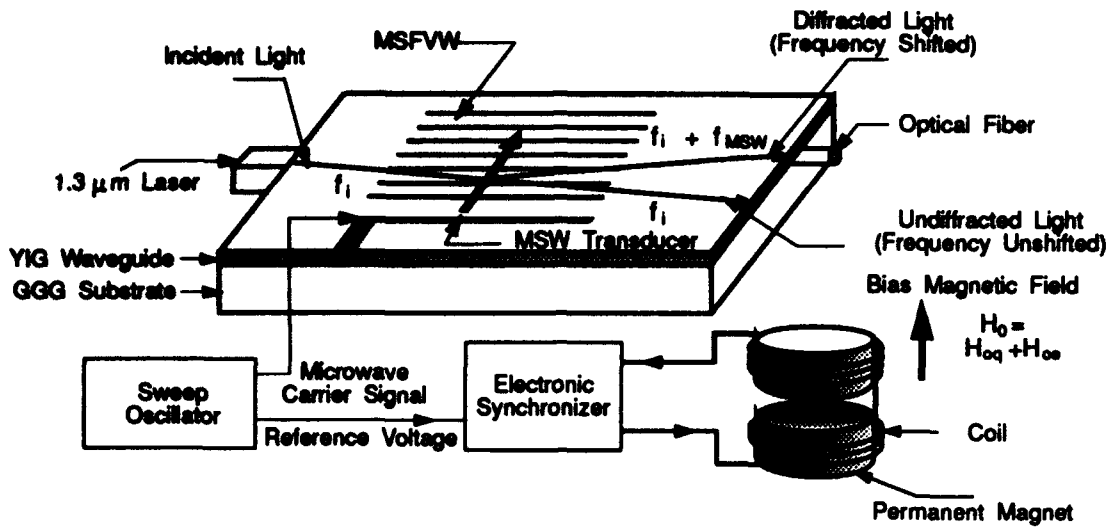


Fig.1 An Electronically Tunable Wideband Integrated Magneto-optic Frequency Shifter

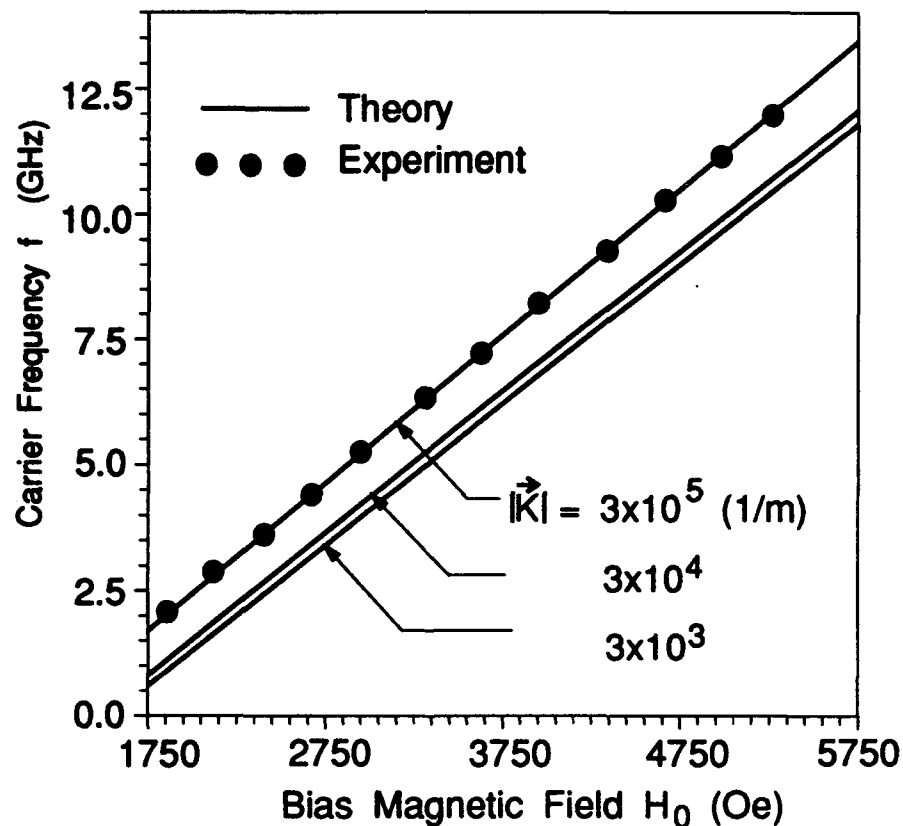


Fig.2 Carrier Frequency versus Bias Magnetic Field with the Wave Number of MSFVW as a Parameter



Optical Waveguide Simulators

ITuC 8:30am-10:15am
Mesquite C/D

Anand Gopinath, *President*
University of Minnesota

**Vector Finite Element Modeling of Dielectric Guides by
Transverse Magnetic Field Formulation**

Z. Abid, K. L. Johnson, A. Gopinath

**University of Minnesota
Department of Electrical Engineering
Minneapolis, MN 55455
(612) 625-3054**

A transverse vector-H finite element formulation for the solution of modes in optical guides has been implemented, and a quantum well laser structure has been analyzed.

Introduction

The vector finite element method usually determines the mode structure of dielectric guides using all three magnetic field (H) components [1,2]. This gives rise to many spurious modes since the basis set does not satisfy the divergence condition. The penalty function method alleviates this problem, however not completely. Furthermore, this formulation requires that the propagation constant be specified, and the frequencies or wavelengths of the propagating modes be determined, which prevents the analysis of guides with loss or gain. Alternate finite element formulations have been proposed [3,4], but none has been shown to be satisfactory.

In this paper, we formulate the vector guide problem in terms of the transverse H fields only, and utilize the corresponding wave equation pair that satisfies the divergence condition. The interface boundary conditions are imposed by a boundary operator, the null set of which is the basis function set for wave equations. Thus, spurious modes are eliminated entirely, and the formulaiton evaluates the propagation constants for a fixed excitation wavelength or frequency.

Formulation

The finite element formulation leads to the integral:

$$F = \int \left\{ \sum -(\nabla H_i)^2 + (k^2 \epsilon - \beta^2) H_i \right\} dx dy, \quad i = x, y \quad (1)$$

Minimizing this integral with respect to the nodal value of H_i , reduces it to a matrix equation of the form

$$[S][H] = \beta^2 [T][H] \quad (2)$$

The continuity of E_z and H_z accross interface boundary conditions in this formulation leads to another matrix equation of the form:

$$[R][H] = 0 \quad (3)$$

where $[R]$ is a $m \times n$ matrix, $m < n$.

The null space of equation (3) is given by:

$$[H] = [N][C] \quad (4)$$

where $[N]$ is a $n \times (n-m)$ matrix, and $[C]$ defines the new vector space. Substituting (what ?) in equation (2) and premultiplying by $[Z]^t$ gives the reduced matrix equation:

$$[N]^t[S][N][C] = \beta^2[N]^t[T][N][C] \quad (5)$$

which is solved to determine the eigenvalues of the propagating modes.

Results

The structure in Fig. 1 was used to compare the results obtained from this technique with those from the literature [1]. Results are within 0.07%, even with an extremely coarse mesh of 22 X 22 nodes. The second case considered is a quantum well separate confinement heterostructure laser at transparency, shown in Fig. 2. Two etch depths are compared with the variable-mesh finite difference semivectorial results [5] shown in Table I. As seen in this table, even with a coarse mesh of 22 X 22 nodes, the eigenvalues are within 0.07% of the finite difference method which has used over 10,000 nodes. Fig. 3 shows a contour plot of the H_x field of the quasi-TE mode propagating on this guide.

Summary

A transverse vector-H finite element method for analyzing dielectric guides with no spurious modes has been proposed. The results, even with a coarse mesh are in excellent agreement with published results in one case, and the semivectorial finite difference in the second case.

References

1. B. M. A. Rahman, J. B. Davies, *IEEE Trans. Microwave Theory and Tech.*, Vol. 32, pp. 20-28, 1984.
2. B. M. A. Rahman, J. B. Davies, *J. Lightwave Tech.*, Vol. 2, pp. 682-688, 1984.
3. K. Hayata, M. Koshihara, M. Eguchi, M. Suzuki, *IEEE Trans. Microwave Theory and Tech.*, Vol. 34, pp. 1120-1124, 1986.
4. C. C. Su, *Electronics Lett.*, Vol. 21, pp. 858-860, 1985.
5. K. Johnson, A. Gopinath, "Variable mesh semivectorial finite difference method for optical waveguides", to be published.

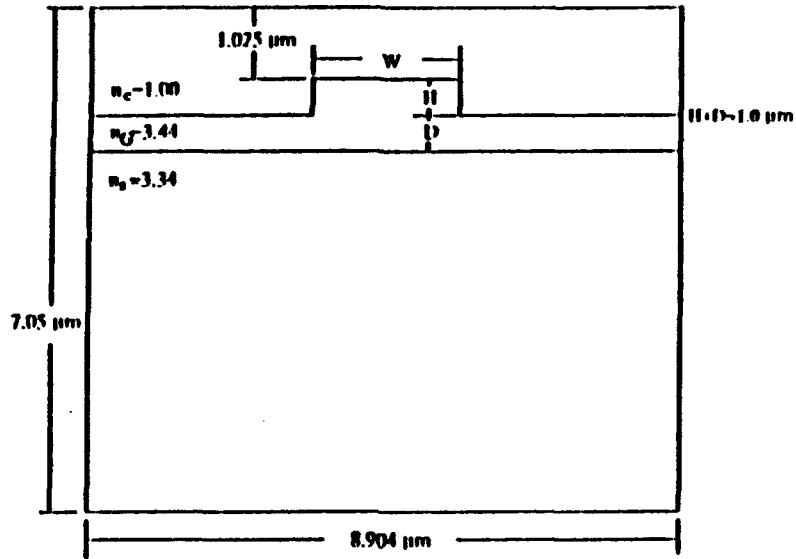


Fig. 1. A dielectric rib waveguide structure

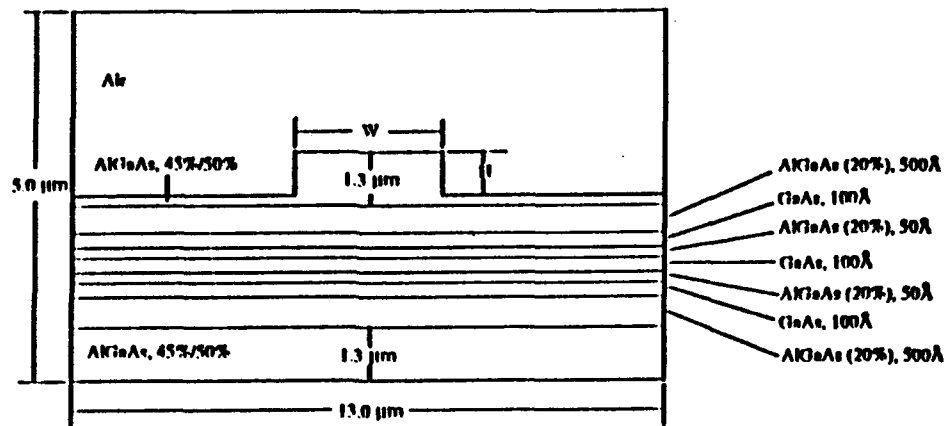
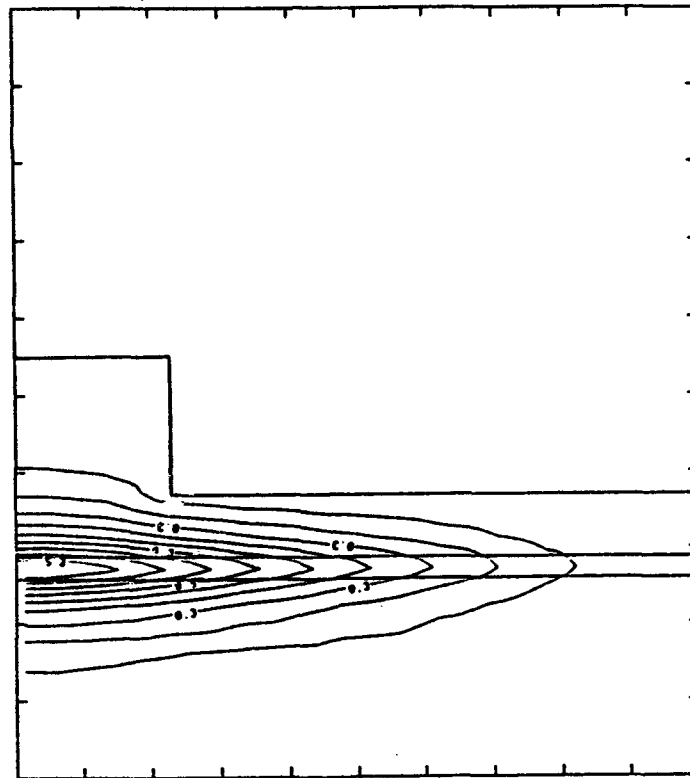


Fig. 2. A multiple quantum well waveguide structure

Table I.

H μm	W μm	Al%	FDM	FEM(E_z, H_z)
1.0	3.0	45	3.35931	3.35708
1.0	4.0	45	3.35975	3.35804
1.0	5.0	45	3.36001	3.35853
1.0	3.0	50	3.34584	3.34341
1.0	4.0	50	3.34624	3.34431
1.0	5.0	50	3.34648	3.34475
0.9	3.0	45	3.35974	3.35790
0.9	4.0	45	3.35999	3.35844
0.9	5.0	45	3.36015	3.35872
0.9	3.0	50	3.34628	3.34201
0.9	4.0	50	3.34649	3.34468
0.9	5.0	50	3.34663	3.34492

Table 1 The computed β_{eff} for the structure shown in Fig 2 for a wavelength of $\lambda=0.86\mu\text{m}$, and for F.D.M. and the F.E.M.



VECTORIAL INTEGRATED FINITE-DIFFERENCE ANALYSIS OF DIELECTRIC WAVEGUIDES

***H. DONG, +A. CHRONOPOULOS, *A. GOPINATH**

***Department of Electrical Engineering, University of Minnesota
200 Union Street SE., Minneapolis, MN 55455. (612)625-3841**

**+Department of Computer Sciences, University of Minnesota
200 Union Street SE., Minneapolis, MN 55455.**

For the step index profile of dielectric waveguides(see Figure 1), the mode-matching techniques[1], the finite-element analysis [2-4], and the finite-difference method[5-7] have been developed for the discretization of the wave equation and the computation of the eigenvalues. In this paper, we present an integrated finite-difference method[8] to discretize the wave equation, and Arnoldi's method[9,10] coupled with multiple deflation[10], followed by the inverse power method[11] combined with an iterative solver[12], for the calculation of eigenvalues and eigenvectors.

The integrated finite-difference approach[8] is formulated in terms of transverse components of the vector magnetic(H) field of the form $\nabla^2 H_i + (k^2 \epsilon_T - \beta^2) H_i = 0$, where $i = x, y$. A nonuniform mesh is used in the cross section of waveguides in this approach. The wave equation for each component of the H field is integrated over each cell of the mesh by the box integration method[8] in three finite difference scheme to discretize the wave equation. The boundary condition at the interface with the nearest neighbor cells is enforced by employing the transverse and longitudinal continuity of the H field and the continuity of the longitudinal E_z . The discretization of these boundary conditions together with the wave equation creates a sparse banded unsymmetric matrix, which has two diagonal sections for H_x and H_y and two off-diagonal sections for the coupling between the H_x and H_y . The exponential decay of the H field at the clad layers is accounted for by choosing a nonuniform mesh at those regions, but the mesh of the guide region is uniform. Only the nonzero elements are stored.

The size of the matrix with coupling between the transverse components is about four times larger than the matrix without this coupling. Solving for all the eigenvalues of the matrix for a large number of nodes is too computer intensive. Since only a few positive eigenvalues need to be obtained, depending on the mode structure of the waveguide, finding a method for accurately computing few eigenvalues of the matrix is highly desirable. We use the modified Arnoldi's method[9] with multiple deflation to calculate few extreme eigenvalues and the corresponding eigenvectors by computing a suitable small size matrix. With the multiple deflation[10], the calculation of eigenvalues only follows the few desired ones. For the strongly guided modes, the convergence of the calculation is fast and accurate. But for single mode waveguides or weak-guided modes, improvement of convergence of the calculation is needed for rapid convergence. We use the inverse power method[11] to continue the calculation after Arnoldi's iteration gives us the initial eigenvalues. This strategy makes the convergence of the calculation very fast. The s-step method[12] is combined with the inverse power method to avoid directly inverting the original matrix.

We consider three examples. The first two dielectric waveguides discussed in the literature have strong guided modes, Figures 1 and 2 show the structures of these waveguides. For these structures, Arnoldi's method(without the use of inverse power method) gives maximum error less than 10^{-11} , where the error is defined as $\|Ax - \lambda x\|$, and A is the original matrix, x is the eigenvector, and λ is the corresponding eigenvalue. Our

error agrees well with the predicted error from Arnoldi's method[9][13]. Figures 1 and 2 show the normalized propagation constant vs. normalized wave vectors. Only the first three largest positive eigenvalues are shown in this figure. The calculation for each set of the eigenvalues at a given wave vector needed an average 17 seconds CPU on Cray X-MP. The last example is for one of a single mode three quantum well waveguide structure(see Figure 3(a)). The maximum error is less than 10^{-8} , and Figure 3(b) shows the normalized propagation constant vs. the normalized wave vectors.

The technique we have presented does not use preconditioning. It is presumed that this method will be more powerful with preconditioning. Currently we use this method to analyze step index profile dielectric waveguides. It is also suitable for continuously variable index profile waveguides, by using the first-order approximation of the Taylor expansion of the index.

References

- [1] E. Goell, 'A circular-harmonic computer analysis of rectangular dielectric waveguides,' *Bell Syst. Tech. J.*, vol. 48, p2133(1969).
- [2] B. M. A. Rahman and J. B. Davies, 'Penalty function improvement of waveguide solution by finite elements,' *IEEE Trans. Microwave Theory Tech.*, vol. MTT-32, p922(1984).
- [3] K. Hayata, 'Vectorial finite-element method without any spurious solutions for dielectric waveguiding problems using transverse magnetic-field component,' *IEEE Trans. Microwave Theory Tech.*, vol. MTT-34, p1120(1986).
- [4] Z. Abid, K. Johnson, and A. Gopinath, 'Analysis of dielectric guides by transverse magnetic field finite element,' submitted.
- [5] K. Bierwirth, N. Schulz, and F. Arndt, 'Finite-difference analysis of rectangular dielectric waveguide structure,' *IEEE Trans. Microwave Theory Tech.*, vol. MTT-34, p1104(1986).
- [6] K. Bierwirth, N. Schulz, and F. Arndt, 'Finite-difference analysis of integrated optical waveguide without spurious solutions,' *Electron. Lett.*, vol. 22, p963(1986).
- [7] A. Galick, T. Kerhoven, and U. Ravaioli, 'Iterative solution of the eigenvalue problem for a dielectric waveguide,' *IEEE Trans. Microwave Theory Tech.*, vol. MTT-40, p699(1992).
- [8] R. Varga, 'Matrix iterative analysis,' Prentice-Hall, Englewood Cliff. HJ: p184(1962).
- [9] W.E. Arnoldi, 'The principle of minimized iterations in the solution of the matrix eigenvalue problem,' *Quart. Appl. Math.*, vol. 9, p17(1951).
- [10] Y. Saad, 'Chebychev Acceleration Techniques for Solving Nonsymmetric Eigenvalue Problems,' *Mathematics of Computations*, vol. 42, April, p567(1984).
- [11] J. Wilkinson, 'The algebraic eigenvalue problem,' Clarendon Press, 1965.
- [12] A. T. Chronopoulos, 's-Step iterative methods for (non)symmetric (in)definite linear systems,' *SIAM J. on Num. Anal.*, vol. 28, No. 6, p1776(1991).
- [13] K. Kim and A. T. Chronopoulos, 'An Efficient Parallel Algorithm for Extreme Eigenvalues of Sparse Nonsymmetric Matrices', *The Int. J. on Supercomputing*, Vol.6, No.1, Spring, p98(1992).

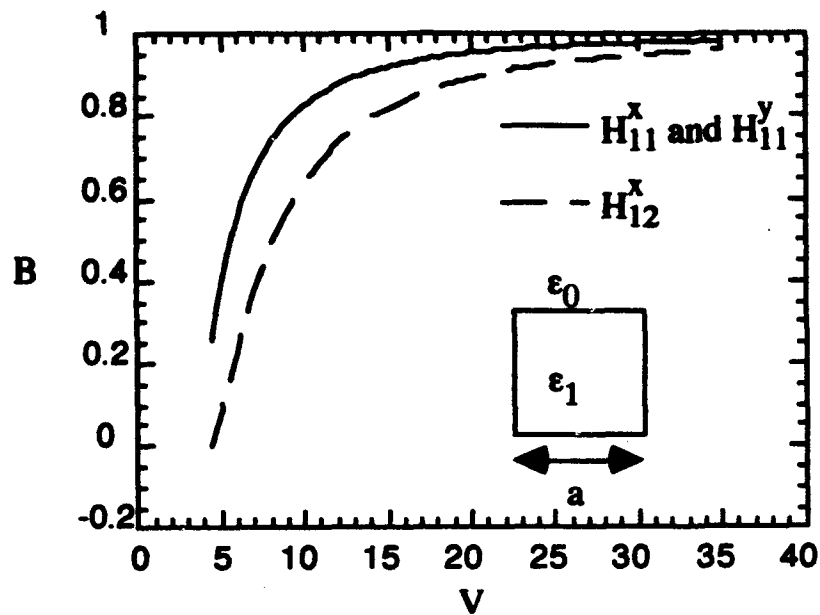


Figure 1. Normalized propagation constant of a square dielectric waveguide, $B = ((\beta/k)^2 - \epsilon_0) / (\epsilon_1 - \epsilon_0)$ vs. normalized wave vector $V = ka(\epsilon_1 - \epsilon_0)^{1/2}$, k is free space wave vector, $a = 1 \mu\text{m}$, $\epsilon_1 = 13.1\epsilon_0$

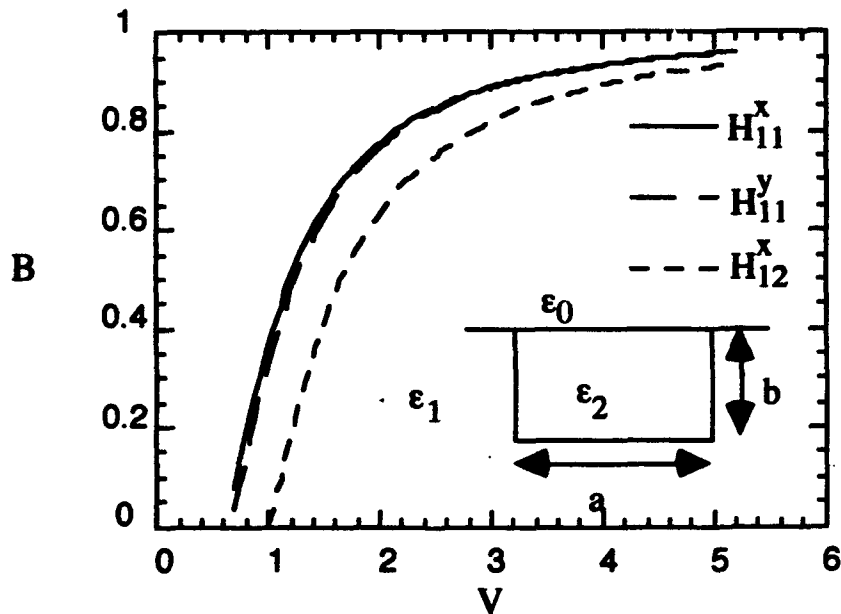


Figure 2. Normalized propagation constant of a channel waveguide, $B = ((\beta/k)^2 - \epsilon_1) / (\epsilon_2 - \epsilon_0)$ vs. normalized wave vector $V = ka(\epsilon_1 - \epsilon_0)^{1/2}$, k is free space wave vector, $a = 2b = 6 \mu\text{m}$, $\epsilon_1 = 2.13\epsilon_0$, $\epsilon_2 = 2.25\epsilon_0$.

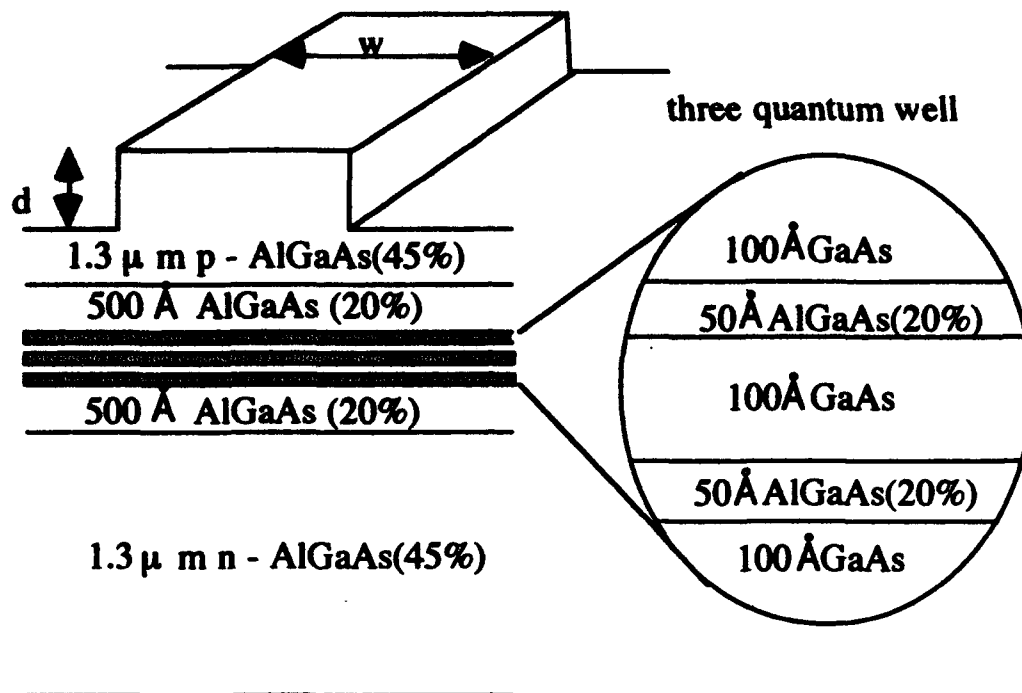


Figure 3(a). A single mode quantum well ridge waveguide, $w=3\mu\text{m}$, $d=0.9\mu\text{m}$.

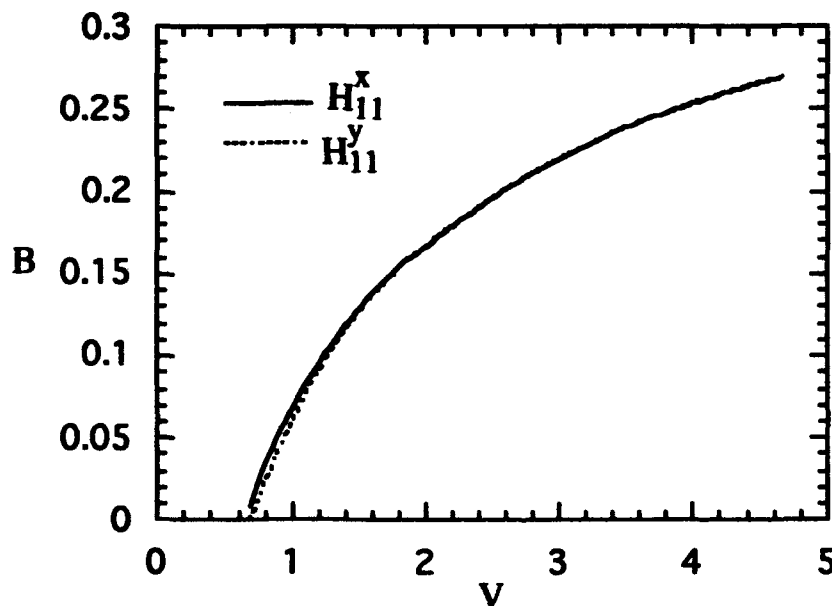


Figure 3(b). Normalized propagation constant $B = ((\beta/k)^2 - \epsilon_{\text{clad}}) / (\epsilon_{\text{core}} - \epsilon_{\text{clad}})$ vs. normalized wave vector $V = 0.14k(\epsilon_{\text{core}} - \epsilon_{\text{clad}})^{1/2}$, k is free space wave vector, ϵ_{clad} is the maximum dielectric constant in the clad layers, the ϵ_{core} is the maximum dielectric constant in the guided region.

Eigenmode propagation analysis of radiation losses in waveguides with discontinuities and grating assisted couplers

J. Willems, J. Haes, R. Baets

University of Gent - IMEC - Laboratory of Electromagnetism and Acoustics

Sint-Pietersnieuwstraat 41, B-9000 Gent, Belgium

Tel. 32-91-643316 Fax. 32-91-643593

G. Sztefka, H.P. Nolting

Heinrich Hertz Institut für Nachrichtentechnik Berlin GmbH

Einsteinufer 37, D-1000 Berlin 10, Germany

Tel. 49-30-31002255 Fax. 49-30-31002558

Introduction

Grating assisted codirectional couplers are very useful for widely tunable lasers and filters. They consist of a directional coupler with periodic discontinuities. These have to be strong to obtain coupling in relatively short devices. Therefore these devices may show substantial radiation losses. Generally, there are two methods to analyse codirectional couplers, one based on a coupled mode formalism [1] and another using mode matching theory at discontinuities and mode propagation in the straight waveguide sections [2]. Both methods can calculate the wavelength of maximum coupling and the coupling length as a function of the structure parameters. BPM calculations may have difficulties with the large refractive index steps. In this paper we present a method to calculate accurately the radiation losses. An optimised design with respect to losses is now possible for this kind of couplers.

Our method is basically an eigenmode propagation method, extended with radiation modes [3]. With this method it is also possible to account for reflections, but in the structures proposed here, these are negligible. An orthogonal discrete set of radiation modes is used by introducing a finite calculation window with fictitious walls which provide zero field outside. This gives rise to a problem however : when radiation modes are propagated, they can reflect at the fictitious walls. Furtheron two solutions are proposed to avoid these reflections.

First we consider a simple slab waveguide structure consisting of three sections (Fig. 1). We calculate the power transfer in the guided mode of the last section, versus the length of the intermediate section, when optical power is launched in the first section. Fig. 1 illustrates the problem of the reflecting radiation modes. The solution using a discrete set of radiation modes is compared with the exact solution. The strong oscillation is due to the recaptured radiation modes. The exact solution is calculated simply by enlarging the calculation window. This latter method however needs a higher number of modes and is very unpractical and CPU-time consuming. In order to take into account correctly the radiation modes, one must know at which point they reflect at the fictitious walls. This can be derived from the well known k -diagram, shown in Fig. 2. Each k -vector represents a mode. A radiation mode reaches the fictitious boundary if

$$\frac{k_x}{k_z} > \frac{W}{L}$$

The next two paragraphs show a solution to the problem of the reflecting radiation modes. In the last section the results are compared by means of a calculation on a grating assisted codirectional coupler.

Using an absorber

In the first technique an absorber at the fictitious walls is introduced to avoid reflection and recapturing of the radiated power at the walls. The absorbing frame is realised with complex refractive indices. This complicates the evaluation of the eigenmodes and eigenvalues which have to be searched in the complex plane, but as an advantage the fast matching and propagation algorithm [3] remains the same. The plane wave Transfer-Matrix-Method [4] is applied to calculate the set of eigenmodes including the discrete set of radiation modes of the slab waveguides in two steps. In the first step we exclude the imaginary part of the refractive indices of the absorber and we search for the roots on the real axis with an adaptive stepsize control. Counting the nodes of the field distribution insures that the N lowest eigenmodes are found. In the second step the imaginary part slowly increases. Starting with the roots on the real axis from the first step and tracking the roots with reduced functions (divided by the known eigenvalues) and checking the orthogonality give us the roots in the complex plane. By a suitable positioning of the ideal metal walls and the absorbers the influence of the boundaries on the eigenvalues and the guided mode shapes is practically eliminated. This is achieved when the imaginary part of the propagation constants of the guided modes vanishes. The simple waveguide coupling in Fig. 1 serves to illustrate the technic. The short-dashed curve in Fig. 3 is calculated with an absorbing frame (4 layers, 10000, 5000, 2500, 1250 cm^{-1} absorption and each 1 μm thick) and a moderate number of 25 modes. The strong oscillations vanish which indicates that the absorber works well for all radiation modes. Since radiation modes with a lower radiation angle are absorbed more efficiently, the absorber remains the same and is applicable to new structures as long as the radiation modes with a significant contribution to the mode matching at the longitudinal discontinuities have a lower radiation angle.

Hybrid propagation method

In a second method reflections at the fictitious walls of propagated radiation modes are also suppressed. With each radiation mode we associate a maximum propagation length $L_{\max} = W' k_z / k_x$. This maximum length can also be written as

$$L_{\max,i} = W' \frac{\beta_i}{\sqrt{\beta_{\text{clad}}^2 - \beta_i^2}}$$

with W' as defined in Fig. 2 and $\beta_{\text{clad}} = 2\pi n_{\text{clad}}/\lambda$, n_{clad} being the refractive index of the cladding. We propose here to omit those radiation modes for which $L_{\max,i}$ is smaller than the total length L in the device. This restriction corresponds to the idea that each radiation mode spreads out with a certain angle. If it is no longer confined in the calculation window, this mode is not taken into account in the calculations. This is justified because the power in these specific radiation modes is located already away from the structure itself. The output power for the slab structure can now be analytically expressed as

$$\text{Power}(L) = \left| a_0^2 \exp(j\beta_0 L) + \sum_{i=1, L_{\max,i} > L}^M a_i^2 \exp(j\beta_i L) \right|^2$$

with a_0 , resp a_i ($i > 0$), the overlap between the guided mode in the first section and the guided mode, resp. radiation mode, in the intermediate section. Note that each term must satisfy a condition, namely $L_{\max,i} > L$, before this term is taken into account in the calculations. This method applied on the slab structure results in the long-dashed line in Fig. 3.

With some modifications this method can also be applied for a grating assisted codirectionally coupled structure. A single radiation mode is now composed of several contributions, because at each boundary of the grating all radiation modes are generated. Each contribution has a different critical length L_{max} .

Grating assisted codirectional coupler

The two methods are illustrated for a grating assisted codirectional coupler. The structure is an InGaAsP/InP based component, described in [5]. Fig. 4 shows the optical power in the two guided modes of the coupler versus the longitudinal direction. Also the total power is shown, giving us an estimate of the radiation loss at the end of the structure. The dashed line is calculated with an absorbing frame and the solid line is the result of the hybrid propagation method. Both methods agree well, indicating a loss of approximately 0.3 dB after one coupling length of about 2200 μm .

As a conclusion we have presented two methods to calculate the radiation loss in e.g. grating assisted codirectional couplers. They are both based on an eigenmode propagation mode with the inclusion of radiation modes. Concerning the estimate of the radiation loss, the two methods agree well.

Acknowledgement

Part of this work was supported by the European RACE project 2069 (UFOS) and by the Belgian IWONL.

References

- [1] G. Griffel, M. Itzkovich, A. Hardy, *IEEE J. Quant. Elec.*, vol. 27, pp. 985-994, 1991
- [2] G. Sztelka, H.P. Nolting, *IEEE Photonics Technology Letters*, in press
- [3] G. Sztelka, *Integrated Photonics Research 1992*, New Orleans, paper TuB4
- [4] J. Chilwell e.a., *J.Opt.Soc.Am.*, p. 742, 1984
- [5] R. Alferness e.a., *Appl. Phys. Lett.*, vol. 59, pp. 2573-2575, 1991

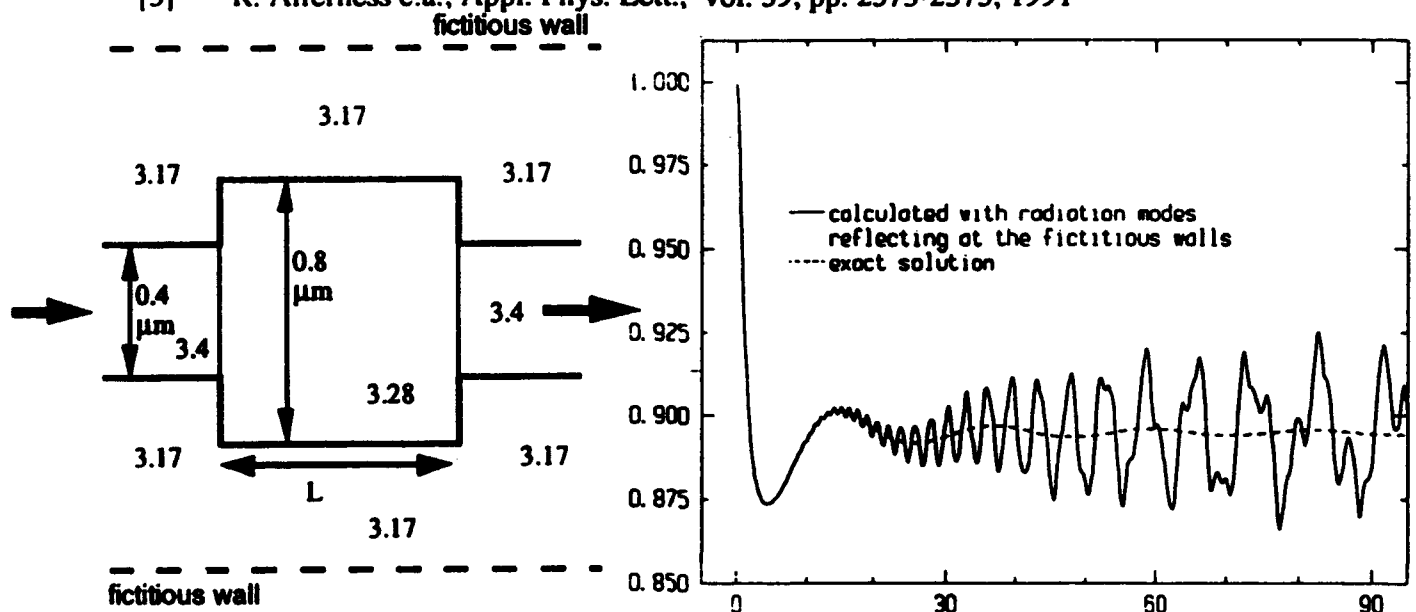


Fig. 1 Schematic of a simple slab structure, for which the amount of output power is calculated for different lengths L of the intermediate section.

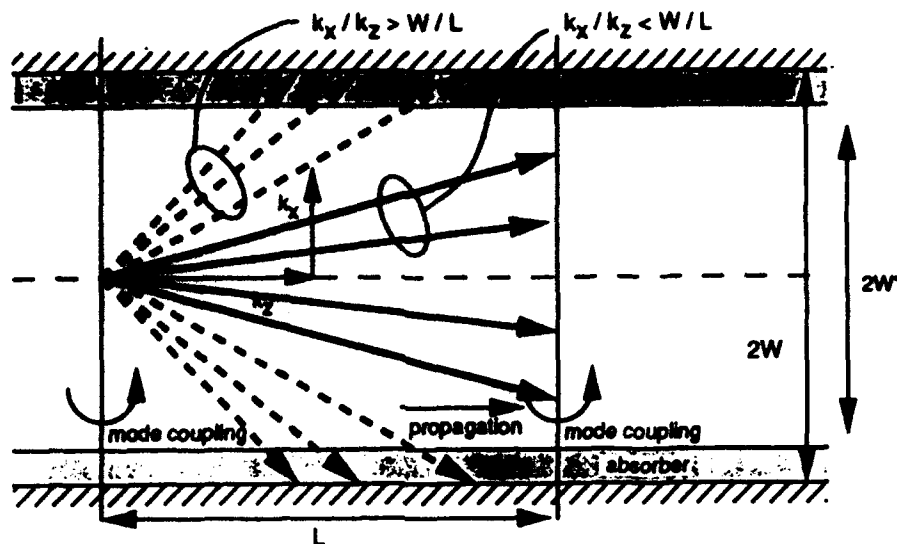


Fig. 2 A k -diagram showing when the radiation modes are no longer confined in the calculation window, defined by the fictitious boundaries.

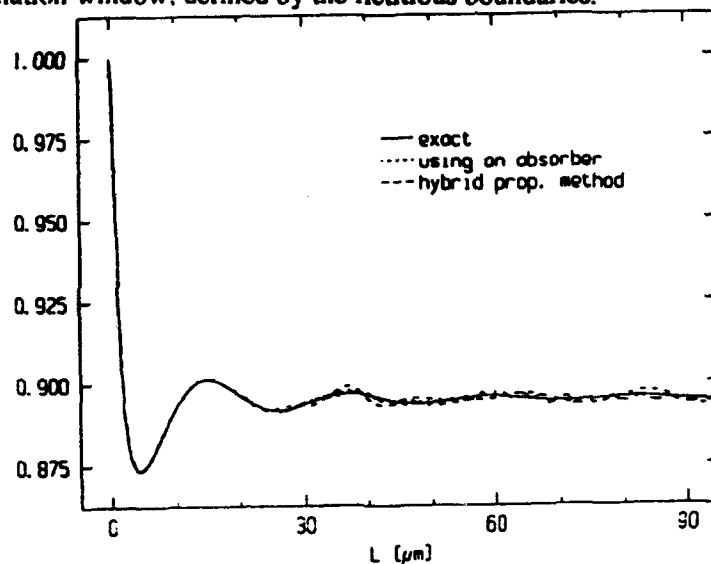


Fig. 3 The amplitude of the guided mode at the output of the simple slab structure in Fig. 1, as a function of the intermediate section length.

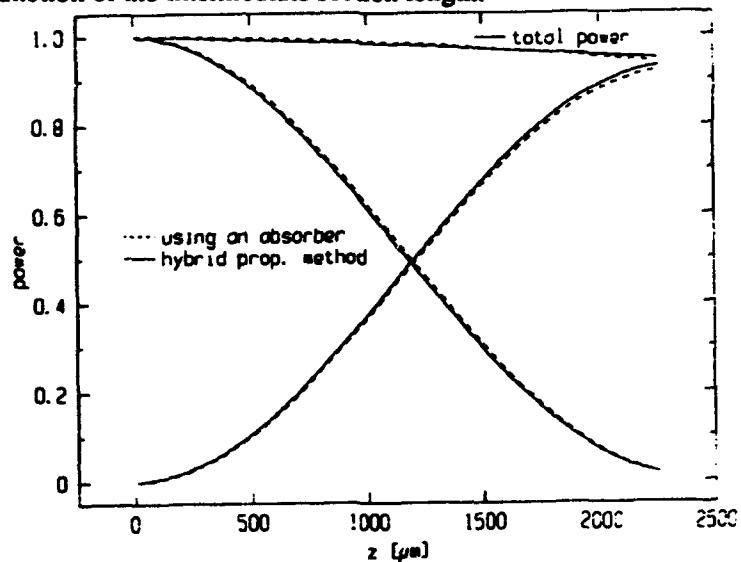


Fig. 4 The power in the two guided modes along the longitudinal direction of the grating assisted codirectional coupler. Also the total power is shown.

**Non-Uniform Finite Difference Analysis of
Quantum Layer Dielectric Ridge Waveguide Structures**

**Klein L. Johnson
University of Minnesota
Dept. of Electrical Engineering
4-174 EE/SCI Bldg.
200 Union Street SE
Minneapolis, MN. 55455
(612) 625-3841**

**Anand Gopinath
University of Minnesota
Dept. of Electrical Engineering
4-174 EE/SCI Bldg.
200 Union Street SE
Minneapolis, MN. 55455
(612) 625-3054**

The semi-vectorial finite difference method has been extended to non-uniform grids by reformulating the matrix equations, making possible the efficient analysis of quantum layer structures.

Finite difference methods for the analysis of dielectric optical waveguides have been extensively explored in literature. [1-8] The semi-vectorial method of [6] is of particular interest to these authors because it allows the evaluation of polarized modes (quasi-TE or quasi-TM) in dielectric layer structures by casting the problem in the form of a simple eigenvalue equation $Ax=\lambda x$.

As presented, the method takes the standard finite difference approach of enclosing the guide cross section in a box over which is imposed a uniform mesh, the index of refraction in the region being a point function defined at the nodes. Discontinuities in refractive index are allowed to occur only at the midpoint of adjacent nodes, and the field on the outer boundary may either be set to zero or modified to represent an exponential decay.

The fact that the mesh is uniform in the lateral directions proves very restrictive in the analysis of quantum well structures where the quantum layer thicknesses may be on the order of $1/1000^{\text{th}}$ the total guide dimension. The large number of node points necessary for modelling such structures gives rise to finite difference matrices of extremely high order.

In order to allow greater freedom in the analysis of waveguides whose geometries contain large dimensional differences, as well as make efficient use of computer resources, the method of [6] was reformulated so that a grid with variable node spacings may be used [1-2]. This approach yields a dramatic reduction in the number of mesh points necessary for guide representation, and by strategic arrangement of the node points, may also lead to an overall improvement in accuracy. [1]

The semi-vectorial finite difference approach is well documented in the reference, so little will be said here about the actual method. The key point to this paper is the inclusion of the full expansion of the finite difference operator for the approximation of the second derivatives of the Laplacian in the matrix equations as derived in [6]:

$$\frac{\partial^2 E}{\partial y^2} \Big|_{z_c} = \frac{E_N}{h_n(h_n+h_s)} - \frac{E_C}{h_n h_s} + \frac{E_S}{h_s(h_n+h_s)}$$

$$\frac{\partial^2 E}{\partial x^2} \Big|_{z_c} = \frac{E_W}{h_w(h_w+h_e)} - \frac{E_C}{h_w h_e} + \frac{E_E}{h_e(h_w+h_e)}$$

When the method is reformulated in this manner, the spacings between the adjacent rows and columns of nodes can be arbitrarily set, allowing a particular guide geometry to be accurately represented with a minimum number of nodes. Of course, the accuracy of any finite difference method will suffer as the node spacings are increased. Therefore, care must be taken to assure that the mesh is fine enough to give an accurate representation of the field.

The semi-vectorial finite difference method, reformulated in

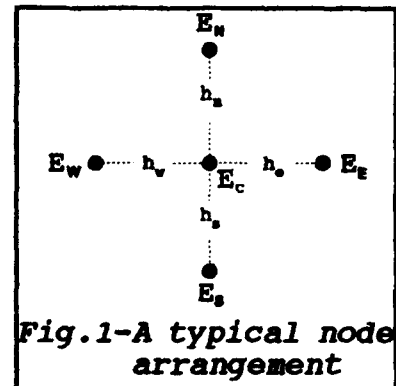


Fig.1-A typical node arrangement

this manner, has been used to analyze ridge waveguide structures previously analyzed in references [4],[6], and [9]. In all cases, excellent agreement with the published results were obtained using significantly fewer mesh points. This is important, because cpu time typically is non-linear in N , where $N=N_x*N_y$ is the order of the matrix, N_x and N_y being the number of mesh points in the lateral directions.

The multiple quantum well structure MQW1 shown in Fig.2 was examined to determine the field profile and effective index of the fundamental quasi TE mode at a wavelength of 860 nm. For comparison purposes, the calculation was performed using both a uniform mesh and the non-uniform mesh depicted in Fig.3. In order to observe the convergence behavior as the number of nodes was increased, the non-uniform calculation was performed several times for different values of N_y . (N_x was held constant in all cases).

Only one uniform mesh calculation was possible due to constraints imposed by the geometry of the guide and the computer used. (CRAY XMP with 64 bit floating point precision). Indeed, this is precisely the reason why the non-uniform implementation was investigated in the first place.

The results of this work are presented in Fig.4. As can be seen, there is very little improvement in the calculated effective index as N is increased by nearly a factor of 5, from 7752 to 38250. For $N=7752$, the effective index has converged essentially to within 1×10^{-5} of its asymptotic value, which agrees very well with the uniform result obtained with $N=38250$. The reduction in cpu time is just as dramatic.

The upward convergence trend of the non-uniform method was unexpected, and has yet to be explained. Similar behavior has been observed in [4], where index discontinuities were placed at the mesh points instead of between them. Where uniform meshes have been used, the convergence has always been observed to be in a downward direction.

Fig. 5 is a plot of the fundamental quasi-TE field profile calculated using the non-uniform method.

In conclusion, a non-uniform implementation of the semi-vectorial finite difference method has been used to evaluate polarized modes in a variety of dielectric waveguides, including quantum well structures. The non-uniform approach has three primary

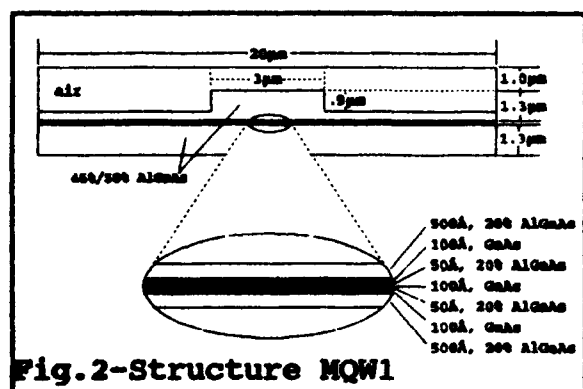


Fig.2-Structure MQW1

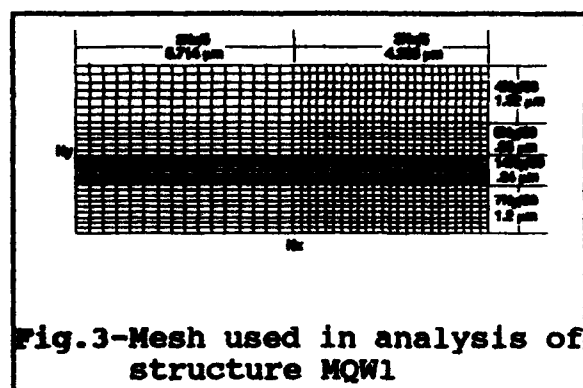


Fig.3-Mesh used in analysis of structure MQW1

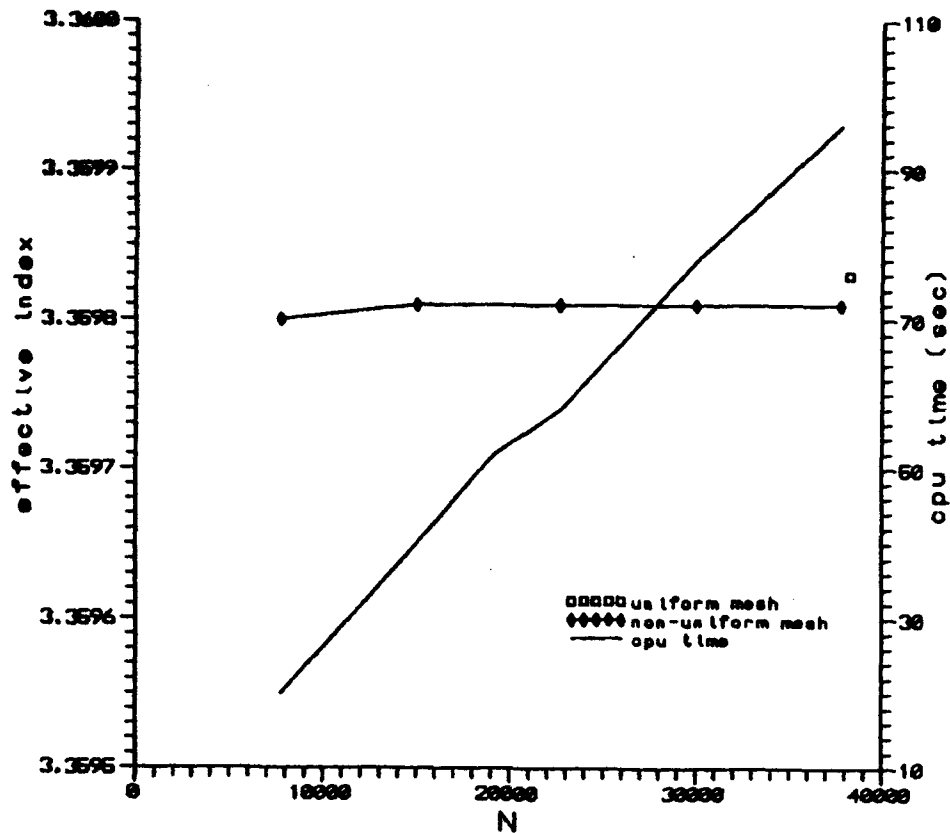


Fig. 4- Graph of effective index and cpu time versus total number of nodes in F.D. mesh for quantum well structure MQW1 of Fig. 2 using the uniform and non-uniform grids described in the text.

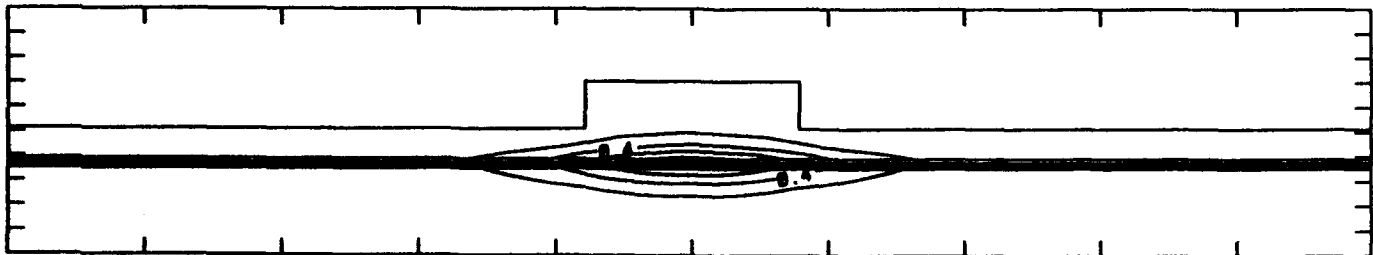


Fig. 5- Contour plot of E-field for fundamental quasi-TE mode of structure MQW1. $\lambda=860\text{nm}$.

advantages: 1) It allows the efficient modelling of structures with large differences in layer thicknesses which would otherwise require unreasonably large finite difference matrices, 2) the number of mesh points may be reduced while still maintaining a high degree of accuracy, which 3) leads to a dramatic reduction in cpu time.

REFERENCES:

- [1] S. Seki, T. Yamanaka, and K. Yokoyama, "Two-Dimensional Analysis of Optical Waveguides with a Non-Uniform Finite-Difference Method", IEE Proc., Vol. 138, Pt.J, No.2, pp.123-127, April 1991.
- [2] C. Kim and R. Ramaswamy, "Modelling of Graded-Index Channel Waveguides Using Nonuniform Finite Difference Method", Journal of Lightwave Technology, Vol.7, No.10, pp.1581-1589, Oct. 1989.
- [3] R. Lagu and R. Ramaswamy, "A Variational Finite-Difference Method for Analyzing Channel Waveguides with Arbitrary Index Profiles", IEEE Journal of Quantum Electronics, Vol. QE-22, No.6, pp.968-976, June 1986.
- [4] M. Robertson, S. Ritchie, and P. Dayan, "Semiconductor Waveguides: Analysis of Optical Propagation in Single Rib Structures and Directional Couplers", IEE Proc., Vol.132, Pt.J, No.6, pp.336-342, Dec. 1985.
- [5] K. Bierwirth, N. Schulz, and F. Arndt, "Finite-Difference Analysis of Rectangular Dielectric Waveguide Structures", IEEE Trans. on MTT, Vol. MTT-34, No.11, pp.1104-1113, Nov. 1986.
- [6] M.S. Stern, "Semivectorial Polarised Finite Difference Method for Optical Waveguides with Arbitrary Index Profiles", IEE Proc., Vol. 135, Pt.J, No.1, pp.56-63, Feb. 1988.
- [7] M.S. Stern, "Semi-Vectorial Polarised H Field Solutions for Dielectric Waveguides with Arbitrary Index Profiles", IEE Proc., Vol.135, Pt.J, No.5, pp.333-338, Oct. 1988.
- [8] E. Schweig and W. Bridges, "Computer Analysis of Dielectric Waveguides: A Finite Difference Method", IEEE Trans. on MTT., Vol.MTT-32, No.5, pp.531-541, May 1984.
- [9] B. Rahman and J. Davies, "Vector H Finite Element Solution of GaAs/GaAlAs Rib Waveguides", IEE Proc., Vol.132, Pt.J, No.6, pp.349-353, Dec. 1985.
- [10] J.H. Wilkinson, "The Algebraic Eigenvalue Problem", (Clarendon Press, 1965)
- [11] R. Burden and J. Faires, "Numerical Analysis", (Prindle, Weber, and Schmidt, 1985)

Coupled-Mode Theory of Vertically Integrated Impedance-Matched Waveguide/ Photodetectors

Ewan M. Wright
Optical Sciences Center
University of Arizona
Tucson, AZ 85721, USA
(602) 621 8267

Raymond J. Hawkins and Robert J. Deri
Lawrence Livermore National Laboratory
P. O. Box 808, Livermore, CA 94550, USA
(510) 422 0581

The future success of guided-wave optoelectronic circuits relies on the development of efficient photodetectors. In conventional photodetector designs the absorbing layer is grown directly adjacent to the waveguide core and the transfer of energy proceeds by evanescent field coupling.^{1,2,3} This strategy leads, however, to small detector absorption coefficients and hence long detector lengths for high quantum efficiency, typically 100 μ m or more, with a concomitant increase in the device capacitance and slow frequency response.^{2,3} Reducing the detector length is therefore a key issue in the development of efficient waveguide photodetectors.

In response to the need for shorter detector lengths Deri and Wada⁴ proposed the Vertically integrated Impedance-Matched waveguide/photodetector, or VIM diode, in which a thin matching-layer is inserted between the waveguide core and the absorbing layer. The VIM detector structure is shown in Fig. 1 along with the parameter values used in the simulations. VIM diode operation can be modelled as a two-step process:⁵ The field coupled into the waveguide is transferred to the matching layer in the double-moded waveguide/matching-layer structure prior to the absorbing region. By judicious choice of the extended-matching-layer length M the optical power then can be concentrated very close to the absorber thereby greatly increasing the evanescent coupling to the absorber and reducing the device length. Device length reductions of 500% over conventional structures have been reported by Deri et al.⁶ in agreement with numerical simulations using the beam propagation method (BPM).⁵

In this talk we shall present a simple coupled-mode theory (CMT) which provides a particularly convenient way of understanding the physics of VIM devices. For example, the CMT exposes the relation between the spatial absorption transients seen in experiments⁶ and BPM simulations,⁵ and the nonhermitian properties of the underlying modes of the problem. Furthermore, CMT allows one to reduce the parameter space of the problem and to extract the key parameters for device optimization, a formidable if not impossible task based on time-consuming BPM simulations alone. Using the CMT we have discovered a new regime of operation of VIM devices in which spatial transients can be eliminated so that the diode absorption is exponential as in conventional devices.

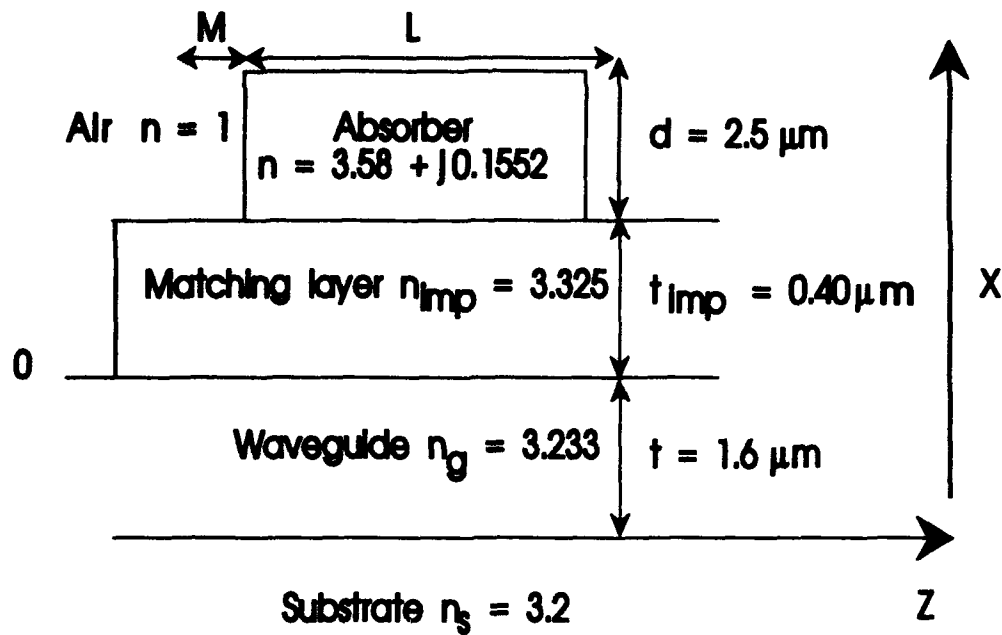


Fig. 1. VIM detector structure used in the simulations.

The CMT is built upon the two-step model outlined above. Before the absorber the waveguide-matching layer system is assumed to support two supermodes described by amplitudes $a_{1,2}$. We assume that the combinations $a_{\pm} = (a_1 \pm a_2)/2$ correspond to distributions concentrated in the waveguide (+) and the matching layer (-). For an extended-matching-layer length M and initial excitation of the waveguide we then have

$$a_+(M) = \cos(\pi M/2L_c) \quad , \quad a_-(M) = i \sin(\pi M/2L_c) \quad , \quad (1)$$

where L_c is the coupling length. In the absorbing region the coupled-mode equations are

$$\frac{d}{dz} \begin{bmatrix} a_+ \\ a_- \end{bmatrix} = \begin{bmatrix} 0 & i\pi/2L_c \\ i\pi/2L_c & -\alpha/2 \end{bmatrix} \begin{bmatrix} a_+ \\ a_- \end{bmatrix} = M \begin{bmatrix} a_+ \\ a_- \end{bmatrix} \quad , \quad (2)$$

where α is the intensity absorption coefficient of the matching layer due to the absorber. Here we have assumed that the field is absorbed only when it is concentrated in the matching layer, thus only a_- is subject to absorption. The CMT equations are to be solved subject to the initial conditions (1) due to the action of the extended-matching-layer.

The solution of Eqs. (1) and (2) is straightforward and can be compared to simulations of the BPM. The CMT parameters L_c and α are obtained from a single BPM simulation without the absorber. Figure 2a shows an example of the CMT results for the total integrated absorption versus diode length for the case shown in Fig. 1 ($\alpha = 0.1\mu\text{m}^{-1}$, $L_c = 26\mu\text{m}$), and is in excellent agreement with previous BPM simulations.⁵ For 90% quantum efficiency the minimum diode length is seen to be $L = 25\mu\text{m}$ for $M = 17\mu\text{m}$. The CMT results also show the spatial transients previously reported,^{5,6} as evidenced by the crossing of the curves for different values of M .

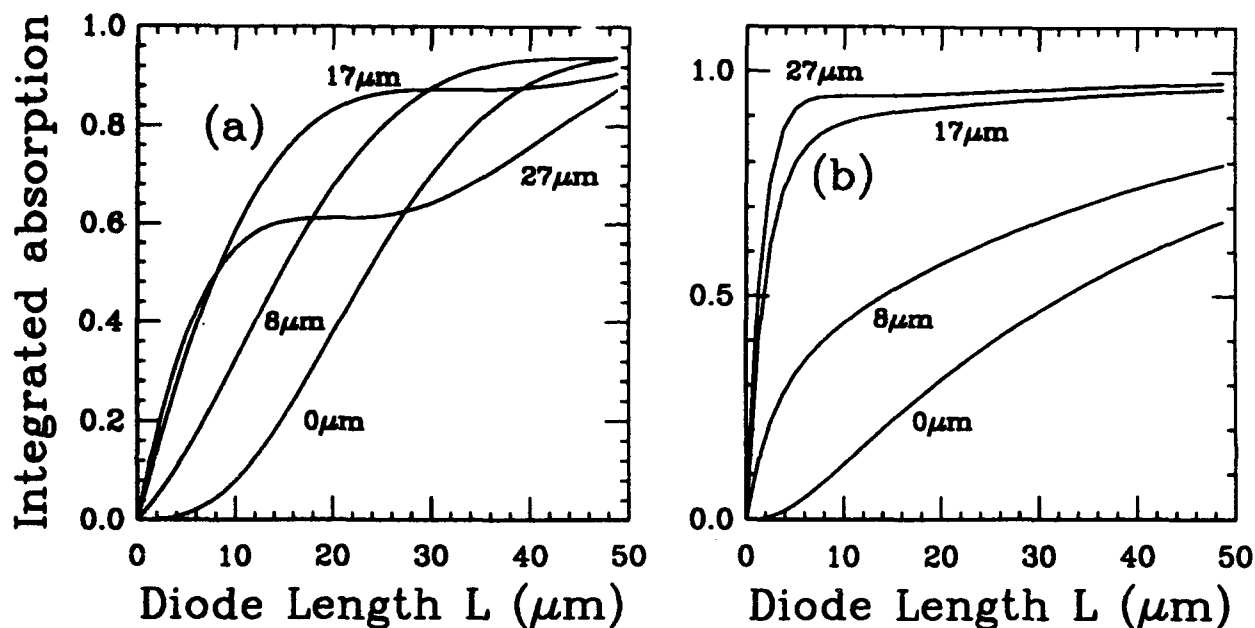


Fig. 2. Total integrated absorption versus diode length: (a) $\alpha = 0.1\mu\text{m}^{-1}$, $L_c = 26\mu\text{m}$, and (b) $\alpha = 0.6\mu\text{m}^{-1}$, $L_c = 26\mu\text{m}$.

The CMT provides a simple physical picture of the spatial transients. First we note that any solution of the propagation problem (2) can be expanded in terms of the eigenvectors of the 2×2 nonhermitian matrix M , which by their nature are biorthogonal, as opposed to power-orthogonal, and have different phase-shifts and exponential absorption coefficients. Now, the initial condition (1) generally corresponds to a linear superposition of the two eigenvectors so that the propagating field is a sum of two exponentially decaying components with different phase-shifts, thus giving rise to the observed spatial transients. Analysis of the coupled mode equations shows that spatial transients are always present if $\alpha L_c < 2\pi$, as was the case in all prior BPM simulations.⁵ However, for $\alpha L_c > 2\pi$ it is possible to mode-match the input (1) to a solitary biorthogonal eigenvector, and hence obtain exponential gain with no spatial transients, by appropriate choice of the extended-matching-

layer length M . This establishes the dimensionless parameter αL_c as a key parameter in device design. Figure 2b shows the evolution of the total integrated absorption as a function of diode length for $\alpha = 0.6\mu\text{m}^{-1}$, $L_c = 26\mu\text{m}$ so that $\alpha L_c > 2\pi$. In this case the spatial transients are notably absent, thus offering a new mode of operation for VIM diodes which may further reduce the device length.

In summary, we shall present a simple CMT of VIM diode operation which exposes their basic operating principles and promises to reveal new designs which may further reduce the device length.

This work was performed, in part, under the auspices of the US Department of Energy by Lawrence Livermore National Laboratory under contract W-7405-ENG-48.

REFERENCES

1. P. Cinguino, et al., Appl. Phys. Lett. **50**, 1515 (1987).
2. F. Mallecot, et al., Appl. Phys. Lett. **53**, 2522 (1988).
3. M. Erman, J. Lightwave Technol. **LT-6**, 399 (1988).
4. R. Deri and O. Wada, Appl. Phys. Lett. **55**, 2712 (1989).
5. R. J. Hawkins et al., Opt. Lett. **16**, 470 (1991).
6. R. J. Deri et al., Appl. Phys. Lett. **56**, 1737 (1990).

A Novel Device Structure for Optical Switches: Three Mode Interference (3MI)

H. - P. Nolting, M. Gravert

Heinrich-Hertz Institut für Nachrichtentechnik Berlin GmbH,
Einsteinufer 37, 1000 Berlin-10, Germany, ++ 30 31002 427

Optical switches with high switching efficiency and low loss are necessary for future optical communication systems. Recently, switches with multiple quantum wells (MQW) of different kind (QCSE, BRAQWET, WSL[1]) for higher efficiency are reported, which sometimes suffer of high loss. Here a novel device structure (similar to [2]) will be proposed and investigated theoretically, which may overcome the problem of high cross talk in Mach-Zehnder type interferometer switches on the basis of the above mentioned layers.

Fig. 1 shows a directional coupler constructed of 3 independent waveguides, where both the outer waveguides are monomode, passive, low loss and serve as input / output ports. The following discussion is based on two different numerical examples Ex1 and Ex2 at wavelength $1.55 \mu\text{m}$, which are described in the table and fig. 1:

	$t_{\text{WG}} [\mu\text{m}]$	$t_{\text{gap}} [\mu\text{m}]$	n_{gap}	n_{WG}	n_{control}	$\alpha [\text{cm}^{-1}]$
Ex1	0.5	1.5	3.2	3.3	3.4	100
Ex2	0.5	0.75	3.2	3.3	3.25	10

The center waveguide may be a multimode waveguide containing the MQW layers and is used as the electrical or optical *control* structure of the switch. Thus this waveguide may be lossy (up to 10 or 100 cm^{-1} , depending on example Ex2 or Ex1) and the refractive index of this layer can be changeable by Δn . In the coupling region the total structure is multimode and the behaviour of the different modes as a function of the thickness of the center waveguide is given in fig. 2. It can be seen by BPM calculation, that the device acts as a coupler with a short coupling length at the 3 mode interference (3MI) crossings of the diagram (marked by a circle) and with a very large coupling length at the two parallel lines (2MI) in between. For switching purposes we use the asymmetric behaviour of the device in the region close to the resonance coupling of the 3 modes. If we change the refractive index of the control layer (or the thickness, or the wavelength), the output energy changes from resonant coupling (energy in the cross state) over an asymmetric coupler with nearly all energy in the same waveguide to the very long two mode interference coupler (parallel state). This is shown for different Δn in fig. 3. The cross talk here is always present but low for a refractive index change of 10^{-2} , which can be realized with suitable MQW-layers.

The advantage of this novel device structure is, that in the case of lossy MQW-layers the total device is symmetric in relation to the passive waveguides. Thus the cross talk in the device is always low, only the output energy in the cross state is reduced a little compared to the parallel state, which is demonstrated in the fig. 4. Due to the fact, that the coupling length of the 3MI device is about a factor of 10 lower compared to the 2MI coupler, the total loss is also reduced drastically.

Suppose we have some freedom in the design of the switch in respect to the choice of the refractive index of the layers and the point of operation in the eigenmode diagram, where multiple three mode interaction points are possible (fig.2). The calculations show the followings trends:

- * For high values of the refractive index of the control layer the device is short (low loss influence) and a high Δn for switching is necessary.
- * For large thicknesses of control layer (higher order of modes) Δn decreases slowly, but device length increases.

The first point has a strong influence, which is demonstrated in the reduction of Δn from 4 to 1 10^{-2} in Example Ex1 and Ex2.

This 1 dimensional calculation shows the principal behaviour of the device, which have also been verified by 2D FD calculations. A real implementation can be realized in a vertical or a horizontal waveguide arrangement.

One advantage of this structure is the possibility to use the center waveguide as optical input waveguide of a control wave for optical switching of the device by nonlinear optical effects. Thus optical signal and control paths can be easily separated.

In the cross state of the switch we have to fulfill a *resonant* condition, but in the parallel state we have a *digital* switching behaviour, that means that beyond a specific switching voltage (optical power), the state maintains stable. To be sure to meet the resonance condition we can use a tapered velocity coupler design for the passive waveguide, thus reducing the fabrication tolerances. For reducing the cross talk a delta beta reversal design can be used. This will be shown on the conference in detail.

To reduce the cross talk of the switch by several orders of magnitudes below the usual 15 dB a cut off switching design of the third mode can be used. If the effective refractive index of the center waveguide operates close to the eigenmode value of the outer waveguides, it is possible to switch the center waveguide structure from a leaky mode condition (sinusoidal behaviour inside) to an evanescent mode condition (exponential behaviour inside). In the latter case the coupling of the outer waveguides decrease drastically to an uncoupled waveguide condition by the larger separation (e. g. if the control waveguide is multimode) of both waveguides. The field distribution are shown in fig. 5 and the switch behaviour in fig. 6.

By "combinig" two 3MI structures to act as a 5MI Y-branch, as shown in fig. 7, the following advantages can be achieved:

- * *symmetric* power divider even with slight fabrication tolerances in the passive state, leading to a symmetric power output for both ports in a switching application,
- * *digital* switching behaviour for both outputs stages, when activating one of the two electrodes.

The device improvements described above can also be used for the 5MI Y branch. For optimum loss and cross talk behaviour the thicknesses have to be optimized for given refractive indices. This device structure is very attractive for optical space switch matrices.

Conclusion

We have proposed and theoretical investigated a novel switch design, which is suitable for optical *lossy* material with high refractive index change by electrical or optical influence like MQW layers. The 3MI switch has a *resonant* and a *digital* state and the 5MI Y branch two *digital* states of operation. The cross talk is always low, even in the presence of loss. To meet the fabrication tolerances of the resonant condition a *tapered velocity design* and/or a *delta beta reversal design* can be used. For extremely low cross talk an operation at *cut off* point is advisable.

- [1] J. E. Zucker, T. Y. Chang, M. Wegener, N. J. Sauer, K. L. Jones and D. S. Chemla, "Large Refractive Index Changes in Tunable-Electron-Density InGaAs/InAlAs Quantum Wells", Photonics Technology Letters, Vol. 2, No. 1, January 1990, p29-31.
- [2] T. Yamaguchi, K. Tada, T. Ishikawa, "A Novel Device Structure of Vertical Multiple Quantum Well Directional Coupler Switch for Low Switching Voltage", Integrated Photonic Research Conference, April 13-16, 1992 New Orleans, Louisiana, Technical Digest Ser. Vol. 10, paper WH4-1, pp 334-335.

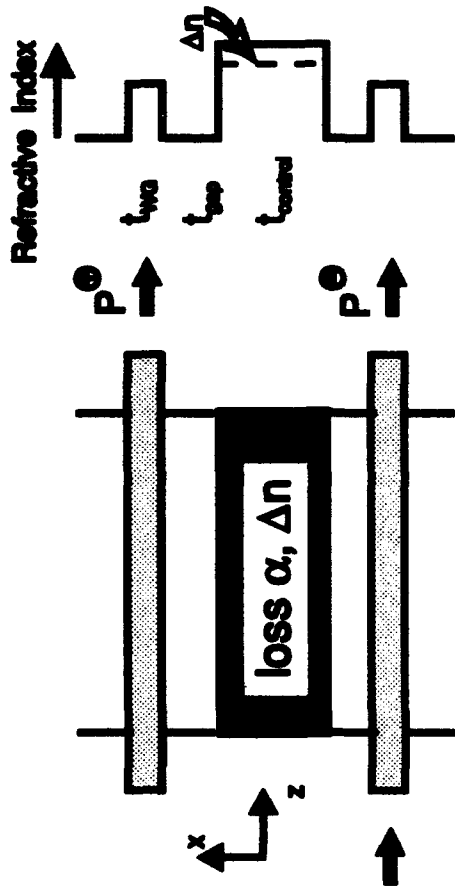


Fig. 1 : Device Structure and 1D Refractive Index Profile of Three Mode Interference (3MI) Switch

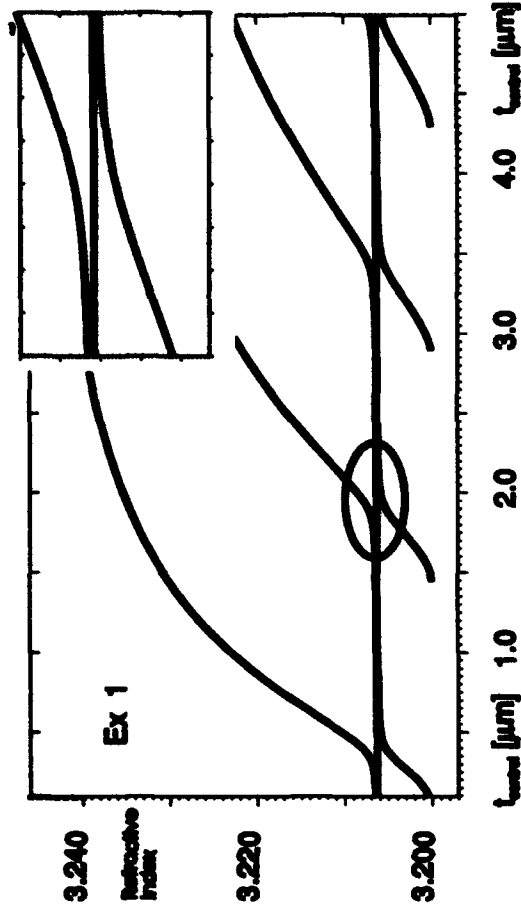


Fig. 2 : Mode Behaviour of Three Mode Switch

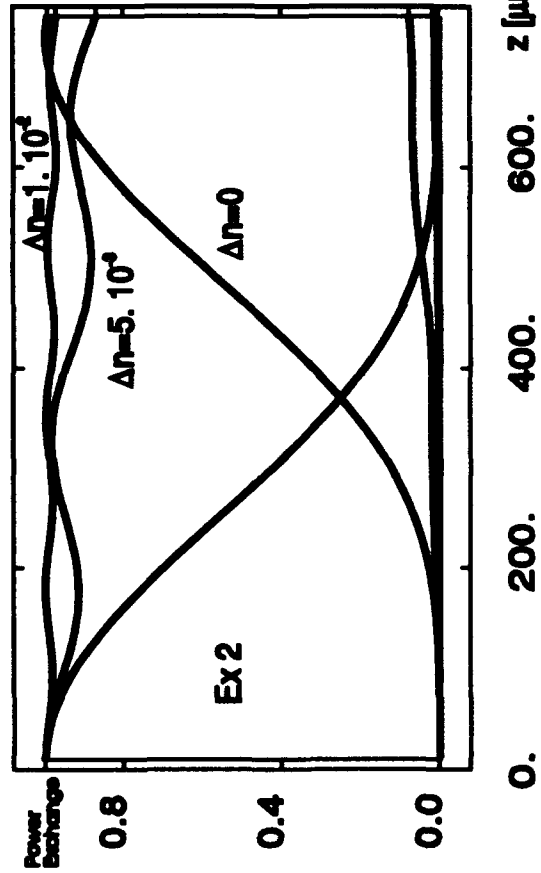


Fig. 3 : Cross and Parallel State of Lossless Switch

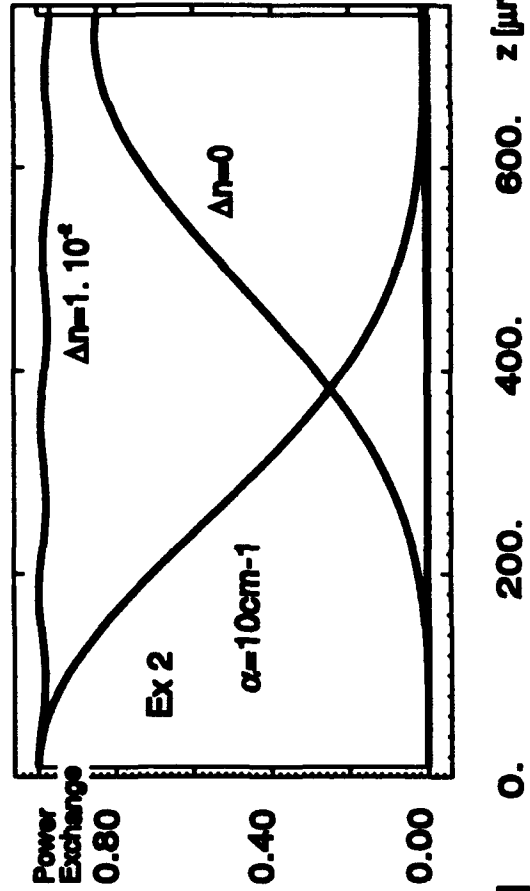


Fig. 4 : Cross and Parallel State of Lossy Switch

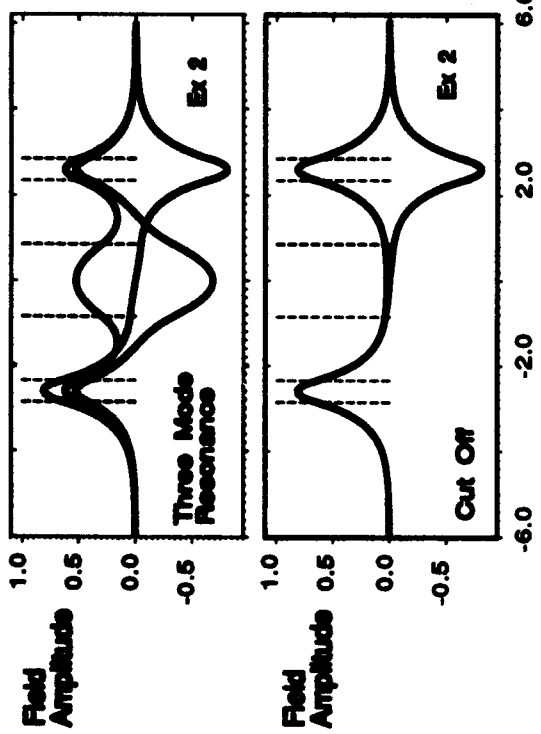


Fig. 5 : Mode Behaviour at Cut Off

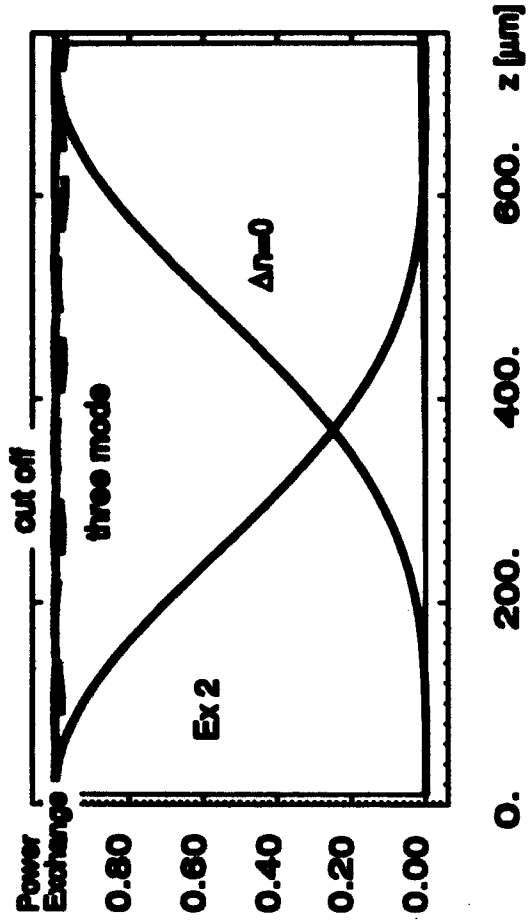


Fig. 6 : Switching Behaviour due to Cut Off

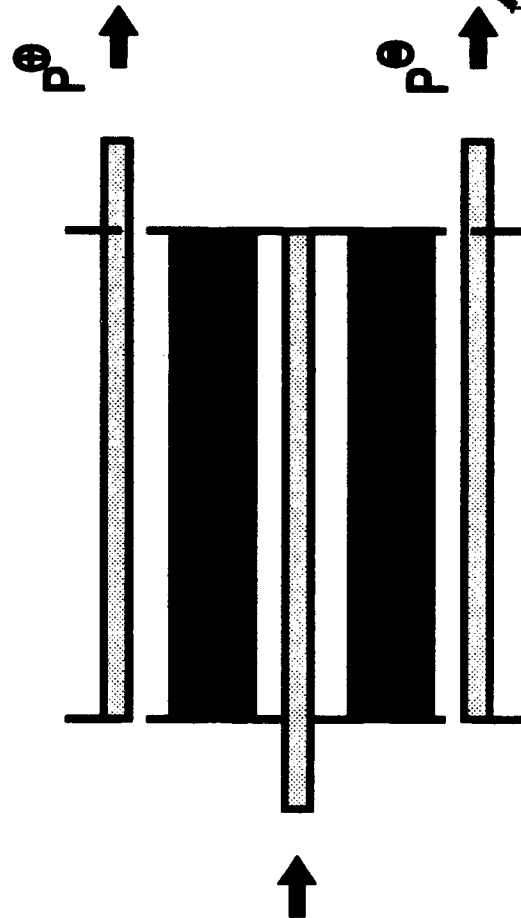


Fig. 7 : Structure of 5MI Y Branch Switch

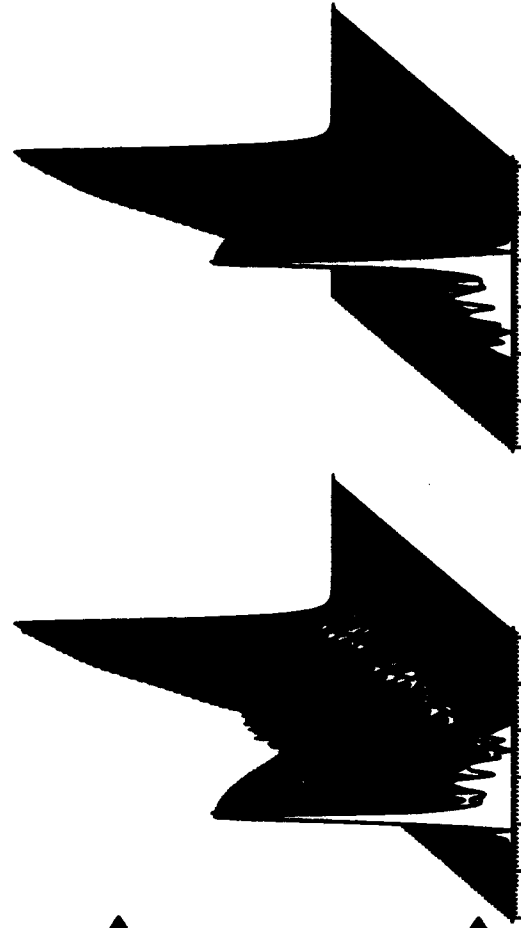


Fig. 8 : BPM Calculation of 5MI Y Branch Switch States

Integrated Optical Pulse Shaping

Kent B. Hill and David J. Brady
 University of Illinois at Urbana-Champaign
 Department of Electrical and Computer Engineering
 Beckman Institute
 Urbana, Illinois 61801
 (217)244-6898 (217)244-5558

1 Introduction

Advances in pulsed lasers have resulted in a growing need for methods and devices for controlling and exploiting the temporal bandwidth of pulsed fields. Mode-locked diode sources with subpicosecond pulse widths have recently been integrated [1]. We consider high-resolution integrated systems for modulating the bandwidth of such pulses. These systems are capable of creating arbitrarily-shaped optical pulses with bandwidths limited only by the bandwidth of the pulsed source. Applications for pulse-shaping devices exist in communications, optical computing, and nonlinear spectroscopy.

We consider integrated systems which use high spatial bandwidth reflection holograms to control the temporal bandwidth of reflected pulses. To analyze the impulse response of such holograms, a numerical method has been developed which efficiently and accurately calculates the reflection spectrum of arbitrary one-dimensional holograms. In Section 2, we describe an optical pulse-shaping system and consider materials which may be used in its fabrication. In Section 3, we discuss some difficulties that arise in methods which have been previously used to analyze multiple-grating holograms. We then describe a numerical method which overcomes these difficulties and provides a means of analyzing complicated one-dimensional holograms. A pulse-coding scheme is also considered. In Section 4, some numerical results showing the impulse response of various holograms are presented.

2 A Pulse Shaping System

In Fig. 1 we show an experimental configuration that may be used for optical pulse shaping. The reference

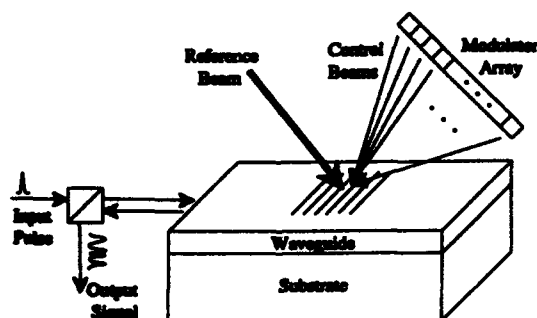


Figure 1: A holographic pulse-shaping system.

beam and the control beams interfere to form a spatial intensity distribution on the waveguide. The waveguide is doped with an active species that responds to the intensity and creates a hologram in the waveguide. The modulator array is used to control the amplitude and phase of each of the control beams. The interference of each control beam with the reference beam creates a sinusoidal modulation whose frequency is determined by the angle between the control beam and the reference beam. In this manner, a holographic modulation is created in the waveguide. The input pulse is injected into the waveguide, and the output pulse is reflected from the hologram in the waveguide. The wavelengths of the beams are chosen

so that the control beams are absorbed by the waveguide to create the modulation, and the signal beam is not absorbed.

As an example, the waveguide in this system may be fabricated with methyl orange doped in a thin film of polyvinylalcohol. Methyl orange absorbs light at 514 nm and undergoes a *cis-trans* conformation change which changes the index of refraction. The hologram may be probed using an infrared pulse which is not absorbed by the methyl orange. This system may also be fabricated using GaAs waveguides in which photorefractive effects may be used to record holograms. These effects can occur on submicrosecond time scales [2].

There are several advantages in using this waveguide configuration for pulse-shaping applications. First, since the waveguide is thin, it may be heavily doped so that all of the energy in the control beams is absorbed in the waveguide. In volume geometries, the absorption must be weak so that the intensity can be uniformly dispersed throughout the volume. This means that the holographic modulation can be much stronger in the waveguide geometry. Second, since Bragg-matching constraints are relaxed in the direction normal to the waveguide, only one reference beam is needed for all of the control beams. Finally, the waveguide geometry is compatible with integrated circuit technology.

3 Impulse Response of Multiple-Grating Holograms

Volume holographic scattering is most commonly analyzed using the coupled mode formalism developed by Kogelnik [3]. Kogelnik's analysis focuses on holograms in which the modulation is sinusoidal, which we refer to as the single grating case. To be useful for pulse shaping, a hologram must consist of a number of gratings. Scattering in multiple grating holograms has previously been analyzed using coupled mode equations based on many-wave Bloch expansions [4, 5] and by finite element integrations [6]. The number of coupled mode equations required in many Bloch expansions may grow combinatorially with the number of gratings. The problem is considerably simplified if we limit our analysis to one-dimensional reflection holograms, but even in this case Bloch expansions have not been used to solve problems involving more than a few gratings. Finite element integrations are performed by representing the hologram as a large stack of homogeneous thin films. The characteristic matrix method for thin-film stacks is then used to model the hologram.

We have developed a numerical method to find the impulse response of multiple-grating holograms which is based on Kepler discretization for problems in celestial mechanics [7, 8]. This method is used to solve the one-dimensional problem of reflection from a hologram in which the modulation $V(x)$ varies only along the direction of propagation. Consider a pulse propagating along the \hat{x} axis with polarization normal to \hat{x} that is reflected by this modulation. The modulation is zero everywhere except between the boundaries of the hologram at $x = 0$ and at $x = L$. We solve the wave equation

$$\frac{\partial^2 \Psi}{\partial x^2} - \frac{1}{c^2}(1 + V(x))\frac{\partial^2 \Psi}{\partial t^2} = 0. \quad (1)$$

for the reflected field under the boundary conditions that a known pulse is incident on the holographic region from negative x and that only a positive propagating field exits the hologram at $x = L$. Ψ is the scalar field, and c is the speed of light in the unmodulated dielectric.

The impulse response of a hologram is found by solving Eq. 1 in the temporal Fourier domain where, for a given frequency, we can write

$$\frac{d^2 \psi}{dx^2} + k^2(1 + V(x))\psi = 0, \quad (2)$$

where $k^2 = \omega^2/c^2$. Applying the boundary condition that a field given by $\exp(j\omega t)$ leaves the hologram at $x = L$, we solve Eq. 2 numerically and find the reflection coefficient, $\Gamma(\omega)$, at $x = 0$. The numerical algorithm uses Deuffhard's discretization of Eq. 2, and, starting at $x = L$, takes small steps back to $x = 0$ to find $\psi(0)$. Polynomial extrapolation is used at each step until the desired accuracy is achieved. Once $\Gamma(\omega)$ is determined over a suitable range of frequencies, FFT techniques are used to find the inverse Fourier transform which yields the impulse response. This method has proved to be very accurate, and it is able to efficiently solve problems with arbitrary modulations, $V(x)$.

Using this numerical method to analyze various modulations, it can be seen that the impulse response of a hologram is nearly proportional to the modulation of the hologram for even strongly scattering holograms. Based on this fact, we have developed a coding scheme which modulates the amplitude of a hologram to produce arbitrarily-shaped pulses. The amplitude modulation is performed by writing a multiple-grating hologram in which the amplitude and phase of each grating is controlled independently. This control can be achieved using the integrated system presented in the previous section.

4 Numerical Results

Using the numerical method described in the previous section, the responses of various holograms have been determined. In Fig. 2 the reflection spectra, $|\Gamma(\omega)|$, and the envelope of the impulse responses, $|r(t)|$, are plotted for a single grating. In Fig. 2a, the strength of the modulation is weak while in Fig. 2b, it is strong. A normalized time parameter $t' = t/\tau$, where $\tau = L/c$ is the transit time through the hologram, is

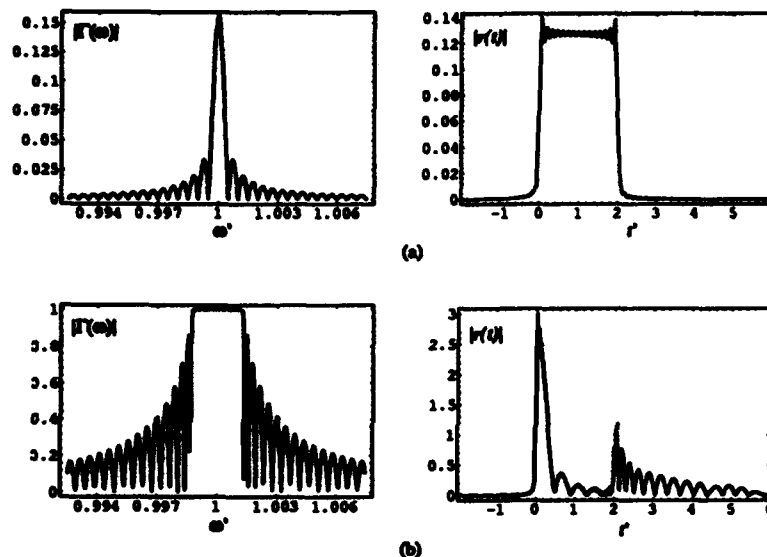


Figure 2: Responses of single grating holograms. $V(x) = A \cos(Kx)$. (a) $A = 0.0001$. (b) $A = 0.005$.

used. According to the Bragg condition, the maximum reflection from a grating with frequency K occurs when $\omega = \omega_0 = Kc/2$. The normalized frequency ω' is given by $\omega' = \omega/\omega_0$. It can be seen that for weak modulation, the impulse response is a simple square wave of duration 2τ as predicted by coupled-mode theory. For strong modulation, multiple scattering effects become significant, and the response continues beyond $t = 2\tau$. There is also a reflection at the output interface which can be seen in the impulse response at $t = 2\tau$. This reflection is caused by a mismatch in the effective index at the interface even though the average index was assumed to be the same on both sides of the interface.

In Fig. 3, the response of a grating with a chirp in its spatial frequency is shown. The phase of the impulse response is seen to follow the phase of the hologram. This effect may be used recover short pulses which have been broadened by dispersion in optical fibers.

Finally, in Fig 4, the response of a hologram which has been coded to produce the bit sequence 1010001110110010 is shown. It can be seen that the code can be readily extracted from the impulse response. If the length of the hologram in this example is chosen to be $L = 1$ mm, then each bit has a pulse width of approximately 500 fs. With integrated pulsed sources approaching 100 fs pulse widths, such a pulse could be produced in an integrated system.

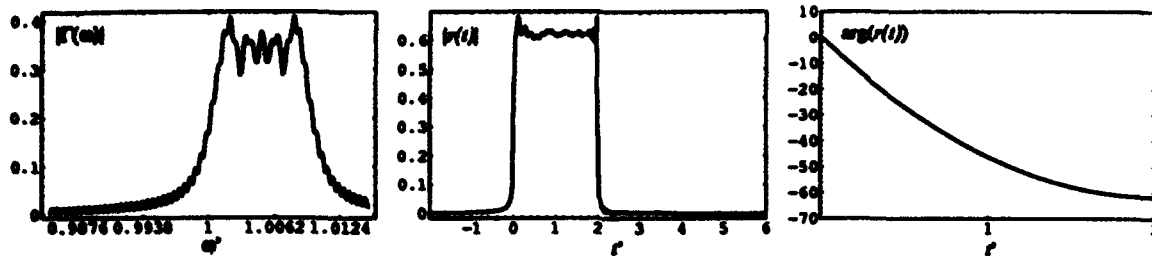


Figure 3: Response of a chirped grating. $V(x) = 0.001 \cos\left(Kx + \frac{(Kx)^2}{400L}\right)$.

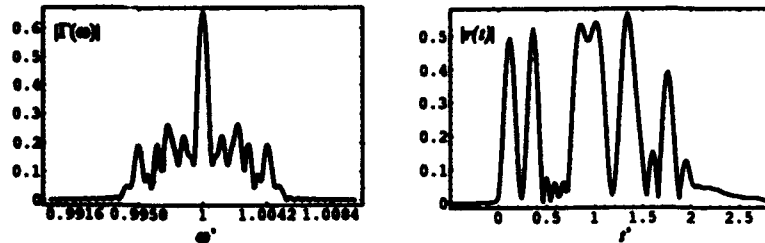



Figure 4: Response of a coded grating with Gaussian pulse shapes.

5 Conclusion

An integrated pulse-shaping system has been described which may be used to modulate the high temporal bandwidth of ultrashort optical pulses. Using a numerical method based on Kepler discretization and polynomial extrapolation, the impulse response of complex reflection holograms has been calculated, and a coding scheme has been developed to produce arbitrary pulse shapes. Applications for this system include dispersion compensation, optical computing, communications, and nonlinear spectroscopy.

References

- [1] Y. K. Chen and M. C. Wu, "Monolithic colliding-pulse mode-locked quantum-well lasers," *IEEE J. Quantum Electron.*, vol. 28, pp. 2176-2185, 1992.
- [2] A. M. Glass, A. M. Johnson, D. H. Olson, W. Simpson, and A. A. Ballman, "Four-wave mixing in semi-insulating InP and GaAs using the photorefractive effect," *Appl. Opt.*, vol. 44, pp. 948-950, 1984.
- [3] H. Kogelnik, "Coupled wave theory for thick hologram gratings," *Bell Syst. Tech. J.*, vol. 48, pp. 2909-2947, 1969.
- [4] R. K. Kostuk, J. W. Goodman, and L. Hesselink, "Volume reflection holograms with multiple gratings: an experimental and theoretical evaluation," *Appl. Opt.*, vol. 25, pp. 4362-4369, 1986.
- [5] D. L. Hecht, "Multifrequency acoustooptic diffraction," *IEEE Trans. on Sonics and Ultrasonics*, vol. SU-24, pp. 7-18, 1976.
- [6] X. Ning, "Analysis of multiplexed-reflection holographic gratings," *J. Opt. Soc. Am. A*, vol. 7, pp. 1436-1440, 1990.
- [7] P. Deuffhard, "A study of extrapolation methods based on multistep schemes without parasitic solutions," *J. Appl. Math. Phys. (ZAMP)*, vol. 30, pp. 177-189, 1979.
- [8] P. Deuffhard, "Kepler discretization in regular celestial mechanics," *Cel. Mech.*, vol. 21, pp. 213-223, 1980.



Optical Switching: Materials and Devices

ITuD 11:00am-12:30pm
Mesquite A

George I. Stegeman, *Presider*
University of Central Florida

OPTICAL SWITCHING USING SECOND ORDER NONLINEARITIES

P.St.J. Russell

Optoelectronics Research Centre,

University of Southampton,

Hampshire SO9 5NH, United Kingdom

Tel +44 703 593083, Fax +44 703 593149

Recently, the use of a cascaded second order nonlinearity has been proposed for all-optical switching [1]. Standard coupled-wave theory of second-harmonic generation (SHG) shows that the pump wave undergoes a nonlinear phase shift when the SHG process is phase-mismatched. This has led to the proposal of a number of novel switching devices, including a push-pull Mach-Zehnder switch [2]. Looking at the origins of linear and nonlinear polarization, a common feature, if the refractive index is to change, is that a frequency component in the driving fields should appear in the resulting nonlinear polarization. In the case of the optical Kerr effect, $P_{\omega}^{(3)} = \chi^{(3)}\{\omega; \omega, \omega_1, -\omega_1\} E_{\omega} E_{\omega_1} E_{\omega_1}^*$. In a similar way, phase changes also appear in the pump wave during degenerate parametric frequency down-conversion: $P_{\omega}^{(2)} = \chi^{(2)}\{\omega; 2\omega, -\omega\} E_{2\omega} E_{\omega}^*$, but none occur during frequency doubling, i.e., $\chi^{(2)}\{2\omega; \omega, \omega\} E_{\omega} E_{\omega}$ contains no term of type $P_{\omega}^{(2)}$. Added to the well-known fact that both up- and down-conversion can occur under phase-matched conditions (the dominant process depending on the relative phase, a balance occurring at the nonlinear eigen-mode point[3]), it does not seem necessary to demand phase mis-matching to obtain a nonlinear phase change in the pump light.

In the cascaded process, the SH is generated and gradually gets out of phase owing to differences in phase velocity between pump and SH. This means (since the direction of conversion depends on the relative phase) that down-conversion begins to appear increasingly as the phase mis-match increases, which yields, according to the argument above, a

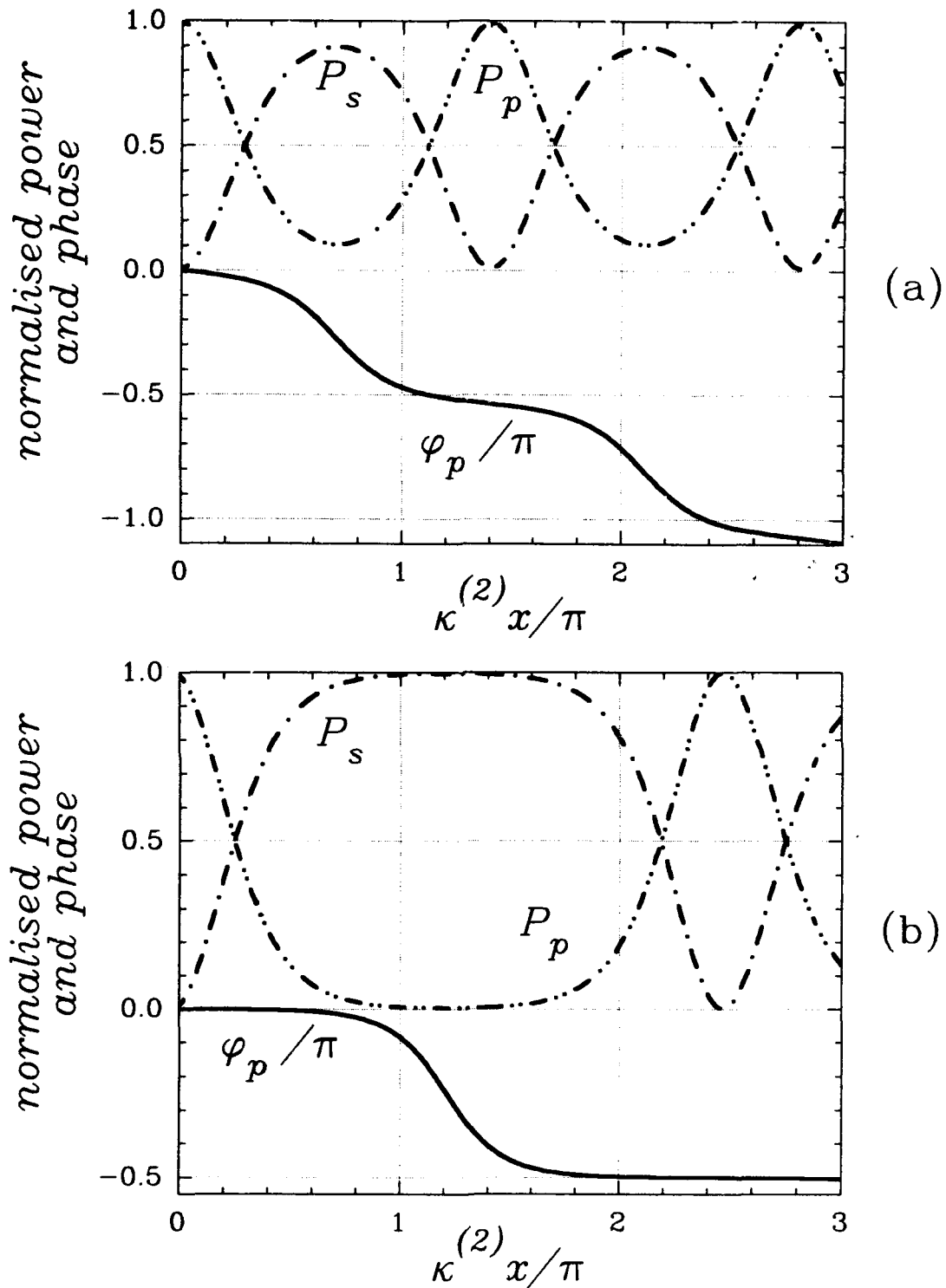


Figure 1 Normalised pump, SH and pump phase evolution with distance for exact phase-matching and 1% injected SH signal at $\kappa^{(2)}L = 3\pi$ for (a) $\psi = 0$ and (b) $\psi = 0.49\pi$. In the absence of the 1% SH seed, the pump phase change is zero. Note that, as expected, the rate of nonlinear phase change with distance is greatest when the down-conversion process is dominant.

nonlinear phase change in the pump wave. This also suggests that pump phase changes may be induced at exact phase-matching if both pump and SH are launched together with an appropriate relative phase. To illustrate this result, I draw upon the distributed feed-forward results in a recent theoretical analysis of reconstruction in nonlinear holograms [3]. Of particular interest are the conserved quantities:

$$\Gamma = 4\kappa^{(2)}\sqrt{P_s P_p} \cos \psi - \vartheta(P_p - P_s) \quad (1)$$

and $P_p + P_s = 1$, which represents power conservation, P_p and P_s being the normalised powers of the pump and SH. ϑ describes dephasing, $\kappa^{(2)}$ is the nonlinear coupling constant (proportional to the square root of the incident power) and $\psi = \phi_s - 2\phi_p$ is the relative phase between SH and pump. From Equation (14) in [3], and using (1), the evolution of the pump phase ϕ_p with distance x is easily shown to be described by:

$$\frac{\partial \phi_p}{\partial x} = -\frac{\vartheta}{2} + \frac{(\vartheta - \Gamma)}{4P_p(x)}. \quad (2)$$

The only varying quantity on the right hand side of this equation is the pump power P_p , and Γ is set by the boundary conditions. If the incoming SH is zero (as in [1]) then inexact phase matching is essential ($|\vartheta| > 0$) for a nonlinear change in pump phase. If it is not, then even when $\vartheta = 0$ it is possible to obtain a nonlinear phase change in the pump wave provided the relative phase ψ is not equal to $\pi/2$.

Some solutions of (2) for exact phase-matching and only 1% injected SH are given in Figure 1. Next, keeping the SH seed power at 1% (for $\vartheta = 0$) while its relative phase is varied (Figure 2), the effects are dramatic: the output slews rapidly between 100% pump (at 0.26π) and 100% SH (at 0.5π). This result may have applications in nonlinear mode-locking of lasers and in clarifying the growth of self-organised $\chi^{(2)}$ gratings in optical fibres.

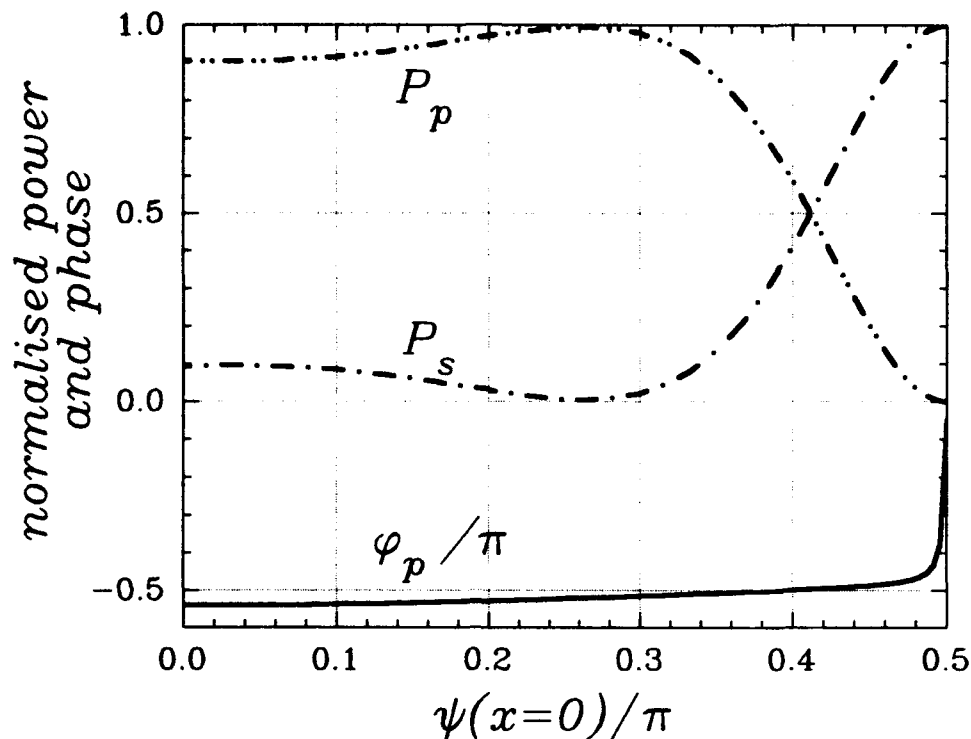


Figure 2 The pump and SH powers and pump phase at the output plane $\kappa^{(2)}L = 3\pi/2$ of a SH generator, plotted as a function of the relative phase ψ at the input surface $x = 0$ for an injected SH power of 1% of the pump. The output swings from zero to complete SH conversion between $\psi = 0.26\pi$ and 0.5π .

References

1. G.I. Stegeman, M. Sheik-Bahae and E.W. Van Stryland, "Very large third order nonlinearities via cascading of second order nonlinearities," International Quantum Electronics Conference, IQEC'92, Paper WeC3, Vienna 1992.
2. C.N. Ironside, J.S. Aitchison and J.M. Arnold, "An all-optical switch employing the cascaded second-order nonlinear effect," Department of Electronics and Electrical Engineering, University of Glasgow report, 1992.
3. P.St.J. Russell, "Theoretical Study of Parametric Frequency and Wavefront Conversion in Nonlinear Holograms," IEEE J Quant. Electr., **27** (830-835) 1991.

Cascaded second order effect in semiconductor waveguides

K. Al-hemyari, F. Laughton, J.S. Aitchison, J. M. Arnold, D. C. Hutchings, J. H. Marsh and C. N. Ironside.

Department of Electronics and Electrical Engineering
University of Glasgow
Glasgow G12 8LT.
U.K.

Introduction

Integrated guided wave, all-optical switches are generally designed to operate via an intensity-dependent refractive index resulting from the third order nonlinear susceptibility, $\chi^{(3)}$ see for example [1], [2]. Recently, De Salvo et al. [3] have shown that nonlinear phase shift and thereby an effective intensity-dependent refractive index can be obtained from cascading the second order nonlinearity $\chi^{(2)}$. They demonstrated that the effective intensity-dependent refractive index $n_{2\text{eff}}$ produced by the cascaded second order nonlinearity could be positive or negative depending on the phase matching conditions, and they also measured $n_{2\text{eff}}$ as $\pm 2 \times 10^{-14} \text{ cm}^2 \text{ W}^{-1}$ for KTP (KTiOPO₄), which has a d_{eff} of $3.1 \times 10^{-12} \text{ m V}^{-1}$. The approximate expression they derived for $n_{2\text{eff}}$ was as follows

$$n_{2\text{eff}} = -\frac{4\pi}{c\epsilon_0} \frac{1}{\lambda} \frac{d_{\text{eff}}^2}{n_{2\omega} n_{\omega}^2} \frac{1}{\Delta k L} \quad (1)$$

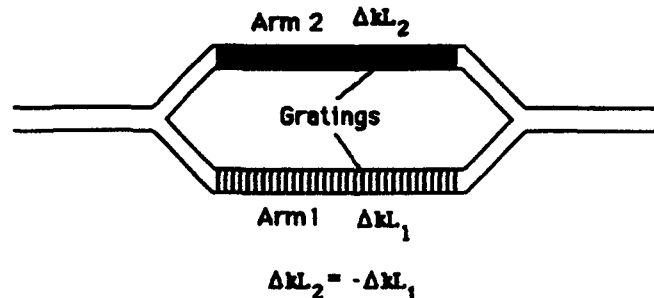
where L is the length of the device, d_{eff} is the effective second order nonlinear coefficient, Δk is the phase mismatch, $n_{2\omega}$ is the refractive index at the second harmonic, and n_{ω} is the refractive index at the fundamental frequency; λ is the wavelength. De Salvo et al. also showed $n_{2\text{eff}}$ is not constant with intensity (i.e. not strictly Kerr law $n = n_0 + n_2 I$), but tends to saturate at phase changes of around $\pi/4$.

We propose here an integrated all-optical switch which uses the cascaded second order effect and is based on the integrated Mach-Zehnder interferometer, illustrated in figure(1). A similar device configuration has already been demonstrated utilising the third-order nonlinearity in AlGaAs [2] where an asymmetric splitting of the input intensity was employed in order to obtain a differential phase shift in the interferometer. The asymmetric splitting reduces the overall throughput of the device. However, with the cascaded second order nonlinearity not only is the intensity dependence of the nonlinear phase shift increased but it is also possible to control the sign of the nonlinear phase shift by appropriate choice of phase matching. The phase matching scheme proposed is the so-called quasi-phase matching (QPM) scheme which has been used to phase match for second harmonic generation in LiNbO₃ [4], LiTlO₃ [5] and KTP [6] and has also been used in a semiconductor, GaAs [7]. With QPM the phase mismatch is given by:-

$$\Delta k = k_{2\omega} - 2k_{\omega} - K \quad (2)$$

where $k_{2\omega}$ is the phase propagation coefficient of the second harmonic light, k_{ω} is that of the fundamental light and $K = 2\pi/\Lambda$ where Λ is the periodicity of the grating. By arranging to have different grating periodicities in each arm of the interferometer it is, therefore, possible to have a different sign of the effective n_2 in each arm of the interferometer. In other words, with the cascaded second-order effect it is possible to operate the device in a "push-pull" mode, where symmetric splitting of the light between the arms of the interferometer can be employed with a subsequent increase in the overall transmission of the device compared to the asymmetric Mach-Zehnder of [2]. We call the proposed device a cascaded, second order, push-pull switch. The phase change required in each arm for an on-to-off transition, or conversely, if the device is biased differently, an off-to-on transition, is $\pi/2$. For this amount of nonlinear phase shift, equation (1) may not be valid and therefore the approximate theory of [3] has to be extended to larger nonlinear phase shifts.

Figure (1) Push-pull Switch



Caption: Schematic of integrated all-optical switch based on the integrated Mach-Zehnder interferometer; each arm of the interferometer has a grating of a different period designed to give a different sign of phase mismatch condition which results in a different sign for the nonlinear phase shift arising from the cascaded the second order nonlinear effect. This device is called a cascaded second order push-pull switch.

Theory of operation

Theory of the nonlinear phase change has to considerable expanded transmission of the switch illustrated in figure(1) is given by :-

$$T = (1 - D) \cos^2 \left(\frac{\theta_{\text{nl}} - \theta_{\text{nl}2} + \xi}{2} \right)$$

where D is the depletion of the fundamental, θ_{a1} and θ_{a2} are the nonlinear shifts in arm1 and arm2 of the interferometer, ζ is the phase offset. The nonlinear phase shift is found by solving the coupled differential equations which describe second harmonic generation is given by:-

$$\theta_{NL} = \theta + \frac{\Delta k z}{2} \quad (3)$$

with

$$\theta = -\frac{1}{\alpha} \Pi(D, \phi | m) \quad (4)$$

Π is the third order elliptic integral with $\alpha = (1+2\varepsilon+(1+4\varepsilon)^{1/2})^{1/2}/2$ where

$$\phi = \arcsin(\operatorname{sn}(Z, m)) \quad (5)$$

with

$$m = \frac{1+2\varepsilon-(1+4\varepsilon)^{1/2}}{1+2\varepsilon+(1+4\varepsilon)^{1/2}} \quad (6)$$

and

$$Z = \frac{\Delta k z}{2\sqrt{2}} \{1+2\varepsilon+(1+4\varepsilon)^{1/2}\}^{1/2} \quad (7)$$

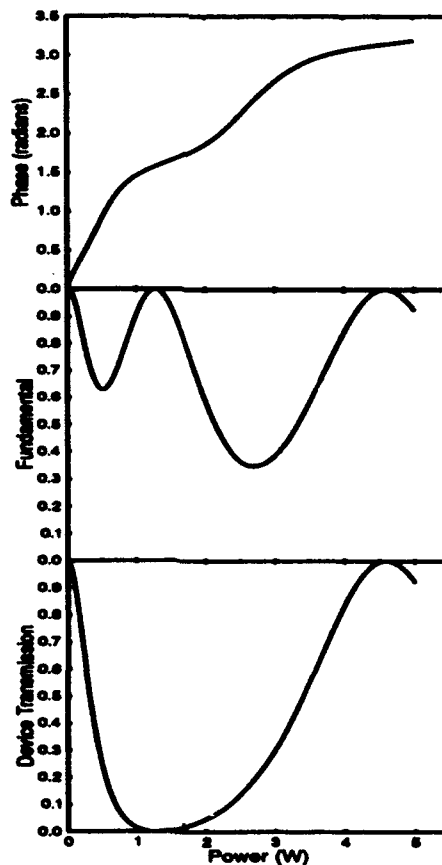
the parameter $\varepsilon = (2\Gamma/\Delta k)^2$ with

$$\Gamma = \frac{k d_{33} E_0}{\sqrt{n_{2e} n_o}} \quad (8)$$

E_0 is the initial fundamental field, k is the magnitude of the fundamental wavevector.

In Figure(2) we show the calculated device characteristics for AlGaAs based material.

Figure(2) Calculated Device characteristics for $\Delta k L = 2\pi$

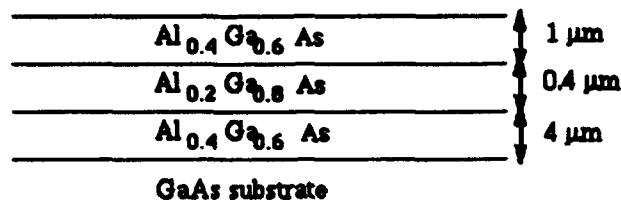


Caption: Top figure shows the nonlinear phase shift in one arm of the push-pull switch; the middle figure shows the fraction in the fundamental; the bottom figure show the response for the push-pull switch; the device parameters are for AlGaAs with $n_{2e} = 3.6$, $n_o = 3.5$, $d_{33} = 150 \text{ pm/V}$, $\lambda = 1.55 \text{ } \mu\text{m}$, $L = 1 \text{ cm}$, $A = 1.6 \times 10^{-11} \text{ m}^2$, phase mismatch $\Delta k L = \pm 2\pi$ and phase offset, $\zeta = 0$.

Device Fabrication

III-V semiconductor materials have a large d coefficient, for AlGaAs $d_{33}=150$ pm/V, and they also have a mature growth and fabrication technology. They are therefore an attractive material for investigating the cascaded second order effect with quasi phase-matching. The following fabrication procedure was adopted to make a sample suitable for the investigation of the cascaded second order effect in AlGaAs semiconductor waveguides at fundamental wavelengths of around 1.55 μm .

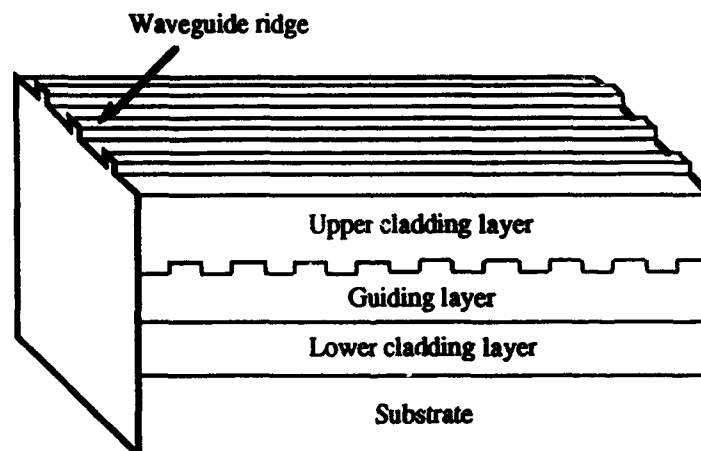
Figure (3) The wafer design for the semiconductor waveguides



Caption The wafer for the semiconductor waveguide employed in second order nonlinear characterisation

At first, only the lower cladding and the guiding regions were grown. A grating was then etched into the top surface of the guiding layer, and the upper cladding layer was then overgrown on top of the grating. Gratings of five different periods were fabricated: 2 μm , 2.5 μm , 3 μm , 3.5 μm and 4 μm . The lines for the gratings ran in the $(0\bar{1}1)$ direction, so that etching gave a V-groove profile. This gives improved overgrowth. The etch depth of the gratings was about 40 nm. A photomask with a variety of waveguide channel widths was employed to put down ridge waveguides perpendicular to the grating: there are about 19 channels whose widths vary in 0.5 μm steps from 1 μm to 10 μm . The distances between the centres of adjacent channels is 50 μm . The resultant chip is illustrated in Figure (4).

Figure(4) The semiconductor waveguide chip



Caption The figure shows the layout of the chip after fabrication

Waveguide Characterisation

The waveguides will be characterised with a tunable F-centre laser in both pulse and CW operation both the efficiency of second harmonic generation and the nonlinear phase shift due to the cascaded second order effect will be investigated

Conclusions

We have proposed an all-optical switch based on an integrated Mach-Zehnder interferometer which employs the cascaded second-order optical nonlinearity and quasi-phase matching to produce a positive and negative $n_{2\text{eff}}$ in opposite arms of the interferometer. A full mathematical treatment of the second order cascaded process has yielded exact solutions for the nonlinear phase shift. The all-optical switch employs a low-loss mechanism which is intrinsically ultrafast.

The fabrication of AlGaAs waveguides for the investigation of the cascaded second order effect has been described and optical characterisation is currently underway.

References

1. Aitchison, J. S., Kean, A. H., Ironside, C. N., Villeneuve, A. and Stegeman, G. I.: "Ultrafast all-optical switching in $\text{Al}_{0.18}\text{Ga}_{0.82}\text{As}$ directional coupler in the 1.55 μm spectral region", *Elect. Letts.*, 27, 1709-1710, 1992.
2. Al-Hemyari, K., Aitchison, J. S., Ironside C. N., Kennedy, G. T., Grant, R.S. and Sibbett, W.: "Ultrafast all-optical switching in GaAlAs integrated interferometer in 1.55 μm spectral region *Electronics Letts* 28 1090-1092 1992.
3. DeSalvo, R., Hagan, D. J., Shiek-Bahae, M., Stegeman, G. I., Vanherzele, H. and Van Stryland, E. W.: "Self-focussing and defocussing by cascaded second order effects in KTP", *Opt. Letts.* 17, 28-30, 1992
4. Lim, E. J., Fejer, M. M., Byer, R. L., Kozlovsky, W. J.: "Blue light generation by frequency doubling in periodically poled lithium niobate channel waveguide", *Electronics. Letts.*, 25, 731-732, 1989.

5. Yamamoto, K., Mizuuchi, K., Taniuchi, : "Milliwatt-order blue-light generation in a periodically domain-inverted LiTaO₃ waveguide" *Opt. Lett.*, 16, 1156-1158, 1991.
6. Van der Poel, C. J., Bierlein, J. D., Brown, J. B., Colak, S.: "Efficient type I second harmonic generation in periodically poled KTiOPO₄ waveguides", *Appl. Phys. Lett.*, 57, 2074-2076, 1990.
7. Van der Ziel, J. P., Ilegems M., Foy P. W. and Mikulyak R. M. "Phased-matched second harmonic generation in a periodic GaAs waveguide" *Appl. Phys. Letts.* 29 775-777 1976.

**Anisotropic Two-Photon Absorption Coefficient and Induced
Nonlinear Refractive-Index in GaAs/AlGaAs Multiple Quantum
Well Waveguides**

C.C. Yang

Department of Electrical and Computer Engineering

The Pennsylvania State University

University Park, PA 16802 USA

Phone: (814) 865-2364

FAX: (814) 865-7065

Alain Villeneuve and George I. Stegeman

CREOL, University of Central Florida

Orlando, FL 32826 USA

Cheng-Hui Lin and Hao-Hsiung Lin

Department of Electrical Engineering

National Taiwan University

Taipei, Taiwan, R.O.C.

Two-photon transitions near the absorption edge in a semiconductor multiple quantum well (MQW) structure are important because they provide information about the energy states involved in the forbidden direct transitions^{1,2} and the induced Kerr-like optical nonlinearity has potential for ultrafast nonlinear switching applications^{3,4}. In the TE polarization mode (the polarization is perpendicular to the MQW growth direction), there are no distinct exciton features because the two-stage transition includes an interband transition and an intraband transition whose final state is a 2P exciton. In the TM polarization mode (the polarization is parallel to the MQW growth direction), distinct exciton features are expected because the intraband transitions are forbidden and intersubband transitions are allowed. In this situation, 1S excitons can be the final states for two-photon transitions.

In this paper, we present measurements of the two-photon absorption coefficient, β_2 , and induced nonlinear refractive-index, n_2 , in both TE and TM modes of GaAs/AlGaAs MQW strip-loaded channel waveguides in the wavelength range between 1490 nm and 1660 nm. The guiding layer included 85 periods of 70 Å GaAs wells and 100 Å $\text{Al}_{0.32}\text{Ga}_{0.68}\text{As}$ barriers, sandwiched by $\text{Al}_{0.27}\text{Ga}_{0.73}\text{As}$ cladding layers. The strip width of the waveguide used for the following results was 5.5 μm . Two samples from the same wafer but with different lengths (1.5 cm and 0.67 cm) and different etching depths were used. The results from the two samples are consistent. The samples were grown by the MBE technique. 4-6 psec (FWHM) almost transform-limited pulses from a color center laser were end-coupled into the waveguides. The coupling efficiency was estimated to be between 30% and 60%. The inverse transmission was recorded for determining the β_2 values and the self-phase modulation, which broadens the signal spectrum, was monitored by a spectrum analyzer for determining the n_2 values.

Theoretical predictions for the wavelength dependence of β_2 were obtained from the calculations of the two-photon transition rates². Those for n_2 were then obtained by using the Kramers-Kronig relation⁵. The error bars in Figs. 1 and 2 show the measured β_2 values in the TE and TM modes, respectively. The continuous curves represent the theoretical values (up to a multiplicative constant) from the contributions of 2D continuous transitions at a low temperature. The excitons are indicated by labelled vertical arrows. In the TE mode, because the contributions from the excitons are weak, the continuous curve is generally in good agreement with the measured values. However, in the TM mode because the 1S exciton contributions are strong, the theoretical result valid at low temperature cannot fit the data well.

Figures 3 and 4 show the measured n_2 values in the TE and TM modes, respectively. The continuous curve in Fig. 3 represents

the theoretical result based on the assumption that the 2P exciton binding energy is 1 meV, the exciton radius is 200 Å, and the Lorentzian broadening width is 12 meV. The choices of the 2P exciton parameters are not critical because the contributions from the 2P excitons are small. The continuous curve in Fig. 4 is the theoretical result for the TM mode with the assumptions that the binding energy of 1S and 2S excitons are 9 meV and 1 meV, respectively, that the exciton radii of C1L2 excitons and C2L1 excitons are 300 Å and 150 Å, respectively, and that the Lorentzian broadening widths of C1L2 excitons and C2L1 excitons are 20 meV and 15 meV, respectively. Different choices of these parameter values will change the shape of the curve slightly but not the major features. However, it seems that the C1L2 (1S) transition is weaker than what the theories predict. This may be attributed to imperfections in the quantum well growth.

References

1. K. Tai, A. Mysyrowicz, R.J. Fischer, R.E. Slusher, and A.Y. Cho, *Phys. Rev. Lett.*, **62**, 1784 (1989).
2. A. Shimizu, *Phys. Rev. B*, **40**, 1403, (1989).
3. A. Villeneuve, C.C. Yang, P.G. Wigley, G.I. Stegeman, J.S. Aitchison, and C.N. Ironside, *Appl. Phys. Lett.*, **147** (1992).
4. K. Al-hemyari, J.S. Aitchison, C.N. Ironside, G.T. Kennedy, R.S. Grant, and W. Sibbett, *Electron. Lett.*, **28**, 1090 (1992).
5. M. Sheik-Bahae, D.C. Hutchings, D.J. Hagan, E.W. Van Stryland, *IEEE J. Quantum Electron.*, **27**, 1296 (1991).

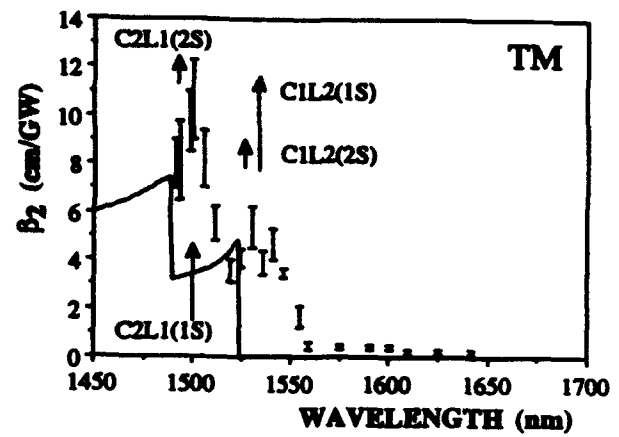
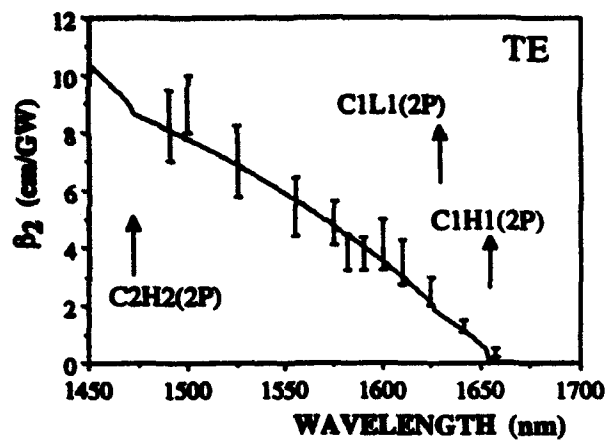


Fig. 1 β_2 values in the TE mode. Fig. 2 β_2 values in the TM mode.

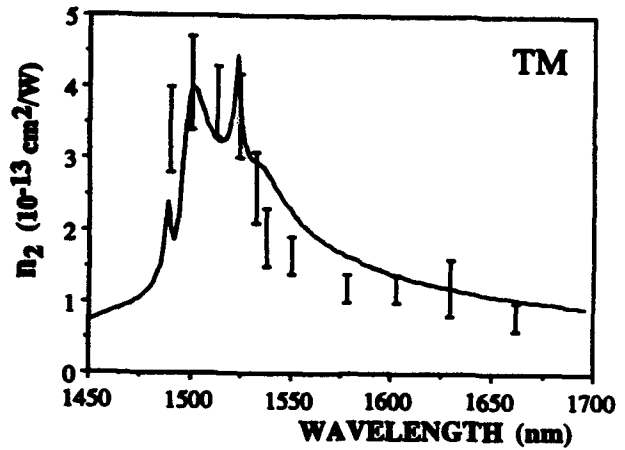
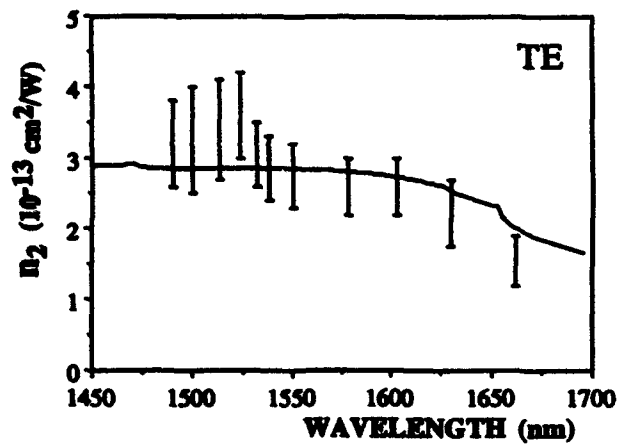


Fig. 3 n_2 values in the TE mode. Fig. 4 n_2 values in the TM mode.

**Effects of Dispersive Two-Photon Transitions on
Femtosecond Pulse Propagation in Multiple Quantum Well Waveguides**

C.C. Yang

**Department of Electrical and Computer Engineering
The Pennsylvania State University
University Park, PA 16802 USA
Phone: (814) 865-2364
FAX: (814) 865-7065**

A. Villeneuve and G.I. Stegeman

**CREOL, University of Central Florida
Orlando, FL 32826 USA**

Cheng-Hui Lin and Hao-Hsiung Lin

**Department of Electrical Engineering
National Taiwan University
Taipei, Taiwan, R.O.C.**

In order to implement ultrafast all-optical switching using the optical nonlinearities induced by two-photon transitions in semiconductors, subpicosecond pulses are usually needed for achieving the required high peak powers¹. However, because the two-photon absorption coefficient and induced nonlinear refractive-index are frequency dependent, particularly when the signal wavelength is close to a strong transition, femtosecond pulses (with large bandwidths) will experience dispersive nonlinear absorption and self-phase modulation. These effects may severely distort the pulses and degrade the switching.

In this paper, we present the results of experimental and theoretical studies on femtosecond pulse propagation in GaAs/AlGaAs multiple quantum well channel waveguides. The guiding layer of the strip-loaded channel waveguides included 85 periods of 70 Å GaAs wells and 100 Å Al_{0.32}Ga_{0.68}As barriers, sandwiched by Al_{0.27}Ga_{0.73}As cladding layers. The strip width and

the length of the waveguide for the following experimental results were 5.5 μm and 1.5 cm, respectively. 400-fsec almost transform-limited pulses, obtained by additive-pulse mode-locking a color center laser, were end-coupled into the waveguide. The output spectrum was monitored by a spectrum analyzer.

Figure 1 shows the output frequency spectrum of the 400-fsec input pulses in the TM mode. The input peak intensity in the waveguide was estimated to be 13 GW/cm². The sharp peak at 1545 nm came from the residual power not additively pulse mode locked in the color center laser. After the additive-pulse mode-locking, the central wavelength was shifted to some value near 1550 nm. From picosecond-pulse measurements of the two-photon absorption coefficient, β_2 , and the nonlinear refractive-index, n_2 , and the theoretical calculations, it was learned that in the TM mode the ClL2 interband transition and ClL2 (1S) exciton transition occur near 1524 nm and 1532 nm, respectively². Therefore, in the wavelength range between 1500 nm and 1600 nm both β_2 and n_2 are expected to be highly dispersive. These dispersion characteristics lead to the strongly asymmetric nature of the spectrum shown in Fig. 1.

The theoretical results were obtained from the equation for the frequency-domain complex amplitude $A(z, \omega)$:

$$\frac{\partial A(z, \omega)}{\partial z} = -\frac{\alpha}{2} A(z, \omega) + \frac{a_2}{2\pi} \int_{-\infty}^{\infty} d\omega_1 \left[\frac{i(\omega + \omega_0)}{c} n_2(\omega + \omega_0, \omega_1 + \omega_0) - \beta_2(\omega + \omega_0, \omega_1 + \omega_0) / 2 \right] p(\omega_1) A(z, \omega - \omega_1). \quad (1)$$

Here, α is the linear loss coefficient which is assumed to be frequency independent, a_2 is a waveguide modal overlap factor which is assumed to be 0.5, c is the speed of light in vacuum, $p(\omega_1)$ is the Fourier transform of the signal intensity, and the ω 's with various subscripts represent angular frequencies. Note that the angular frequencies ω_0 and ω_1 are defined to be the

deviations from the input central frequency ω_0 . The nondegenerate β_2 and n_2 can be obtained from the calculations for the two-photon transition rates³ and the use of the Kramers-Kronig relation⁴. Their absolute values and frequency dependences are justified by the measurements of degenerate β_2 and n_2 values. Fig. 2 shows an output frequency spectrum obtained by solving Eq. (1) to simulate the situation leading to the results in Fig. 1. The theoretical and experimental results share the same asymmetry trends.

The solid curve in Fig. 3 shows the theoretical result of the pulse shape corresponding to the spectrum in Fig. 2. The input pulse is also plotted as the dashed curve for comparison. It can be seen that the self-phase modulation has broadened the pulse. More importantly, the dispersive two-photon transitions have shifted the pulse peak towards the trailing edge. This phenomenon is similar to femtosecond pulse propagation in a silica fiber in which Raman scattering also tilts the pulse toward the trailing side⁵.

References

1. A. Villeneuve, C.C. Yang, P.G. Wigley, G.I. Stegeman, J.S. Aitchison, and C.N. Ironside, *Appl. Phys. Lett.*, **62**, 147 (1992).
2. C.C. Yang, A. Villeneuve, G.I. Stegeman, C.H. Lin, and H.H. Lin, submitted to *Electronics Lett.* (1992).
3. A. Shimizu, *Phys. Rev. B*, **40**, 1403 (1989).
4. M. Sheik-Bahae, D.C. Hutchings, D.J. Hagan, and E.W. Van Stryland, *IEEE J. Quantum Electronics*, **27**, 1296 (1991).
5. R.H. Stolen, J.P. Gordon, W.J. Tomlinson, and H.A. Haus, *J. Opt. Soc. Am. B*, **6**, 1159 (1989).

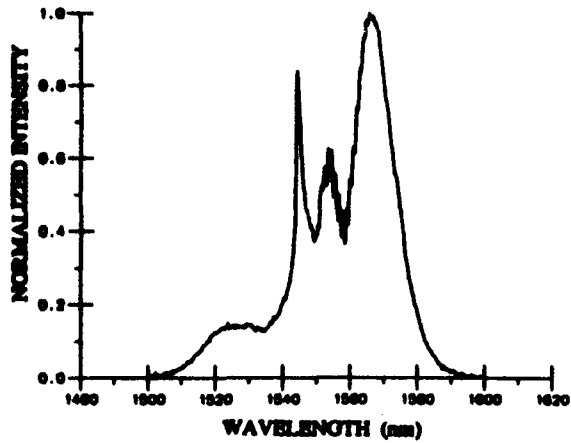


Fig. 1 Experimental output frequency spectrum of a 400-fsec pulse.

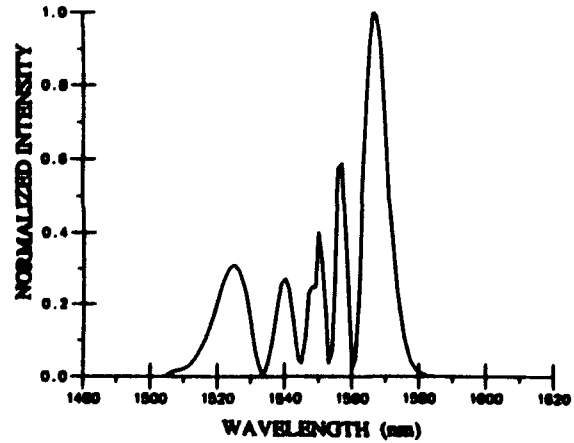


Fig. 2 Theoretical output frequency spectrum simulating the result in Fig. 1.

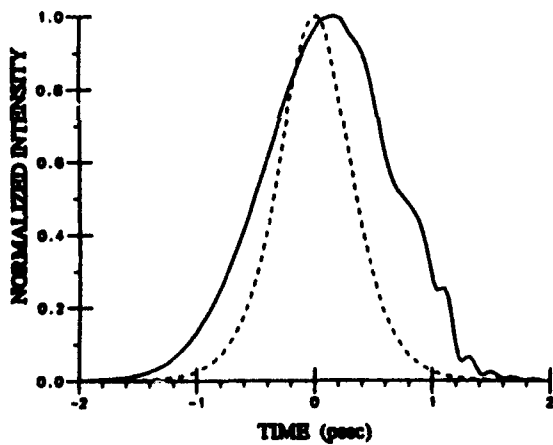


Fig. 3 Theoretical result of the pulse shape corresponding to the spectrum in Fig. 2.

ULTRAFAST REFRACTIVE NONLINEARITY DISPLAYED BY ORGANIC MONOMODE FIBRE WAVEGUIDES

R J Manning, R Kashyap, S N Oliver and D Cotter
BT Laboratories, Martlesham Heath, Ipswich, Suffolk IP5 7RE, UK
Tel: +44 473 645920 Fax: +44 473 646885

This paper reports an investigation of the nonlinear properties of monomode fibre waveguides consisting of glass capillaries (bore radius $\sim 1 \mu\text{m}$) filled with organic liquids. We demonstrate, for the first time, ultrafast ($< 1 \text{ ps}$ response) refractive nonlinearity, and the effective use of organic materials engineered to provide a large electronic refractive nonlinearity.

If, in the future, optical switching and signal processing devices are to have a significant role in computing and telecommunications, they must perform in ways that electronics cannot. One important differentiator will be speed. Devices with ultrafast response will allow optical switching and processing at rates greater than 100 Gb/s, reaching far beyond the fundamental speed limitations of electronics. Truly ultrafast response ($< 1 \text{ ps}$) in guided wave devices will be necessary so that non-dissipative operations using optical solitons as the natural 'bits' can be achieved, thus ensuring high efficiency [1]. So far, the most successful ultrafast switching devices have been based on silica fibre [2]. However, the nonlinear refraction coefficient n_2 for silica is small, so that the product of switching power P and device length L is necessarily high: $PL \approx 1 \text{ kW m}$ typically. To keep the power requirements within practical limits, it is typically found necessary to use device lengths of several hundreds or thousands of metres. However, the corresponding latency of operation ($0.5\text{--}5 \mu\text{s}$) is a severe limitation for all but the most simple applications. For many key processes in future advanced optical communications (including ultrafast clock recovery, regeneration and packet switch control), a practical target is $L \approx 1 \text{ m}$ ($< 5 \text{ ns}$ latency) and $PL \approx 1 \text{ W m}$, implying the need for a 1000-fold reduction in PL compared to silica fibre devices.

One approach is to fabricate fibre devices using special glasses with high n_2 , and considerable success has been obtained recently [3]. We are investigating an alternative approach based on liquid-filled fibres which offers the prospect of obtaining significantly lower PL . Liquid-filled multimode waveguides were first devised many years ago [4] in early attempts to lower the optical loss of fibre. The potential of liquid-filled guides for nonlinear optics [5] has received greater attention recently [6-8]. The refractive nonlinearity due to forced molecular orientation in

capillaries filled with nitrobenzene [6] and DEANST [7,8] exhibits response times of 35 ps and 4 ps respectively. In our current work, we are focusing attention on the *ultrafast* (<1 ps response) electronic nonlinearity. A great advantage of the liquid-filled waveguide approach is that the various organic materials that have been specially developed recently for large electronic n_2 can now be used effectively. This approach overcomes the previous major difficulty of fabricating these special organic materials in the solid state in the form of low loss optical waveguides. An additional advantage, as described later, is the ability to use path lengths of several tens of centimetres and relatively low molecular concentrations, thus avoiding other fundamental problems that have also previously prevented the use of these materials for ultrafast switching and signal processing.

Figure 1 shows one result from a theoretical analysis of the lowest-order eigenmode of a step-index waveguide in which the core region has a nonlinear refraction coefficient n_2 , whilst the nonlinearity of the cladding glass is assumed to be negligible. The total power in the guided mode is P , and λ is the wavelength. The optically-induced change in the effective refractive index for the mode (Δn_{eff}) is plotted in Fig. 1 versus the fibre V value, showing that $V \approx 2.0$ is optimal. An assumption in Fig. 1 is that Δn_{eff} is much smaller than the core-cladding index step Δn . Further analysis shows that for values of $|\Delta n_{\text{eff}}| > 0.01 \Delta n$, there are significant deviations from Fig. 1 and the behaviour then depends on whether the refractive nonlinearity is self-focusing or self-defocusing; for $n_2 > 0$ the maximum value of $\Delta n_{\text{eff}} \lambda^2 / n_2 P$ is enhanced, whereas it is reduced if $n_2 < 0$.

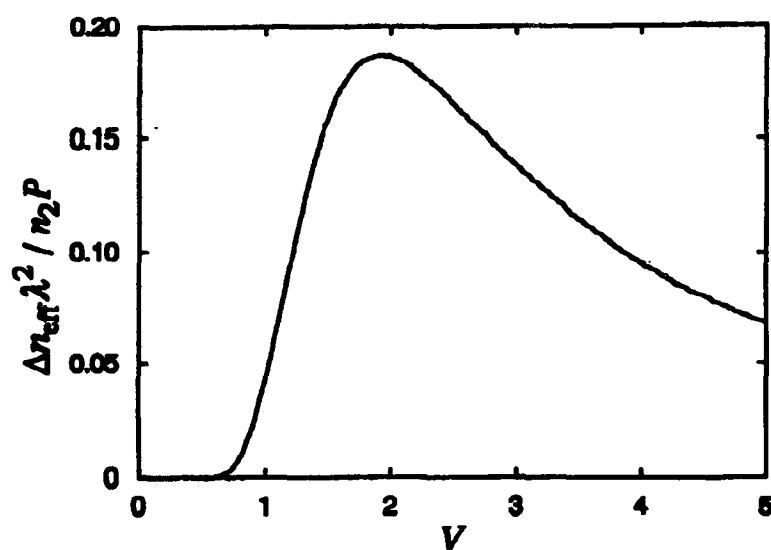


Figure 1: Theoretical change in mode index (Δn_{eff}) versus V value for a fibre with a weakly nonlinear core.

For the experiments in progress, the waveguide consists of a fibre capillary (fabricated by drawing down glass tubing in a fibre pulling rig) suspended between

two specially-designed cuvettes. The cuvettes are filled with the organic liquid which is then allowed to fill the fibre core by capillary action. The fibre can be readily demounted from the cuvettes, allowing different fibres and liquids to be examined. Light is coupled in and out of the fibre through the cuvettes using microscope objectives. The coupling efficiency is only slightly lower than for a conventional fibre. With the addition of anti-reflection coatings on the cuvette walls, this small reduction in efficiency could be eliminated. The nonlinear properties are investigated using a pump-probe interferometer in a split unbalanced Michelson configuration. Transient fringe shifts caused by changes in the effective mode index (Δn_{eff}) of the fibre are measured with sub-picosecond time resolution. The light source is a continuous mode-locked Nd:YLF laser together with a fibre-grating pulse compressor, providing 1.5 ps pulses at 1.05 μm . First experiments were carried out using a simple solvent, methyl benzene (toluene), as the core liquid. Figure 2 shows the measured fringe phase shift as a function of pump-probe pulse time delay τ for peak pump powers of 43 W. The observed temporal response can be explained as a combination of an ultrafast component of the refractive nonlinearity (centred at $\tau \approx 0$) due to electronic deformation, and a weaker slow component (with relaxation time 8 ps) due to forced molecular orientation. The orientational component is negative in Fig. 2 because the pump and probe pulses have orthogonal linear polarisations in the waveguide. The solid curve in Fig. 2 is the best fit to the data using a simple rate-equation analysis. To our knowledge, the electronic refractive nonlinearity of simple solvents such as toluene has not been observed previously. A key observation is that with pulses as short as 1.5 ps, the slower rotational component is effectively suppressed compared to the ultrafast nonlinearity. The electronic n_2 for toluene is found to be $+1.3 \times 10^{-19} \text{ m}^2 / \text{W}$, some 4 times greater than silica.

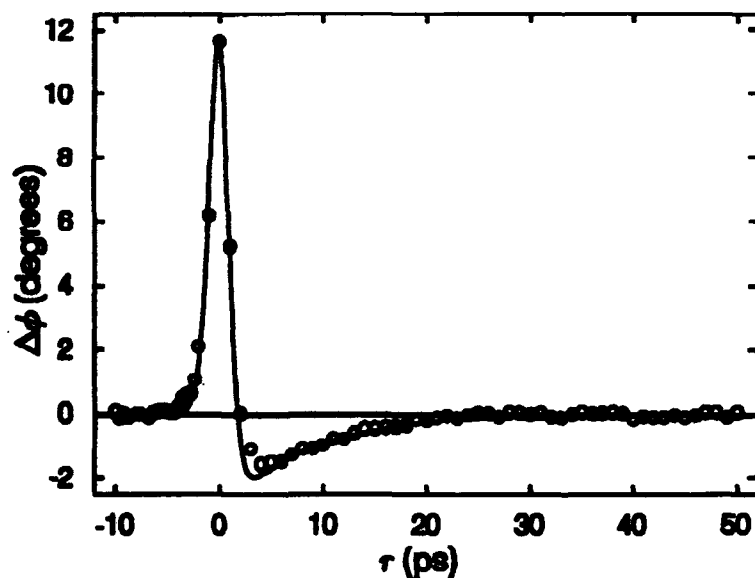


Figure 2: Measured fringe phase shift $\Delta\phi$ versus pump-probe pulse delay τ for a 100 mm long toluene-filled monomode fibre at a peak pump power of 43 W in a 1.5 ps pulse. The solid curve is a theoretical fit.

Further experiments are in progress using as the core liquid solutions of a nickel dithiolene complex in nitrobenzene. Our previous measurements of the bulk properties of this material have shown a refractive nonlinearity some 100 times greater than silica at a molecular concentration of 10^{18} cm^{-3} [9]. We have also previously reported measurements of the two-photon absorption coefficient and of the ratio of the real and imaginary parts of the third-order susceptibility ($R = |\text{Re}\chi^{(3)} / \text{Im}\chi^{(3)}|$) for nickel dithiolene complexes at higher concentrations in polymethylmethacrylate films [10]. The ratio R is an important figure of merit for nonlinear devices; for a Mach-Zehnder device $R \approx 2\pi$ or greater is required to avoid the deleterious effect of two-photon absorption [11]. We showed that R depends on the molecular concentration C ; at $C > 10^{20} \text{ cm}^{-3}$ then $R \approx 1.4\pi$ which is close to being acceptable, but with increasing C two-photon absorption begins to dominate (R decreases rapidly) possibly due to molecular aggregation. Therefore a key aspect of the liquid-filled fibre approach is the ability to optimise readily the device length and C , to ensure a satisfactory nonlinear figure of merit.

To conclude, monomode capillary fibres using organic materials engineered for large electronic nonlinearity have great potential for ultrafast signal processing applications, particularly those in which device latency must be minimised. We have demonstrated, for the first time, sub-picosecond refractive nonlinearity in a liquid-filled guide. This approach greatly simplifies the process of waveguide fabrication and also allows the key material figures of merit to be optimised readily.

REFERENCES

- [1] K J Blow et al, *Opt. Lett.* **14**, 754 (1989)
- [2] M N Islam, *Ultrafast Fiber Switching Devices and Systems*, Cambridge Univ. Press (1992)
- [3] M Asobe et al, *IEEE Photon. Technol. Lett.* **4**, 362 (1992)
- [4] W A Gambling et al, *Opt. Comm.* **6**, 317 (1972)
- [5] E P Ippen et al, *Appl. Phys. Lett.* **24**, 190 (1974)
- [6] R Kashyap and N Finlayson, *Opt. Lett.* **17**, 405 (1992)
- [7] H Kanbara et al, *IEEE Photon. Technol. Lett.* **3**, 795 (1992)
- [8] H Kanbara et al, Fourth Optoelectronics Conference, Paper 16B1-5 (1992)
- [9] C S Winter et al, *J. Mater. Chem.* **2**, 443 (1992)
- [10] C S Winter et al, *Opt. Comm.* **90**, 139 (1992)
- [11] V Mizrahi et al, *Opt. Lett.* **14**, 1140 (1990)

A NEW KIND OF MAGNETO-OPTICAL BISTABLE ELEMENT

USING THE NONLINEARITY OF A PHOTOCONDUCTOR LAYER

A D Boardman

Applied Optics Group, Department of Physics,

University of Salford, Salford, M5 4WT

Tel: (061)-745 5253, FAX: (061)-745 5903

A I Voronko, P M Vetoshko, V B Volkovoy

Institute of Radio Engineering and Electronics of RAN

Vvedenskii sq., 1, Fryazino, 141120, Russia

Tel: (095)-526 9191, FAX: (095)-203 8414

The reflection of light from a five-layered structure (Fig. 1) containing a magneto-optic (MO) and a photoconducting (PC) film, separated by a metal layer, is investigated. The incident light consists of TE and TM polarized plane waves, with amplitudes $A = A_0 \exp(i\Phi_1)$ and $B = B_0 \exp(i\Phi_2)$, respectively. Linear polarized incident light ($\Phi_1 = \Phi_2$, with arbitrary values of A_0 and B_0) and circular polarized light ($\Phi_1 \neq \Phi_2$) are considered.

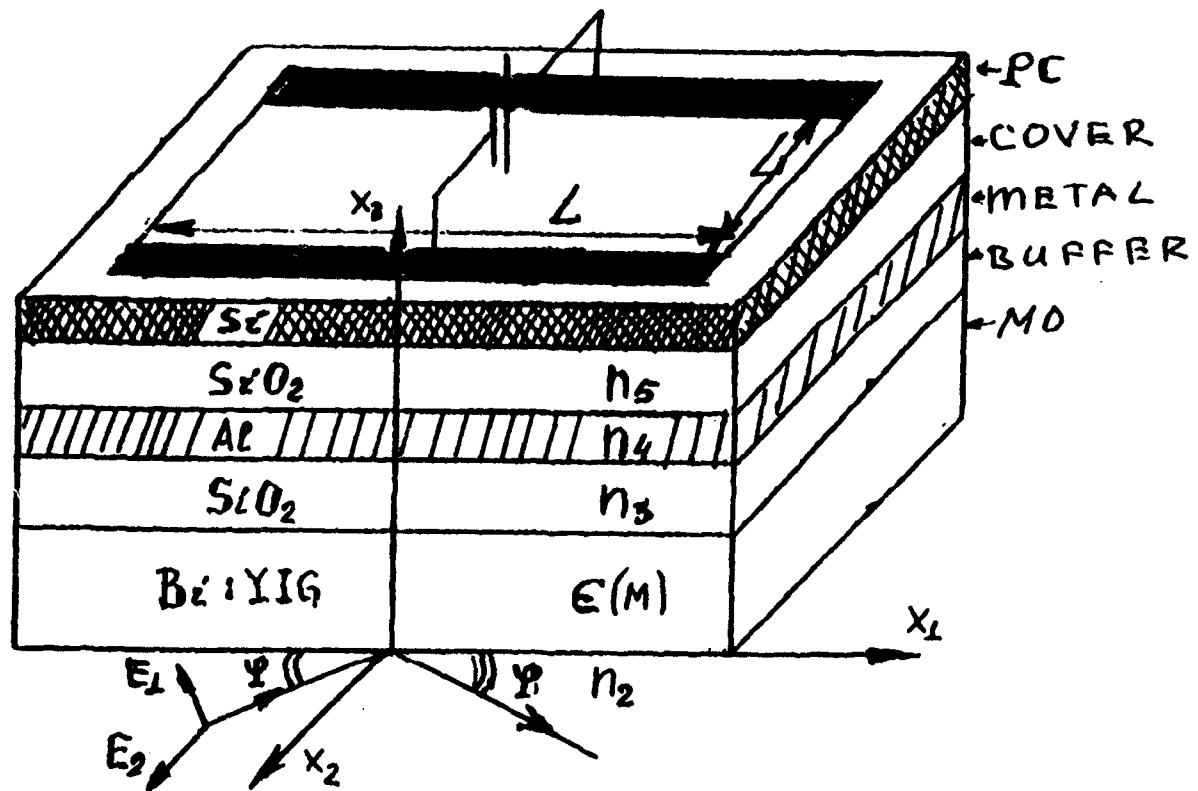


Fig. 1. Oblique incidence of light at an angle of incidence equal to ϕ . $E_3 = E_i \cos(\phi)$ - component of the TM - polarized light, E_2 - TE light. Si is a photoconducting layer.

The MO layer is magnetized in the plane, shown in Fig. 1, and has a gyrotropic type of dielectric permittivity given by

$$\epsilon_1 = \begin{vmatrix} n_1^2 & ig & 0 \\ -ig & n_1^2 & 0 \\ 0 & 0 & n_1^2 \end{vmatrix} \quad (1)$$

where, if g is positive, the magnetic moment vector has the orientation shown in Fig. 1. If g is negative, the vector has the opposite orientation. Note that $n_1 > n_2 > n_3$, a situation that can easily be achieved in practice. The angle of incidence of the light can be varied in the range $\phi = (0, \cos^{-1}[n_2/n_1])$, which corresponds to total internal reflection. Hence, in the buffer layer n_3 , there is an evanescent field.

For linearly polarised light, Fig. 2 shows the TM and TE reflection coefficients as a function of the angle ϕ for the five layered structure, with $d = 1.5 \mu\text{m}$ (MO layer), $b = 0.5 \mu\text{m}$ (buffer layer), $h = 120 \text{ \AA}$ (metal layer), $n_1 = 2.25 + i0.008$, $g = 0.05$, $n_2 = 1.95$, $n_3 = 1.5$, $n_4 = 1.5$, $n_5 = 0.826 + i6.23$, where ϕ is varied from zero to the angle of total internal reflection $\phi_1 = 39.8^\circ$. Fig. 3 shows the same dependence, but for $g = -0.05$. Note that these dependencies are calculated for the wavelength $\lambda = 0.516 \mu\text{m}$ for which the YIG film containing Bi can have huge values of g . One can see that Figs. 2,3 have min/max points, where the biggest energy transfer from one polarization to other occurs. This is due to a spatial resonance that occurs when the angle of incidence ϕ satisfies the condition $k_0 d \cos(\phi_1) = 2\pi N + \Delta$, where $k_0 = 2\pi/\lambda$, ϕ_1 is the

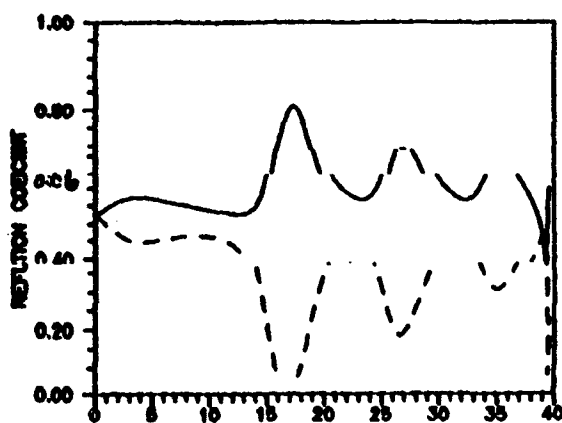


Fig. 2 Energy reflection coefficients

solid line: TE; dashed line: TM

$g = 0.05$

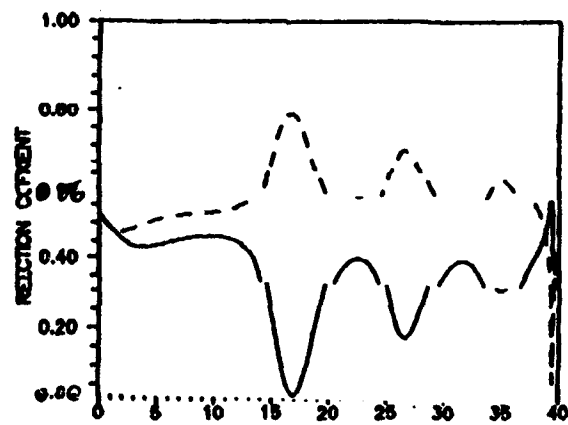


Fig. 3. Energy reflection coefficients

solid line: TE waves

dashed line: TM waves

$g = -0.05$

angle of the light propagation in the MO layer ($n_1 \cos(\phi_1) \simeq n_2 \cos(\phi)$) and Δ is a phase shift at the MO film - buffer layer boundary. For this structure, the incident angles for resonance are $\phi \simeq 17^\circ$, 25° and 35° . Besides these angles, however, there is another very interesting possibility for the angle incidence. It is well-known that a metal layer can support

surface plasmons (SP) that are TM in nature. Hence, if the angle of incidence of the light is chosen to satisfy the phase-matching conditions $n_2 \cos(\phi) = n_{sp}^r$, where n_{sp}^r is the SP propagation constant, we will have energy transfer from the incident light into the SP. Note that the TE polarized light does not connect to the SP for a non-magnetic structure ($g = 0$). In a gyromagnetic layer, energy transfer from TE to TM polarized lights occurs and, because of this fact, TE light can now excite the SP mode as well. Also, in a practical system, the thickness of the buffer layer would be quite small ($b \leq \lambda$), where λ is the wavelength. This is required for efficient excitation of the SP. It is clear that the dispersion curves of the SP have to be calculated for the complete five layered structure, i.e. we must include all layers. The SP modes are located upon the metal layer (n_4 in our geometry) but the small values of the thicknesses d and b are of interest here. The dispersion curve of SP for Al is shown in Fig. 4, where the Fig.4(a) is the dependence of the SP propagation constant on the Al thickness and Fig. 4(b) is the attenuation constant dependence. Note that an Al-thickness of 120 Å corresponds to SP excitation at $\phi \simeq 39^\circ$, in Figs. 2,3. The part of Figs. 2,3 in that region of the angle of incidence, is shown in Fig. 5 and this shows a very important result. This is that the phase-matching conditions are different for the $g = 0.05$ and $g = -0.05$ (inverse orientation of M).

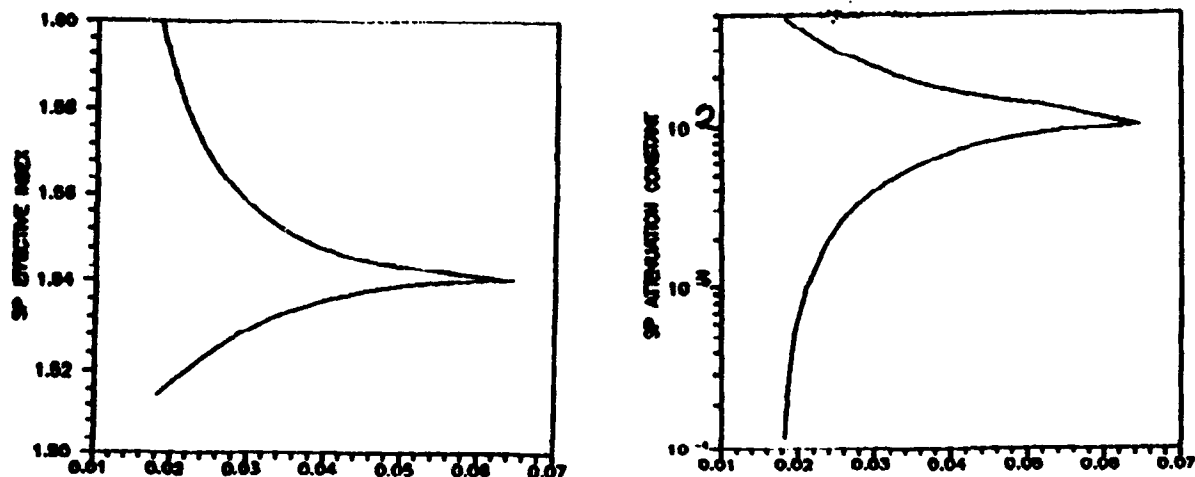


Fig. 4 Surface polaritons in the five-layer structure

Since the system can easily be tuned to $\phi = 39.37^\circ$ we can use the SP response, as opposed to the spatial resonances. The advantage of this move is that the SP resonance is sharp with a high signal-to-noise ratio. For the angle $\phi = 39.37^\circ$, the reflection coefficients of a TE wave (R_{TE}) and a TM wave (R_{TM}) are, $R_{TE} = R_{TM} = 0.35$, for $g = 0.05$, and for $R_{TE} = 0.1$, $R_{TM} = 0.6$, for $g = -0.05$. This means that the polarisation rotation of the reflected light, for $g = 0.05$, is $F = 0^\circ$ while for $g = -0.05$, it is $F \simeq 40^\circ$. For both cases, the total insertion losses are $\alpha = 1.5$ dB. Note that to get a Faraday rotation of 40° in a pure MO film would involve $\alpha = 4.5$ dB. Clearly then, this is one of the advantages of such a structure. Fig. 6 shows that there exists a resonance with a non-symmetric SP. A typical feature of the SP non-symmetric branch is the inverse proportionality of the SP attenuation constant upon the metal (Al) film thickness (Fig. 4b). From Fig. 5 we can estimate the half-width of the SP resonance to be $0.2^\circ / 40^\circ = 0.05$, which corresponds to a value of attenuation constant of an SP in that region of Al thickness (Fig. 4b).

For nonlinear applications it is profitable to use a resonance with a SP. In that case, light tunnelling into the PC layer causes the appearance of a current I , and an associated magnetic field H_{pc} that can reorient the magnetic moment to $M_{\rightarrow} - M$, if $H_{pc} > H_a$, where H_a is the anisotropy field of the YIG film. For the [111] orientation H_a could be less than 1.0 Oe. The light intensity in the PC layer creating the switching photocurrent is estimated to be $P_{sw} = H_{pc}^2 2L/\gamma$ (for Si the parameter $\gamma \simeq 0.4$ A/W). If $H_{pc} = 1.0$ Oe, and the cell size is $L = 10 \mu\text{m}$, then $P_{sw} = 0.5$ mW with a power density of $5 \text{ kW}/\text{cm}^2$.

If the initial value g is 0.05 (direct orientation) and the light intensity in the PC layer achieves the value P_{sw} then the magnetic field of the photocurrent will switch the orientation of the magnetic moment to the back orientation ($M_{\rightarrow} - M$). From Fig. 5 we can see that the field amplitude in the PC layer for $g = -0.05$ is three times more than for $g = 0.05$. This means that when the light intensity decreases the back reorientation ($-M_{\rightarrow} M$) will take

place only for $P \approx 0.1 P_{sw}$. Hence, the TE reflected light will show a bistable dependence, as shown in Fig. 7.

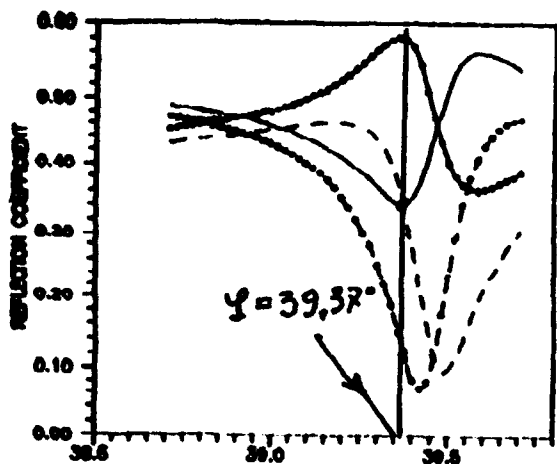


Fig. 5 Reflection coefficients

Solid lines: TE;

Dashed lines: TM

Smooth lines: $g = 0.05$

Marked lines: $g = -0.05$

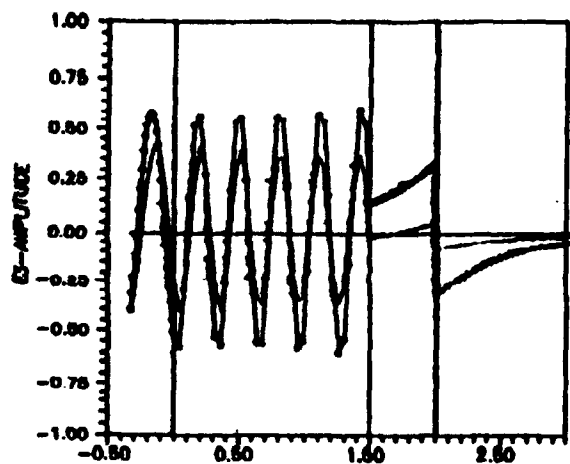


Fig. 6 Field envelope of the TM light

Angle of incidence = 39.37°

Smooth line: $g = 0.05$

Marked line: $g = -0.05$

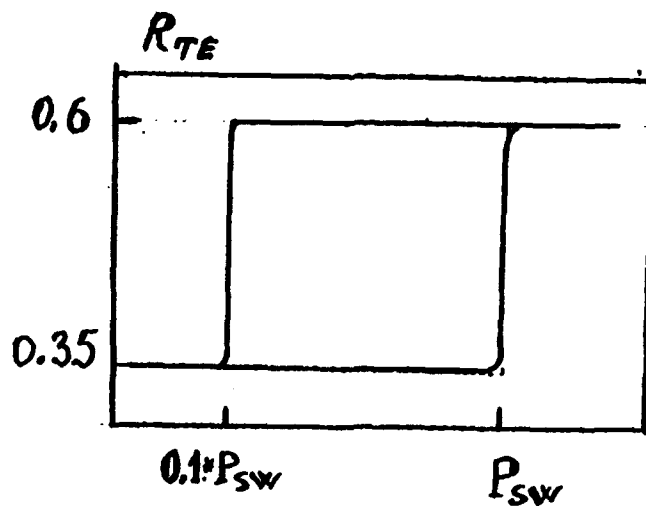


Fig. 7 Bistable dependence of the reflection coefficient of the TE polarized light from the structure of Fig. 5.



Silica on Silicon 1

ITuE 11:00am-12:15pm
Mesquite B

Charles H. Henry, *Presider*
AT&T Bell Laboratories

Recent Progress in Silicon Based Integrated Waveguide Devices

K. Okamoto and M. Kawachi

NTT Optoelectronics Laboratories,
Tokai 162, Naka-Gun, Ibaraki Pref.,
319-11, Japan
Telephone : +81-292-87-7680

Introduction

Planar lightwave circuits (PLCs) are circuits that integrate fiber-matched optical waveguides on Silicon substrate to provide an efficient means of interaction for the guided-wave optical signals[1]. This paper describes the recent progress in PLCs such as star couplers, arrayed-waveguide grating WDM/FDM circuits, transversal filters, and polymer and Er-doped waveguides for possible active devices.

 $N \times N$ Star Coupler

$N \times N$ star couplers are quite useful in high-speed, multiple-access optical networks, since they evenly distribute the input signal among many receivers and make possible the interconnection between them. Dragone's type integrated-optic star couplers, in which a slab waveguide region is located between the fan-shaped input and output channel waveguide arrays, are quite advantageous to construct large scale $N \times N$ star couplers[2],[3]. Figure 1 shows the waveguide pattern of the 256×256 star coupler. The chip size is $80 \text{ mm} \times 80 \text{ mm}$. The input power, from any one of the 256 channel waveguides in the input array, is radiated to the dielectric slab region and it is received by the output array. In order to get the uniform power distribution into 256 output waveguides, the radiation pattern at the output side slab-array interface should be uniform over a sector of 256 guides. Since the radiation pattern is the Fraunhofer pattern of the field profile at the input side slab-array interface, proper sidelobes must be produced by the mode coupling from the excited input waveguide to neighboring guides. The star coupler parameters such as the aperture angle, the radius of curvature, and others were optimized by using Beam Propagation Method so as to get the maximum output and good splitting uniformity. Figure 2 shows the splitting loss histogram of 256×256 star coupler measured at $\lambda = 1.55 \text{ } \mu\text{m}$. The essential splitting loss when light is evenly distributed into 256 output waveguides are 24.1 dB. Therefore, the average of the excess losses in Fig.2 is $\alpha = 2.77 \text{ dB}$, and the standard deviation of the splitting losses is $\sigma = 1.42 \text{ dB}$, respectively. In Fig.2, the additional loss of 1.4 dB, which includes the propagation loss ($\sim 0.6 \text{ dB}$) and coupling losses with single-mode fibers ($\sim 0.4 \text{ dB/point}$), are not included. We have fabricated a series of star couplers

ranging from 8×8 to 256×256 . Table I summarizes the average excess losses and standard deviations of the fabricated $N \times N$ star couplers. Fiber attachment to the $N \times N$ star couplers has been successfully achieved by using 8-fiber ribbons with YAG laser welding[4]. The packaging excess loss for each point is about 0.6 dB.

Arrayed-waveguide grating

An arrayed-waveguide grating WDM (or FDM) circuit utilizes the wavelength (or frequency) dependent wavefront tilting which is caused by the sequential optical path length difference in the waveguide arrays[5],[6]. The arrayed-waveguide grating (Fig. 3) consists of input/output waveguides, two focusing concave slab waveguide regions and a phase-array of multiple channel waveguides with the path length difference ΔL between the adjacent waveguides. The light beam from the input waveguide radiates to the slab waveguide and then couples into the arrayed channel waveguides. After travelling through the arrayed waveguides, the light converges to a focal points in the second slab region where the output waveguides are located. The dispersion of the focal position x with respect to the wavelength λ is given by

$$\frac{d x}{d \lambda} = \frac{f m}{n_s d} \quad (1)$$

where f is the focal length of the converging lens, n_s is the effective index in the slab region, d is the pitch of the channel waveguides at their exits. The diffraction order m is given by $m = n_o \Delta L / \lambda$ where n_o is the effective index of the channel waveguide. It is shown that the multiple WDM or FDM signals are simultaneously focused to each prescribed position in the arrayed-waveguide grating. A 1-nm spaced 13-channel WDM operation and 10-GHz spaced 11-channel FDM operation have been achieved in $1.55 \mu\text{m}$ region[7].

Transversal Filter

Optical signal processing using waveguides as a delay line has the advantage of being able to process broadband signals. Coherent optical transversal filter (Fig.4) consists of the tunable splitters, the thermo-optic(TO) phase shifters, the delay lines with fixed delay time $k \tau$ (k : integer), and the beam combiner[8]. An arbitrary frequency characteristics of

$$H(\omega) = \sum_{k=0}^{n-1} a_k \exp(-jk \omega \tau) \quad (n : \text{number of taps}) \quad (2)$$

can be produced by the transversal filter. The complex tap coefficient a_k is expressed by controlling the amplitude and phase of the optical field using TO tunable splitters and phase shifters. A 16-tap transversal filter with $\tau = 50$ ps (a unit

delay line length 10 mm) has been fabricated on a single Si substrate[9]. Arbitrary m channels ($m = 0 \sim 8$) can be selected out of eight channels which are equally spaced with 2.5 GHz.

Er-doped Waveguide Laser and Amplifier

Rare-earth doped glass waveguides are attractive since they provide the active function to passive PLCs. Among them Er-doped waveguides are particularly important because they operate in the $1.5 \mu\text{m}$ spectral region. Er-doped glass waveguide amplifier with a small signal gain of 13.7 dB and a 0 dB gain pump threshold of 25 mW was achieved[10]. Fig. 5 shows the gain coefficient per unit length. A 0.65 dB/cm gain coefficient is more than four times larger than the waveguide loss. Laser oscillation in Er-doped ring resonator has recently been demonstrated[11]. The ring resonator configuration has advantages of a precisely controlled free spectral range and a possible integration with various optical circuits because the resonator does not require any waveguide facet mirrors.

Polymer Waveguide

The major advantages of the polymer waveguides are potential for low cost and fabrication flexibility. Channel waveguides composed of polymers synthesized from deuterated methacrylate and deuterated fluoromethacrylate monomers show low propagation loss of 0.1 dB/cm at $1.3 \mu\text{m}$ [12]. The ring resonator fabricated with the above polymer waveguide had a finesse of 14.8[13].

These Er-doped waveguides and polymer waveguides will provide various kinds of functions to PLCs on silicon substrate.

Acknowledgements

The authors would like to thank M.Nakahara and all members of Photonic Component Laboratory, NTT Opto-electronics Laboratories, for their contributions.

References

- [1] M.Kawachi, *Opt. & Quantum Electron.*, 22, p.391 (1990)
- [2] C.Dragone et al., *IEEE Photon. Tech. Lett.*, 1,p.241 (1989)
- [3] K.Okamoto et al., *IEEE Photon. Tech. Lett.*, 4, no.9 (1992)
- [4] K.Kato et al., *OEC'92 Chiba, Japan*, PD-1, July 15-17 (1992)
- [5] M.K.Smit, *Electron. Lett.*, 24, p.385 (1988)
- [6] H.Takahashi et al., *Electron. Lett.*, 26, p.87 (1990)
- [7] H.Takahashi et al., *OEC'92 Chiba, Japan* 17C1-3, July (1992)
- [8] K.Sasayama et al., *Electron. Lett.*, 25, p.1508 (1989)
- [9] K.Sasayama et al., *OFC'92 San Jose, TuC2*, Feb. (1992)
- [10] T.Kitagawa et al., *Electron. Lett.*, 28, p.1818 (1992)
- [11] T.Kitagawa et al., *ECOC'92, Berlin*, Th PD II.5 (1992)
- [12] S.Imamura et al., *Electron. Lett.*, 27, p.1342 (1991)
- [13] Y.Hida et al., *OEC'92 Chiba, Japan* 16B3-4, July (1992)

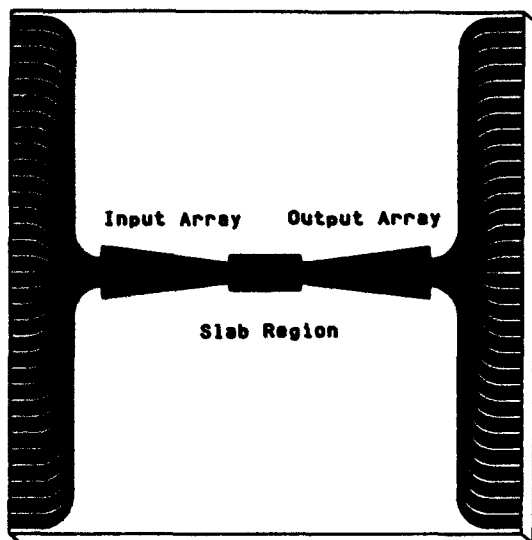


Fig.1 PLC 256x256 star coupler

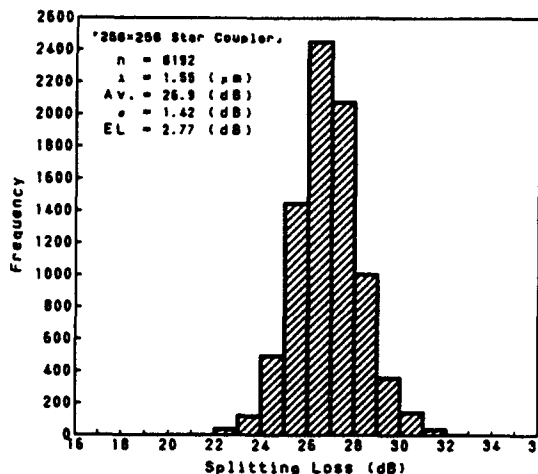


Fig.2 Splitting loss histogram of 256x256 star coupler

Table I Average excess losses and standard deviations of N x N star couplers

N	Av. Ex. Loss (dB) ¹⁾	St. Dev. (dB)	Number of Data
8	1.6	0.44	8x8=64
16	2.0	0.55	16x16=256
32	2.5	0.56	32x32=1024
64	3.1	0.92	64x25=1600
144	3.4	1.47	144x28=4032
256	4.2	1.42	256x32=8192

1) Excess loss from theoretical loss of $-10\log(1/N)$. Fiber coupling losses and propagation loss are included.

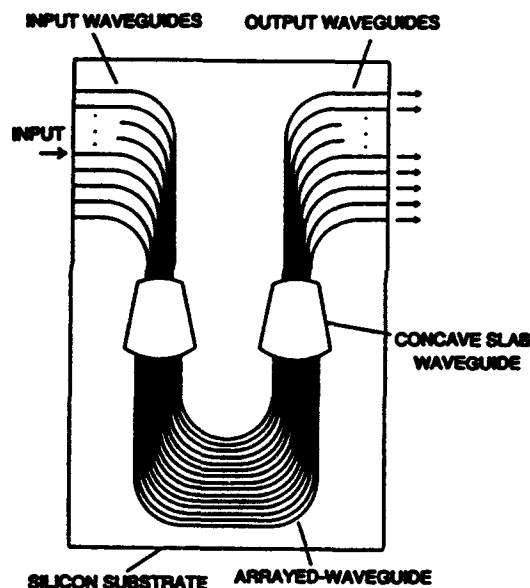


Fig.3 Arrayed-waveguide grating WDM/FDM circuit

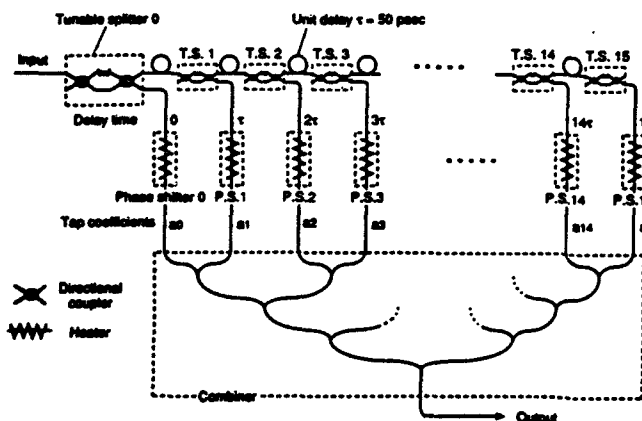


Fig.4 16-tap coherent optical transversal filter

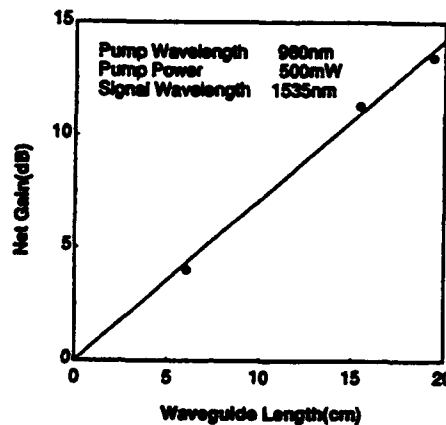


Fig.5 Gain vs waveguide length in Er-doped waveguide amplifiers

PHASE COHERENCE OF OPTICAL WAVEGUIDES

R. Adar, C. H. Henry, M. A. Milbrodt and R. C. Kistler
AT&T Bell Laboratories, Murray Hill, NJ 07974

By measuring null wavelength fluctuations of Mach Zehnder interferometers of different order we verify a proposed random walk model for accumulating phase in optical waveguides. A coherence length equal to $\approx 27M$ was found to characterize our silica on silicon waveguides.

1. INTRODUCTION

Optically integrated waveguide interferometer filters and multiplexers are widely used in optical communication applications. These devices principally consists of Mach Zehnder interferometers (MZI) and array multiplexers [1-4]. We have found that there is an element of randomness in the phase change ϕ along the waveguide, which is associated with device processing. The fluctuations $\Delta\phi$ affect device spectral characteristics. The accumulation of phase fluctuations along a waveguide undergoes a random walk with $\langle\Delta\phi^2\rangle$ proportional to the waveguide length. This process is characterized by a coherence length L_{coh} which is an intrinsic property of the waveguide. It can be defined as the length L of a batch of nominally identical waveguides for which a mean square $\langle\Delta\phi^2\rangle = 2 \text{ rad}^2$. We show that the expected linear dependence of $\langle\Delta\phi^2\rangle$ on L is obeyed and we report our measured value of L_{coh} for our silica on silicon waveguide technology.

2. THEORY

Suppose that due to fluctuations in dimensions and composition of the waveguide, n_{eff} , the local mode effective refractive index deviates from its average value: $n_{eff}(x) = \langle n_{eff} \rangle + \Delta n_{eff}(x)$. We expect that these processing associated fluctuations are only correlated over a length of a few microns or less, a length that is small compared to the waveguide length L . These assumptions imply that the phase fluctuation among an ensemble of waveguides averages to:

$$\langle\Delta\phi(L)^2\rangle = \left(\frac{2\pi}{\lambda}\right)^2 \int_0^L dx \int_0^L dx' \langle\Delta n_{eff}(x)\Delta n_{eff}(x')\rangle \equiv \frac{2L}{L_{coh}} \quad (1)$$

where in the last equality, we have defined a coherence length L_{coh} to describe the relation between the waveguide length and the phase fluctuations.

Since $\Delta\phi(L)$ is the sum of many random variables, it will be Gaussian distributed according to the central limit theorem [5]. It can, thus, be shown that

$$\langle e^{i\Delta\phi} \rangle = e^{-\frac{L}{L_{\text{coh}}}} \quad (2)$$

The above formalism is similar to that used to describe phase noise in semiconductor lasers.

Associated with phase fluctuations in the arms of an ensemble of MZIs are fluctuations in their null wavelength $\Delta\lambda$. $\langle \Delta\lambda^2 \rangle$ is related to L_{coh} by

$$\frac{L}{L_{\text{coh}}} = \frac{\pi^2 m^2 \langle \Delta\lambda^2 \rangle}{\lambda^2} \quad (3)$$

where m is the MZI order and L is the arm length. This relation is used in this work to measure L_{coh} .

3. EXPERIMENTAL RESULTS

Six groups of MZI interferometers were designed to have arm path length difference corresponding to orders 1.5, 3.5, 9.5, 27.5, 81.5 and 243.5. Table 1 lists the MZI long arm length, L_{MZ} , and the null wavelength, λ_{null} , for each group, which was designed to be close to 1560 nm. The shape of the MZIs is illustrated in the inset in Fig. 1. The directional couplers were identical in all groups and close to 3 dB near 1560 nm. The MZIs were made with our silica channel waveguides with phosphorus doped cores that are formed on silicon substrates [6].

Fig. 1 shows an example of the cross state insertion loss spectra measured on 5 adjacent identical MZIs with order $m=9.5$. Five closely placed MZIs of each group in Table 1 were measured in 3 different wafers of the same run. The results of the null wavelength fluctuation are summarized in Fig. 2. In the groups of low order, $m < 27$, a decrease in null wavelength fluctuations with increasing order is observed. In the higher order groups, however, this trend is changed and the fluctuations seem to saturate. In Fig. 3, the data of Fig. 2 is replotted as wavelength standard deviation versus $\sqrt{L_{\text{MZ}}}/m$. The dependence for the lower order MZIs is nicely fitted to a straight line in accordance with the prediction of (3). The fitted slope of $0.97 \cdot 10^{-7} \sqrt{M}$ is used in (3) to calculate a coherence length of 27 Meters.

The theoretical derivation of (3) predicts that the straight line fit in Fig. 3 should pass through the origin. Measurements, however, indicate that, in addition to the uncorrelated phase fluctuations included in this model, another contribution to phase fluctuation in MZIs is present in our waveguide devices, which is of a different nature. We suggest and have supporting measurement results that mask errors or irregularities substantially account for this observed floor in the wavelength fluctuations.

4. DISCUSSION AND SUMMARY

Waveguide interferometers like Mach Zehnder interferometers, have small scale random processing variations which can dominate their spectral fluctuations, especially for low order devices. These variations can be quantified in terms of a phase coherence length, L_{coh} . We determined $L_{\text{coh}} \approx 27M$ by measuring the rms fluctuations in null wavelength of various order Mach-Zehnder interferometers in the cross state. The

exact physical nature of the waveguide variations leading to the finite phase coherence length in our silica on silicon waveguides is currently not identified. A probable mechanism might be the dry etching process and its associated side wall roughening. The experimental assessment of L_{coh} for a given waveguide technology is, however, of major importance even in the absence of its physical understanding, both as a tool in modeling expected yields and average performances and as a design parameter in selecting a preferred device design for a particular application.

REFERENCES

- [1] R. Adar, C. H. Henry, R. F. Kazarinov, R. C. Kistler and G. R. Weber, *Journal of Lightwave Technology*, vol. 10, pp. 46-50 (1992).
- [2] T. Ikegami and M. Kawachi, *Physics World*, vol. 4, pp. 50-54 (1991).
- [3] C. Dragone, C. A. Edwards and R. C. Kistler, *IEEE Photonics Technology Letters*, vol. 3, pp. 896-899 (1991).
- [4] R. Adar, C. H. Henry, C. Dragone, R. C. Kistler and M. A. Milbrodt to be published in *Journal of Lightwave Technology*, 1992.
- [5] J. M. Wozencraft and J. M. Jacobs, Wiley, New York, 1956, chapter 2.
- [6] C. H. Henry, G. E. Blonder and R. F. Kazarinov, *Journal of Lightwave Technology*, vol. 7, pp. 1530-1539 (1989).

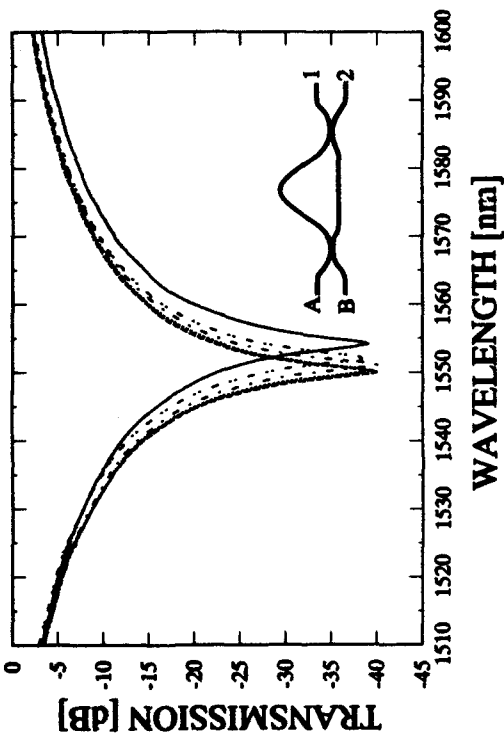


Fig. 1 Cross state transmission loss (fiber to fiber) of 5 nominally identical adjacent Mach Zehnder interferometers with order $m=9.5$.

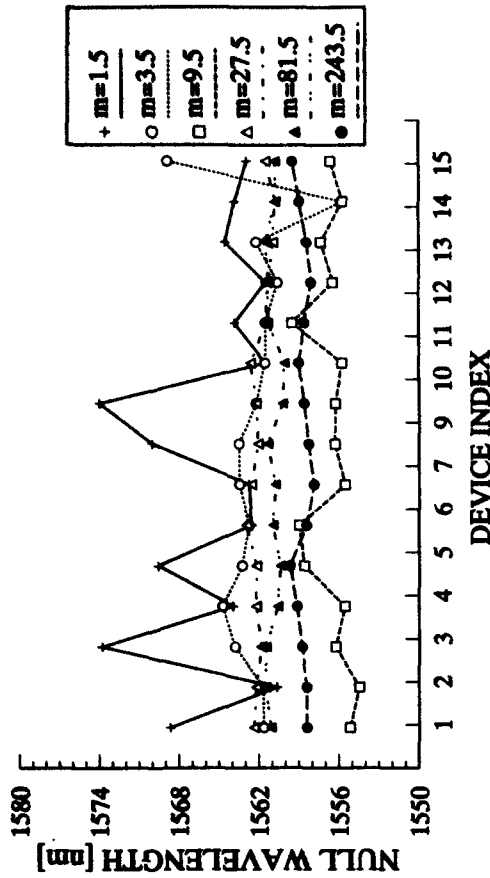


Fig. 2 Null wavelength fluctuations of 15 nominally identical Mach Zehnder interferometers of each group of Table 1.

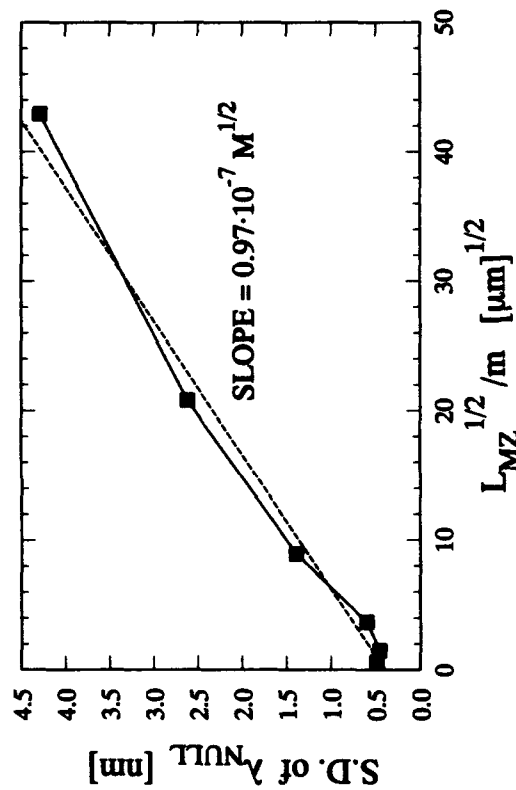


Fig. 3 The null wavelength fluctuations of Fig. 2 vs. the square root of L_{MZ} over the order m .

TABLE 1 Design parameters for the various order Mach Zehnder devices measured.

ORDER m	$L_{MZ}[\mu m]$	$\lambda_{MZ}[\mu m]$
1.5	4146	1556.3
3.5	5286	1563.3
9.5	7226	1556.9
27.5	10220	1559.2
81.5	14648	1559.5
243.5	21110	1559.2

SILICON-BASED RADIATIVE STAR POWER SPLITTERS

S. Day, R. Bellerby, G. Cannell, M. Grant, S. Rosser, P. Wensley
BNR Europe Limited, London Rd., Harlow, Essex.

I. Wilson, N. Lambert
Northern Telecom Optoelectronics, Brixham Rd., Paignton.

INTRODUCTION

The successful development of optical fibre networks towards fibre to the home systems will require the development of low cost passive optical branching components. Silica-on-silicon integrated optics technology is well suited to the fabrication of such devices. A key feature of this technology is that v-grooves for holding the input and output fibres can be precisely defined in the silicon substrate as part of the waveguide fabrication process, allowing passive fibre to waveguide alignment, leading to low cost device assembly and rugged fibre to waveguide coupling. Low loss (0.1 dB/cm) single mode channel waveguides with low interface loss to single mode fibre (0.2 dB/interface) (ref 1) have previously been demonstrated at BNR Europe Limited.

RADIATIVE STAR

For medium to high port count splitters or couplers, the radiative star coupler (ref 2) represents a very flexible attractive component. It can be designed for use either as a tree (1 X N) or a star (M x N) coupler. Unlike components made by other techniques such as concatenated directional couplers or Y junction devices, the number of input and outputs is not constrained to be a power of 2. Another key feature of the component is that the excess loss of the device is independent of the number of output ports. In contrast, for splitters based on Y junctions, the excess loss increases with each increase in splitting level.

The radiative star power splitter is shown schematically in figure 1. It consists of an input channel waveguide, a planar waveguide where the optical field radiates freely and an array of output waveguides which collect the radiated field. The optimum length of the planar region is that which maximises the power coupled into the outermost waveguide. A computer model has been developed which enables M x N components to be designed. The model is currently being used to produce 1 x 16 and 2 x 16 power splitters.

COMPONENT CHARACTERISATION

The first stage in developing components is to fabricate test components in chip form, before producing optimised components with integrated v-grooves. Active alignment of input and output fibres is required to measure such chip components. A semi-automated measurement system has been developed where alignment of fibres is performed manually and a personal computer is used for automated logging of signals. The test equipment that has been developed is shown schematically in figure 2. The optical fibre from a semiconductor laser source is mounted on a micromanipulator to enable active alignment with an input port of a test component. The wafers are sawn up into rectangular blocks, each block containing a number of test components. The blocks are mounted on a micromanipulator which can be traversed horizontally enabling different components to be rapidly aligned. Initial

alignment of the input fibre is performed by imaging the output via a lens onto an infra-red camera. The lens assembly is then removed and replaced with an array of multimode fibres. The signals from the multimode array are connected to a 16 channel detector/amplifier unit. A personal computer is used to record the signals via a 16 channel analogue to digital convertor. A monitor signal is taken via a fused fibre coupler, enabling drifts in the laser output power to be compensated for. Using this measurement technique, test devices can be characterised very rapidly. For example a block of five 4 x 16 components can be characterised in about 1 hour, a total of 640 measurements being recorded.

RESULTS FOR 1 x 16 SPLITTERS

From the theoretical modelling, 1 x 16 power splitters based on an array of uniform width waveguides have an intrinsic uniformity of 2.1 dB. Devices have been fabricated with a worst case insertion loss of 18.9 dB (ref 3). A further improvement in performance can be achieved by varying the width of the waveguides across the output array, so that outer waveguides are wider, enabling them to capture a higher fraction of the incident power.

The variable width approach has been used to fabricate 1 x 16 power splitters with integrated v-grooves. The components had a waveguide spacing (edge to edge) of 6 μm , a height of 5 μm , a Δn of 12×10^{-3} and widths varying between 6 μm for the central waveguide to 16 μm for the outer waveguides. The waveguides fan out to a final spacing of 250 μm , using S-bends with a radius of curvature of 20 mm, to give a device length, excluding v-grooves, of 30 mm. The spacing of 250 μm enables components to be pigtailed with commercially available 8-way ribbon fibre. Heat curing epoxy resin was used to bond the fibres into the v-grooves. The use of variable width waveguides has reduced the worst case loss from 18.9 dB to 17.3 dB. The insertion losses include the intrinsic splitting loss of 12 dB.

The pigtailed components have been environmentally cycled over the temperature range -40°C to $+70^{\circ}\text{C}$. All 16 ports have a loss variation less than ± 0.4 dB over the entire temperature range. These results demonstrate the feasibility of producing rugged components based on passive alignment using silicon v-grooves.

RESULTS FOR 2 x 16 POWER SPLITTERS

Future systems architecture will require more than one input to allow for head end redundancy, maintenance and future upgradability. To produce this component using Y junctions, it would be necessary to produce a chip containing a 2 x 2 directional coupler followed by two separate 1 x 8 splitters. However, using the radiative approach, two or more input waveguides can be positioned adjacent to each other, both pointing at the central member of the output array. This is clearly a much simpler arrangement and can be achieved with very little loss penalty above that of a radiative 1 x 16 power splitter.

Test wafers of 2 x 16 power splitters have been designed and fabricated. These test wafers did not include v-grooves, enabling 30 components to be produced on one wafer, figure 3 shows a photograph of the wafer. The devices were measured using the test equipment described above. Figure 4 shows a histogram of the insertion loss measurements of the 16 output ports for both input ports, giving a total of 32 points. The worst case insertion loss for this device was 16.5 dB. Insertion losses have been measured as a function of wavelength. Figure 5 shows a graph of the insertion loss of one port of a 2 x 16 power

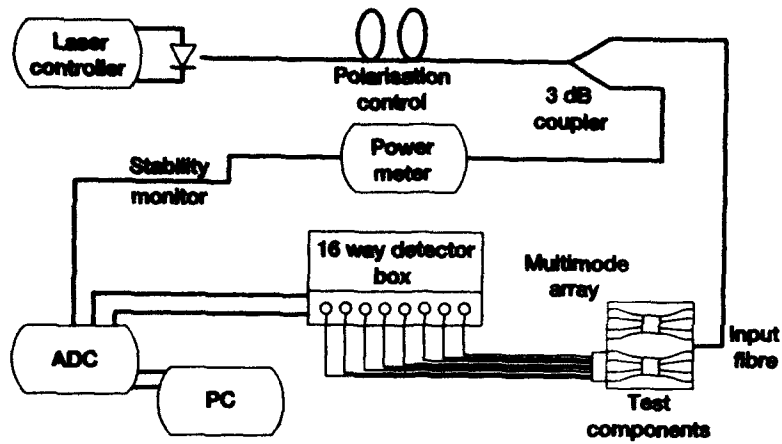


Fig. 2 Semi-automated test equipment

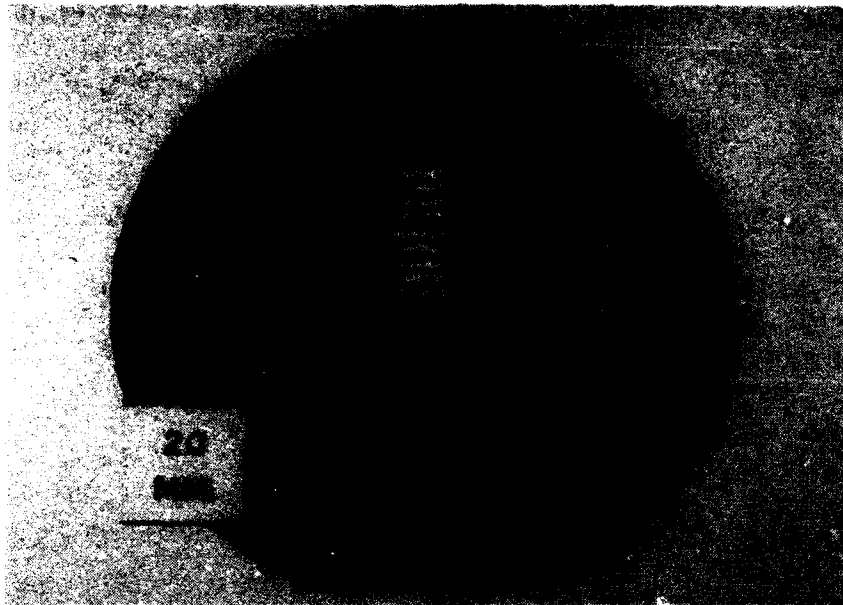


Fig. 3 Wafer containing 30 2 x 16 components

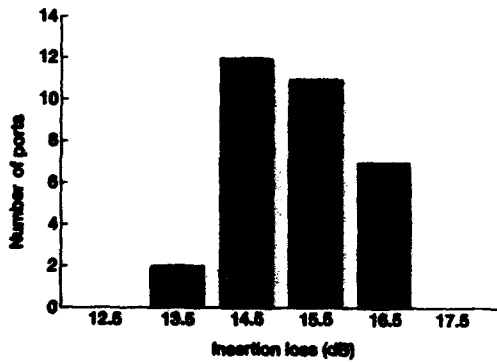


Fig. 4 Histogram of losses of 2 x 16

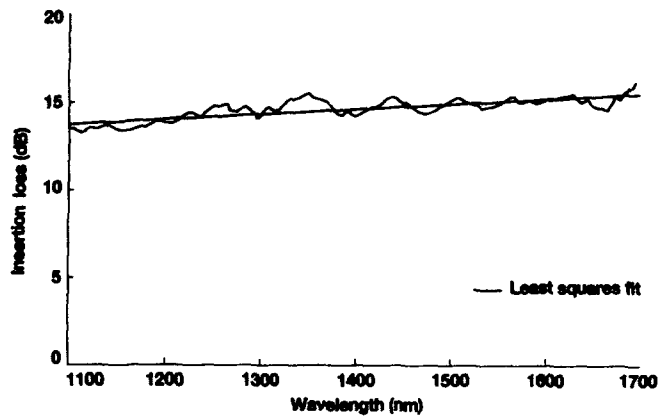


Fig. 5 Spectral loss of a 2 x 16 radiative star

splitter. From the results, it can be seen that the components are spectrally flat over both the 1300 nm and 1550 nm windows. The results from the test wafer have been used to develop optimised 2 x 16 designs with integral v-grooves. Further results on fibre pigtailed 2 x 16 devices will be presented at the conference.

CONCLUSIONS

The feasibility of producing ruggedised silica on silicon components has been demonstrated by fabricating 1 x 16 power splitters with a worst case insertion loss of 17.3 dB. Pigtailed components have been environmentally cycled over the range -40°C to +70°C and have shown less than ± 0.4 dB change in loss. 2 x 16 components with a worst case insertion loss of 16.5 dB have also recently been produced. Spectral measurements have shown that the components are wavelength insensitive.

ACKNOWLEDGEMENTS

The authors would like to thank the directors of BNR Europe Limited for permission to publish this letter. This work has been partially funded by the Commission of the European Communities under RACE project 1089.

REFERENCES

1. M. Grant et al, "Low loss coupling of ribbon fibres to silica on silicon integrated optics using preferentially etched v-grooves", Integrated Photonics Research 92 Proc., April 1992.
2. C. Dragone et al, "Efficient multichannel integrated optics star coupler on silicon", IEEE Photonics Technology Letters, Vol 1, No. 8, August 1989, pp 241-243.
3. S. Day et al, "A silicon-based fibre pigtailed 1 x 16 power splitter", Electronics Letters, 7th May 1992, Vol. 28, No. 10 pp 920-921.

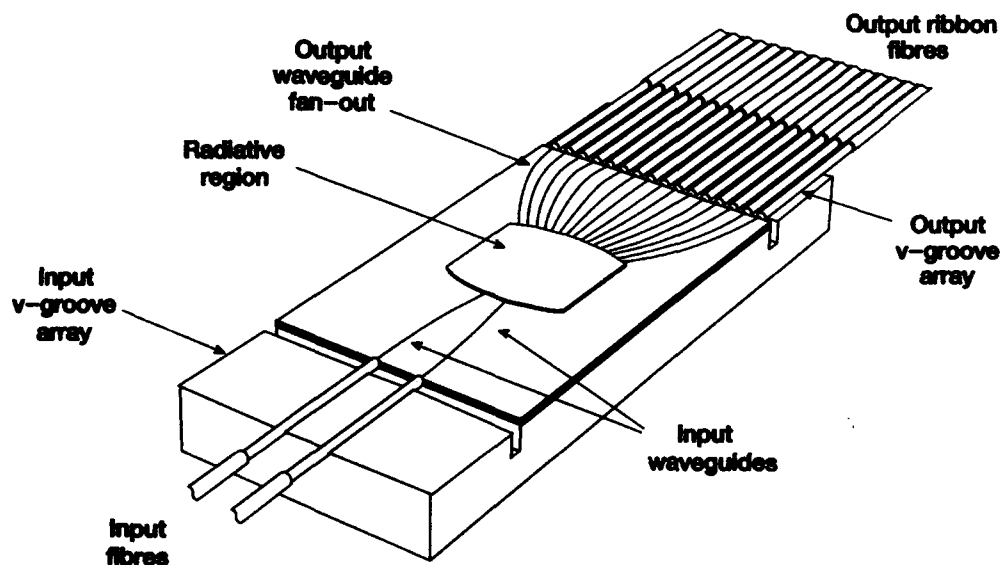


Fig. 1 Radiative star 2 x 16 power splitter

Three-dimensional optical interconnects by stacked ARROW waveguides

S. Asakawa, Y. Kokubun, T. Baba* and M. Ohyama

Yokohama National University

Division of Electrical and Computer Engineering
156 Tokiwadai, Hodogayaku, Yokohama, 240 JAPAN
Phone +81-45-335-1451 Ext. 2368

*Tokyo Institute of Technology
Precision and Intelligence Lab.

The stacked configuration of photonic circuits is important to the dense integration of photonic devices and the flexible construction of photonic circuits. In this study, we developed a stacked configuration of ARROW's with a coupling region to establish three-dimensional optical interconnects.

Since the confinement factor of conventional waveguides is not large enough to avoid the cross talk resulting from the light coupling, these waveguides are not suitable for the dense optical interconnects. In contrast to this, ARROW-type waveguides[1],[2] have much thinner cladding and much larger confinement factor than those of conventional waveguides. In addition, the coupled waveguide structure with controlled coupling efficiency can be constructed[4]. In our previous report[3], we realized a stacked configuration of ARROW. However, since the loss discrimination of higher order modes was not large enough in the upper waveguide, single mode propagation was not obtained. To solve this problem, we introduce a new configuration for stacking ARROW-type waveguides.

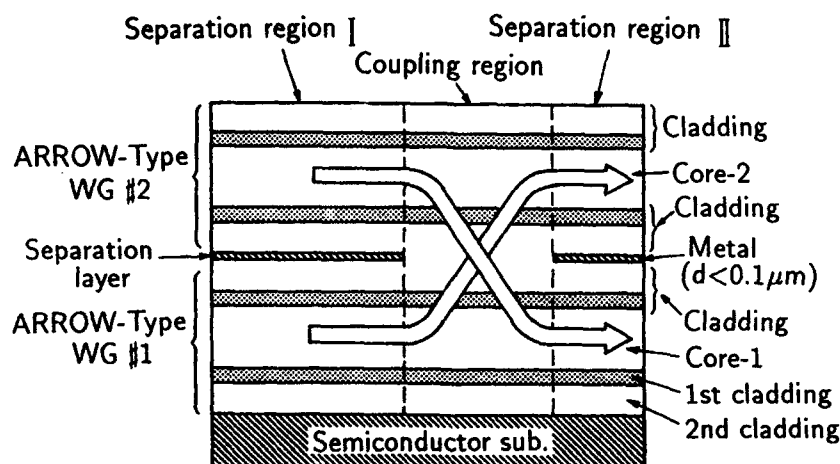


Fig. 1 Fundamental structure of 3-dimensional optical interconnects by stacked ARROW-type waveguides.

The fundamental structure of the stacked configuration using ARROW-type waveguides is shown in Fig. 1. The stacked waveguides are symmetric ARROW's which have two pairs of interference cladding upper and under the core. The ARROW-type waveguides are separated by a thin metal layer of less than $0.1\mu\text{m}$ thick. Since higher order modes are radiated and absorbed in this layer, each waveguide can achieve single-mode propagation. In addition, since the separation layer prevents the light from leaking into the adjacent waveguide, the crosstalk is completely suppressed. The loss increase due to the use of this metal layer is negligibly small. Another advantage of this configuration is that a coupling region can be easily constructed by eliminating partly the separation region, because the separation layer is very thin and the thickness of the second cladding is a half of the core. In the following, let us call this region as a coupling region, and the region in which waveguides are separated as a separation region, as shown in Fig. 1.

The propagation and coupling characteristics of this stacked configuration were analyzed by solving the Maxwell's equations directly for the whole waveguide structure and by using the quasi-guided mode approximation[5]. We adopted an ARROW-B which consists of NA45 glass core ($n_c=1.54$, $d_c=3\mu\text{m}$) and SiO_2 first cladding ($n_1=1.46$, $d_1=0.5\mu\text{m}$). The wavelength was assumed to be $0.633\mu\text{m}$ which made the experiment easy. The TE polarization was assumed in this analysis.

We simulated the case in which the fundamental mode in the waveguide #2 is transformed into that in the waveguide #1 through the coupling region. When the fundamental mode of waveguide #2 is incident on the coupling region, it is expanded into three coupled modes TE_0^c , TE_1^c , and TE_2^c . Fig. 2 shows the field distributions of these coupled modes just after the incidence on the coupling region ($z=0$). Fig. 2 (d) shows the actual field, i.e. the superposition of the three coupled modes. The coupling efficiency from the fundamental mode of waveguide #2 to the field shown in Fig. 2 (d) reaches $\eta = 0.997$. The propagation constants of these coupled modes are very close to each other, and the difference between the propagation constants of the TE_0^c and TE_1^c modes are almost the same as that between the TE_1^c and TE_2^c modes. To achieve the power exchange from the waveguide #2 to #1, the coupling region should have the length $L=\pi/|\Delta\beta|$, where $\Delta\beta$ is the difference of propagation constants between the TE_0^c and TE_1^c modes. In the case of $d_c=3\mu\text{m}$, L is 3.7mm. When the phase difference between the TE_0^c and TE_1^c modes $\Delta\phi_{01}$ is $-\pi$ at the end of the coupling region, the difference between the TE_0^c and TE_2^c modes $\Delta\phi_{02}$ is -2π and the field is localized in the bottom core, as shown in Fig. 3. In addition, this total field is very close to the fundamental mode in the waveguide #1 in the separation region, so that the coupling efficiency from the coupling region to the waveguide #1 is as high as $\eta=0.997$. Thus the overall power coupling efficiency between the upper and lower waveguides is theoretically greater than 0.99. The same results are led in the

case of coupling from the waveguide #1 to #2 as well as for the stacked configuration with ARROW.

The stacked configuration with ARROW-B was fabricated by the RF sputtering technique, and the coupling characteristics were measured. The thickness of NA45 glass core d_c was $2\mu\text{m}$ and that of SiO_2 first cladding d_1 was $0.6\mu\text{m}$. The metal separation layer of $0.06\mu\text{m}$ thick was formed by the vacuum evaporation using $\text{Cr}(n=2.6+j3.0)$. In addition, the coupling region was formed by eliminating partly the separation layer. Although the optimum length of the coupling region was theoretically $L=2.1\text{mm}$ for $d_c=2\mu\text{m}$, various lengths were prepared in consideration of the fabrication error in the film thickness.

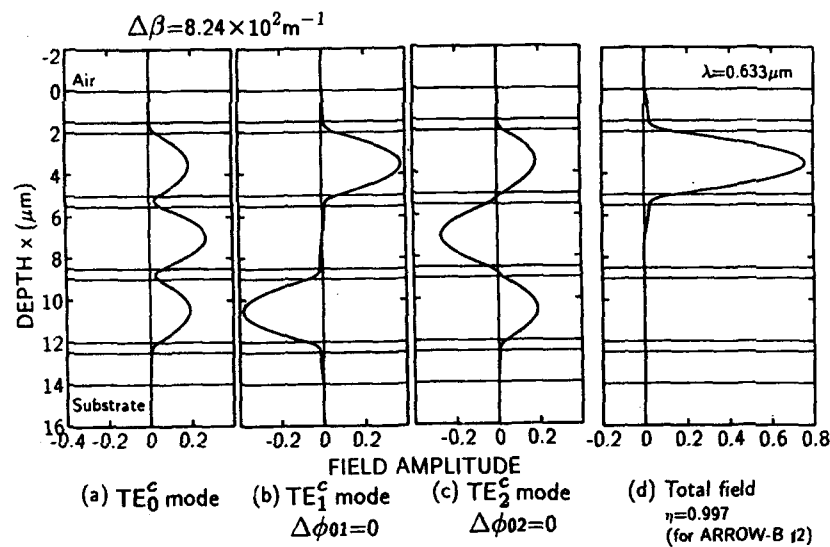


Fig. 2 Field distributions of coupled modes excited by TE_0 mode of ARROW-B #2. ($z=0$)

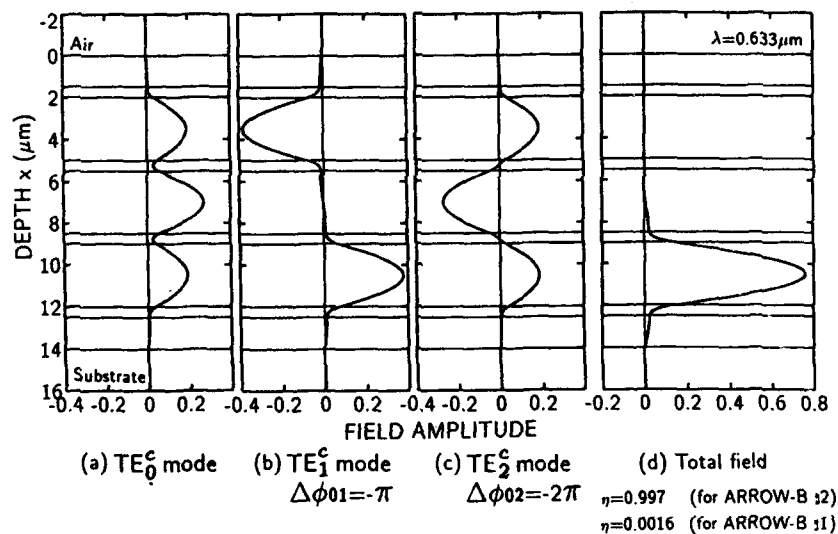


Fig. 3 Field distributions of coupled modes at end of coupling region. ($z=L=3.7\text{mm}$)

Near field patterns of the output light at the separation region are shown in Fig. 4 (a) and (b). It can be seen that a completely independent propagation in each waveguide and single-mode propagation were successfully achieved. Fig. 5 shows the near field patterns at the separation region after passing through the coupling region. When the light was incident on the upper or the lower core, the light output was observed from the opposite waveguide. Thus almost the complete light coupling between the upper and lower waveguides was observed. However, the length of the coupling region was 6mm, and this discrepancy between theoretical and experimental results seems to be caused by the fabrication error of the film thickness. Since the multilayer waveguides like ARROW's have several light control functions, this configuration can be an element of vertical coupler-type devices such as polarization splitters and wavelength demultiplexers.

References

- [1] M. A. Duguay, Y. Kokubun, T. L. Koch and L. Pfeiffer: *Appl. Phys. Lett.*, vol.49, p. 13 (1986)
- [2] T. Baba and Y. Kokubun: *IEEE Phot. Tech. Lett.*, vol.1, p. 232 (1989)
- [3] T. Baba, Y. Kokubun, T. Sakaki and K. Iga: *J. Lightwave Tech.*, vol.6, p. 1440 (1988)
- [4] M. Mann., U. Trutschel., C. Waechter, L. Leine and F. Lederer: *Opt. Lett.*, vol. 6, p. 805 (1991)
- [5] Y. Suematsu and k. Furuya, *IEEE Trans. Microwave Theory and Tech.*: vol.MTT-23, p. 170-175 (1975)

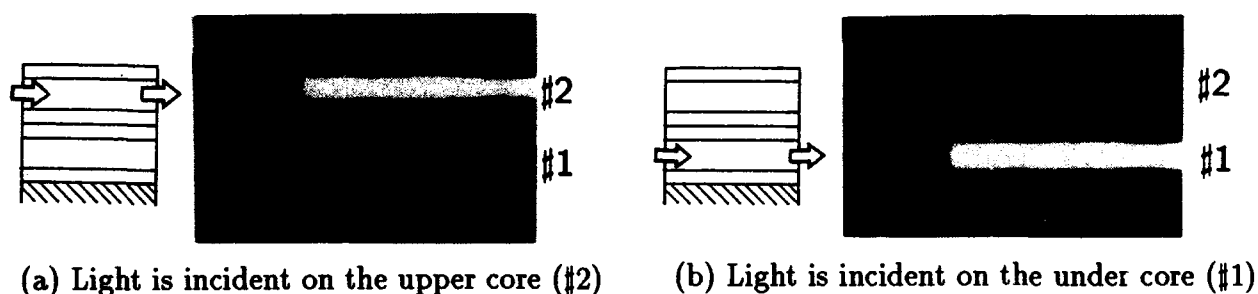


Fig. 4 Near field patterns at the separation region. ($\lambda=0.633\mu\text{m}$)

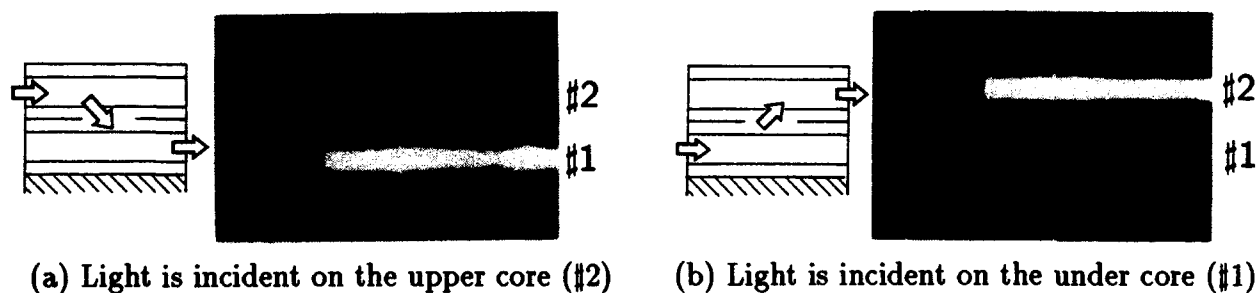


Fig. 5 Near field patterns after passing the coupling region. ($\lambda=0.633\mu\text{m}$)



Nonlinear Wave Propagation

ITuF 11:00am-12:30pm
Mesquite C/D

Govind Prasad Agrawal, *President*
University of Rochester

Solitons in Birefringent Optical Fibers

C. R. Menyuk
 Department of Electrical Engineering
 University of Maryland
 Baltimore, MD 21228-5398
 tel. no. (410)-455-3501

It has long been known that so-called single-mode fibers are really bimodal due to fiber birefringence.¹ As a consequence, the fundamental equation which describes nonlinear pulse propagation is not, in general, the nonlinear Schrödinger equation. It is instead a set of coupled equations which can be written in the form²

$$\begin{aligned} i\frac{\partial u}{\partial s} + i\delta\frac{\partial u}{\partial s} + \frac{1}{2}\frac{\partial^2 u}{\partial s^2} + (|u|^2 + B|v|^2)u &= 0, \\ i\frac{\partial v}{\partial s} - i\delta\frac{\partial v}{\partial s} + \frac{1}{2}\frac{\partial^2 v}{\partial s^2} + (B|u|^2 + |v|^2)v &= 0, \end{aligned} \quad (1)$$

where ξ is normalized distance along the optical fiber, s is normalized retarded time, and u and v are normalized complex envelopes of the two polarizations, δ is proportional to the strength of the birefringence, and B is the ratio of the cross-coupling to the self-coupling in the Kerr effect. In a linearly birefringent fiber $B = 2/3$, and all fibers are linearly birefringent unless they are specially prepared.

In contrast to the nonlinear Schrödinger equation, Eq. (1) is not integrable and cannot be solved by using the inverse scattering method unless $B = 1$ which requires specially fabricated, elliptically birefringent fibers.² Nonetheless, Eq. (1) still retains many of the properties of the nonlinear Schrödinger equation, and soliton-like solutions of mixed polarization will exist in general. The existence of soliton-like solutions, which we will refer to here simply as solitons, could be—and were—anticipated on the grounds that Eq. (1) is a Hamiltonian deformation of an integrable Hamiltonian system.³

When a single pulse of mixed polarization is injected into an optical fiber, the portion of the pulse in each polarization tends to shift its central frequency in such a way that the group velocities approach each other. Linearly, the two polarizations would walk off from one another due to the differing group velocities. If the walkoff length is shorter

than the nonlinear scale length, the length over which the Kerr effect would lead to a 2π rotation of the phase, then the nonlinearity is too weak to shift the central frequencies of the two polarizations sufficiently far to create a self-trapped structure. Conversely, when the walkoff length is long compared to the nonlinear scale length, the two polarizations will self-trap and will form a soliton. The specific value at which self-trapping occurs must be determined numerically. In the case in which

$$u(\xi = 0) = v(\xi = 0) = \frac{A}{\sqrt{2}} \operatorname{sech} s, \quad (2)$$

one finds that when $\delta = 0.5$, the threshold amplitude for self-trapping is $A = 1$.⁴

The nonlinear frequency shift which occurs when nonlinear pulses in different polarizations interact has been used as the basis of soliton dragging and trapping gates.⁵ An architecture in which these gates would be used to read packet headers has been designed.⁵ In modeling a network in which a large number of these gates would be used, one must be able to solve simultaneously for the behavior of a large number of gates. This sort of CAD program requires the use of a reduced set of equations since the simultaneous solution of Eq. (1) for a large number of gates is not numerically feasible. We have developed an approach which relies on solving a set of coupled ordinary differential equations rather than Eq. (1). This approach should also be useful in dealing with architectures based on loop mirrors.⁶

In long-distance communications, the solitons are of 50 ps duration as opposed to 1 ps or less in the switching application. As a consequence, the walkoff length assuming a fixed birefringence is short compared to the nonlinear scale length. The walkoff length is roughly 100 km, while the nonlinear scale length is roughly 1000 km. So, why do solitons exist? It is because the birefringence is rapidly and randomly varying relative to these long scale lengths. Averaging over the rapid variations, one finds⁷ that Eq. (1) becomes, at lowest order in an expansion in powers of (polarization correlation length)/(nonlinear scale length),

$$\begin{aligned} i \frac{\partial u}{\partial s} + \frac{1}{2} \frac{\partial^2 u}{\partial s^2} + \frac{8}{9} (|u|^2 + |v|^2) u &= 0, \\ i \frac{\partial v}{\partial s} + \frac{1}{2} \frac{\partial^2 v}{\partial s^2} + \frac{8}{9} (|u|^2 + |v|^2) v &= 0, \end{aligned} \quad (3)$$

where u and v can be *any* set of orthogonal polarizations. Equation (3) can be solved using the inverse scattering method,² and, if we assume that every point of time is initially in the same polarization state, then Eq. (3) reduces to the usual nonlinear Schrödinger equation. Thus, we now understand from a fundamental standpoint why the nonlinear Schrödinger equation is such a good model for an optical fiber in the parameter regime of interest for long-distance communications.

Carrying out the expansion which leads to Eq. (3), we find the extent to which the randomly varying birefringence will tend to depolarize single solitons over long lengths. The conclusion is that to maintain solitons in a single state of polarization (as a function of time—the polarization state rapidly changes as a function of position) one must use good optical fibers, but fibers that are within the parameter range of standard communication fibers.

This work was supported by DOE and NSF. The numerical work was done at SDSC and NERSC.

REFERENCES

1. I.P. Kaminow, *IEEE J. Quantum Electron.* **QE-17**, 15 (1981).
2. C.R. Menyuk, *IEEE J. Quantum Electron.* **QE-23**, 174 (1987); C.R. Menyuk, *IEEE J. Quantum Electron.* **QE-25**, 2674 (1989).
3. C.R. Menyuk, *Opt. Lett.* **12**, 614 (1987); C.R. Menyuk, *J. Opt. Soc. Am. B* **5**, 392 (1988).
4. C.R. Menyuk in *Guided Wave Nonlinear Optics*, D. B. Ostrowsky and R. Reinisch, eds. (Kluwer, Dordrecht, 1992), pp. 457–488.
5. M.N. Islam, *Opt. Lett.* **14**, 1257 (1989); **15**, 417 (1990); M.N. Islam, C.E. Soccolich, and D.A.B. Miller, *Opt. Lett.* **15**, 909 (1990); M.N. Islam and J.R. Sauer, *IEEE J. Quantum Electron.* **27**, 843 (1991); J.R. Sauer, M.N. Islam and S.P. Djaili, "A soliton ring network," to be published in *J. Lightwave Tech.*
6. N.J. Doran in *Guided Wave Nonlinear Optics*, *loc. cit.*, pp. 535–552.
7. P.K.A. Wai, C.R. Menyuk, and H.H. Chen, *Opt. Lett.* **16**, 1231 (1991); P.K.A. Wai, C.R. Menyuk, and H.H. Chen, *Opt. Lett.* **16**, 1735 (1991).

A Modified Beam Propagation Method for Modeling Nonlinear Effects in Optical Fibers

Peter S. Weitzman and Ulf Osterberg, Thayer School of Engineering,
Dartmouth College, Hanover, NH 03755
(603)646-1466

I. Theory

The Beam Propagation Method (BPM) has been used extensively to model propagation in optical fibers [1,2]. In this paper we extend this technique to model propagation in the presence of a second and third order nonlinear susceptibility in the glass. Using this technique, nonlinear effects such as second harmonic generation (SHG), self phase modulation (SPM) and cross phase modulation (XPM) can be modeled.

The propagation of light can be modeled by the following scalar wave equation

$$\nabla^2 E - \frac{1}{c^2} \frac{\partial^2 E}{\partial t^2} = -S \quad (1)$$

where E is the electric field, c is the speed of light and S is a source term which depends on the material as

$$S = -\mu_0 \frac{\partial^2 P}{\partial t^2} \quad (2)$$

where P is the induced polarization in the material. For the examples presented in this paper we consider induced polarizations of the form:

$$P = \chi^{(1)}E + \chi^{(2)}EE + \chi^{(3)}EEE \quad (3)$$

Where $\chi^{(1)}$, $\chi^{(2)}$, and $\chi^{(3)}$ are the linear, second and third order nonlinear susceptibilities of the material. The technique presented in this paper can be easily generalized to any order of nonlinearity.

As an example of the technique, SHG in the presence of SPM and XPM is modeled. When considering the recently discovered phenomena of SHG in glass optical fibers [3], the induced second harmonic light is at least two orders of magnitude less intense than the fundamental light. We therefore make the approximation that the pump beam at the fundamental wavelength is not depleted as the second harmonic is generated. In addition to this we assume that the $\chi^{(2)}$ present in the fiber is not altered by the generated second harmonic light. With these approximations, the equation for the propagation of second harmonic light ($E_{2\omega}$) in the presence of radiation at the fundamental wavelength (E_{ω}) becomes:

$$(\nabla^2 + k_{2\omega}^2)E_{2\omega} = S \quad (4)$$

where

$$S = -\mu_0 \omega^2 \chi^{(2)} E_{\omega} E_{\omega} - 3\mu_0 \omega^2 \chi^{(3)} E_{\omega} E_{\omega}^* E_{2\omega} \quad (5)$$

and $k_{2\omega}$ is the wavevector of the second harmonic light given by

$$k_{2\omega}(x,y,z) = \frac{2\pi}{\lambda_{2\omega}} n_{2\omega}(x,y,z) \quad (6)$$

where $n_{2\omega}$ is the local refractive index for second harmonic light and $\lambda_{2\omega}$ is the wavelength. Several physical models have been proposed recently to explain the phenomena of SHG in glass optical fibers [4,5]. Each of these models is in agreement that a DC field generated by an interaction of fundamental and second harmonic light and the intrinsic $\chi^{(3)}$ in the glass creates a periodic $\chi^{(2)}$ structure which is capable of efficient SHG and has exactly the

right periodicity so that the phase-matching condition for SHG is satisfied. Based on this model, the induced $\chi^{(2)}$ in the glass is given by

$$\chi^{(2)} = \gamma \chi^{(3)} \text{Re} \left\{ E_{\omega w} E_{\omega w} E_{2\omega w}^* \right\} \quad (7)$$

Where $E_{\omega w}$ is the field of the fundamental light used for writing the grating, $E_{2\omega w}$ is the field of the second harmonic light used to write the grating and γ is a parameter of the material which determines the proportionality between the DC field and the induced $\chi^{(2)}$. Substituting (7) into (5), we obtain the form of the source term used for the results presented in this paper.

$$S = \gamma \chi^{(3)} \text{Re} \left\{ E_{\omega w} E_{\omega w} E_{2\omega w}^* \right\} E_{\omega} E_{\omega} \quad (8)$$

where E_{ω} is the fundamental field used to read out the second harmonic light and γ has absorbed the other constants found in (5). The $\chi^{(3)}$ term in equation (5) models the effect of cross phase modulation (XPM) and has been brought over to the left side of equation (4) by considering an intensity dependent refractive index of the form:

$$n_{2\omega}(x, y, z) = n_{2\omega 0}(x, y, z) + n_2 I_{\omega}(x, y, z) \quad (8)$$

where I_{ω} is the intensity of the fundamental light, $n_{2\omega 0}$ is the unperturbed index of refraction and n_2 is the Kerr effect coefficient.

To simplify the numerical solution of equation (4), it is useful to employ the slowly varying envelope approximation [1]. This reduces the scalar wave equation to the paraxial form

$$[\nabla_T^2 - 2i\bar{k} \frac{\delta}{\delta z} + (k^2 - \bar{k}^2)]E = S e^{i\bar{k}z} \quad (10)$$

where ∇_T is the transverse Laplacian operator and \bar{k} is the usual average wavenumber for the problem. Equation (10) remains accurate as long as the refractive index difference between the core and cladding of the fiber remains small compared to the refractive index. To solve equation (10) using a finite difference technique, we first re-arrange the terms in the form

$$\frac{\delta E}{\delta z} = \frac{\nabla_T^2 E}{2i\bar{k}} + \frac{(k^2 - \bar{k}^2) E}{2i\bar{k}} - \frac{S e^{i\bar{k}z}}{2i\bar{k}} \quad (11)$$

A direct finite difference solution of equation (11) would involve the solution of a banded system of equations where the bandwidth would be determined by the number of grid points per dimension used in the finite difference approximation. A solution of this banded system would be computationally inefficient. Several researchers have presented techniques where the x and y derivatives in the transverse Laplacian are solved separately in two steps, each of which generates tridiagonal systems of equations which can be solved efficiently [6,7]. Using a similar technique, a finite difference approximation for each propagation step Δz involves the solution of the following two equations

$$\begin{aligned} & \frac{-1}{2i\bar{k}\Delta_x^2} E(x+1, y, \frac{\Delta z}{2}) + \left(\frac{2}{\Delta z} + \frac{1}{i\bar{k}\Delta_x^2} - \frac{(k^2 - \bar{k}^2)}{4i\bar{k}} \right) E(x, y, \frac{\Delta z}{2}) - \frac{1}{2i\bar{k}\Delta_x^2} E(x-1, y, \frac{\Delta z}{2}) \\ & = \frac{1}{2i\bar{k}\Delta_y^2} E(x, y-1, 0) + \left(\frac{2}{\Delta z} - \frac{1}{i\bar{k}\Delta_y^2} + \frac{(k^2 - \bar{k}^2)}{4i\bar{k}} \right) E(x, y, 0) + \frac{1}{2i\bar{k}\Delta_y^2} E(x, y+1, 0) \\ & \quad - \frac{S e^{i\bar{k}z}}{2i\bar{k}} \quad (12) \end{aligned}$$

$$\begin{aligned}
& \frac{-1}{2i\bar{k}\Delta_y^2} E(x, y+1, \Delta z) + \left(\frac{2}{\Delta z} + \frac{1}{i\bar{k}\Delta_y^2} - \frac{(k^2 - k^2)}{4i\bar{k}} \right) E(x, y, \Delta z) - \frac{1}{2i\bar{k}\Delta_y^2} E(x, y-1, \Delta z) \\
& = \frac{1}{2i\bar{k}\Delta_x^2} E(x-1, y, \frac{\Delta z}{2}) + \left(\frac{2}{\Delta z} - \frac{1}{i\bar{k}\Delta_x^2} + \frac{(k^2 - k^2)}{4i\bar{k}} \right) E(x, y, \frac{\Delta z}{2}) + \frac{1}{2i\bar{k}\Delta_x^2} E(x+1, y, \frac{\Delta z}{2}) \\
& \quad - \frac{S e^{ikz}}{2i\bar{k}} \quad (13)
\end{aligned}$$

In order to use the finite difference equations (12) and (13), it is necessary to employ a boundary condition at the edges of the computational window. The actual fields of bound fiber modes extend infinitely far into the cladding so some type of artificial boundary condition which approximates this behavior must be utilized. We have chosen to use the radiation boundary condition recently presented by Hadley [8]. Hadley's technique involves calculating the ratio of fields at points close to the boundary. When a zero occurs in the field, such as in an asymmetric fiber mode, a singularity results which cannot model the physical situation. This problem has been avoided by checking for this condition and substituting $k_{\perp} = k$ so that the field is assumed to be propagating normal to the boundary.

This modification has been found to eliminate the numerical instability associated with Hadley's procedure. To test stability and convergence of this boundary condition, we propagated exact asymmetric modes (LP₁₁, and LP₂₁) in a step-index fiber for 100,000 propagation steps of one wavelength each and observed that the modes were not significantly changed by the algorithm despite the zeroes in the field.

When propagating the intense fundamental light, the intensity dependent refractive index will depend on the unknown field solution for the next propagation step. To simplify the computation, we calculate the refractive index for the current step explicitly from the known field from the previous propagation step. This approximation assumes that the intensity distribution does not change appreciably over a distance Δz . In order to achieve an algorithm which is stable and converges to the correct result, we have experimentally determined that the Δz step should be on the order of one wavelength at the second harmonic frequency. It is reasonable to assume that the intensity distribution does not change over this distance.

II Results

Using the source term in equation (8), propagation and growth of Second Harmonic light in the presence of an intense fundamental beam has been modeled. The results presented in this paper are for a step index fiber with a core radius of 3 μm , and Δn of 0.017 between the core and cladding. The computational window is a square with a side of length 4 core radii. This window contains a 64 by 64 grid of points which were used in the finite difference calculations. The propagation step used was one wavelength at the second harmonic frequency in the core material. The wavelengths used are representative of the output of a Nd:YAG laser (fundamental 1.064 μm , second harmonic 0.532 μm). In the example presented here, the $\chi^{(2)}$ grating is given by equation (7) where E_{ω} and $E_{2\omega}$ are in the LP₁₁ mode and $E_{2\omega}$ is in the LP₀₁ (Fundamental) mode. E_{ω} , $E_{\omega\omega}$, $E_{2\omega\omega}$, and the generated SH light are all plotted in figure 1. The SH light is generated in the LP₀₁ mode. In general, the SH light will be generated in whichever SH mode was used to seed the grating, the efficiency of the growth will depend on the overlap integral between $E_{2\omega\omega}$, $E_{\omega\omega}^2$, and E_{ω}^2 . The length dependence of this growth can be modeled using the nonlinear BPM.

To study the effect of SPM and XPM on the phase matching condition, three simulations were run. The three cases all used reading and writing beams in the LP₀₁ mode. In case 1, SPM and XPM were not included. In case 2, SPM and XPM were included in $E_{2\omega\omega}$ and $E_{\omega\omega}$, but not in E_{ω} or the generated SH. In case 3, SPM and XPM were included in the reading and writing beams. It was observed that when different intensities are used for reading and writing, the efficiency of SHG is decreased. When the same intensity is used for reading and writing, the effect of SPM and XPM in reading and writing cancel each other out and the efficiency is the same as the $n_2 = 0$ case. This is in agreement with the result predicted by Ouellette [9] using a plane wave approximation to the actual fiber modes.

The nonlinear BPM has been shown to work for the modeling of SHG, SPM and XPM in optical fibers. It should be noted that this is a very general algorithm which can be used for any refractive index profile and many other nonlinear interactions other than those presented in this short summary.

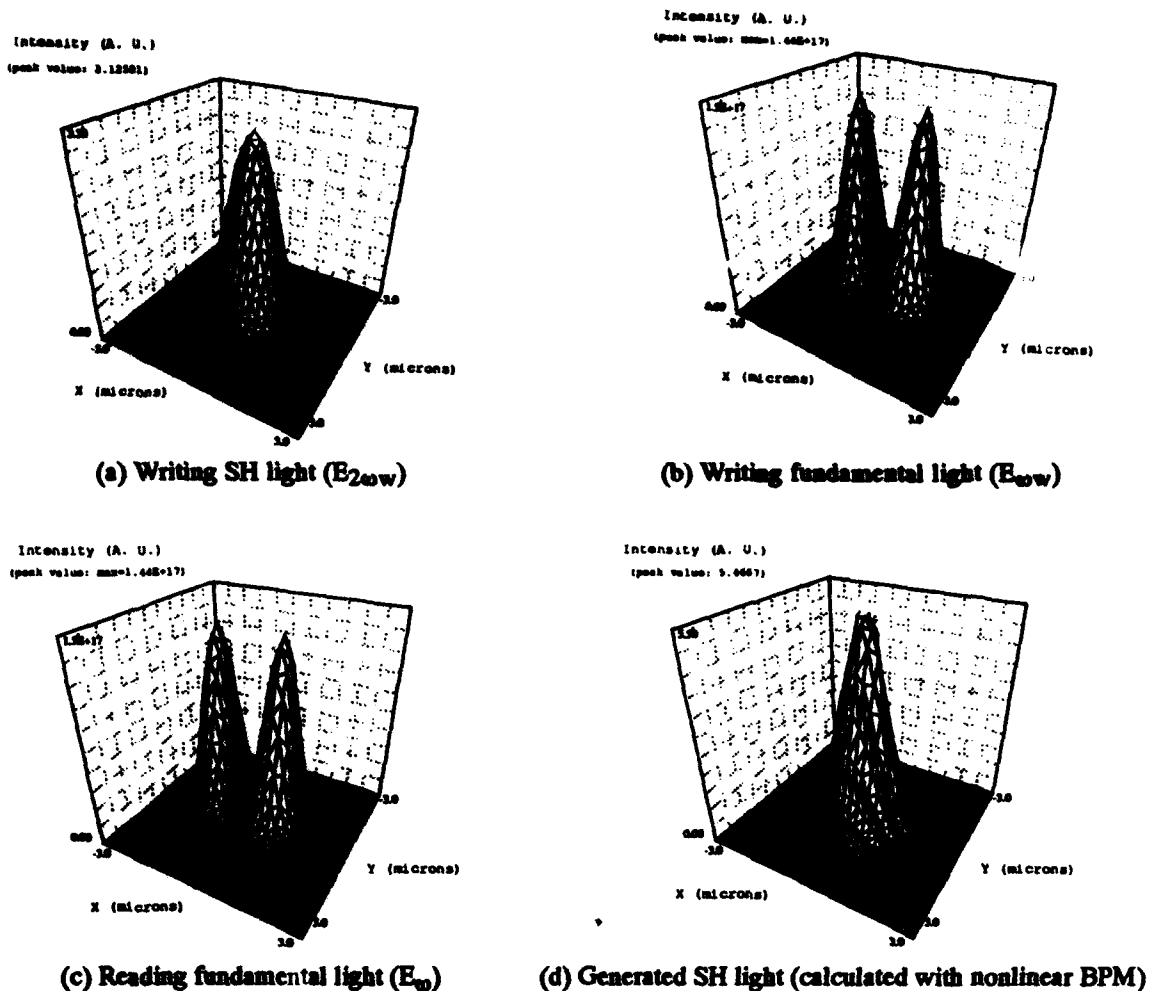


Figure 1. Fiber Cross Section Intensity Profiles

REFERENCES

- [1] M. D. Feit and J. A. Fleck Jr., "Light propagation in graded-index optical fibers," *Applied Optics*, vol. 17, pp. 3990 - 3998, 1978
- [2] J. Saijonmaa and D. Yevick, "Beam-propagation analysis of loss in bent optical waveguides and fibers," *J. Opt. Soc. Amer. Vol. 73*, pp. 1785 - 1791, 1983.
- [3] U. Osterberg and W. Margulis, "Dye Laser Pumped by Nd:YAG Laser Pulses Frequency Doubled in an Optical Fiber," *Optics Letters*, vol. 11, p. 516, 1986.
- [4] D. Z. Anderson, "Efficient second-harmonic generation in glass fibers: The possible role of photoinduced charge redistribution.," *Proc. SPIE 1148*, pp. 186-192 (1989).
- [5] E. M. Dianov, P. G. Kazansky, D. Yu. Stepanov, "On the Problem of Photoinduced Second-Harmonic Generation in Optical Fiber," *Sov. J. Quantum Electron.*, vol. 19, pp. 575-576, 1989.
- [6] D. Yevick and B. Hermansson, "Efficient Beam Propagation Techniques," *IEEE J. Quant. Elec.*, vol. 26, pp. 109 - 112, 1990.
- [7] J. Yamauchi, T. Ando, and H. Nakano, "Beam Propagation Analysis of Optical Fibres by Alternating Direction Implicit Method," *Electronics Letters*, vol. 27, pp 1663 - 1665, 1991.
- [8] G. R. Hadley, "Transparent Boundary Condition for the Beam Propagation Method," *IEEE J. Quant. Elec.* vol. 28, pp. 363 - 370, 1992.
- [9] F. Ouellette, "Axial Dependence of X(2) Gratings in Optical Fiber: Effect of the Intensity-Dependent Detuning," *Electronics Letters*, vol. 26, pp. 740 - 741, 1990.

A Theoretical Investigation Of Soliton Decoupling In Cross-Phase Modulation Systems

Min Du, Andrew K. Chan and Charles K. Chui
Dept. of Electrical Engineering, Texas A&M University
College Station, Texas 77843
(409)-845-7458

Cross-phase modulation (XPM) in nonlinear optical fibers has been investigated for several purposes in recent literature^{[1],[2]}. Several XPM-induced soliton devices, such as Kerr shutters, intensity discriminators, soliton switches^{[2],[6]}, have been developed for applications in optical soliton communication. To our knowledge, most of these investigations are limited to designs of coupling or switching devices. Few works are devoted to optical soliton multiplex communication system by compensating the fiber XPM effect. Although the XPM effect is always exist when two or more optical waves copropagating inside a nonlinear fiber, we have found that these mutual-modulating effects can be greatly reduced to near zero under certain condition. This condition provides a possibility to realize an optical soliton multiplex communication system. That is, two solitons at two different wavelengths or two different polarizations may copropagate in a nonlinear fiber without interfering each other.

We report here the condition for obtaining two decoupled soliton solutions to the coupled nonlinear Schrödinger equation. A general XPM system with asymmetric SPM and XPM nonlinear coefficients $\{\gamma_{ij}\}$ is considered. The coupled equations are written as

$$j \frac{\partial u}{\partial z} + j\beta_{1u} \frac{\partial u}{\partial \tau} - \frac{\beta_{2u}}{2} \frac{\partial^2 u}{\partial \tau^2} + (\gamma_{uu} |u|^2 + \gamma_{uv} |u_2|^2) u + \alpha_u u = 0, \quad (1)$$

$$j \frac{\partial v}{\partial z} + j\beta_{1v} \frac{\partial v}{\partial \tau} - \frac{\beta_{2v}}{2} \frac{\partial^2 v}{\partial \tau^2} + (\gamma_{vu} |u|^2 + \gamma_{vv} |u_2|^2) v + \alpha_v v = 0 \quad (2)$$

where u and v represent the slow varying complex envelopes of the two optical fields respectively. In these equations, z , $\tau = t - z/v_g$, β_2 and β_1 denote the propagation distance, the reduced local time and dispersive parameters of the medium respectively. $\{\gamma_{ij}\}$ represents the nonlinear coefficient matrix (including SPM and XPM). α is the fiber loss. These equations are applicable to either two-wavelength XPM in nonlinear fibers or two-polarization XPM in nonlinear birefringent fibers.

Assuming that optical pulses have identical soliton pattern $q(\tau, z)$ for both u and v . The exact fundamental soliton solutions of (1) and (2) can be written as

$$u(\tau, z) = q(\tau, z) e^{j\Phi_u(\tau, z)}, \quad (3)$$

$$v(\tau, z) = \sqrt{\sigma} q(\tau, z) e^{j\Phi_v(\tau, z)}. \quad (4)$$

Here $q(\tau, z)$ denotes the fundamental soliton envelope and σ is a coefficient by which the independent soliton co-propagation condition is determined. $\Phi_u(\tau, z)$ and $\Phi_v(\tau, z)$ are phase factors associated with the solitons. For the case of two-wavelength XPM, β_{1u} and β_{1v} represent the group velocity respect to two different wavelengths (λ_1 and λ_2). β_{2u} and β_{2v} are GVD coefficients for λ_1 and λ_2 , respectively. The elements of $\{\gamma_{ij}\}$ become: $\gamma_{uu} = \gamma_1$, $\gamma_{uv} = 2\gamma_1$, $\gamma_{vu} = 2\gamma_2$, and $\gamma_{vv} = \gamma_2$. γ_1 and γ_2 are the fiber nonlinear coefficients for λ_1 and λ_2 respectively, with $\gamma_i = 2\pi n_2/\lambda_i A_{eff}$. For the two-polarization XPM case, u and v stand for amplitudes along the x and y axes. $\Delta\beta = \beta_{1x} - \beta_{1y}$ or $\delta = \Delta\beta T_0/2|\beta_2|$ is the wavenumber mismatch due to linear birefringence of the fiber. In this case,

the elements of $\{\gamma_{ij}\}$ are reduced to $\gamma_{uu} = \gamma_{vv} = \gamma$, and $\gamma_{uv} = \gamma_{vu} = \frac{2}{3}\gamma$. It is important to note that the nonlinearity parameter γ is the same for both polarisations because of their degenerate frequencies.

Let us discuss the exact solutions for the two families of solitary waves as in the following:

Case (I). For fundamental solitary wave solution, we have phase terms given by

$$\Phi_u(\tau, z) = (k_u + \alpha_u) z - \frac{\beta_{1u}^2}{2\beta_{2u}} z + \frac{\beta_{1u}}{\beta_{2u}} \tau, \quad (5)$$

$$\Phi_v(\tau, z) = (k_v + \alpha_v) z - \frac{\beta_{1v}^2}{2\beta_{2v}} z + \frac{\beta_{1v}}{\beta_{2v}} \tau \quad (6)$$

where k_u and k_v are soliton phase constants. In anomalous-dispersion regime ($\beta_2 < 0$), the fiber supports a bright soliton when the initial distribution ($z = 0$) is that of a bright soliton. It has the hyperbolic secant distribution given by

$$q(\tau, z) = \sqrt{\frac{2k_u}{\sigma\gamma_{uv} + \gamma_{uu}}} \operatorname{sech} \left[\sqrt{-2\frac{k_u}{\beta_{2u}}} \tau \right]. \quad (7)$$

In normal dispersion regime ($\beta_2 > 0$), a dark soliton solution of the form

$$q(\tau, z) = \sqrt{\frac{k_u}{\sigma\gamma_{uv} + \gamma_{uu}}} \tanh \left[\sqrt{\frac{k_u}{\beta_{2u}}} \tau \right] \quad (8)$$

can exist in the fiber with proper initial profile. From the above equations, it can be shown that the soliton wavenumber k_u can be determined from initial input pulse at $z = 0$. Furthermore, the soliton envelope of both bright and dark soliton depend only on local time τ , and not on distance z . Hence, the shapes are invariant during propagation.

Case (II). For soliton modulated wave solution with velocity $v_m = 1/\beta_m$, traveling bright or dark soliton modulated CW signals are supportable by the fiber. These solutions are slightly different from those above. The phase terms are expressed by

$$\Phi_u(\tau, z) = (k_u + \alpha_u) z - \frac{1}{2\beta_{2u}} (\beta_{1u}^2 - \beta_m^2) z + \frac{1}{\beta_{2u}} (\beta_{1u} - \beta_m) \tau, \quad (9)$$

$$\Phi_v(\tau, z) = (k_v + \alpha_v) z - \frac{1}{2\beta_{2v}} (\beta_{1v}^2 - \beta_m^2) z + \frac{1}{\beta_{2v}} (\beta_{1v} - \beta_m) \tau. \quad (10)$$

The traveling bright and dark soliton modulated waves take the form of

$$q(\tau, z) = \sqrt{\frac{2k_u}{\sigma\gamma_{uv} + \gamma_{uu}}} \operatorname{sech} \left[\sqrt{-2\frac{k_u}{\beta_{2u}}} (\tau - \beta_m z) \right], \quad (11)$$

$$q(\tau, z) = \sqrt{\frac{k_u}{\sigma\gamma_{uv} + \gamma_{uu}}} \tanh \left[\sqrt{\frac{k_u}{\beta_{2u}}} (\tau - \beta_m z) \right] \quad (12)$$

in the anomalous and normal dispersive regime respectively. These soliton modulated CW profiles move with the speed of v_m along distance z . The two propagation constants k_u and k_v are determined by the input soliton power with the relationship

$$\frac{k_u}{\beta_{2u}} = \frac{k_v}{\beta_{2v}}$$

for both cases (I) and (II). In order to realize independent soliton propagation for both fields (or components), the coefficient σ must satisfy the equation

$$\sigma = \frac{\beta_{2u}\gamma_{vu} - \beta_{2v}\gamma_{uu}}{\beta_{2v}\gamma_{uv} - \beta_{2u}\gamma_{vv}} \quad (13)$$

which sets the criterion for designs of two-wavelength (λ_1 and λ_2) or two-polarization division multiplex soliton communication system. For two-wavelength systems, $\sigma = (2\gamma_2\beta_{2u} - \gamma_1\beta_{2v}) / (2\gamma_1\beta_{2u} - \gamma_2\beta_{2v})$ and $\sigma = 1$ for birefringent fiber ($\beta_{2u} = \beta_{2v}$). Under this criterion, two solitons will co-propagate in a fiber without interaction. Thus, it is important to determine the relative soliton amplitude by the coefficient σ for soliton wavelength division multiplex (WDM) or polarization division multiplex (PDM) communication.

As a confirmation, we simulated the propagation process numerically for several cases. Figure 1 and 2 demonstrate the independent soliton profile evolution during propagation by appropriately choosing the value of σ . Fig.1 is the simulation of the pulse intensity $|u(\tau, z)|^2$ and $|v(\tau, z)|^2$ vs. z in a WDM system. For a bright soliton propagation, the parameters are chosen to be: $\lambda_1 = 1.50 \mu m$, $\beta_{2u} = -18.25 ps^2/km$, $\gamma_1 = 20.67 W^{-1}/km$ and $\lambda_2 = 1.55 \mu m$, $\beta_{2v} = -20.00 ps^2/km$, $\gamma_2 = 20.00 W^{-1}/km$, $\sigma = 0.685$. Figure 2 is a plot of the solution in equation (3) and (4) using the same parameters. Figure 3 demonstrate the propagation of two solitons when the independence criterion is not met ($\sigma = 1.20$).

In summary, we have theoretically derived two families of solitary wave solution to a XPM system with $\beta_{1u} \neq \beta_{1v}$. Both fundamental soliton solution and soliton modulated solution expressions are given in detail. Numerical simulations have been conducted for a non-symmetric XPM nonlinear system using the local cardinal interpolation spline approach [4]. The results agree well with theoretical prediction. The soliton independent propagation condition provides a useful criterion in designs of optical soliton multiplex communication systems.

The authors acknowledge the assistance of Jun Zha to provide the numerical simulation program. This research project is supported by Texas Higher Education Coordinating Board under Grants No: 32135-70800 and No: 32130-70440.

References

- [1] R. S. Tasgal and M. J. Potasek, "Exact Soliton Solutions in a Periodically Twisted Birefringent Fiber," in *Integrated Photonics Research*, Vol. 10, OSA, Technical Digest Series (Optical Society of America, Washington,DC 1992), pp.22-23.
- [2] M. J. Potasek and J. M. Fang, "Optical Switching for a Nonlinear Directional Coupler Including the Effects of Two Photon Absorption," in *Integrated Photonics Research*, Vol. 10, OSA, Technical Digest Series (Optical Society of America, Washington,DC 1992), pp.12-13.
- [3] P. A. Bélanger and C. Paré, "Soliton Switching and Energy Coupling in Two-mode Fibers: Analytical Results," *Physical Review A*, Vol. 41, No. 9, May, 1990, pp.5254-5256.
- [4] A. K. Chan, C. K. Chui, J. Zha and Jieren Bian "Local Cardinal Interpolation Spline Method For Solving Coupled Nonlinear Schrödinger Equations: A Comparison With BPM," in *Integrated Photonics Research*, Vol. 10, OSA, Technical Digest Series (Optical Society of America, Washington,DC 1992), pp.224-225.
- [5] G. Agrawal "Nonlinear Fiber Optics," *Academic Press, Inc, New York*, 1989

A Numerical and Asymptotic Solution of Maxwell's Equations for Nonlinear Optical Pulse Propagation

Cheryl V. Hile and William L. Kath

Engineering Sciences and Applied Mathematics

McCormick School of Engineering and Applied Science

Northwestern University, 2145 Sheridan Rd., Evanston, IL 60208-3125

Phone: (708) 491-5585 Fax: (708) 491-2178

Recent interest in the development of all-optical switching devices and in the utilization of nonlinear optical fibers for long distance communication systems has lead to extensive research on the propagation of nonlinear optical pulses. A particularly important example is the optical soliton [1], whose propagation in nonlinear optical media is frequently modelled by the nonlinear Schrödinger (NLS) equation [1, 2]. While the NLS equation is an appropriate model for sufficiently wide pulses, some approximations implicit in this equation are no longer valid for narrow or high-powered pulses. To account for these types of pulses, the NLS equation has been extended to include higher-order linear and nonlinear dispersion, as well as effects due to Raman scattering [1, 2].

Here we present a mathematical model and one-dimensional numerical solution of the full-vector Maxwell's equations for pulses in nonlinear optical media. This model is similar to the one derived by Goorjian and Taflove [4], for it includes both linear dispersion and a Kerr nonlinearity. The linear dispersion is expressed in the time domain as a convolution integral involving the electric field and a causal susceptibility function [3], which is then transformed into a second-order differential equation. Unique to this model is a coordinate system moving with the group velocity of the pulse, which allows the pulse to remain in the center of the computational grid. This significantly reduces the size of the computational grid, for the number of computational points required becomes independent of the distance over which the pulse propagates. The model also utilizes circularly polarized waves to more easily obtain the envelope of the field magnitudes.

Such a model can be shown to be governed by the nondimensional equations

$$H_t - \alpha H_x = E_x, \quad (1a)$$

$$D_t - \alpha D_x = H_x, \quad (1b)$$

$$\Phi_t - \alpha \Phi_x = U, \quad (1c)$$

$$U_t - \alpha U_x = -2\gamma U - \omega_1^2 \Phi + \beta_1 \omega_1^2 E, \quad (1d)$$

$$D = E + \Phi + a|E|^2 E, \quad (1e)$$

where α is the speed of the moving coordinate system, a is the strength of the Kerr nonlinearity, ω_1 is the resonance frequency, β_1 is its strength, and γ is a small phenomenological damping included for computational stability.

A key feature of the work presented here is an asymptotic analysis which reduces these equations to the NLS equation. This allows the direct generation of initial conditions for the equations corresponding to solutions of the NLS equation (such as soliton solutions), thus providing a method for the direct comparison of the numerical results and solutions of the NLS equation. This asymptotic analysis utilizes a slowly-varying envelope approximation in the limit of high frequency, strong dispersion, and weak nonlinearity. Also obtained from this analysis is the equality,

$$A^2 x_0^2 = 2k\omega'' / \omega^2 \omega' a,$$

which relates the pulse's amplitude, A , and width, x_0 , to the properties of the medium (i.e. the dispersion coefficients and the strength of the nonlinearity) and must be satisfied for dispersion and nonlinearity to balance one another. This relationship is quite similar to the one obtained (and verified experimentally) for the case of soliton propagation in nonlinear optical fibers [2].

A standard approach for the direct time integration of Maxwell's equations for linear and nonlinear dispersive media is the application of the conventional finite difference time domain (FD-TD) electromagnetic solver [4]. While this approach normally provides an efficient numerical description of the physics underlying Maxwell's equations, it does not seem to allow a straightforward implementation of them in a moving coordinate system. This is due to the spatial derivative terms multiplied by α in equations (1). Consequently, the numerical method employed here to solve equations (1) is a leap-frog scheme which uses second-order central differencing in space and time. In addition, radiation boundary conditions based on the wave equation are used.

Using the initial conditions derived from the asymptotics, numerical results are obtained and describe the propagation of pulses corresponding to a first-order NLS soliton, a second-order soliton, and a pulse which radiates energy and decays to a soliton. Figure 1 shows the magnitudes of the electric field, magnetic field and electric displacement for a second-order soliton-like pulse propagating for one soliton period. Numerical results also include the collision of two co-propagating and two counter-propagating solitons.

When applicable, these numerical results are compared to the corresponding solution of the NLS equation and are found to be in good agreement. This provides confidence that nonlinear Maxwell equation solvers like the one formulated and implemented here can provide a method for correctly modeling soliton-like pulse propagation in two and three-dimensional optical devices in situations where the NLS equation is not appropriate [5]. These direct comparisons also show, however, that the NLS equation provides an excellent approximation of one-dimensional nonlinear optical pulse propagation even when a pulse contains as few as 10-15 optical cycles. This suggests that in one dimension extended NLS equations [1, 2], as long as they approximately model the underlying physics, should give very good results even at quite short pulse widths.

This work was supported in part by the AFOSR and the NCSA.

References

- [1] A. Hasegawa. *Optical Solitons in Fibers*, (Springer-Verlag, New York, 1989).
- [2] G. P. Agrawal. *Nonlinear Fiber Optics*, (Academic Press, New York, 1989).
- [3] R. M. Joseph, S. C. Hagness, and A. Taflove, "Direct time integration of Maxwell's equations in linear dispersive media with absorption for scattering and propagation of femtosecond electromagnetic pulses", *Opt. Lett.*, vol. 16, 1412 (1991).
- [4] P. M. Goorjian and A. Taflove, "Direct time integration of Maxwell's equations in nonlinear dispersive media for propagation and scattering of femtosecond electromagnetic solitons", *Opt. Lett.*, vol. 17(3), 180-182 (1992); P. M. Goorjian, A. Taflove, R. M. Joseph and S. C. Hagness, "Computational modeling of femtosecond optical solitons from Maxwell's equations", *IEEE J. Quant. Elect.*, vol. 28(10), 2416-2422 (1992).
- [5] R. W. Ziolkowski and J. B. Judkins, "Full-wave vector Maxwell equation modeling of the self-focusing of ultrashort optical pulses in a nonlinear Kerr medium exhibiting a finite response time", submitted to *JOSA B*, March 1992.

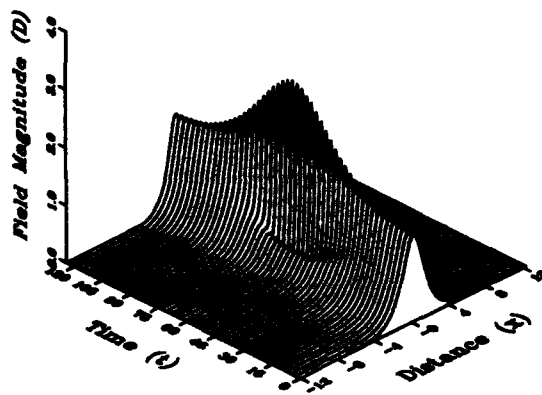
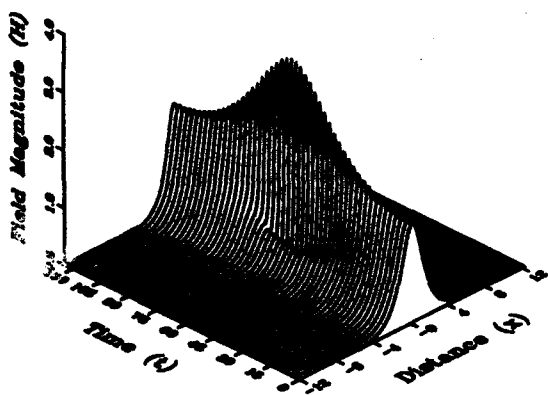
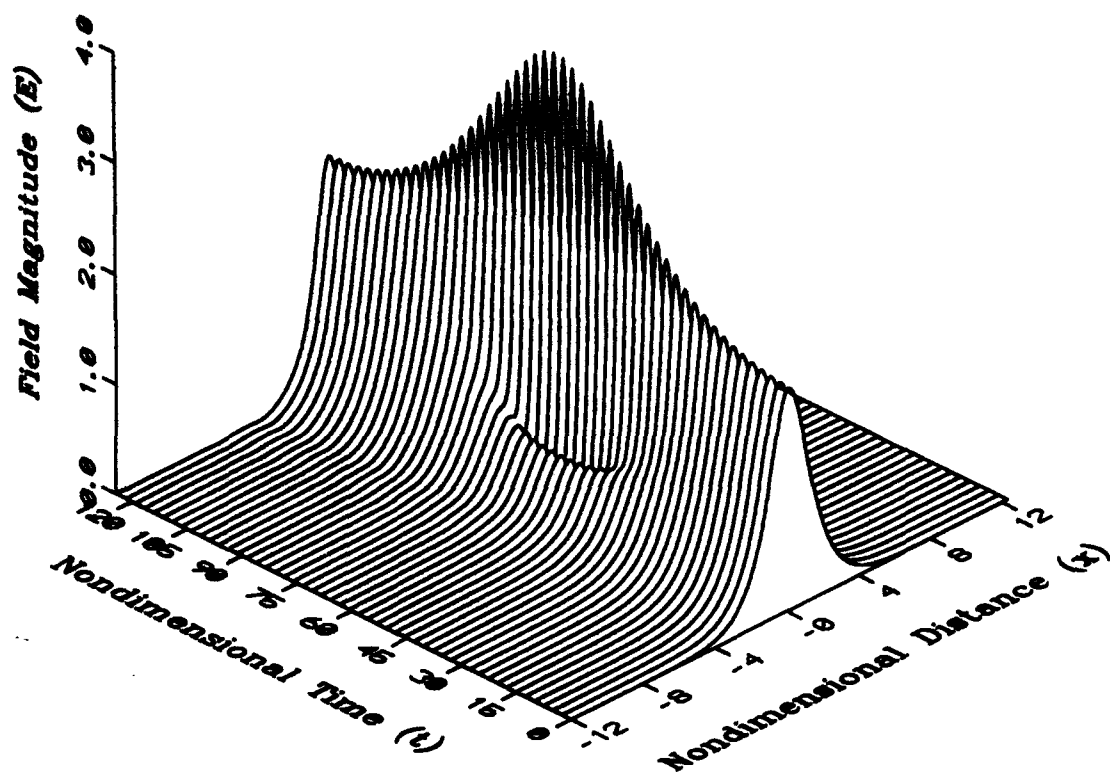


Figure 1: Field magnitudes ($|E|$, $|H|$, and $|D|$) of a second-order soliton-like pulse propagating for one soliton period.

Spatial gap-soliton in periodic nonlinear structures

R. F. Nabiev and P. Yeh

Department of Electrical and Computer Engineering
University of California at Santa Barbara Santa Barbara, CA 93106

D. Botez

TRW Space & Technology Group
One Space Park, D1/2519, Redondo Beach, CA 90278, USA

Waveguiding properties of nonlinear periodic dielectric structures have recently been a subject of intensive exploration [1-3]. Active structures typical for arrays of antiguided semiconductor lasers have some interesting nonlinear properties [5]; for instance, waves propagating in such structures may undergo either self-focusing or self-defocusing depending on the parameters of structure. This paper is devoted to the investigation of the static properties of periodic nonlinear dielectric structures. The results can be explained in terms of spatial gap solitons analogous to temporal gap solitons [6].

Nonlinear electromagnetic modes of the form $A(x)\exp(i\beta z)$ propagating along the structure with dielectric constant $\epsilon(x)$ periodic in x direction and possessing Kerr-like nonlinearity with nonlinearity n_2 obey the nonlinear Schrodinger equation

$$\frac{d^2 A}{dx^2} - A[\beta^2 - \epsilon(x)] + \text{sign}(n_2)|A|^2 A = 0 \quad (1)$$

where the positive or negative sign of nonlinear term depends on whether medium possess self-focusing or self-defocusing nonlinearity (positive or negative sign of n_2). The lateral coordinate x is normalized to $\lambda/2\pi$ (λ is the wavelength of photon in a vacuum).

Dispersion of optical waves propagating along linear periodic structures differs significantly from that of the waves in homogeneous medium, namely, there are forbidden bands corresponding to Bragg reflection of waves in such structures [4]. Each point of dispersion curve (dependence of propagation constant β on wavevector of photon k_x in direction perpendicular to structure) represents a Bloch mode of the infinite periodic structure. These modes are solutions of nonlinear problem (1) only for infinitesimal intensity of field when the nonlinear term can be neglected. As was shown in Refs. 5 periodic arrays of antiguided lasers may lase at points of high symmetry of Brillouin zone (BZ), namely either in the center ($k_x=0$) or in the edge of BZ ($k_x = \pi/d$, d is a period of structure), depending on structure parameters. The center of BZ corresponds to in-phase mode and the edge to the out-of-phase one. Figure 1 represents the behavior of forbidden gaps and a differential gain $d \text{Im}(\beta) / d \text{Im}(\epsilon_2)$ [5] under pumping of antiguiding regions, as a function of the width of guiding region d_1 for the structures which lase in fundamental in-phase mode with parameters $d_2 = 3\mu\text{m}$, $\epsilon_1 = \epsilon_2 + \Delta\epsilon$, $\epsilon_2 = 12.25$, $\Delta\epsilon = 0.2$, where $d_1, \epsilon_1, d_2, \epsilon_2, \Delta\epsilon$ are the widths and dielectric constants of the guiding and antiguiding regions and dielectric constant step, respectively. The modes with maximal gain correspond to the top of allowed band (negative "photon mass" [5]) for $d_1 > d_1^*$ and to the bottom of the nearest allowed band (positive "photon mass") for $d_1 < d_1^*$, where $d_1^* = 2.692\mu\text{m}$ is the point of zero-gap structure corresponding to resonant optical waveguide (ROW) array [7] (see Fig. 1). Therefore, choosing the widths of antiguiding regions one can force lasing of mode $k_x=0$ with either negative or positive "photon mass". All these modes have propagation constant $\beta < (\epsilon_2)^{1/2}$ corresponding to "leaky" modes of structure.

We solved numerically nonlinear equation according to method described in Ref. 8. In the nonlinear regime β depends on intensity of light launching along the structure because refractive index of structure elements depends on the light intensity. Figure 2 shows a distribution of electromagnetic field across the dielectric structure ($d_1 = 3\mu\text{m}$, positive nonlinearity) for two values of propagation constant: $\beta=3.49785$ (Fig. 2a) and $\beta=3.4996$ (Fig. 2b). Both of these constants lie in the forbidden gap (Fig. 1) of the dispersion of the linear structure. These two

distributions of field correspond to different energy integrals $I = \int |A(x)|^2 dx$ (which are proportional to total launched power of light), namely $I=0.1268$ and $I=0.5756$, respectively. These nonlinear modes are the core Bloch functions $k_x=0$ modulated by slowly varying envelope [5] which is analogous to wave functions of shallow impurities in solid state theory. The figures demonstrate clearly self-focusing of the Bloch modes of structure with increasing of intensity of light. Actually, the process of self-focusing is determined by the difference $\beta - \beta_0$ (β_0 is the propagation constant of linear problem corresponding to the top of allowed zone), the more this value, the more trapping of the field. The self-consistent solution of the nonlinear problem results in spatial soliton which can be referred to as spatial gap soliton analogously to temporal gap solitons in the problem of propagation of pulses perpendicular to periodic nonlinear structure [6].

The $I(\beta)$ dependence in nonlinear medium determines the stability of nonlinear waves [8]. Stable nonlinear waves in self-focusing medium should have positive slope of this dependence. Figure 3a shows this dependence for two different widths of waveguiding regions $d_1 = 3\mu m$ and $d_1 = 2.8\mu m$. From this figure it is obvious that the second structure ($d_1 = 2.8\mu m$), which is closer to resonance, resists self-focusing stronger. This result agrees with the results on self-stabilization of fundamental in-phase mode of finite arrays of antiguided lasers close to ROW structures [9].

For an uniform Kerr-like medium, the $I(\beta)$ dependence is rather simple for sech-like spatial solitons: $I^2 = 32\beta_0(\beta - \beta_0)$. In this case β_0 is equal to linear part of refractive index of medium $n_0 = \sqrt{\epsilon}$. The dashed-dotted line in the Fig. 3a shows this dependence for the uniform medium. The $I(\beta)$ dependence of periodic structure differs considerably from that for the uniform medium. One can see that uniform medium suffers from self-focusing more severely than both cases of periodic structures.

As was indicated in Ref. 5, nonlinear properties of periodic structure depend on the sign of "effective mass" of photon in lateral direction, or on sign of curvature of the dispersion curve. For the case of positive curvature, waves propagating along the structure have to feel the self-defocusing influence of a structure possessing local self-focusing nonlinearity. Because exploration of self-defocusing effects in infinite periodic structure in static regime is impossible, we consider a solution of Eq. (1) with negative sign of nonlinear term what corresponds to self-defocusing Kerr-like local nonlinearity. We expect that the structures with $d_1 < d_1^*$ have to show self-focusing properties for large scale perturbation. Indeed, Figs. 2c and 2d show two examples of amplitude distributions for $d_1 = 2.5\mu m$, and for propagation constants $\beta=3.4967$ and $\beta=3.4958$ corresponding to energy integrals $I=0.2105$ and $I=0.5951$, respectively. Higher intensity of field corresponds to lower propagation constant because of negative nonlinearity, and nevertheless electromagnetic field undergoes self-focusing. These figures represent gap spatial solitons in periodic structure with negative Kerr-type nonlinearity. The $I(\beta)$ dependence for this structure is shown in the Fig. 3b. Although, this dependence has negative slope we believe that the spatial solitons are stable under propagation along the structure. The edge of corresponding zone for linear problem (the bottom of allowed zone) corresponds to propagation constant $\beta_0=3.4968$ (see Fig. 1). We present for comparison the $I(\beta)$ dependence for uniform medium with refractive index $n_0 = \beta_0$ possessing negative Kerr-like nonlinearity, $I^2 = 32\beta_0(\beta_0 - \beta)$, by dashed-dotted line. In this case of positive "photon mass", periodic structure resists also stronger to self-focusing process comparatively to uniform medium.

These results show that the properties of the nonlinear periodic structures depend strongly on their parameters. Particularly, fundamental in-phase mode of the structures with proper geometric parameters can undergo the self-defocusing even if intrinsic local nonlinearity of medium is positive. It gives a unique possibility to search for dark spatial solitons in these rather simple periodic structures.

If guiding regions of periodic structure are under pumping the lasing mode is the evanescently coupled fundamental mode [5]. Previous computer simulations [10-12] showed that evanescently coupled laser arrays suffer severely from spatial hole burning of gain profile and self-focusing of fundamental in-phase supermode. This effect can be explained easily also by the sign of curvature of the dispersion curve. In-phase fundamental mode corresponds

to the center of BZ of the highest dispersion curve of infinite periodical structure, and curvature is always negative. Therefore, this mode undergoes always self-focusing in structures with positive nonlinearity.

In conclusion, we have analyzed the effect of self-focusing in periodic Kerr-like nonlinear structures. We have found, for the first time, the effect of self-focusing in periodic medium with negative nonlinearity for the case of periodic array of antiguides. The results obtained can be explained in terms of spatial gap solitons. The analysis and comparison show that the antiguided arrays can possess both self-focusing and self-defocusing properties depending on the sign of curvature of dispersion curve whereas evanescently coupled arrays always show self-focusing of fundamental in-phase mode if the medium has positive nonlinearity. In addition, periodic structures with positive nonlinearity should be able to support propagation of dark solitons.

References:

- [1]. U. Trutshel, F.Lederer, and M. Goltz, *IEEE J. of Quantum Electronics*, QE-25, 194 (1989).
- [2]. U. Langbein, F. Lederer, T. Peschel, U. Trutshel, and D. Mihalache, *Physics Reports*, 194, 325 (1990).
- [3]. P.M. Lambkin and K.A. Shore, *IEEE J. of Quantum Electronics*, QE-27, 824 (1991)
- [4]. A. Yariv, P. Yeh, *Optical Waves in Crystals*. John Wiley & Sons, Inc., 1984.
- [5]. R.F. Nabiev and A.I. Onishchenko. *IEEE J. of Quantum Electronics*, QE-28, 2024 (1992)
- [6]. J.E. Sipe and H.G. Winful, *Optics Letters*, 13, 132 (1988).
- [7]. C.A. Zmudzinski, D. Botez and L.J.Mawst, *Appl. Phys. Lett.*, 60, 1049 (1992).
- [8]. A.A. Kolokolov. *Zh. Prikl. Mekh. Tech. Fis. (Applied Mechanics and Technical Physics)*, 3, 153 (1973) (in Russian).
- [9]. R.F. Nabiev, P.Yeh, and D. Botez "Self stabilization of fundamental in-phase mode in resonant antiguided laser arrays" - submitted to *Applied Physics Letters*.
- [10]. K.-L. Chen, S. Wang. *Appl.Phys. Lett.*, 47, 555 (1985).
- [11]. J. Katz, W.K. Marshall. *Electronics Lett.*, 21, 974 (1985).
- [12]. J.E.A. Whiteaway, G.H.B. Thompson, A.R.Goodwin. *Electronics Lett.*, 21, 1194 (1985).

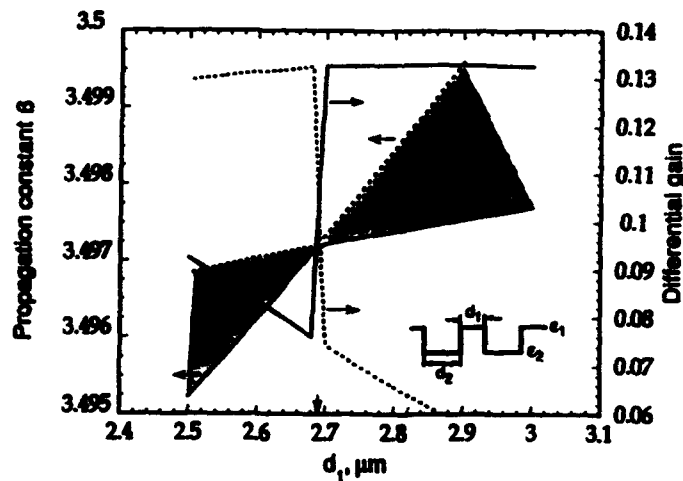


Fig. 1. Dependence of band edges and a differential gain $d \text{Im}(\beta) / d \text{Im}(\epsilon_2)$ of the wave propagating along the periodical structure on the width of guiding region d_1 . Solid and dashed lines correspond to the top and the bottom of allowed zones of β , respectively. Shaded region indicate band gap of β . Other parameters of the structure are: $d_2 = 3 \mu\text{m}$, $\epsilon_2 = 12.25$, $\Delta\epsilon = 0.2$ (see the inset).

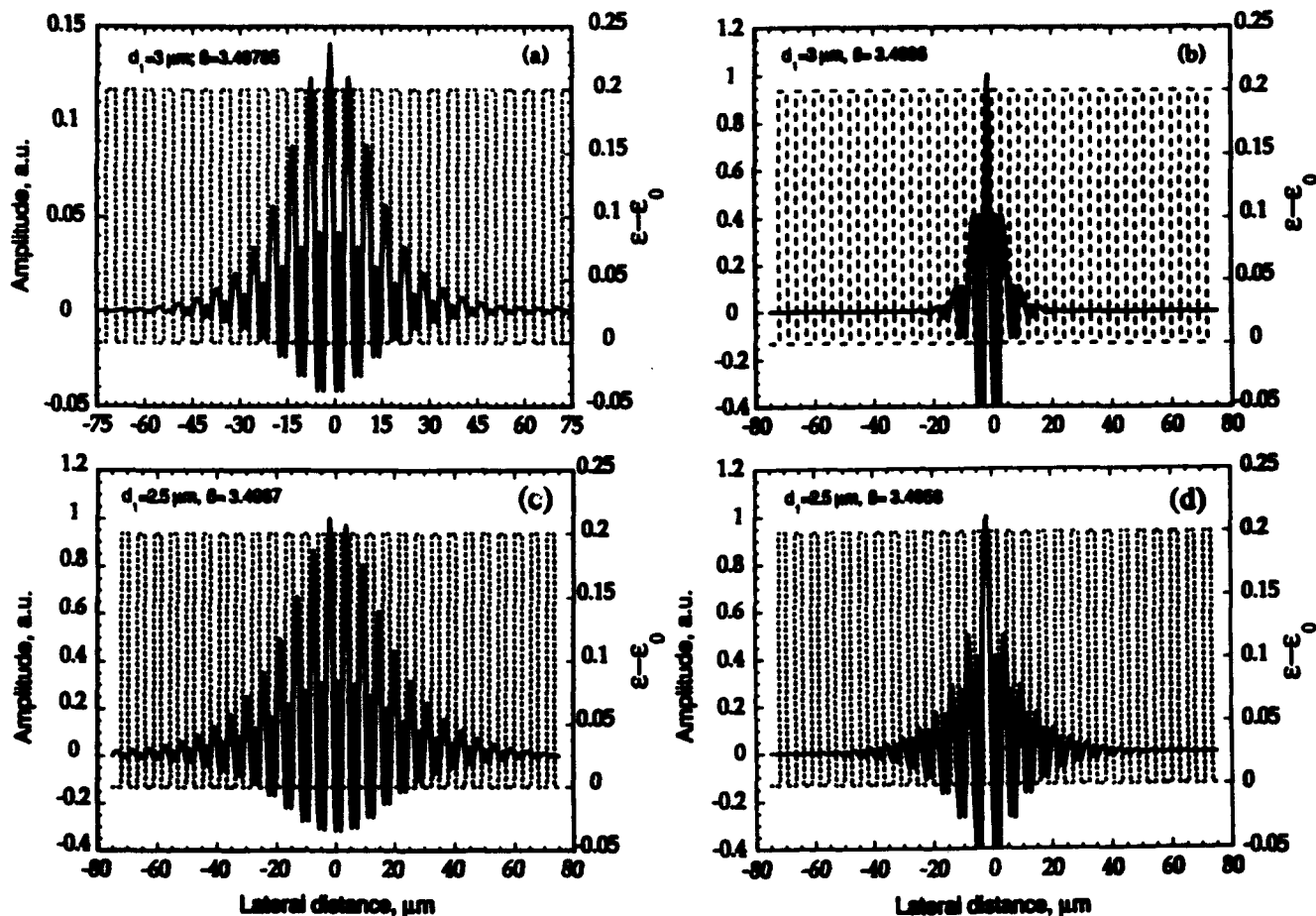


Fig. 2. Electromagnetic field profile of spatial solitons in structures with positive (a,b) and negative (c,d) nonlinearities. Parameters of the structure are: $d_1 = d_2 = 3 \mu\text{m}$, $\epsilon_2 = 12.25$, $\Delta\epsilon = 0.2$. Dashed line shows the profile of dielectric constant $\epsilon(x)$.

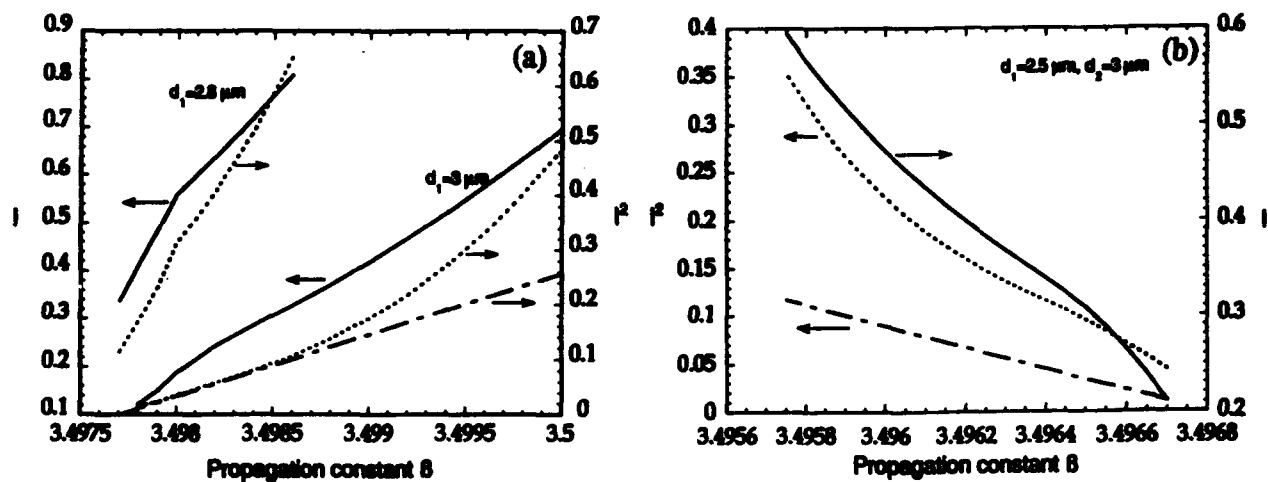


Fig. 3. Dependence of energy integral I (solid lines) and its square I^2 (dashed lines) on propagation constant β for periodic structures with positive (a) and negative (b) nonlinearity. Parameters of structure are: $d_2 = 3 \mu\text{m}$, $\epsilon_2 = 12.25$, $\Delta\epsilon = 0.2$, $d_1 = 2.8 \mu\text{m}$, $3 \mu\text{m}$ (a) and $2.5 \mu\text{m}$ (b). Dashed-dotted line corresponds to sech-like spatial soliton in uniform Kerr-like medium.

Semiconductor Lasers

ITuG 1:30pm-3:30pm
Mesquite A

Constance J. Chang-Hasnain, *Presider*
Stanford University

Surface Emitting Lasers

— How Small Is Small Enough and How Large Is Large Enough ? —

K. Iga

Tokyo Institute of Technology, P&I Lab.
4259 Nagatsuta, Midoriku, Yokohama, Japan 227
Fax +81-45-921-0898

The progress of vertical cavity surface emitting lasers is very rapid, i. e., a new field such as optical computing, optical interconnects and so on, is accelerating it¹.

The importance of 1.3 or 1.55 μm devices is currently increasing, since parallel lightwave systems are wanted. However, the GaInAsP/InP system has some substantial difficulties for making SE lasers due to such reasons that the Auger recombination and intra-valence band absorption are noticeable, the index difference between GaInAsP and InP is relatively small, valence band offset is large, and so on. Pulsed operation has been obtained at near room temperature², at room temperature³, and at 66 °C⁴. Recently, a hybrid mirror technology is being developed. One is to use a semiconductor/dielectric reflector, which is demonstrated by CBE⁵ as shown in Fig 1. The other is epitaxial bonding of quaternary/GaAs-AlAs mirror, where 144 °C pulsed operation was achieved by optical pumping⁶. Thermal problems for CW operation are now extensively studied. A MgO/Si mirror with good thermal conductivity is demonstrated⁷. For realizing a reliable devices, the buried heterostructure (BH) is crucial. We have fabricated a BH SE laser exhibiting a relatively small threshold⁸ as shown in Fig.2.

In the GaAlAs/GaAs system, an SE laser of 5 μm long and 6 μm in diameter⁹ and room temperature CW operation¹⁰ were first realized among other systems. At present, devices exhibiting $I_{th} \cong 2 \sim 15$ mA and 10 mW of output power are available in the laboratory level¹¹. A very high coupling efficiency to a single mode fiber ($\cong 90\%$) was reported¹². The spectral linewidth of 50 MHz is obtained with an output power of 1.4 mW¹³.

The GaInAs/GaAs strained pseudomorphic system grown on a GaAs substrate emitting 0.98 μm exhibits a high laser gain and has been introduced into surface emitting lasers together with using GaAlAs/AlAs multi-layer reflectors. A low threshold ($= 1$ mA at CW) has been demonstrated¹⁴. The minimum threshold reported so far is 0.7 mA¹⁵ and 0.65 mA¹⁶. The minimum J_{th} is 8 $\mu\text{A}/\mu\text{m}^2$, which is approaching to the similar level of stripe lasers. Also, relatively high power is becoming possible¹⁷.

By overcoming those technical problems, such as making tiny structures, ohmic resistance of electrodes and improving heat sinking, we believe that we can obtain a 1 μA device¹⁸. A lot of efforts toward improving the characteristics of surface emitting lasers have been made¹⁹, including surface passivation in the regrowth process for buried heterostructure, micro-fabrication, and fine epitaxies. The ohmic resistance of semiconductor DBR is reduced down to the order of low $10^{-5} \Omega\text{cm}^2$ ²⁰.

Spontaneous emission control is considered by taking the advantage of micro-cavity structures. The spontaneous emission factor has been estimated on the basis of 3-D mode density analysis²¹. The result is shown in Fig. 3. The possibility of no distinct threshold devices is suggested.

Another interesting topic for micro-cavity SE lasers is photon recycling. By covering the side-bounding surfaces of the cavity, some amount of spontaneously wasted photons can be recycled. It has been demonstrated that the device appears to have no distinct threshold²². The efficiency of photon recycling has been estimated²³ as shown in Fig. 4. The quantum noise characteristics are being studied, such as RINs²⁴ and linewidths¹³.

Lastly, we consider some possible applications including optical interconnects, parallel fiber-optic subsystems, and so on by featuring high power capabilities and largely extending

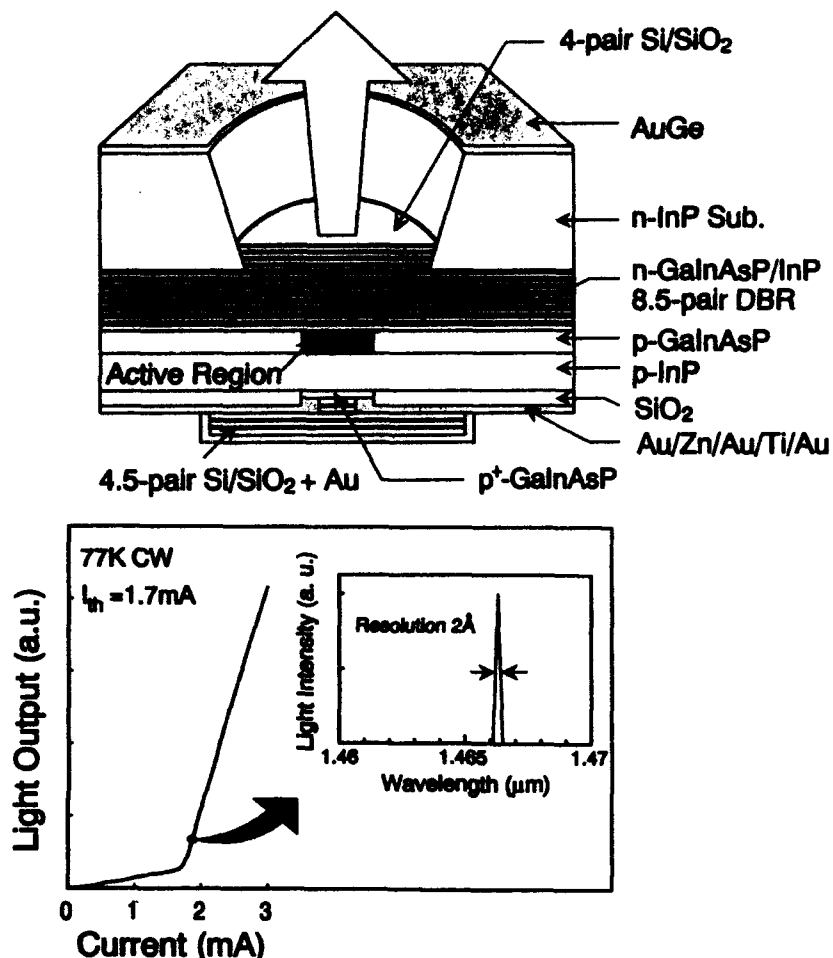


Fig 1 A CBE grown GaInAsP/InP 1.55 μm SE laser using a hybrid mirror.

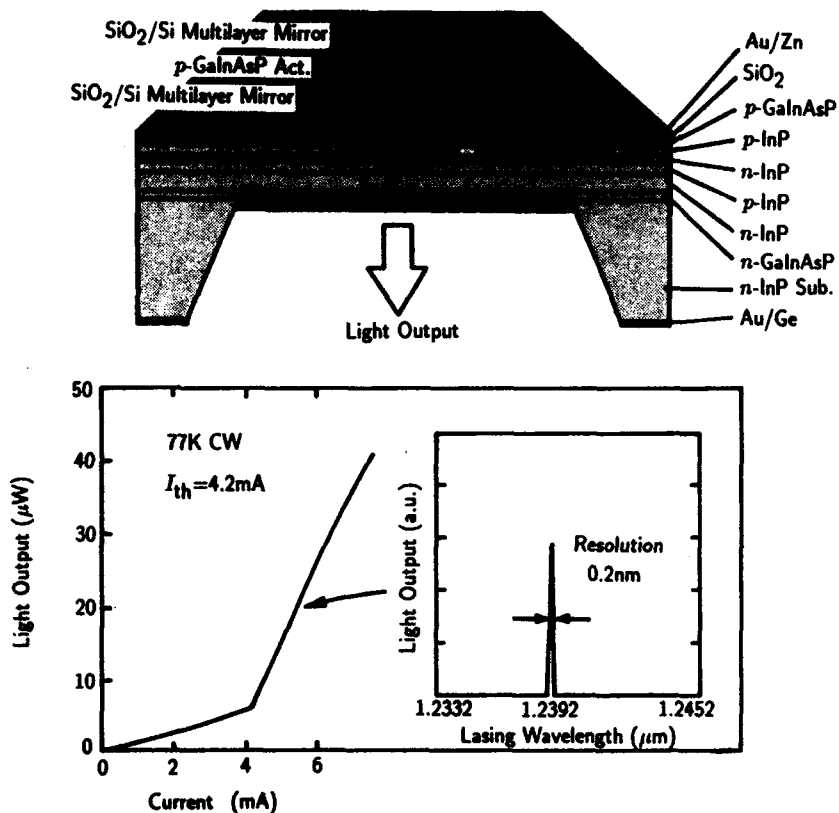


Fig. 2 A buried structure GaInAsP/InP 1.3 μm SE laser.

2-D arrays. For the purpose of realizing coherent arrays, coherent coupling of these arrayed lasers has been tried by using a Talbot cavity²⁵ and phase compensation is considered²⁶. It is pointed out that 2-D arrays are more suitable to make a coherent array than a linear configuration, since we can take the advantage of 2-D symmetry²⁷. The research activity is now forwarded to monolithic integration of SE laser based optical circuits by taking the advantage of its small cavity dimension. Densely packed arrays have also been demonstrated for the purpose of making high power lasers and coherent arrays.

In addition to surface emitting lasers, surface emitting laser-type optical devices such as optical switches, frequency tuners^{28,29}, optical filters³⁰, using ultra-minute structures such as quantum wells and super-lattices have become very active. In Fig. 5 we show a 40 Å continuous tuning by the use of an external reflector. Wide variety of functions, such as polarization control³¹, amplification, detecting, and so on can be integrated along with surface emitting lasers by stacking. The polarization control will become very important for SE lasers. One of the methods is shown in Fig. 6, where a stress effect is incorporated³¹. Vertical optical interconnection of LSI chips and circuit boards may be another interesting point. From this point of view, the device should be small enough, and no limitation exists to form a 2-D array as large as possible.

Lastly, the author would like to acknowledge the members of his laboratory for collaborations and data.

References

1. K. Iga, F. Koyama, and S. Kinoshita, *IEEE J. Quant. Electron.*, **OE-24**, **9**, p. 1845, Sept. 1988.
2. M. Oshikiri, H. Kawasaki, F. Koyama and K. Iga, *Photo. Tech. Lett.*, **1**, **1**, p.11, Jan., 1989; M. Oshikiri, F. Koyama, and K. Iga, *Electron. Lett.*, **27**, **22**, p.2038, Oct. 24, 1991.
3. Y. Imajo, A. Kasukawa, S. Kashiwa and H. Okamoto, *Jpn. J. appl. Phys.*, **29**, **7**, p.L1130, July, 1990.
4. H. Wada, D. I. Babic, D. L. Crawford, J.J. Dudley, J. E. Bowers, E. L. Hu, and J. L. Merz, *Device Research Conference, Post Deadline Paper, A-8*, June, 1991.
5. T. Miyamoto, T. Uchida, N. Yokouchi, Y. Inaba, F. Koyama, and K. Iga, *LEOS Annual DLTA13.2*, 1992.
6. J. E. Bowers, 13th IEEE Semiconductor Laser Conf., PD-, 1992. 7. H. Tanobe, M. Oshikiri, M. Araki, F. Koyama, and K. Iga, *LEOS Annual, DLTA12.2*, 1992.
8. T. Baba, K. Matsuoka, F. Koyama, and K. Iga, *Optoelectronics Conf. (OEC'92)*, **16C2-3**, 1992
9. K. Iga, S. Kinoshita and F. Koyama, *Electron. Lett.*, **23**, **3**, p.134, Jan. 1987.
10. F. Koyama, S. Kinoshita, and K. Iga, *Appl. Phys. Lett.*, **55**, **3**, p. 221, July 1989.
11. K. Tai, G. Hasnain, J. D. Wynn, R. J. Fischer, Y. H. Wang, B. Weir, J. Gamelin, A. Y. Cho, *Electronics Letters*, **26**, **19**, p. 1628, Sept. 1990.
12. K. Kojima, R. A. Morgan, T. Mullally, G. D. Guth, M. W. Focht, R. E. Leibenguth, M. T. Asom, and W. A. Gault, 13th IEEE Semiconductor Laser Conf., PD-2, 1992.
13. H. Tanobe, F. Koyama, and K. Iga, *Trans. IEICE of Jpn.*, **J73C-1**, p.241, 1990.
14. J. L. Jewell, A. Scherer, S. L. McCall, Y. H. Lee, S. Walker, J. J. P. Harbison, L. T. Florez, *Electron. Lett.*, **25**, **17**, p.1123, Aug. 1989.
15. R. S. Geels and L. A. Coldren, 48th Device Research Conference, VIII A-1, June 1990.
16. T. Wipiejewski, K. Panzlaff, E. Zeeb, and K. J. Ebeling, 18th European Conf. on Opt. Comm. (ECOC'92), PDII-4, 1992.
17. F. H. Peters, M. G. Peters, D. B. Young, J. W. Scott, B. J. Tibeault, S. W. Corzine, and L. A. Coldren, 13th IEEE Semiconductor Laser Conf., PD-1, 1992.
18. T. Tamanuki, F. Koyama and K. Iga, *J. J. of Appl. Phys.*, **30**, **4A**, p. L593, April 1991; *J. J. of Appl. Phys.*, **31**, p. 3292, Oct. 1992.
19. T. Baba, T. Harano, F. Koyama and K. Iga, *IEEE J. Quant. Electron.*, **27**, **6**, p. 1991, *ibid*, **28**, p.1310, 1992.
20. K. L. Lear, S. A. Chalmers, and K. P. Kileen, *LEOS Annual*, PD3, 1992.
21. T. Baba, T. Hamano, F. Koyama, and K. Iga, *IEEE J. Quant. Electron.*, **27**, 1347, 1991; *ibid*, **28**, 1310, 1992.
22. T. Numai, M. Sugimoto, I. Ogura, H. Kosaka and K. Kasahara, *J. J. Appl. Phys.*, **30**, **4A**, p. L602, April 1991.
23. T. Tamanuki, F. Koyama, and K. Iga, *Jpn J. Appl. Phys.*, **31**, 1810, 1992.
24. F. Koyama, K. Morito, and K. Iga, *IEEE J. Quant. Electron.*, **27**, p.1419, 1992.
25. E. Ho, F. Koyama, and K. Iga, *MOC/GRIN'89*, **J2**, p. 242, Oct. 1989.
26. M. E. Warren, P. L. Gourley, G. R. Hadley, G. A. Vawter, T. M. Brennan, B. E. Hammons, and K. L. Lear, *CLEO'92 JThA5*, 1992.
27. M. Orenstein, E. Kapon, N. G. Stoffel, J. P. Harbison, L. T. Florez, and J. Wullert, *Appl. Phys Lett.*, **58**, **8**, p. 804, Feb. 1991.
28. M. W. Maeda, C. J. Chang-Hasnain, C. Lin, J. S. Patel, H. A. Johnson, and J. A. Walker, *IEEE Photonics Tech. Letts.*, **3**, **3**, p. 268, March 1991
29. N. Yokouchi, F. Koyama and K. Iga, *The Trans. of IEICE*, **E73**, **9**, p.1473, Sept. 1990; *Photonics Tech. Lett.*, **7**, p.701, 1992.
30. F. Koyama, S. Kubota, and K. Iga, *IEICE Trans.*, **E74**, **6**, p.1689, June, 1991.
31. T. Mukaiyama, F. Koyama and K. Iga, *IPR'92*, MC-5, 1992.

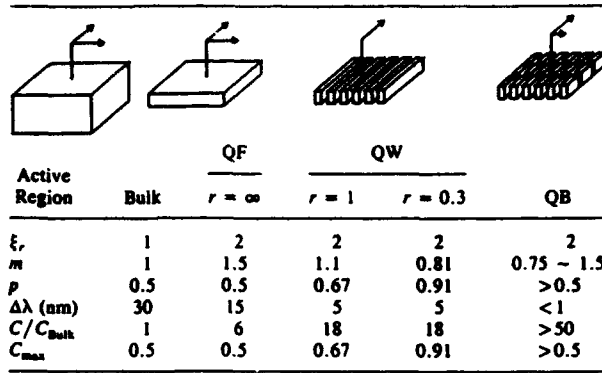


Fig. 3 Spontaneous emission coefficients for micro-cavity lasers with various active media.

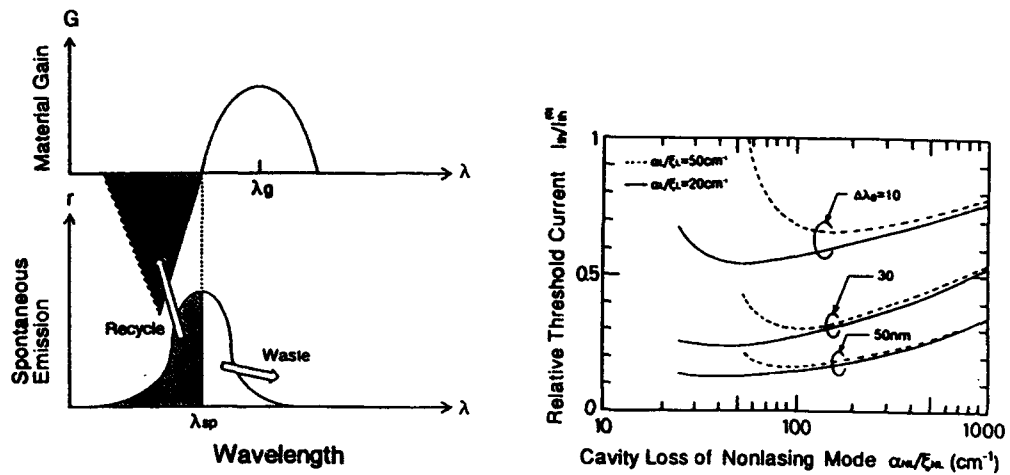


Fig. 4 Photon recycling probability for micro-cavity SE lasers.

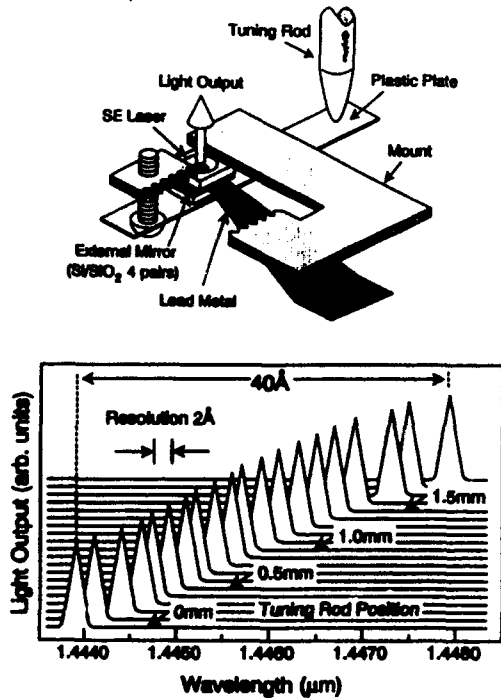


Fig. 5 40 Å continuous tuning of SE laser by an external reflector.

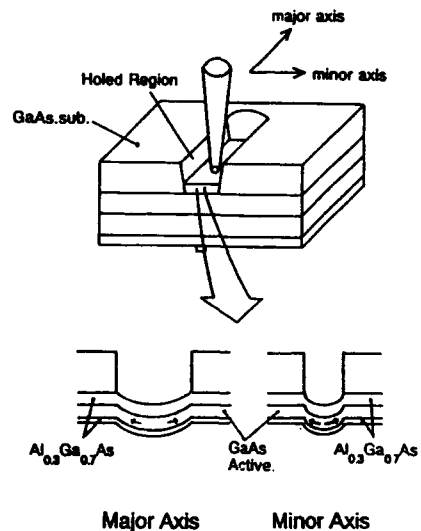


Fig. 6 Polarization control using a stress effect.

**Vertical Cavity Surface Emitting DOES Lasers with Dielectric
Top Reflectors for Opto-Electronic Integration**

P. A. Ewaldsson, G. W. Taylor, P. W. Cooke, P. A. Kiely, S. K. Sargood and D. P. Docter
AT&T Bell Laboratories, Holmdel, New Jersey, 07733-1988, Tel. (908) 949-9033
ARL, Fort Monmouth, New Jersey, 07703-5016

A very significant application of the Vertical Cavity Surface-Emitting Laser (VCSEL)^{(1) (2) (3)}⁽⁴⁾ will be in the area of wide-band opto-electronic interconnect of electronic processors. To realize this goal the VCSEL should be considered as an addition to an electronic technology base and therefore compatible in growth and fabrication with viable logic circuits. Further, a planar structure is essential for performing the photolithographic processes to form the fine circuits as required for the gates of high speed transistors, with gate dimensions less than $1\mu\text{m}$. The processing compatibility results in the simplest technology approach and thus realizes the highest circuit yield.

Recently⁽⁵⁾, we reported on a family of vertical cavity devices, including surface emitting switching lasers (DOES), resonant cavity photodetectors and Heterostructure Field Effect Transistors realized from a single epitaxial growth sequence and compatible processing sequences. Here, we have improved the performance significantly of the two-terminal DOES VCSEL by replacing the grown top mirror with a dielectric stack consisting of $\text{SiO}_2/\text{TiO}_2$, deposited during the fabrication. Previously, Jewell and coworkers⁽⁶⁾ demonstrated the lowest threshold voltage (1.7V) obtained for a VCSEL, using a dielectric stack for the top mirror. Several other advantages arise from the use of the dielectric stack including 1) it allows adjustment of the cavity mode position by etching back the cavity 2) it provides optimized planarity for fine feature circuits 3) it functions as passivation and interlevel dielectric for electrical cross-overs 4) it allows independently a deposition of fewer pairs for the photodetector to trade off bandwidth for responsivity.

The inversion channel structure was grown in the form of a 5λ cavity on a $27\frac{1}{2}$ pair quarter wave stack consisting of GaAs/AlAs, as shown in figure 1. The mode position of the as grown wafer was $1.015\mu\text{m}$ and the sample was therefore etched prior to fabrication to position the mode at $0.985\mu\text{m}$. Both two-terminal and three-terminal devices were fabricated as DOES VCSELs. The two-terminal processing used two Au lift-offs, hydrogen blocking implants, mesa etching, and alloying of contacts at 450°C . The

three-terminal processing utilizes refractory ohmic gate/emitter contacts and a self-aligned (to the gate) silicon implant to form source contacts to the inversion channel followed by a rapid thermal anneal at 950°C for 10s. The electrical switching characteristics of the two- and three-terminal devices are shown in figure 2a and b. The switching voltage has decreased from 11V to 6V, which is attributed primarily to leakage through the third terminal. It is noted that full switching control is obtained with 60μA input to the source terminal. Next, a dielectric stack consisting of 7 pairs of SiO₂/TiO₂ was deposited on the two-terminal devices, and the L-I characteristic for a 14μm diameter is shown in figure 3. Continuous wave threshold currents as low as 5.6 mA (typically 6.5mA) were obtained with slope efficiencies of 0.45mW/mA and maximum c.w. output powers of 2.5mW. Figure 4 shows the emission spectrum with a resolution limited (0.1nm) FWHM at a peak wavelength of 0.986μm. To demonstrate the electronic compatibility Heterostructure Field Effect Transistors (HFET) were fabricated from the same layer structure (without a bottom stack) using the same fabrication sequence. For the HFET sources and drains are formed to contact the inversion channel and are synonymous with the third terminal source contact of the DOES. The drain output characteristics of a nominal 1μm×25μm device are shown in figure 5a and the current gain versus frequency in figure 5b. A peak transconductance of 110mS/mm and a unity current gain cut-off frequency of 10.5 GHz for an effective gate length of 1.3μm were obtained. Fabrication of HFETs and DOES lasers from the stack material is now in progress. These results form the basis for the design of an OEIC technology.

REFERENCES

1. K. Iga, F. Koyama, and S. Kinoshita, IEEE J. Quantum Electron., QE-24, pp. 1845-1855, 1988
2. C. J. Chang-Hasnain, J. P. Harbison, G. Hasnain, A. C. von Lehmen, L. T. Florez, and N. G. Stoffel, IEEE J. Quantum Electron., vol. 27, pp. 1402-1409, 1991
3. J. L. Jewell, J. P. Harbison, A. Scherer, Y. H. Lee, and L. T. Florez, IEEE J. Quantum Electron., vol. 27, pp. 1332-1346, 1991
4. R. S. Geels and L. A. Coldren, Electron. Lett., vol. 28, pp. 1984-1985, 1991
5. P. A. Evaldsson, S. Daryanani, P. Cooke, G. W. Taylor, Opt. and Quantum Electron., vol. 24, pp. 133-146, 1992
6. J. L. Jewell, A. Scherer, M. Walthre, J. P. Harbison, and L. T. Florez, CLEO, Post Deadline, L. A. 1992

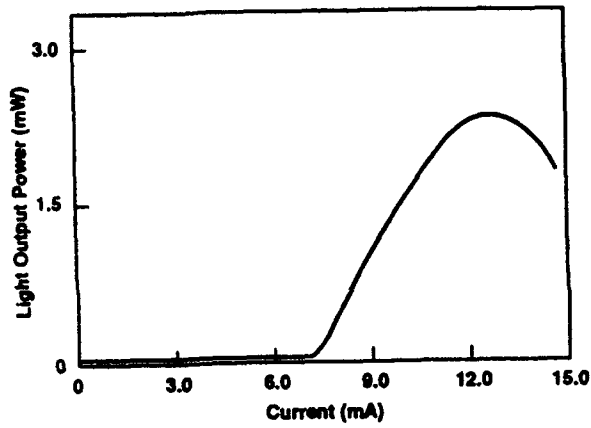


Figure 3 L-I characteristic for a 14 μ m diameter laser under continuous wave operation

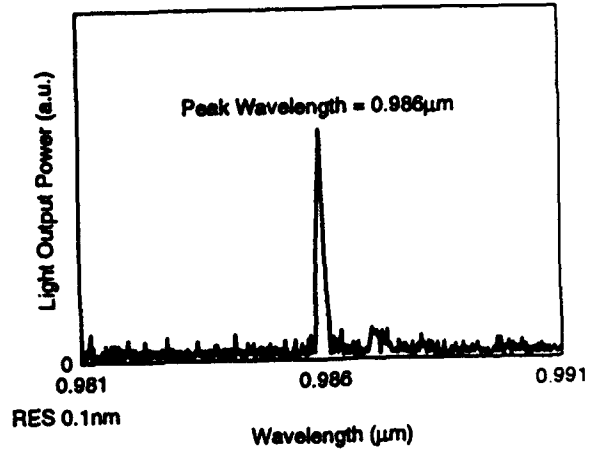
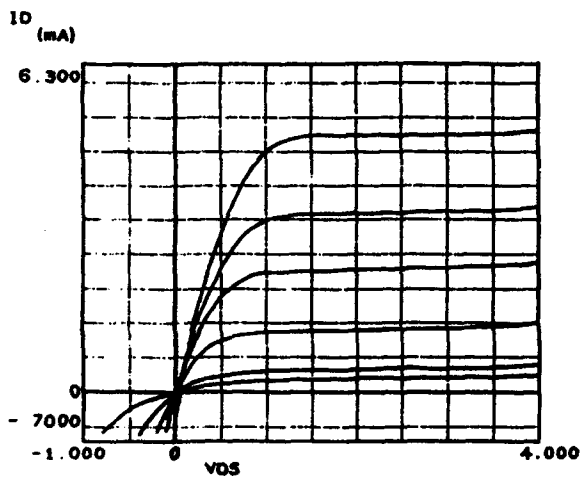
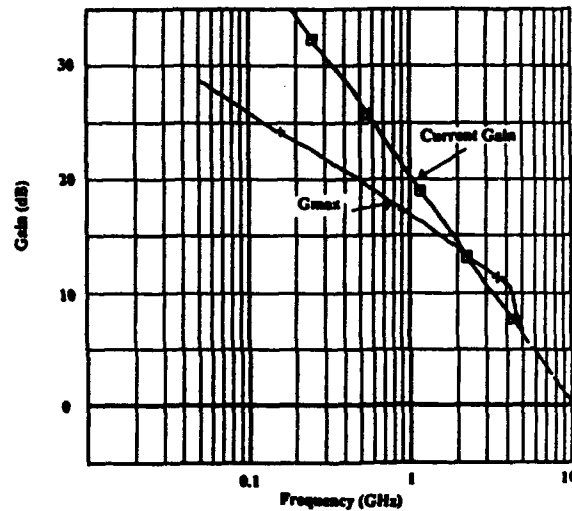


Figure 4 Emission spectrum for the VCSEL DOES



a)



b)

Figure 5 a) Drain Output characteristic for a nominal 1 μ m \times 25 μ m HFET for gate voltages of -0.5, 0.0, 0.5, 1.0, 1.5 and 2.0V

b) Current gain versus frequency for a 1.3 μ m gate length HFET showing a unity current gain cut-off frequency of 10.5GHz

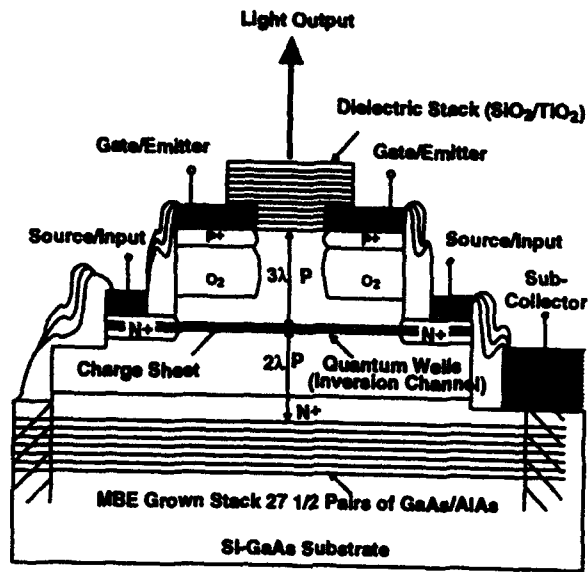


Figure 1 Schematic cross-section of the three-terminal Vertical Cavity Double Heterostructure Switching Laser

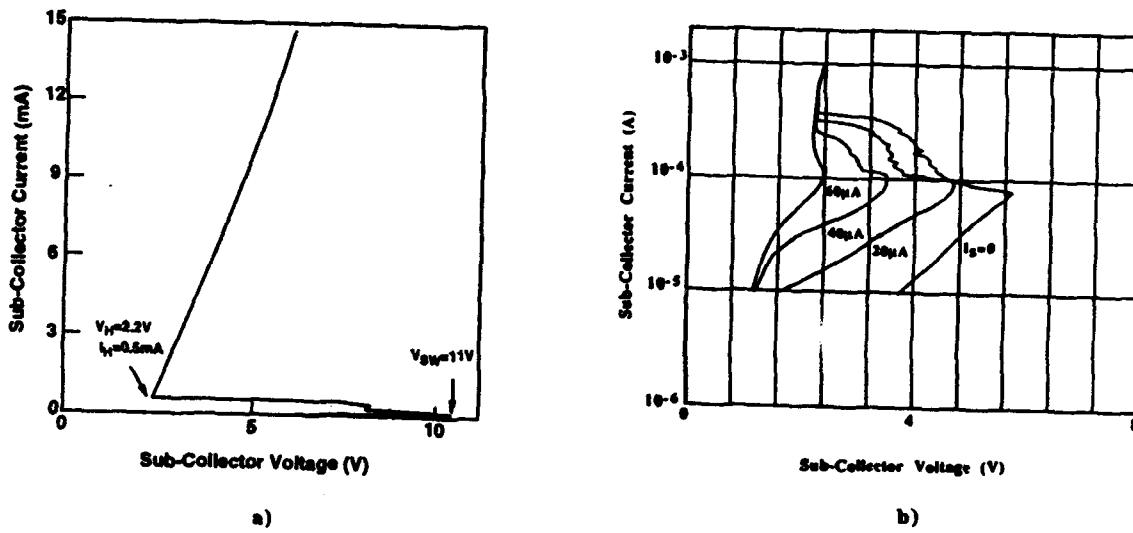


Figure 2 a) I-V characteristic for the two-terminal DOES
 b) I-V characteristic for the three-terminal DOES

Band Structure Dependence of Carrier Transport Effects Direct Modulation of Quantum Well Lasers

T.C. Wu, S.C. Kan, D. Vassilovski and K.Y. Lau

Two forms of carrier transport impose upper limits on the maximum modulation bandwidth of quantum well lasers : real-space and state-space transport [1-3]. The former refers to carrier transport across the barrier region[2], while the latter refers to capture of carriers from the 3-D electronic states in the barrier region to the 2-D electronic states in the quantum well[3]. Both effects can be significant and must be considered concurrently. So far, real space transport in the barrier region has been considered in the context of diffusion only, i.e., a flat-band situation was assumed. While this may be applicable in structures with step-barrier designs, it is not the case in graded barrier designs, in which a substantial electric field is expected to be present. It is the purpose of this paper to consider the effect of such band structure variations on the overall modulation bandwidth limitation.

To take into account the carrier drift process, we write down the small signal rate equations and the continuity equation as below[3]:

$$i\omega s = \frac{1}{1 + \epsilon S_o} (\Gamma A S_o n_2 - \frac{\epsilon S_o}{\tau_p} s) \quad (1)$$

$$i\omega n_2 = \frac{j_2}{qd} - \left(\frac{A S_o}{1 + \epsilon S_o} + \frac{1}{\tau_n} \right) n_2 - \frac{s}{\Gamma(1 + \epsilon S_o)\tau_p} \quad (2)$$

$$i\omega n_b(x) = D_n \frac{d^2 n_b}{dx^2} + \mu_n E \frac{dn_b}{dx} - \frac{n_b}{\tau_n} \quad (3)$$

$$i\omega n_3 = \frac{j_3}{qd} - \frac{j_2}{qd} \quad (4)$$

$$\frac{j_2}{qd} = \frac{n_3}{\tau_{cap}} - \frac{n_2}{\tau_{esc}} \quad (5)$$

We assume the quantum well is sitting at $x = 0$, the total length of SCH region is L , The boundary conditions are: $j_b(\frac{L}{2}) = j_{pump}$, $j_b(-\frac{L}{2}) = 0$, $j_b(0^+) - j_b(0^-) = j_3$, and $n_b(0^+) = n_b(0^-) = n_3$, where j_b is calculated as $j_b(x) = qD_n \frac{dn_b}{dx} + q\mu_n n_b E$.

The electric field $E(x)$ is a function of band structure design as well as carrier density distribution as given by Poisson's Equation. It can be shown that under a dynamic situation, the effect of a time-varying E -field is relatively unimportant so that we can analyse laser dynamics by assuming the E -field to be equal to the steady state distribution. Further, calculations of real band structures show that the E -field is well approximated as piecewise constant, i.e. $E = E_L = \text{constant}$ for $-\frac{L}{2} < x < 0$ region and $E = E_R = \text{constant}$ for $0 < x < \frac{L}{2}$ region.

Four cases are considered which correspond to band structures shown in Fig. 1. Analytical results can be obtained from Eq. 1-5 and are shown in Fig.2 to Fig.4, where we plot the maximum 3dB bandwidth versus electric field (E), carrier capture time (τ_{cap}) and $1/R(= \tau_{esc}/\tau_{cap})$, respectively. One can clearly see from Fig.2, with $E = 0$, the carrier diffusion process, in conjunction with a finite capture time of τ_{cap} of 0.5ps, cause a maximum 3dB bandwidth to be limited to 27 GHz for a step barrier width of 3000Å. However, with proper grading, one can restore this bandwidth back to >50 GHz.

Fig.3 shows the τ_{cap} effect on maximum 3dB bandwidth for different E-field arrangements. In each case, we see a large variation for τ_{cap} between 0.1 ps to 1 ps, which illustrates the importance of this time constant in high speed laser design. With a small τ_{cap} , one can even increase the maximum f_{3dB} back to >70 GHz when $E_R = -E_L = 3000V/cm$. Fig.4 basically describes the τ_{esc} effect on modulation speed for the same E-field arrangements as in Fig.2. From the point of view of τ_{esc} , we want this time constant long enough compared with τ_{cap} (> 100 times). This can readily be accomplished for quantum well depth of >0.15eV.

In summary, we analyze the dependence of modulation speed on band structure design of the barrier region. With a proper band structure design, the E -field, one can reduce the the carrier transport effect to a minimum even for relatively wide separate confinement regions. Real space carrier transport is therefore **NOT** a fundamental limitation in high speed quantum well lasers.

References

- [1] RIDEOUT, W., SHARFIN, W. F., KOTELES, E. S., VASSEL, M. O., and ELMAN, B., *IEEE Photon. Technol. Lett.*, **3**, 784 (1991).
- [2] ISHIKAWA, M., NAGARAJAN, R., FUKUSHIMA, T., WASSERBAUER, J. G., and BOWERS, J. E., *IEEE Quantum Electron.*, **28**, 1835 (1992).
- [3] KAN, S. C., VASSILOVSKI, D., WU, T. C., and LAU, K. Y., *Appl. Phys. Lett.*, **61**, 752 (1992).

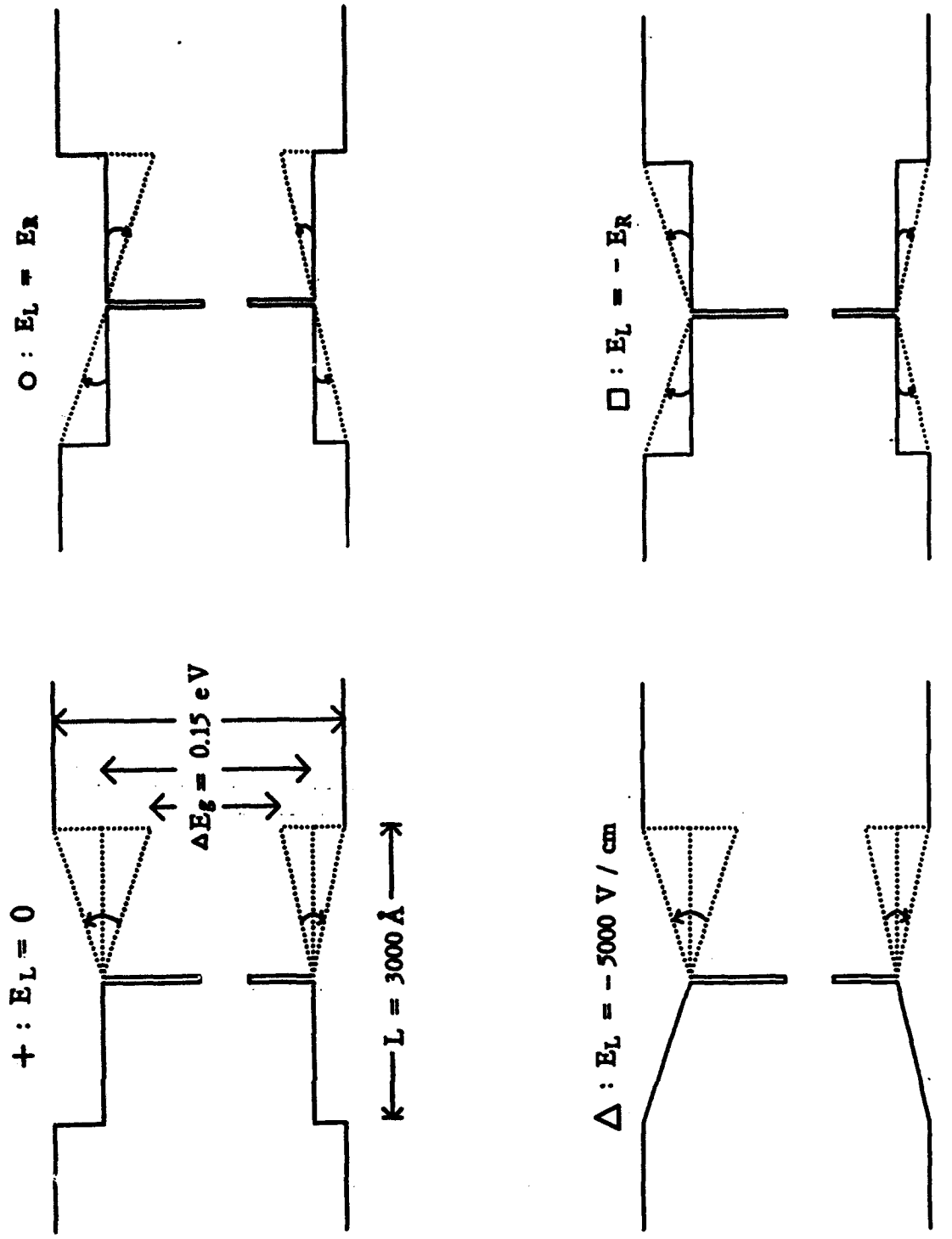


Figure 1. Band structures under consideration.

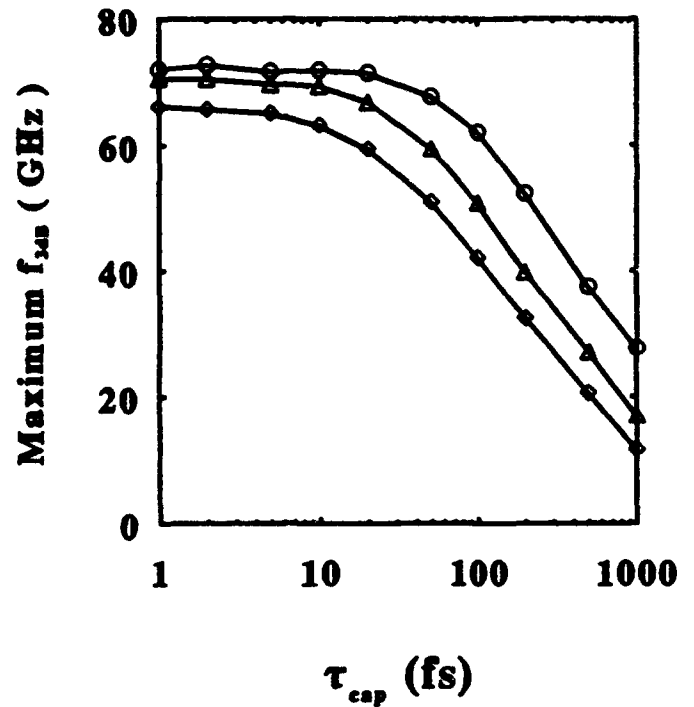
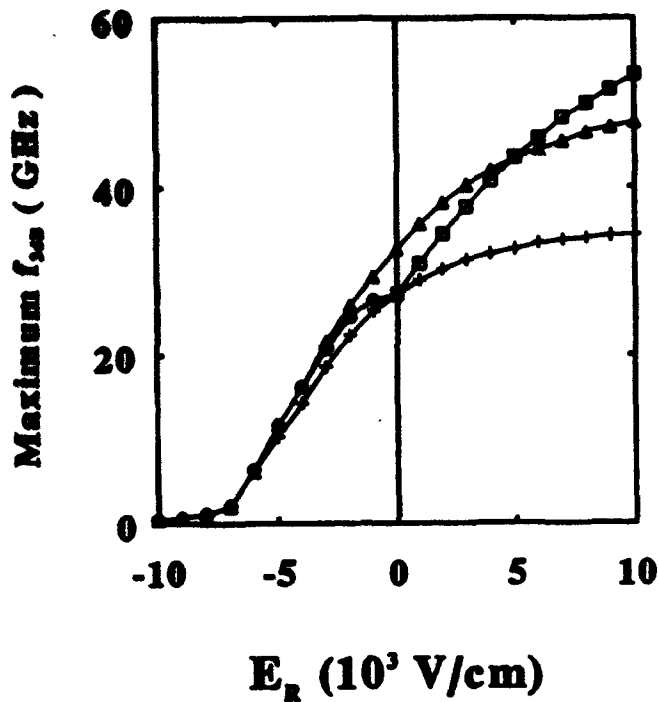


Figure 2. E field dependence of maximum f_{3dB} with $\tau_{cap} = 0.5ps$ and $R = 10^{-3}$.
 \square : $E_L = -E_R$, \triangle : $E_L = -5000V/cm$,
 $+$: $E_L = 0$, \circ : $E_L = E_R$.

Figure 3. Capture time dependence of maximum f_{3dB} with $R = \tau_{cap}/\tau_{esc} = 10^{-3}$.
 \circ : $E_R = -E_L = 3000V/cm$, \triangle : $E_R = E_L = 0$,
 \diamond : $E_R = E_L = -3000V/cm$.

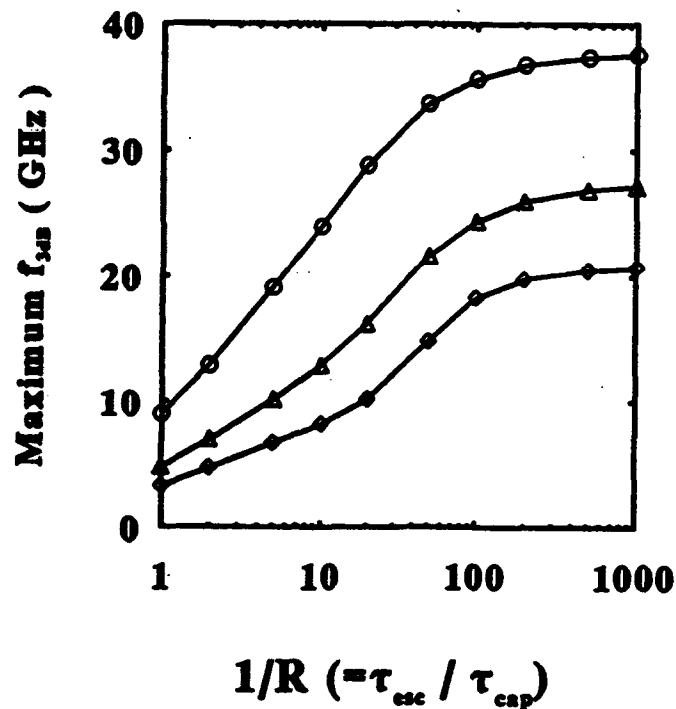


Figure 4. Escape time dependence of maximum f_{3dB} with $\tau_{cap} = 0.5ps$.
 \circ : $E_R = -E_L = 3000V/cm$, \triangle : $E_R = E_L = 0$, \diamond : $E_R = E_L = -3000V/cm$.

**Theoretical Study of Carrier Distribution
and Small Signal Response
in InGaAsP/InP Multiple Quantum Well Lasers**

Takuya Ishikawa, Radhakrishnan Nagarajan, and John E. Bowers*

Department of Electrical and Computer Engineering,

University of California, Santa Barbara, CA93106

TEL 805-893-8376 Fax 805-893-3262

**on leave from Furukawa Electric, Chiba, Japan.*

InGaAsP / InP multiple quantum well (MQW) lasers are one of the most important and promising active components for 1.3 or 1.55 μm optical communication systems. There have been a lot of work on the physical phenomena in the MQW lasers. In such an effort, especially in analyzing the small signal modulation dynamics as well as steady state characteristics in the MQW lasers, the carrier density or number in each well is usually assumed to be uniform among all the MQWs. However, it is not correct especially for the InGaAsP / InP MQWs, whose energy discontinuity of the valence band is larger than that of the conduction band, since the transport of holes is much slower. It is of great importance to know how uniformly carriers are distributed in order to investigate the high speed performance of the laser with many number of quantum wells. This theoretical work describes the distribution of both electrons and holes among the InGaAsP / InP MQW lasers by solving coupled rate equations with barrier states, three-dimensional like well states, and two-dimensional well states.

An separate confinement heterostructure (SCH) MQW laser structure with InGaAs wells and InGaAsP barriers is assumed for the simulation. The coupled rate equations with barrier states and 3-dimensional like states in well region for electrons can be written as follows [1];

$$\begin{aligned} \frac{dB_i}{dt} &= \frac{N_i^{(3)}}{\tau_{d(i)}} + \frac{N_{i+1}^{(3)}}{\tau_{d(i+1)}} - \frac{2B_i}{\tau_d} - \frac{B_i}{\tau_{sp}} \\ \frac{dN_i^{(3)}}{dt} &= \frac{B_{i-1} + B_i}{\tau_d} + \frac{N_i^{(2)}}{\tau_{esc}} - \frac{2N_i^{(3)}}{\tau_{d(i)}} - \frac{N_i^{(3)}}{\tau_{cap}} - \frac{N_i^{(3)}}{\tau_{sp}} \\ \frac{dN_i^{(2)}}{dt} &= \frac{N_i^{(3)}}{\tau_{cap}} - \frac{N_i^{(2)}}{\tau_{esc}} - \frac{2N_i^{(2)} - N_{i-1}^{(2)} - N_{i+1}^{(2)}}{\tau_{tun}} - \frac{N_i^{(2)}}{\tau_{sp}} - \frac{\Gamma_i G_i S}{1 + \epsilon \Gamma_i S} \end{aligned}$$

$$\frac{dS}{dt} = \sum_{i=1}^M \frac{\Gamma_i G_i S}{1 + \epsilon \Gamma_i S} - \frac{S}{\tau_p} + \frac{\beta}{\Gamma_{\text{sum}}} \sum_{i=1}^M \frac{N_i^{(2)}}{\tau_{\text{sp}}}$$

where M is the number of wells, B_i the carrier number in i -th barrier, $N_i^{(3)}$ the carrier number of 3-dimensional like state in i -th well region, $N_i^{(2)}$ the carrier number of quantum well, τ_d the diffusion time, τ_{esc} the escape time, τ_{cap} the capture time, τ_{sp} the spontaneous emission lifetime, τ_{tun} the tunneling time, ϵ the gain compression factor, S the total photon number, G_i the optical gain, β the spontaneous emission feedback factor, τ_p the photon lifetime, Γ_i the confinement factor with $\Gamma_{\text{sum}} = \sum \Gamma_i$, respectively. The coupled rate equations for holes can be described in a similar manner.

We assumed the charge neutrality where the number of electrons and holes is the same in the identical well (or barrier). In such a case, the diffusion time is expressed as the average of electron and hole diffusion times [2]. We used a thermionic emission time for the escape time. Operation wavelength of 1.55 μm , gain compression factor ϵ of $1 \times 10^{-17} \text{ cm}^{-3}$, and capture time of 0.1 ps are used. Carriers in the SCH regions are neglected here for simplicity, although the transport of the carriers through the regions have been shown to play an important role in the high speed phenomenon [2]. We have used an analytical formula for the carrier density dependent gain function [3]. The carrier distribution at the steady state is obtained by solving the above coupled rate equations.

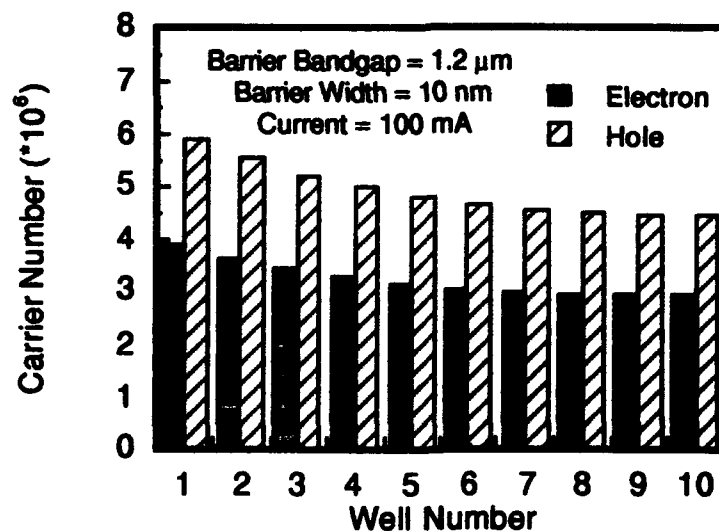


Fig. 1 Distribution of electrons and holes in a 10 quantum well laser.

Figure 1 shows the calculated distributions of electrons and holes of the 2-dimensional states in 10-well laser with barrier bandgap of $1.2 \mu\text{m}$ and width of 10 nm at 100 mA bias. Non-uniform carrier distribution is observed. In addition, the number of electrons in the quantum well is much smaller than that of holes. This is due to the much shorter thermionic emission time (escape time) of electron. The number of electrons of the 3-dimensional like state is larger than that of holes, so that the charge neutrality is satisfied.

Small signal response of the laser can be calculated based on the above rate equations. The differential gain in an individual well is different from each other depending on the steady state number of electrons and holes in the well. This effect will be taken into account in the following simulation. Figure 2 shows the small signal modulation response of a 10-well laser with barrier bandgap of $1.2 \mu\text{m}$ and width of 10 nm at four bias points. We believe that this is the first simulation of the small signal modulation response with non-uniform carrier injection taken into account.

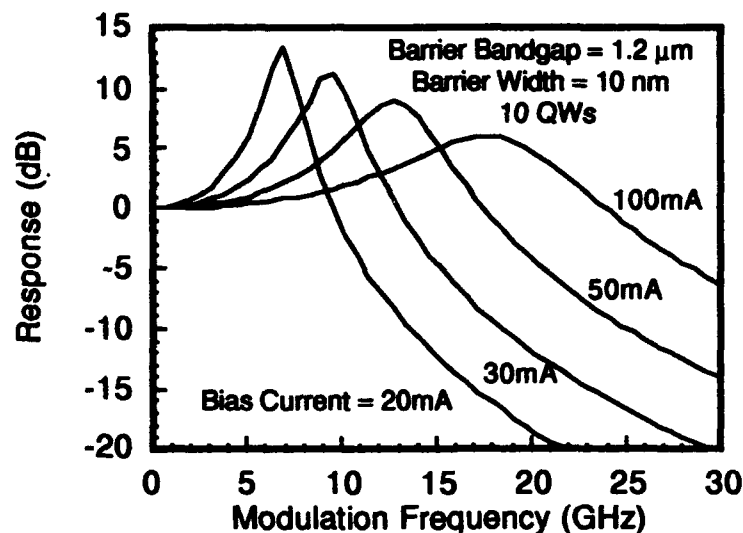


Fig. 2 Small signal modulation response of a 10-well laser.

Figure 3 shows the calculated dependence of 3dB modulation bandwidth on the number of wells at 100 mA bias. The result obtained by the conventional analysis method, where the carrier distribution is completely uniform and all the carriers are in the quantum well, is also plotted for comparison. It is evident that the conventional analysis

overestimates the 3dB bandwidth. In actual devices, the carriers in barrier and 3-dimensional like states in well region cannot contribute to the optical gain, leading to the degradation of the modulation bandwidth. In addition, there exists an optimum number of wells to obtain the maximum modulation bandwidth.

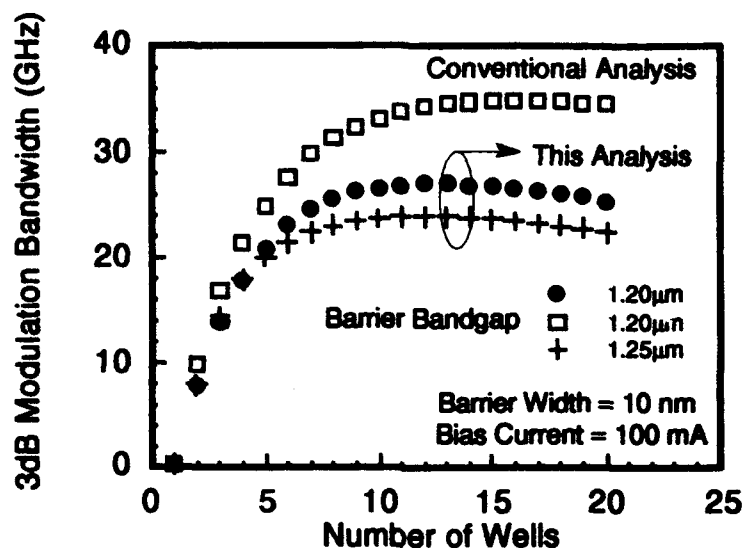


Fig. 3 Calculated dependence of 3dB modulation bandwidth on the number of wells at 100 mA bias.

In summary, we have calculated the distribution of electrons and holes among the InGaAsP / InP MQW lasers. Non-uniform carrier distribution has been observed in a steady state. The dependence of 3dB modulation bandwidth on the number of wells has been calculated with spatially varying differential gain taken into account.

References

- [1] N. Tessler, R. Nagar, D. Abraham, and G. Eisenstein, *J. Appl. Phys.*, 60 (6), pp.665-7 (1992).
- [2] R. Nagarajan, M. Ishikawa, T. Fukushima, R. S. Geels, and J. E. Bowers, *J. Quantum Electron.*, 28 (10), pp.1990-2008 (1992).
- [3] K. J. Vahala, and C. E. Zah, *Appl. Phys. Lett.*, 52 (23), pp. 1945-7 (1988).

2.2 GHz active mode-locking in a 2.0 cm long monolithic extended-cavity laser

G. Raybon, P. B. Hansen, U. Koren, B. I. Miller, M. G. Young,
M. A. Newkirk, M.-D. Chien, B. Tell, and C. A. Burrus

AT&T Bell Laboratories,

Crawford Hill Laboratory, Holmdel, NJ 07733

(908) 888-7221

Monolithic mode-locked semiconductor lasers are compact and reliable pulse sources for optical communication systems employing short pulses such as optical time division multiplexed systems and long distance soliton transmission [1]. These sources offer the advantage and flexibility for integration with filters, amplifiers, modulators, saturable absorbers, or other photonic components which can enhance the versatility and reliability of the transmission source [2,3]. However, the repetition rate at which the mode-locked laser operates is inversely proportional to the cavity length. Therefore, very long cavity lengths are required for operation at frequencies which are of practical interest for systems deployed today, such as those designed for the Sonet standard rate, OC-48 (2.488 Gbit/s). Maturing growth and processing techniques of III-V materials have enabled fabrication of very long 1.55 μm laser devices, that are suitable for mode-locking at repetition rates below 10 GHz [4]. Recent results indicate a trend toward lower, more practical operating frequencies and increased integration. Here, we report a semiconductor laser with a length twice that of any previously reported monolithic mode-locked laser. The resultant fundamental repetition rate is 2.2 GHz. Active mode-locking at the fundamental frequency, and at higher harmonics, yields optical pulses with widths ranging from 9.0-12.0 ps.

High quality photonic integrated circuits are fabricated using MOVPE based growth and processing techniques described in ref. 5. Advancements in the processing of InP based circuits allows for more complex integration and increased device area. The laser, shown

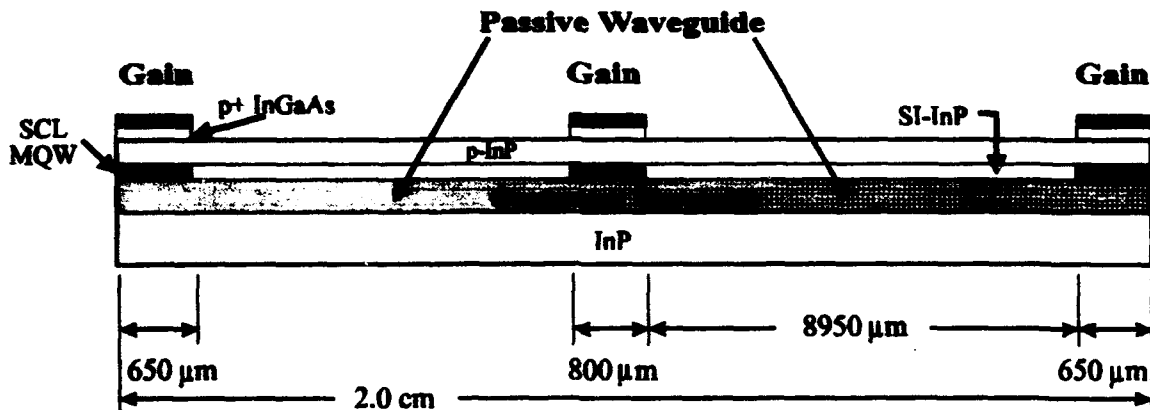


Fig. 1: Schematic drawing of the 2.0-cm long multi-segment monolithic mode-locked laser. SCL: strain compensated layer. MQW: multiple quantum well.

schematically in Fig. 1, consists of three multiple quantum well (MQW) gain regions separated by two long, low loss, passive waveguides. A quaternary guiding layer extends the full length of the 2.0 cm device with the active segments, defined above the guiding layer at each end and in the middle of the device. The lengths of these segments are 650 μm , 800 μm , and 650 μm respectively, for a total length of 2,100 μm . This gives a ratio of gain to passive waveguide of 11.7 %. Each gain segment is a buried heterostructure, as shown in the cross section view of Fig. 2a, and is comprised of six, 35 \AA thick strain-compensated (1.2% compressive) quantum wells separated by 90 \AA thick barriers. The two segments of passive waveguide separating the gain regions, are buried rib waveguides consisting of a 0.12- μm thick 1.3- μm quaternary layer grown on top of a 0.2- μm thick, 1.1- μm quaternary layer. This composite waveguide structure is shown as a lightly hatched single layer in Fig. 2b. Semi-insulating InP is regrown to act as the upper cladding layer for the passive waveguide and to provide low capacitance current blocking in the active regions.

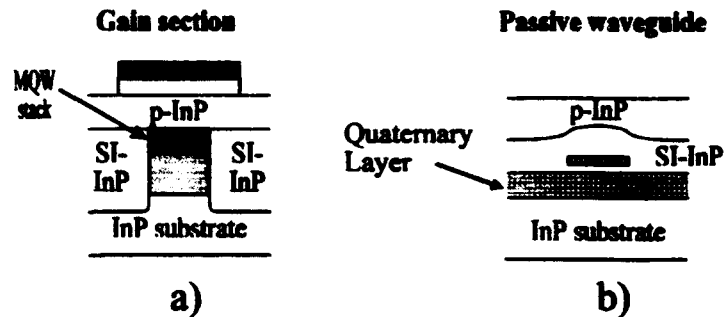


Fig. 2: Cross section view of a) buried heterostructure MQW active region and b) buried rib quaternary passive waveguide.

The laser exhibits a DC threshold current of 102 mA at 20 $^{\circ}\text{C}$ and an external quantum efficiency of 5.0 % per facet when all three contacts are biased in parallel. A measurement of the small signal response as shown in Fig. 3, reveals a strong response at the fundamental resonance frequency and at higher harmonics. Only the fundamental and the first harmonic are shown in the figure, but strong resonances are observed up to 20 GHz, which is the limit of the measurement system.

Active mode-locking at the fundamental resonance frequency is achieved by driving one of the end gain segments with a 2.2 GHz, 1W RF sinusoid superimposed on a small DC current of 21 mA. The other two contacts are shorted together and biased with a DC current of 130 mA. These active regions act as intra-cavity optical amplifiers to maintain a high-Q cavity. Figure 4 shows the pulses as observed on a Hamamatsu synchroscan streak camera when the laser is mode-locked at the fundamental repetition rate of 2.2 GHz. The measured pulse width is 12.0 ps with a

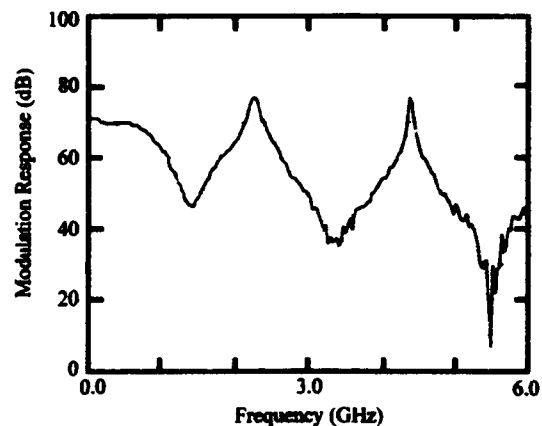


Fig. 3: Small signal response of the monolithic laser showing the fundamental resonance and the first harmonic.

corresponding peak power of 51.7 mW. The pulses exhibit a on/off ratio greater than 23 dB and the resultant pulse stream has a very low duty cycle of 2.6%. This corresponds to a 12 ps pulse every 450 ps. Similar pulse profiles are observed at the first and second harmonics. At 4.3 GHz, and 6.5 GHz, pulses as short as 9.0 ps were observed. An Avantek 2-8 GHz power amplifier provides the 1W drive power allowing access to the fundamental and first two harmonics by simply tuning the RF source. The corresponding optical spectrum has a half width of 7 nm. The broad spectral width can be limited through an integrated or external filter to obtain a narrower or transform limited spectrum as has been shown previously [1,4]. Figure 5 shows the dependence of the pulse width and the peak optical power on the modulation frequency. The pulse width and peak power reach a minimum and maximum, respectively, at a frequency near 2.2 GHz. The pulse broadens more rapidly as the frequency is tuned below the optimum frequency than when the frequency is tuned above the optimum. This behavior is characteristic of active mode-locking and is qualitatively in agreement with the calculations reported by Morton, et. al. in ref. 6.

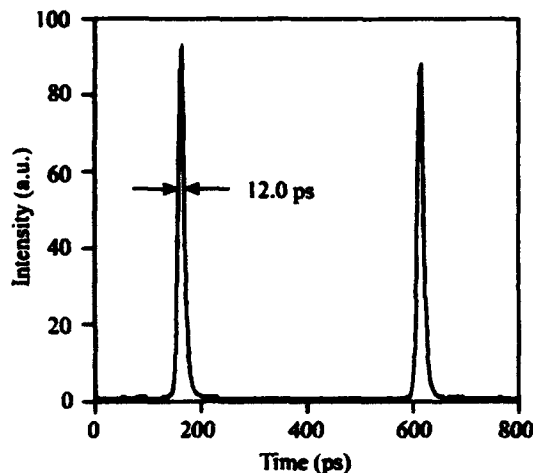


Fig. 4: Low duty cycle pulse stream as measured on a streak camera.

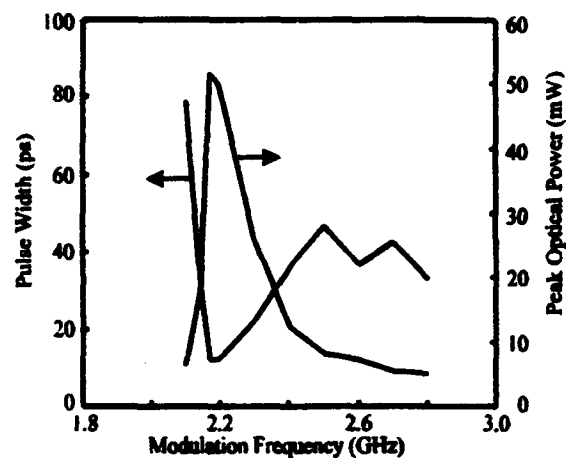


Fig. 5: Measured pulse width and optical peak power versus frequency.

In summary, active mode-locking at the fundamental repetition rate of 2.2 GHz has been achieved in a 2.0-cm long monolithic semiconductor laser. This is the lowest repetition rate, by a factor of two, reported for any mode-locked monolithic semiconductor laser device. Consequently, we have demonstrated that it is feasible to design an optical transmitter using a monolithic mode-locked laser for application in pulse transmission systems operating at rates being deployed commercially such as the Sonet rate of 2.488 Gbit/s.

References:

- [1]: C. R. Giles, et. al., "Soliton transmission over 4,200 km using a mode-locked monolithic extended-cavity laser as a soliton source", Conf. on Optical Fiber Communication, February, 1993, San Jose, CA.

- [2]: D. J. Derickson, et. al., "Short pulse generation using multisegment mode-locked semiconductor lasers", IEEE Journ. of Quan. Electron., Vol 28, No. 10, pp. 2186-2201, 1992.
- [3]: P. B. Hansen, et. al., "Mode-locked extended-cavity laser with a Bragg reflector monolithically integrated with an electro-absorption modulator operating at 4.5 Gbit/s", 13th IEEE Semiconductor Laser Conf., Paper PD-6, Kagawa, Japan, Sept. 1992.
- [4]: G. Raybon, et. al., "Active mode-locking at 4.4 GHz in 1-cm long monolithic extended cavity laser", LEOS'92 Annual Meet., Paper DLTA4.3, Boston, Massachusetts, 1992.
- [5]: T. L. Koch, and U. Koren, "Semiconductor photonic integrated circuits", IEEE Journ. Quantum Electron., Vol. 27, No. 3, pp 641-653, 1991.
- [6]: P. A. Morton, et. al., "Dynamic detuning in actively mode-locked semiconductor lasers", IEEE Journ. of Quantum Electron., Vol. 25, No. 12, pp. 2621-2633, 1989.

Intrinsic Modulation Response of a Gain-Coupled MQW DFB Laser with an Absorptive Grating

*Yoshiaki Nakano^{1,2}, Marian L. Majewski¹, Larry A. Coldren¹,
Hong-li Cao², Kunio Tada², and Haruo Hosomatsu³*

¹Department of Electrical and Computer Engineering
University of California, Santa Barbara, CA 93106
Phone: (805) 893-2875, Facsimile: (805) 893-4500

²Department of Electronic Engineering, University of Tokyo
7-3-1 Hongo, Bunkyo-ku, Tokyo, 113, Japan
Phone: +81-3-3812-2111, Facsimile: +81-3-5684-3645

³Devices Lab., Yokogawa Electric Co., Ltd.
2-11-13 Naka-cho, Musashino-shi, Tokyo, 180, Japan
Phone: +81-422-52-5744, Facsimile: +81-422-55-8080

Introduction

Semiconductor lasers with gain-coupled distributed optical feedback (DFB) have been revealed to be superior to traditional index-coupled DFB devices, as they exhibit excellent single mode property,¹⁻⁵⁾ reflection insensitivity,^{6,7)} low-chirping short optical pulse generation capability,^{8,9)} and immunity to longitudinal spatial hole burning.¹⁰⁾ All these features are certainly to benefit the integrated photonics applications. One of the remaining issues is a high-speed small signal modulation capability of the device as there have been only a few reports.¹¹⁾

In this paper we describe measurement of intensity noise spectra of a multiple quantum well (MQW) gain-coupled DFB laser with an absorptive grating as well as the resulting intrinsic modulation response. Based on simple small signal Rate Equations, an anomalous behavior of the device damping factor observed has been explained.

Device Structure

A schematic cross-sectional picture of the device measured here is shown in Fig. 1. The SCH-MQW active layer consists of three 8nm-thick GaAs quantum wells separated by two 8nm-thick Ga_{0.8}Al_{0.2}As barriers, and two 75nm thick Ga_{0.8}Al_{0.2}As optical confinement layers which sandwich the quantum wells in between.

Since bulk GaAs has a narrower band gap than the quantum wells by approximately 70meV, the periodically embedded GaAs is highly absorptive to the lasing light, thus making an absorptive grating. It is a third-order grating with a 376nm period. The grating duty cycle W/Λ is controlled to be ~ 0.2 in order to limit extra loss, yet to acquire large gain coupling.^{12,13)} An additional grating layer is formed during the second step epitaxy on the absorptive grating, namely "anti-phase index grating", which is to reduce the index perturbation produced by the absorptive grating.

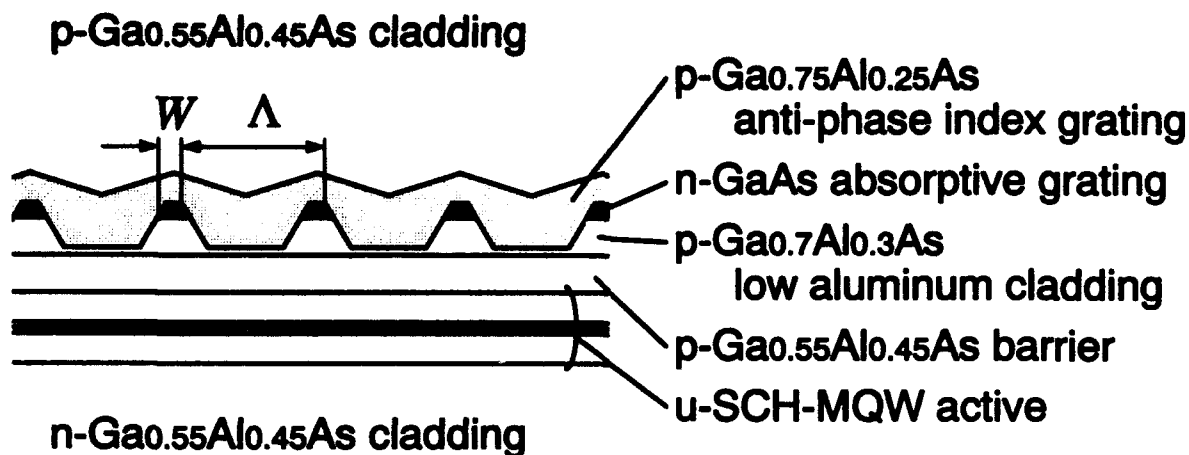


Fig. 1. Schematic longitudinal cross section of the MQW GC DFB laser with an absorptive grating used here.

The laser has a $4\mu\text{m}$ -wide ridge waveguide and a $200\mu\text{m}$ -long cavity. The cleaved facets are left uncoated. DC characteristics of the laser at 20°C are threshold current of 11.3mA , oscillation wavelength of 841nm , differential efficiency of $0.27\text{mW}/\text{mA}/\text{facet}$, and side mode suppression of more than -30dB at 2mW .

Measurement

The CW light output was collected via a GRIN rod lens into a single mode fiber, and connected to a high speed photodetector with a post-amplifier (New Focus 1404 and 1422). The RF output signal was monitored using a microwave spectrum analyzer (HP8566B). This system was capable of measuring signals at frequencies up to $\sim 20\text{GHz}$. Intensity noise spectra were taken at different optical output powers. These noise spectra allowed us to obtain the relaxation resonance frequency and the damping factor corresponding to the device intrinsic response.

The squared resonance frequency and the damping factor are plotted as functions of output power per facet, as shown in Fig. 2. It can be seen from the figure that the squared resonance frequency is proportional to the

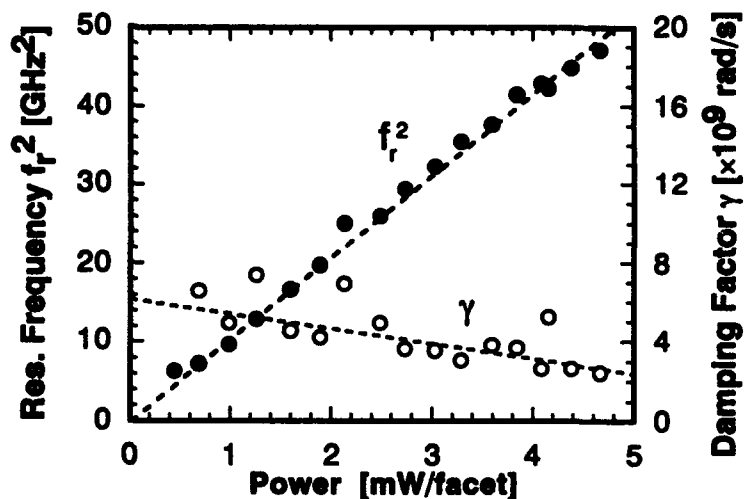


Fig. 2. Resonant relaxation frequency and damping factor vs. optical power obtained from the intensity noise spectra.

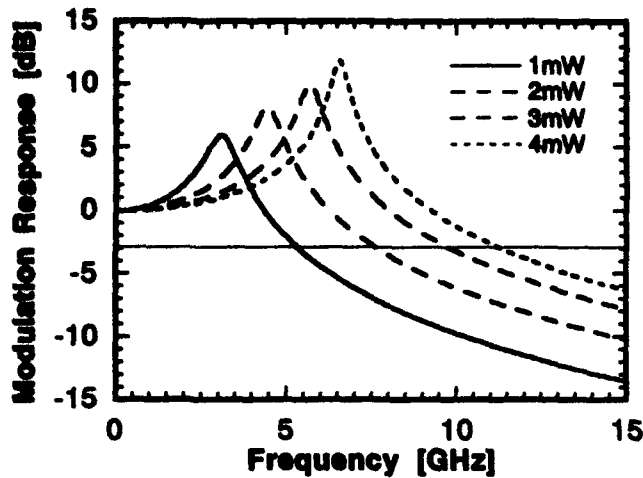


Fig. 3. Intrinsic intensity modulation response calculated from the experimental data shown in Fig. 2.

factor with power, the relaxation resonance peak becomes sharper and the -3dB bandwidth continuously increases. As is shown in Fig. 4, the -3dB bandwidth can be enhanced proportionally to the square root of the output power. It easily reaches 12GHz at powers around 5mW.

Discussion

There are several factors which may cause the uncommon behavior of the damping factor of our device. One of them is the saturable nature of the absorption of the GaAs grating.¹⁴⁾ If we introduce another Rate Equation to account for the carrier density in the absorptive grating, and add to the Rate Equation for the photon density another term which deals with the absorption in the grating, we obtain the following expression for the damping factor,

$$\gamma = (\epsilon_s G + G' - \epsilon_a A + A')S + \frac{1}{\tau_s} + \frac{1}{\tau_a}$$

where S is the photon density, G and A are gain and absorption coefficients of the active and grating layers, G' and A' are differential gain and absorption, ϵ_s and ϵ_a are gain and absorption compression factors, and τ_s and τ_a are recombination lifetimes corresponding to each

power, which agrees with the standard theory. In other words, the gain compression is not very large at power levels below 5mW. The slope of 10.4GHz²/mW is good and indicates that the device has a potential for broadband modulation. What is interesting to notice from Fig. 2 is that the damping factor decreases with increasing power. This tendency is just opposite to what is commonly seen in most lasers where the damping factor typically increases with power.

If we calculate the intrinsic small signal intensity modulation response using the values shown in Fig. 2, we obtain Fig. 3. Due to the decreasing damping

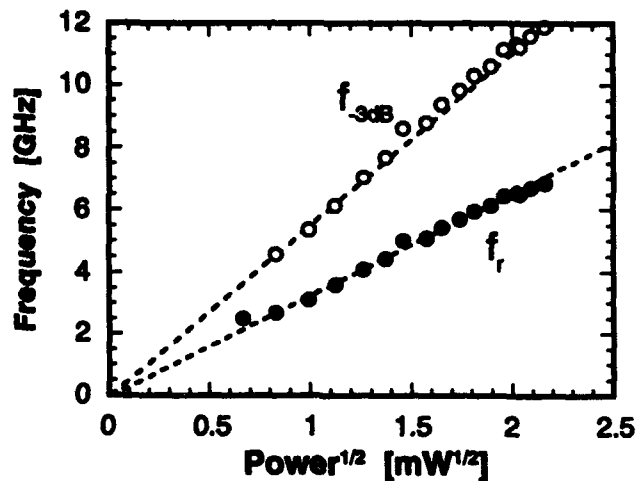


Fig. 4. Relaxation resonance and -3dB modulation bandwidth frequencies vs. the square root of optical power.

layer, respectively. In obtaining the above expression, we assumed that the photon density is moderate thus it does not cause a severe gain nor absorption compression.

If τ_s is small and ϵ/A is larger than the rest of the terms in the parentheses in front of S , the damping factor vs. photon density relation results in a negative slope with a large offset at null photon density, which is what can be seen in Fig. 2. The assumption made may be valid here because the grating faces re-growth interface and the absorption used is highly nonlinear in nature.

Another factor that might contribute to the behavior of the damping factor is the photon-density-dependent photon lifetime in the gain-coupled cavity.⁹⁾ This may play an essential role after the parasitic index coupling and the facet reflectivity are reduced significantly.

Conclusion

It has been found that the gain-coupled DFB laser with absorptive gratings exhibits an uncommon intrinsic modulation response where the damping factor decreases with optical output power. Because of this effect, the modulation bandwidth of the device has no limitations due to damping. Modified Rate Equations developed have successfully explained this anomalous behavior. Measurements of different devices as well as time-domain characterization are currently under way.

References

- 1) H. Kogelnik and C. V. Shank, *J. Appl. Phys.* **43** (1972) 2327.
- 2) Y. Luo, Y. Nakano, and K. Tada, *SSDM'88, Tokyo, D-4-4*.
- 3) Y. Luo, Y. Nakano, K. Tada, T. Inoue, H. Hosomatsu, and H. Iwaoka, *Appl. Phys. Lett.* **56** (1990) 1620.
- 4) K. David, G. Morthier, P. Vankwikelberge, and R. Baets, *Electron. Lett.* **26** (1990) 238.
- 5) G. Morthier, P. Vankwikelberge, K. David, and R. Baets, *IEEE Photon. Technol. Lett.* **2** (1990) 170.
- 6) Y. Nakano, Y. Luo, and K. Tada, *Appl. Phys. Lett.* **55** (1989) 1606.
- 7) Y. Nakano, Y. Deguchi, K. Ikeda, Y. Luo, and K. Tada, *IEEE J. Quantum Electron.* **27** (1991) 1732.
- 8) Y. Luo, R. Takahashi, Y. Nakano, K. Tada, T. Kamiya, H. Hosomatsu, and H. Iwaoka, *Appl. Phys. Lett.* **59** (1991) 37.
- 9) Y. K. Chen, M. C. Wu, W. T. Tsang, F. S. Choa, R. A. Logan, M. A. Chin, and A. M. Sergent, *CLEO'92, Anaheim, CTuF4*.
- 10) K. David, G. Morthier, P. Vankwikelberge, R. Baets, T. Wolf, and B. Borchert, *IEEE J. Quantum Electron.* **27** (1991) 1714.
- 11) B. Borchert, B. Stegmuller, R. Gessner, and I. Karger, *1992 IEEE International Semiconductor Laser Conf., Takamatsu, PD-10*.
- 12) Y. Luo, H.-L. Cao, M. Dobashi, H. Hosomatsu, Y. Nakano, and K. Tada, *IEEE Photon. Technol. Lett.* **4** (1992) 692.
- 13) H.-L. Cao, Y. Luo, Y. Nakano, K. Tada, M. Dobashi, and H. Hosomatsu, to appear in the October 1992 issue of *IEEE Photon. Technol. Lett.*
- 14) K. Y. Lau and N. Bar-Chaim, *IEEE Photon. Technol. Lett.* **4** (1992) 118.

Tensile Strained InGaAs/InGaAsP Quantum Well Optical Amplifier with a Wide Spectral Gain Region at 1.55 μm

B. I. Miller, U. Koren, M. A. Newkirk, M. G. Young, R. M. Jopson, and M. D. Chien. AT&T Bell Laboratories, Rm. 4F-335, 101 Crawfords Corner Road, Holmdel, NJ 07733, 908-949-6341

Recently, several new designs for wide range tunable lasers have been demonstrated, using different structures for the tuning element such as Y branch interferometers [1,2], sampled gratings [3], and vertical coupler filters [4].

A tunable laser is composed of a gain medium and a tunable filter. The tuning range of a laser may be limited by the filter, or by the ability of the gain medium to provide enough gain to overcome the cavity losses over a wide spectral range [4]. For integrated tunable lasers, and for external cavity lasers, it is important to develop a gain medium that can provide optical gain over a large spectral range. Furthermore, it is important to achieve this gain coverage with low injection current, as lower bias currents can improve the laser efficiency, output power and long term reliability.

Quantum well (QW) lasers have been suggested for this application, utilizing the lower density of states in quantum wells to obtain an inverted carrier population at higher photon energies. Population inversion of the $n=1$ and $n=2$ quantum levels has been shown to be important for broadening of the gain spectrum in the GaAs [5-7] and the InP material systems [8].

In the present work we suggest and demonstrate the use of the $n=1$ and $n=2$ electron to light hole transitions in tensile strained quantum wells for effectively broadening the range of available gain. This broad gain range is achieved with significantly less injection current than with other quantum well configurations. It has been argued by Yablonovitch and Kane [9] that strained QW's can diminish the current injection level required for lasing due to the reduction of the hole effective mass and density of states.

As the selection rules forbid transitions between different n subbands (such as electron $n=2$ to holes $n=1$) it is necessary to invert the hole $n=2$ level in order to obtain gain from $n=2$ transitions. Therefore, by the same argument it should be expected that the limiting factor in obtaining useful gain from $n=2$ transitions in unstrained or compressively strained QW's is the need to invert the heavy holes population at the $n=2$ subband which can be done only at high injection currents. In contrast, it is very advantageous to use tensile strained quantum wells for this purpose, as the light holes have lower effective mass and lower density of states for the $n=1$ and $n=2$ subbands. Therefore, useful gain can be obtained from $n=2$ transitions in tensile strained quantum wells with significantly less carrier injection than in other quantum well configurations, for a given volume and carrier lifetime.

The band diagram used in the tensile strained amplifiers of the present work is shown in Fig. 1. The structure was grown by atmospheric pressure metalorganic vapor-phase epitaxy (MOVPE) using strain compensation [10] to minimize any deleterious effects arising from the large tensile strain in the QW's. The wells and barriers were approximately 160Å and 270Å thick respectively; the wells were $\text{In}_{0.39}\text{Ga}_{0.61}\text{As}$ and were under tensile strain of 1%. The barriers were compressively strained InGaAsP ($E_g=0.95$ eV) about 0.15% to partially compensate the tension in the wells. Shown in the figure is the $n=1$ and $n=2$ electron (e) to light hole (lh) transi-

tions for the quantum wells. The electron to heavy hole transition does not play a significant role in this structure. The room temperature photoluminescence is shown in Fig. 2. Two peaks corresponding to the $e \rightarrow lh$ for $n=1$ and $n=2$ transitions are shown at $1.566 \mu\text{m}$ and $1.48 \mu\text{m}$ respectively and agree well with theory.

After the growth of the base wafers, lasers and optical amplifiers were made using two additional MOVPE regrowths for the blocking layers and the p-type cladding layers. Fabry-Perot lasers were cleaved with various cavity lengths. The lasing wavelength for a $350 \mu\text{m}$ long laser was $1.58 \mu\text{m}$ with current threshold of about 10 mA and differential quantum efficiency of 30%/facet. The cavity absorption (α) for these lasers was $\approx 12 \text{ cm}^{-1}$. Optical amplifiers were made with $650 \mu\text{m}$ long gain sections and $20\text{--}40 \mu\text{m}$ long window sections at both ends adjacent to the facets. Single SiO layers were used for AR coatings on the facets. The residual reflectivities of these amplifiers are estimated to be about 8×10^{-5} .

The amplified spontaneous emission (ASE) coming from both compressive and tensile amplifiers is shown in Fig 3. The compressive amplifier, shown for sake of comparison is $800 \mu\text{m}$ long. The wavelength of the compressive amplifier (TE mode) shifts very slightly with current from $1.58 \mu\text{m}$ to $1.55 \mu\text{m}$, while the tensile amplifier (TM mode) undergoes a very large shift from $1.56 \mu\text{m}$ to $1.46 \mu\text{m}$. The small shift of the compressive peak and the maintenance of its shape with current point to a single $e \rightarrow hh$, $n=1$ transition. The tensile amplifier however shows much more change: at low currents we see that the predominant source of gain for the tensile amplifier comes from the $n=1$, $e \rightarrow lh$ transition, at higher currents the gain comes from both the $n=1$ and $n=2$ levels, while at the maximum current the gain is predominately from the $n=2$ level. This is summarized in Fig. 4 where the peak wavelength of both the compressive and tensile amplifiers is plotted vrs. current. The shift in wavelength of the compressive amplifier is small compared to the tensile one. For example, at 60 mA the shift of wavelength of the compressive amplifier is $\approx 25 \text{ nm}$, compared to $\approx 84 \text{ nm}$ for the tensile amplifier. This large shift in wavelength with moderate currents is essential for achieving large tuning ranges in integrated tunable lasers.

The internal gain of the tensile strained amplifier is shown in Fig 5. As in Fig. 3 we see that at moderate currents (50 mA) both the $n=1$ and $n=2$ levels contribute equally to the gain and give a very wide 3 dB bandwidth of $\geq 92 \text{ nm}$ at a peak gain of 17 dB. At higher pump power the gain is dominated by the $n=2$ transition and gains of 24 dB can be realized. Even at this gain, 3 dB bandwidths in excess of 50 nm are obtained. As expected from theory the TE gain is very low, about 15 dB below the TM at 150 mA as can be seen in Fig. 6.

In conclusion we have demonstrated that it is possible to achieve wide bandwidth gain by using tensile strained quantum wells. The range in wavelength where there is over 5 dB gain (suitable for lasing) at a moderate current of 50 mA, makes it possible to realize tunable lasers covering a range of more than 125 nm.

The Authors would like to acknowledge J. E. Zucker for suggesting we study tensile quantum well lasers and amplifiers, and H. M. Presby for supplying the micro-machined lensed fibers used for coupling into the amplifier.

REFERENCES:

- [1] M. Schilling, K. Dütting, W. Idler, D. Baums, G. Laube, K. Wünnstel, and O. Hildebrand, *Electron. Lett.*, vol. 28, pp. 1698-1699, 1992

- [2] M. Kuznetsov, P. Verlangieri, A. G. Dentai, C. H. Joyner, and C. A. Burrus, *IEEE Photon. Tech. Lett.*, vol. 4, pp. 1093-1095, 1992.
- [3] V. Jayaraman, D. A. Cohen, and L. A. Coldren, *Appl. Phys. Lett.* vol. 60, pp. 2321-2323, 1992.
- [4] R. C. Alferness, U. Koren, L. L. Buhl, B. I. Miller, M. G. Young, T. L. Koch, G. Raybon, and C. A. Burrus., *Appl. Phys. Lett.* vol. 60, pp. 3209-3211, 1992
- [5] M. Mittelstein, Y. Arakawa, A. Larsson, A. Yariv., *Appl. Phys. Lett.* vol. 49, pp. 1689-1691, 1986.
- [6] P. S. Zory, A. R. Reisinger, L. J. Mawst, G. Costrini, C. A. Zmudzinski, M. A. Emanuel, M. E. Givins, and L. J. Coleman, *Electron. Lett.* vol. 22, p. 475, 1986
- [7] D. Mehuys, M. Mittelstein, A. Yariv, R. Sarfaty, J. E. Ungar, *Electron. Lett.* vol. 25, pp.143-145, 1989
- [8] K. Berthold, A. F. J. Levi, Tanbun-Ek, and R. A. Logan, *Appl. Phys. Lett.* vol. 56, pp. 122-124, 1990.
- [9] E. Yablonovitch and E. O. Kane, *J. of Lightwave Technol.* vol. 8, pp. 1292-1299, 1988.
- [10] B. I. Miller, U. Koren, M. G. Young, and M. D. Chien, *Appl. Phys. Lett.* vol. 58, pp. 1952-1954, 1991

FIGURES

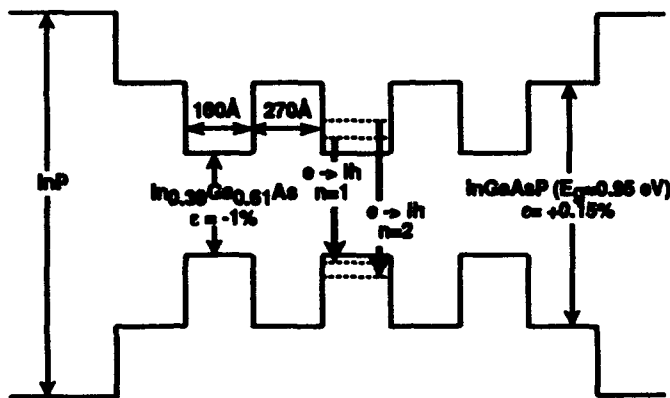


FIG. 1 Band Diagram for 3 tensile-strained quantum well structure used in this work. The $e \rightarrow lh$ transitions are shown for $n=1$ and $n=2$.

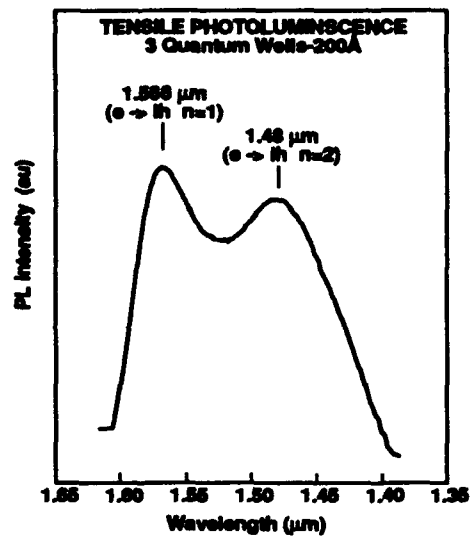


FIG. 2. Room temperature PL of the structure in Fig. 1. The peaks corresponding to the $n=1$ and $n=2$ transitions are shown.

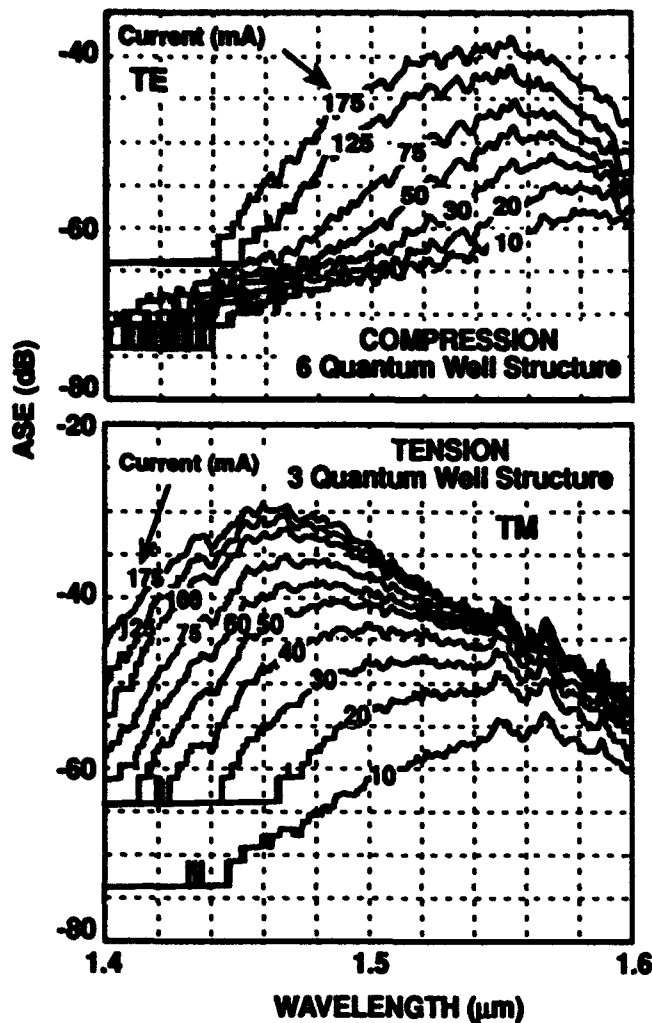


FIG. 3 ASE spectra of compressive and tensile strained-layer quantum well structures.

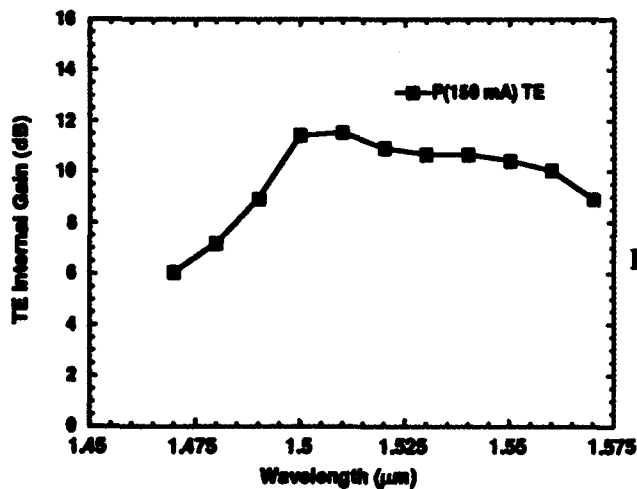


FIG. 6 TE internal gain of 3-quantum well tensile amplifier at 150 mA. The TE gain is 15 dB below the TM at 150 mA.

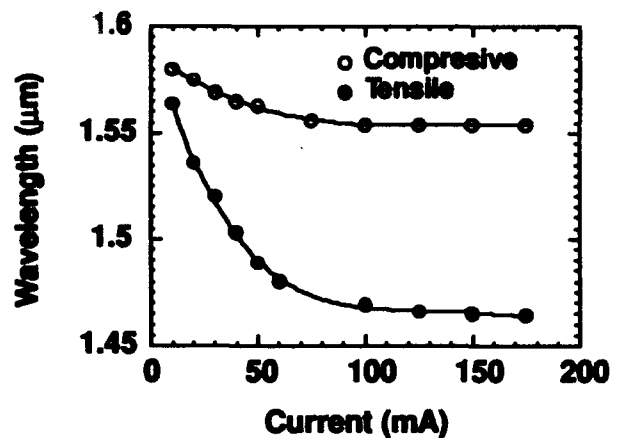


FIG. 4 ASE peak wavelength vrs current for compressive and tensile quantum well structures. At 60 mA, the wavelength is shifted 25 nm for compressive compared to 84 nm for tensile strain.

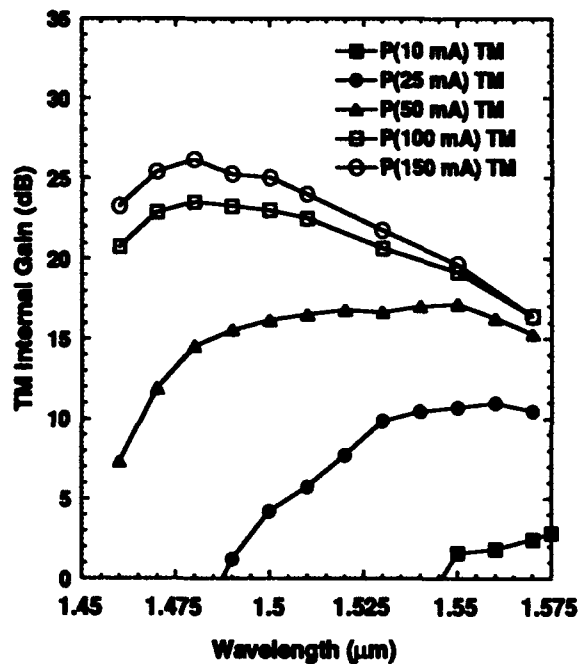



FIG. 5 Internal gain of 3-quantum well tensile amplifier at several pump currents.



**LiNbO₃ and LiTaO₃
Devices**

ITuH 1:30pm-3:30pm
Mesquite B

Gar Lam Yip, *Presider*
McGill University

Optically pumped solid state lasers in LiNbO₃

Eric Lallier

Thomson-CSF, Laboratoire Central de Recherches

91404 Orsay Cedex, France.

Phone: (33-1) 60 19 78 54

Fax: (33-1) 60 19 74 16

LiNbO₃ is a well-known and widely used crystal for its good electro-optic, acousto-optic, and non-linear properties. The combination of such properties with the laser gain of rare-earth ions in the same medium permits the construction of many interesting systems including self-Q-switched, self-mode-locked, and self-frequency-doubled laser devices. Since LiNbO₃ benefits from well-established techniques to form low loss waveguides and complex integrated optical functions, the further combination of rare-earth doped LiNbO₃ properties in a single-mode waveguide configuration can yield to efficient and monolithic multifunction compact devices. To name a few, the integration of modulators can simply mode-lock or Q-switch the laser with respectively a high-frequency and peak-power capability for low-drive voltages. Using the acousto-optic or electro-optic effect it is also possible to fabricate tunable single-frequency lasers with a potentially narrow linewidth. Compact visible laser sources can be fabricated by intra-cavity second-harmonic-generation using for instance the recently developed quasi-phase-matching techniques. Finally, implementing the already demonstrated large range of integrated optical functions on doped LiNbO₃ substrate should eventually provide insertion loss compensated amplified optical circuits.

Within the last years, good progress has been achieved towards the experimental demonstration of such devices. The 1.08 μm Nd³⁺ transition has been studied first and efficient single mode channel waveguide lasers have been demonstrated⁽¹⁾. Laser thresholds on the order of 1 mW and 50 % conversion efficiency compatible with low power diode laser pumping have now been achieved. The integration of a traveling-wave phase modulator allowed for mode-locked operation yielding 7 ps pulses with 250 mW peak-power at a 6 GHz repetition rate (fig. 1)⁽²⁾. Repetition rates ranging from one to several tens of GHz should be possible using different lengths and harmonic mode-locking. More recently the integration of a directional coupler permitted Q-switched operation (fig. 2)⁽³⁾. Although the modulator is not yet optimized, this device has now been able to produce 300 ps wide pulses with 350 W peak-power for less than 15 mW of 0.814 μm coupled pump power⁽⁴⁾. Such characteristics are already interesting for time-multiplexed fiber sensors system applications and should be useful for intra-cavity non-linear interactions (frequency-doubling, parametric oscillation).

Other ions are of interest and in particular the Er³⁺ 1.5 μm transitions for telecommunication applications. Although this is a quasi-three-level system, the single mode waveguide configuration eases its operation as for fiber lasers. Brinkman *et al.* have demonstrated Er:LiNbO₃ laser operation near 1.53 μm using an indiffused evaporated Er layer⁽⁵⁾. This technique permits to use large-size and high-quality undoped LiNbO₃ substrates and eventually to perform local doping through standard photolithographic techniques. This is particularly important for

the further integration of passive and active components. It also permits tailoring the doping profile with respect to the guided pump mode thus minimizing the laser signal reabsorption. These authors have then operated low thresholds lasers (≈ 10 mW) at different wavelengths near 1.56 and 1.58 μm and shown broad-band amplification in the range of 1.53-1.61 μm indicating the potential for a tunable laser (6). They also expect to achieve 10 dB gain in an optical amplifier with optimized dopant and waveguide profiles. Such a gain should be sufficient to compensate for the insertion losses of many LiNbO_3 integrated optical devices. In this talk we shall review in more details the recent development in rare-earth doped LiNbO_3 waveguide lasers and amplifiers, their applications and future prospects.

References:

- (1) E. Lallier, JP. Pocholle, M. Papuchon, M. De Micheli, M. J. Li, Q. He, D. B. Ostrowsky, C. Grezes-Besset, and E. Pelletier, "Nd:MgO:LiNbO₃ channel waveguide laser devices", IEEE J. Quantum Electron., vol. 27, no. 3, pp. 618-625, 1991.
- (2) E. Lallier, JP. Pocholle, M. Papuchon, M. De Micheli, Q. He, D. B. Ostrowsky, C. Grezes-Besset, and E. Pelletier, "Integrated Nd:MgO:LiNbO₃ FM mode-locked waveguide laser", Electron. Lett., Vol. 27, no. 11, pp. 936-937, 1991.
- (3) E. Lallier, JP. Pocholle, M. Papuchon, Q. He, M. De Micheli, and D. B. Ostrowsky, "Integrated Q-switched Nd:MgO:LiNbO₃ waveguide laser", Electron. Lett., Vol. 28, no. 15, pp. 1428-1429, 1992.
- (4) E. Lallier, JP. Pocholle, M. Papuchon, M. De Micheli and D. B. Ostrowsky, "Short pulse, high power Q-switched Nd:MgO:LiNbO₃ waveguide laser", submitted for publication in Electron. Lett..
- (5) R. Brinkmann, W. Sohler, and H. Suche, "Continuous-wave erbium-diffused LiNbO₃ waveguide laser", Electron. Lett., Vol. 27, no. 5, pp. 415-417, 1991.
- (6) P. Becker, R. Brinkmann, M. Dinand, W. Sohler, and H. Suche, "Erbium-doped integrated optical amplifiers and lasers in lithium niobate", in Optical Amplifiers And Their Applications, Vol. 17 of 1992 OSA Digest Series, invited paper ThB4-1, pp. 109-112.

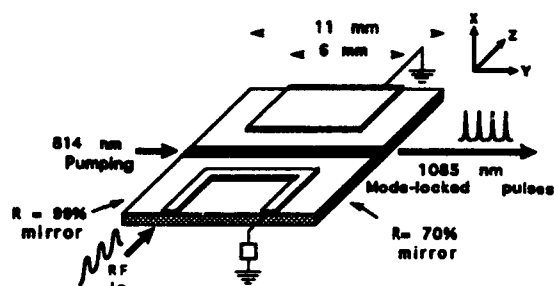


Figure 1: Integrated mode-locked laser

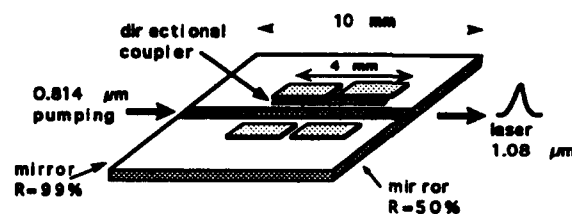


Figure 2: Integrated Q-switched laser

EXCITED STATE LIFETIME REDUCTION IN Nd:MgO:LiNbO₃ AND Nd:LiTaO₃ PROTON EXCHANGED WAVEGUIDES

S. Nouh, P. Baldi, M. De Micheli, G. Monnon and D.B. Ostrowsky

Laboratoire de Physique et de la Matière Condensée

Université de Nice-Sophia Antipolis

Parc Valrose, 06108 Nice Cedex 2, France

Tel. +33 93 52 98 82

E. Lallier, and M. Papuchon

L.C.R. Thomson-CSF, Domaine de Corbeville

91404 Orsay Cedex, France

Tel. +33 (1) 60 19 74 57

Introduction:

In this paper, we present the measurement of the Nd fluorescence decay lifetimes in Nd doped lithium niobate and lithium tantalate. In proton exchanged waveguide we studied the influence of the proton concentration on this lifetime and we show that, in some cases, proton exchange drastically reduces this important parameter for laser oscillation. Finally, we present a Nd:LiTaO₃ waveguide laser whose threshold is on the order of 40 mW, this high threshold is largely explained by the excited state lifetime reduction.

Fluorescence lifetime:

In our fluorescence experiment on Nd doped lithium niobate and lithium tantalate, we pumped with a Ti:Sapphir laser tuned to 0,816 μm which modulated with an acousto-optic device. For an unexchanged Nd doped lithium niobate sample ,S0, with 0,1 mole % Nd the lifetime was 110 μs . For Nd doped lithium tantalate we did the measurement on two samples, S1, with 0,1 mole % Nd and ,S2, with 0,2 mole % Nd and we found that the lifetime was 123 μs and 105 μs for S1 and S2 respectively. Here we can note three things :

a) these measurements confirm the results published in reference {1} for Nd doped lithium niobate; the Nd³⁺ ion can replace a Nb⁵⁺ ion as well as a Li⁺ ion and the two sites of Nd have the same lifetime. The same observation was made for Nd doped lithium tantalate.

b) Comparing the results obtained on S1 and S2 we can see that the lifetime is reduced when the Nd concentration is increased as expected.

c) The comparison of S1 and S0 show that the matrix slightly influences the lifetime which is shorter in lithium niobate. For this reason and for the tantalate's reputation for having a considerably higher optical damage threshold, it seemed interesting to develop laser devices in Nd doped lithium tantalate to improve the results obtained in Nd doped lithium niobate {ref. 2,3}.

The easiest technique available to fabricate waveguides in lithium tantalate is proton exchange and different waveguides were realized using this technique. For PEI {ref. 4} waveguides where

the proton-lithium replacement ratio is between 0.5 and 0.8, we observed two lifetimes, far shorter than those observed in the bulk. In figure (1), we present in logarithmic coordinates the experimental points and the best numerical fits obtained with the function $f(t) = A \exp(-t/T1) + B \exp(-t/T2)$ where $T1$ and $T2$ are the lifetimes to measure and A and B are weighting factors. For S1 we found $T1 = 2.8 \mu s$, $T2 = 33 \mu s$, $A = 0,64$ and $B = 0,36$ and For S2 we found $T1 = 3.7 \mu s$, $T2 = 43 \mu s$, $A = 0.4$ and $B = 0.6$. This has to be compared to the results obtained for analogous waveguide realized on S0 where we found $T1 = 1.8 \mu s$, $T2 = 10.8 \mu s$, $A = 0.66$ and $B = 0.34$. With these results we can suggest that the two Nd sites are no longer degenerate in highly exchanged waveguides.

LiTaO₃ waveguide laser:

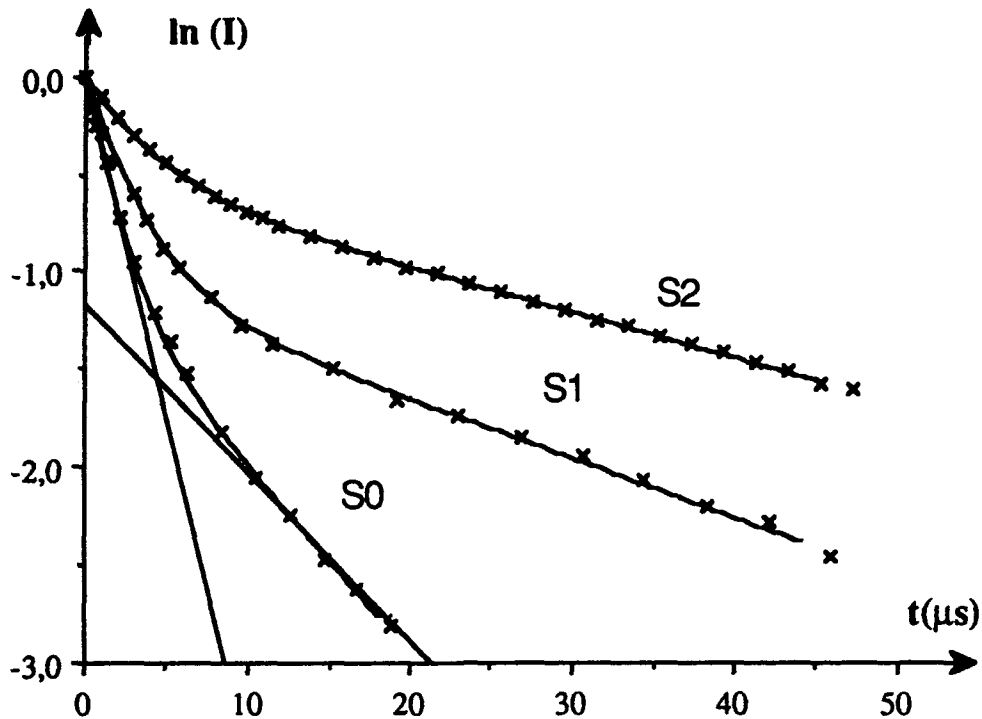
For PE_I proton exchanged waveguides fabricated on the sample S1, dielectric mirrors were deposited on the end-faces having 94% transmissivity at the pump wavelength ($\lambda = 0,816 \mu m$) and a reflectivity of 99% at the laser wavelength ($\lambda = 1,094 \mu m$), at the entrance face, and a reflectivity of 70% at $1,094 \mu m$ at the output face. Pumping with a Ti:Sapphire laser tuned to $0,816 \mu m$, a decaying laser action was observed. The initial output power versus absorbed pump power is given in figure (2). In this figure we can observe a high threshold value on the order of 40 mW which may be mainly attributed to the reduction of the lifetime by the proton concentration. The optical damage at the pump wavelength being essentially responsible for the decaying laser action. Further investigations using a Nd:LiTaO₃ waveguide laser on S2 are underway to separate the influence of these two effects .

Conclusion:

We demonstrate that a high proton-lithium replacement ratio radically reduces the excited state lifetime. two lifetimes appear, suggesting the removal of the degeneracy of Nd³⁺ sites.

References :

- 1) T. Y. Fan, A. Cordova-Plaza, M. J. F. Digonnet, R. L. Byer, and H. J. Shaw : "Nd:MgO:LiNbO₃ spectroscopy and laser devices", J. Opt. Soc. Am. B/Vol. 3, No.1 January 1986.
- 2) E. Lallier, J.P. Pocholle, M. Papuchon, C. Grezes-Beset, E. Pelletier, M. De Micheli, M.J. Li, Q. He and D.B. Ostowsky: "Laser oscillation of single-mode channel waveguide in Nd:MgO:LiNbO₃", Electron. Lett. Vol. 25, pp. 1491-1492, 1989.
- 3) R. Brinkman, W. Sohler and H. Suche: "Continuous-wave erbium-diffused LiNbO₃ waveguide laser", Electron. Lett. vol. 27, pp. 415-417, 1991.
- 4) M. J. Li, M. De Micheli, D. B. Ostrowsky and M. Papuchon : " R alisation sur LiNbO₃ de guides d'onde pr esentant une forte variation d'indice et de tr es faibles pertes" , Annales des T el ecommunications, 43, n  1-2, pp. 73-77 ,1988.



Figure(1) : Fluorescence curves of Nd:MgO:LiNbO₃ (S₀) and Nd:LiTaO₃ (S₁,S₂) :

- x are experimental points,

- lines are the numerical fits with a function $f(t) = A \exp(-t/T_1) + B \exp(-t/T_2)$. As shown, for the sample S₀, T₁ and T₂ are determined by the slope of two straight lines. The different lifetimes in μs are given in the following table.

	S ₀	S ₁	S ₂
T ₁	1.8	2.8	3.7
T ₂	10.8	33	43

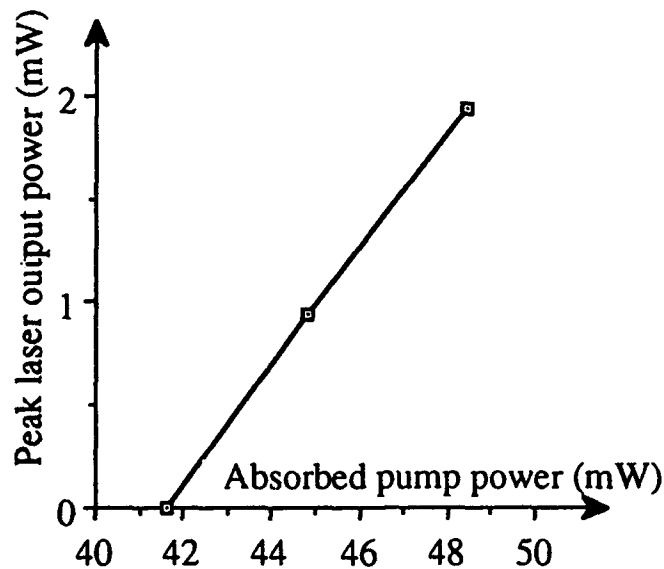


Figure (2). Characteristics of the Nd:H_xLi_{1-x}TaO₃ waveguide laser

Measurement of Optical Damage in LiNbO₃ Waveguide Devices

G. E. Betts, F. J. O'Donnell, and K. G. Ray
Lincoln Laboratory, Massachusetts Institute of Technology
Lexington, MA 02173-9108
(617) 981-4429

Operation of LiNbO₃ devices at high optical power levels has become a practical issue owing to the use of the devices in analog optical links [1]. Optical damage at high power and long wavelength has not been well characterized, especially with respect to its effects in an actual interferometric modulator. We report here the results of long-term (up to 200 h), high-power (up to 400 mW) tests, at 1321-, 1064-, and 850-nm wavelengths, of LiNbO₃ waveguide devices made using both Ti-indiffused and proton-exchanged waveguides.

The basic optical damage mechanism is the photorefractive effect, in which illuminated regions experience a refractive index change [2]. This can manifest itself in several ways in an optical waveguide: (1) the optical path length (the total phase shift of the light passing through a given length of waveguide) can be altered, (2) the waveguide loss can increase because the photorefractive index change reduces the waveguide/substrate index difference, (3) TE-polarized light can be converted to TM by an induced index grating [3], and (4) the mode shape can be altered because of changes in the waveguide index profile.

In an interferometric modulator, illustrated in Figure 1, these waveguide variations affect the modulation performance. Different changes in total phase shift in the two arms (due to any slight imbalance in power or damage sensitivity) alter the modulator bias point, which is the relative phase difference between the arms. The bias point change is usually the most sensitive measure of damage, but it is a practical problem only in applications that do not actively control the modulator bias point. The on-to-off, or extinction, ratio can be degraded by unbalanced losses in the two arms or by unbalanced splitting at the Y-branches due to a photorefractive index change. The total optical insertion loss can increase because of an increase in the waveguide loss. These latter two effects will be a problem in almost any application if they are severe enough.

The design of a modulator has an important influence on how photorefractive index changes will translate to performance degradation. For example, the interferometric modulator should be less sensitive to photorefractive index changes in its waveguides than the directional coupler [4], because it is a balanced device and index changes in one arm should compensate index changes in the other. We have chosen to focus primarily on measurements on actual modulators, instead of test structures, to give us the best information on the power-handling capabilities of practical devices.

The majority of our samples used Ti-indiffused waveguides on commercial optical waveguide substrates. The diffusion was done at 1050°C in wet O₂. The devices using proton-exchanged waveguides were exchanged in pure benzoic acid at 215°C, then annealed in wet O₂ at 360°C. All devices were X-cut and Y-propagating. The waveguide losses were <0.1 dB/cm (at 1321 nm) to 0.5 dB/cm (at 850 nm). The modulators all had a 250-nm-thick SiO₂ buffer layer under the electrodes. All devices were annealed in wet O₂ after the oxide deposition as the final high-temperature process step.

We used lens coupling for most of our measurements. (We tested some fiber-coupled devices at 1321 nm at power levels up to 300 mW and temperatures from +40 to -60°C, but did not see any substantial difference from the room-temperature lens-coupled results.) The waveguide output was detected either with a thermal detector (for accurate absolute power measurements), a photodiode, or a beam profile scanning system. Optical power levels quoted here refer to the power in the waveguide just after input coupling. Since the losses in the Y-branch, the propagation, and the output lens are approximately known and are all small (except in the 850-nm tests), and the Fresnel loss at the waveguide/air interface is known, the input guide power can be calculated accurately from the measured output power. The interferometric modulator bias point was accurately measured by applying a 1-kHz sine wave to the electrodes and measuring the first and second harmonic outputs. Most of our measurements were made with the dc voltage between the electrodes held at 0 V, to evaluate the bias drift in a device with no bias control.

Devices made using Ti-indiffused waveguides showed good power-handling ability, especially at longer wavelengths, as seen in Table 1. The maximum optical power levels used were determined by our maximum laser power and best coupling efficiency. The only severe damage effect was the drift in bias point; this is illustrated in Figure 2. The TE:TM ratio remained >30 dB for the 1321-nm devices shown in Table 1. The waveguides had elliptical modes with $1/e^2$ -intensity dimensions of approximately $7.5 \mu\text{m}$ (along Z) \times $5.0 \mu\text{m}$ (along X) at 1321 nm; the mode size scaled linearly with the wavelength. The size and shape of the mode did not seem to change significantly during the damage runs, but our measurement repeatability was limited to about $\pm 1 \mu\text{m}$ and changes of that order or smaller could have occurred.

Our results at 1064 nm seem to show a substantially less significant photorefractive problem than might be expected from the measurements at that wavelength by Fujiwara et al. [5]. Our maximum power density of about $1 \text{ MW}/\text{cm}^2$ is about 500 \times larger than the power levels used in that work, and yet we see only minor device effects. There are several possible reasons for this apparent disagreement. First, the magnitudes of effects in an actual device are difficult to predict from approximate knowledge of basic effects. As mentioned above, the device design plays an important role in translating basic phenomena to observed effects. Furthermore, basic constants are not known accurately. For example, whether we are in the high-intensity limit, where photoconductivity is much larger than dark conductivity, is not clear; both the dark conductivity and the photoconductivity are known to within only an order of magnitude [6]. Second, the purity and composition of the substrate vary from one crystal grower to another, and some of these variations are significant for optical damage. The optical waveguide substrates used in this work had an Fe concentration of approximately 1 ppm by weight (spark source mass spectrometry was used to determine concentration) and even smaller concentrations of other transition metals such as Cu and Mn that might have contributed to the photorefractive effect. We obtained some substrates from an alternative source that contained 2 to 4 ppm of Fe, and these showed a substantially larger photorefractive effect. Third, there are processing steps that can greatly increase the sensitivity to optical damage. We found that a final anneal at temperatures as low as 200°C in nonoxygen atmospheres can increase photorefractive sensitivity [7].

Proton-exchanged waveguides were not immune to optical damage. Our results are summarized in Table 2. At 1321 nm, the proton-exchanged guides showed approximately the same small (but nonzero) effects as Ti-indiffused devices. At shorter wavelengths, the proton-

exchanged devices did appear somewhat more stable than the Ti-indiffused devices. This difference is most visible at 850 nm. The measurements at 850 nm reported here are our initial ones at that wavelength, and the power levels are uncertain by a factor of two; further work is in progress that will give more reliable results at the 850-nm wavelength. The proton-exchanged devices maintained their excellent polarization properties (TE:TM ratio >41 dB) in all our results so far.

We made a few measurements with a dc voltage applied to the electrodes to look for photoconductive problems. We evaluated a Ti-indiffused modulator at 1064 nm with 90 mW in the input waveguide and a dc bias voltage of approximately 9 V across the 5- μ m electrode gap. The voltage required to maintain a fixed bias point only changed by 0.5 V in 70 h, indicating that the photoconductivity was not large enough to seriously interfere with the use of a dc bias voltage. An ion-exchanged device, tested with 300 mW at 1321 nm, also showed only a small photoconductive drift.

We have measured photorefractive effects in interferometric modulators on LiNbO₃ at three wavelengths of practical significance. The power-handling capability is large enough for dependable long-term operation in analog systems, although some improvement is desirable for systems that do not have active control of the dc bias point. Proton-exchanged waveguides do show some advantage over Ti-indiffused waveguides at the shorter wavelengths, but more work is needed to reliably determine the extent of this improvement.

This work was supported by the Department of the Air Force.

REFERENCES

1. G. E. Betts, L. M. Johnson, and C. H. Cox III, *Devices for Optical Processing, SPIE Proceedings*, vol. 1562, p. 281, 1991.
2. A. M. Glass, *Opt. Eng.*, vol. 17, p. 470, 1978.
3. J. F. Lam and H. W. Yen, *Appl. Phys. Lett.*, vol. 45, p. 1172, 1984.
4. G. T. Harvey, G. Astfalk, A. Y. Feldblum, and B. Kassahun, *J. Quantum Electron.*, vol. QE-22, p. 939, 1986.
5. T. Fujiwara, S. Sato, and H. Mori, *Appl. Phys. Lett.*, vol. 54, p. 975, 1989.
6. R. Gerson, J. F. Kochhoff, L. E. Halliburton, and D. A. Bryan, *J. Appl. Phys.*, vol. 60, p. 3553, 1986.
7. G. E. Betts, F. J. O'Donnell, and K. G. Ray, *LEOS Annual Meeting Technical Digest*, paper OTA1.3, 1992.

TABLE 1. TI-INDIFFUSED DEVICE RESULTS

Damage Test			Result		
Wavelength (nm)	Optical Power (mW)	Time (h)	Change in Bias Point (deg)	Change in Optical Transmission (dB)	Worst Extinction (dB)
1321	100	168	<1	0	>20
1321	400	145	3.5	<-0.15	22
1064	20	24	15	-0.6	19
1064	140	24	25	-0.3	18
850	10	41	430	<-1	

TABLE 2. PROTON-EXCHANGED DEVICE RESULTS

Damage Test			Result		
Wavelength (nm)	Optical Power (mW)	Time (h)	Change in Bias Point (deg)	Change in Optical Transmission (dB)	Worst Extinction (dB)
1321	205	200	18	-1.0	25
1064	45	90	5	<-1	
850	5	24	<20	0	

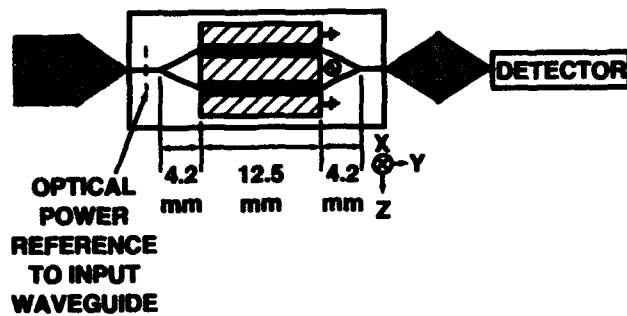


Figure 1. Diagram of interferometric modulator used in experiments.

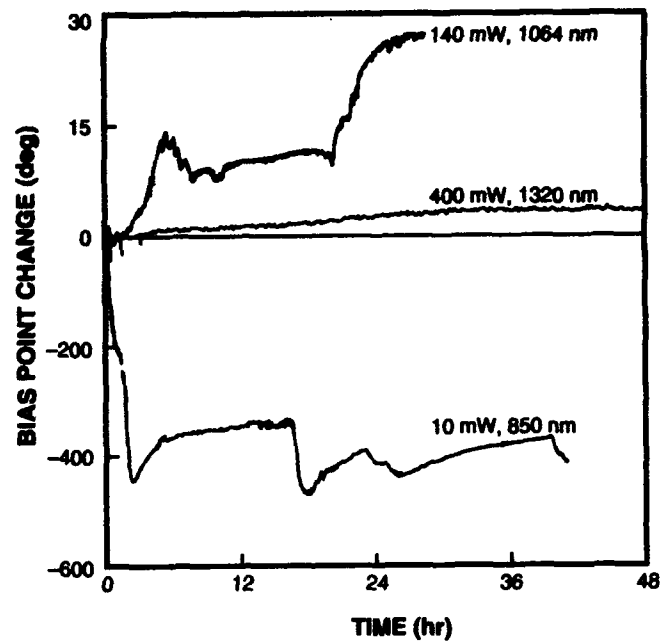


Figure 2. Change in interferometer bias point (i.e., change in phase difference between arms) as a function of time for Ti-indiffused devices. Note different vertical scale for 850-nm measurement.

Loss mechanisms in high δn_e PE planar waveguides.

S. Chen, M.P. De Micheli and D.B. Ostrowsky

C.N.R.S. - Université de Nice Sophia Antipolis
Laboratoire de Physique de la Matière Condensée
06108 Nice Cedex2, FRANCE

Tel. +33 93 52 98 82, Fax. +33 93 52 98 08

A. Leycuras

C.N.R.S. Sophia Antipolis
Laboratoire de Physique du Solide et de l'Energie Solaire
06560 Valbonne, FRANCE

Tel. +33 93 95 42 00

G. Tartarini and P. Bassi

Università di Bologna
Dipartimento di Elettronica Informatica e Sistemistica
Viale Risorgimento 2, 40136 Bologna, ITALY

Tel. +39 51 64 43 050

Introduction

High δn_e Proton Exchanged (PE) waveguides in LiNbO_3 ¹ are extremely interesting when dealing with phenomena where power confinement is a key factor. However it was noted that in many cases it was not possible to keep the losses under several dB/cm. In this paper we will show how a correlation between the crystalline and the optical properties of these waveguides allows us to explain the propagation losses either by scattering induced by the presence of dislocations in the exchanged layer, or by stress induced rotation of the principal axes of the exchanged layer with respect to the substrate axes, or a combination of the two. The importance of these loss mechanisms is strongly related to the fabrication parameters, especially the temperature of the exchange melt, and we will show that increasing this temperature dramatically improves the crystalline quality of the layer and the properties of the waveguide.

Disorder and dislocations in high δn_e PE waveguides

The disorder which is sometimes introduced in the exchanged layer can be seen by different techniques, among which Rutherford Back Scattering (RBS) is the most effective. RBS results are shown in figure 1 where we see that the number of α particles back scattered by the Nb ions increases rapidly when the exchange temperature is reduced². At 300°C, the exchange layer presents the same spectra as a virgin sample, which means that at this temperature, no disorder is introduced by the exchange. This phenomenon is corroborated by a number of other observations, such as the monitoring of Bragg reflections on crystalline plans in X-ray rocking curve experiments³. Figure 2 shows a set of rocking curves obtained on samples realized at different temperatures. On samples exchanged at temperatures higher than 300°C the signature of the exchanged layer is a well defined peak showing that the layer has the same crystalline cell as the substrate but with slightly different parameters. On the contrary, samples processed at temperatures under 300°C, no longer present a peak for the exchanged layer, but a faint signal for a great range of parameter values, which is the signature of a layer presenting a lot of dislocations and a poor crystalline quality. All these material properties are strongly correlated to the optical characteristics of the waveguides.

We will concentrate here on the properties of planar waveguides realized in pure benzoic acid. The waveguides exchanged at temperatures under 300°C always show losses of at least several dB/cm, important in-plane scattering, and when they are multimode, they exhibit a strong mode coupling. All these properties can easily be explained by a strong scattering due to the disorder created in the layer by the exchange.

An important point to make to understand the disappointing quality of high δn PE waveguides, is that the boiling temperature of benzoic acid under normal pressure conditions is 250°C. Thus most waveguides have been realized below this temperature

which explains their poor optical quality. The sealed ampoule technique⁴, allows using exchange temperatures up to 350°C. As can be seen in figure 2, despite the fact that the index profiles are nearly the same, the strains are reduced and the elastic energy stored in the exchanged layer remains inferior to the dislocation threshold. As we shall see in the next paragraph, these strains are responsible for the hybrid nature of the guided modes, which, depending on their n_{eff} values, show either high or low losses.

Stresses and hybrid modes in high δn_e PE waveguides

During the exchange, the crystalline cell tends to expand⁵, but as in the interface plane the layer parameters have to fit the substrate ones, the elongation occurs only perpendicularly to the surface. This induce strains and stresses in the exchanged layer. In the case of LiNbO₃ these strains [S] create permittivity modifications [$\delta\epsilon$] by two different processes, the photoelastic effect [Ph] and the combination of the piezoelectric [Pz] and the electrooptic effect [R] following the equation (1).

$$[\delta\epsilon^{-1}] = \{[\text{Ph}] + [\text{R}].[\epsilon].[\text{Pz}]\} [\text{S}] = [\text{T}] [\text{S}] \quad (1)$$

In the case of planar waveguides, the strains are uniform which implies that there is no shearing. The coefficients of the different tensors are taken equal to the substrate value⁶. This is qualitatively justified by the fact that the exchanged layer has the same crystalline structure as the substrate (the nonvanishing terms are the same in the substrate and in the layer) but this is quantitatively wrong because the values of these coefficients are modified by the exchange⁷. The last point to make is that the strains are defined by $S_{ii} = (d''_{ii} - d'_{ii})/d'_{ii}$ rather than by $S_{ii} = (d''_{ii} - d_{ii})/d_{ii}$ ⁸ where d'' , d' and d refers to a cell parameter respectively in the strained exchanged layer, in a powder of the same composition as the layer where the cell is free to expands and in the substrate.

With these conditions, using the classical index contraction convention $xx=1, yy=2\dots$, we obtain the following set of equations :

$$S_4 = S_5 = S_6 = 0 \text{ (no shearing) and } \left\{ \begin{array}{l} \delta \epsilon_1^{-1} = t_{11}S_1 + t_{12}S_2 + t_{13}S_3 \\ \delta \epsilon_2^{-1} = t_{12}S_1 + t_{11}S_2 + t_{13}S_3 \\ \delta \epsilon_3^{-1} = t_{31}S_1 + t_{31}S_2 + t_{33}S_3 \\ 2 \delta \epsilon_4^{-1} = t_{41}(S_1 - S_2) \\ \delta \epsilon_5^{-1} = 0 \\ \delta \epsilon_6^{-1} = 0 \end{array} \right. \quad (2)$$

We now have to distinguish two cases depending on the substrate orientation. In the case of Z-cut plate, there is no elongation in the XOY plane. Thus, $S_1=S_2$ which implies that the index matrix of the exchanged layer remains that of an uniaxial layer with the same principal axes as the substrate. The modes supported by the waveguide are then the classical TM modes, the strains and stresses are just responsible for a small part of the ordinary and extraordinary index variations. The situation is completely different in the case of an X-cut substrate where the only permitted elongation is along OX. Thus $S_1 \neq S_2$ which implies that $n_1 \neq n_2$ and $n_4 \neq 0$. The index matrix of the layer is now that of a biaxial medium with principal axes different from those of the substrate. The propagation equations of the different polarizations of the field are now coupled by a source term whose amplitude is proportional to n_4 . For any direction of propagation, the modes are now hybrid modes⁹, which, because of the negative birefringence of LiNbO₃, have to be classified in two families depending on the value of n_{eff} compared to the substrate ordinary index value n_0 . If n_{eff} is greater than n_0 , the ordinary component is evanescent in the substrate, the mode is perfectly guided, behaves like a classical TM mode and can be used in a practical device¹⁰. If n_{eff} is smaller than n_0 , the ordinary component radiates into the substrate, the mode is semi-leaky which, from the device point of view, is intolerable.

We have been able to verify experimentally and numerically these different properties of high δn_e PE waveguides realized on LiNbO₃. Measuring, for different propagation

directions ϕ , the effective indices of the modes at $\lambda=0.632,8\text{nm}$ of an X-cut planar PE waveguide realized at 200°C in pure benzoic acid, we obtained the results reported in fig. 3. Using a specially developed program¹¹, we have been able to fit these results with the following waveguide parameters : $n_o=2.285$, $n_e=2.205$, $\delta n_o=-0.05$, $\delta n_e=0.115$ and $\theta=10^\circ$, where θ is the angle in the XOY plane between the principal axes in the layer and in the substrate. This fit degrades dramatically if θ is changed by more than $\pm 2^\circ$. This value of θ is confirmed by the observation that the effective index of the fundamental mode goes through a maximum for $\phi=10^\circ$ as the theory predicts when $\phi=\theta$. The semi-leaky modes show very high losses up to 140 dB/cm !

In the case of waveguides exchanged at 300°C , we no longer have scattering problems, and we get a good fit with the measured effective indices for $\delta n_e=0.108$, $\delta n_o=-0.025$ and $\theta=0^\circ$. Looking carefully for the maximum of the effective index of the fundamental mode versus the propagation direction, we were able to measure it for $\phi=1^\circ \pm 0.5^\circ$ (Fig. 4). This rather small value of θ is nevertheless important for the propagation of the semi-leaky modes which still exhibit losses of several dB/cm.

Conclusion

In this paper we have shown that the losses in high δn_e PE planar waveguides are associated with two different mechanisms. In the case of waveguides fabricated with an exchange melt temperature smaller than 300°C we observed dislocation induced scattering and strain induced semi-leaky hybrid modes. Using an exchange melt temperature of 300°C allows avoiding the dislocations and the related scattering and considerably reduces the strain influence which improves drastically the quality of the waveguide without suppressing the semi-leaky modes. Studies are under way to test waveguides realized at even higher temperatures.

References

- 1 J.L. Jackel, C.E. Rice and J. Veselka, *Appl. Phys. Lett.* **41**, p.607 (1982)
- 2 M.P. De Micheli *et. al.* *J. Light; Tech.* **4** (7), p.743 (1986)
- 3 Thèse de S. Chen, Nice 1992
"Modes hybrides dans les guides réalisés par échange protonique sur LiNbO_3 "
- 4 M.P. De Micheli *et. al.* *Opt. Comm.* **42**, p.102 (1982)
- 5 C.E. Rice and J.L. Jackel, *Mat. Res. Bull.*, **119**, p.591 (1984)
- 6 A. Raüber, *Current Topics in Materials Sciences Vol. 1*, Ed. E. KALDIS, North Holland Publ.
- 7 See for example M. Minakata *et al.* *Appl. Phys. Lett* **49**, p.992 (1986)
- 8 V.A. Ganshin and Yu. N. Korkishko *J. Opt. Comm.* **13** (2) (1992)
- 9 A. Knoesen *et al.* *J. Light. Tech.* **6** (6), p.1083 (1988)
- 10 T. Taniuchi and K. Yamamoto, *SPIE Proc.* 864-09, Cannes, FRANCE (1987)
- 11 G. Tartarini *et al.* to be published

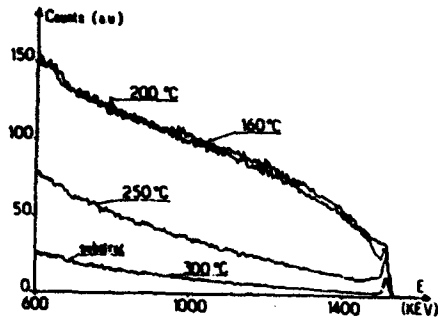


Fig. 1. Rutherford backscattering spectra in aligned condition of PE waveguides realized, in pure benzoic acid, at different temperature.

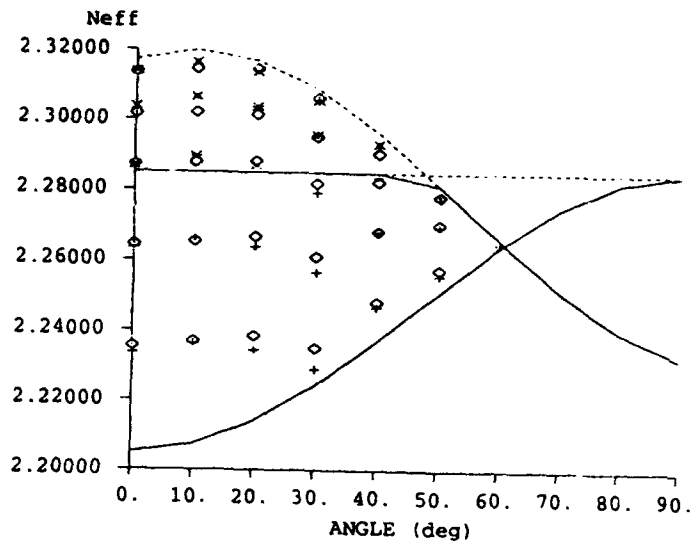


Fig. 3: Measured (\odot) and calculate (* and +) n_{eff} of a PE waveguide realized at 200°C as a function of the propagation direction

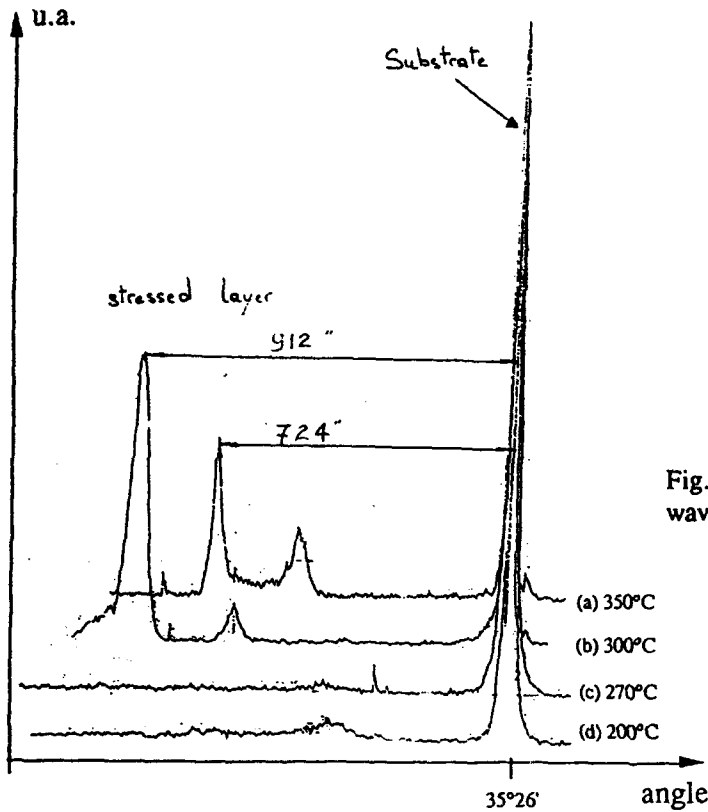


Fig. 2: Rocking curves of PE waveguides realized, in pure benzoic acid, at different temperature. Crystalline plane (220)

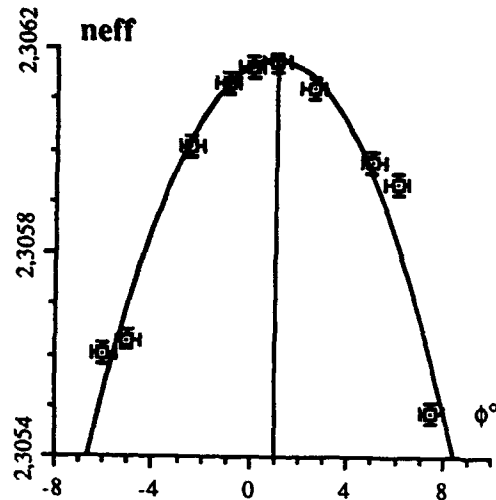


Fig. 4: n_{eff} of the fundamental mode of a PE waveguide realized at 300°C

Measurement of RF Drive Voltage and Intermodulation Distortion of a TW LiNbO₃ Modulator

G.K. Gopalakrishnan*, W.K. Burns †, and C.H. Bulmer†

*Maryland Advanced Development Laboratory, Greenbelt, MD 20770

†Naval Research Laboratory, Code 5671, Washington D.C. 20375-5000

Traveling wave (TW) LiNbO₃ optical modulators with performance extending well into the millimeter-wave frequency spectrum have been recently reported [1,2]. In these devices, a near velocity match between microwave and optical signals was achieved by using thick electrodes [3] in a coplanar waveguide (CPW) configuration. For application of TW modulators in optoelectronic systems, a fundamental parameter of interest is the electrical to optical conversion loss. This loss limits the strength of the modulated optical signal and is primarily dependent on the RF Drive Voltage ($V_r(f)$). It is therefore of interest to measure $V_r(f)$ directly. Below, we discuss a technique to carry out this measurement and compare results with theoretical calculations.

The electrical and optical characteristics of the device considered herein were recently reported [1]. A CPW electrode structure whose average thickness was 18 μm was electroplated on z-cut LiNbO₃, with an intervening SiO₂ buffer layer 0.9 μm in thickness. The center strip of the electrode was 8 μm wide and the gaps were 15 μm wide. The device length was 2.4 cm and the DC V_r was 5 V. At 40 GHz, the device rolled-off by about 7.5 dB(electrical) at an operating wavelength of 1.3 μm . Considering the voltage drop across the buffer layer and the asymmetry of the electrode structure with respect to the interferometer, the resulting optical-electrical overlap integral δ was 0.77 - 0.65. $V_r(f)$ can be obtained from the optical response using:

$$V_r(f) = V_r(0) \left(\frac{Z_D + Z_0}{2Z_D} \right) e^{\left(\frac{-OR}{20} \right)} \quad (1)$$

where $V_r(0)$ is the DC V_r , OR is the optical response (obtained from ref. 1) in dB(electrical), Z_D is the device impedance (approx. 35 Ω) and Z_0 is the line impedance (50 Ω). The result plotted in fig. 2 shows a variation of $V_r(f)$ from 5 to 15 Volts over a 40 GHz frequency span.

$V_r(f)$ can also be directly measured using the setup shown in fig. 1. This setup is the same as that used to measure intermodulation distortion in TW modulators [4]. Two synthesized sources operating at identical power levels at frequencies f_1 and f_2 that are marginally offset ($f_1 - f_2 = 40$ MHz in our case) are used to drive the modulator. A matched amplifier pair is used in conjunction with the sources to obtain power levels in excess of 10 dBm to be applied to the modulator. This is necessary to obtain signals of measurable strength in the third order frequency terms ($2f_2 - f_1$ and $2f_1 - f_2$). $V_r(f)$ can then be obtained from the ratio of power levels in the fundamental ($P_1(f)$) and third order ($P_3(f)$) terms as follows:

$$V_r(f) = \frac{\pi V}{2\sqrt{2}} \left(\frac{P_1(f)}{P_3(f)} \right)^{0.25} \quad (2)$$

where V is the input voltage applied to the modulator. The data obtained from this measurement are shown in fig. 2. Measurements conducted up to 17.5 GHz compare well with theory; above 17.5 GHz, we were limited by non-availability of equipment. We have also used the same technique to measure intermodulation distortion (IMD) upto 17.5 GHz.

In conclusion, we have presented a technique to directly measure $V_r(f)$ of TW modulators; measurements agree well with theory. We also measured the IMD of the device and obtained good agreement with theory; these results will be presented at the meeting.

REFERENCES

- [1] G.K. Gopalakrishnan et al.: '40 GHz low half-wave voltage Ti:LiNbO₃ intensity modulator', *Electron. Lett.*, 1992, **28**, pp. 826-827.
- [2] D.W. Dolfi and T.R. Ranganath: '50 GHz velocity-matched broad wavelength LiNbO₃ modulator with multimode active section', *Electron. Lett.*, 1992, **28**, pp. 1197-1198.
- [3] M. Seino et al.: '20 GHz 3 dB bandwidth Ti:LiNbO₃ Mach-Zehnder modulator', *ECOC*, 1990, paper ThG1-5.
- [4] B.H. Kolner and D.W. Dolfi.: 'Intermodulation distortion and compression in an integrated electrooptic modulator', *Applied Optics*, 1987, **26**, pp. 3676-3680.

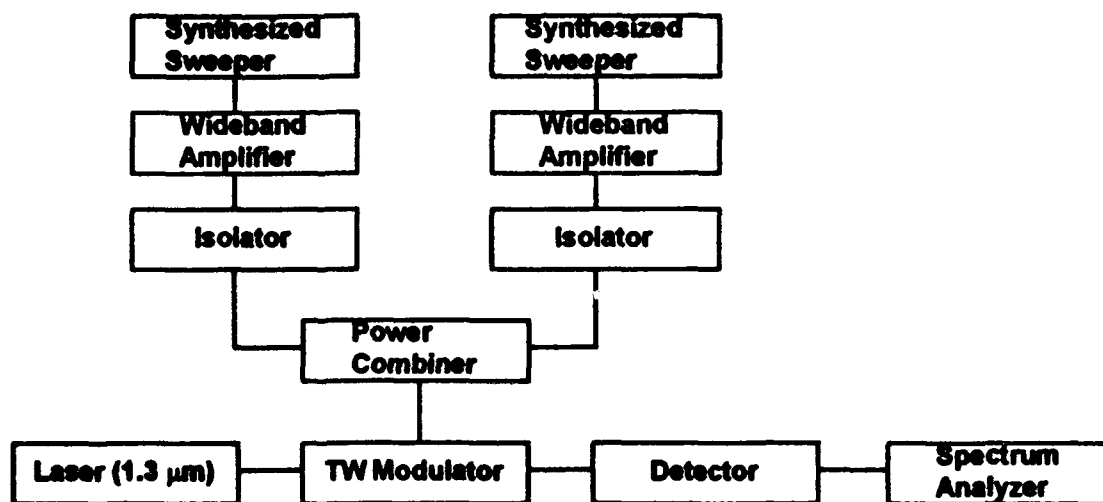


Fig. 1

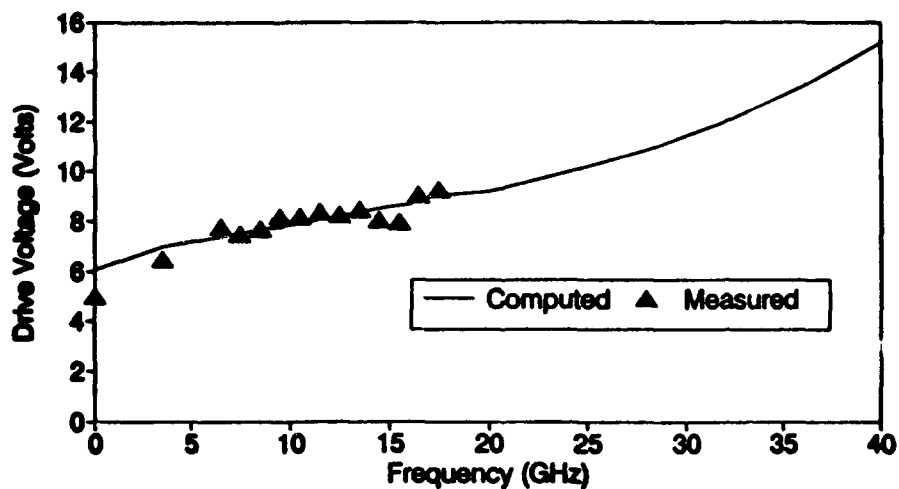


Fig. 2

Evaluation of Electrical Losses in TW LiNbO₃ Modulators

G.K. Gopalakrishnan* and W.K. Burns†

*Maryland Advanced Development Laboratory, Greenbelt, MD 20770

†Naval Research Laboratory, Code 5671, Washington D.C. 20375-5000

Recently, traveling wave (TW) LiNbO₃ optical modulators with performance extending well into the millimeter-wave frequency spectrum have been fabricated by engineering a near velocity match between microwave and optical signals [1,2]. In these devices, the dimensions of the coplanar waveguide (CPW) electrode in the active section are typically very narrow; for the device reported in ref. 1, the center strip width (w) = 8 μm and gap width (g) = 15 μm . To facilitate external microwave and optical access to the modulator, CPW tapers and bends are designed in conjunction with the active section of the device. Previously, high frequency operation of these devices, in the velocity matched condition, has been believed to be limited by only the conductor loss (\sqrt{f} loss) of the electrode. However, other losses such as dielectric loss (proportional to f) that stems from the loss tangent of the material and radiative loss that stems from radiation from discontinuities such as tapers and bends may also become significant at high-frequencies. Since tapers and bends are integral components of the device, losses that occur in these sections affect the overall device response. We investigate such losses in a TW modulator [1] and assign independent loss coefficients to different sections of the device.

As shown in the inset of fig. 2, a typical TW modulator consists of an input/output section (whose dimensions match those of a microwave connector), a pair of tapers, a pair of bends and the active section. To evaluate losses in each section of the device, we fabricated a set of test structures whose layouts are shown in fig 1. These structures were fabricated on z-cut LiNbO₃ with the following parameters: substrate thickness = 0.2 mm, SiO₂ buffer layer thickness = 0.9 μm and gold electrode thickness = 15 μm . For the input/output section corresponding to fig. 1(a), the dimensions of the CPW line were: $w = 305 \mu\text{m}$ and $g = 305 \mu\text{m}$. Since this section does not contain any discontinuities that cause radiation, the total loss was assumed to consist of contributions from conductor and dielectric losses. The taper in our device (fig. 1(b)) was a linear taper whose dimensions at one end matched those of the input/output section while at the other end it matched the waveguide section. To allow for radiation in this section (in addition to conductor and dielectric losses) we tried to fit a polynomial to the total response, and observed that coefficients of f^2 and other higher order terms were negligibly small; the same was also true for the structure with bends shown in fig. 1(d) (radius of bend = 100 μm). However, in both cases the \sqrt{f} and f terms provided an excellent fit to the data. Using the four test structures of fig. 1, we obtained loss coefficients (\sqrt{f} and f) of each section by a scheme of sequential de-embedding. These loss coefficients are given in Table 1. Although the taper and bends are unique to our design and their loss coefficients may not strictly be distributed entities, we still define them per unit length to facilitate comparison of losses in different sections. The loss coefficient proportional to f is similar in each section except for the bends, where it is significantly larger, due to either radiation or mode mismatch. Loss tangents (at 40 GHz) obtained from these measurements are given for the input and waveguide sections. These numbers compare well with the loss tangent of bare LiNbO₃ at 40 GHz (.0016) [3]. In fig. 2 we show the individual $\sqrt{f} + f$ loss contributions for each section and the resulting total device loss which fits well with the measured data from an experimental modulator.

In conclusion, we have evaluated electrical losses in TW modulators and have shown that dielectric and bend losses proportional to f must be accounted for in the total device loss at high frequencies. The loss coefficients obtained may be used in conjunction with microwave-optical index mismatch information to completely specify broadband optical performance of TW modulators.

REFERENCES

- [1] G.K. Gopalakrishnan et al., Electron. Lett., 1992, 28, pp. 826-827.
- [2] D.W. Dolfi and T.R. Ranganath, Electron. Lett., 1992, 28, pp. 1197-1198.

[3] W.M. Robertson et al., Electron. Lett., 1991, 27, pp. 175-176.

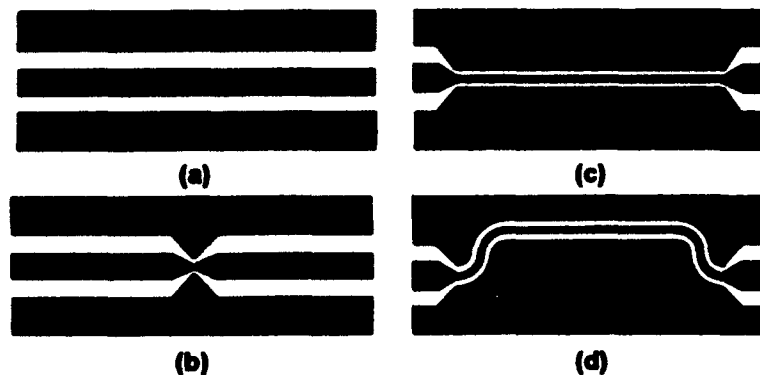


Fig. 1

Section (Length)	\sqrt{f} Loss dB/ $\sqrt{\text{GHz cm}}$	f Loss dB/GHz cm	Loss Tgt. @ 40 GHz
Input (.9 mm)	.133	.0134	.002
Taper (2.1 mm)	.28	.019	-
Bends (.16mm)	.375	.95	-
Waveguide (24 mm)	.585	.0117	.0067

Table 1

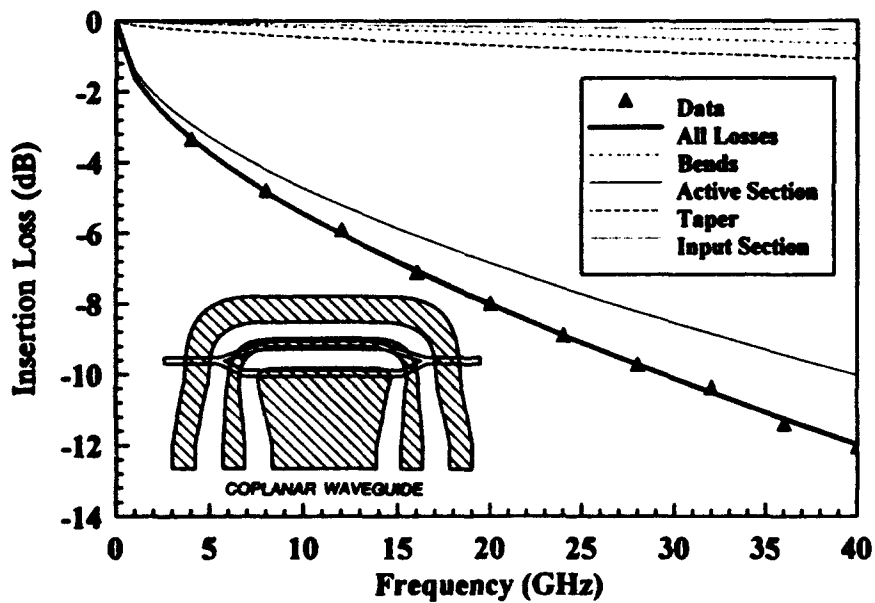


Fig. 2

**Velocity Matched Resonant Slow-Wave Structure
for Optical Modulator**

Mark Yu and Anand Gopinath

**Department of Electrical Engineering
University of Minnesota
Minneapolis, MN 55455
Tel: (612)625-3841**

A slow-wave resonant electrode structure for the phase velocity matching in optical modulators is proposed. This technique is scalable to millimeter-wave frequencies.

I. Introduction

It is well known that efficiency and bandwidth of traveling-wave electro-optic modulators are limited by the mismatch of the optical and electrical phase velocities. The phase difference between two waves caused by this velocity mismatch requires a short interaction length, which results in an increase of the RF drive level requirement for adequate modulation. To lower the drive voltage and power, a long device length is required. However, without velocity matching, the run-out limits the device length. Most broad-band modulators reported to date [1-2] still require high drive power.

Any phase velocity mismatch causes the optical phase front to walk-off from the electrical phase front. The optical lag will vary sinusoidally with this walk-off and modulation will cancel out altogether if the mismatch is severe enough or if the interaction length is too long. Since the optical phase velocity is constrained by the material indices and the waveguide conditions, small changes in optical phase velocity could result in large changes in the optical propagation characteristics or in the electrooptic interaction. As a result, only the electrical phase velocity can be adjusted for velocity-matching. Since the electrical phase velocity in III-V semiconductor structures is larger than the optical phase velocity, we, therefore, design a slow wave electrode structure to reduce this difference.

A new state-of-the-art design of slow wave periodic structure is proposed. For the planar structure, the proposed velocity-matched electrode configuration employs a coplanar waveguide (CPW) design as shown in Fig. 1, which consists of the usual center conductor segmented into a series of Z-shaped cascaded resonators. A similar electrode design may be used for III-V semiconductor ridge guides. With this design, the effective quality factor, Q , of the resonant structure will result in the decrease of driving voltage. Thus, the power requirement can be reduced by a factor of Q^2 for a bandwidth of 10%. In addition, the bandwidth design can be improved by using Chebyshev design for coupled-line filters.

The emphasis in this paper is to demonstrate that the reduction of RF phase velocity can be achieved. Thus, we will not discuss any further the propagation losses in this structure.

II. Analysis and Simulations

The general physical configuration of the coupled-line bandpass filter, which forms the bases of the proposed structure, is illustrated in Fig. 2a. Consider the case of a parallel coupled directional coupler, for a V_0 voltage incident at port 1 and a matched load terminating port 4, the voltage at ports 2 and 3 are given by [3]. V_2 and V_3 may be regarded as the voltages of the waves incident onto the open-circuit terminations at their respective port. Now, V_2 and V_3 are reflected from the open circuits with a phase change of 0° and may be regarded as an incident waves at port 2 and port 3. Because of the matched termination at port 4, V_4 does not produce a reflected wave at this port. Thus, the outward voltages gives

$$V_1 = \frac{V_0^2}{\Delta} (1 - k_{12} - k_{12}^2 \sin^2 \theta) \quad (1a)$$

$$V_4 = \frac{V_0^2}{\Delta} (2jk_{12} \sqrt{1 - k_{12}^2} \sin \theta) \quad (1b)$$

where

$$\Delta = ((1 - k_{12}^2) \cos^2 \theta - \sin^2 \theta) + j\sqrt{1 - k_{12}^2} \sin 2\theta \quad (1c)$$

where $\theta = 2\pi l / \lambda$, and k_{12} is the coupling coefficient. For the special case of $l = \lambda/4$, (1b) gives the phase delay of -90° . When θ is small, $\sin\theta \approx \theta$ and $\cos\theta \approx 1$, voltage at port 4 is j times a constant, or the outward phase response at port 4 is advanced by 90° .

We have performed simulations of coupled-line structure with extensions, as shown in Fig. 2b, which constitutes a component of resonant structure, based on the CAD program Touchstone. The resonators were λ at 4.4 GHz, and the phase velocities are plotted for various overlap length l . v_0 is the phase velocity of RF signal traveling through a line with the same length as coupled-line with extensions. We note that the phase velocity leads to phase of up to 90° for overlap length $l \leq \lambda/4$, which is due to the strong lumped capacitive coupling. As we increase the overlap length, the distributed capacitive coupling starts taking over until the overlap reaches to $\lambda/4$, at which length, the phase delay is 90° and thus the velocity ratio of v/v_0 is unity over this coupled length. With further increase in overlap, the phase delay increases and thus the velocity ratio over the coupled length becomes less than one, and when the overlap reaches to $\lambda/2$ where the additional phase delay over the coupling length lags by 90° . If this distributed capacitive coupling can be changed into inductive coupling by bridging the gap, then the phase velocity reduction would be possible with such coupling even in the first $\lambda/4$ overlap region. In Fig. 3, we have used coupling coefficient $k_{12} = 0.36$. Simulation results by using Touchstone simulation program are in good agreement with Eg. 1b. Because the coupling is both capacitive and inductive and existing theory is not capable of analyzing this structure, we have, therefore, used this simulation program for the remainder of the study.

The proposed resonant slow-wave structure, as shown in Fig. 1, is formed by cascading a series of Z-shaped resonators with length λ , and each resonator is equally spaced by a gap g , and is connected by a narrow strip line over the overlap section to allow for dc biasing of the structure. A mixed lumped-distributed equivalent circuit model, as shown in Fig. 4, is developed by taking into account all possible coupling effect. The inductance LL is accounted for the continuity of traveling wave across within the resonator. The value is estimated to be $LL = 0.6nH$. A gap discontinuity, g , between two adjacent resonators is introduced

to provide a dominant capacitive reactance. Its equivalent circuit is a π -network of three capacitances. The dc inductive strip line is represented by a single inductance, $L_{dc}=1.6\text{nH}$. The value is optimized over a 1 GHz band with other calculated parameters to match the center frequency at 4.4 GHz using the EEsof Touchstone program.

III. Experimental Results

Since the propagation loss is neglected, only the phase de-embedding for characterizing the device-under-test is considered in this paper. The test fixture, made of RT/duroid 5880, $\epsilon_r=2.2$, with the CPW through line on 0.06-in thick RT/duroid 6002 substrate, $\epsilon_r=2.94$, was used for measurements. A CPW through line consisting of a uniform 50- Ω CPW line with the corresponding aspect ratio of 15/17 is terminated at both ends by a 4.5-cm mobile delay-line launcher which is excited by a SMA connector. The pair of delay-line launcher and the coaxial connectors form a part of the test fixture and are phase de-embedded for all the cases measured.

Fig. 5 shows both the experimental results for three different number of cascades and the simulation results based on the equivalent circuit model. We can see that the experimental and simulation results for the phase velocity ratio from 0.7 to 0.8 agree very well in the overlap length from 0.1λ to 0.25λ . This result suggest that for the GaAs/AlGaAs waveguide, the optical phase velocity is 2.65/3.61 times smaller than RF phase velocity, with the proposed electrode design the RF phase velocity can be reduced by simply adjusting the resonator spacing.

IV. Conclusion

We have given a description of the design of a resonant slow-wave electrode design. Although the design of the structure used in the experiment is at 4.4 GHz, it can be easily scaled to higher frequencies. With the current design, the bandwidth can be increased by means of the usual coupled-line resonator Chebyshev filter design up to 50%. The experimental measurements show that phase velocity mismatch between RF signal and optical signal can be reduced by simply adjusting the resonator spacing. For the case of GaAs/AlGaAs waveguide, the overlap of about 0.2λ would provide the necessary velocity match.

V. References

1. R. C. Alferness, S. K. Korotky, and E. A. J. Marcatili, "Velocity-matching techniques for integrated optic traveling wave switch/modulators," *IEEE J. Quantum Electron.*, Vol. QE-20, pp. 301-309, 1984.
2. T. Yoneyama, K. Niinuma, and S. Kanno, "Velocity-matched LiNbO₃ waveguide optical modulator using inverted slot line," *IEEE Microwave Guided Wave Lett.*, Vol. 1, NO. 8, pp.192-194.
3. E. M. T. Jones and J. T. Bolljahn, "Coupled-strip-transmission-line filters and directional coupler," *IRE Transactions on Microwave Theory and Techniques*, Vol. MTT-4, pp.75-81, April, 1956.

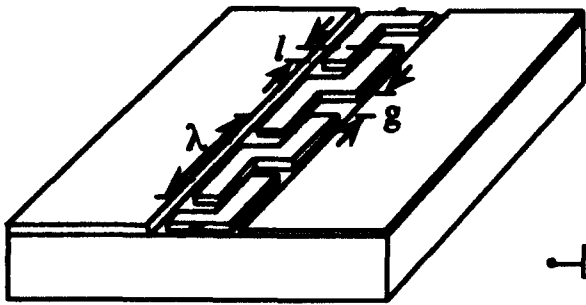


Figure 1 Proposed Z-shaped cascaded resonant slow-wave structure

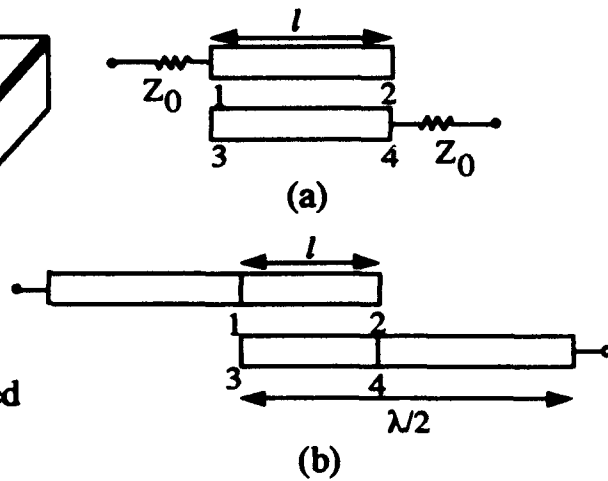


Figure 2 (a) A coupled-line bandpass filter with variable length l . (b) with addition of delay line at input and output ports.

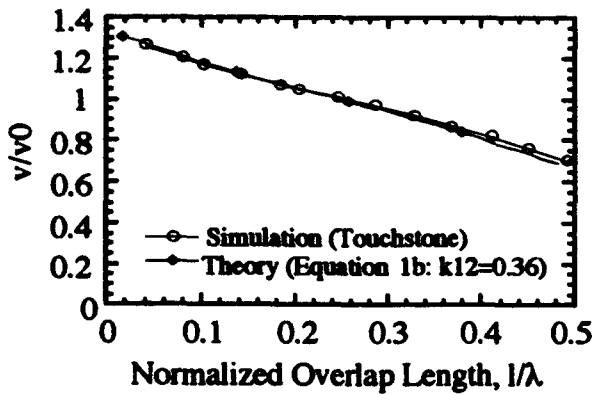


Figure 3 Velocity reduction ratio as a function of normalized overlap length

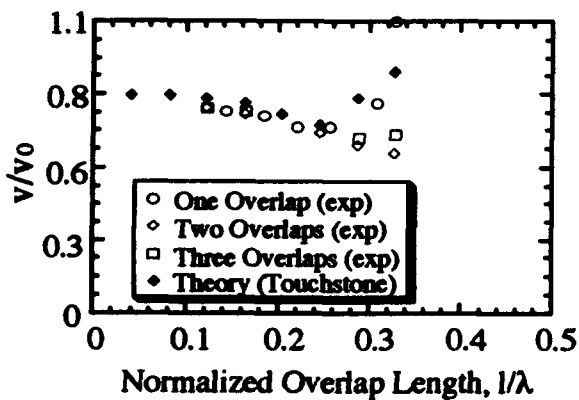


Figure 5 Velocity reduction ratio vs. normalized overlap length for both theoretical and experimental results

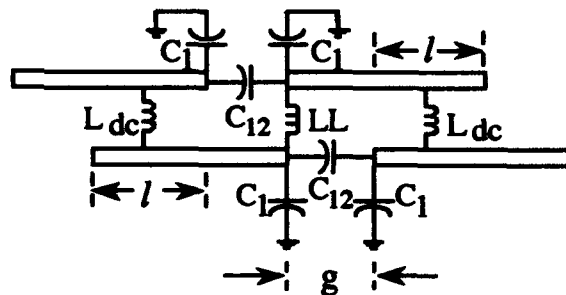


Figure 4 A lumped-distributed equivalent circuit model of slow wave structure

Beam Propagation Methods

ITul 1:30pm-3:30pm
Mesquite C/D

David O. Yevick, *President*
Queens University

Transparent boundary conditions using Green's function technique for beam propagation methods

G. Hugh Song

Bellcore, 331 Newman Springs Road, Red Bank, New Jersey 07701-7040, (908)758-3310

Introduction: The beam propagation method (BPM) has proven to be a powerful simulation technique in integrated photonics. The method is basically a numerical solution procedure for the paraxial wave equation or the Schrödinger equation,¹ as time-harmonic electromagnetic (optical) waves are approximately described by the paraxial wave equation.²

In practical applications of BPM we often encounter an infinite medium which cannot be handled because of limited computer resources. A few methods were previously introduced^{3, 4, 5} to find the boundary condition simulating the transparent boundary for the BPM based on finite-difference method. After testing these methods for two-dimensional (2-D) problems, we have observed that Hadley's modified method referred to as "TBC" in Ref. 5 is superior to the method by Accornero et al.³ for certain problems. However, for other problems, both the modified and the "simpler (STBC)" methods of Hadley often give solutions with anomalous reflection, while the one by Accornero et al. still gives solutions with no such reflections. We have also found that the "TBC" of Hadley is not robust enough to be used on all kinds of problems. In this paper, we introduce a new technique which employs Green's function method which do not have such problems and which is more accurate than the method by Accornero et al. In the case of 2-D problems, this technique yields three closed-form formulae, one of which generalizes the method of Accornero et al.³

Theory: We consider the $+z$ -propagating Green's function in an semiinfinite region Ω of x and x' outside of the BPM computational window on $0 \leq z' < z$.

$$(\partial/\partial z - D\nabla^2 + V)G(\mathbf{r}|\mathbf{r}') = \delta(x-x')\delta(z-z'),$$

$$V(\mathbf{r}) \equiv Dk_0^2 [n_r^2 - n^2(\mathbf{r})],$$

where $D \equiv i/2n_r k_0$. We integrate by parts $G(\partial/\partial z' - D\nabla'^2 + V)\psi - \psi(\partial/\partial z' - D\nabla'^2 + V)G$, which vanishes over Ω and $0 \leq z' \leq z - \epsilon$ with ϵ being an arbitrary, small, positive number. By this technique, we use three kinds of Green's functions with different boundary conditions to obtain the following three formulae for the solution to the potential-less paraxial equation at position (x, z) outside our BPM computational window where the medium is homogeneous with refractive index n_r .

$$\psi(x, z) = I_a \equiv \int_0^z \psi(x_b, z') \frac{|x - x_b|}{2\sqrt{\pi D}(z - z')^{3/2}} \times \exp\left[-\frac{(x - x_b)^2}{4D(z - z')}\right] dz', \quad (1)$$

$$\psi(x, z) = I_c \equiv \mp \int_0^z \frac{\partial \psi}{\partial x}(x_b, z') \sqrt{\frac{D}{\pi(z - z')}} \times \exp\left[-\frac{(x - x_b)^2}{4D(z - z')}\right] dz', \quad (2)$$

$$\psi(x, z) = (I_a + I_c)/2, \quad (3)$$

where ' \mp ' sign is for $x \geq x_b$.

Example 1: The plot of Fig. 1 is obtained by simulating a similar situation which was taken originally in Ref. 4. Two Gaussian beams centered initially at $x = 25 \mu\text{m}$ and $82.5 \mu\text{m}$ are launched with tilt 11.5° and 5.7° , respectively, on a BPM window of $0 \mu\text{m} < x < 100 \mu\text{m}$. Snapshots of the two beams at $30 \mu\text{m}$ intervals are shown in Fig. 1 of Ref. 4. Note that the method of Eq. 2 gives 'N.1' and 'N.2' showing roughly the same level of reflectivities for all lateral sampling sizes of Δx . We have found that it is because the

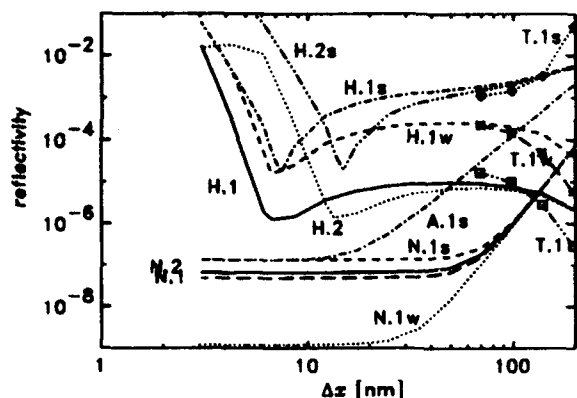


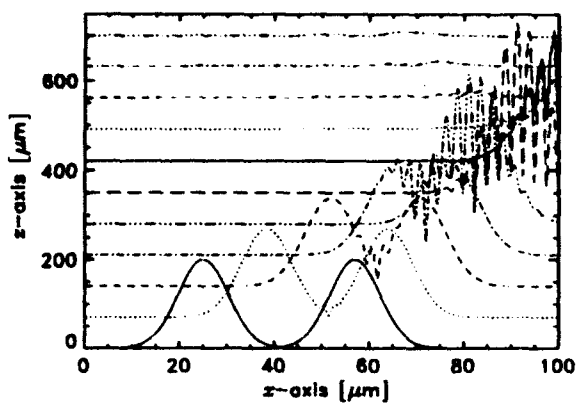
Fig. 1. Reflectivities with two Gaussian beams with respect to lateral sampling size Δz for different boundary condition schemes. The portion of energy still remained in the BPM computational window is defined as 'reflectivity.' Letters H, N, A, and T represent "STBC", Eq. (2), Accornero et al., and "TBC", respectively. Numerals '1' and '2' represent the step size $\Delta z = 0.1 \mu\text{m}$ and $0.2 \mu\text{m}$ of BPM, respectively. Curves H.1, H.2, N.1, N.2, H.1w, N.1w, T.1, and T.1w are obtained by launching two beams with tilts 11.5° and 5.7° , centered initially at $x = 25 \mu\text{m}$ and $x = 82.5 \mu\text{m}$, respectively. Curves H.1, H.2, N.1, N.2, H.1s, H.2s, N.1s, and N.2s are obtained with simulations on $0 \mu\text{m} < x < 100 \mu\text{m}$, while curves with postfix 'w' (H.1w, N.1w, and T.1w) are obtained with on $0 \mu\text{m} < x < 110 \mu\text{m}$. Curves with the postfix 's' are obtained with the second beam centered at $x = 57 \mu\text{m}$ instead of $x = 82.5 \mu\text{m}$. Curves T.2, T.2w, and T.2s are not plotted as they are almost identical to T.1, T.1w, and T.1s, respectively.

boundary at $x = 100 \mu\text{m}$ has not been taken at enough distance from the beam centered initially at $x = 82.5 \mu\text{m}$. In fact, this kind of cases require a term which we have neglected in the derivation of Eqs. (1)–(3) under the assumption that no initial field is present outside of the BPM window. This assertion can be confirmed by curve 'N.1w,' in which the postfix 'w' signifies that the curves have been obtained with the BPM window increased to $0 \mu\text{m} < x < 110 \mu\text{m}$ so that the tails of the Gaussian beam outside of the BPM window are initially negligible. Note that curve 'H.1w,' on the other hand, has risen by an order of magnitude. This is because that the tails of the two beams begin to meet as they pass through the

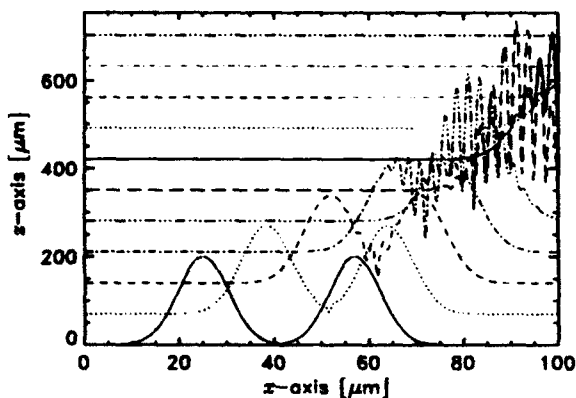
boundary, causing trouble in Hadley's methods. To confirm this observation, we have moved the center of the second beam from $x = 82.5 \mu\text{m}$ to $x = 57 \mu\text{m}$, so that the two beams interfere with each other strongly when they are hitting the boundary. Interestingly, Hadley's methods give curves 'H.1s,' 'H.2s,' and 'T.1s' showing two orders of magnitude higher reflectivities than their counterparts, 'H.1,' 'H.2,' and 'T.1,' while method of Eq. (2) gives curve 'N.1s' which stays roughly at the same level as 'N.1.' The reason for increased reflectivity levels in curves 'H.1s,' 'H.2s,' and 'T.1s' can be explained as follows: When the two beams meet around the boundary at $x \sim 100 \mu\text{m}$, they interfere each other creating a spatial oscillation of local energy in the lateral direction. Once the spatial energy is moved out of the BPM boundary, the approximate algorithms of Hadley do not give back its energy inwards. This results in a considerable increase of energy reflection in the solution whose magnitude is shown in Fig. 2(a), while our scheme shows no such appreciable reflection as in Fig. 2(b). In addition to the problems involved with interference, the "TBC" method in Ref. 5 sometimes fails when the $\text{Re } k_x$ evaluated according to Eqs. (15)–(19) in Ref. 5 becomes inaccurate between longitudinal steps or becomes even greater than $n_r k_0$, as we decrease Δx . All three curves showed unacceptably high reflectivities when Δx goes down below 50 nm .

From this first example, we can conclude that the method based on Green's function technique is superior to all other methods. The spurious reflection always decreases with smaller sampling sizes, while Hadley's "STBC" method seemingly has a certain range of lateral sampling size to work. When the beam is highly structured, "STBC" suffers to a significant degree. We have also found that the method of Accornero et al. (e.g., curve 'A.1s') gives 1–2 orders of magnitude higher reflectivities than the methods using Eqs. (1)–(2) as the former suffers from lateral discretization errors.

Example 2: The second example is devised



(a)



(b)

Fig. 2. Plots of waveforms at every $\sim 75 \mu\text{m}$ using two different boundary condition algorithms with $\Delta z = 97.7 \text{ nm}$ and $\Delta z = 0.2 \mu\text{m}$. (a) Using Hadley's "STBC" method. (b) Using Eq. (2).

as in Fig. 3 to check the amount of error due to approximation which is taken in the "STBC" method of Hadley. It is a tapered planar waveguide with staircase-like layers. This taper structure is designed to transfer the fundamental-mode input of wavelength $1.523 \mu\text{m}$ from the top to the fundamental-mode output to the bottom between a semiconductor waveguide component and a standard single-mode fiber. For this example structure, it is found that the "STBC" method of Hadley gives a solution with anomalous reflections, while that of Accornero et al.

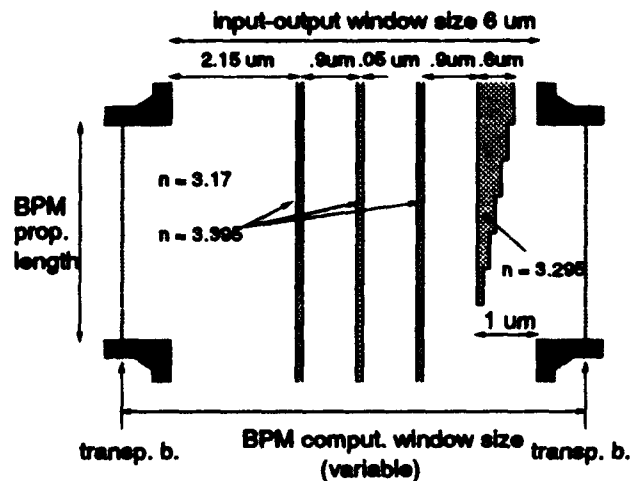
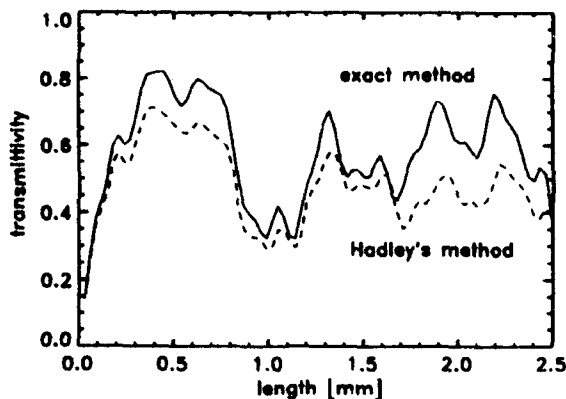


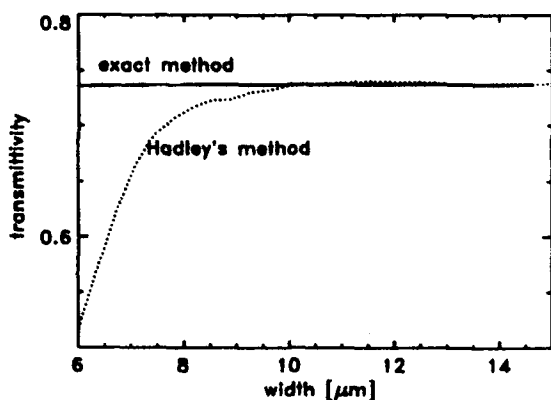
Fig. 3. A refractive index profile devised to show the difference between the "STBC" method of Hadley and the method of Green's function.

and ours do not show such reflection in the solution plots. The adaptive method of Hadley, the "TBC"⁵ does not work at all since the parameter $\text{Re } k_x$ evaluated according to Eqs. (15)–(19) in Ref. 5 is often found to be greater than $k \equiv n_T k_0$. Artificial metallic walls are included for the sake of error analysis. For the plot in Fig. 4(a), it is supposed that the BPM window size is set at $6 \mu\text{m}$ while the taper length is varied. By calculating the result with overlap integral, the efficiency of energy transmittance is plotted for the two methods—the "STBC" of Hadley and the Green's function method of Eq. (2). It is observed that the two results are quite different.

To check the validity and convergence of the solution, we fixed the taper length at 1.9 mm , while increasing the BPM window from $6 \mu\text{m}$ to $15 \mu\text{m}$. The resulting overlap integrals are plotted in Fig. 4(b). We can see clearly that the results from the Green's function method do not vary more than $\pm 0.1 \%$. On the contrary, Hadley's "STBC" method does not approach this level of accuracy until the width is increased to $\sim 13 \mu\text{m}$. It is observed that any interference of the propagated waves in the vicinity of boundaries causes a significant increase in the reflection error. To reduce this error, the simu-



(a)



(b)

Fig. 4. Quantified difference measured as an overlap integral with the fundamental mode at the output end of the taper assuming that a fundamental mode input is launched. (a) Result with a varying taper length at a fixed BPM window size of $6 \mu\text{m}$. (b) Result with a varying BPM window size at a fixed taper length 1.9 mm .

lation window has to be increased, which offsets the original purpose of the transparent boundary condition. However, it should be noted that the exact method requires extra computation time for the integration along the boundary. The amount of this overhead depends on the computational accuracy requirement and the aspect ratio of the problem size in terms of numbers of lateral and longitudinal sampling points. We expect that an efficient integration algorithm can reduce this overhead significantly.

3-D Problems: Use of Green's function gives an intuitive idea about generalizing the transparent boundary conditions into the 3-D FD-BPM problems under the paraxial approximation.

$$\psi(\mathbf{r}) = - \int_0^z \int_{\partial\Omega} \psi(\rho'_b, z') D \nabla G(\mathbf{r}|\rho'_b, z') \cdot \hat{n} dl'_b dz' + \int_0^z \int_{\partial\Omega} G(\mathbf{r}|\rho'_b, z') D \nabla \psi(\rho'_b, z') \cdot \hat{n} dl'_b dz',$$

$$G(\mathbf{r}|\rho', z') \equiv \frac{H(z-z')}{4\pi D(z-z')} \exp\left[-\frac{|\rho-\rho'|^2}{4D(z-z')}\right],$$

where $\int_{\partial\Omega} dl'_b$ represents integration along the boundary perimeter, and \hat{n} represents the direction normal to the boundary surface. However, computational efficiency of the method becomes a question due to limited computer resources.

Conclusion: Exact formulae which give boundary conditions simulating an infinite medium in FD-BPM are found via a Green's function technique, and are demonstrated with examples. We have found that the Green's function method is the most robust for the most general problems, especially in 2-D applications. However, there is some computational overhead which can be overcome in 2-D applications. Although the local approximate method developed by Hadley (referred to as "STBC"⁵) is found to be useful, it does not give a correct solution when any interference of waves in the vicinity of boundaries is present. We have also found that the "TBC" method of Hadley sometimes fails even when a modest level of scattering is present at the boundary.

REFERENCES

1. A. Goldberg, H. M. Schey, and J. L. Schwartz, *Amer. J. Phys.* **35**, 177 (1967).
2. M. D. Feit and J. A. Fleck, Jr., *Appl. Opt.* **18**, 2843 (1979).
3. R. Accornero, M. A. Artiglia, G. Coppa, P. Di Vita, G. Lapenta, M. Potenza, and P. Ravetto, *Electron. Lett.* **26**, 1959 (1990).
4. G. R. Hadley, *Opt. Lett.* **16**, 624 (1991).
5. G. R. Hadley, *IEEE J. Quantum Electron.* **28**, 363 (1992).

Investigation of the inherent errors in the Lanczos propagation method

M. D. Feit, J. A. Fleck, Jr., and R. P. Ratowsky
Lawrence Livermore National Laboratory, Livermore, California 94550

A propagation scheme for solving the scalar Helmholtz wave equation, based on matrix diagonalization in a low-dimensional Lanczos space has been previously proposed.¹ We review the scheme briefly here.

After factoring the carrier $\exp(-ikz)$ from the electric field, one can express, without loss of generality, the scalar Helmholtz equation in the form

$$-\frac{1}{2k} \frac{\partial^2 \psi}{\partial z^2} + i \frac{\partial \psi}{\partial z} = H \psi, \quad (1)$$

where ψ is the field and the operator H is given by

$$H = \frac{1}{2k} \nabla_{\perp}^2 \psi + \frac{k}{2} \left(\frac{n^2(x, y, z)}{n_0^2} - 1 \right). \quad (2)$$

If the field is expressed as an N' -dimensional vector ψ , representing the solution value of ψ at each of N' points on a computational grid, and H is a matrix representation of the operator H , in terms of some basis, say plane waves, sampled on the same grid, one can solve Eq. (1) by matrix diagonalization. The solution can be expressed as

$$\psi(z) = U^\dagger \exp\{ikz[1 + 2\beta'/k]^{1/2}\} U \psi(0), \quad (3)$$

where $\beta'_1, \beta'_2, \dots, \beta'_{N'}$ are the eigenvalues of H and $\beta' = \text{diag}[\beta'_1, \beta'_2, \dots, \beta'_{N'}] = U H U^\dagger$.

Unfortunately, application of Eq. (3) requires diagonalization of an $N' \times N'$ matrix, which greatly restricts the number of grid points that can be used. In the Lanczos method one resorts instead to a much lower dimensional space, spanned by the Krylov vectors $\psi(0), H\psi(0), \dots, H^N\psi(0)$, where $N \ll N'$. The orthonormal Lanczos vectors q_0, q_1, \dots, q_N are determined from the Krylov vectors by setting $q_0 = \psi(0)$ and using the three-term recursion relation

$$H q_n = \beta_{n-1} q_{n-1} + \alpha_n q_n + \beta_n q_{n+1}, \quad (4)$$

where $\beta_{-1} = 0$, and $\langle q_n | H | q_n \rangle = \alpha_n$, $\langle q_{n-1} | H | q_n \rangle = \langle q_n | H | q_{n-1} \rangle = \beta_{n-1}$, are the matrix elements of H in the $N+1$ -dimensional Lanczos subspace. The matrix representation of H in the Lanczos subspace, which we call H_N , is a symmetric tri-diagonal matrix that can be diagonalized to give the solution to Eq. (2) in the form

$$\psi(\Delta z) = U_N^\dagger \exp\{ik\Delta z[1 - (1 + 2\beta'_N/k)^{1/2}]\} U_N \psi(0), \quad (5)$$

where, in analogy to Eq. (3), $\beta'_N = \text{diag}\{\beta'_0, \beta'_1, \dots, \beta'_N\} = U_N H_N U_N^\dagger$.

If one expands the square root in Eq. (5) in a linear Taylor series, one obtains the following solution to the Fresnel or Paraxial wave equation

$$\psi(\Delta z) = U^\dagger \exp\{-i\beta' z\} U \psi(0) \quad (6)$$

The Lanczos propagation scheme, as summarized by Eqs. (4) and (5), has been shown to give exceedingly accurate results for propagation in quadratic refractive index waveguides, as determined by comparing numerical and analytic results.¹ It has been reported in Ref.2 on the other hand, that propagation in a rib-waveguide Y-junction device, calculated using Eqs. (4) and (5), shows erratic numerical convergence properties, with respect to both Lanczos order $N+1$ and propagation step Δz . This

behavior makes it difficult to judge the accuracy of the Lanczos propagation scheme applied with the square root operator. Application with the paraxial operator, as in Eq. (6), on the other hand, showed smooth convergence properties.

It is difficult to say whether the numerical difficulties involved with the square root operator are due to numerical differentiation errors inherent in rib index profiles or to the basic Lanczos algorithm itself. Therefore we have undertaken to study the inherent accuracy of the Lanczos scheme without involving numerical differentiation of any kind. To this end we consider propagation over a single step of length Δz in free space of a one-dimensional Gaussian beam. We take as the initial field

$$\psi(x,0) = \exp(-x^2 / 2\sigma^2) / \sqrt{\sigma\pi^{1/4}}. \quad (7)$$

For free space propagation $H = (1/2k)\partial^2 / \partial x^2$. After applying Eqs.(7) with the Lanczos recursion relation (4), one obtains the following analytic expressions for the Lanczos vectors and the Lanczos coefficients

$$q_n = N_n H_n(x/\sigma), \alpha_n = -\frac{1}{k\sigma^2}(n+1/4), \beta_n = \frac{1}{4k\sigma^2} \sqrt{(2n+1)(2n+2)}, \quad (8)$$

where N_n is a normalization coefficient. By using Eqs.(8) in connection with Eqs. (5) or (6), one can generate Lanczos solutions to either the Helmholtz or Fresnel equations without numerical differentiation. Numerical errors for these Lanczos solutions are determined by comparing with numerical evaluations of

$$\psi(\Delta z) = \int dk_x \exp\left\{ik\Delta z \left[1 - (1 - k_x^2/k^2)^{1/2}\right]\right\} \tilde{\psi}(0), \quad (9a)$$

$$\psi(\Delta z) = \int dk_x \exp\left\{i\frac{k_x^2}{2k^2} \Delta z\right\} \tilde{\psi}(0), \quad (9b)$$

respectively, where $\tilde{\psi}(0)$ is the Fourier transform of $\psi(0)$.

Results are shown in Figs. 1-4 for various propagation beam angles, where the beam angle is measured by the rms average for the initial Gaussian, $\theta_{rms} = \sin^{-1}(1/k\sigma)$. Figure 1 shows both amplitude and phase error for the square root or Helmholtz Lanczos calculation as a function of transverse position, measured in units of σ , for the angle $\theta = 9.6^\circ$, which is approximately the limit for accuracy of the paraxial equation. The error, which is extremely small, exhibits no systematic characteristics. Figure 2 shows amplitude error at the origin as a function of propagation step, measured in units of the Rayleigh range, $k\sigma^2$. Both Helmholtz and Fresnel calculations exhibit improved accuracy for increasing Lanczos order and decreasing propagation step. Accuracy for Helmholtz Lanczos is very good, but error for Fresnel Lanczos is significantly smaller for any specific order or propagation step. Figure 3 compares amplitude error at beam center for $\theta = 9.6^\circ$ and $\theta = 90^\circ$. Clearly error for the smaller angle is far smaller than for the large angle, but the accuracy can be regarded as still acceptable for the large angle. Figure 4, which compares amplitude error as a function of position on the beam for beam angles $\theta = 11.5^\circ$, $\theta = 30^\circ$, and $\theta = 90^\circ$, shows that the error function undergoes a significant shape change as one goes from small to large angles. What is interesting is that for the central portion of the beam the error for $\theta = 30^\circ$ is smaller than it is for $\theta = 90^\circ$. Thus, while the accuracy can be considered acceptable for both angles, it does not behave monotonically.

REFERENCES

1. R. Ratowsky, J. A. Fleck, Jr., and M. D. Feit, *J. Opt. Soc. Amer. A*, **9**, 265 (1992).
2. B. Hermansson, D. Yevick, W. Bardyszewski, and M. Glasner, *J. Lightwave Technol.*, **10**, 772 (1992).

Work performed under auspices of the U. S. Department of Energy by the Lawrence Livermore National Laboratory under contract No. W-7405-ENG-48.

Fig. 1: Amplitude and Phase Errors for n=9 One Step Propagation

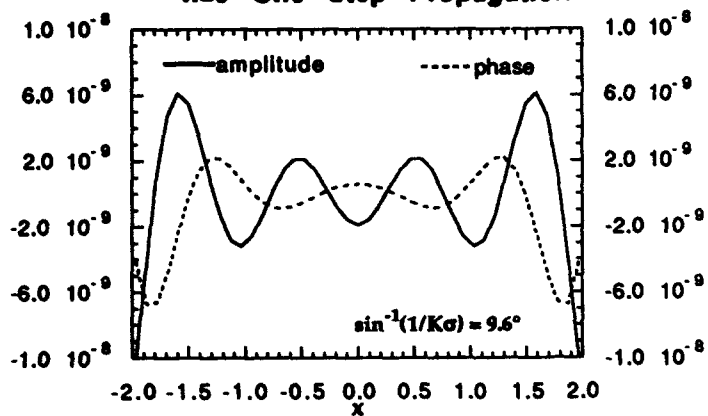


Fig 2: Lanczos Propagation of Gaussian through One Step

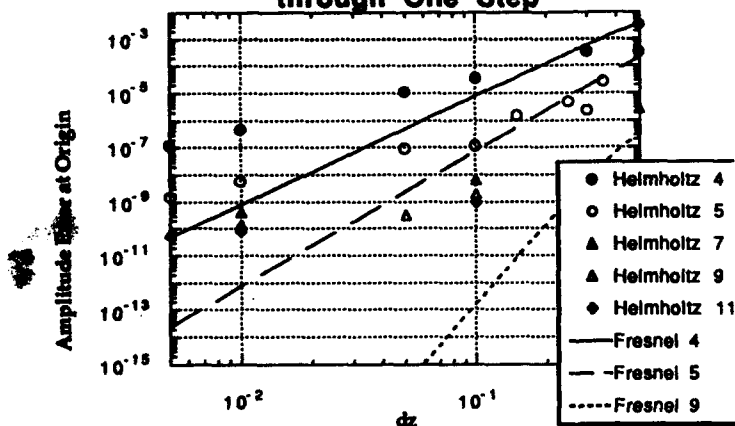


Fig. 3: One Step Propagation via n=9 Helmholtz Lanczos

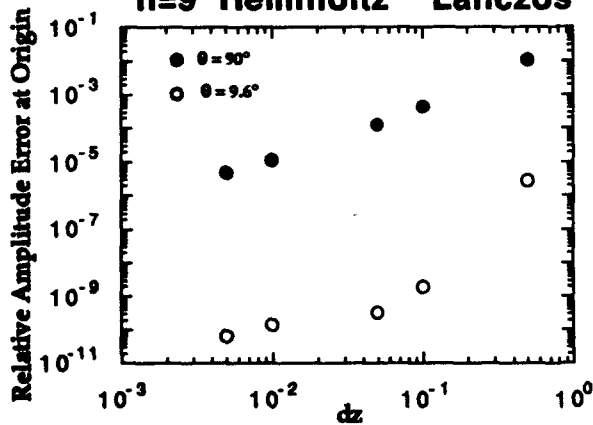
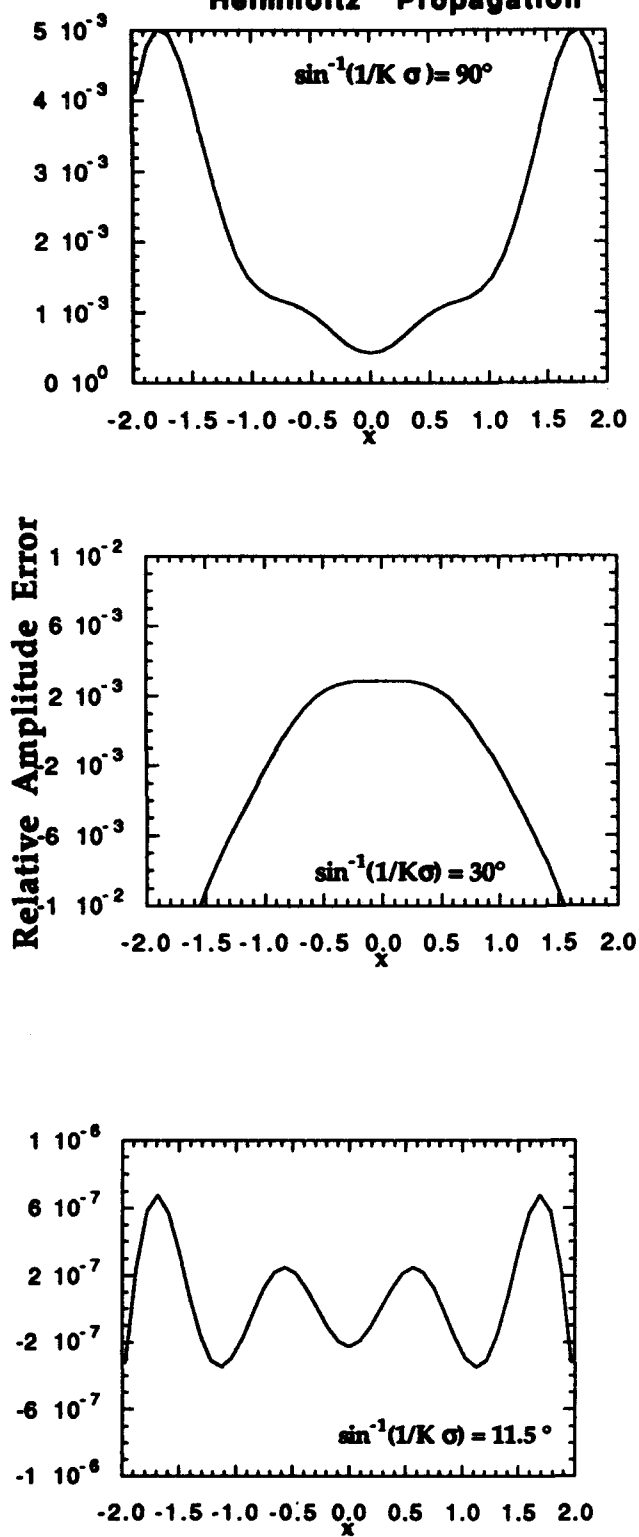


Fig. 4: Accuracy of n=9 One Step Helmholtz Propagation



Accurate Solution of the Paraxial Wave Equation Using Richardson Extrapolation

V. R. Chinni, C. R. Menyuk, and P. K. A. Wai

Department of Electrical Engineering, University of Maryland

Baltimore, MD 21228-5398

Tel. No. (410) 455-3545

It is useful to have highly accurate, yet rapid schemes for solving the paraxial wave equation in order to be able to separate inaccuracies inherent in the numerical methods from inaccuracies due to the paraxial wave approximation itself.

In this presentation, we describe a scheme based on Richardson extrapolation which allows one to efficiently and simply obtain an arbitrarily accurate solution of the paraxial wave equation. In Richardson extrapolation, numerical solutions with lesser accuracy are extrapolated to zero step size to obtain a more accurate solution. This method is often used to solve ordinary differential equations,^{1, 2} but has not been widely applied to the solution of partial differential equations. In the present context, the extrapolation technique is used to eliminate discretization errors in both the propagation and the transverse direction. Pulse propagation in a straight waveguide is analyzed using Richardson extrapolation and the mid-step Euler finite difference beam propagation method.³ This finite difference method is efficient but is also unstable. We shall show that the addition of Richardson extrapolation stabilizes the numerical scheme as well as leads to arbitrarily high accuracy. We note that this scheme works

at least as well with the implicit, finite difference beam propagation method, but we do not present those results here.

In Richardson extrapolation, the sequence of estimates obtained by varying the step size of a numerical calculation are used to extrapolate to zero step size. We may write

$$A(h, N) = S(h) + \epsilon_1(h) \frac{1}{N} + \epsilon_2(h) \frac{1}{N^2} + \dots \quad (1)$$

where $A(h, N)$ is the outcome of a numerical calculation over a very short interval h , $S(h)$ is the exact solution, and $\Delta = h/N$ is the step size used inside the interval. From Eq. (1), the leading error term can be eliminated by taking a linear combination of results calculated by using two different values of N . For example, we find

$$2A(h, 2) - A(h, 1) = S(h) + \epsilon_2(h) \left(-\frac{1}{2}\right) + \dots \quad (2)$$

This procedure can be repeated to arbitrarily high order by generating a sequence of solutions with different step size Δ . We use $h, h/2, h/4, h/8$, etc. By comparing the solutions at each stage of the extrapolation with the previous stages, we obtain an estimate of the error.

As an example, we consider light propagation in a straight waveguide with a symmetric step-index profile. The input to the waveguide is a Gaussian beam. We have done simulations extrapolated below error thresholds of 10^{-8} and 10^{-12} , where error = $\int e^2 dx$ and e is the difference between the solutions which are obtained at two consecutive levels of the Richardson extrapolation. The calculations are repeated with different values of Δx , the grid size in the transverse dimension. Then the solutions

obtained are extrapolated in x to eliminate errors due to the discretization in x . In the actual calculations, the extrapolation in the transverse dimension are not done at each step. In fact, for the simple cases we studied, it is sufficient to extrapolate at the end of the calculation.

The solutions obtained at distances of 1000, 2000, 3000 and 4000 μm in the propagation direction are extrapolated for accuracy in the transverse direction. The extrapolation is made from the solutions obtained with grid sizes of 512, 1024 and 2048 points in the transverse dimension. The order of error obtained in extrapolating the solutions in the transverse dimension at propagation distances of 1000, 2000, 3000, and 4000 μm are compiled in the following table. Note that when the accuracy threshold is set at 10^{-8} , the estimated accuracies are actually lower for 1000 μm - 3000 μm than the error threshold. That happened because the actual error was significantly below threshold in this case as determined by comparison with the case in which the accuracy threshold was 10^{-12} .

Distance μm	Accuracy limit in z direction	
	$10\text{e-}8$	$10\text{e-}12$
1000	$1.7\text{e-}11$	$9.7\text{e-}12$
2000	$2.7\text{e-}10$	$1.6\text{e-}11$
3000	$6.8\text{e-}09$	$1.2\text{e-}11$
4000	$6.3\text{e-}08$	$1.1\text{e-}11$

This work was supported by the Department of Energy. Computational work was carried out at the San Diego Supercomputer Center and the National Energy Research Supercomputing Center.

References

- [1] William H. Press, Brian P. Flannery, Saul A. Teukolsky and William T. Vetterling, *Numerical recipes in C: The art of scientific computing*, New York: Cambridge University press, 1988, pp. 582-588.
- [2] Forman S. Acton, *Numerical methods that work*, New York: Harper and Row, 1970, pp. 105-107.
- [3] David Yevick, Moses Glasner, and B. Hermansson, "Numerical studies of split-operator finite-difference alternating-direction implicit propagation techniques based on generalized Padé approximants," *Optics Letters*, vol. 17, pp. 725-727, 1992.

An Explicit Finite Difference Wide Angle Beam Propagation Method

Youngchul Chung and Nadir Dagli
Department of Electrical and Computer Engineering
University of California
Santa Barbara, CA 93106

Phone) 805-893-4847

Fax) 805-893-3262

1. Introduction

In recent years, significant improvements in the beam propagation method(BPM) have taken place mostly to be able to design and analyze various photonic integrated circuits(PIC). The efficiency of the scalar paraxial BPM has been improved through finite difference algorithms. The vector nature of the wave propagation in PICs has been studied using the paraxial vector BPM. In addition, several wide angle beam propagation algorithms have been developed using a higher order expansion of a Helmholtz propagation operator[1] with the operator splitting or using a recursive Pade formula[2][3]. All the reported algorithms are implicit schemes which require the solution of linear matrix equation[2][3] or that in combination with the fast Fourier transform[1]. The purpose of this paper is to introduce a simple explicit finite difference wide angle BPM. This wide angle propagation technique is compared with the paraxial BPM through numerical examples which are a tilted propagation in a dielectric waveguide and the diffraction of a focused gaussian beam in homogeneous media.

2. Formulation

The scalar wave equation

$$\left(\nabla_t^2 + \frac{\partial^2}{\partial z^2} + k_0^2 n^2(x,y,z)\right)E(x,y,z) = 0 \quad (1)$$

is transformed with the substitution of a solution of the form

$$E(x,y,z) = \exp(-jk_0 n_r z)E(x,y,z), \quad k_0 = 2\pi/\lambda \quad (2)$$

into the following equation for the slowing varying complex amplitude $E(x,y,z)$:

$$\left(\frac{\partial^2}{\partial z^2} - j2k_0 n_r \frac{\partial}{\partial z} + \nabla_t^2 + k_0^2(n^2(x,y,z) - n_r^2)\right)E(x,y,z) = 0 \quad (3)$$

where n_r is the reference refractive index. This amplitude Helmholtz equation can be written as a factorized form[4]

$$\left(\frac{\partial}{\partial z} - jk_0 n_r + jk_0 n_r \left(1 + \frac{\nabla_t^2 + k_0^2(n^2(x,y,z) - n_r^2)}{(k_0 n_r)^2}\right)^{1/2}\right) \left(\frac{\partial}{\partial z} - jk_0 n_r - jk_0 n_r \left(1 + \frac{\nabla_t^2 + k_0^2(n^2(x,y,z) - n_r^2)}{(k_0 n_r)^2}\right)^{1/2}\right) E(x,y,z) = 0. \quad (4)$$

It is noticed that the propagation of the forward going (positive z direction) wave is described by the following wave equation:

$$\frac{\partial E}{\partial z} = jk_0 n_r \left(1 - (1 + L)^{1/2} \right) = jk_0 n_r \left(-\frac{1}{2}L + \frac{1}{8}L^2 - \frac{3}{48}L^3 \dots \right) \quad (5)$$

where $L = \frac{\nabla_t^2 + k_0^2 (n^2(x,y,z) - n_r^2)}{(k_0 n_r)^2}$. The wave equation (5) reduces to the paraxial wave equation if the square of L and the higher order terms are ignored. In this paper, we consider the first order correction to the paraxial equation where the terms only to the L^2 term are retained in Eq. (5), which is given as

$$\frac{\partial E}{\partial z} = \frac{\nabla_t^2 + k_0^2 (n^2 - n_r^2)}{j2k_0 n_r} \left(1 - \frac{\nabla_t^2 + k_0^2 (n^2 - n_r^2)}{4(k_0 n_r)^2} \right) \quad (6)$$

The higher order terms can be included into the propagating algorithm to get the higher accuracy. If a Crank-Nicholson scheme is employed to solve Eq. (6), it can be transformed into a pentadiagonal linear matrix equation in two-dimensional case and a more complicated matrix equation in the three dimensional case. On the other hand, Eq. (6) can also be explicitly solved using a center finite difference approximation to the z -derivative, i.e. $\frac{\partial E}{\partial z} = \frac{E(z+\Delta z) - E(z-\Delta z)}{2\Delta z}$. As a demonstration of this scheme, the two-dimensional case is considered, and the resulting explicit propagating algorithm can be expressed as follows:

$$E_p(z+\Delta z) = E_p(z-\Delta z) - jaE_p(z) - jb\{E_{p+1}(z) + E_{p-1}(z)\} - jc\{E_{p+2}(z) + E_{p-2}(z)\} \quad (7)$$

where

$$a = \Delta w \left(-\frac{2}{\Delta u^2} + \left(\frac{n^2}{n_r^2} - 1 \right) + W \cdot \left[-\frac{3}{2\Delta u^4} + \left(\frac{n^2}{n_r^2} - 1 \right) \frac{1}{\Delta u^2} - \frac{1}{4} \left(\frac{n^2}{n_r^2} - 1 \right)^2 \right] \right),$$

$$b = \Delta w \left(\frac{1}{\Delta u^2} + W \cdot \left[\frac{1}{\Delta u^4} - \frac{1}{2} \left(\frac{n^2}{n_r^2} - 1 \right) \frac{1}{\Delta u^2} \right] \right), \quad \text{and } c = W \cdot \Delta w \left(-\frac{1}{4\Delta u^4} \right).$$

In the above equations, $\Delta w = k_0 n_r \Delta z$, $\Delta u = k_0 n_r \Delta x$, and $W = 1$ for the wide angle propagation and 0 for the paraxial propagation. It should be noted that the extension of this algorithm to a three-dimensional structure is straightforward. Being explicit, the algorithm represented by Eq. (7) is stable and power-conserving only when the condition $\Delta z < k_0 n_r \left(\frac{4}{\Delta x^2} + \frac{4}{(k_0 n_r)^2 \Delta x^4} \right)^{-1}$ is satisfied. For the values $n_r = 3.3$, $\lambda = 1 \mu\text{m}$, $\Delta x = 0.05 \mu\text{m}$, the propagation step size Δz should be smaller than $0.006 \mu\text{m}$. It should be noted that, even though the propagation step size should be very small for the stability and power conservation, the computational effort could be limited because only the sparse matrix multiplication is necessary at each propagation step.

3. Numerical Results and Discussions

The propagation of an eigenmode in a 30° tilted waveguide as shown in the inset of Fig. 1 is considered to check the accuracy of the present wide angle propagation scheme. At the input of the tilted waveguide, the tilted eigenmode is launched. The overlap integral of the output optical field at the output of the tilted waveguide ($z = 20 \mu\text{m}$) is calculated for various values of reference index n_r using the wide angle BPM and also using the paraxial BPM. In the calculation, the window size is $L_x = 30 \mu\text{m}$, and the number of mesh points is $M_x = 1024$, and $\Delta z = 0.0008 \mu\text{m}$. In Fig. 1, it is observed that the results obtained from the wide angle BPM ($W=1$) are insensitive to the choice of the reference index whereas those obtained from the paraxial BPM ($W=0$) are greatly dependent on the reference index, and are accurate for the proper reference index.

As a further example, a diffraction of a focused gaussian beam in a homogeneous medium (air in this example) is simulated using both the wide angle and the paraxial BPMs. The full width at e^{-2} intensity of the input gaussian beam is $0.8 \mu\text{m}$. In the calculations, $L_x = 60 \mu\text{m}$, $M_x = 1024$, and $\Delta z = 0.00025 \mu\text{m}$. The diffracted beam profiles upon $5 \mu\text{m}$ propagation are shown in Fig. 2. The results are compared with the exact solutions obtained using plane wave decomposition technique. The diffraction pattern calculated using the wide angle BPM is almost the same as the exact diffraction pattern. On the other hand, the diffraction pattern obtained using the paraxial BPM is quite different from the exact diffraction profile. This again shows the improvement over the paraxial BPM

4. Conclusions

In conclusion, we presented the simple explicit wide angle BPM, and it is shown that this new scheme is suitable for the wide angle propagation. The wide angle propagation using the first order correction is pretty good in practical cases, and it is expected that the higher accuracy can be obtained using higher order expansion terms. In addition, this algorithm can be easily extended to three-dimensional structures.

References

1. D. Yevick and M. Glasner, "Wide-Angle Beam Propagation in Semiconductor Rib Waveguides," *Opt. Lett.*, Vol. 15, pp. 174 - 176, 1990.
2. G. R. Hadley, "Wide-Angle Beam Propagation with a Transparent Boundary Condition," *Integrated Photon. Res.*, New Orleans, paper WE3-1, 1992.
3. W. P. Huang and C. L. Xu, "A Wide-Angle Vector Beam Propagation Method," *IEEE Photon. Technol. Lett.*, Vol. 4, pp. 1118 - 1120, 1992.
4. A. Wunsche, "Transition from the paraxial approximation to exact solution of the wave equation and application to Gaussian beams," *J. Opt. Soc. Am. A*, Vol. 9, pp. 765 - 774, 1992.

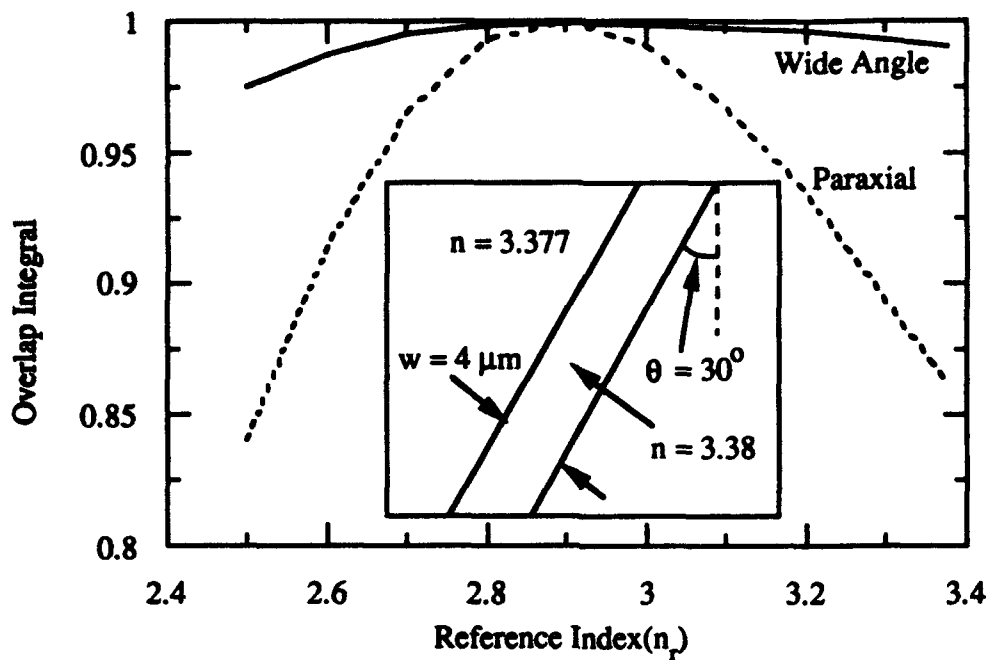


Fig. 1 The overlap integral for the different values of the reference index. The tilted eigenmode the slab waveguide is excited at the input. The overlap integral is calculated upon $20 \mu\text{m}$ propagation. The wavelength is $1.15 \mu\text{m}$.

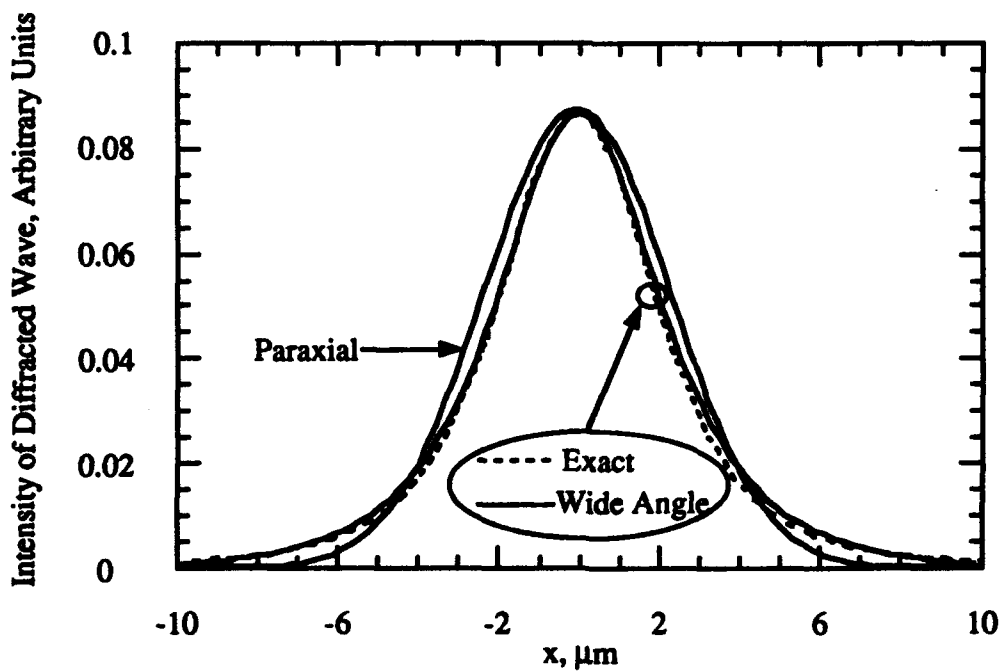


Fig. 2 The diffracted wave pattern of the focused gaussian beam after $5 \mu\text{m}$ propagation in the air. The propagation is simulated using the wide angle BPM, paraxial BPM, and exact plane wave decomposition approach. The wavelength is $1.15 \mu\text{m}$.

A Multistep Method for Wide Angle Beam Propagation

G. Ronald Hadley
Sandia National Laboratories
Albuquerque, New Mexico 87185-5800
(505) 844-4015

The beam propagation method has proven to be an extremely important tool in the simulation of guided-wave optics since its inception. Although initially limited to the study of paraxial beams, methods have been recently reported¹⁻⁴ that include approximate treatments of wide-angle propagation. However, all the methods presently available suffer from serious drawbacks. Those based upon eigenfunction expansions³ require recalculation of the eigenfunctions whenever there is a change in waveguide structure. Another method based upon an expansion of the field in terms of a set of so-called Lanczos vectors² has been found to exhibit convergence problems⁵. Several authors^{1,4,6} have employed various Pade approximations of the Helmholtz operator. In one case⁶ this approach leads to difference equations that are only first order accurate in the propagation step size. Otherwise, the lower order Pade approaches¹ are numerically attractive, but their range of validity is still somewhat limited.

In an attempt to broaden this range, a recent method⁴ utilized a sequence of higher-order Pade approximant propagation operators. Unfortunately, this increase in accuracy was obtained only at the expense of a corresponding increase in matrix bandwidth. In this paper, a simple finite difference beam propagation method is presented whereby the higher-order Pade approximant operators derived previously⁴ are expressed as factors of Pade(1,1) operators, thus resulting in a simplified multi-step algorithm. Because each component step is tridiagonal, wide-angle propagation may now be performed using well-known, efficient solution

algorithms . Furthermore, the fact that each component step is tridiagonal also allows a straightforward usage of the transparent boundary condition algorithm previously reported for paraxial propagation⁷.

A description of the present simplified method begins with the scalar propagation equation obtained using a Pade(n, n) approximation of the true Helmholtz operator⁴

$$\frac{\partial H}{\partial z} = \frac{iN}{D}H \quad (1)$$

where N and D are polynomials of degree n in the operator P , defined as

$$P \equiv k_0^2 \left(\frac{\epsilon(\bar{x})}{\epsilon_0} - \bar{n}^2 \right) + \nabla_{\perp}^2 \quad (2)$$

If Eq. (1) is discretized using standard centered differencing, we obtain

$$D(H^{m+1} - H^m) = \frac{i\Delta z}{2}N(H^m + H^{m+1}) \quad (3)$$

where the superscript indicates position along the z axis. Equation (3) may be conveniently recast in the form

$$H^{m+1} = \frac{\sum_{i=0}^n \xi_i P^i}{\sum_{i=0}^n \xi_i^* P^i} H^m \quad (4)$$

where $\xi_0 = P^0 = 1$ and the other ξ_i 's are easily determined from the coefficients of the polynomials N and D . Since a polynomial of degree n can always be factored in terms of its n roots, we may rewrite Eq. (4) as

$$H^{m+1} = \frac{(1+a_1P)(1+a_2P)\dots(1+a_nP)}{(1+a_1^*P)(1+a_2^*P)\dots(1+a_n^*P)} H^m \quad (5)$$

It is apparent from the form of Eq. (5) that an n^{th} order Pade propagator may be decomposed into an n -step algorithm for which the i^{th} partial step takes

the form

$$H^{m+\frac{i}{n}} = \frac{1+a_i P}{1+a_i^* P} H^{m+\frac{i-1}{n}} \quad (6)$$

Each such partial step is unitary and tridiagonal (block tridiagonal for propagation in 3D). These two important properties imply that the resulting algorithm is fast and unconditionally stable. The runtime for an n^{th} order propagator is obviously n times the paraxial runtime. Thus, the resulting algorithm is capable of providing extremely accurate wide-angle propagation with only a modest numerical penalty.

We now demonstrate the accuracy and utility of the above approach using a two-dimensional test case involving the propagation of an initial Gaussian beam through a uniform medium at an angle of 45 degrees with respect to the Z axis. The beam was propagated with a $0.01 \mu\text{m}$ step size on a field of width $50 \mu\text{m}$ using a three-step ($n=3$) method, and compared with a known analytic solution for true Helmholtz propagation. The resulting intensity profiles are shown in Figure 1, along with the paraxial result to provide additional perspective. The results are highly accurate, reproducing the analytic results to within 1%. More importantly, however, these results were obtained with virtually no increase in code complexity, and only a threefold increase in runtime over the paraxial method.

In conclusion, this paper describes the simplification of the Pade approximant approach to wide-angle beam propagation to a multi-step method whose component steps are each tridiagonal in form. This simplification allows the use of well-developed, efficient paraxial solution techniques to accomplish accurate wide-angle propagation and thus make possible the modeling of a wider variety of photonic devices.

References

1. D. Yevick and M. Glasner, *Optics Lett.* Vol. 15, No. 3, 174(1990).
2. R. P. Ratowsky and J. A. Fleck, Jr., *Optics Lett.* Vol. 16, No. 11, 787(1991).
3. J. Gerdes and R. Pregla, *J. Opt. Soc. Am. B*, Vol. 8, 389(1991).
4. G. R. Hadley, *Optics Lett.* Vol. 17, No. 18, 1426(1992).
5. B. Hermansson, D. Yevick, W. Bardyszewski and M. Glasner, *IEEE J. Lightwave Tech.* Vol. 10 No. 6, 772(1992).
6. M. D. Collins, *J. Acoust. Soc. Am.* Vol. 87, No. 4, 1535(1990).
7. G. R. Hadley, *IEEE J. Quantum Electron.* Vol. 28, No. 1, 363(1992).

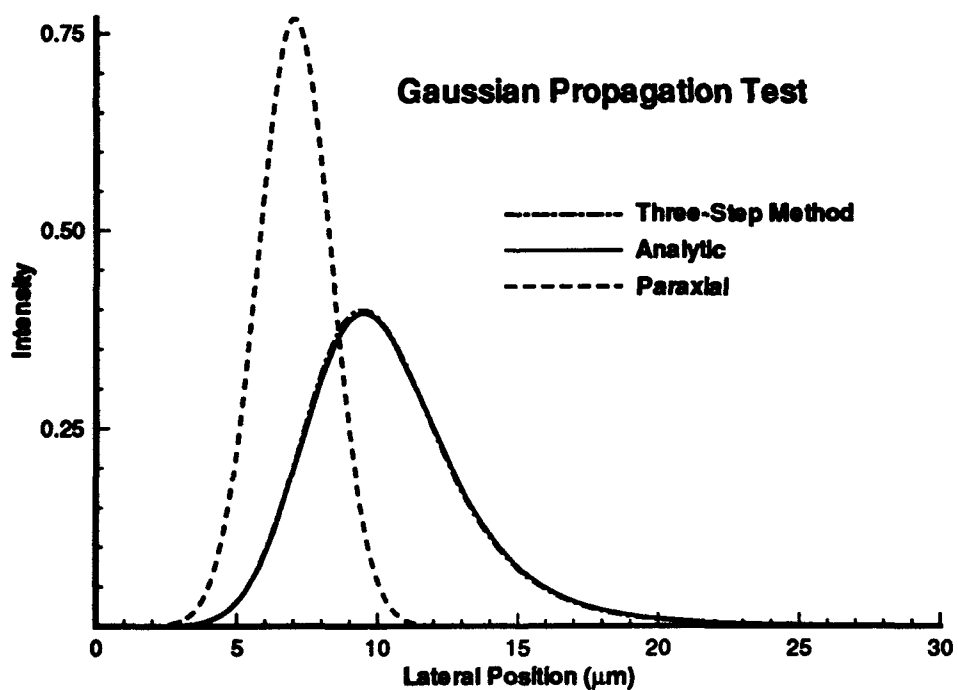


Fig. 1. Intensity profiles resulting from the propagation of an initial Gaussian beam having a 45 deg phase tilt a distance of 10 μm through a uniform medium. Results for the three-step method are compared to the exact analytic results.

Efficient Vectorial Analysis of Propagation in Three-Dimensional Optical Devices

R.D. Ettinger, F.A. Fernandez, J.B. Davies
Department of Electronic and Electrical Engineering
University College London,
Torrington Place
London WC1E 7JE, UK
phone: +44 71 387 7050
and

H. Bissessur
Alcatel Alsthom Recherche
Route de Nozay
91460 Marcoussis, France
phone: +33 1 64 49 14 82

There is a need for reliable and efficient analysis of three dimensional integrated optical components. This can usually be met by employing a propagation algorithm where a given excitation is followed in space and/or time, with the advantage that only the fields at relevant recent steps need be kept at any stage of the analysis.

This paper reports a time-harmonic, fully vectorial modeling technique suitable for devices where the transverse cross-section, represented using finite elements, is arbitrarily complicated but the longitudinal features vary sufficiently gradually that reflections can be ignored. Furthermore, this technique can be easily extended to deal with arbitrary index nonlinearities. No distinction needs to be made between special cases (TE or TM modes). This method deals naturally with mode conversion in general cases.

Similar vectorial propagation problems have already been treated using finite differences [1]-[4] or the discrete Fourier transform [5] to model the fields in the transverse section. These have been demonstrated mainly in 2-dimensional cases due to the high computing cost in 3-dimensions. Such methods are inefficient in the discretization of the transverse section, relying on rectangular (even uniform) grids. In contrast, the use of finite elements in the transverse plane, which so far has only been applied to one transverse-dimensional propagation modeling [6]-[8] allows the efficient distribution of nodal points and further permits adaptive techniques to be used [9], [10].

As the structures of interest have constant magnetic permeability but inhomogeneous permittivity, it is advantageous to formulate the problem in terms of the magnetic field $H \exp(j\omega t)$. Eliminating the electric field from Maxwell's curl equations gives:

$$-\nabla^2 \mathbf{H} = \nabla l \times (\nabla \times \mathbf{H}) + \epsilon \mu \omega^2 \mathbf{H} \quad (1)$$

where ω , $\epsilon(x,y)$ and μ are the frequency, permittivity and permeability, respectively and $l(x,y)$ represents $\ln(\epsilon)$.

Expressing the magnetic field as $\mathbf{H} = (\mathbf{H}_t + \hat{z}H_z)e^{-j\beta z}$, using only the transverse components of equation (1) and assuming isotropic permittivity, we obtain:

$$(\partial_z l + 2j\beta)\partial_z \mathbf{H}_t = (\nabla^2 + \omega^2 \epsilon \mu - \beta^2)\mathbf{H}_t + (M + j\beta \partial_z l)\mathbf{H}_t + (\partial_z l)\nabla_t H_z$$

where

$$M = \begin{bmatrix} (-\partial_y l)\partial_y & (\partial_y l)\partial_x \\ (\partial_x l)\partial_y & (-\partial_x l)\partial_x \end{bmatrix}$$

A third equation is obtained from the divergence condition:

$$\partial_z H_z = -\nabla_t \cdot \mathbf{H}_t + j\beta H_z \quad (2b)$$

It is assumed in our implementation that the slowly varying amplitude approximation is applicable in equation (2a) so that the ∇^2 can be reduced to ∇_t^2 by neglecting the second order z -derivative (a paraxial approximation), but this assumption can of course be lifted. It should be emphasized that all three components of \mathbf{H} are present in the model.

The modified coupled equations (2a) and (2b) are discretized spatially in (x,y) using the Galerkin/finite element method with a nonuniform mesh of triangles and first order basis functions. This results in a large but sparse unsymmetric matrix differential equation in z , which is finally converted to an algebraic problem using finite differences in the longitudinal direction (Crank-Nicolson).

An advantage of this formulation is that it includes the coupling between different optical polarizations, even if the materials themselves are isotropic. The coupling operator M is zero within homogeneous dielectric regions but has a contribution from any inhomogeneity of ϵ , including a delta function term at dielectric interfaces in the transverse section. Note that when all z derivatives are set to zero in equations (2a) the resulting pair of equations reduces to that used for modal analysis by Williams and Cambrell [11].

The method has firstly been tested using problems where the solution is known or available through other methods. Two further examples are shown here. The first is a ridge coupler structure [12] which was excited in the left arm by an elliptic gaussian input of wavelength 1.52 μm . The cross-section was discretized using a mesh of 900 triangles and each propagation step took 0.8 sec. on a SUN sparcstation. Fig. 1 shows 3-D plots of the H_y component at three different distances from the input. Fig. 2 shows the contour plots of H_y in two of these cases. The results show the capture of the gaussian input and illustrate the coupling effect. The observed coupling length is 270 μm , in reasonable agreement with our own modal analysis (for the same mesh) and with [12] although some discrepancy is expected since a spatial filter is used here as a simple treatment of the boundary truncation.

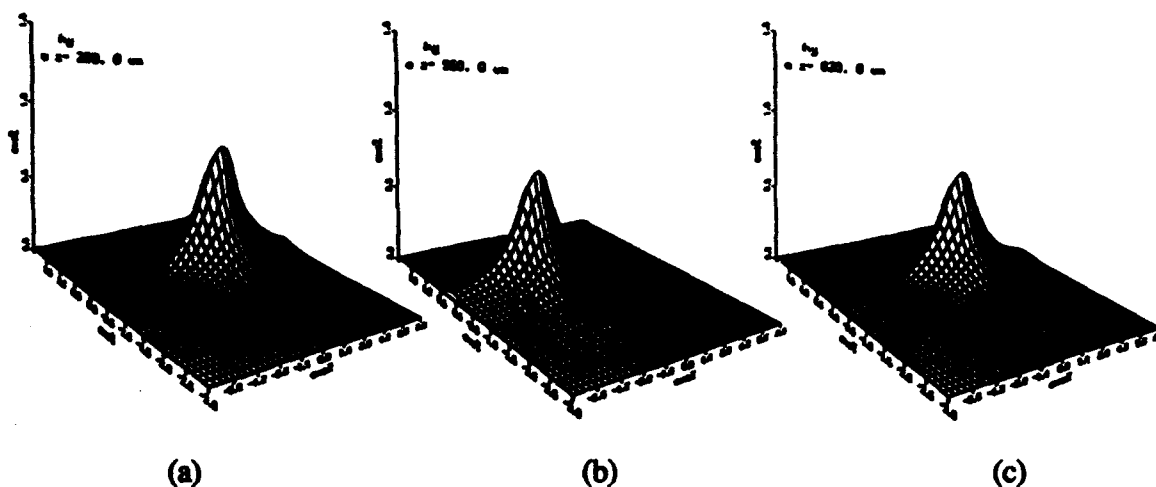


Fig. 1 3-D plots of the dominant field component H_y in the ridge coupler of reference [12]. (a) $z = 280 \mu\text{m}$, (b) $z = 550 \mu\text{m}$ and (c) $z = 820 \mu\text{m}$.

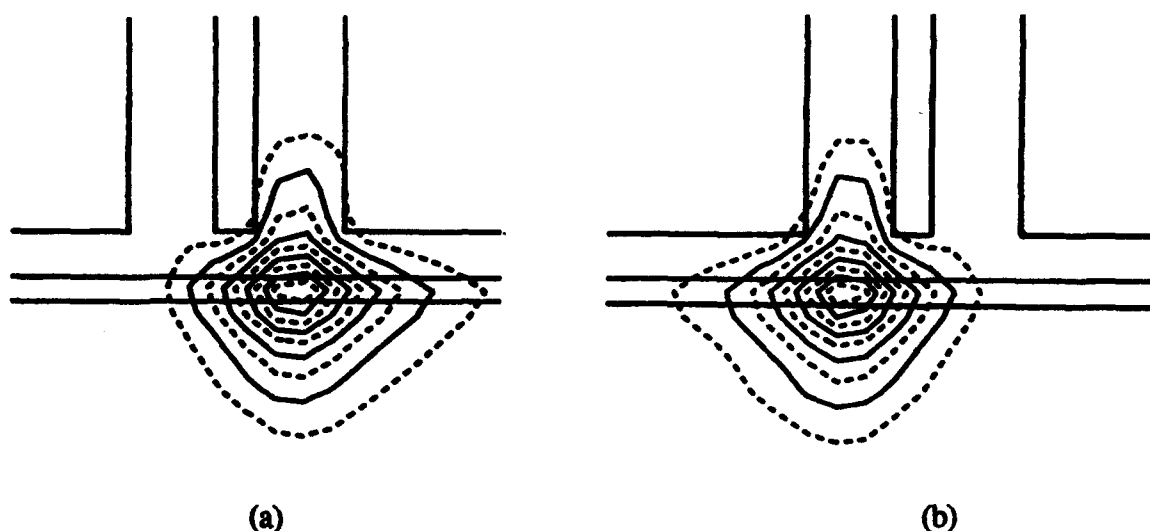


Fig. 2 Contour plots of H_y at (a) $z = 280 \mu\text{m}$ and (b) $z = 550 \mu\text{m}$.

As a second example, Fig. 3 illustrates a 2-dimensional simulation of the reflection of the slab-guided wave at a diagonal facet. The slab guide has a refractive index of 3.2 and a width of $1.2 \mu\text{m}$ on a substrate of refractive index 3.17. The air interface is cut at an angle of 7° . Such a large refractive index will pose a stringent condition on the step size for the Fourier BPM.

We have observed that careful treatment of the transverse boundary condition is necessary to avoid stability problems. These problems sometimes occur in the results for the less significant field components.

By taking advantage of our adaptive remeshing technique [9] for the distribution of nodes in the cross-section and using efficient sparse matrix algorithms, the present method does not require massive computer resources.

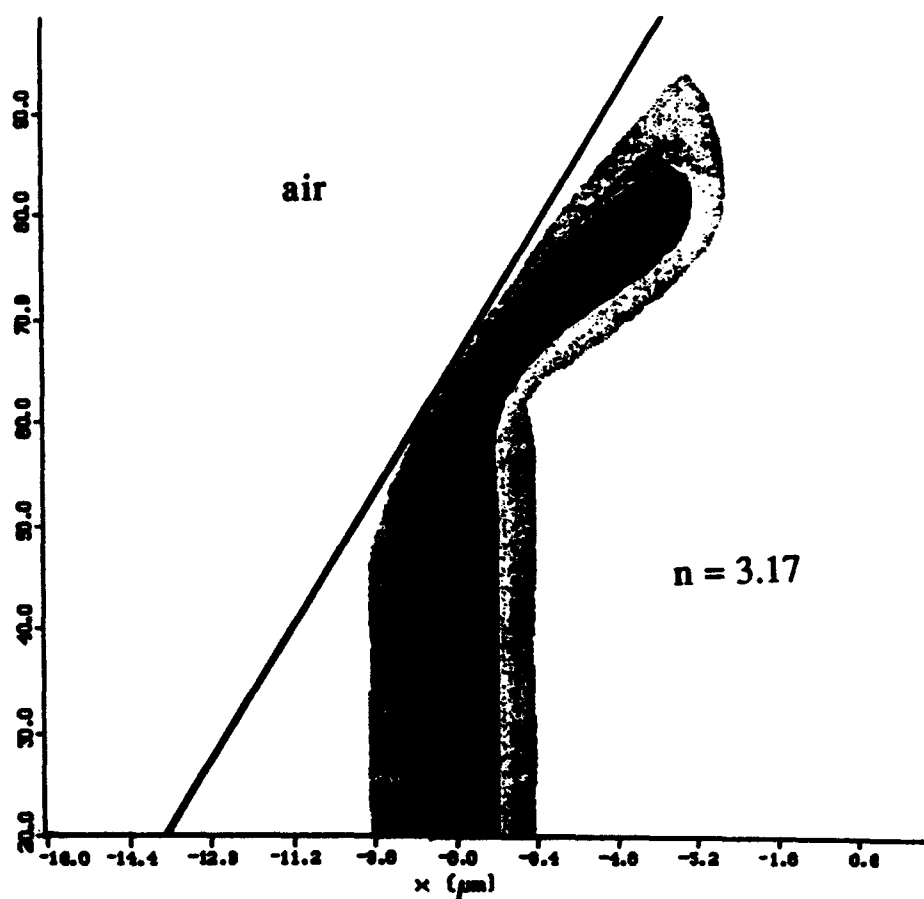


Fig. 3 Reflection of the guided wave in a facet cut on a slab waveguide at an angle of 7° .

REFERENCES

- [1] M. Bothe, A. Splatt, D. Uhlendorf, and K. Petermann, *Integrated Photonics Research*, Vol.10 of OSA Tech. Digest Series (1992), pp. 300-301.
- [2] W.P. Huang, C.L. Xu, and S.K. Chaudhuri, *IEEE Photonics Tech. Lett.* (1991), pp. 1117-1120.
- [3] Y. Chung, N. Dagli, and L. Thylén, *Electronics Lett.* (1991), pp. 2119-2121.
- [4] O.J.F. Martin, R. Clauberg, and P. von Allmen, 17th European Conference on Optical Communications, Paris (1991).
- [5] J.M. Liu and L. Gomelsky, *J. Opt. Soc. Am. A* (1992), pp. 1574-1585.
- [6] T.B. Koch, J.B. Davies, and D. Wickramasinghe, *Electronics Lett.* (1989), pp. 514-516.
- [7] K. Hayata, A. Misawa, and M. Koshiba, *J. Opt. Soc. Am. B* (1990), pp. 1268-1280.
- [8] H.E. Hernandez-Figueroa, *Nonlinear Guided-Wave Phenomena*, Vol.15 of OSA Tech. Digest Series (1991), pp. 92-95.
- [9] R.D. Ettinger, F.A. Fernandez, and J.B. Davies, in "Directions in Electromagnetic Wave Modeling", H.L. Bertoni and L.B. Felsen (Eds.), Plenum Press, New York (1991), pp. 239-246.
- [10] F. Schmidt and H.-P. Nolting, *Integrated Photonics Research*, Vol.10 of OSA Tech. Digest Series (1992), pp. 302-303.
- [11] C.G. Williams and G.K. Cambrell, *IEEE Trans. Microwave Theory Tech.* (1974), pp. 329-330.
- [12] Working Group I, COST 216, *Proc. IEE J* (1989), pp. 273-280.

Three-Dimensional Vectorial Beam Propagation Method for Anisotropic Medium

Olivier J.F. Martin, Rolf Clauberg and Franz-Karl Reinhart*

IBM Research Division, Zurich Research Laboratory, CH-8803 Rüschlikon, Switzerland
+ 41-1-724.84.21 (tel.) + 41-1-724.17.89 (fax)

*Institute of Micro- and Optoelectronics, Swiss Federal Institute of Technology
CH-1015 Lausanne, Switzerland

There has been a strong effort recently to develop so-called vectorial beam propagation methods (VBPM) [1-7]. The aim of this effort is to overcome the scalar limitation of the classical beam propagation method (BPM) [8-10]. We present here a new approach to the VBPM that can handle three-dimensional anisotropic media. This new method allows the study of the vectorial properties of the electromagnetic fields, such as polarization effects and coupling between the field components.

Numerical method

We start with the wave equation for the electrical field $\vec{E}(x, y, z)$:

$$-\vec{\nabla} \times \vec{\nabla} \times \vec{E}(x, y, z) + k_0^2 \varepsilon(x, y, z) \vec{E}(x, y, z) = \vec{0} \quad (1)$$

where we have assumed the usual time dependence $e^{-i\omega t}$. In order to treat anisotropic medium, we take the tensorial character of ε into account:

$$\varepsilon(x, y, z) = \begin{pmatrix} \varepsilon_{xx} & \varepsilon_{xy} & \varepsilon_{xz} \\ \varepsilon_{yx} & \varepsilon_{yy} & \varepsilon_{yz} \\ \varepsilon_{zx} & \varepsilon_{zy} & \varepsilon_{zz} \end{pmatrix}. \quad (2)$$

Similarly to the BPM, we consider a beam propagating in the z -direction and assume that the main dependence of the field is described by the term $e^{ik_0 n_{ref} z}$, where n_{ref} is a reference refractive index. For the remaining z -dependence, we expect that $|\partial_{zz} E_x| \ll |2ik_0 n_{ref} \partial_z E_x|$ and $|\partial_{zz} E_y| \ll |2ik_0 n_{ref} \partial_z E_y|$. As the electrical field is predominantly transversely polarized in a weakly guiding structure, we neglect the longitudinal field component. With these assumptions, Eq. (1) becomes

$$\partial_z \begin{pmatrix} E_x \\ E_y \end{pmatrix} = \frac{i}{2k_0 n_{ref}} \begin{pmatrix} \partial_{yy} + k_0^2 (\varepsilon_{xx} - n_{ref}^2) & -\partial_{xy} + k_0^2 \varepsilon_{xy} \\ -\partial_{yx} + k_0^2 \varepsilon_{yx} & \partial_{xx} + k_0^2 (\varepsilon_{yy} - n_{ref}^2) \end{pmatrix} \begin{pmatrix} E_x \\ E_y \end{pmatrix}. \quad (3)$$

The discretized form of Eq. (3) is then solved using the Crank-Nicolson algorithm [11]

$$(1 - \alpha \Delta z A^{z+\Delta z}) \vec{E}_\perp^{z+\Delta z} = (1 + (1 - \alpha) \Delta z A^z) \vec{E}_\perp^z \quad (4)$$

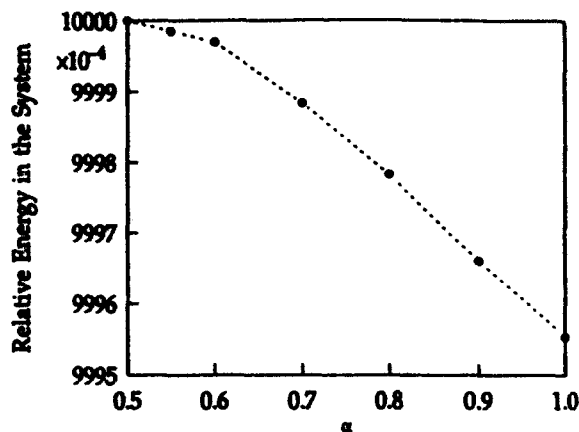
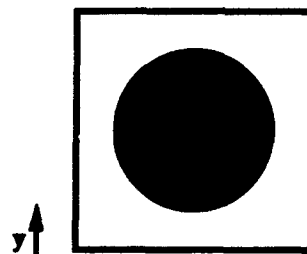


Figure 1. Propagation of an HE_{11} mode in an isotropic fiber. Energy remaining in the system after a propagation length of $100 \mu\text{m}$ as a function of the numerical parameter α (Eq. 4).



radius = $4 \mu\text{m}$
 $\lambda = 1 \mu\text{m}$
 $n_{\text{ref}} = 3.60046$
 propagation = $250 \mu\text{m}$
 Isotropic medium :
 $n_{\text{core}} = 3.601$ $n_{\text{cladding}} = 3.600$
 Anisotropic medium :
 $n_{\text{core-x}} = 3.601$ $n_{\text{core-y}} = 3.602$
 $n_{\text{cladding-x}} = 3.600$ $n_{\text{cladding-y}} = 3.601$

Figure 2. Cross section and parameters of the system used for the simulations.

where A is the differential operator on the right-hand side of Eq. (3) and α is introduced to control the stability of the method. Indeed this numerical scheme is unconditionally stable for $0.5 < \alpha < 1$ and marginally stable for $\alpha = 0.5$ [12].

The parameter α also leads to some numerical absorption as can be seen in Fig. 1 where we report results of the propagation of an HE_{11} mode in the isotropic fiber depicted in Fig. 2. The energy remaining in the system after a propagation length of $100 \mu\text{m}$ is reported as a function of α . The numerical absorption increases with α . Therefore the energy remaining in the system decreases with α . In the following, we choose a value of $\alpha = 0.55$ which gives a good numerical stability with a very small numerical absorption. Finally, transparent boundary conditions [13] are used at the edges of the computational window.

Stability of the method

To establish the influence of the mesh size Δx , Δy and of the propagation step Δz on the stability of the method, we introduce the overlap integral:

$$\theta(z) = \sum_{\mu=x,y} \frac{\langle E_{\mu}(z) | E_{\mu}(z=0) \rangle}{\langle E_{\mu}(z=0) | E_{\mu}(z=0) \rangle} \quad (5)$$

When the shape and the energy of the field are conserved during the propagation, $\theta(z)$ remains equal to unity.

Values of $\theta(z)$ for the propagation of an HE_{11} mode over a length of $100 \mu\text{m}$ in the aforementioned isotropic fiber are given in Fig. 3. The energy of the field is conserved; only the shape of the field changes slightly. $\theta(z)$ depends mainly on the mesh size Δx , Δy whereas the propagation step Δz has a limited influence. Hence it is possible to use quite large values of Δz

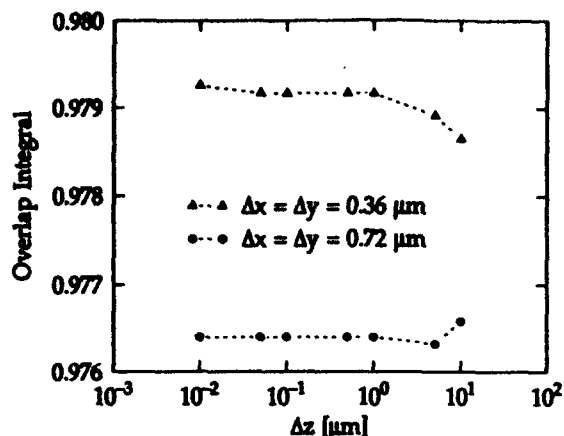


Figure 3. Overlap integral of the field after $100 \mu\text{m}$ of propagation. Isotropic fiber, as a function of the mesh size Δx , Δy and of the propagation step Δz .

without loss of stability. Even for large mesh size Δx , Δy , the overlap integral remains very close to unity.

Propagation in anisotropic medium

When an HE_{11} mode is propagated in an isotropic fiber, its polarization is conserved, as can be seen in Figs. 4a and b. On the other hand, if we launch the same mode into the anisotropic fiber of Fig. 2, the polarization direction changes as the propagation proceeds (Fig. 4c). This is easily understood from Eq. (3): In any medium, the two field components are coupled by the antidiagonal terms of (3). For an HE_{11} mode in an isotropic medium, the two ∂_{xy} terms com-

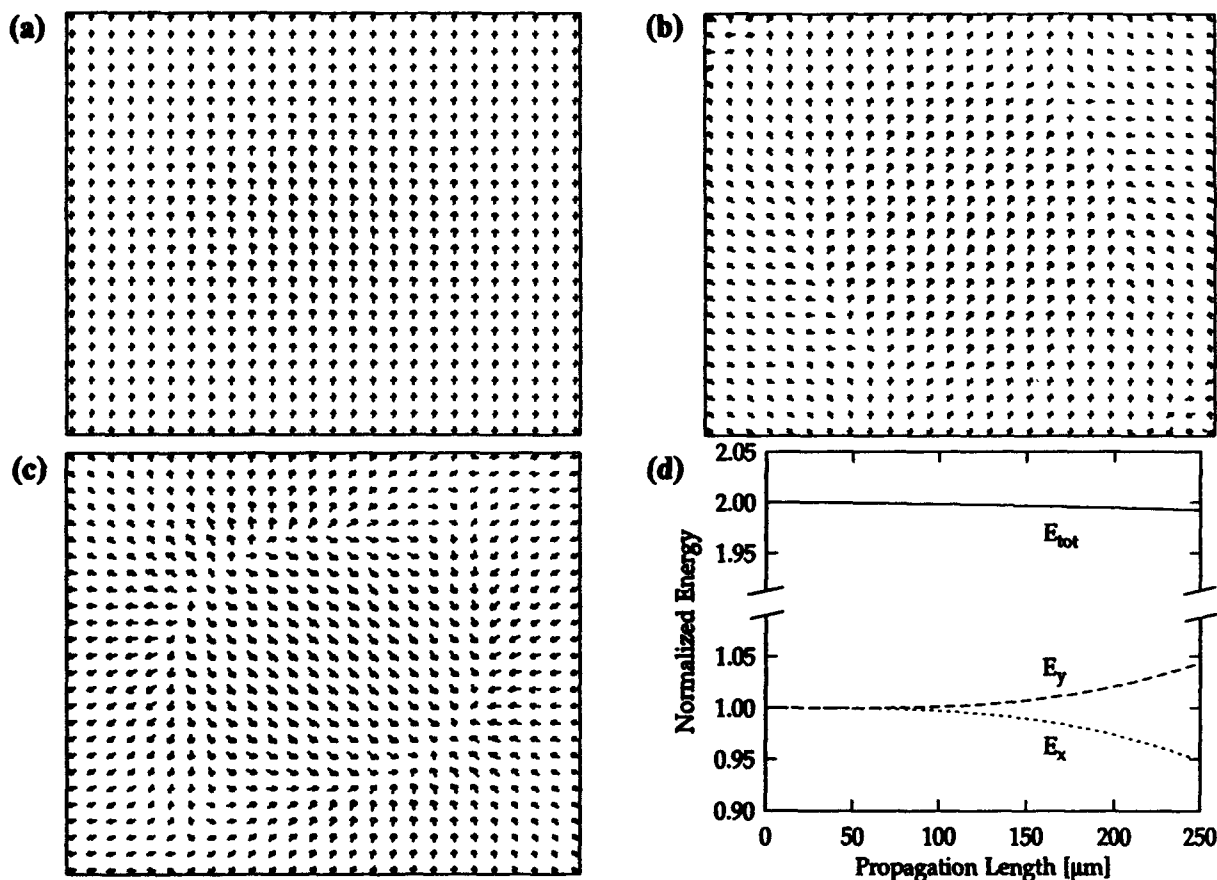


Figure 4. Propagation of an HE_{11} mode in isotropic and anisotropic fibers. (a) Polarization of the starting field. Polarization after $250 \mu\text{m}$ of propagation in isotropic fiber (b) and in anisotropic fiber (c). In the anisotropic case, the polarization direction changes during the propagation and energy is transferred from the E_x to the E_y field component (d).

pensate each other and both field components are conserved independently. On the other hand, the difference between ϵ_{xx} and ϵ_{yy} in the anisotropic fiber generates a difference between E_x and E_y . This leads to different values of the ∂_{xy} term for each field component. The balance between these two coupling terms is upset and energy can transfer from one field component to the other. This is visible in Fig. 4c, which depicts the energy of each field component. As the propagation progresses, energy is transferred from the E_x -component to the E_y -component. This is no numerical artefact, as the total energy of the system is conserved, except for some numerical absorption due to α (Fig. 4c).

Thus, the ability of our method to handle vectorial properties of electromagnetic fields is demonstrated.

References

1. R. Clauberg and P. von Allmen, *Electron. Lett.* **27** 654-655 (1991).
2. W.P. Huang, C.L. Xu, S.T. Chu and S.K. Chaudhuri, *IEEE Photon. Technol. Lett.* **3** 910-913 (1991).
3. Y. Chung, N. Dagli and L. Thylén, *Electron. Lett.* **27** 2119-2120 (1991).
4. W. Huang, C. Xu, S.T. Chu and S.K. Chaudhuri, *IEEE J. Lightwave Technol.* **10** 295-305 (1992).
5. R. Pregla, J. Gerdes, E. Ahlers and S. Helfert, *Proc. Integrated Photon. Research, New Orleans, April 13-16 1992*, 32-33 (1992).
6. M. Bothe, A. Splett, D. Uhlendorf and K. Peterman, *Proc. Integrated Photon. Research, New Orleans, April 13-16 1992*, 300-301 (1992).
7. J.M. Liu and L. Gomelsky, *J. Opt. Soc. Am. A* **9** 1574-1585 (1992).
8. M.D. Feit and J.A. Fleck, Jr, *Appl. Opt.* **17** , 3990-3998 (1978).
9. J. van Roey, J. van der Donk and P.E. Lagasse, *J. Opt. Soc. Am.* **71** , 803-810 (1981).
10. D. Yevick and B. Hermansson, *IEEE J. Quantum Electron.* **26** , 109-112 (1990).
11. J. Crank and P. Nicolson, *Proc. Cambridge Philos. Soc.* **43** , 50-67 (1947).
12. A.R. Mitchell and D.F. Griffiths, "The finite difference method in partial differential equations," (J. Wiley and Sons, Chichester, 1990)
13. G.R. Hadley, *IEEE J. Quantum Electron.* **28** 363-370 (1992).

Bidirectional beam-propagation method based on the Method of Lines

Johannes Gerdes and Reinhold Pregla

Allgemeine und Theoretische Elektrotechnik
FernUniversität

Postfach 940, D-5800 Hagen, Germany

(Phone: +49 2371 566 255 FAX: +49 2371 51898)

Introduction

There is an increasing need of including reflected waves into beam - propagation algorithms. Example is the publication [1], in which reflected waves are approximated by a split-operator formalism. Alternative algorithms are given in [2] and [3] for multiple discontinuities. Recently new analysis methods for single discontinuities in slab waveguides were presented in [4] and in [5].

To improve the accuracy in analyzing longitudinal discontinuous waveguide structures with high transverse index steps and to treat problems with multiple discontinuities we extend the beam-propagation method based on the Method of Lines (MoL-BPM) to a bidirectional propagation scheme. Thus we arrive at an approach, which describes wave propagation in forward and backward direction in an analytical way. The semianalytical approach also leads to a drastical reduction of storage requirements in comparison with the above mentioned split-step methods [1].

The general algorithm

Starting point is the normalized semivectorial wave equation for quasi TE or TM polarisation

$$\frac{\partial^2}{\partial \bar{z}^2} \psi_{e,h} + \bar{\nabla}_t \psi_{e,h} + n^2 \psi_{e,h} = \frac{1}{n^2} \frac{\partial}{\partial \xi} n^2 \frac{\partial}{\partial \xi} \psi_{e,h}$$

with

$$n = n' - jn'', \quad \xi = x, y$$

It should be emphasized, that material with complex refractive index is included in the analysis. The transverse operators are discretized with finite differences, which take into account the boundary conditions of the normal or tangential field components at dielectric discontinuities, i.e. the transverse vectorial character of the field [6]. The field potential $\psi_{e,h}$ are discretized resulting in an two dimensional array $\psi_{e,h}$ which is then converted into a vector $\hat{\psi}_{e,h}$. The result of the discretization is an ordinary differential equation. To solve

this equation a diagonalization of the discretized transverse wave operator $\widehat{Q}_{e,h}$ is performed:

$$\frac{d^2}{dz^2} \widehat{\psi}_{e,h} - \widehat{Q}_{e,h} \widehat{\psi}_{e,h} = 0 \quad \Rightarrow \quad \frac{d^2}{dz^2} \widehat{\psi}_{e,h} - \widehat{\lambda}_{e,h}^2 \widehat{\psi}_{e,h} = 0$$

with

$$\widehat{T}_{e,h}^{-1} \widehat{Q}_{e,h} \widehat{T}_{e,h} = \widehat{\lambda}_{e,h}^2, \quad \widehat{\psi}_{e,h} = \widehat{T}_{e,h}^{-1} \widehat{\psi}_{e,h} \quad (1)$$

This ansatz is a characteristic feature of the MoL - BPM [7]. The columns of the matrices $\widehat{T}_{e,h}$ are the eigenvectors of the transverse operator $\widehat{Q}_{e,h}$ of the discretized wave equation and the diagonal matrix $\widehat{\lambda}_{e,h}^2$ contains the eigenvalues of the transverse operator, which have the meaning of the propagation constants of the eigenvectors in the discretized representation. The general solution of the diagonalized wave equation including reflected waves is [4]:

$$\widehat{\psi}_{e,h} = e^{-\widehat{\lambda}_{e,h} z} \widehat{F}_{e,h} + e^{\widehat{\lambda}_{e,h} z} \widehat{G}_{e,h} \quad (2)$$

It should be mentioned that this solution is exact, that means it solves the discretized wave equation analytically in z direction and therefore propagation steps of arbitrary length are possible.

After the propagation in the transformed domain the field in the original domain is obtained by inverse transformation. The solution describing the propagation in the original domain including reflected waves using eqns. (1,2) is:

$$\widehat{\psi}_{e,h}(z) = \widehat{T}_{e,h} \left(e^{-\widehat{\lambda}_{e,h} z} \widehat{F}_{e,h} + e^{\widehat{\lambda}_{e,h} z} \widehat{G}_{e,h} \right) \quad (3)$$

The coefficients $\widehat{F}_{e,h}$ and $\widehat{G}_{e,h}$ are determined from field matching at longitudinal discontinuities at and supplying an incident wave $\widehat{\psi}_{e,h}^i$ at the position z_0 , i. e. $\widehat{F}_{e,h}^-(z_0) = \widehat{T}_{e,h1}^{-1} \widehat{\psi}_{e,h}^i(z_1)$

Propagation scheme for multiple discontinuities

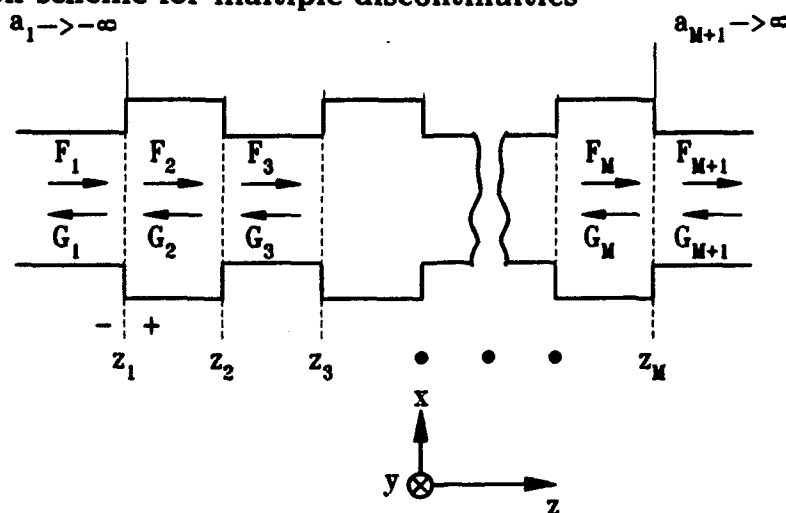


Fig. 1: Bidirectional propagation scheme for multiple slab waveguide discontinuities

To determine the coefficients field matching is performed in the original domain on the left (-) and right (+) side of a discontinuity for the discretized potentials, i. e. $\hat{\psi}_- = \hat{\psi}_+$ and $\frac{\partial}{\partial \bar{z}} \hat{\psi}_- = \frac{\partial}{\partial \bar{z}} \hat{\psi}_+$ which leads together with eqn. 3 to the transfer matrix A_k^D of a discontinuity and thus to a relation between the coefficients of reflected and transmitted waves

$$\begin{pmatrix} \mathbf{F}_{k+1}^+ \\ \mathbf{G}_{k+1}^+ \end{pmatrix} = A_k^D \begin{pmatrix} \mathbf{F}_k^- \\ \mathbf{G}_k^- \end{pmatrix}$$

The transfer matrix of a homogeneous region results from the conventional MoL-BPM algorithm

$$\begin{pmatrix} \mathbf{F}_{k+1}^- \\ \mathbf{G}_{k+1}^- \end{pmatrix} = A_k^P \begin{pmatrix} \mathbf{F}_k^+ \\ \mathbf{G}_k^+ \end{pmatrix} \quad \text{with} \quad A_k^P = \begin{bmatrix} e^{-\bar{\lambda}_{e,h_k} \bar{d}} & \\ & e^{\bar{\lambda}_{e,h_k} \bar{d}} \end{bmatrix}, \quad \bar{d} = \bar{z}_{k+1} - \bar{z}_k$$

Thus the solution for M discontinuities runs

$$\begin{pmatrix} \mathbf{F}_{M+1} \\ \mathbf{G}_{M+1} \end{pmatrix} = A_M^D \cdot \prod_{k=1}^{M-1} (A_k^P A_k^D) \begin{pmatrix} \mathbf{F}_1 \\ \mathbf{G}_1 \end{pmatrix} = \tilde{A}_M \cdot \begin{pmatrix} \mathbf{F}_1 \\ \mathbf{G}_1 \end{pmatrix}$$

From $\mathbf{G}_{M+1} = 0$ ($a_{M+1} \rightarrow \infty$, $a_1 \rightarrow -\infty$) follow the reflected and transmitted fields

$$\mathbf{G}_1 = r_M \cdot \mathbf{F}_1, \quad \mathbf{F}_{M+1} = t_M \cdot \mathbf{F}_1$$

at the input and output of the waveguide structure. An important extension in conjunction with the presented algorithm is the numerical reduction of the eigenwave system, i. e. the number of used eigenvalues and eigenvectors is reduced, which leads also to a reduction of size of the transfer matrix.

$$\bar{\lambda} \rightarrow \bar{\lambda}^r, \quad T \rightarrow T^r \quad \Rightarrow \quad \tilde{A}_M \rightarrow \tilde{A}_M^r$$

Only numerical significant eigenvectors are used for propagation. This leads to a drastical decrease in storage requirements and computation time.

Numerical Results

The first results were obtained from analyzing TE wave propagation in slab waveguide discontinuities, i. e. $\partial/\partial y = 0$. By using the above derived formalism and the known incident field represented by the coefficient $\mathbf{F}_{h1}^- = T_{h1}^{-1} \mathbf{E}_y(z_1^-)$ [4] the total reflected and transmitted power was calculated for a finite number of periodic discontinuities. The results for a slab waveguide with finite number of periodic discontinuities are shown in Fig. 2. They were computed using only 12 eigenvectors from the transverse operator discretized on 136 lines, i. e. only 10 % of the total number of eigenvectors. The runtime was a few seconds on a workstation. The results are in good agreement with [2]. This shows the efficiency of the

presented method.

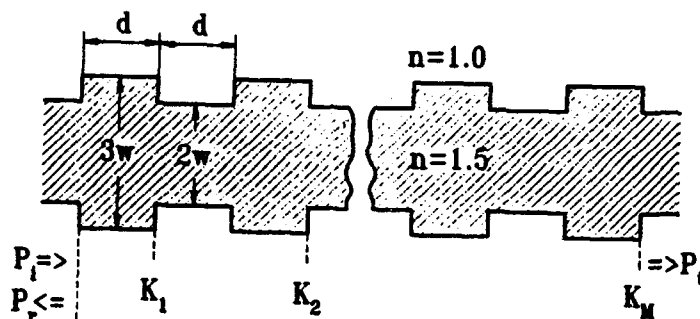


Fig. 2a: Waveguide with finite number of discontinuities

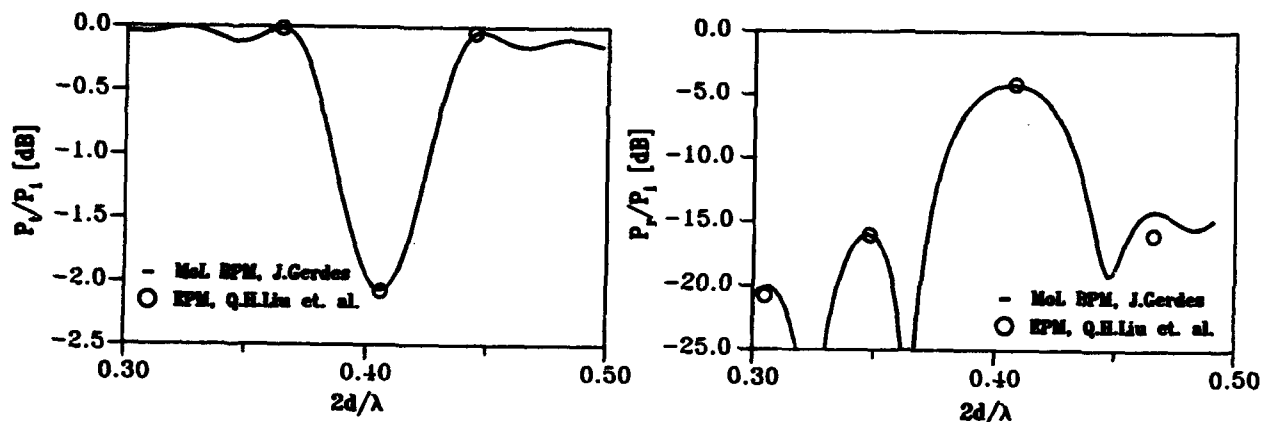


Fig. 2b: Calculated Power flow in slab waveguide with finite Number of discontinuities versus normalized period $2d/\lambda_0$. $k_0w = 2/3$, $w = 1 \mu\text{m}$. $M = 10$

References

- [1] D. Yevick, W. Bardyszewski, B. Hermansson and M. Glasner. 'Split-Operator Electric Field Reflection Techniques', IEEE Photonic Techn. Lett., vol. 3, 1991, pp. 527 - 529.
- [2] Q. H. Liu, W. C. Chew, 'Analysis of Discontinuities in Planar Dielectric Waveguides: An Eigenmode Propagation Method'. IEEE Microwave Theory and Techn.. Vol. 39, March 1991, pp. 422 - 430.
- [3] G. Sztefka, 'A Bidirectional Propagation Algorithm for Large Refractive Index Steps and Systems of Waveguides Based on the Mode Matching Method', in Technical Digest on Integrated Photonics Research, Vol. 10, Optical Society of America, Washington, D. C., 1992, S. 134 - 135.
- [4] J. Gerdes, B. Lunitz, D. Benish, R. Pregla, 'Analysis of Slab Waveguide Discontinuities Including Radiation and Absorption Effects', Electronics Letters, Vol. 28, May 1992, pp. 1013 - 1014.
- [5] D. Yevick, W. Bardyszewski, B. Hermansson. 'Lanczos reduction techniques for Electric Field Reflection', Journal of Lightwve. Techn.. Vol. 10, Sept. 1992, pp. 1234 - 1237.
- [6] R. Pregla, J. Gerdes, E. Ahlers, S. Helfert. 'MoL-BPM Algorithms for Waveguide Bends and Vectorial Fields', in Technical Digest on Integrated Photonics Research, Optical Society of America, Washington, D. C., 1992, Vol. 10, pp. 32 - 33.
- [7] R. Pregla and J. Gerdes, 'New beam-propagation algorithm based on the method of lines', in Technical Digest on Integrated Photonics Research, Optical Society of America, Washington, D. C., 1990, Vol. 5, pp. 29-30.



Photonic Integrated Circuits and Applications

IWA 8:30am-10:30am
Mesquite A

Thomas L. Koch, *Presider*
AT&T Bell Laboratories

Long wavelength photonic integrated circuits for telecommunications

U. Koren, AT&T Bell Laboratories, Holmdel, N.J. 07733

In recent years the number of reports, by different groups, in the field of photonic integration is increasing dramatically. Many groups have demonstrated new devices with new functionality for different application areas. To name a few, one can mention WDM communications [1-7], coherent detection [8-12], tunable lasers [13-17], optical switching [18,19], high power sources [20,21], extended cavity lasers [22-25], and others. In this talk we describe some of our own recent work concerning photonic integration in the areas of extended cavity mode locked lasers, and WDM components.

Extended cavity lasers combine active and passive waveguides to form a long laser cavity. These lasers provide an instructive demonstration of photonic integrated circuits (PIC's) as these are simple devices, yet highly sensitive to optical losses and reflections at the active-passive transitions. A schematic description of an extended cavity laser is shown in fig. 1, where the waveguide is composed of a short active gain section and a long passive section forming the laser cavity between the two cleaved facets. Mode locked pulses are obtained at the frequency $c/2nl$ - the inverse of the round trip time in the cavity, requiring cavity length of about 2 cm for 2.5 GHz operation. Although in principle, lasers with active region only (without passive sections) can be made that long, the internal losses will result in very low efficiencies. In contrast, active-passive extended cavity lasers can have reasonable quantum efficiencies in the range of 5-10 %/facet as shown in fig.2.

The efficiency of lasers is related to the internal loss. In an extended cavity laser the loss is composed of the active and passive propagation losses, and the active passive transitions loss. These losses can be measured using several methods, and are estimated in the range of 40-80 dB/cm, 2-5 dB/cm, and less than 1 dB/transition respectively.

Back reflections at the active passive transitions are an important issue. These reflections cause a ripple in the spectrum of the laser with a period corresponding to the active section length. If these reflections are large, control over the spectral behavior and pulse shape is not possible. From studies of integrated optical amplifiers, the internal reflections for well designed active-passive transitions can be as low as 5×10^{-5} .

For obtaining transform limited pulses the spectral width of the gain medium must be reduced. This has been achieved by integrating a DBR grating in the laser cavity [22]. Such lasers can be used as compact soliton sources, and have been used in long distance soliton transmission experiments [25]. Recently, a mode locked laser integrated with an electroabsorption (EA) modulator was also demonstrated [24] using an 9.1 mm long extended cavity laser with an integrated DBR grating. A digitally modulated pulse train at 4.5 Gbit/sec, using the integrated electroabsorption modulator, is shown in Fig.3. The time-bandwidth product for the mode locked pulses obtained with this device was recently reduced to 0.60.

Another area where photonic integration technology can make an important contribution is in WDM communications. One basic component is a tunable laser that can be tuned over a standard set of predetermined optical frequencies. Because of mode partitioning noise and chirp problems it is likely that such lasers will be externally modulated. Fig. 4. shows a tunable laser integrated with an electroabsorption modulator [26]. Fig. 5. shows the sensitivity of the receiver before and after transmission through 674 km of

conventional optical fiber (using EDFA's) and tuning the laser to four different optical frequencies. The sensitivities obtained with the PIC in this experiment were similar to those obtained with an external LiNbO₃ modulator. The switching time for changing optical frequencies with these lasers is of the order of a few nsec [27]

Another component under development that has been reported by several groups is a WDM laser array [5-7]. In such an array each laser is separately modulated, using a dedicated optical frequency, and then combined into a single fiber, thus increasing the transmission capacity by the number of lasers in the array. Fig. 6 shows a schematic diagram of a WDM array currently being developed by us. Each laser is followed by an integrated electroabsorption modulator and combined using a recently reported high performance InP based 1x16 splitter/combiner [28]. In this configuration an integrated optical amplifier is used to compensate for the 1xN splitting losses. However, when operating near the saturation output power the output amplifier will introduce cross talk due to gain saturation effects. Another attractive possibility would be to use a WDM multiplexer as in ref. [3] for a combiner which will eliminate splitting losses and the need for a booster amplifier.

In conclusion, the field of photonic integration has seen very rapid growth in the last few years. Progress in photonic integration technology will lead to the introduction of PIC's to several application areas in optical telecommunications.

References

1. C. Cremer et al, IEEE Photonic Tech. Lett. 4, 108, (1992).
2. J.B.D. Soole et al, Post deadline Proc. Integrated Photonic Research Conf. page 1, New Orleans, La (1992).
3. M. Zirngibl et al, IEEE Photonic Tech. Lett. November, (1992).
4. C.M. Ragdale et al, Electronics Lett. 28, 712, (1992).
5. U. Koren et al, Appl. Phys. Lett. 54, 2056, (1989).
6. M. Yamaguchi et al, Proc. 12th IEEE intl Semiconductor Laser Conf. page 160, Davos, Switzerland, (1990).
7. C.E. Zah et al, Proc. of the 13th IEEE intl. Semiconductor Laser Conf. page 194, Kagawa, Japan (1992).
8. T.L. Koch et al, Electronics Lett. 25, 1621, (1989).
9. H. Takeuchi et al, IEEE Photonic Tech. Lett. 1, 398 (1989).
10. R.J. Deri et al, IEEE Photonic Tech. Lett. 2, 581 (1990).
11. H. Heidrich et al, Proc. 17th European Conf. Optical Communications
12. R. M. Deri et al, Proc. Integrated Photonic Research Conf. , page 328, New Orleans, La, (1992).
13. M. Schilling et al, Electronics Lett. 28, 1698, (1992).
14. M. Kuznetsov et al, IEEE Photonic Tech. Lett. 4, 1093 (1992).
15. S. Illek et al, Electronics Lett. 27, 2207 (1991).
16. R.C. Alferness et al, Appl. Phys. Lett. 60, 3209, (1992).
17. V. Jayaraman et al, Appl. Phys. Lett. 60, 2321, (1992).
18. M. Janson et al, Post Deadline Proc. European Conf. on Optical Communications, page 28, Paris (1991).
19. U. Koren et al, Appl. Phys. Lett. 61, 1613, (1992).
20. U. Koren et al, Appl. Phys. Lett, 59, 2351, (1991).
21. J. H. Abeles et al, Post Deadline Proc. 13th IEEE Intl. Semiconductor Laser Conf. , page 23, Kagawa, Japan (1992).
22. P.B. Hansen et al, IEEE Photonic Tech. Lett. 4, 215, (1992).

24. P.B. Hansen et al, Post Deadline Proc. 13th IEEE Intl Semiconductor Laser Conf., page 11, Kagawa, Japan (1992).
25. C. R. Giles et al, Conf. On Optical Fiber Communications, San Jose, Ca (1993).
26. U. Koren et al, Proc. Conf. Optical Fiber Communications, page 124 San Jose, Ca, (1992).
27. B. Glance et al, Proc. Conf. Optical Fiber Communications, page 200 San Jose Ca, (1992).
28. M. Zirngibl et al, Electronics Lett. 28, 1212, (1992).

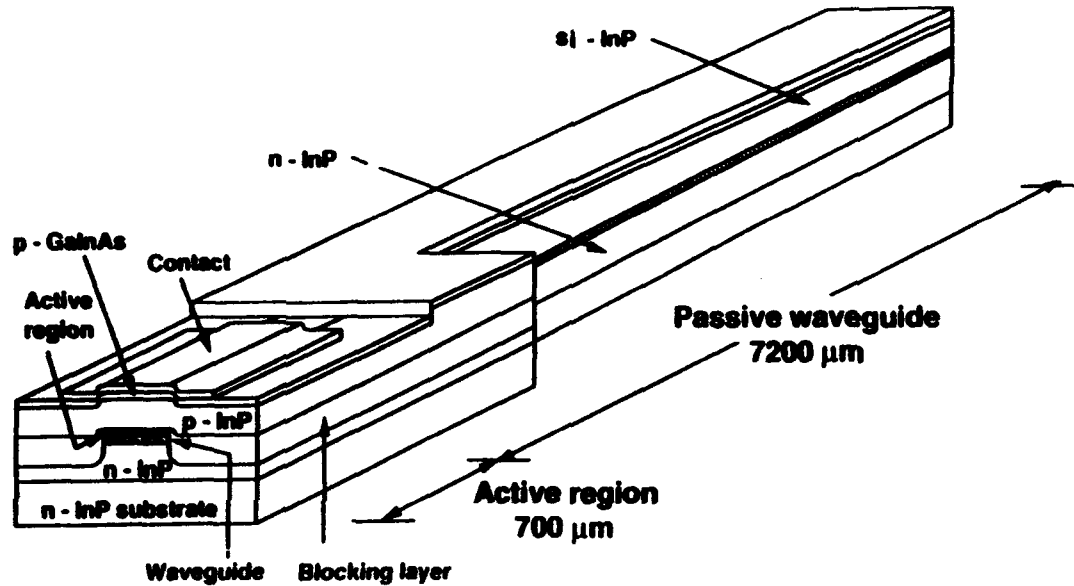


Fig.1. Schematic description of an extended cavity laser with total cavity length of 7.9 mm.

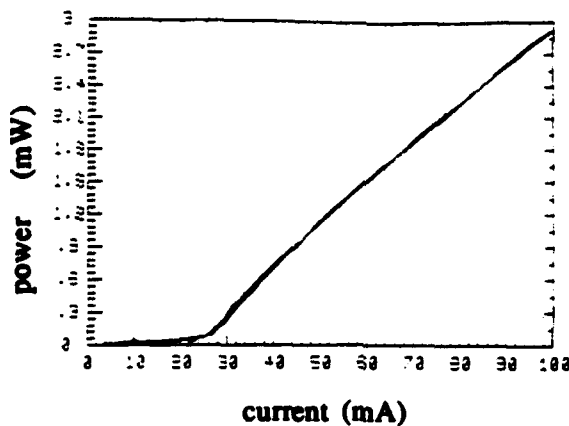


Fig.2. Light current characteristics of the extended cavity laser shown above. I_{th} is 25 mA. η is 6.5 %/facet.

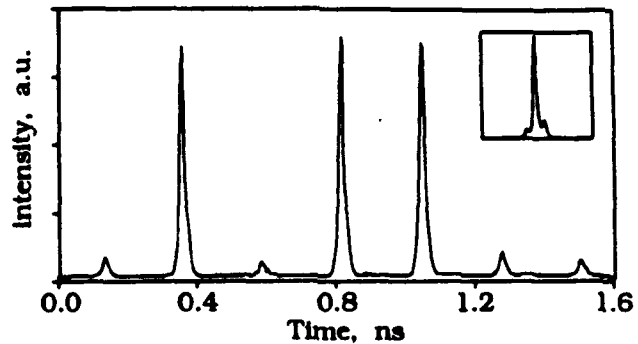


Fig.3. Mode locked pulses modulated with the bit pattern (0101100) using an integrated EA modulator.

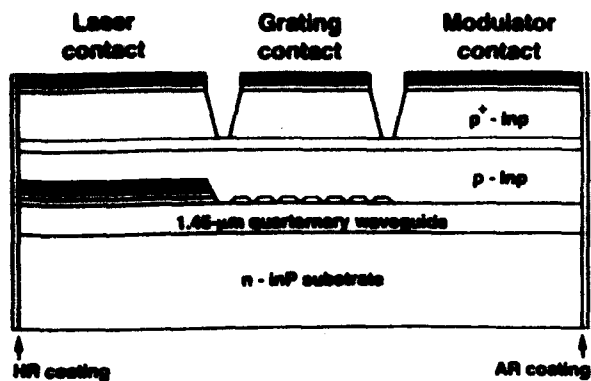


Fig. 4. Schematic diagram of a tunable laser with an integrated EA modulator.

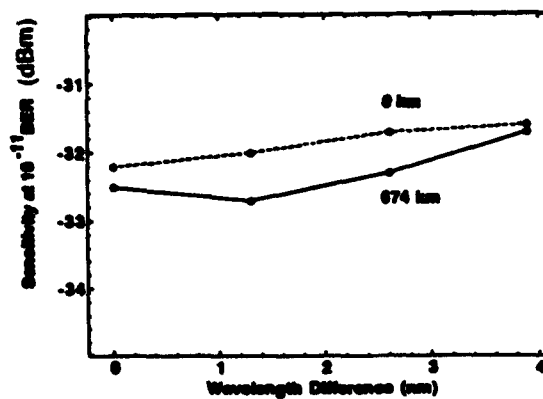


Fig. 5. Receiver sensitivities at 2.5 Gbit/sec at four wavelengths, using the laser-modulator PIC.

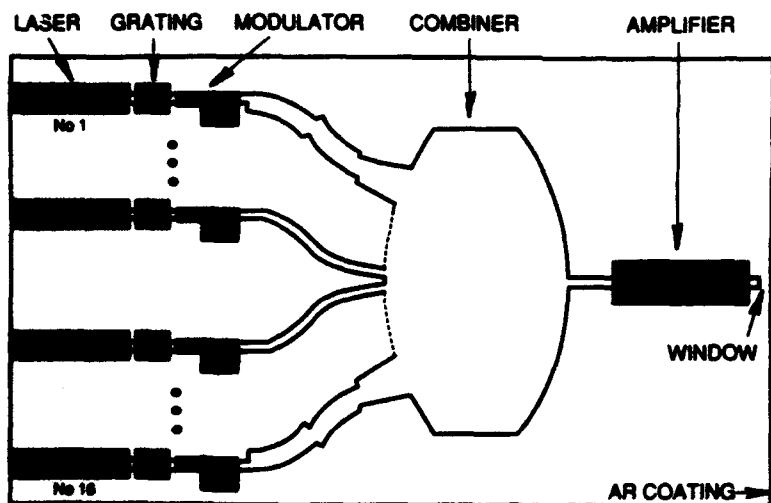


Fig. 6. Schematic diagram of a 16x1 WDM array with DBR lasers and integrated EA modulators.

Integrated Multi-wavelength Light Sources for WDM Lightwave Communication Systems

C. E. Zah, F. Favire, B. Pathak, L. Curtis, P. S. D. Lin, A. S. Gozdz
R. Bhat, C. Caneau, N. C. Andreadakis, D. D. Mahoney, V. S. Shah
R. E. Spicer, M. A. Kozza, G. H. Song, W. C. Young and T. P. Lee
Bellcore, 331 Newman Springs Road, Red Bank, NJ 07701, USA
Tel: (908) 758-3290, Fax: (908) 758-4372

With the recent advances in erbium-doped fiber amplifiers, the transmission distance is no longer loss limited but rather fiber dispersion limited. By the use of wavelength multiplexing, the bit rate of each wavelength can be substantially lower than the aggregated bit rate, such that not only cost-effective electronics are available but also the maximum transmission distance can be substantially increased. Moreover, the wavelength can be used as an address to route information without going through opto-electronic conversion. Recently, DARPA has funded a project on all optical network to study the potential of multi-wavelength switching.¹ A substantial part of the total cost for a packaged DFB laser module is the packaging cost to include a fiber pigtail, a thermoelectric cooler and an optical isolator. The total cost of a multi-wavelength laser transmitter made of discrete packaged DFB laser modules is proportional to the number of wavelengths. For WDM lightwave systems to be cost effective, it is desirable to fabricate the multi-wavelength laser transmitters by photonic integration to reduce the per wavelength cost of packaging and control circuitry by sharing them among all the wavelengths.

Previously, 20-wavelength DFB laser arrays made of bulk,² compressive-, and tensile-strained³ multiple quantum well active layers have been reported in the 1.5 μm wavelength region. However, for system applications, it is necessary to combine all the channels with different wavelengths into a single mode fiber for signal transmission or distribution. The conventional approach is to couple the individual outputs of a laser array to a fiber array, and then combine the signals using a fiber star coupler or a grating multiplexer. A 4-wavelength DFB laser array module has been demonstrated with 4.5 to 4.8 dB coupling loss per channel using bulk lenses.⁴ In this method, active alignment is required and the number of lasers that can be efficiently coupled to a fiber array is limited because the lens aperture is finite and the fiber spacing has to be at least 125 μm . Passive fiber coupling using a silicon waferboard is more desirable for an array with more than ten lasers. So far, the coupling loss per channel demonstrated with a 4-channel laser array is relatively high (8.5-14.6 dB).⁵ Another approach is to combine all the laser outputs with different wavelengths on chip, and then couple the combined signal into a single mode fiber. Integrated power combiners have been demonstrated previously with distributed Bragg reflector laser arrays of 2 to 4 wavelength channels.^{6,7} The insertion loss of the integrated combiner can be compensated by an efficient fiber coupling (0.45 dB)⁸ and/or optical amplification.⁶ Moreover, an efficient 19x19 optical star coupler has been demonstrated on silicon⁹, which distributes uniformly the light from each input to all outputs. Also, a 15x15 arrayed waveguide multiplexer consisting of two star couplers has recently been demonstrated on InP substrate.¹⁰ We present here a brief review of our recent work on the integration of a multi-wavelength DFB laser array with a star coupler and optical amplifiers on one chip.¹¹

Fig. 1 shows the top view of a finished chip. The 21-wavelength DFB laser array is connected to the center input waveguides of a 25x25 star coupler. Two remaining input waveguides on each side are dummy waveguides utilized to eliminate the edge effect. The DFB laser array is divided into two groups, ten lasers on the right and eleven lasers on the left. The top electrode of each laser is connected to a pad for wire bonding. The electrode spacing is twice the optical waveguide spacing to minimize the electrical crosstalk. Two of the output waveguides are fed to two optical amplifiers, 400 μm long each, and the remaining output waveguides are passive. The star coupler is formed by radially spacing the input (output) waveguides with an angular increment of 0.6° on a 750 μm radius circle centered at the middle of the output (input) waveguides. Each DFB laser is 450 μm long and connected to the input waveguide through a bend of 1 mm radius. Since the light from each DFB laser uniformly radiates across all the output waveguides of the star coupler, only one fiber pigtail is required to collect all the wavelengths into a single mode fiber. The total chip area is 1 mm by 4 mm.

The samples were grown by low-pressure organometallic chemical vapor deposition at 625°C . To achieve low threshold, low chirp and high speed lasers over a wide wavelength range, the active layer of the DFB lasers and optical amplifiers is chosen to be six compressive-strained $\text{In}_{0.7}\text{Ga}_{0.3}\text{As}$ wells separated by GaInAsP barrier layers (1.25 μm bandgap wavelength, 10 nm thick each). Under the active layer is the passive waveguide layer (1.25- μm quaternary, 200 nm thick) separated from the active layer by a n-doped InP etch stop layer, 50 nm thick, as shown in Fig. 2(a). Above the active layer is the grating layer (1.3- μm quaternary layer, 60 nm thick). $\lambda/4$ -shifted first-order gratings with twenty-one different periods were generated by electron-beam lithography using a high speed resist and etched into the grating layer by reactive ion etching using a noncorrosive gas mixture of CH_4/H_2 .¹² The grating periods vary from 2325 to 2450 \AA in 6.25 \AA increments such that each laser has a unique wavelength. The center to center spacing for two neighboring gratings is 36 μm . Outside the regions of DFB lasers and optical amplifiers, the active layer is selectively etched away and replaced with a regrown 1.3- μm quaternary layer as shown in Fig. 2(b). A single masking step is used to simultaneously define both active and passive waveguides together with the star coupler. The SiO_2 mask is kept only on top of the lasers and the optical waveguides during the regrowth for the lateral confinement. A semi-insulating planar buried heterostructure was grown for lateral optical and current confinement. Semi-insulating InP is also grown on top of the passive waveguides and the star coupler (see Fig. 2(b)), so that the optical loss is minimized.⁶ To achieve good electrical isolation, islands are formed for the lasers and the optical amplifiers by selectively etching down to the semi-insulating InP around each laser or optical amplifier. The leakage current between neighboring lasers is measured to be less than 30 μA at ± 3 volts bias. Antireflection facet coatings were applied to both facets of the chip.

Fig. 3 shows the CW lasing wavelength and the threshold current of the 21 lasers as a function of grating period. The wavelength channel spacing is 3.7 nm with a standard deviation of 0.34 nm except for one wavelength. The side-mode suppression ratio is typically better than 35 dB. The threshold current increases monotonically with decreased wavelength mainly because of the large negative wavelength detuning between the Bragg

wavelength and the gain peak wavelength ($\lambda_p = 1.6 \mu\text{m}$). By adjusting the bandgap of the quantum well, we expect to obtain low threshold over a wide wavelength range from 1500 to 1580 nm.

A finished chip has been packaged with a single mode fiber pigtail as an optical output, 50 Ω microstrip lines for DC and RF inputs and a thermoelectric cooler under the laser submount to maintain a constant temperature. A lensed single mode fiber is aligned to the middle output waveguide of the star coupler. With this packaged module, simultaneous fifteen wavelengths coupling into a single mode fiber has been achieved for the first time with a laser array. The lasers are biased at 20 mA above threshold using a current divider driven from a common voltage supply. The output optical spectrum is shown in Fig. 4(a). From the wavelength shifts, the temperature rises under simultaneous operation are estimated to be about 6-11 °C, depending upon where each laser is located within the chip. At constant driving current, the power variations among channels are due to the path length difference of the input waveguides of the star coupler in the longer wavelength region and the high laser threshold in the shorter wavelength region. The optical power can be boosted up by an erbium-doped fiber amplifier as shown in Fig. 4(b). The on-chip amplifier did not provide enough gain because of the shift of the gain peak during processing which will be corrected in the future. The inherent splitting loss of the star coupler can be avoided by forming a wavelength multiplexer with two star couplers as demonstrated in ref. [10].

In summary, we have demonstrated that photonic integration is useful for simplifying the coupling between laser arrays and single mode fibers. The optimal number of wavelengths to be integrated depends on the yield of the integrated chip, which will improve as the technology matures. Using photonic integration technology, we expect an integrated multi-wavelength laser transmitter for WDM lightwave systems to have a cost comparable to that of a single wavelength laser transmitter.

- [1] Optical Networks Technology Consortium, SOL BAA 91-14, 1992.
- [2] M. Nakao, et al., *IEEE Journal on Selected Areas in Communications*, 1990, 8, 1178-1182.
- [3] C. E. Zah, et al., *Electron. Lett.*, 1992, 28, 824-826, also 1585-1587.
- [4] S. Sekine, et al., *Tech. Dig., Optical Fiber Commun. Conf.*, San Diego, February 18-22, 1991, WC2.
- [5] C. A. Armiento et al., *Electron. Lett.*, 1991, 27, 1109-1111.
- [6] T. L. Koch and U. Koren, *J. of Lightwave Technol.*, 1990 8, 274-293.
- [7] M. Yamaguchi, et al., *Tech. Dig., 12th IEEE, Int. Semiconductor Laser Conf.*, Davos, Switzerland, 1990, 160-161.
- [8] H. M. Presby, *Tech. Dig., Optical Fiber Commun. Conf.*, San Jose, February 2-7, 1992, PD24.
- [9] C. Dragone, et al., *IEEE, Photon. Tech. Lett.*, 1989, 1, 241-243.
- [10] M. Zirngibl, et al., *LEOS Summer Topical Meeting on Integrated Optoelectronics*, 1992, PD3.
- [11] C. E. Zah, et al., *Tech. Dig., 13th IEEE, Int. Semiconductor Laser Conf.*, Takamatsu, Kagawa, Japan, September 21-25, 1992, 194-194.
- [12] A. S. Gozdz, et al., *Electronics Letters*, . 24, 1988, 123-125.

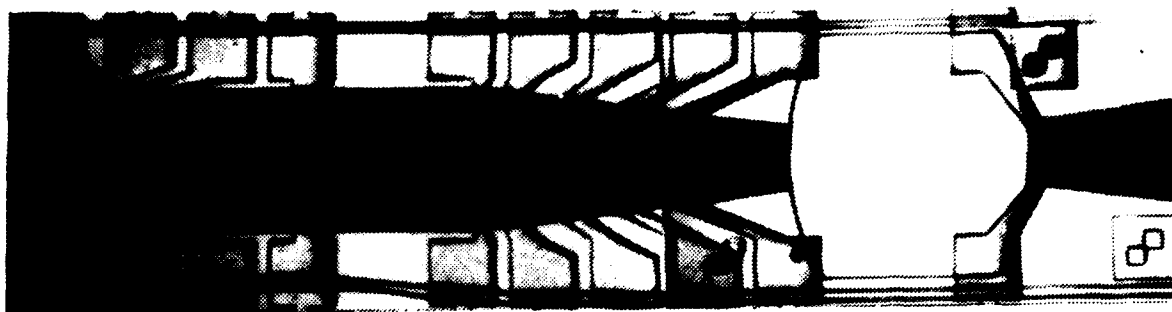


Fig. 1 Top view of a finished chip consisting of a multi-wavelength DFB laser array integrated with a star coupler and two optical amplifiers.

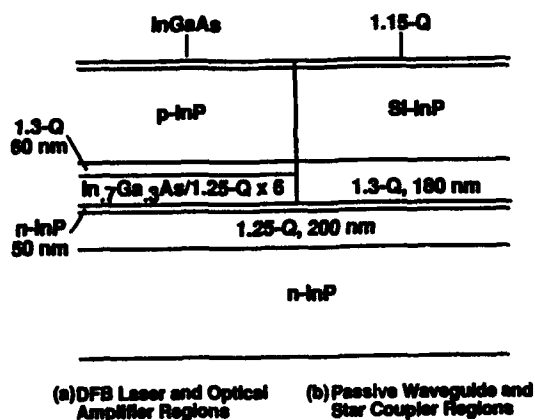


Fig. 2 Longitudinal cross-section of the layer structures. 1.25-Q stands for a quaternary layer with a bandgap wavelength of 1.25 μm .

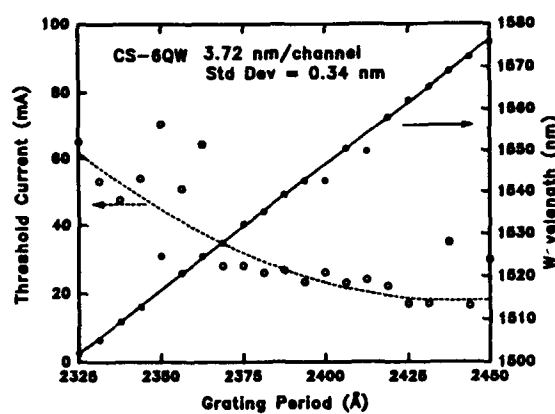


Fig. 3 Lasing wavelength and threshold current as a function of the grating period under CW operation at 15 °C heat sink temperature.

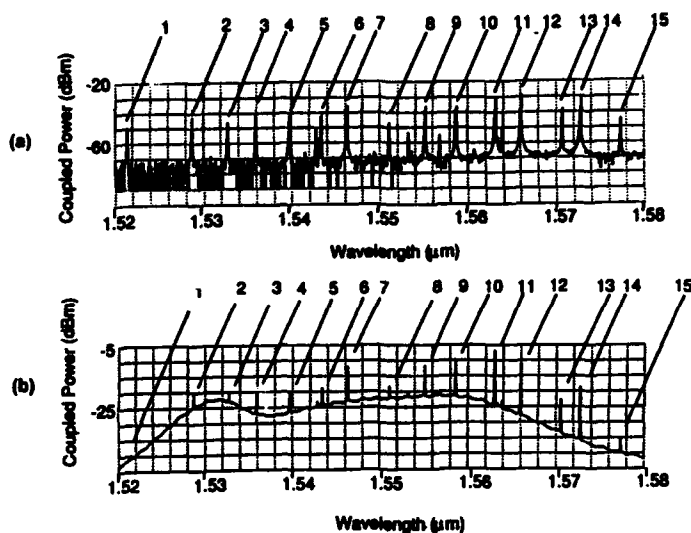


Fig. 4 Output optical spectrum from a packaged multi-wavelength laser module (a) without and (b) with amplification by an erbium-doped fiber amplifier. The noise floor comes from the amplifier spontaneous noise.

A 16x1 WDM Transmitter with Integrated DBR Lasers and Electroabsorption Modulators

M. G. Young, U. Koren, B.I. Miller, M.A. Newkirk, M. Chien, M. Zirngibl, C. Dragone, B. Tell, H.M. Presby, and G. Raybon

AT&T Bell Laboratories, Holmdel, New Jersey 07733
(908) 949-5974

Semiconductor laser arrays are being realized for wavelength-division-multiplexed (WDM) lightwave communication systems. Such arrays can increase the amount of transmitted information through a fiber link, or can be used for optical switching applications. By combining the signals on chip, the alignment of fibers to individual lasers is eliminated.

Recently, laser arrays with integrated combiners have been demonstrated [1-3]. Here we report a 16x1 laser array combining 16 distributed Bragg reflector (DBR) lasers with different optical frequencies into a single output. By using a recently reported high performance 1x16 splitter [4,5] and an integrated output amplifier we achieve high optical power coupled into a single fiber. The use of repeated holographic exposures for the Bragg gratings results in wavelength distribution from 1.544 μm to 1.554 μm with a channel spacing of approximately 6.7 \AA which is suitable for dense WDM applications.

A schematic diagram of the device is shown in Fig. 1. The array is grown on an InP substrate using four metal organic vapor phase epitaxial (MOVPE) growth steps. The active layer, providing the gain, is a strain-compensated stack of six compressively strained 35 \AA thick InGaAs quantum wells, separated by 100 \AA thick tensile strained 1.25 μm quaternary barriers [6]. These layers are selectively etched away, exposing the underlying waveguide layer to define the passive section as well as to allow the growth of a 1.46 μm quaternary layer to act as an electro-absorption modulator [7]. The passive 1.3 μm quaternary waveguides employ the buried rib configuration [8]. As mentioned, the gratings for the sixteen DBR lasers were defined by repeated holographic exposures using a window mask and transverse stage to align to the individual lasers. Wet chemical etching was then used to form the gratings. The signals from the lasers, spaced 250 μm apart, are combined using a novel combiner incorporating a free space radiation region. A more detailed description of the combiner can be found in references 4 and 5. The output waveguide consists of an amplifier to compensate for signal loss as well as a window region (see Fig. 1) with no waveguide to reduce the amount of reflection. The amplifier as well as the lasers and modulators are made with the semi-insulating blocked planar buried heterostructure (SIPBH) configuration and the active-passive transitions are obtained using photonic integration techniques as described previously [9]. The total width of the device is 4 mm and the total length is 6 mm.

The integration of external modulators allow the lasers to operate CW, thereby reducing mode partition noise and chirp. The response of an integrated electroabsorption modulator is shown in Fig. 2, using the output amplifier of the device as a photodetector. The modulation voltage to obtain an extinction ratio of 10 dB is approximately 2.5 volts. These modulators can operate at 2.5 GHz, which is sufficient for currently used transmission systems.

The distribution of CW lasing wavelengths for the 16 laser array is shown in Fig. 3. The wavelengths range from 1.544 μm to 1.554 μm with an average spacing of 6.7 \AA . Laser number 8 did not lase. Although the device was fabricated so that the Bragg wavelength could be electrically tuned, the results in Fig. 3 are obtained without active tuning. However, we are currently tuning the lasers using current injection in the Bragg sections in addition to resistive heating with a platinum resistor adjacent to the laser/grating pair (not shown in Fig. 1). In This way, we can adjust the laser frequencies to a set of predetermined values with high precision.

The performance of the combiner is shown in Fig. 4. By operating the output amplifier as a photodetector, we can determine the power launched into the output amplifier from each individual laser. In order to compensate for varying thresholds, the current to individual lasers was adjusted so that all would have the same output power. An average coupled power into the

amplifier of -15 dBm was obtained with a range of ± 2.5 dBm. The shape of the response shown in Fig. 4 is reproducible, and is similar to the splitter response in [5].

Figure 5 shows the power coupled into a recently developed micromachined lensed fiber [10] with a 56% coupling efficiency. In this case, all the lasers were kept at a constant injection current of 55 mA, and the output amplifier was kept at 70 mA. The highest coupled power was -4.4 dBm, with the average over the device being approximately -8 dBm per channel. The variation in the coupled power is due mainly to the variation in threshold current of the lasers, and not a result of the multiplexing, as demonstrated in Fig. 4.

In conclusion, we have demonstrated a 16x1 laser array with integrated external modulators using a previously reported passive splitter/combiner. The single output waveguide with integrated optical amplifier coupled an average of -8 dBm per channel into a single mode fiber. The performance of the combining region was demonstrated with a very uniform coupling into the output optical amplifier. Using holographic techniques and wet chemical etching, the operating wavelengths of 1.544 μm to 1.554 μm with a 6.7 Å channel spacing was obtained. We will present results of improved wavelength control with tuning by means of current injection and resistive heating.

REFERENCES

- [1] U. Koren, et al., *Appl. Phys. Lett.*, Vol. 54, 2056, 1989
- [2] M. Yamaguchi, et al., *Tech. Dig., 12th IEEE, Int. Semiconductor Laser Conf.*, 160, Davos, Switzerland, 1990
- [3] C.E. Zah, et al., *Tech. Dig., 13th IEEE, Int. Semiconductor Laser Conf.*, 194, Kagawa, Japan, 1992
- [4] U. Koren, et al., *Appl. Phys. Lett.*, Vol. 61, 1613, 1992
- [5] M. Zirngibl, et al., *Electron. Lett.*, 28, 1212, 1992
- [6] B.I. Miller, et al., *Appl. Phys. Lett.*, Vol. 58, 1952, 1991
- [7] U. Koren, et al., *Tech. Dig., Optical Fiber Communication Conf.*, 124, San Jose, 1992
- [8] T.L. Koch and U. Koren, *IEEE J. Quantum Electron.*, 27, 641, 1991
- [9] U. Koren, et al., *Tech. Dig. of the Int. and Guided Wave Optics Conference*, Paper MDD2., Houston, TX, 1989
- [10] H.B. Presby and C.A. Edwards, *Electron. Lett.*, 28, 582, 1992

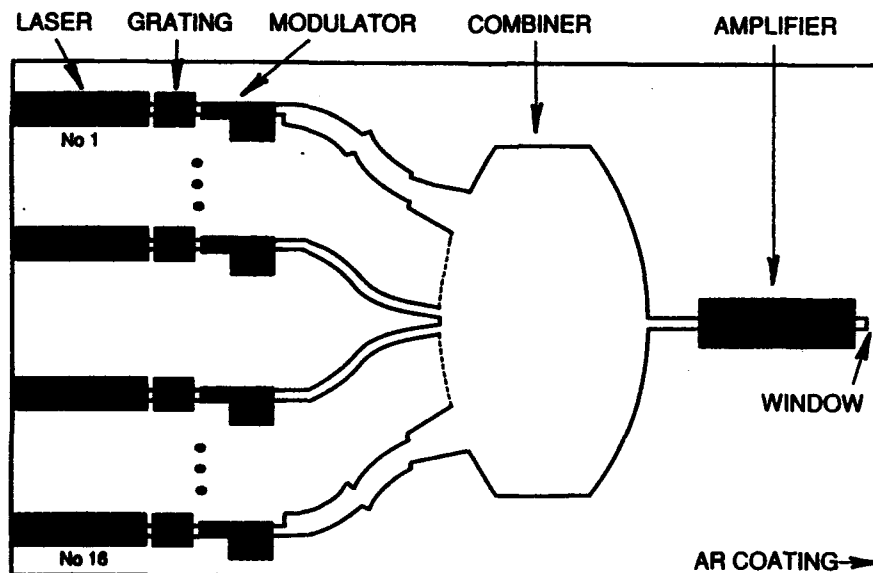


Fig. 1 Schematic diagram of the device.

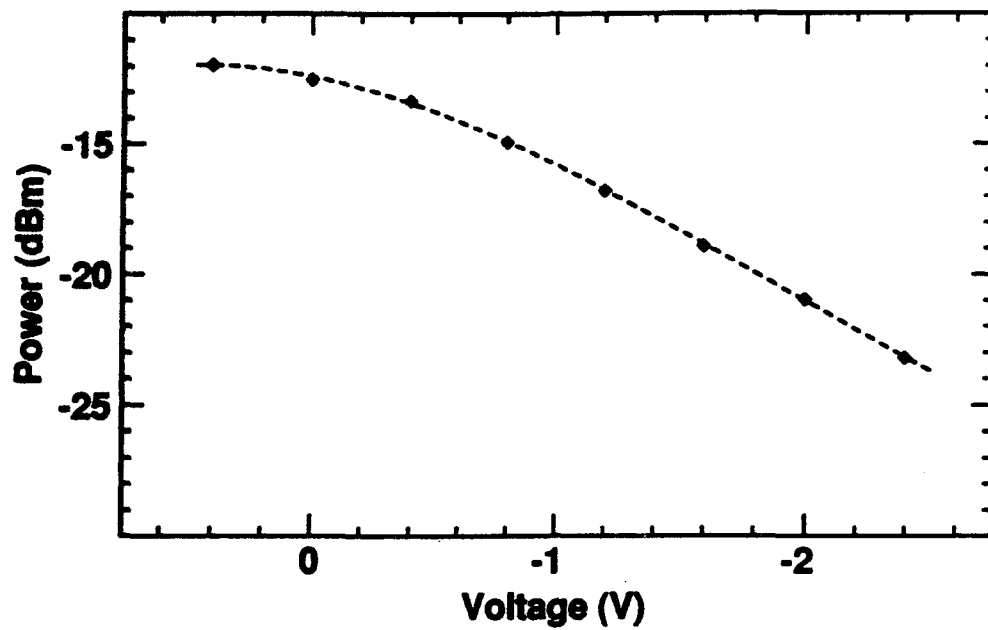


Fig. 2 Modulation response of one of the electroabsorption modulators. This is measured by operating the output amplifier as a photodetector.

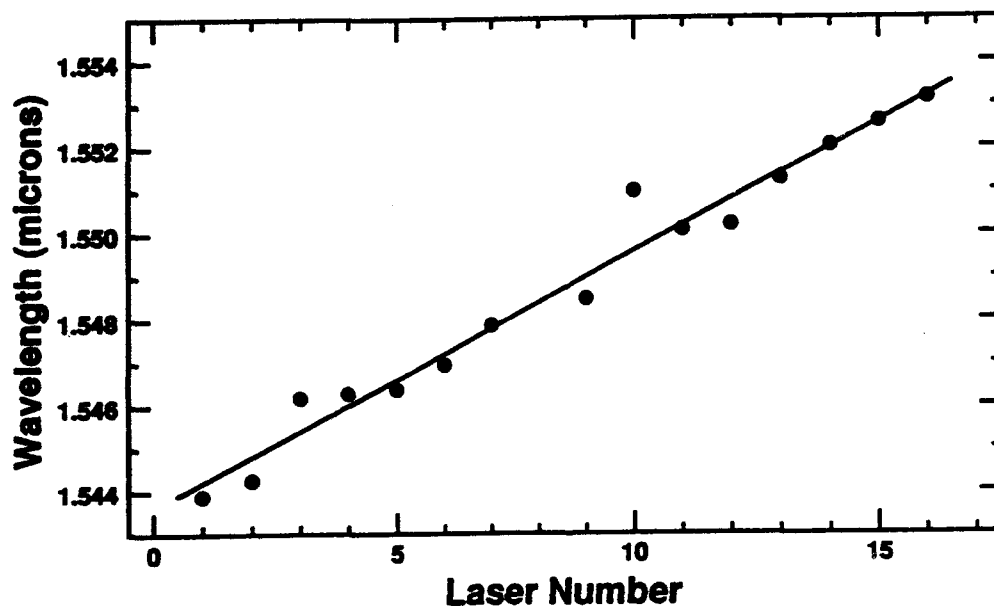


Fig. 3 Lasing wavelengths as a function of laser number. The average spacing is 6.7 Å.

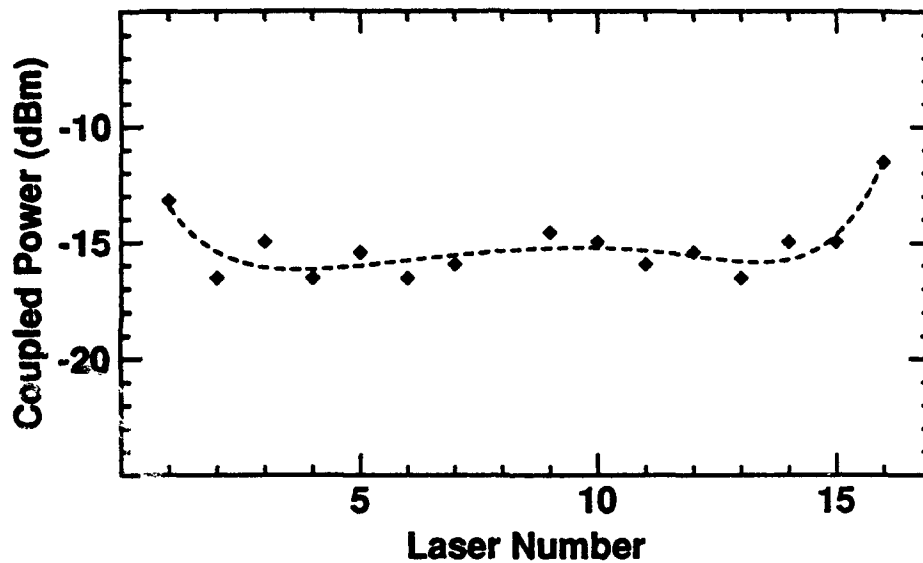


Fig. 4 Power launched into the output amplifier from each individual laser. This is measured by operating the output amplifier as a photodetector. The modulators are unbiased, and the lasers are held at constant power.

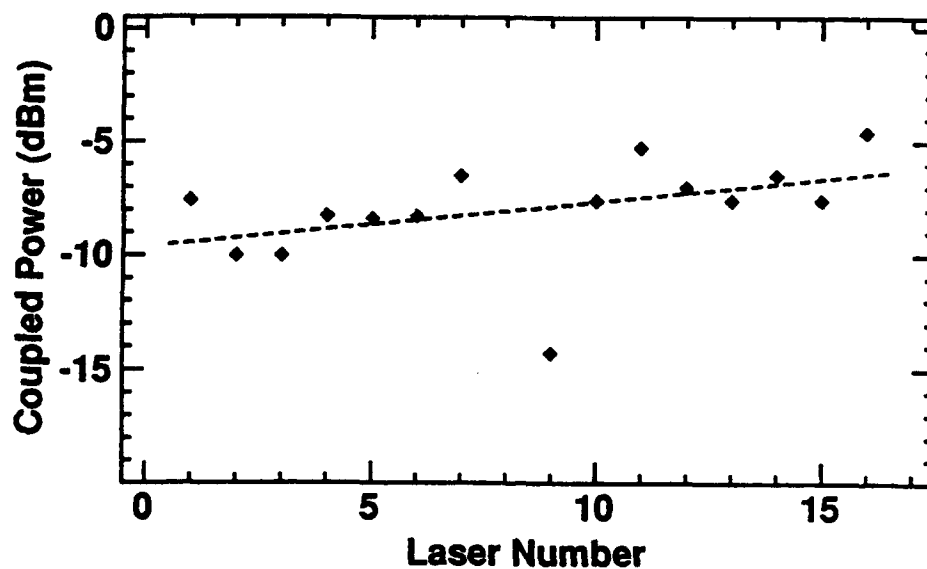


Fig. 5. Power coupled into micromachined lensed fiber. All lasers were held at a constant current of 55 mA, and the output amplifier was held at 70 mA.

A Detector-Switched GaAs Monolithic Time-Delay Network for Microwave Phased Arrays at L and X Band

W. Ng, D. Yap, A. Narayanan, R. Hayes
Hughes Research Laboratories
3011 Malibu Canyon Road
Malibu, CA 90265
(310) 317-5704

A. Walston
Hughes Aircraft Company
Radar Systems Group
Los Angeles, CA 90009

Recently, there has been much interest in the development of photonic techniques for steering microwave phased array radar over multiple microwave bands. In these optically controlled phased array antennas, guided lightwave is used as a carrier for distributing and delaying the microwave signals that drive and "phase-up" the antenna radiation elements. A first demonstration of the above concept was reported by Ng et al¹ using fiber-delay-lines. As described in Ref. 1, these optically controlled phased array antennas displayed instantaneous bandwidths of almost one frequency decade — from 2 to 9 GHz — which was previously unattainable. In this paper, we will report on the demonstration of a GaAs monolithic time-delay network (Fig. 1) for steering phased arrays from L (1-2.6 GHz) to X (8-12 GHz) band. Specifically, the monolithic time-delay network integrates the delay lines (curved GaAlAs/GaAs rib-waveguides) and MSM detectors that serve as optoelectronic switches on a GaAs substrate. Aside from compactness, the GaAs time-shift network offers more precision for the RF phase than fiber-delay-lines¹ because the lengths of the waveguides on the GaAs wafer, as defined by photolithography, can be fabricated to micrometers of accuracy. Finally, the integration of detectors to the optical waveguides eliminates a delicate fiber-device interface between the delay-lines and optoelectronic switches that control the delay times.

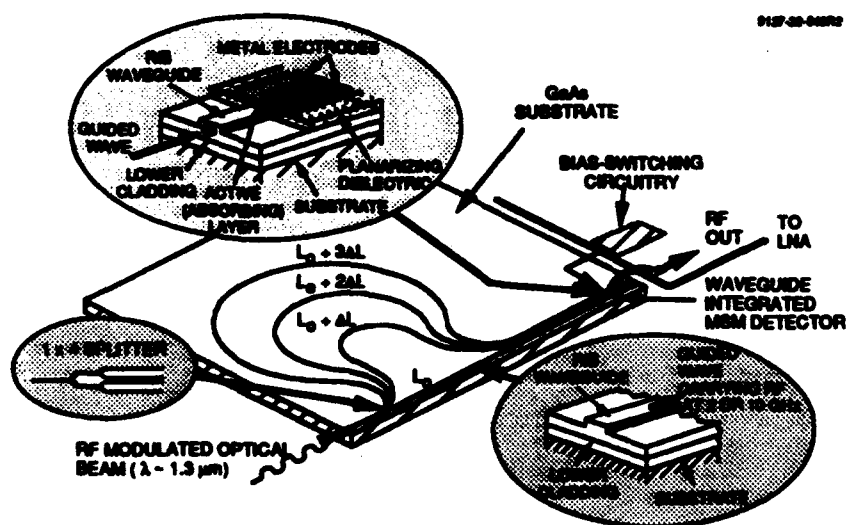


Fig. 1. Monolithic time-delay network integrating rib-waveguides and waveguide-coupled MSM detectors on GaAs substrate.

As shown in Fig. 1, the optical input to the network is an RF-modulated beam from a $\lambda = 1.3 \mu\text{m}$ GaInAsP/InP laser. The RF output from each of these networks addresses a specific antenna radiating element after amplification. As a 2-bit time-shifter, the depicted network consists of four delay lines whose lengths are designed to be $L_0, L_0+\Delta L, L_0+2\Delta L, L_0+3\Delta L$. After going through a 1×4 splitter, the RF signal is delayed by the propagation time ($t_0, t_0+\Delta t, t_0+2\Delta t, t_0+3\Delta t$) of its optical carrier in the four rib waveguides. The detector array coupled to the waveguides serves as an optoelectronic switch that "selects" a designated delay time for the radiating element it addresses. For example, by turning on the bias of the detector integrated to the waveguide with length $L_0+2\Delta L$, we "switch" out the RF signal delayed by $t_0+2\Delta t$. Because the photo-currents of MSM detectors are always clamped to a null at zero bias, we routinely achieve² on/off ratios of better than 40 dB for the RF output from the detector array.

The monolithic time-delay network were fabricated from epitaxial layers grown by MOVPE. The rib waveguides, fabricated by RIE, consist of a GaAs waveguiding layer and a $\text{Al}_{0.1}\text{Ga}_{0.9}\text{As}$ lower cladding layer that are $1.5 \mu\text{m}$ and $3.0 \mu\text{m}$ respectively. We characterized the propagation losses of straight segments of these waveguides with the Fabry-Perot resonance technique, and measured losses as low as 0.3 dB/cm. Figure 2 shows the combined optical losses of rib waveguides (rib height = $1.1 \mu\text{m}$) with S-bend geometries designed to have different radii (R) and rib widths (W). The overall waveguide loss of these S-bends included contributions from the propagation loss, bend loss, and transition loss between the curved and straight segments in the S-bend. As shown, the combined optical loss was only ~ 1 dB/cm for S-bends with R and W greater than 2 mm and $2 \mu\text{m}$, respectively. The waveguide losses shown in Fig. 2 are comparable to some of the best reported³ for S-bend geometries. Figure 3 shows a mask layout for two delay networks with different L_0 and ΔL . To minimize the optical, and therefore RF insertion loss, the radii of curvature of the curved waveguides in the network were all designed to be 3 mm or larger. Their rib width is $\sim 6 \mu\text{m}$. The waveguide-integrated MSM detectors at the end of the delay lines are spaced $700 \mu\text{m}$ apart to facilitate coupling to an off-chip hybrid circuit designed for bias control and RF-matching.

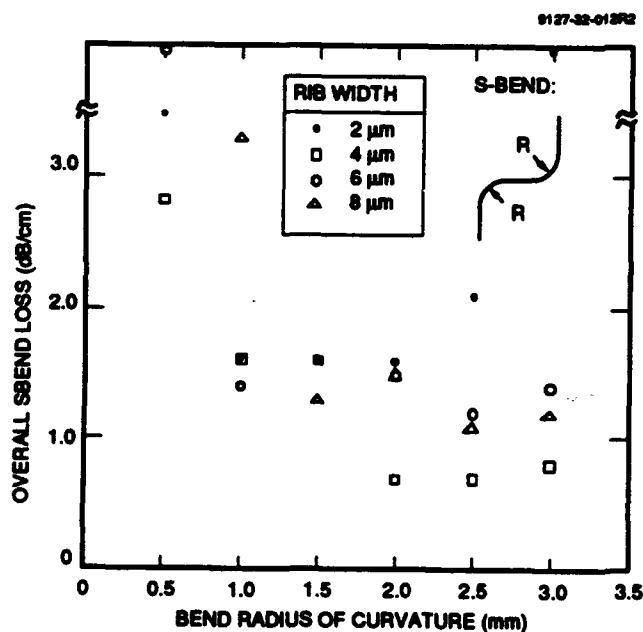


Fig. 2. Measured loss of S-bend waveguides plotted versus bend radius of curvature (R) and rib-width.

Figure 4 shows the SEM photograph of an $\text{In}_{0.35}\text{Ga}_{0.65}\text{As}/\text{GaAs}$ MSM detector array integrated at the end of four waveguide-delay-lines. The active area of the detector is $\sim 100 \times 10 \mu\text{m}$. Their Ti-Pt-

Au fingers, spaced $1.5 \mu\text{m}$ apart, are $2 \mu\text{m}$ wide. Figure 5 shows the detectors' RF response, measured with cascade-probes, when they were excited by a pigtailed semiconductor laser coupled to the delay-lines. The $1.3 \mu\text{m}$ GaInAsP/InP laser was biased to a resonance frequency of ~ 9 GHz. In this particular wafer, the lengths of the waveguides integrated with the detectors were ~ 1.3 cm. Using a microwave network analyzer, we characterized the differential RF insertion phase ($\Delta\phi$) between different delay lines on the same chip. We obtained a $\Delta\phi$ of ~ 10 degree/mm of length difference (ΔL_0) between the delay lines at an RF frequency (f) of 3 GHz. This is in rough agreement with the theoretical value of 12.6 degree/mm given by $\Delta\phi/\Delta L_0 = (2\pi f n)/c$, where n is the effective index of the waveguides. Further details will be presented in the talk.

ACKNOWLEDGMENT:

This work is partially supported by the Rome Laboratory, Griffiss AFB, NY 1344-5700.

REFERENCES:

1. W. Ng, A. Walston, G. Tangonan, J.J. Lee, I. Newberg, and N. Bernstein, *J. Lightwave Technol.* vol. LT-9, pp. 1124-1131, 1991.
2. W. Ng, A. Narayanan, R. Hayes, and D. Yap, Paper TuA2-1, Integrated Photonics Research Conference, April 13-16, 1992, New Orleans, Louisiana.
3. R. Deri and E. Kapon, *IEEE J. Quantum Electron.*, vol. QE-27, pp. 626-640, 1991.

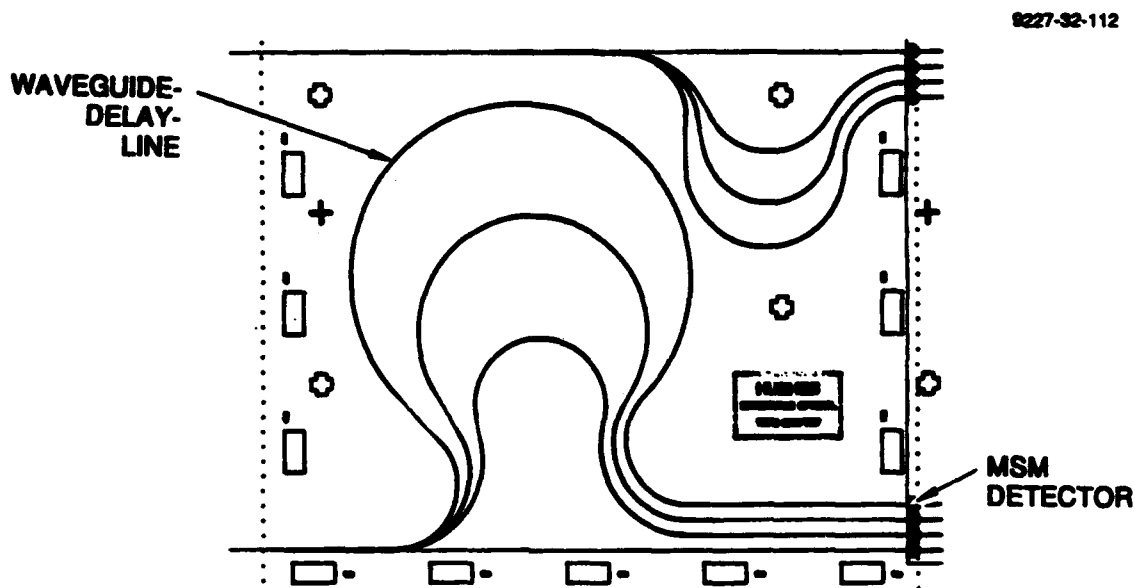


Fig. 3. Mask layout (x 4) for two 2-bit delay networks.

9227-32-105

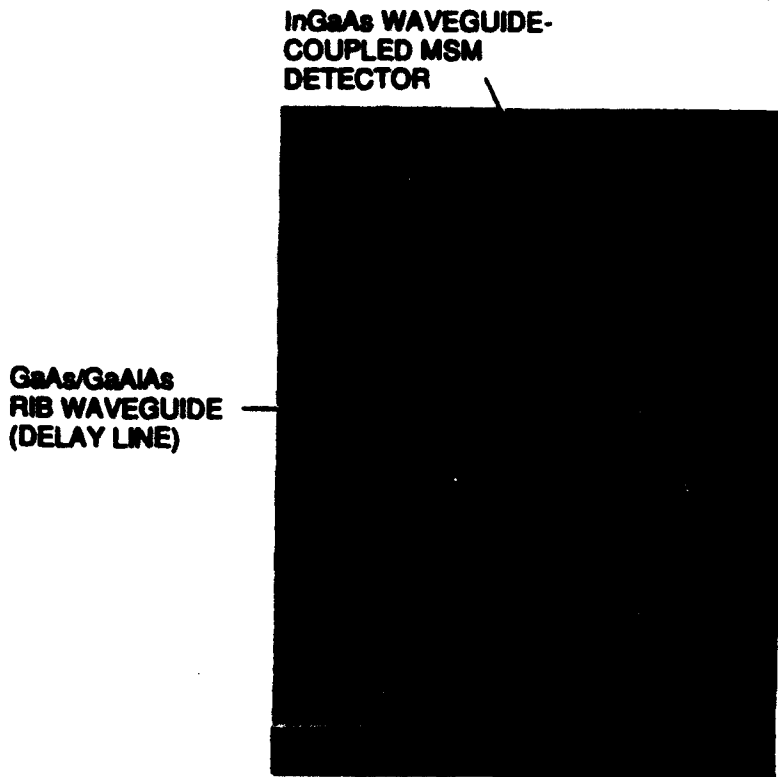


Fig 4. SEM photograph of MSM detector array integrated to delay lines.

9227-32-102

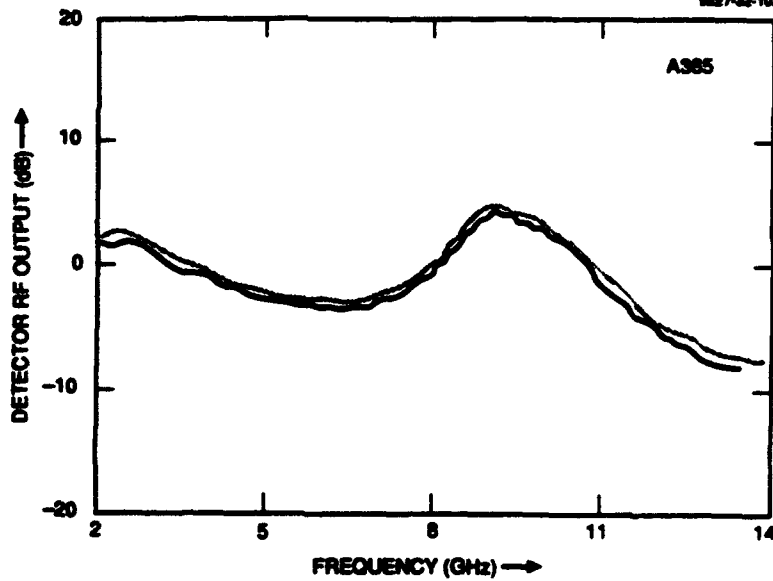


Fig. 5. Frequency response of on-chip detectors excited by 1.3 μ m diode laser.

Electroabsorption Effect in $\text{Ge}_x\text{Si}_{1-x}/\text{Si}$ Multiple Quantum Wells at Room Temperature

Suhail Murtaza, Andalib A. Chowdhury, M. Mahbub Rashed, Christine M. Maziar, Joe C. Campbell
Microelectronics Res. Ctr., Dept. of Elec. & Comp. Eng., Univ. of Texas at Austin, Austin, TX 78712

A red shift of the fundamental absorption edge due to an electric field applied perpendicular to the multiple quantum wells (MQWs) may result from quantum effects such as the Quantum Confined Stark Effect (QCSE) [1] and has already been demonstrated in several compound semiconductors, e.g. the GaAs/AlGaAs system [2] and the InP/InGaAs system [3]. However, no such room-temperature effects have been reported for the $\text{Ge}_x\text{Si}_{1-x}$ system although the presence of the QCSE has been indicated and photocurrent measurement results at 77 K have been shown [4]. In this communication we present room temperature photocurrent measurements in $\text{Ge}_x\text{Si}_{1-x}/\text{Si}$ MQWs grown by Remote Plasma-enhanced Chemical Vapor Deposition (RPCVD) [5],[6]. These measurements indicate that optoelectronic devices such as optical modulators [7] and Self Electrooptic Devices (SEEDs) [8] operating at the technologically important wavelengths of 1.3 μm and 1.55 μm can be realized.

A schematic cross-section of the device is shown in Fig. 1. A 0.5 μm -thick, p-doped ($5 \times 10^{17} \text{ cm}^{-3}$) $\text{Ge}_{0.2}\text{Si}_{0.8}$ buffer layer was grown by RPCVD on top of a p-type ($5 \times 10^{17} \text{ cm}^{-3}$), (100) Si substrate. The buffer layer allows the MQWs and barriers that follow to be symmetrically strained [9],[10]. This relaxes the critical thickness limitations, thus allowing a larger number of quantum wells to be grown [11]. Twenty-five 80 Å-thick $\text{Ge}_{0.4}\text{Si}_{0.6}$ QWs were grown on top of the buffer layer with twenty-five 80 Å-thick Si barriers. The MQWs were not doped intentionally. The MQW region was followed by a 0.1 μm , n-doped ($5 \times 10^{17} \text{ cm}^{-3}$) $\text{Ge}_{0.2}\text{Si}_{0.8}$ layer and a n⁺-doped ($5 \times 10^{18} \text{ cm}^{-3}$) Si contact layer. The structure is, in essence, that of a p-i-n photodiode with MQWs in the intrinsic region (to allow the maximum electric field to appear across the quantum wells). The devices were isolated from each other by etching 1.0 μm -deep mesas using a CF_4 plasma. This was followed by a 0.3 μm wet etch to remove the plasma damage. The resulting mesa depth was 1.3 μm and the diameter was approximately 470 μm . The top Al contact was 75 μm in diameter. Thus, most of the mesa area was available for top illumination.

Figure 2 shows the dark current and the photoresponse of one of the diodes. At a reverse bias of 8 V, the dark current was 314 nA. Capacitance-voltage measurements show the QWs to be fully depleted at zero bias. This is important as we want to ensure that the electric field across the intrinsic region varies linearly with the applied reverse voltage.

We used photocurrent measurements to demonstrate the shift in band edge with applied bias. Photocurrent spectra were taken as a function of wavelength for different biases. To eliminate the effects of increased carrier transport due to bias, these spectra were normalized with respect to a wavelength (1160 nm) where any changes in the absorption coefficient with bias were negligible. In the absence of any band gap change with bias, all the normalized spectra would be expected to lie neatly on top of one another in the whole wavelength range of interest. However, with the red shift in the absorption edge, the normalized photocurrent was found to increase with increasing bias, more so at near-band-gap energies.

We used a tungsten-halogen light source to illuminate a spectrometer grating. The light output from the spectrometer was passed through a series of six long-pass filters to suppress the higher-order shorter wavelengths. Each filter was made of 3 mm-thick black glass, had a cut-off wavelength of approximately 1000 nm, and provided an attenuation of more than 10^{-5} at wavelengths shorter than 800 nm. The filters were needed because of the much higher absorption coefficient of the thick silicon substrate at these short wavelengths as compared to the $\text{Ge}_x\text{Si}_{1-x}$ response at the longer wavelengths. After mechanically chopping the light beam, it was focused on to the photodetector by a microscope objective. The photocurrent was measured with a lock-in amplifier which was phase locked to a reference signal from the chopper. Figure 3 shows the normalized photocurrent measurements for different applied electric fields.

The band alignment in the Quantum Wells is staggered type II. Under an applied electric field ϵ , the change in transition energy may be written as $\Delta E_1 + \Delta H H_1 \pm e\epsilon L$ where ΔE_1 and $\Delta H H_1$ are the shifts in the ground state electron and heavy hole energy levels, respectively, and L is the width of the quantum wells. The last term is responsible for the large linear energy shifts seen in type II structures. It can be shown that for thicknesses much less than the absorption length ($1/\alpha$), the absorption coefficient α is proportional to the product of the photocurrent (I) and the photon energy ($h\nu$). Figure 4 shows a plot of $Ih\nu$ versus $h\nu$. It is observed that near 800 meV (the transition energy of the MQW) α varies as $(h\nu - E_{g0})^{1/2}$ for different applied electric fields. From this fit, the absorption edge (E_{g0}) may be estimated at different electric fields. A linear edge shift towards lower energies with increased electric field may be observed in Figure 5. Figure 5 illustrates the good agreement found between the experimentally obtained shift and that calculated within the framework of the envelope function approximation [12], neglecting intervalley interaction. The bandoffsets were estimated from the combination of self-consistent *ab initio* pseudopotential results [13] and the phenomenological deformation potential theory [14]. To understand the spectra at higher energies, we have subtracted the $(h\nu - E_{g0})^{1/2}$ dependency from the measured data and obtained the shape of the absorption curve of the $\text{Si}_{0.8}\text{Ge}_{0.2}$ buffer layer (Figure 6). This is found to be similar to the shape reported by Braunstein, et al. [15]. It is interesting to note the square root dependence of absorption coefficient on photon energy (which is characteristic of bulk direct band gap materials) is different from that of ref. 4, where Park et al. observed a square dependence.

In conclusion, we have presented the first room temperature measurements of electro-absorption effects in $\text{Ge}_x\text{Si}_{1-x}/\text{Si}$ multiple quantum wells. The MQWs and the buffer layers were grown by RPCVD. These measurements can be used to design optoelectronic devices that operate at 1.3 and 1.55 μm . These devices will have the advantages of low costs of manufacturing and the robustness of mature silicon technology.

We are thankful to B. G. Streetman and D. L. Kwong for their encouragement and valuable suggestions. The Si wafers used as substrates for crystal growth were supplied by MEMC and the work was supported by grants from National Science Foundation (ECS-N101187) and The Office of Naval Research (ONR-N00014-92-J-1085).

References

1. D. A. B. Miller, D.S. Chemla, T.C. Damen, A. C. Gossard, W. Wiegmann, T. H. Wood, and C. A. Burrus, "Band-Edge Electroabsorption in Quantum Well Structures: The Quantum-Confined Stark Effect," *Phys. Rev. Lett.* 53, 2173, 1984.
2. T. H. Wood, C. A. Burrus, D. A. B. Miller, D. S. Chemla, T. C. Damen, A.C. Gossard, and W. Wiegmann, "3 ps optical modulation in semiconductor multiple quantum wells," *IEEE J. Quantum Electronics*, 21, 117, 1985.
3. U. Koren, B. I. Miller, R.S. Tucker, G. Eisestein, I. Bar-Joseph, D. A. B. Miller, and D. S. Chemla, "High frequency InGaAs/InP multiple quantum well buried mesa electroabsorption optical modulator," *Electron. Lett.* Vol.23, 621, 1987.
4. J. S. Park, R. P. G. Karunasiri, and K. L. Wang, "Observation of large Stark shift in $\text{Ge}_x\text{Si}_{1-x}$ multiple quantum wells," *J. Vac. Sci. Technol.*, B 8 (2), Mar/Apr 1990.

5. L. Meiners, "Indirect Plasma Deposition of SiO₂," J. of vacuum science and technol., 21 (2), 655 (1982).
6. D. Kinosky, R. Qian, J. Irby, T. HSu, B. Anthony, S. BAnerjee, A. Tasch, C. Magee, and C. L. Grove, "Low-temperature growth of Si_{1-x}Ge_x/Si heterostructures on Si (100) by remote plasma-enhanced chemical vapor deposition," Appl. Phys. Lett. 59 (7), p817 (1991).
7. T. H. Wood, "Multiple Quantum Well (MQW) Waveguide Modulators," J. Lightwave Technol., vol. 6, no. 6, June 1988.
8. D. A. B. Miller, D. S. Chemla, T. C. Damen, A.C. Gossard, W. Wiegmann, T. H. Wood, and C. A. Burrus, "Novel hybrid optically bistable switch: The quantum well self electrooptic device," Appl. Phys. Lett., 45 (1), July 1984.
9. R. Hull, J. C. Bean, F. Cerdeira, A.T. Fiory, and J. M. Gibson, "Stability of Strained-Layer Superlattices," Appl. Phys. Lett. 48, 56, (1986).
10. J. C. Bean, "Silicon Based Semiconductor Heterostructures: Column IV Bandgap Engineering," To be published in the Proceedings of the IEEE.
11. Roosevelt People, "Physics and applications of Ge_xSi_{1-x} strained layer," IEEE J. Quantum Electron., vol. 22, no. 9, September 1986.
12. G. Bastard, and J. A. Brum, J. Quantum Electronics 22, 1625 (1986).
13. C. G. Van de Walle and R. M. Martin, J. Vac. Sci. Technol. B 4, 1055 (1986).
14. R. People, Physical Rev. B 34, 2508 (1986).
15. R. Braunstein, A. R. Moore, and F. Herman, Phys. Rev. 109, 695 (1958).

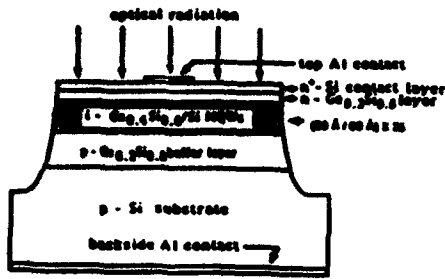


Fig. 1: A schematic cross-section of the device studied.

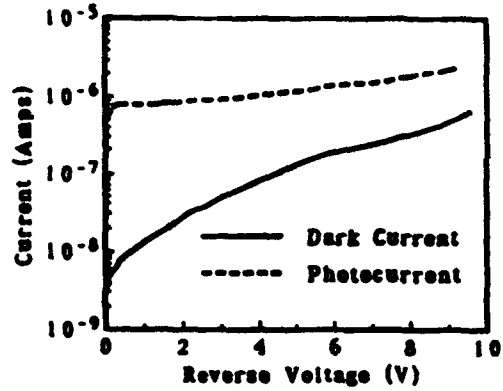


Fig. 2: Dark current and photocurrent versus reverse voltage for the device of Fig.1.

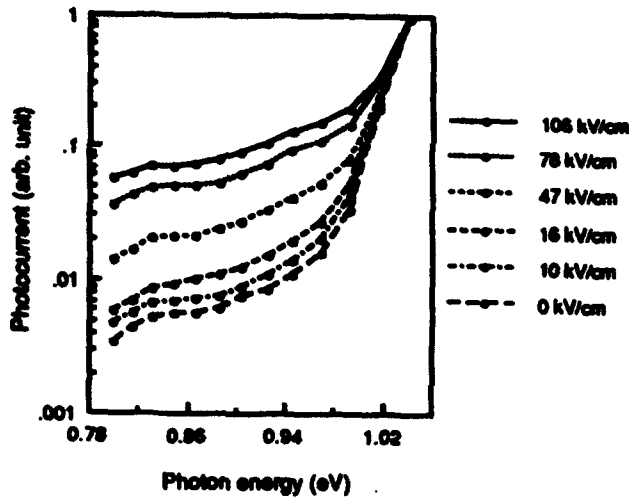


Fig. 3: The measured room temperature photocurrents as a function of photon energy under different estimated electric fields.

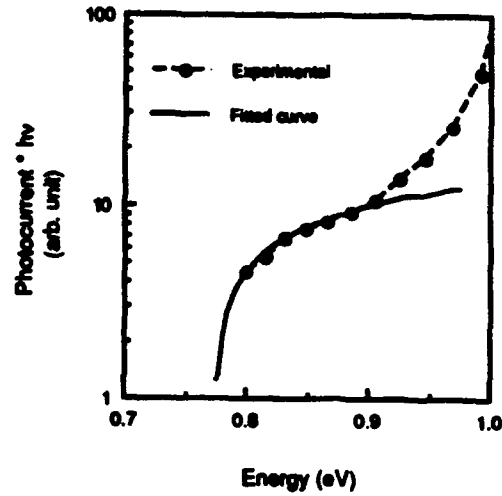


Fig. 4: Typical example of the curve fitting procedure at lower energies. The applied electric field in this case was 16 kV/cm.

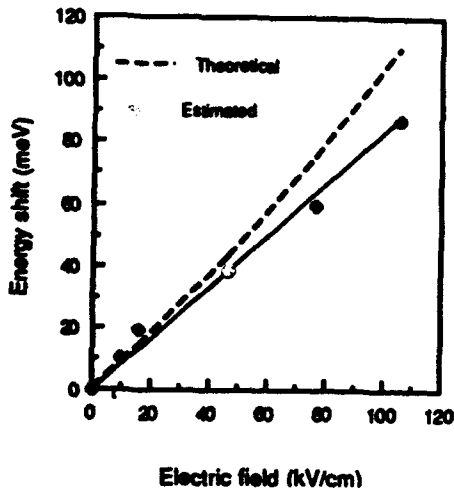


Fig. 5: Magnitude of the absorption edge shift as a function of electric field. The reference point was taken at zero electric field.

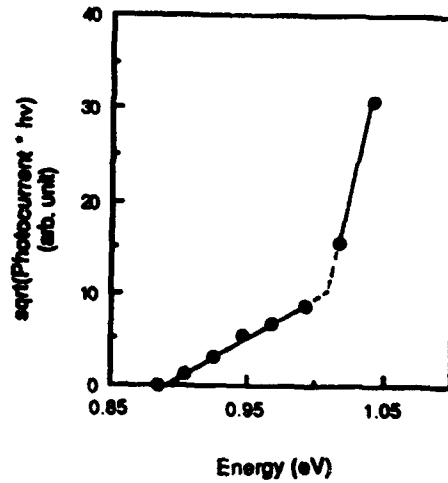


Fig. 6: Sqrt of (photocurrent * hv) as a function of photon energy. These points were obtained by subtracting the $(hv - E_{g0})^{1/2}$ dependency (Fig. 4) from the measured results.

Millimeter Wave Optical Transmission Using a Tunable Laser Beatnote Source with Feedforward Compensation

Olav Solgaard, John Park, John B. Georges, Petar K. Pepeljugoski, Kam Y Lau.
 University of California at Berkeley,
 Department of Electrical Engineering and Computer Science
 231 Cory Hall, Berkeley, CA 94720.
 Phone (415) 643-5849

High frequency optical modulation is required in many applications in satellite communication, mm-wave distribution and phased array radar. Traditionally this is achieved by direct modulation of a semiconductor laser diode, or through the use of an external modulator. Direct modulation has been demonstrated up to 30 GHz [1] and traveling wave LiNbO₃ external modulators to beyond 40 GHz [2]. We present a modulation technique which potentially can be used at frequencies >100 GHz. We have experimentally demonstrated simulated radar pulse transmission at 40 GHz. The technique is based on the use of a low frequency external modulator to compensate for the phase noise on the beatnote of two laser diodes as shown in Fig. 1.

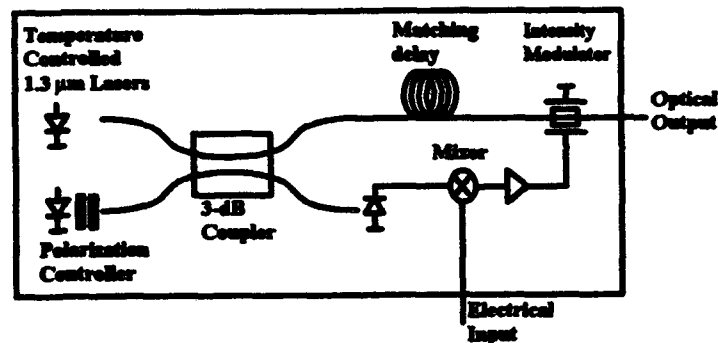


Figure 1 Schematic drawing of the optical modulator. The input is mixed with the detected laser beatnote, and the down converted signal drives the optical modulator to create an optical modulation proportional to the input.

The outputs of the two single frequency laser diodes are combined in a directional coupler, producing an intensity beatnote whose spectral width is approximately twice that of the laser linewidth (>1MHz). One of the coupler outputs is detected and mixed with the input signal to the modulator. The up-converted beat note is filtered out and the down converted mixer product is amplified and applied to the optical modulator that modulates the other output from the fiber optic directional coupler. Assuming that the modulator is operated in the linear region, we can express the output as

$$I_{out} = \frac{I_0}{2} \{1 + k \cos[\omega_b t + \Theta(t)] - m \cos[(\omega_m - \omega_b)t + \Theta(t + \tau)] - \frac{km}{2} (\cos[(2\omega_b - \omega_m)t + \Theta(t + \tau) + \Theta(t)] + \cos[\omega_m t + \Theta(t) - \Theta(t + \tau)])\} \quad (1)$$

where I_0 is the total intensity of the two lasers, k is the modulation index of laser beat note, m is the modulation depth achieved by the down converted mixer product driving the modulator, $\Theta(t)$ is the time dependent phase of the laser beat note, τ is the difference in time delay of the two paths from the coupler to the modulator, ω_b is the laser beat note frequency, ω_{in} is the frequency of the input signal. The last term represents the electrical input modulating the optical carrier, and we note that the phase noise of this component goes to zero if the delay difference, τ , is set to zero. To quantify the influence of the delay difference, we find the power spectrum of the last term in the above equation. Assuming that the input is a pure sine wave and that the laser beat note has a Gaussian distribution with a coherence time t_b (i.e. the beat note is a Lorentzian with a $1/\pi t_b$ linewidth), the power spectrum is

$$S(\omega) = 2\pi e^{-\frac{|\omega|}{t_b}} \delta(\omega) + \frac{2t_b}{\omega^2 t_b^2 + 1} \left\{ 1 - \left(\frac{|\tau| \sin(\omega|\tau|)}{t_b \omega|\tau|} + \cos(\omega|\tau|) \right) e^{-\frac{|\omega|}{t_b}} \right\} \quad (2)$$

where ω is the frequency offset from ω_{in} . This simplifies to a delta function for $\tau=0$, as we would expect from Eq. 1.

The frequency of operation and the tunability of this modulation technique is determined by the tunability of the lasers, while the usable bandwidth of this modulation technique will be limited by the bandwidth of the optical modulator, and the required signal-to-noise ratio, which sets a lower limit on the frequency difference of the signal and the beatnote (see Eq. 4 below).

It is clear from the above that in addition to shot noise, thermal noise and laser relative intensity noise, which are the traditional noise sources influencing fiber optic links, there are two extra noise sources which must be considered when analyzing the above described modulation technique. It is realistic to assume that the delay difference can be reduced to less than 1 ps, which corresponds to roughly 200 μm of propagation in a silica waveguide. We then have $\tau \ll t_b$ and $\tau \ll 1/\omega$, and the spectrum can be simplified to

$$S(\omega) = 2\pi e^{-\frac{|\omega|}{t_b}} \delta(\omega) + \frac{|\tau|^2}{t_b} \quad (3)$$

Note that under the above assumptions, the noise is not a function of the frequency offset, and the signal-to-noise ratio (S/N) is given simply by $2\pi t_b / |\tau|^2$. It follows that in a well-designed system with ps control of the time delay, and lasers with a coherence time larger than 10 ns, the noise side bands on the signal are negligible. The term $k \cos[\omega_b t + \Theta(t)]$ in Eq. 1 will also contribute noise in the signal band (the other terms are further removed from the signal and therefore less important). The S/N due to this term is given roughly by

$$S/N = \frac{m^2 \omega_d^2 t_b}{8B} \quad (4)$$

where ω_d is the difference frequency $\omega_{in} - \omega_b$. With $m=0.7$, $f_d=20$ GHz and $t_b=160$ ns (corresponding to a beat note linewidth of 2 MHz), this evaluates to 142 dB (1 Hz), showing that high S/N is possible.

The experiment shown schematically in Fig. 1 was carried out using two 1.3 μm DFB lasers. Thermo-electric coolers were used to stabilize and control the temperature of the lasers. The laser beat note was tunable over a wide range (>100 GHz), can be accurately modeled as a

Lorentzian with a 25 MHz full-width-at-half-maximum (corresponding to a coherence time of 13 ns) close to the line center, but has roughly 5 dB of extra noise more than 2 GHz away from the peak. We used an optical modulator with a 3 dB bandwidth of 4 GHz.

Fig. 2 shows a typical intensity spectrum for the modulated light. The input frequency and the beat note components from Eq. 1 can be identified. The delay is adjusted to maximize the ω_{in} component. The S/N of the replica of the input signal is 103.3 dB (1 Hz), in good agreement with Eq. 4 that gives $S/N=108$ dB (1 Hz) with $m=0.5$, $t_b=13$ ns and $f_d=2$ GHz. The linewidth of the output signal is narrower than the resolution bandwidth of our spectrum analyzer and is assumed to be limited by the microwave input.

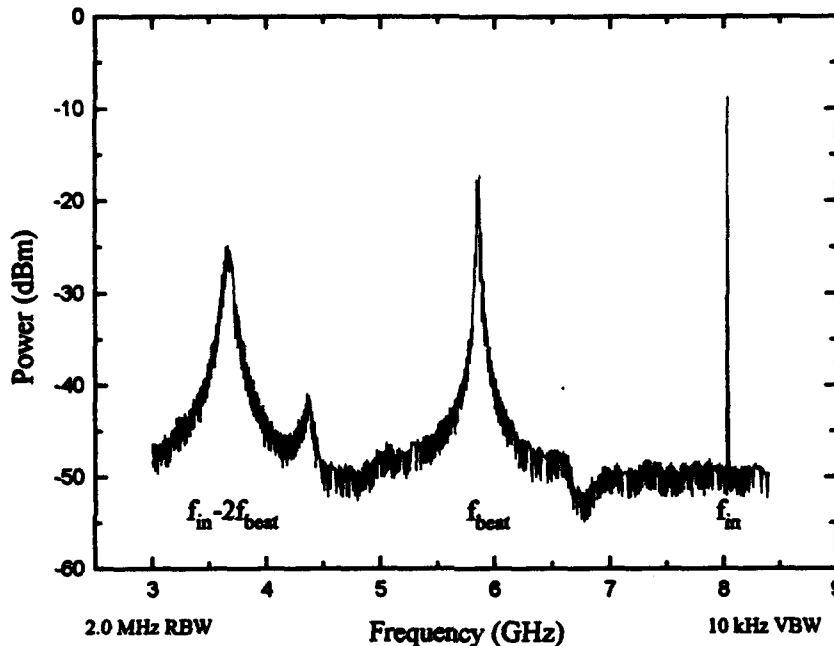


Figure 2 Typical power spectrum showing the modulator output with a pure sine wave at 8 GHz as input. The ω_b , the $\omega_{in}-2\omega_b$ and the ω_{in} terms of Eq. 1 are shown. The carrier-to-noise ratio of the replica of the input is 103.3 dB (1 Hz). The component around 4.4 GHz is the second harmonic of the down converted signal created by the nonlinearity of the optical modulator.

To demonstrate the high frequency capability of this modulation technique, we performed transmission experiments of a simulated radar pulse (1.3 μ s pulse width) at 40 GHz. Fig. 3 shows a the received spectrum as compared to the spectrum of the input simulated radar signal. The input signal is created by switching a 20 GHz carrier at 250 KHz with a duty cycle of roughly 35 %, followed by a frequency doubling. The result is a 250 KHz comb function with a sinc function squared envelope centered at 40 GHz and with the first nulls close to the third harmonic. The excellent correspondence between the input and output spectra demonstrates that a 40 GHz signal can be transmitted with good fidelity.

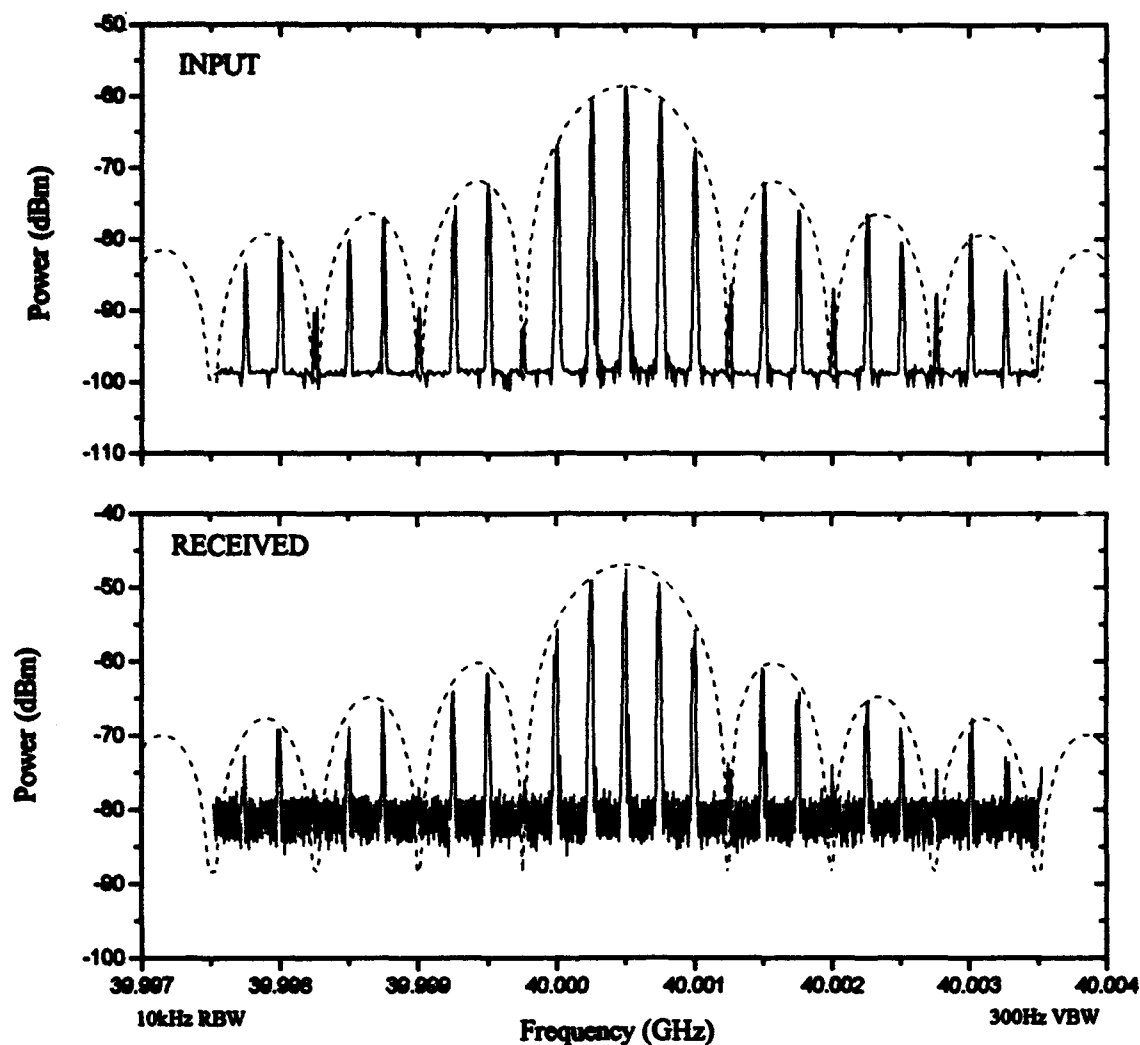


Figure 3 Comparison of input and received spectrum, showing that the modulation technique can be used for transmission with good fidelity at 40 GHz.

We have described a novel type technique for high speed, band limited optical modulation. Experimentally we measured a signal-to-noise of 103.3 dB (1 Hz) at 8 GHz, and demonstrated transmission at 40 GHz with good fidelity. With proper optimization of parameters, the S/N can exceed 140 dB (1 Hz). The wide tunability and good signal quality, make this modulation technique a promising candidate for high frequency optical signal distribution in phased array antenna systems and satellite communication.

References

- 1 S. D. Offsey, L. F. Lester, W. J. Schaff, L. F. Eastman, "High-speed modulation of strained-layer InGaAs-GaAs-AlGaAs ridge waveguide multiple quantum well lasers", *Appl. Phys. Lett.*, vol. 58, no. 21, pp. 2336-2338, 27 May 1991.
- 2 R. L. Jungerman, C. Johnson, D. J. McQuate, K. Salomaa, M.P. Zurakowski, R. C. Bray, G. Conrad, D. Cropper, P. Hernday, "High Speed Modulator for Applications In Instrumentation", *Journal of Lightwave Technology*, vol. 8, no.9, pp.1363-1370, September 1990.

Wednesday, March 24, 1993

Semiconductor Device Modeling 1

IWB 8:30am-10:30am
Mesquite B

Nadir Dagli, *President*
University of California

Vertical Cavity Laser High Speed Dynamics and Modeling

by

**John Bowers, Dubravko Babic, Gary Wang,
Dan Tauber, Wenbin Jiang, and Radhakrishnan Nagarajan****Department of Electrical and Computer Engineering
University of California
Santa Barbara, CA 93106
805/893-8447**

Vertical cavity lasers have been demonstrated with low thresholds and high efficiency. Wafer level testing is possible and packaging is simpler with excellent coupling to optical fibers. Two dimensional arrays of these lasers offer a new set of applications for semiconductor lasers. The design and properties of vertical cavity lasers are significantly different from in-plane lasers and present difficult theoretical design and analysis problems. Three important examples will be discussed here: Coupling between waveguides and DBR reflectors, relaxation oscillation dynamics, and chirping of vertical cavity laser output.

Many different vertical cavity laser structures have been demonstrated. Fig. 1 summarizes the different methods of transverse mode definition. The study of open resonators with plane or spherical mirrors has been extensive[1]. Historically, laser cavities were large compared to the wavelength, and the mirror diameter was small compared to the mirror separation. It was therefore possible to employ scalar diffraction theory and the Fresnel approximation to solve for the cavity modes. Vertical cavity surface emitting lasers (VCSELs), on the other hand, have dimensions on the order of a wavelength and hence require rigorous treatment of the electromagnetic wave propagation that considers the vector nature of the electromagnetic field as well. VCSEL cavities are generally realized as open resonators since the mode confinement is typically realized only in a part of the optical cavity while a part of the cavity is left unguided. The reason for this is the compromise between the optical, electrical and thermal properties of VCSEL structures. Beam propagation methods are commonly used in obtaining both scalar and vector solutions.

We analyze the common VCSEL structure which has semiconductor DBRs with no or weak lateral guiding. The magnitude of the diffraction loss is important and limits the maximum modal reflectivity of the mirror. Fig. 2 shows a calculation of the reflectivity of a mode from quarter wavelength mirrors[2]. In the Fresnel diffraction limit, an equivalent model for the DBR mirror can be obtained by placing a hard mirror at a suitable location beyond the surface of the real mirror (Fig. 2).

The high speed dynamics of VCSELs are another important theoretical challenge. Experimental measurements have indicated that 80 GHz relaxation oscillations are possible[3], higher than one would expect based on in-plane laser results. VCSELs have an extra design possibility, namely, tuning the laser wavelength to the short wavelength side of the gain peak so that the gain increases with increasing carrier temperatures rather than decreases, as is usually the case.

Recent calculations indicate that this could lead to a negative gain suppression factor. This results in a reduction in damping and thus higher frequency operation. These results are shown in Fig. 3. This figure shows analytic calculations of the small signal relaxation oscillation frequencies for positive and negative values for the gain suppression coefficient ϵ . It also shows large signal calculations of relaxation oscillation frequency (the inverse of the ringing time) for a laser with negative ϵ . The large and small signal resonant frequencies have a similar dependence on drive current when operating at high current levels. This figure also shows experimental measurements where such high relaxation oscillation frequencies were observed. In contrast to conventional lasers, the dependence of relaxation oscillation frequency is not as the square root of current above threshold.

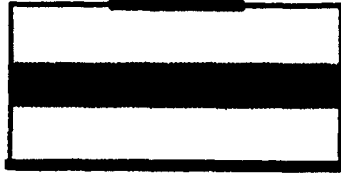
A final interesting problem in the analysis of VCSELs is the chirp behavior of gain switched or mode locked lasers. It has been experimentally observed that the lasers can either be blue[4] or red[5] chirped. We analyze the excess optical bandwidth generation in these lasers and find that self phase modulation due to injection pumping and gain saturation is the dominant factor in inducing laser pulse chirping. The chirp due to self phase modulation is typically four orders of magnitude greater than the value caused by intracavity material dispersion or mirror dispersion. The relative amounts of gain saturation or absorption saturation give rise to chirp of either sign. With proper design, short pulses with minimal chirp can be generated[6]. In recent work, 190 fs transform limited pulses have been generated from optically pumped mode locked VCSELs[7]. These are the shortest pulses directly generated from any mode locked semiconductor laser.

In summary, the optimal design of the optical, electrical and thermal characteristics of VCSELs is quite difficult, and many interesting theoretical challenges need to be solved. The initial experimental results are exciting, with relaxation oscillation frequencies above those measured for in-plane lasers and mode locked pulses shorter than have been achieved with in-plane lasers. However, additional work is needed to combine all of these desirable properties into one robust vertical cavity laser.

References

1. A. G. Fox and T. Li, "Resonant modes of a maser interferometer", *Bell System Tech. Journal*, **40**, 453(1961).
2. D. I. Babic, Y. Chung, N. Dagli, and J. E. Bowers, "Modal reflection of quarter wave mirrors in vertical cavity lasers", submitted to *J. Quantum Electron.* (1992).
3. D. Tauber, G. Wang, R. S. Geels, J. E. Bowers, and L. A. Coldren, "Large and small signal dynamics of vertical cavity surface emitting lasers", *Appl. Phys. Lett.* **62**(1993).
4. W. H. Xiang, S. R. Friberg, K. Watanabe, S. Machida, W. B. Jiang, H. Iwamura and Y. Yamamoto, "Femtosecond external cavity surface emitting InGaAs/InP multiple quantum well laser," *Opt. Lett.* **16**, 1394(1991).
5. "Mode-locked GaAs Vertical Cavity Surface Emitting Lasers," W. B. Jiang, R. Mirin, and J. E. Bowers, *Appl. Phys. Lett.*, **60**(6), 677-679, Feb. (1992).
6. "Analysis of Laser Pulse Chirping in Mode-locked Vertical Cavity Surface Emitting Lasers," W. B. Jiang, D. Derickson, R. Mirin, and J. E. Bowers, *J. Quantum Electron.*, **29**(1993).
7. "Femtosecond Periodic Gain Vertical-Cavity Lasers," W. B. Jiang, M. Shimizu, R. P. Mirin, T. E. Reynolds, and J. E. Bowers, *Photon. Tech. Lett.*, **5**(1993).

Top mirror determines
transverse mode



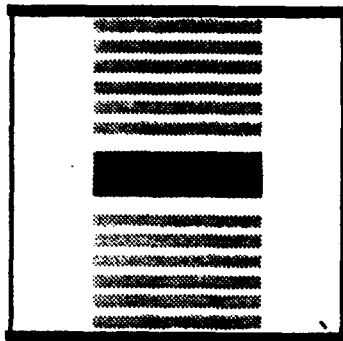
a)

Gain or partial index guiding
determines transverse mode



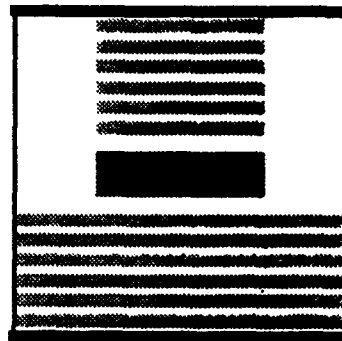
b)

"Complete" index guiding



c)

Partial index guiding



d)

Confocal resonator



e)

Figure 1. Schematic diagram of different methods of transverse mode definition in vertical cavity lasers.

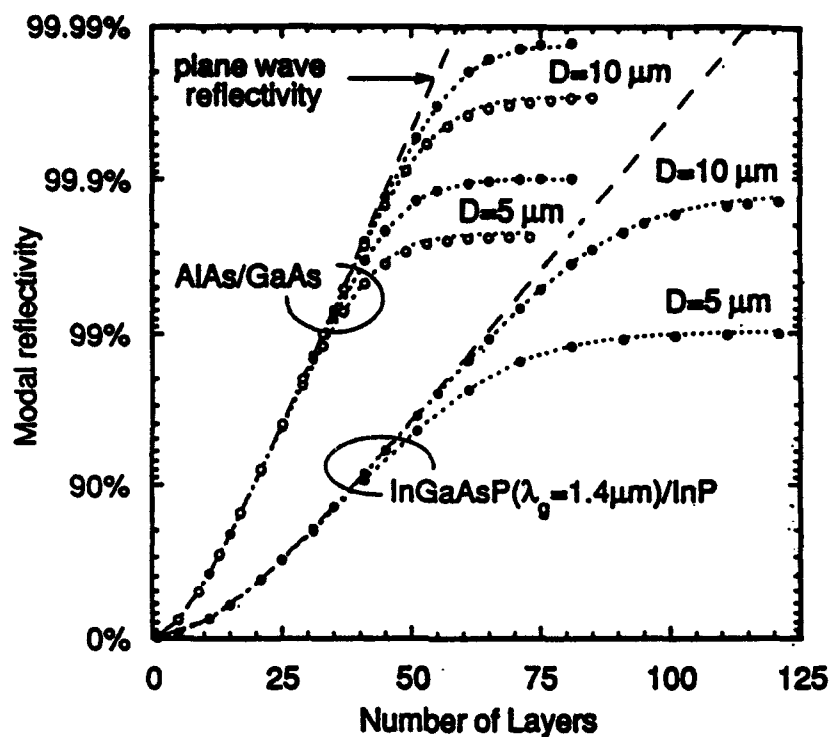


Figure 2. Modal Reflectivity of 5 μm and 10 μm air-clad InP waveguides on two types of mirrors as a function of the number of mirror layers. The dots indicate the numerical solution while the dashed lines indicate an approximate, analytic solution. The vertical axis shows $1-R$ on a reverse logarithmic plot labeled in reflectivity values.

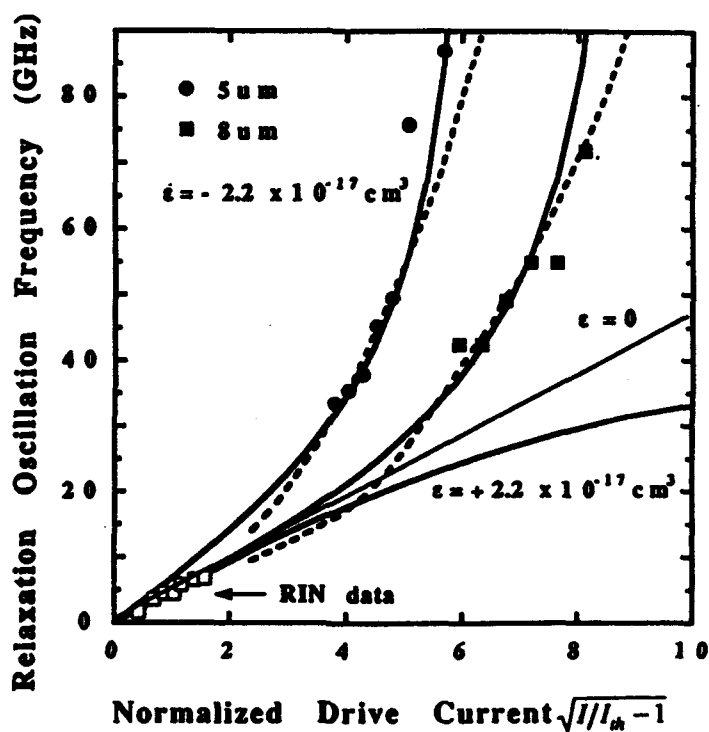


Figure 3. Dependence of relaxation oscillation frequency on drive current. The solid lines are an analytic small signal solution, the dashed lines are a numerical large signal solution and the dots are measurements on two sizes of devices.

Theoretical Study of Gain Saturation Coefficients in InGaAs/InGaAsP Strained Layer Quantum Well Lasers

Shunji Seki, Takayuki Yamanaka and Kiyoyuki Yokoyama

NTT Opto-electronics Laboratories

3-1 Morinosato Wakamiya, Atsugi, Kanagawa, 243-01 JAPAN

(Tel +81-462-40-3173, Fax +81-462-40-2859)

Paul Sotirelis and Karl Hess

Beckman Institute, University of Illinois at Urbana-Champaign,

405 North Mathews Avenue, Urbana, IL 61801, USA

I. Introduction

Strained layer quantum well lasers (SL-QWLs) have attracted much interest since the application of band structure engineering [1], [2] can improve lasing properties such as lower threshold currents and larger differential gains. It has been expected that the larger differential gain due to strain can enhance modulation bandwidths of QWLs [3]. However, the highest bandwidths found so far are much smaller than expected. One reason for this is that gain saturation also influences the modulation bandwidths of QWLs as well as the differential gain [4], [5]. We have already shown that the gain saturation coefficient increases with compressive strain in GaAs-based SL-QWLs due to an increase of the intra-subband relaxation times [6]. Recent experimental work has also shown that the gain saturation coefficient increases with compressive strain in InGaAs/InGaAsP SL-QWLs [7]. It is, therefore, necessary to take into account the effects of strain not only on differential gains but also on gain saturation coefficients to properly evaluate the enhancement of modulation bandwidths in SL-QWLs.

The purpose of this paper is to clarify the relationship between gain saturation coefficients and the amount of strain in InP-based SL-QWLs. The gain saturation coefficients of a tensile-strained, a lattice-matched and a compressive-strained InGaAs/InGaAsP quantum well laser are analyzed on the basis of spectral hole burning theory. The intra-subband relaxation times are calculated by taking into account the strain effects within the common framework of carrier-carrier and carrier-phonon interactions. We demonstrate here that the gain saturation coefficient in *tensile-strained* QWLs *remains constant* independent of the amount of strain, while it *increases* with strain in *compressive-strained* QWLs.

II. Mathematical Formulation

In an analysis of gain saturation in QWLs, it is essential to calculate intra-subband relaxation times on the basis of the realistic valence band structure with strain-dependent valence band mixing effects [6]. Thus, the valence subband energies and the wave functions were obtained by solving the multi-band effective mass equation. We used a 6×6 Luttinger-Kohn Hamiltonian [8], which includes the strain-dependent coupling among heavy-hole, light-hole and spin-orbit split-off subbands. The influence of strain was introduced to the Hamiltonian on the basis of the deformation theory for

valence bands. We assumed that the conduction band was decoupled from the valence bands. Hence, the conduction subband energy and the wave function were calculated by a parabolic-band scalar effective mass equation.

Using these band structures, the intra-subband relaxation time was calculated within the random phase approximation (RPA) [9], [10]. The intra-subband relaxation time of a carrier occupying the lowest subband in a quantum well is then obtained from the scattering-in and scattering-out rates $\Gamma_{\mathbf{k}_1}^{\text{in}}$ and $\Gamma_{\mathbf{k}_1}^{\text{out}}$, respectively:

$$\Gamma_{\mathbf{k}_1}^{\text{in}} = \frac{2\pi}{\hbar} \frac{2}{(2\pi)^2} \int d^2q n_f(E_{1\mathbf{k}-\mathbf{q}}) n_b(\omega) \frac{f_{1111}(q) v_q}{2\pi} \text{Im} \left(\frac{-1}{\epsilon_{1111}(q, \omega)} \right). \quad (1)$$

$\Gamma_{\mathbf{k}_1}^{\text{out}}$ is obtained by replacing $n_f \leftrightarrow 1 - n_f$ and $n_b \leftrightarrow n_b + 1$ in Eq. (1) [10]. The functions $n_f(E_{1\mathbf{k}-\mathbf{q}})$ and $n_b(\omega)$ are the Fermi-Dirac and the Bose statistic factors, respectively. The energy $\hbar\omega = E_{1\mathbf{k}} - E_{1\mathbf{k}-\mathbf{q}}$ is the scattered carrier's energy loss to the thermal distribution of the carriers and the lattice (LO-phonons). The function $f_{1111}(q)$ represents a form factor involving the overlap of the wave functions. The function v_q is the two-dimensional Fourier transform of the coulomb interaction and $\epsilon_{1111}(q, \omega)$ is the complex RPA dielectric function. Included in the dielectric function are the polarizabilities of the lattice (with LO-phonons) and the carriers (electrons and holes). The effects of carriers occupying the higher subbands are also included in the dielectric function. The region of integration is determined by simple energy conservation and includes emission and absorption.

By using the calculated intra-subband relaxation times and the dipole moments, the gain saturation coefficients are then obtained for the dominant polarization mode of lasing oscillation.

III. Results and Discussions

We analyzed $\text{In}_x\text{Ga}_{1-x}\text{As}/\text{InGaAsP}$ ($\lambda_g = 1.2\mu\text{m}$) single quantum well structures with the Indium content, x , varying in the range from 0.3 to 0.8. These values correspond to 1.6 % tensile strain and 1.8 % compressive strain, respectively. The well width is 5 nm for all kinds of wells. The Luttinger parameters for $\text{In}_x\text{Ga}_{1-x}\text{As}$ and $\text{In}_x\text{Ga}_{1-x}\text{As}_{1-y}\text{P}_y$ were interpolated by using these values for the binary compounds. The band offset parameter was assumed to be $\Delta E_c = 0.4 \Delta E_g$.

Figures 1 (a), (b) and (c) show the calculated valence subband structures for a 1.6 % tensile-strained, a lattice-matched and a 1.8 % compressive strained quantum well, respectively. Applying the tensile strain, the light-hole subband moves up enough to become the ground state in the valence band. Since the LH1 is the ground state, the dominant polarization of lasing oscillation becomes the TM mode in strained QWLs with large tension. In the lattice-matched case, strong nonparabolicity is observed and LH1 has a negative effective mass at the zone center. This is mainly due to the interactions between heavy and light hole subbands at $\mathbf{k}_{\parallel} \neq 0$. When compressive strain is introduced, the strain lowers the light-hole subbands, which gives rise to a much decreased effective mass in the heavy hole ground state HH1.

Figure 2 shows the calculated results of intra-subband relaxation times for electrons and holes at the edge of the lowest subband at 300 K. Note that the intra-subband

relaxation times in the tensile-strained QWLs remains constant when the strain increases. On the other hand, they monotonically increase with the amount of strain in the compressive-strained QWLs. These results clearly indicate that it is essential to include strain effects on band structures in the calculation of intra-subband relaxation times in SL-QWLs.

Figure 3 shows the relationship between the gain saturation coefficient and the strain in the quantum wells. Note that the gain saturation coefficients show the different tendency between tensile- and compressive-strained QWLs. In the case of tensile strain, the gain saturation coefficient remains constant independent of the amount of strain. On the other hand, the gain saturation coefficient in compressive-strained QWLs markedly increases with the amount of strain. This increase is mainly due to the increase of the intra-subband relaxation times shown in Fig. 2.

Differential gains tend to increase with the amount of strain in both tensile- and compressive-strained QWLs. Hence, the results shown in Fig. 3 suggest that tensile-strained InGaAs/InGaAsP QWLs can have greater potential for high-speed operation since the increase of differential gain may be canceled out by the increase of the gain saturation coefficient in compressive-strained QWLs.

IV. Summary

In summary, we have studied the effects of strain on the gain saturation coefficient in InGaAs/InGaAsP SL-QWLs on the basis of the spectral hole burning theory. Intra-subband relaxation times have been calculated including carrier-carrier and carrier-phonon interactions by taking into account the effect of strain on the band structure. We have shown that the gain saturation coefficient in tensile-strained QWLs remains constant even when the amount of strain increases, while the coefficient in compressive-strained QWLs markedly increases with the strain. It has been suggested from these results that tensile-strained InGaAs/InGaAsP QWLs can have greater potential for high-speed operation as compared with compressive-strained ones.

References

- [1] E. Yablonovitch and E. O. Kane, *IEEE Lightwave Technol. LT-4*, 504 (1986).
- [2] A. R. Adams, *Electron. Lett.* **22**, 249 (1986).
- [3] I. Suemune, L. A. Coldren, M. Yamanishi and Y. Kan, *Appl. Phys. Lett.* **53**, 1378 (1988).
- [4] G. P. Agrawal, *Appl. Phys. Lett.* **57**, 1 (1990).
- [5] K. Uomi, T. Tsuchiya, M. Aoki and N. Chinone, *Appl. Phys. Lett.* **58**, 675 (1991).
- [6] S. Seki, P. Sotirelis, K. Hess, T. Yamanaka and K. Yokoyama, *Conference Digest of the 13th IEEE International Semiconductor Laser Conference, D-4* (1992).
- [7] H. Yasaka, R. Iga, Y. Noguchi and Y. Yoshikuni, *IEEE Photon. Technol. Lett.* **4**, 826 (1992).
- [8] J. M. Luttinger and W. Kohn, *Phys. Rev.* **97**, 869 (1955).
- [9] G. f. Giuliani and J. J. Quinn, *Phys. Rev. B* **26**, 4421 (1982).
- [10] R. Binder, D. Scott, A. E. Paul, M. Lindberg, K. Henneberger and S. W. Koch, *Phys. Rev. B* **45**, 1107 (1992).

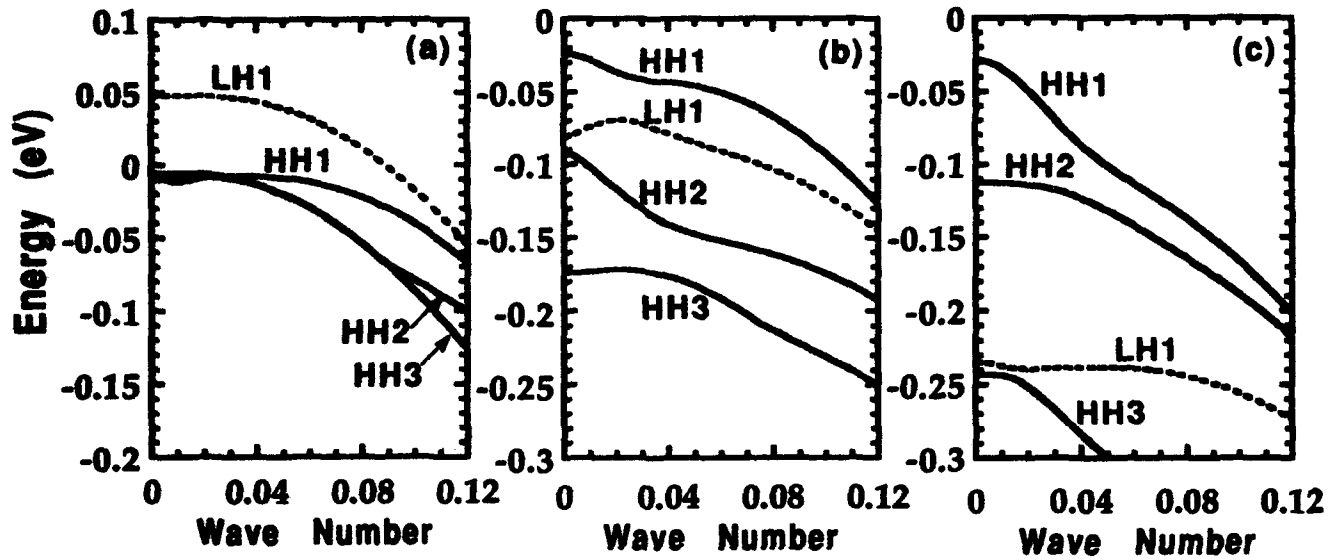


Figure 1
S. Seki et al.,
"Theoretical Study of Gain Saturation ..."

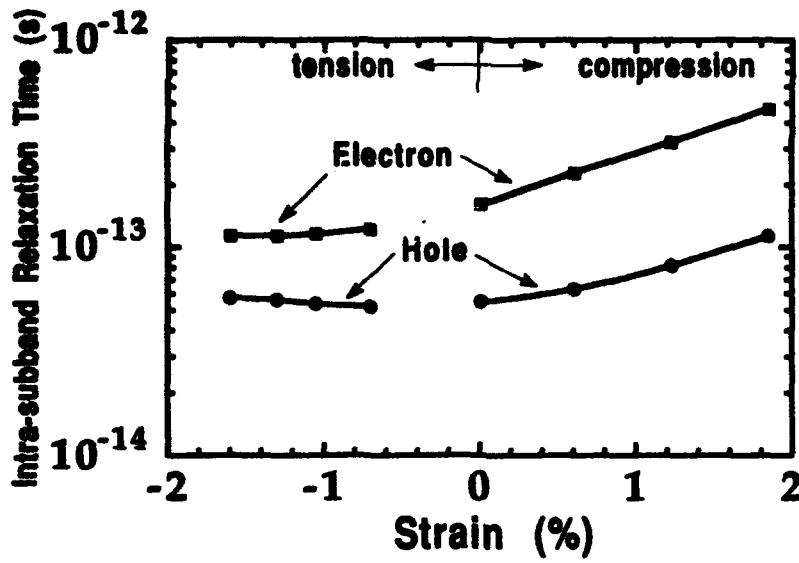


Figure 2
 S. Seki et al.,
 "Theoretical Study of Gain Saturation ..."

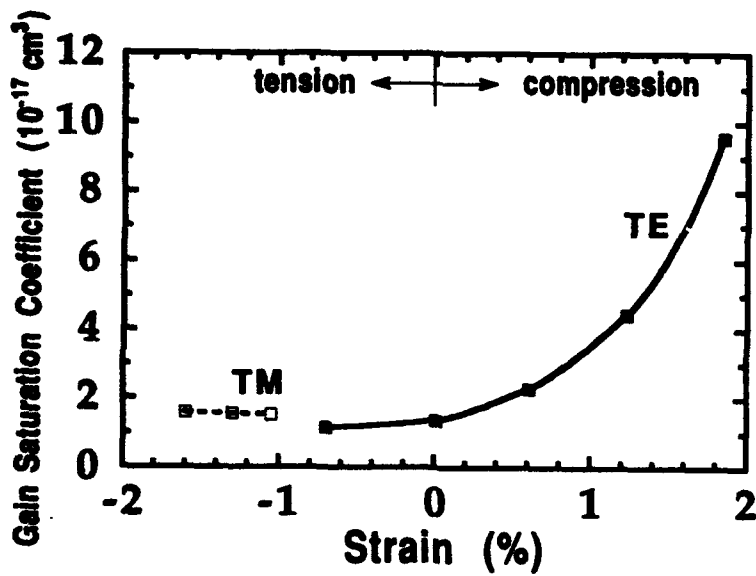


Figure 3
 S. Seki et al.,
 "Theoretical Study of Gain Saturation ..."

Finite-Element Analysis of Quantum Wire Arrays with and without Strain.**Jong Chang Yi and Nadir Dagli****Electrical and Computer Engineering Department
University of California
Santa Barbara
CA 93106
Phone: 805 893 4847
Fax: 805 893 3262**

Quantum wire structures, which provide quantum confinement in two dimensions, have undergone extensive study and development for their interesting physical phenomena and potential device applications [1]-[3]. It is widely believed that quantum wires will have superior optical and transport properties compared to quantum wells. Therefore, the fabrication of quantum wires is a very active research area and many different approaches such as growth on vicinal substrates [4], re-growth on V-grooves [5] and cleaved edges [6], partial strain release [7] are actively pursued by different groups. Obviously the main purpose of fabricating quantum wires is to generate semiconductor heterostructures with properties superior to quantum wells. However, a quantitative analysis of under what conditions a quantum wire array is superior to a quantum well is still lacking. The purpose of this paper is to investigate this issue and provide guidelines towards an optimum geometry. This is a very complicated task due to the large number of parameters available for optimization and the complexity of the calculations required. In this paper this problem will be investigated by taking a certain quantum well and chopping it into an array of quantum wires and comparing the optical properties of the two as this transformation goes on. Therefore, in this study we will concentrate on the effect of the lateral dimension and wire fill factor on the optical properties of the quantum wire structures fabricated in GaAs/AlGaAs and InGaAs/AlGaAs systems. As a basis of comparison we will calculate the threshold current and the differential gain of a laser whose active area is either a quantum well or a quantum wire of certain lateral dimensions made out of the quantum well.

The starting point of the analysis is the calculation of the energy band diagram of an array of quantum wires. The calculation of the energy band diagram of a semiconductor structure in the presence of two dimensional quantum confinement is generally very complicated and cannot be done analytically. Recently, several numerical techniques have been developed for quantum wire structures, including finite-element method [8] finite-difference method [9] effective bond orbital method [10], and tight binding method [11]. In this study, we use the finite-element method [12] to solve the Schrodinger equation. The advantage of this method is that the energy and wavefunction of eigenstates of arbitrarily shaped structures can be obtained without further complications such as coordinate transformations. Furthermore, wide range of the quantum wire dimensions can be analyzed using a non-uniform mesh, which reduces the required computational effort. In the calculations for the analysis of the conduction band a single band model is used. The calculations on the valence band are more complicated due to band mixing induced by two dimensional quantum confinement. In the valence band calculations a four band $k \cdot p$ analysis is used [13]. This presents a difficulty, however, because the variational expression needed for the finite-element analysis is not known. This expression is derived and verified through the Euler equation [14]. Furthermore, the flux continuity conditions at each boundary is assured. The resulting equations are far too complicated to present in this short abstract, but they will be presented and discussed in detail in the conference. This finite-element method is applied to calculate the conduction and valence energy band diagrams of quantum wire arrays as well as wavefunctions. Once these quantities are calculated, density of states functions, momentum matrix elements and optical properties such as gain of loss are calculated. In cases where strain is present, the strain tensor coefficients are also calculated by using finite element method [15].

The additional contribution by the strain coefficients are included in the Hamiltonian for conduction and valence bands in InGaAs/AlGaAs quantum wire structures [7].

The cross-sectional profile of an array of quantum wires analyzed is shown in figure 1. This quantum wire array can be regarded as made out of a quantum well structure by replacing part of the well material with a higher bandgap material. In this calculations the quantum wire thickness is fixed at 100Å, while the lateral dimension is changed from 10Å to 1000Å. Figure 2 shows the conduction and the valence energy subband positions of such an array as a function of wire width. In this calculation $W = S = D/2$ and the wire and barrier material are GaAs and Al_{0.5}Ga_{0.5}As, respectively. C_{mn} denotes the conduction band eigenstates where the envelope part of the eigenfunction has m maxima along the growth direction and n maxima along the lateral direction. HH_{mn} and LH_{mn} denote those of heavy hole and light hole bands. Other higher eigenstates are omitted in the plot for clarity. Subband energies of the 100 Å thick GaAs quantum well are shown on the right margin. When W is greater than 500 Å, the quantum wire eigenstates are closely spaced and deviate slightly from the eigenstates of the 100Å thick GaAs quantum well. When W is reduced to 200 Å, the energy gap between the lowest subbands in the conduction band becomes greater than $1 kT$ at room temperature. As W decreases further, the gap between subband energies increases. However, if the W becomes smaller than 40 Å the coupling between wires over the thin barriers becomes significant due to reduced barrier width since $W = S$. This results in broadening of the subbands into minibands as shown in Figure 2. This broadening is more significant for the conduction band due to lighter electron effective mass which results in increased the wire to wire coupling. Due to the miniband broadening, the array becomes quasi two dimensional and energy gap between the subbands is reduced. Therefore, for this case the largest subband separation can only be obtained when W is between 50 to 100 Å. Figure 3 shows the variation of the threshold current and differential gain of a laser when the same quantum wire array is used as the active medium as a function of wire width for different total loss values of the laser cavity. In the threshold current and differential gain calculation, the gaussian lineshape function with 6 meV of energy broadening and an optical confinement factor of 0.0115 were assumed. The corresponding values for the 100 Å quantum well when the total loss is 70 cm^{-1} are again shown on the right margin. Both the differential gain and the threshold current improve in the width range of 40-80 Å. When $W=55\text{Å}$, the threshold current is 3 times smaller and the differential gain is 4 times greater than that of the 100 Å GaAs quantum well. However, when quantum confinement becomes weak, i.e., when $W > 100\text{Å}$, or a quasi two dimensional system is formed, i.e., when $W < 40\text{Å}$, the improvements over the quantum well are rapidly lost. Further calculations on the effect of wire filling ratio on the threshold current density and differential gain indicate that optimum wire filling ratios result when $W = 0.4 - 0.5 D$. For high wire filling ratios the optical confinement factor is enhanced, hence the gain is enhanced by the same ratio of the increase in the density of wires. As the wire width to period ratio decreases or wire filling ratio gets smaller improvements over quantum well rapidly decrease.

Figure 4 shows the conduction and valence band energy subband positions as a function of wire width for an In_{0.3}Ga_{0.7}As/Al_{0.2}Ga_{0.8}As strained quantum wire array. Due to the compressive strain within the InGaAs wire material, the light and heavy hole subbands are split further from one another, resulting in about a 1.5 times enhancement in differential gain compared to the unstrained GaAs/AlGaAs system[11]. Further results of calculations and comparisons including the effects of unavoidable imperfections and limits on the tolerances will be presented at the conference.

References:

1. M. Asada, Y. Miyamoto, and Y. Suematsu, Jpn. J. Appl. Phys, 24, L95 (1985).
2. M. Asada, Y. Miyamoto, and Y. Suematsu, IEEE J. Quantum Electron., QE-22, 1915 (1986)
3. I. Suemune and L. A. Coldren, IEEE J. Quantum Electron., QE-24, 1778 (1988).

4. P. M. Petroff, M. S. Miller, Y. T. Lu, S. A. Chalmers, H. Metiu, H. Kroemer and A. C. Gossard, *J. Crystal Growth*, **111**, 360 (1991).
5. E. Kapon, D. M. Hwang, and R. Bhat, *Phys. Rev. Lett.*, **63**, 430 (1989).
6. Y.-C. Chang, L. L. Chang, and L. Esaki, *Appl. Phys. Lett.*, **47**, 1324 (1985).
7. I.-H. Tan, M. Y. He, J. C. Yi, E. Hu, N. Dagli, and A. Evans, *J. Appl. Phys.*, **72**, 546 (1992).
8. K. Kojima, K. Mitsunaga, and K. Kyuma, *Appl. Phys. Lett.*, **55**, 882 (1989).
9. Craig Pryor, *Phys. Rev. B* **44**, 12912 (1991).
10. D. S. Citrin and Y.-C. Chang, *Phys. Rev. B*, **40**, 5507 (1989-I).
11. T. Yamauchi, Y. Arakawa and J. N. Schulman, *Surface Science*, **267**, 291 (1992)
12. K.-J. Bathe and E. L. Wilson, *Numerical Methods in Finite Element Analysis*, Prentice-Hall, Inc., Englewood Cliffs, New Jersey (1976)
13. J. M. Luttinger and W. Kohn, *Phys. Rev.*, **97**, 869 (1955).
14. D. Marcuse, *Principles of quantum electronics*, Academic Press, Inc., London (1980).
15. Z. Xu and P. Petroff, *J. Appl. Phys.*, **69**, 6564 (1991)

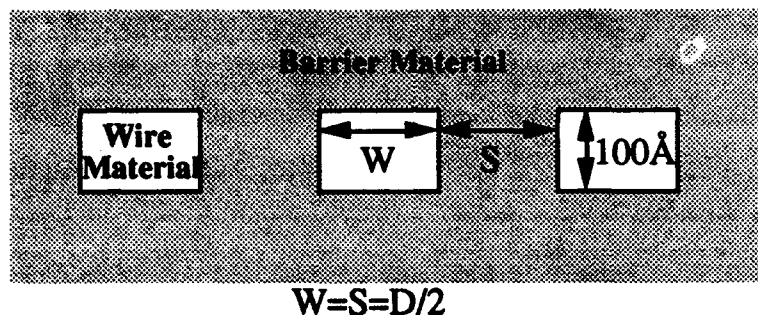


Figure 1. Cross sectional profile of quantum wire array.

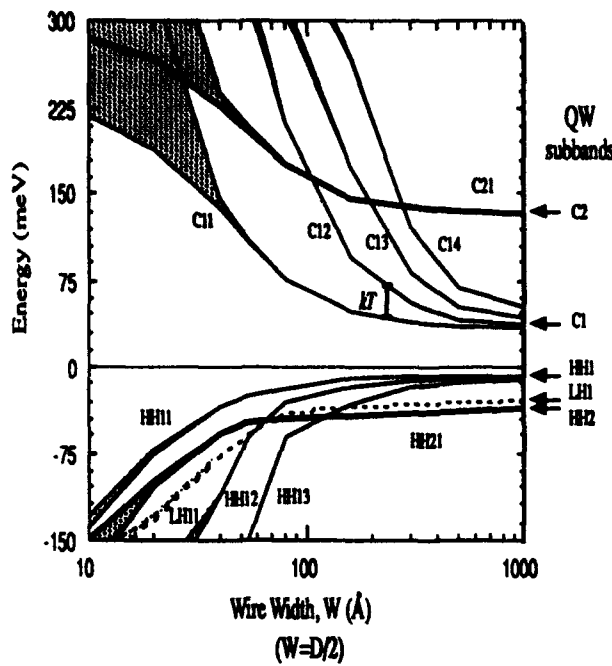


Figure 2. Energy subband positions of a GaAs/Al_{0.5}Ga_{0.5}As quantum wire array. In all the subsequent figures, the marks on the right margin show the values for the quantum well when $W=\infty$ and $S=0$.

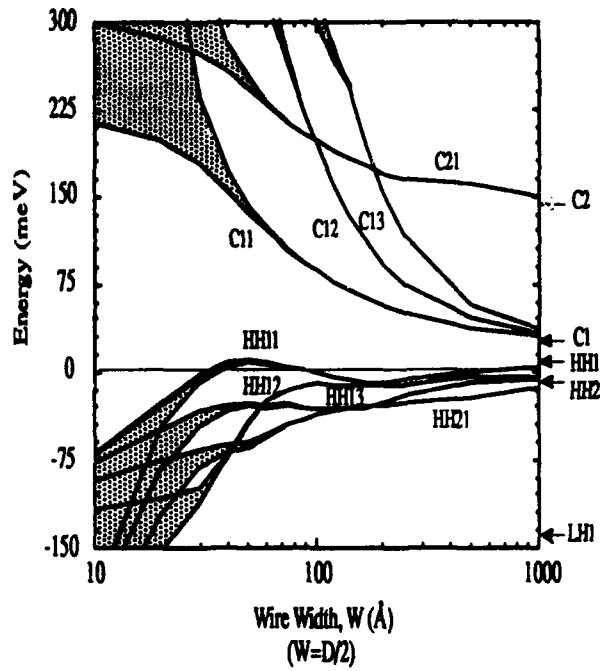


Figure 4. Energy subband positions of an In_{0.3}Ga_{0.7}As/Al_{0.2}Ga_{0.8}As strained quantum wire array.

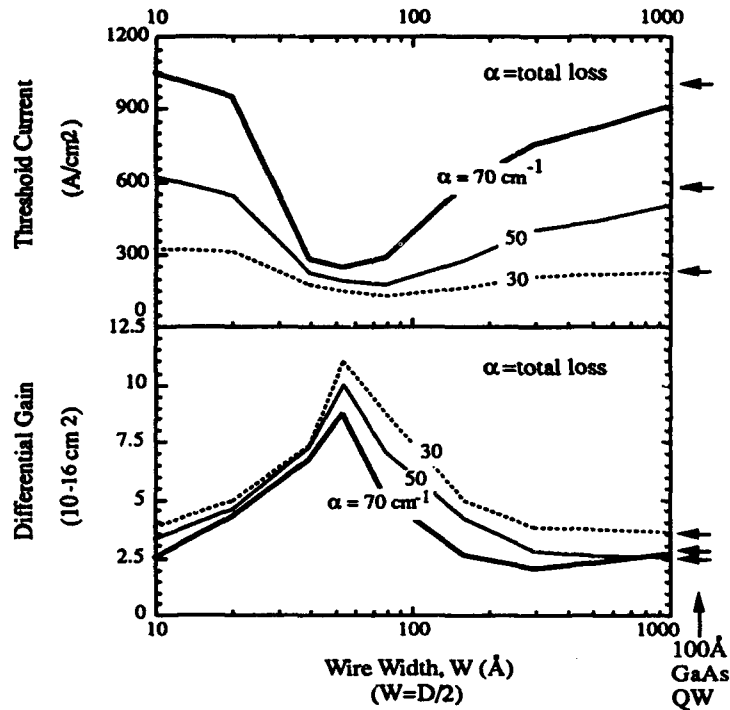


Figure 3. Threshold current density and differential gain of a GaAs/Al_{0.5}Ga_{0.5}As quantum wire array.

Comparison of different DFB laser models within the European COST 240 collaboration

G. Morthier and R. Baets (University of Gent), C. F. Tsang and J. E. Carroll (University of Cambridge), H. Wenzel (Humboldt University Berlin), A. Mecozzi and A. Sapia (Fondazione Ugo Bordonini), P. Correc (CNET Bagneux), S. Hansmann and H. Burkhardt (DBP), R. Bonello and I. Montrosset (Politecnico di Torino), H. E. Lassen and H. Olesen (TFL), R. Schatz (KTH, Stockholm), H. Bissessur (Alcatel Alsthom Recherche), J-L. Vey and G. Duan (ENST).

contact address: Laboratory of Electromagnetism & Acoustics
University of Gent, Sint-Pietersnieuwstraat 41
B-9000 Gent, Belgium - Tel. +32 91 643344

Working group I of COST 240 concentrates on the comparison of modelling results and experimental results obtained in different laboratories on DFB lasers. In a first stage, the results of different European laser models obtained for static, dynamic and noise related characteristics have been compared. Several perfectly AR-coated, $\lambda/4$ -shifted DFB lasers and one DFB laser with cleaved facets have been or are currently being investigated. Here, we will briefly describe some of the results on $\lambda/4$ -shifted lasers, but more details will be presented at the meeting. From the numerical results obtained so far, it seems that an excellent agreement can be obtained in most cases (the differences between the different results are usually smaller than a typical experimental uncertainty).

I. Description of the different laser models

For the COST exercises, the gain as well as the refractive index were assumed to vary linearly with the carrier density and to be independent of the wavelength. Carrier diffusion and thermal effects have been neglected.

The static characteristics are obtained using a detailed nonlinear longitudinal description in all models. Linear, bimolecular and Auger recombination as well as stimulated emission depending on the local intensity are thereby included. Most models assume a constant current injection in the active layer. Only the model of HUB (Humboldt University Berlin) [1] assumes a constant voltage between the contacts and the current injection therefore depends on the series resistance and the junction voltage. The carrier density rate equation is

linearized above threshold in the model of FUB (Fondazione Ugo Bordonini)[2]. The wave propagation in the lasers is generally described by the coupled mode equations. The models of DBP (Deutsche Bundespost) [3], UA (University of Athens) [4] and AAR (Alcatel Alsthom Recherche) [5] are based on a transfer matrix algorithm applied to a cavity divided into sections with uniform refractive index, carrier density and photon density.

To calculate the dynamic and noise related characteristics, different approaches have been used. The most detailed calculations are obtained with the models from TFL [6], [7], UG (University Gent) [8] and PT (Politecnico di Torino) [9], in which linearized coupled mode and carrier rate equations are still solved taking into account all longitudinal variations as well as longitudinally varying Langevin functions representing the noise. The solution of these longitudinal equations is based on the application of a finite difference scheme in the axial dimension in the model of UG and PT, while the model of TFL incorporates an exact solution of the linearized equations. To this end, the TFL group has implemented two independent numerical schemes: one is based on a Greens' function approach [6] and the other is based on solving the adjoint set of equations [7]. (These two methods give the same results.) The models of KTH (Royal Institute of Technology, Stockholm) and FUB are based on a similar small signal theory, but the equations are solved within the envelope approximation (modulation and noise do not change the longitudinal field distribution around its steady state). The linewidth calculation of UA and AAR is based on a negative conductance oscillator formalism. All other results for the FM-response at low modulation frequencies were calculated from the incremental wavelength shift and for the linewidth from a modified Schawlow-Townes formula using an effective linewidth enhancement factor and a longitudinal K-factor [6]. The model from UC (University Cambridge) [10] is a large signal, mixed time-frequency domain model with non-uniform carrier and photon density and based on transfer matrices driven by spontaneous emission. The linewidth is calculated using the modified Schawlow-Townes formula (using α_{mat} and a longitudinal K-factor).

II. Numerical results

Here we will only describe numerical results concerning the static or low-frequency dynamic and noise related behaviour of AR-coated $\lambda/4$ -shifted lasers (for which linear gain has been assumed). Other results will be given at the meeting. Both bulk and MQW lasers with different κL values ($L=300 \mu\text{m}$: $\kappa L=1, 2$ and 3 , $L=1\text{mm}$ and $\kappa L=1$) have been modelled. For general reference, the other parameters are summarized in table I. It can be remarked that the choice of $n_{e,0}$ and Λ leads to an unusual emission wavelength of $\pm 1.65 \mu\text{m}$.

Since most models use a similar approach to find the steady state solutions, the results on threshold current, emission wavelength, threshold gain difference and P-I relation show

in general an excellent agreement. Fig. 1 shows the P-I relation as obtained with the different models for the bulk laser with $\kappa L=2$. The dashed lines give the most deviating results, but most results coincide with the full line. For this laser, we found $I_{th} = 23.75 \pm 0.05$ mA, $\lambda_{th} = 1.6583 \pm 0.0008$ μm and $2\Delta\alpha L = 1.46-147$. The model of HUB, which uses an interpolation scheme, gave a slightly higher $I_{th} = 24.1$ mA.

An idea of the agreement on linewidth, FM etc. can be obtained from table II, which, for bulk and MQW lasers with $\kappa L=2$, gives the current (in mA) required to obtain an output power of 5 mW, the linewidth (in MHz), the FM-response (in GHz/mA) and the wavelength difference (in pm) with the threshold value for this current. Only the best agreeing results are listed however. The larger FM and wavelength shift of CNET are due to the choice a higher effective index (determined by the dispersion relation $n_e = n_g - (n_g - n_{e,0}) \lambda/\lambda_0$ with $\lambda_0 = 1.55$ μm).

We finally report on the results for a 1mm long, bulk $\lambda/4$ -shifted laser with $\kappa L=1$, a laser which becomes unstable at high power levels. The linewidth results for this laser, shown vs. the injected current in fig. 2, are particularly interesting. The rebroadening which accompanies the instability is found only with the models of UG and TFL, i.e. if possible small signal fluctuations in the longitudinal mode profile are taken into account. This result is the only one where a significant influence of the mode profile fluctuations is observed.

References

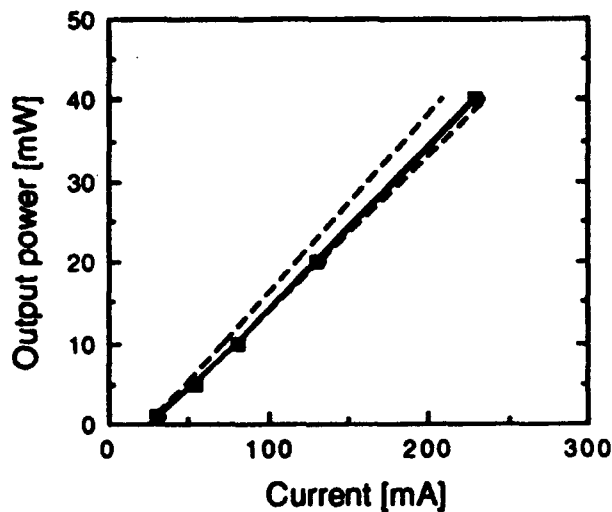
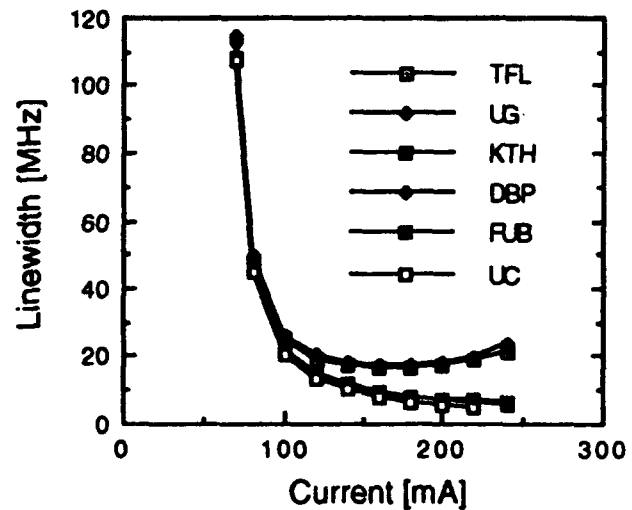
- 1/ H.J. Wünsche, U. Bandelow, H. Wenzel, submitted to IEEE J. Quant. El.
- 2/ A. Mecozzi, A. Sapia, P. Spano, H. Burkhard, S. Hansmann, H. Hillmer, Proc. ECOC-IOOC '91, TuPS1-21, 1991.
- 3/ S. Hansmann, IEEE J. Quant. El., Vol. 28, pp. 2589-2595, 1992.
- 4/ I. Orfanos, T. Sphicopoulos, A. Tsigopoulos, C. Caroubalos, IEEE J. Quant. El., Vol. 27, pp. 946-956, 1991.
- 5/ H. Bissessur, to be published in J. Lightw. Techn.
- 6/ B. Tromborg, H. Olesen, X. Pan, IEEE J. Quant. El., Vol. 27, pp. 178-192, 1991.
- 7/ B. Tromborg, H. E. Lassen, H. Olesen, X. Pan, IEEE Phot. Techn. Lett., Vol. 4, pp. 985-988, 1992
- 8/ P. Vankwikelberge, G. Morthier, R. Baets, IEEE J. Quant. El., Vol. 26, pp. 1728-1741, 1990.
- 9/ R. Bonello, I. Montrosset, J. Lightw. Techn., Vol. 10, October 1992.
- 10/ L.M. Zhang, J.E. Carroll, IEEE J. Quant. El., Vol. 28, pp. 604-611, 1992.
- 11/ G-H. Duan, P. Gallion, G. Debarge, IEEE J. Quant. El., Vol. 26, pp. 32-44, 1990.

Parameter	bulk	MQW
Grating period Λ [μm]	244.5	244.5
Bragg order m	1	1
Stripe width w [μm]	1.5	1.5
Active layer thickness d [μm]	0.2	0.1
Confinement factor Γ	0.3	0.15
Eff. refr. index $n_{e,0}$ without injection ($N=0$)	3.4	3.4
Group index n_g	3.6	3.6
Absorption α_{int} [cm^{-1}]	50	40
Differential gain a [10^{-16}cm^2]	2.5	7
Transp. carrier dens. N_t [cm^{-3}]	10^{18}	$1.5 \cdot 10^{18}$
Carr. dens. dependence of the index in act. layer [10^{-20}cm^3]	-1.5	-1.5
Inversion factor n_{sp}	2	2
Carrier lifetime τ [ns]	10	10
Bimolec. coeff. B [$10^{-10} \text{cm}^3/\text{s}$]	1	1
Auger coeff. C [$10^{-29} \text{cm}^6/\text{s}$]	7.5	7.5

Table I

bulk	I	$\Delta\nu$	FM	$\Delta\lambda$
TFL	54.0	21.50	0.174	-50.7
UG	54.0	22.60	0.178	-53.7
PT	54.0	22.40	0.176	-50.0
KTH	54.0	22.80	0.200	-51.0
DBP	54.0	23.00	0.187	-52.9
FUB	49.6	27.70	0.239	x
CNET	54.0	x	0.204	-60.2
HUB	53.4	21.90	x	x
MQW				
TFL	37.8	3.52	0.016	-6.2
UG	37.8	3.61	0.016	-6.5
PT	37.8	3.60	0.016	-6.0
KTH	37.8	3.61	0.017	-6.2
DBP	37.8	3.64	0.017	-6.4
FUB	34.9	3.70	0.015	X
CNET	37.9	X	0.026	-9.9
HUB	37.5	3.40	x	x

Table II

Fig. 1: P-I characteristic found for the $\lambda/4$ -shifted bulk laser with $L=300 \mu\text{m}$, $\kappa L=2$.Fig. 2: $\Delta\nu$ -I characteristic found for the $\lambda/4$ -shifted bulk laser with $L=1 \text{mm}$, $\kappa L=1$.

**DIFFUSION AS A MECHANISM OF GAIN
SATURATION IN QUANTUM WELL LASERS**
G.W. Taylor (Rm 4D423, Tel 9089490515) and P.R. Claine,
AT&T Bell Laboratories, Holmdel, N.J. 07733

The role of transport in determining the high frequency response of quantum well lasers has been studied in depth lately in an effort to bring the calculated frequency response into line with various experimental results[1-3]. In these descriptions a transport factor is introduced which describes the exchange of electrons(holes) between the n-contact(p-contact) and the well. The mechanism of transport is considered to be diffusion in these regions and the concentration of carriers is introduced as a new variable resulting in a third rate equation. However the carrier transport is not considered for the carriers on the far side of the well. Also, in these studies the loss of gain with increasing power level is modeled via the non-linear gain or gain compression factor which is the standard phenomenological approach.

In this work we consider transport from a new perspective. The energy band diagram for the p-n laser is shown in Fig. 1a at equilibrium and in Fig.1b in the lasing state. Often the inverted refractive index profile is used as shown in Fig.1c which can be misleading for the interpretation of carrier flow especially as regards hot electron or ballistic effects. The current components and stored charge components are shown in Fig.1b. It is noted that the electrons (holes) between the n+ contact (p+ contact) and the well are considered as majority carriers inasmuch as they are flowing by the drift mechanism [4] with an impedance which has been well established as

$$R_i = \frac{V_i}{I_F} = \left[\frac{3kTW}{8qD_s \tau_s} \right] \frac{1}{I_F} \quad (1)$$

The electrons (holes) flowing between the well and the p+ contact (n+contact) are minority carriers as in standard pn junction theory [4] and hence the current transport is by diffusion. The minority carriers stored in these regions to support the diffusion flow are indicated and constitute a diffusion capacitance whose low frequency magnitude is [4]

$$C_{deo} = \frac{q^2 L_n n_{po}}{2kT} e^{V_i/V_T}, \quad C_{dho} = \frac{q^2 L_p p_{no}}{2kT} e^{V_i/V_T} \quad (2a)$$

and which varies with frequency as

$$C_{de} = C_{deo} / \left[1 + b\sqrt{\omega} \right] \quad (2b)$$

In addition to the diffusion capacitance there is a depletion capacitance which can be neglected for a wide intrinsic SCH region . In practice the background doping always results in small depletion regions so this component can become important. Taken together these components comprise an electrical RC circuit for the laser as shown in Fig.2 which simply attenuates the applied electrical signal according to the pole $(1+sRC)^{-1}$. For a linear system analysis, this pole multiplies the opto-electronic modulation response of the laser to obtain the overall response.

In the regions past the well(s) the current flow is by diffusion [4] (standard p-n theory) and the magnitude of this flow is of critical importance in determining the damping of the laser and the effective gain compression. We start with the time-dependent current continuity equation for the laser

$$qL_x \frac{dn}{dt} = J - J_{RL} - J_{NR} - J_{DIFF} \quad (3)$$

where J_{NR} is the non-radiative recombination component, J_{RL} is the radiative component (stimulated and spontaneous) and J_{DIFF} is the diffusion component. The diffusion component determines the carrier confinement factor η_c which may be expressed as the simple ratio of the carrier components at threshold

$$\eta_c = \frac{J_{NRT} + J_{SPT}}{J_{NRT} + J_{DIFFT} + J_{SPT}} \quad (4)$$

Since the diffusion increases above threshold according to $(J - J_{TH})(1 - \eta_c)$ then the junction voltage increases with optical power as shown typically for a quantum well laser in Fig 3. The small signal frequency response of the diffusion current has been well established[4] as

$$\delta J_D = \delta E_{FT} [A + sB] \quad (5)$$

and thus represents an additional frequency dependence in the laser response which varies as the small signal of the appropriate Fermi level. Here, A and B are functions of τ_n the recombination lifetime of the diffusing carriers. We include this frequency response in the small signal form of (3) and derive the laser response $\delta F/\delta J$ in terms of one rate equation for the system Fermi level and one rate equation for photons. The concept of the stimulated lifetime[5] is used to represent the stimulated emission process. With this expedient the photon density is expressed in terms of the system Fermi level which thus becomes the parameter which links together the small signal carrier and photon amplitudes. With this approach the small signal diffusion parameters A and B in (5) have a major effect on the traditional second order response for two reasons. First they increase with optical power so that above some level they totally control the damping term and second they depend upon the frequency themselves. Thus above this critical level the response becomes very non-linear and the resonance frequency saturates.

This behavior is illustrated in Fig.4 which shows the frequency response of a single quantum well laser for increasing power levels. In Fig.4b we show the same response when the additional electrical pole due to $R_i C_{DIFF}$ is included. One key feature of this result is the low frequency roll-off which is introduced by the $R_i C_{DIFF}$ time constant. Obviously the wider the SCH region the lower the frequency at which this effect becomes important which is in agreement with experiment. Another key feature is the saturation of the frequency response as the power is increased and the reduction in height of the resonant peak. Both of these effects result from the dominance of diffusion as the power is increased. This is most clearly shown by the resonant frequency versus root power variation in Fig.5 which indicates the initial linear response at low powers of a second order system and then the saturated response at higher powers of a non-linear system. The theory predicts a maximum resonant frequency

$$\omega_{max} = \left[\frac{1}{\tau_{ST}^*} \sqrt{\frac{2}{\tau_n} \frac{\eta_e}{1-\eta_e}} \right]^{\frac{2}{3}} \quad (6)$$

and shows that speed is limited by both the diode recombination time and the differential stimulated lifetime. It also shows a strong dependence on the confinement factor η_e . Since η_e is fairly sensitive to temperature as we show in Fig. 6 then the heating in the laser at increased power levels can further contribute to the saturation of the resonant frequency. In essence the diffusion mechanism represents a shunt path for carriers through the diode and imposes an upper limit on the laser response. We also note that the K factor is continuously varying as the power is increased up to ω_{max} (where it is determined by diffusion) and so is of little utility in predicting maximum bandwidth.

The approach applies equally well to strained layer and multi-quantum well lasers. We show a comparison of ω_r versus $\sqrt{\text{power}}$ in Fig.7 for the unstrained single and multiple well situations and the single strained layer device all on a GaAs substrate. The multiquantum well achieves a higher response than the single well due to the superior η_e . The strained well is superior due to both a larger η_e and a lower τ_{ST}^*

To compare with conventional approaches the differential gain is shown to be related to the differential lifetime as

$$g_0^{-1} = v_g \tau_{ST}^* \frac{dn}{dE_{FT}} kT \quad (7)$$

Although a maximum g_0 provides the maximum frequency at a given power in the linear regime it is clear that the maximum frequency is determined by τ_{ST}^* and η_e .

In summary a new approach has been introduced to describe the non-linear gain mechanism and to predict the maximum laser frequency. The approach describes both the low frequency roll-off due to the RC diode time constant and the excessive damping observed in practise. The technique provides analytical results for all quantum well structures and provides a new interpretation in terms of the system Fermi level.

- [1] R.Nagarajan, M.Ishikawa, T. Fukushima, R. Geels and J.E. Bowers. Journ. of Quantum Electronics, Vol.28, No.10, pp.1990
- [2] M. Ishikawa, R. Nagarajan, T. Fukushima, J. Wasserbauer, and J.E. Bowers. IEEE Journ. Quant. Electronics, Vol. 28, No. 10, pp 2230

- [3] N. Tessler, R. Nagar, and G. Eisenstein, IEEE Journ. Quant. Electronics, Vol.28, No.10 pp2242
- [4] S.m. Sze, Physics of Semiconductor Devices, J. Wiley & Sons Inc.
- [5] G.W. Taylor, J. Appl. Phys. 70 (5), 1991, pp2508

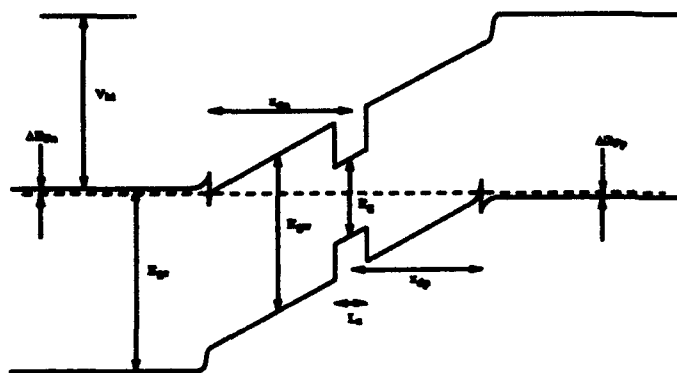


Fig 1a Energy band diagram at equilibrium

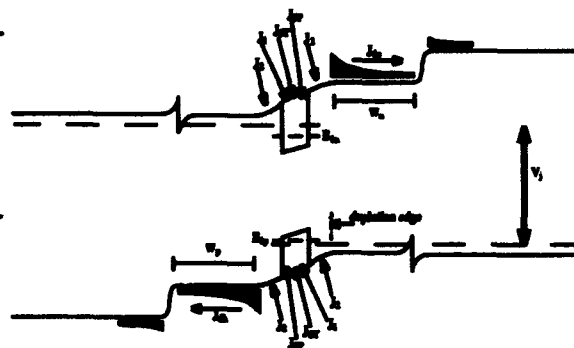


Fig 1b Energy band diagram at lasing



Fig 1c Inverted refractive index profile

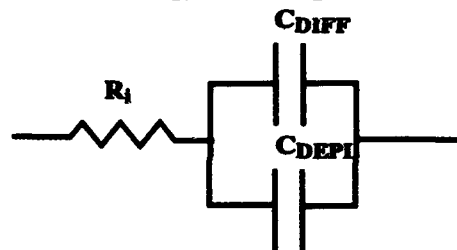


Fig 2 Equivalent electrical circuit of parasitic resistance and capacitance

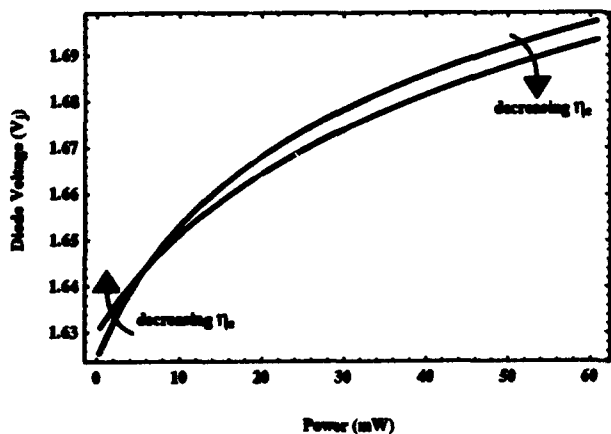


Fig 3 Variation of diode voltage with optical power

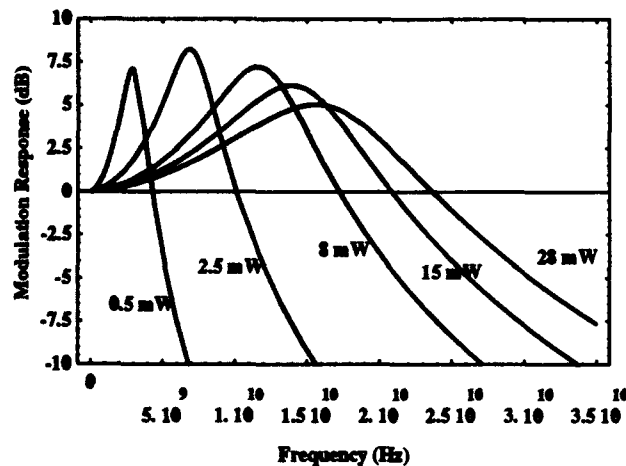


Fig 4a Small signal modulation response of diode laser

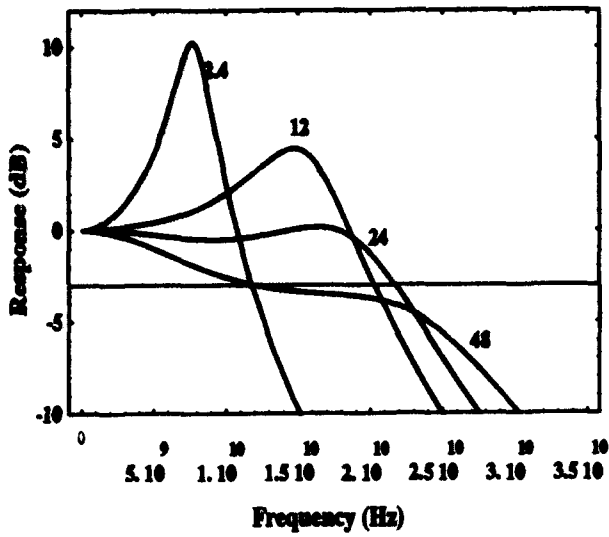


Fig 4b Small signal response with additional electrical pole

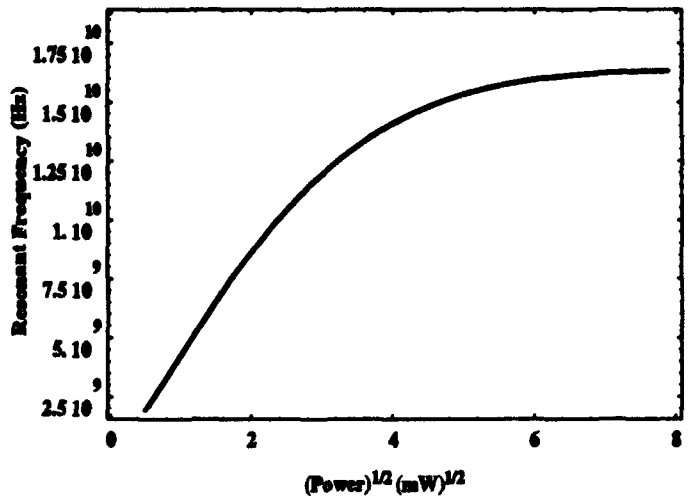


Fig 5 Resonant frequency versus square root of optical power

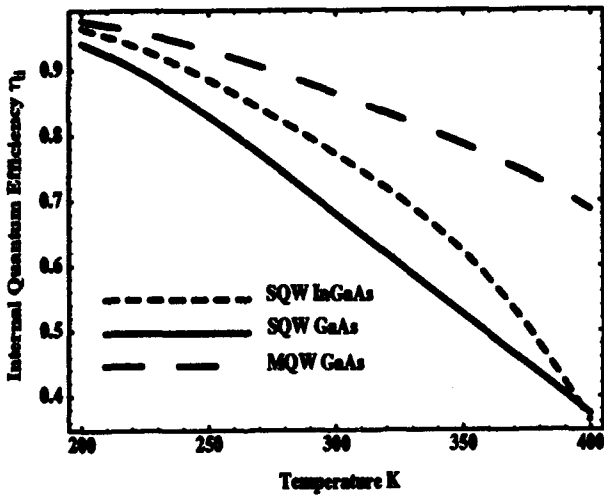


Fig 6 Temperature dependence of electrical confinement factor

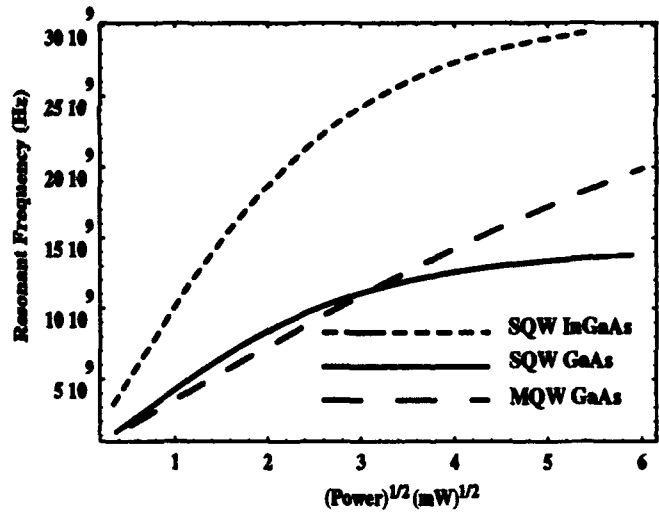


Fig 7 Variation of resonant frequency for strained layer and multi-quantum well lasers

**A Self-Consistent Finite Difference Simulation Method for
Quantum Well Electron Transfer Structures**

C.M. Weinert and N. Agrawal

Heinrich-Hertz-Institut für Nachrichtentechnik Berlin GmbH

Einsteinufer 37, D 1000 Berlin 10, Germany

Tel. + +30 31002 255

Electroabsorptive and electrorefractive effects due to phase space filling by electron transfer into quantum well (QW) layers are suitable for the design of high speed space switches [1]. Recently, electron transfer structures (ETS) based on the InGaAsP/InP material system have been reported in which electrons were transferred into modulation doped wells [2] and superlattices [3]. The great number of design parameters to be considered in such heterostructures necessitates a fast and reliable numerical design tool for their optimization. In this work a self-consistent finite difference simulation method is presented which simultaneously solves Poisson's equation, continuity equation and Schrödinger's equation for these nipin structures. In contrast to the previous work [1,4] this method goes beyond the space charge layer approximation and, therefore, accurately describes the electron transfer and leakage current.

For a description of the present method consider the InGaAsP/InP/InAlAs ETS schematically shown in Fig 1. Determination of band bending $\Psi(x)$ for evaluation of the band structure and charge distribution for electrons $n(x)$ and holes $p(x)$ under bias requires solution of Poisson's equation, which is

$$\frac{\partial^2 \Psi}{\partial x^2} = \frac{\epsilon_0}{\epsilon} (N_D - n - N_A + p) \quad (1)$$

where N_D and N_A are the donor and acceptor concentrations respectively. For the electron transfer structures considered here current is carried almost entirely by majority carriers, namely, electrons. Since the recombination current is negligible, in the steady state the current density j and the continuity equations are

$$j = \mu n \frac{\partial F}{\partial x} \quad (2)$$

$$\frac{\partial j}{\partial x} = 0 \quad (3)$$

where μ is the electron mobility and F is the Fermi energy. In the bulk layers $n(x)$ and $p(x)$ are given by the Fermi integrals over the three dimensional density of states

(DOS). Moreover, since relatively high n and p doping levels (degenerate semiconductor) are required within the modulation doped electron transfer structures, the Fermi statistics is used. In the QW region charge density is given by [4]

$$n^{QW}(x) = \sum_i Z_i \Phi_i^2(x) \quad (4a)$$

$$Z_i = \frac{m^* k_B T}{\pi \hbar^2} \ln(1 + \exp(\frac{F - E_i}{k_B T})) \quad (4b)$$

where Z_i is the number of electrons per unit area for the i -th QW-level and $\Phi_i(x)$ is the i -th eigenfunction which is evaluated by solving Schrödinger's equation for the QW-potential obtained from the solution of Poisson's equation.

Equations (1-4) are solved at discretized mesh points located at x_k . If Ψ , $d\Psi/dx$, F and j at x_k are denoted by Y_{1k} , Y_{2k} , Y_{3k} , and Y_{4k} , respectively, then equations (1-3) can be converted into Finite Difference equations as

$$(Y_{1k} - Y_{1k-1}) - (A_{1k} - A_{1k-1})(x_k - x_{k-1})/2 = 0 \quad (5)$$

with $A_{1k} = Y_{2k}$, $A_{2k} = e_0(N_D - n - N_A + p)/\epsilon$, $A_{3k} = j/(\mu n)$, and $A_{4k} = 0$. This set of coupled equations can be solved iteratively by the relaxation method [5], i.e. the procedure is started with a trial solution and deviations from the exact solution are found and corrected by the derivatives of equations (5) with respect to Y_{ik} and Y_{ik-1} . Transformation of the coupled equations into block diagonal form ensures rapid diagonalization. The first iteration step is done using a trial solution. Next the energy levels and eigenfunctions of the QW are evaluated by the well known transfer matrix method for the actual potential distribution around the well from which the QW electron density is obtained using equation (4). Note that shape of the potential for the quantum well varies continuously with the applied bias. For the purposes of calculating the electron distribution in the well the wavefunction is truncated outside the well because the electron probability density outside the well is almost negligible. This procedure allows us to handle this complicated transition of the dimension of the density of states from 2D to 3D between different layers. The so obtained new QW electron density and band-bending is used for the next iteration step. Such an iterative process is continued until the convergence is reached.

As an example, we show in figure 1 the calculated band diagram and the charge density for an externally applied forward bias of $U = 0.75V$. A comparison of n calculated by using the 2D DOS in the QW layer and an approximate treatment using a 3D bulk DOS shows that the electron density is underestimated for a QW with thickness less than 200 Å. Therefore, in the present case of QW's with 100 Å thickness, the wells are filled at much lower bias than predicted by the 3D approximation. Filling at zero bias is unfavourable since it increases free carrier absorption. From figure 2 it is seen that low filling at zero bias and low leakage currents are obtained for high p doping of the barrier although ΔZ is reduced.

In addition to the refractive index change which is proportional to bandfilling, it is necessary to reduce the leakage current to low values for high speed applications. One important technological step to reduce leakage currents in the MOVPE grown ETS devices was to substitute the InP barrier by InAlAs barrier layers [3]. However, bandfilling and leakage current density also strongly depend upon the reservoir doping. In figure 2 we summarize the results for the QW structure for various doping levels N_D and N_A of the reservoir and barrier layers, respectively. Figure 2a shows filling of the QW at zero bias measured as the sum of Z_i of the QW levels (which for this structure is one). Considerable filling of the level already occurs at reservoir doping below 10^{18} cm^{-3} especially if p-doping in the barrier is low. On the other hand, figure 2b shows that the change $\Delta Z = Z(U=0.75V) - Z(U=0)$ first increases rapidly with N_D but is saturated at values above 10^{18} cm^{-3} . The calculated leakage current density (fig. 2c) shows a drastic increase of several orders of magnitude for the doping variations considered. N_D should be carefully chosen in order to get a large ΔZ close to saturation yet with a small leakage current.

Concluding, we have developed an effective numerical method which allows fast and accurate simulations of a variety of properties which are crucial to the design of QW electron transfer structures. Further examples of simulations of such structures including the issues involved in optimizing the multiple superlattice structures [3] with respect to a lower voltage-length product will be discussed at the conference.

[1] M. Wegner, J. E. Zucker, T. Y. Chang, N. J. Sauer, K. L. Jones, and D. S. Chemla, Phys. Rev. B 41, 3097 (1990).

[2] N. Agrawal, D. Hoffmann, D. Franke, K. C. Li, U. Clemens, A. Witt, and M. Wegner, Appl. Phys. Lett. 61, 249 (1992).

[3] N. Agrawal, F. W. Reier, H. Selber, C. Bornholdt, C. M. Weinert, K. C. Li, D. Franke, D. Hoffmann, L. Berger, and M. Wegner, Proceedings of the 18-th European Conference on Optical Communication, Berlin, Germany, pp. 213-216 (1992).

[4] J. Wang, J. P. Leburton, and A. J. Sengers, IEEE Photon. Technol. Lett. , 3, 709 (1991).

[5] W. H. Press, B. P. Flannery, S. A. Teukolsky, and W. T. Vetterling, "Numerical Recipes", (Cambridge: Cambridge University Press), pp. 588-608, (1986).

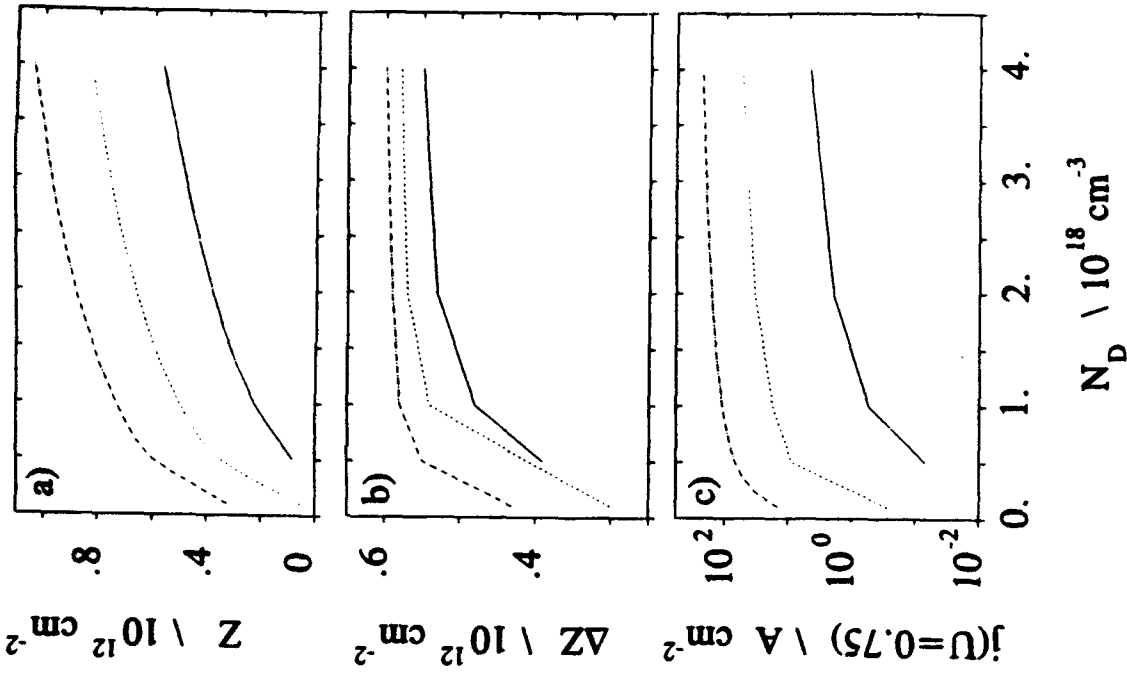


Figure 2: a) Bandfilling Z at $U=0$, b) charge transfer ΔZ for $U=0.75$ V, and c) leakage current j , as a function of reservoir n-doping N_D for different p-doping of the barrier (solid line: $N_A = 10^{18} \text{ cm}^{-3}$, dashed line: $N_A = 5 \cdot 10^{17} \text{ cm}^{-3}$, dashed-dotted line: $N_A = 10^{17} \text{ cm}^{-3}$)

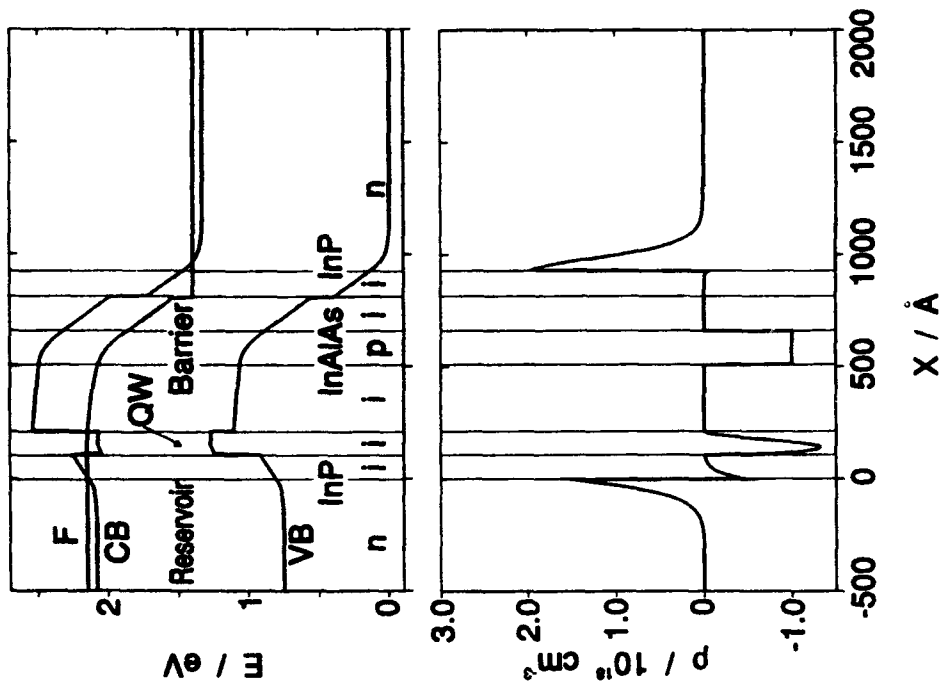


Figure 1: Layer structure and energy band diagram for an electron transfer structure with a QW of 100 \AA thickness (InGaAsP, $\lambda_Q = 1.55 \text{ \mu m}$) for $U=0.75$ V. Charge density ρ in the QW is calculated by Eqs. (4).

Spatio-Temporal Behavior of Y Junction Semiconductor Laser Arrays

Prasad Subramanian, Herbert G. Winful

Dept. of Elec. Eng. & Comp. Science, Univ. of Michigan, 1301 Beal, Ann Arbor, MI 48109

Y junction semiconductor laser arrays have attracted attention because they tend to favor in-phase operation and therefore generate predominantly single lobe output beams [1, 2]. Recent streak camera measurements, however, have indicated that these lasers exhibit sustained self-pulsations under CW pumping [4]. These pulsations have not yet been properly explained. In this paper we use a propagation model to examine the spatio-temporal dynamics of Y junction lasers and arrays. We find that even a single Y junction laser is capable of exhibiting sustained pulsations.

The propagation model is based on the following partial differential equations for the lateral field $\psi(x, z, t)$ and the carrier density N :

$$2ik \frac{\partial}{\partial z} \psi + \frac{\partial^2}{\partial x^2} \psi + k_0^2 \Gamma \Delta \epsilon(x, z) \psi = 0. \quad (1)$$

Here the dielectric perturbation $\Delta \epsilon$ includes the built-in refractive index distribution, gain, loss, and carrier-induced index antiguiding. The time dependence of the carrier density is governed by

$$\frac{\partial}{\partial t} N = \frac{J}{qd} + D \frac{\partial^2}{\partial x^2} N - \frac{N}{\tau_{nr}} - \Gamma \frac{g(N)}{h\omega} |\psi|^2. \quad (2)$$

The first term on the right hand side of the equation represents the pumping. Carrier diffusion is represented by the second term and the third and fourth terms represent spontaneous carrier recombination and stimulated emission respectively.

We examine the temporal behavior of single element Y junction lasers as well as dual element Y junction arrays. Computer simulations show that even a single Y junction laser is capable of rich dynamic behavior. Figure 1 shows the output of a single Y junction laser driven a constant pump current. The laser exhibits sustained self pulsations at a multigigahertz rate. The mechanism for the self pulsations is as follows: Constructive interference at the Y junction creates an intense in-phase mode

which strongly depletes the carriers at the center. The hole burnt in the carrier profile means that the out-of-phase mode will have a better overlap with the gain distribution and will begin to grow at the expense of the in-phase mode. However, the out-of-phase mode is much more lossy and gets converted largely into radiation. The output intensity drops as the intense in-phase mode is converted into the lossy out-of-phase mode. This allows the depleted carriers to be pumped up again and the process repeats itself indefinitely. This laser structure is essentially a device with a periodic modulation of loss. In addition to the above mentioned mechanism, antiguiding induced refractive index changes also play an important role in the dynamics of such a laser. Single element Y junction lasers with higher index steps are seen to be relatively more stable than ones with lower index steps.

A twin element weakly guided array is seen to exhibit chaotic temporal behavior. A strongly guided twin element array, on the other hand, is seen to exhibit small amplitude high frequency oscillations which are accompanied by rapid, periodic changes in the spatial field pattern (Figure 2). The behavior of the far field pattern is also seen to be periodic. Simulation results for multi-element arrays will also be presented.

References

- [1] W. Streifer, D. F. Welch, P. S. Cross and D. R. Scifres, "Y-Junction Semiconductor Laser Arrays: Part 1-Theory" *IEEE J. Quantum Electron.*, vol. QE-23, pp. 744-751, 1987.
- [2] D. F. Welch, W. Streifer, P. S. Cross and D. R. Scifres, "Y-Junction Semiconductor Laser Arrays: Part 2-Experiments" *IEEE J. Quantum Electron.*, vol. QE-23, pp. 752-756, 1987.

- [3] M. Taneya, M. Masumoto, S. Matsui, S. Yano and T. Hijikata, "0° phase mode operation in phased-array laser diode with symmetrically branching waveguide" *Appl. Phys. Lett.*, vol. 47, pp. 341-343, 1985
- [4] N. Yu, R. K. Defreez, D. J. Bossert, R. A. Elliot, H. G. Winful and D. F. Welch, "Observation of Sustained Self-Pulsation in CW operated Flared Y- Coupled Laser Arrays" *Electron. Lett.*, vol. 19, pp. 1203-1204, 1988.

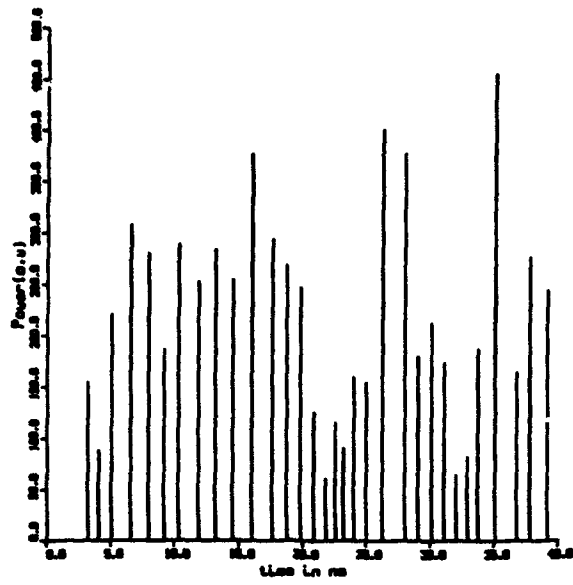


Figure 1

Sustained self pulsations from a single element Y junction laser

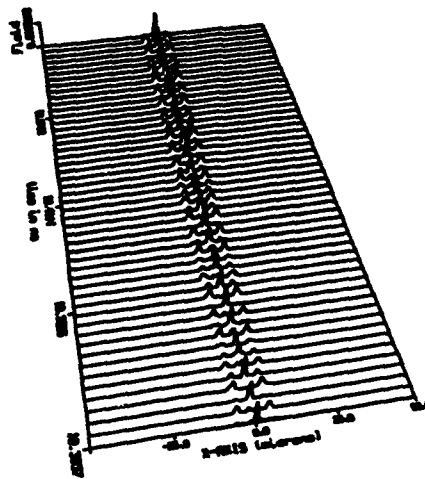


Figure 2

Time evolution of the near field from a twin element Y junction array

Wednesday, March 27, 1995

Waveguide Frequency Conversion

IWC 8:30am-10:30am
Mesquite C/D

Martin M. Fejer, *Presider*
Stanford University

Quasi-phasematched second harmonic generation in periodically poled lithium niobate waveguides

Masahiro Yamada and Naoji Nada

Applied magnetic Research Department, Corporate Research Laboratories, Sony Corp.
141, Kita-Shinagawa 6-7-35, Shinagawa-ku, Tokyo, Japan
Tel. 81-3-3448-2547, Fax. 81-3-3448-4308

To realize a compact coherent blue light source, second harmonic generation (SHG) in a waveguide has been studied. Quasi-phasematching (QPM) is being investigated intensively among several candidates for phasematching because it gives a higher conversion efficiency using the largest component of the nonlinear susceptibility tensor. QPM requires a periodic modulation of the optical nonlinear coefficient. Such a periodic domain structure can be obtained by alternating the crystal orientation periodically. The conversion efficiency of QPM-SHG depends strongly on the shape of inverted domain structure. An ideal domain structure is a rectangular shape at any depth in the waveguide. For KTP anisotropic diffusion of Ba yields the rectangular domain shape with a large aspect ratio [1], and $>20\text{mW}$ blue output with the normalized conversion efficiency of $>400\%/W\text{cm}^2$ was generated [2]. For lithium tantalate (LiTaO_3), an around $2\mu\text{m}$ deep semicircular inverted domain was obtained by proton-exchange and heat treatment just below the Curie temperature, and blue output of $>20\text{mW}$ was observed [3]. For lithium niobate (LiNbO_3) the periodic domain structure was fabricated mainly by Ti indiffusion [4] or Li_2O outdiffusion [5]. In spite of the relatively larger nonlinear coefficient in lithium niobate, the conversion efficiencies of the actual waveguide devices had been lower than those of KTP and lithium tantalate waveguides. This was mainly due to the shallow triangular domain. Because of change in the duty cycle of domains throughout the cross section of the waveguide using the diffusion methods for domain inversion of lithium niobate, higher conversion efficiencies can not be expected.

We have succeeded in fabricating the fine domain structure which the domain boundary is parallel to the c-axis of lithium niobate crystal by applying an external electric field. This method enabled the fabrication of ideal domain structure for the first-order QPM-SHG waveguide devices [6]. And $>20\text{mW}$ blue light with the normalized efficiency of $600\%/W\text{cm}^2$ was obtained [7].

Recently we applied this method to x-cut lithium niobate and succeeded in realizing the TE-mode QPM-SHG waveguide device that can produce mW order blue light.

In this paper current results about our QPM-SHG devices using z-cut and x-cut lithium niobate will be presented.

references

- [1] C.J. van der Poel, J.D. Bierline, J.D. Brown, and S. Colak, *Appl. Phys. Lett.*, **57**, 2074 (1990)
- [2] J.D. Bierline, *CLEO 91*
- [3] K. Mizuuchi, *CLEO 92*
- [4] E.J. Lim, M.M. Fejer, and R.L. Byer, *Electron Lett.*, **25**, 174 (1989)
- [5] J. Webjorn, F. Laurell, and G. Arvidsson, *IEEE Photonics Technol. Lett.*, **1**, 316 (1989)
- [6] M. Yamada, N. Nada, and K. Watanabe, *IPR 92*
- [7] M. Yamada, N. Nada, M. Saitoh, and K. Watanabe, *Appl. Phys. Lett.*, to be published

Electro-optic Tuning and Modulation of Second Harmonic Generation in Quasi-Phase Matched LiNbO₃ Waveguides

X. F. Cao
E-TEK Dynamics Inc.,
1885 Lundy Ave., San Jose, CA 95131

Second harmonic generation (SHG) by quasi-phase matching (QPM) in LiNbO₃ waveguides has recently attracted a great deal of attention. Using periodically domain inverted grating on LiNbO₃, normalized conversion efficiency of order of 20 ~ 80%/W.cm² have been achieved.¹⁻⁴ However, the phasematching bandwidth length product is rather small for QPM waveguides, thus imposes a very critical limit on the diode pump sources. Temperature tuning of the QPM wavelength in LiNbO₃ waveguide have been demonstrated,³ a tuning rate which is comparable to the diode laser temperature tuning can be achieved. However, in order to obtain stable SHG output, a fast responding fine tuning scheme is required for the electronic feedback stabilization system. In this paper, we demonstrate the wavelength tuning and modulation of the quasi-phase matched SHG signal using the electro-optic (EO) effect in LiNbO₃ waveguide.

The QPM LiNbO₃ waveguide fabrication was described elsewhere.⁴ The period of the domain inversion grating was chosen to match the required second order QPM period at 852 nm. The 18 mm long channel waveguides were design to be single mode at the fundamental wavelength and support three modes at the harmonic wavelength. A 120 nm thick SiO₂ buffer layer was sputtered on substrate surface in order to reduce waveguide loss. A three sections coplanar waveguide electrode pattern was defined by lift-off and gold plating. The electrode center width, gap and thickness is 8, 4, and 3 μm , respectively. The length of each electrode is 5 mm. Due to the large difference in the modesize at the fundamental wavelength λ^0 and the harmonic wavelength $\lambda^{2\omega}$, the small electrode gap give raises a large difference in the electric-optical field overlap factor at λ^0 and $\lambda^{2\omega}$, and thus results in a large electric field induce mode index mismatch.

In the SHG experiment, a high power single mode diode laser (SDL-5422) was used as pump source, the experimental setup is described in Ref. 4. First, the diode laser was temperature tuned to the QPM wavelength, and it was fine tuned around the QPM wavelength. The fine tuning of the diode laser wavelength was achieved by modulating the drive current. The QPM wavelength was monitored by a wavemeter, and fine tuning in wavelength was determined from the injection current/wavelength curve given by the manufacturer. The QPM wavelength was measured as a function of applied voltage (same voltage was applied to three

electrodes). The EO tuning curve is shown in Fig. 1, a 0.5 nm tuning range is obtained with ± 15 V applied voltage.

Due to the waveguide nonuniformity and the narrow QPM bandwidth, it is very difficult to maintain phase matching condition over long interaction length. We have demonstrated that the phase mismatch due to the waveguide nonuniformity can be partially corrected by the EO effect using multi-section electrode structures, and therefore increase the effective interaction length. As shown in Fig. 2(b), by separately biasing three electrodes, up to a factor of five enhancement in SHG power can be obtained due to the increased effective interaction length. At the same time the QPM bandwidth is decreased by a factor of 2.2. On the other hand, if a large QPM bandwidth is desired, three electrodes can be biased in such way that the phase matching wavelength is shifted by equal amount to both the short and long wavelength direction, thus providing a broad QPM bandwidth. As shown in Fig. 2 (c), QPM bandwidth as large as 0.3 nm can be obtained when the three electrode were biased at -15 V, 0 V, and 15 V, respectively. Such a wide QPM bandwidth is potentially useful for QPM frequency doubling of a multimode high power diode lasers.

The experimental result of EO modulation of the QPM second harmonic signal is shown in Fig. 3, a modulated SHG signal with twice of the applied voltage signal frequency was obtained. One interesting fact of this modulation scheme is that the duty cycle of the modulated SHG signal can be controlled by the amplitude of the applied voltage. The modulation bandwidth of up to 500 MHz (limited only by the pulsed voltage source) has been demonstrated.

In conclusion, we have demonstrated SHG wavelength tuning and intensity modulation, utilizing the electro-optic effect in a quasi-phase matched LiNbO₃ waveguide. A 0.5 nm tuning range of phase matched wavelength has been achieved by applying a voltage of ± 15 V at the diode laser wavelength of 852 nm. Stable modulation of the frequency doubling output with a minimum bandwidth of 500 MHz has also been demonstrated. In addition, we have shown that an five fold enhancement in the SHG conversion efficiency can be obtained with a three sections electrode fine tuning scheme.

References:

1. E. J. Lim, M. M. Fejer, and R. L. Byer, *Electron Lett.* **25**, 174 (1989).
2. K. Mizauchi, K. Yamamoto, and T. Taniuchi, *Appl. Phys. Lett.* **60**, 301 (1992).
3. N. Noda, O. Kawakubo, and K. Watanabe, *CLEO'91*, Baltimore, MD, paper CTuV7, (1991).
4. X. F. Cao, B. Rose, R. Srivastava and R. V. Ramaswamy, *Optics Lett.* **17**, 795 (1992).

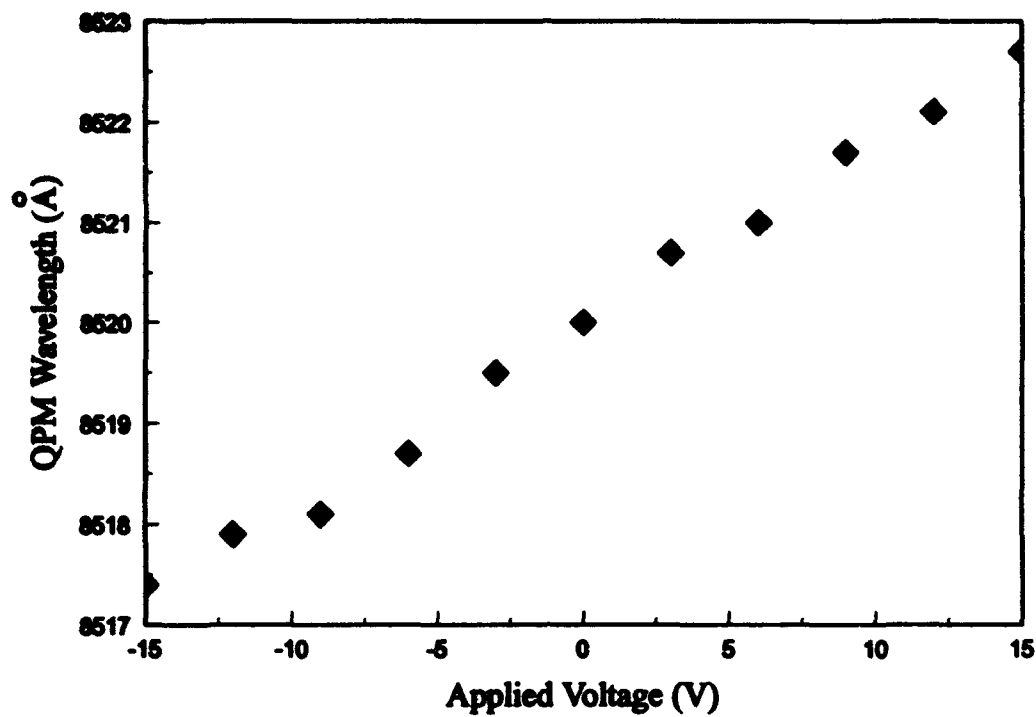


Fig.1 QPM wavelength as a function of applied voltage in the QPM waveguide.

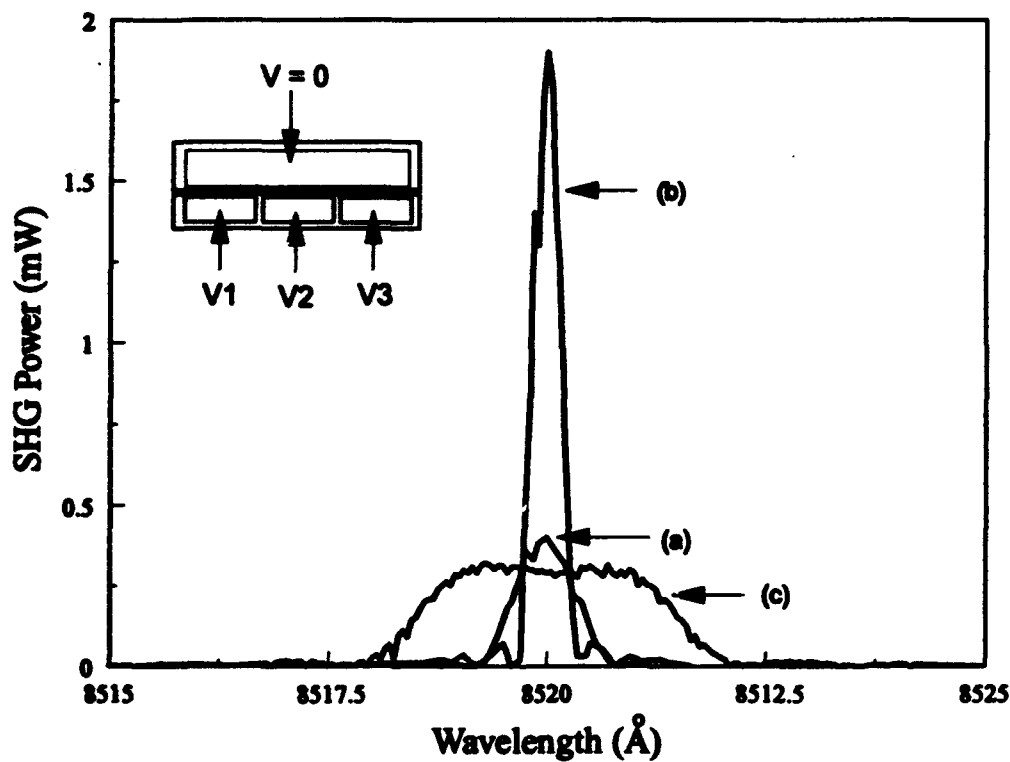


Fig. 2 QPM bandwidths for three different applied voltage combinations; (a) $V_1=V_2=V_3=0$ (V); (b) $V_1=-0.5$ (V), $V_2=1.2$ (V), $V_3=1.6$ (V); (c) $V_1=-5$ (V), $V_2=0$ (V), $V_3=5$ (V).

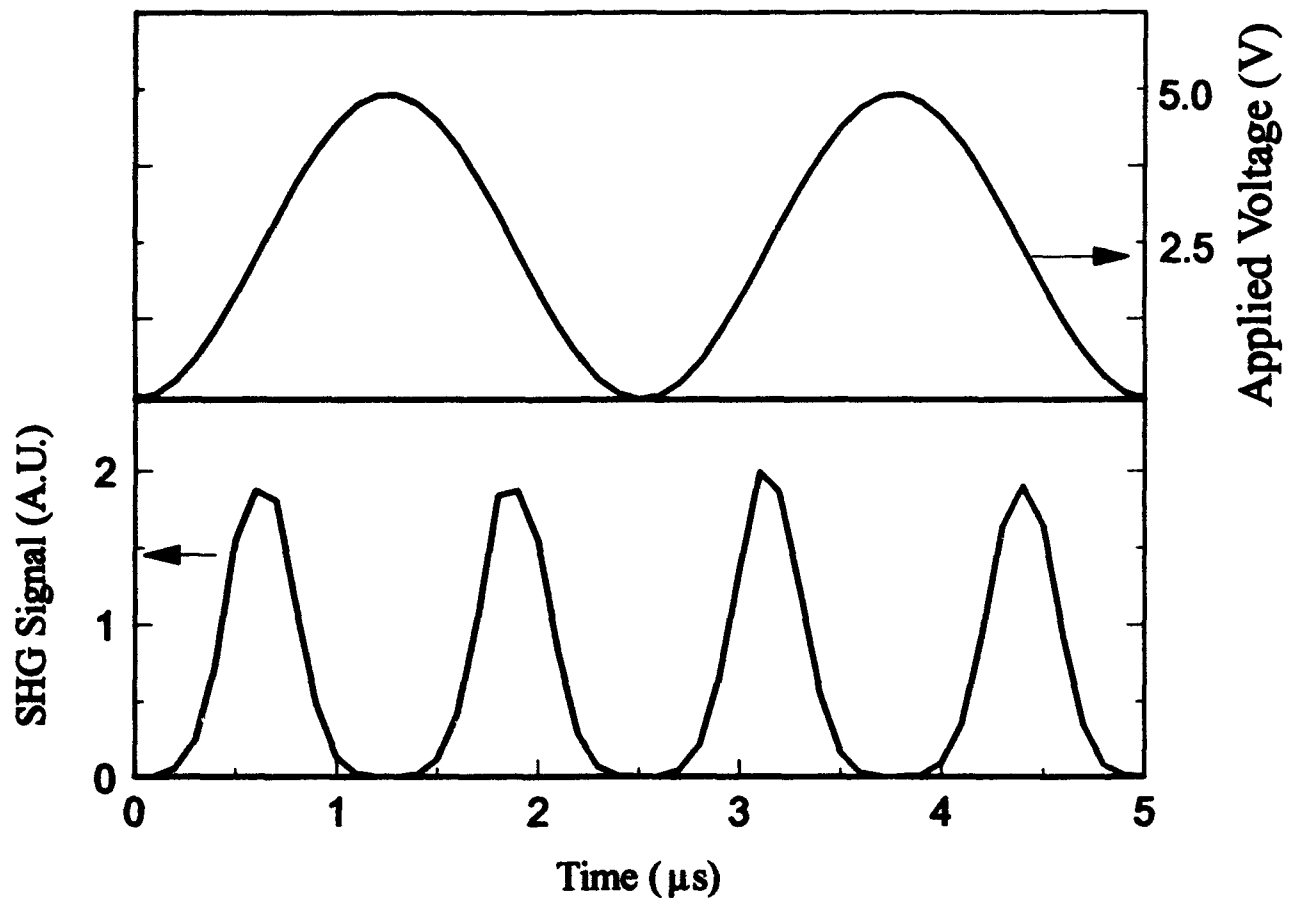


Fig. 3 Electro-optic modulation of the QPM second harmonic signal.

Depth Profiling of the d_{33} Nonlinear Coefficient in Annealed Proton Exchanged LiNbO₃ Waveguides

M. L. Bortz, L. A. Eyres, and M. M. Fejer

*E. L. Ginzton Laboratory, Stanford University, Stanford, California 94305
415-725-2282*

Quasi-phasematched frequency conversion in LiNbO₃ waveguides offers an efficient method for the generation of short wavelength radiation from infrared laser diodes. While different techniques have been used to form the ferroelectric domain grating necessary for quasi-phasematching, the annealed proton exchange (APE) process has been used exclusively to provide waveguide confinement. Contradictory measurements of the nonlinear optical properties of proton exchange (PE) and APE-LiNbO₃ waveguides have been reported for several years.^{1,2,3,4,5,6} The d_{33} coefficient of PE-LiNbO₃ has been reported to be between 0⁴-⁵ and 0.63³ the bulk LiNbO₃ value. No successful guided wave frequency conversion devices have been fabricated using unannealed PE waveguides. The effect of annealing is similarly controversial, with reports of d_{33} in APE-LiNbO₃ varying from 0⁴ to 90³ % of the bulk value. Recently demonstrated^{7,8} guided wave quasi-phasematched frequency doublers with normalized conversion efficiencies of > 600 %/W-cm² indicate that APE-LiNbO₃ waveguides must have a large nonlinear coefficient. In this letter we report depth profiling of the d_{33} nonlinear coefficient in APE-LiNbO₃ waveguides using reflected second harmonic generation (SHG) from wedged samples. The data explains the variation in the d_{33} values reported in the literature. Normalized conversion efficiencies calculated using the depth profiles of the d_{33} nonlinear coefficient are consistent with those observed from guided wave quasi-phasematched SHG devices.

Measurement of the d_{33} coefficient in APE-LiNbO₃ is complicated by the graded refractive index profile and the unknown spatial variation in the d_{33} coefficient. We have measured the depth dependence of the d_{33} coefficient in APE-LiNbO₃ waveguides using reflected SHG from wedged samples. With a 532 nm fundamental wavelength the 266 nm SH wavelength is above the APE-LiNbO₃ band edge and only SH generated within a 0.05 μm^4 absorption depth of the surface is observed. The samples were wedged so that depth into the sample was mapped into lateral position, allowing depth profiling via lateral translation.

APE waveguides were fabricated on x-cut LiNbO₃ by proton exchanging in pure benzoic acid at 173 °C for 66 minutes to a depth of 0.42 μm^9 , and annealing in air at 333 °C for varying times. The samples were subsequently polished at a wedge angle ≤ 2 mrad, with the exact relationship between lateral position and depth determined using surface profilometry. Frequency doubled 532 nm radiation from an injection seeded Q-switched Nd-YAG laser was focussed at normal incidence to a 30 μm FWHM diameter spot with a peak intensity of ≤ 150 MW/cm². The samples were scanned under the focussed spot using a motorized micrometer and the reflected 266 nm SH was detected vs. lateral position using a dichroic mirror, a solar blind photomultiplier, and a gated integrator. The fundamental and SH fields were polarized parallel to each other and the z-axis of LiNbO₃ and were coupled by the d_{33} nonlinear coefficient. To discriminate against polishing artifacts each sample had an internal, unexchanged LiNbO₃ reference formed by masking 1/2 the sample with Al prior to proton exchange, which was removed by etching in NaOH prior to annealing. Only samples that displayed constant reflected SH over the entire unexchanged side, with

intensities equal to that from bulk LiNbO_3 , were used in this study. A portion of the sample remained unwedged, so that data from the original surface could be obtained. Also, care was taken to obtain SHG and profilometry data over the whole surface to eliminate errors associated with polish skew. Figure 1 shows the sample orientation and geometry, with the dashed line indicating the the beginning of the wedged portion of the sample and the origin of the lateral position; negative values of lateral position represent data from the unwedged portion of the sample and thus the original surface.

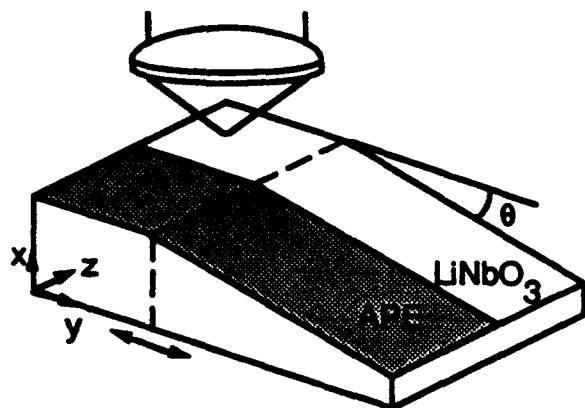


Figure 1. Wedged sample used for reflection SHG measurements. The dashed line indicates the beginning of the wedged portion of the sample.

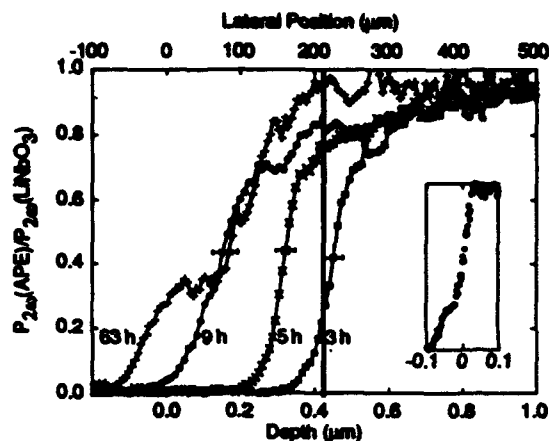


Figure 2. Reflected 266 nm SH power, normalized to that from bulk LiNbO_3 , vs. lateral position (top scale) or depth into the waveguide (bottom scale) for APE- LiNbO_3 annealed for 3, 5, 9, and 63 hrs.

Figure 2 shows the reflected SH power at 266 nm, normalized to the signal from bulk LiNbO_3 , vs. depth and/or lateral position for APE- LiNbO_3 annealed for 3, 5, and 9, and 63 hrs. The error bars represent the variation in the depth measurement for 5 different scans. The figure inset shows the spatial step response of the detection system projected onto depth, measured by scanning the focussed spot off the end of a bulk LiNbO_3 sample. This demonstrates a depth resolution of $\leq 0.05 \mu\text{m}$. For the APE- LiNbO_3 sample annealed for 3 hr no reflected SH signal is observed from the original surface or from the portion of the wedged surface corresponding to the original PE layer. However, there is an abrupt increase from zero to 80% of the bulk LiNbO_3 value at a position corresponding to the interface between the original PE film and the LiNbO_3 substrate. At lateral positions corresponding to depths greater than the initial PE depth the reflected SH power approaches that measured from bulk LiNbO_3 , and at depths $\geq 1 \mu\text{m}$ the measured reflected SH power is indistinguishable from that of bulk LiNbO_3 .

With further annealing, the position of the abrupt increase in the reflected SH power moves towards the surface and the reflected power approaches that from bulk LiNbO_3 at shallower positions. No reflected signal was ever observed from the original surface regardless of annealing time (the sample annealed for 63 hrs had a polishing defect between lateral positions $-75 \mu\text{m}$ and $+50 \mu\text{m}$ resulting in the enhanced signal near the origin. However, no signal was observed over the rest of the unwedged portion of this sample). For the longest anneal times the reflected power rises to that from bulk LiNbO_3 at depths equal to or less than the original PE depth. Since the refractive index profiles had 1/e depths of 0.9, 1.3, 2.0, and $9.2 \mu\text{m}$ respectively, the modes extend significantly deeper than the

region of varying d_{33} coefficient. Comparison between these results and previously published values for d_{33} in APE-LiNbO₃ will be discussed.

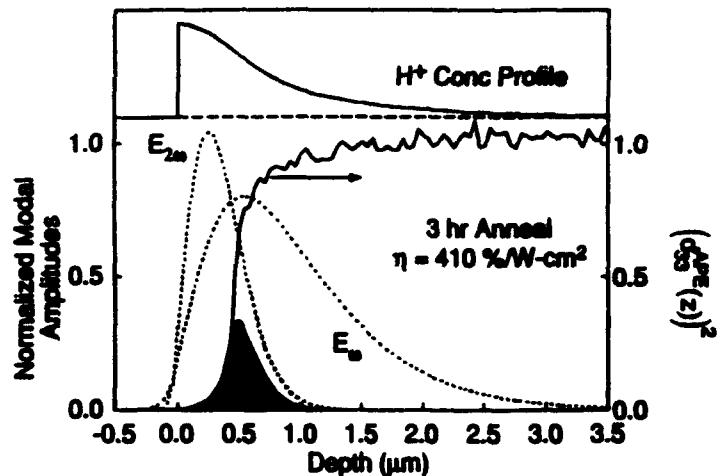
The measurements of the d_{33} coefficient as a function of depth into the waveguide shown in Figure 2 can be used with the optical modes to determine the actual normalized conversion efficiency for any guided wave nonlinear optical interaction. As an example, we compute the normalized conversion efficiency for frequency doubling $\lambda_{00} = 850$ nm radiation in a z-cut, x-propagating APE-LiNbO₃ waveguide. We assume 1st order quasi-phaseshifting with a uniform, depth independent ferroelectric domain grating, which can be fabricated using an electric field⁷ or electron beam⁸ poling technique. This grating greatly simplifies the depth overlap integral calculation since the magnitude of the Fourier component used to quasi-phaseshift is constant in depth. With the output SH power given by $P_{2\omega} = \eta P_{\omega}^2$, the normalized conversion efficiency η is defined as:

$$\eta = \frac{8\pi^2 (d_{\text{eff}})^2}{n_{\omega}^2 n_{2\omega}^2 c \epsilon_0 \lambda_{00}^2} \left| \int_{-\infty}^{+\infty} \int_0^{+\infty} d_{33}^{\text{APE}}(z) E_{\omega}^2(y, z) E_{2\omega}(y, z) dy dz \right|^2$$

where $d_{\text{eff}} = 2d_{33}^{\text{LiNbO}_3}/\pi$, $d_{33}^{\text{APE}}(z)$ is normalized to $d_{33}^{\text{LiNbO}_3}$, and the fields are normalized to carry unity power. We model a waveguide fabricated with a proton exchange depth of 0.42 μm and annealed at 333 $^{\circ}\text{C}$ for 3 hours, which represent typical device processing parameters. The depth dependence of the refractive index profile was determined using a one-dimensional nonlinear diffusion model for the APE process¹⁰ and we assumed a 4 μm wide top-hat dependence for the lateral refractive index profile. We assume separable modes $\{E(y, z) = E_y(y)E_z(z)\}$, and computed the mode profiles at $\lambda_{00} = 850$ nm and $\lambda_{2\omega} = 425$ nm using the effective index method. Shown in Figure 3 are the optical modes, the normalized reflected SH power proportional to $(d_{33}^{\text{APE}}(z))^2$, and the modal overlap $d_{33}^{\text{APE}}(z)E_{\omega}^2(z)E_{2\omega}(z)$ vs. depth. Also shown is the H^+ concentration profile, proportional to the index profile. The normalized conversion efficiency assuming the d_{33} coefficient to be independent of depth and equal to the bulk LiNbO₃ value is 2010 %/W-cm².¹¹ The shaded area is the depth overlap of the modes with the measured d_{33} value, and using this depth overlap we compute a normalized conversion efficiency of 410 %/W-cm². For unannealed waveguides the efficiency is zero since $d_{33}=0$ for PE-LiNbO₃ and for very long anneal times the modal overlap is essentially removed from the initial proton exchange region and the conversion efficiency decreases because of reduced confinement. Figure 3 shows that the variation in conversion efficiency with annealing is not due to a restoration in the d_{33} coefficient of the APE waveguide as much as a variation in the overlap integral due to a spatial redistribution of the modal fields away from the initial PE region.

There are two recent reports of guided wave quasi-phaseshifted SHG using depth-independent ferroelectric domain gratings, and normalized conversion efficiencies of 680⁷ and 700⁸ %/W-cm² were reported from devices with APE waveguides fabricated similar to the one modeled above, with the exception that the annealing was performed at 350 $^{\circ}\text{C}$ rather than 333 $^{\circ}\text{C}$. These observed efficiencies are near the calculated values, indicating that the general form of the d_{33} depth profile presented here allows reasonably accurate device modeling. Measurements of the efficiencies of guided wave QPM devices as a function of waveguide processing parameters will be presented to refine the models for the linear and nonlinear optical properties of APE-LiNbO₃, and optimization of the processing parameters to achieve a maximum normalized conversion efficiency for a given quasi-phaseshifting grating will be discussed.

Figure 3. The optical modes, the normalized reflected SH power proportional to $(d_{33}^{APB}(z))^2$, and the modal overlap $d_{33}^{APB}(z)E_{\omega}^2(z)E_{2\omega}(z)$ (shaded) vs. depth. Also shown is the H^+ concentration profile, proportional to the index profile.



- 1 T. Suhara, H. Tazaki, H. Nishihara, *Electron. Lett.* 25, 1326 (1989).
- 2 R. W. Keys, A. Loni, and R. M. De La Rue, *Electron. Lett.* 26 624 (1990).
- 3 X. Cao, R. Srivastava, R. V. Ramaswamy, and J. Natour, *IEEE Photon. Tech. Lett.* 3, 25 (1991).
- 4 F. Laurell, M. G. Roelofs, and H. Hsiung, *Appl. Phys. Lett.* 60, 301 (1992).
- 5 M. L. Bortz and M. M. Fejer, *Opt. Lett.* 17, 704 (1992).
- 6 W. Hsu, C. S. Willand, V. Gopalan, and M. C. Gupta, *Appl. Phys. Lett.* 61, 2263 (1992).
- 7 M. Yamada, N. Nada, and K. Watanabe, *Integrated Photonics Research Topical Meeting, 1992* (Optical Society of America, Washington, D. C., 1992), Paper TUC2.
- 8 M. Fujimura, K. Kintaka, T. Suhara, and H. Nishihara, *Electron. Lett.* 28, 1868 (1992).
- 9 T. Maciak and M. Sokolowski, *Optica Applicata*, 19, 423 (1989).
- 10 M. L. Bortz and M. M. Fejer, *Opt. Lett.* 16, 1844 (1991).
- 11 We used the following values in the calculation: $d_{33}=34.5$ pm/V, $n_{\omega}=2.1708$, and $n_{2\omega}=2.3036$.

Organic Crystal Cored Fibers for Efficient Frequency Doublings

**Shinsuke Umegaki
Keio University
1404-1 Katakura-Cho Hachioji
Tokyo, Japan 192**

Summary not available at time of printing.

Orientation Patterning of II-VI Semiconductor Films for Quasi-phasematched Nonlinear Devices

M. J. Angell, R. M. Emerson, J. L. Hoyt, and J. F. Gibbons
 Solid State Laboratory, Stanford University
 226 McCullough 4055
 Stanford, California 94305
 (415) 723-4194

M.L. Bortz, L.A. Eyres, and M.M. Fejer
 E. L. Ginzton Laboratory
 Stanford University
 Stanford, California 94305

Waveguide frequency conversion based on quasi-phasematched (QPM) nonlinear optical interactions has been actively studied over the past several years as a means for efficiently generating radiation at wavelengths where no convenient source exists. Quasi-phasematching requires modulation of the nonlinear susceptibility every coherence length (typically several microns), so these devices require media with nonlinear susceptibilities that can be spatially patterned. All efficient QPM waveguide devices fabricated to date have used ferroelectrics with periodically reversed domains to accomplish the necessary modulation of the effective nonlinear coefficient.

II-VI semiconductors have large nonlinear susceptibilities and wide bandgaps, making them attractive media for waveguide nonlinear optics. They are particularly interesting since they can be grown on GaAs substrates, suggesting monolithic integration with pump lasers. To take advantage of this

potential, methods of patterning the nonlinear susceptibility of II-VI films on GaAs must be developed. Patterning the orientation of the films during epitaxial growth provides such an opportunity, as the effective nonlinear coefficient depends on the orientation of the crystal. In this presentation we demonstrate a technique to pattern the orientation of II-VI films on GaAs substrates suitable for use in a QPM frequency doubler.

A possible device geometry is shown schematically in Figure 1. The waveguide consists of a ZnTe core and a ZnSe cladding on a GaAs substrate. Quasi-phasematching is achieved by periodic rotation of the film orientation. For TM polarization of the incident beam the effective nonlinear coefficient $d_{eff} = 2 d_{14} / \sqrt{3}$ in the $\langle 111 \rangle$ oriented regions while $d_{eff} = 0$ in the $\langle 100 \rangle$ regions.

Our method for growing such a patterned film is based on the observation that the orientation of a CdTe film on a GaAs

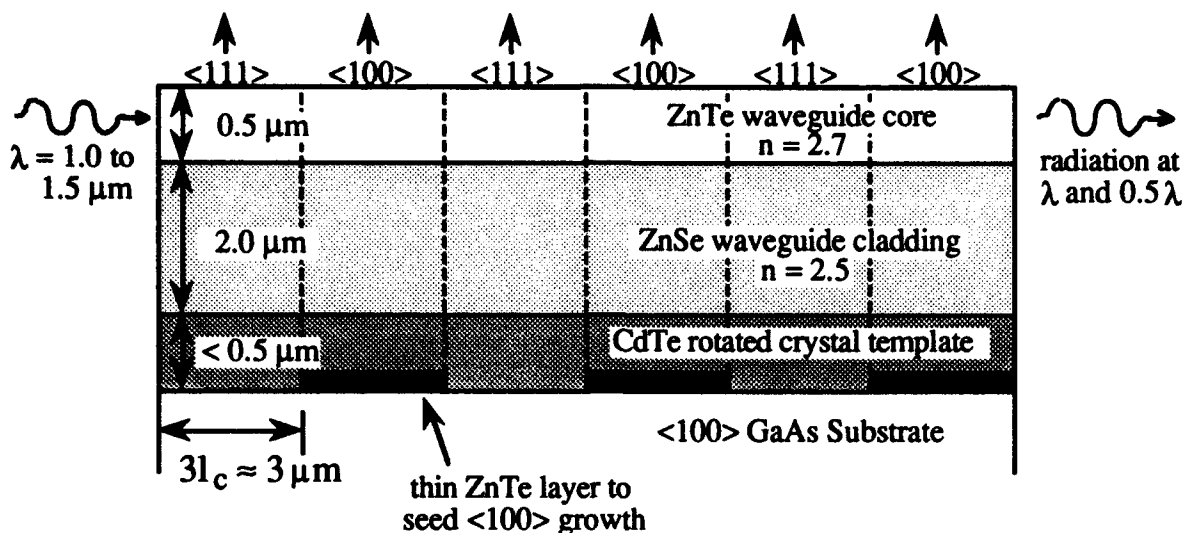


Figure 1. Proposed device geometry for a quasi-phased-matched frequency doubler.

substrate depends on the surface preparation.¹ CdTe grows with a $\langle 111 \rangle$ orientation on a clean $\langle 100 \rangle$ GaAs substrate, but when the substrate is seeded with a thin ZnTe layer, the CdTe preserves the $\langle 100 \rangle$ orientation of the substrate. The film patterning procedure is illustrated in Figure 2. A $\langle 111 \rangle$ CdTe film is grown on a bare GaAs substrate, and then is masked with the desired grating periodicity and etched back to the GaAs substrate using KI:I:HBr.² After a low temperature in-situ cleaning, developed to prepare the sample for regrowth, a thin ZnTe layer is deposited and the CdTe growth is resumed. The result is $\langle 100 \rangle$ CdTe in the etched regions and $\langle 111 \rangle$ CdTe in the masked areas.

The modulation of the nonlinear susceptibility was confirmed using reflected second harmonic generation. The $1.06 \mu\text{m}$ s-polarized output of a Q-switched Nd:YAG laser was weakly focused on the surface of the sample at an incidence angle of 45 degrees, and the reflected p-polarized second

harmonic output measured as the wafer was rotated around the surface normal. The dependence of the second harmonic on azimuthal angle is shown in Figures 3a and 3b. The solid curves are the theoretical expressions for the reflected SHG from a $\langle 111 \rangle$ oriented CdTe film, and a $\langle 100 \rangle$ CdTe film misoriented 3° towards $\langle 010 \rangle$. This tilt results from both the use of substrates misoriented 2° towards $\langle 011 \rangle$ and a further tilt of the CdTe film towards $\langle 01\bar{1} \rangle$.¹ The good agreement with the theoretical expressions confirms the $\langle 100 \rangle$ film orientation in the etched region and the $\langle 111 \rangle$ orientation in the masked regions, as is necessary for modulating d_{eff} to achieve quasi-phasing.

The patterned CdTe film can now serve as a template for the growth of the remaining layers of the waveguide structure. ZnTe films grown on $\langle 111 \rangle$ and $\langle 100 \rangle$ CdTe have followed the CdTe orientation, indicating that the rotated template established in the CdTe layer can be propagated upwards

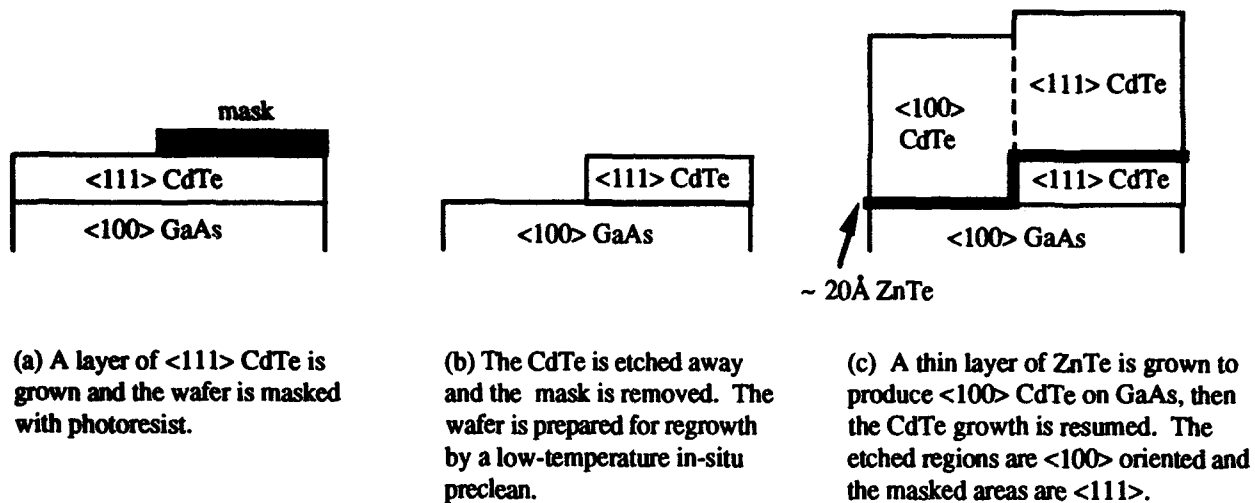


Figure 2. Processing steps for orientation patterning of CdTe on GaAs.

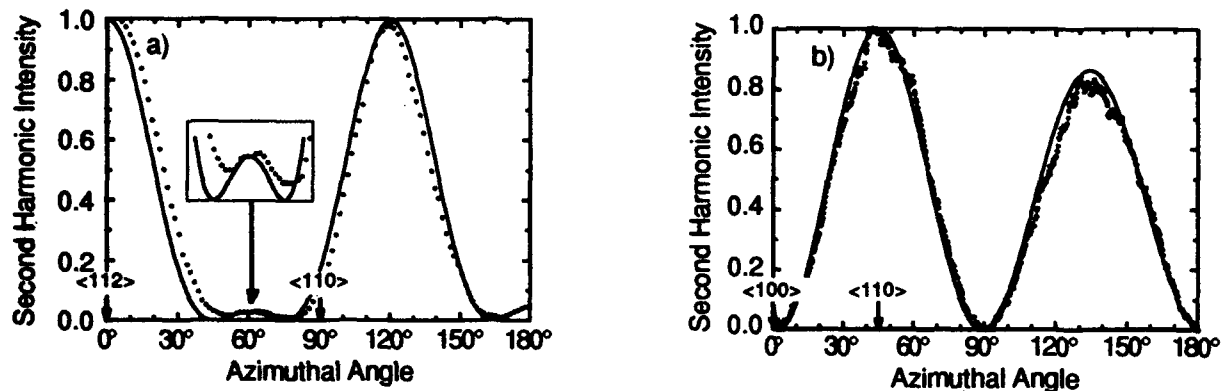


Figure 3. Reflected SHG vs. azimuthal angle of a) $\langle 111 \rangle$ and b) $\langle 100 \rangle$ CdTe on $\langle 100 \rangle$ GaAs. The solid lines are the theoretical predictions.

through the ZnSe/ZnTe waveguide layers. Progress towards the growth and testing of complete waveguide structures will be described. Successful implementation of these patterned semiconductor structures will be important both for monolithically integratable visible light sources as well as for extension of quasi-phases matching techniques to longer wavelengths beyond the infrared absorption edges of common oxide ferroelectrics.

- 1 Hadas Shtrikman, M. Oron, A. Raizman and G. Cinader, *J. Electronic Materials* 17, 105 (1988).
- 2 P. W. Leech, P. J. Gwynn, M. H. Kibel, *Appl. Surface Sci.* 37, 291 (1989).

LENGTH DEPENDENCE OF CERENKOV SHG IN LOSSY WAVEGUIDES

M. R. Shenoy, V. Mahalakshmi and K. Thyagarajan
 Department of Physics
 Indian Institute of Technology
 New Delhi 110016, INDIA

1. INTRODUCTION : Second harmonic generation (SHG) in waveguides is being widely studied for the realization of a compact blue source. Obtaining SHG in the Cerenkov configuration [1] has the important advantage of automatically satisfying the 'phase matching condition'. In this paper, using a coupled mode analysis (similar to that in Ref 4) , we obtain an expression for the Cerenkov SHG efficiency, taking into account propagation loss in the waveguide. We have also fabricated planar waveguides in Z-cut LiNbO_3 by the proton exchange technique, and have measured the length dependence of the second harmonic power, generated in the Cerenkov configuration. The results of our measurements are in agreement with the theory.

2. THEORY Following the same procedure as in Ref 4 we obtain the variation of amplitude coefficient $b_2(\beta, z)$ of the second harmonic radiation mode with propagation direction as

$$\frac{db_2}{dz} = - \frac{\beta_1^3 P_0^\omega}{2 \omega^2 \epsilon_0^2} e^{\Delta\beta z} \quad d = C e^{\Delta\beta z} \quad - (1)$$

where P_0^ω is the power carried by the guided mode, $\Delta\beta = \beta_2 - 2\beta_1$ and

$$d = \int_0^\omega \frac{1}{n_{e1}^4 n_{e2}^2} H_{y1}^2(\beta_1, x) d_{33} H_{y2}^*(\beta_2, x) dx \quad - (2)$$

H_{y1} and H_{y2} are the y-components of the magnetic fields of the power normalised guided and radiation modes respectively. In the notation of various parameters, the subscript 1 (or 2) refers to fundamental (or second harmonic) wavelength.

Equation (1) is usually solved assuming no pump depletion, i.e. $P^\omega(z) = P_0^\omega$. For a waveguide possessing loss, one has

$$P^\omega(z) = P_0^\omega e^{-\alpha z} \quad - (3)$$

where α is the attenuation constant. Thus Eq.(1) becomes

$$\frac{db_2}{dz} = C e^{(L\Delta\beta - \alpha)z} \quad - (4)$$

Integrating Eq.(4), we obtain the following expression for the power generated at second harmonic

$$P^{2\omega}(z) = \frac{\pi C^2}{\alpha} \left[1 - e^{-2\alpha z} \right] \quad - (5)$$

3. EXPERIMENT: Proton exchanged planar waveguides were fabricated in Z-cut LiNbO_3 by soaking in neat melt benzoic acid/orthophosphoric acid. A schematic of the experimental arrangement to study the waveguide-length dependence of second harmonic power is shown in Fig.1. In our experiment, we have measured the second harmonic power as a function of ξ .

4. RESULTS AND DISCUSSION: Figure 2 shows the variation of second harmonic power $P^{2\omega}$ with ξ for a waveguide with $\Delta n(1.06 \mu\text{m})=0.09$ and the thickness = $0.73 \mu\text{m}$. The crosses represent the measured values of $P^{2\omega}$ at different values of ξ and the solid line corresponds to a least square fit of the following functional

form (cf. R.H.S. of Eq. 5) with α (the loss coefficient) and B as parameters:

$$P^{2\omega}(\xi) = A + \frac{B}{\alpha} \left[1 - e^{-2\alpha\xi} \right] \quad - (6)$$

Figure 3 shows experimental results and the fitting on a pair of highly lossy LiNbO_3 waveguides. Actually, in this case the substrates were cut using a blunt saw, and consequently the waveguide fabricated on this substrate was highly lossy ($\approx 63\text{dB/cm}$). Annealing the substrate before fabricating the waveguide resulted in reduction of loss to about 23 dB/cm. The results clearly show a saturating behaviour. A straight forward implication of this result is that in a practical device using waveguides with finite loss in the above configuration, the minimum length of the waveguide that needs to be used to obtain maximum second harmonic power, corresponding to the saturation region, can be estimated.

5. REFERENCES

- [1] P.K. Tien, R. Ulrich and R.J. Martin, Appl.Phys.Lett., Vol. 17, pp.447-450, 1970.
- [2] T.Taniuchi and K.Yamamoto, presented at the Conf.Lasers Electro Opt., Apr.26-May 1, 1987, Baltimore, MD, paper WP-6
- [3] N.A. Sanford and J.M. Connors, J. Appl.Phys., vol. 65. pp 1429-1437, 1989.
- [4] H.Tamada, IEEE J.Quantum Electron., vol.QE-27, pp.502-508, 1991.

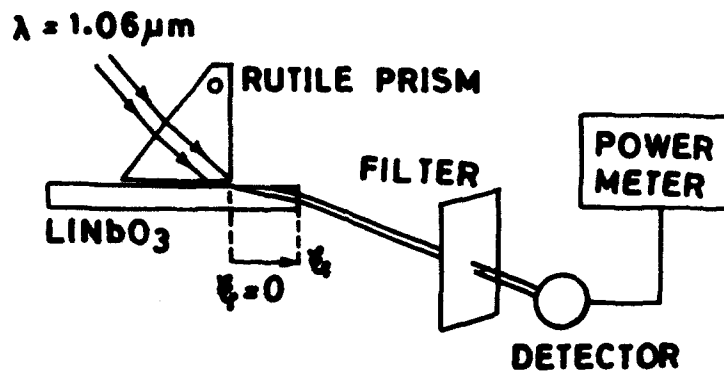


Fig 1 The experimental set up

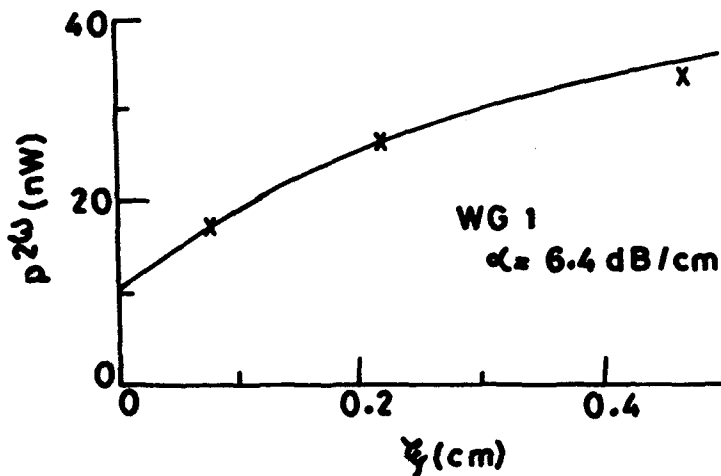
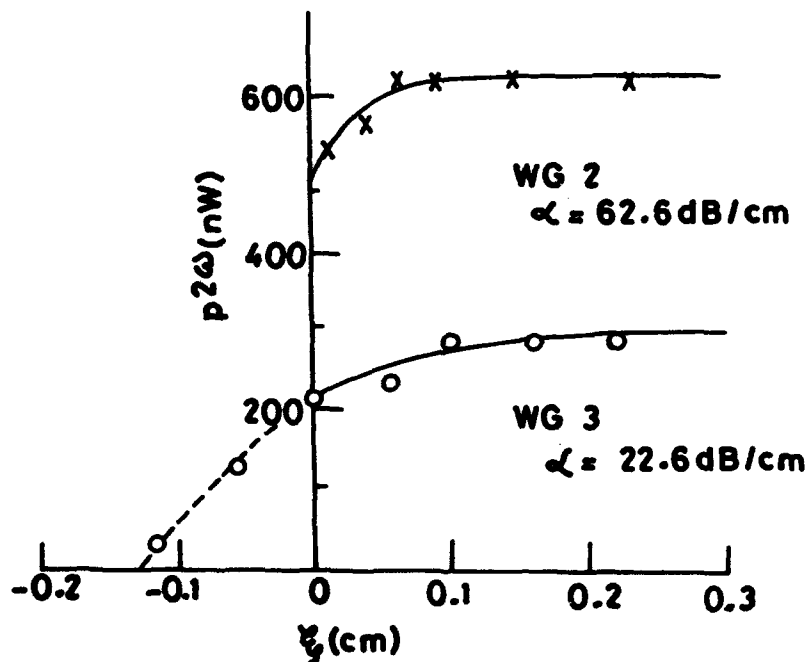
Fig 2. Variation of second harmonic power with interaction length for a proton exchanged waveguide with $\Delta n = 0.09$ and $d = 0.73 \mu\text{m}$.

Fig 3. Variation of second harmonic power with interaction length for highly lossy waveguides. WG3 corresponds to a waveguide grown after annealing the substrate.

Silica on Silicon 2

IWD 11:00am-12:15pm
Mesquite A

Steven Korotky, *President*
AT&T Bell Laboratories

Active silica-based optical waveguides on Si

Yoshinori Hibino

NTT Opto-electronics Laboratories

Tokai, Ibaraki 319-11, Japan

1. Introduction

Silica-based optical waveguides have been developed for the purpose of constructing efficient optical fiber communication systems[1]. The waveguides, which are fabricated by a combination of fiber fabrication and LSI technologies, have the advantages of low loss and a fiber-matched structure. Various kinds of planar lightwave circuit (PLC) have been successfully formed on Si.

PLCs with active functions are required in order to expand their field of application. Here we describe active silica-based optical waveguides on Si which have recently been developed. These include rare-earth doped waveguide lasers and amplifiers, lasers integrated with laser diodes (LDs) and photosensitive waveguides.

2. Rare-earth doped waveguide lasers and amplifiers

Rare-earth doped silica-based waveguides on Si are very attractive as integrated lasers and amplifiers. Lasing in a straight Nd-P₂O₅-codoped silica waveguide was first attained at 1.05 μm in 1989[2]. The waveguide has a Nd concentration of about 2000 ppm and was 5 cm long. By redesigning the waveguide structure, the threshold of the Nd-doped waveguide laser was reduced to 26 mW, thus making LD pumping possible[3].

The fluorescence of Er ions at 1.54 μm is the result of a three-level energy system, and so the doping conditions and the Er and codopants (P₂O₅) concentrations have to be precisely controlled to avoid concentration quenching. In this way, a Fabry-Perot type Er-doped silica waveguide laser was realized in 1991[4]. Recent progress enabled us to form a ring laser with a free spectral range (FSR) of 2.3 GHz on Si (Fig. 1)[5]. Furthermore, the Er concentration dependence of the gain has

been investigated in detail to enable a short waveguide amplifier to be constructed on Si(Fig. 2)[6]. Based on the result, a maximum net gain of 13.7 dB has been obtained in an amplifier 19.4 cm long with an Er concentration of 5000 ppm. These results indicate the potential for introducing various active functions into low loss PLCs.

3. LD-integrated waveguide laser

Another way to provide silica waveguides with efficient active functions is hybrid integration with LDs. Recently we have succeeded in incorporating a semiconductor laser amplifier (SLA) into a waveguide ring resonator with a very low coupling loss[7]. The configuration of the SLA-integrated ring laser is shown in Fig. 3. The total ring length is 10.2 cm which corresponds to an FSR of 2 GHz. The low coupling loss was attained with lensed optical fibers, which are coupled to the SLA as input and output fibers, and fiber-guiding grooves. The fiber guiding grooves allowed us to insert the small SLA module into the ring without alignment. The coupling loss between the optical fiber and waveguide at the groove was about 1.2 dB/point. The lasing threshold was 17 mA, which was by only 5 mA higher than that of the SLA without antireflection coating before insertion. The lasing spectrum of the ring laser at an input current of 40 mA is shown in Fig. 4. Multimode lasing with an interval of 2 GHz is observed, which corresponds to the FSR of the ring. This configuration enables us to design a laser with a precisely-controlled FSR and to combine it with other types of PLC.

4. Photosensitivity

Photosensitivity, which was first observed in GeO_2 -doped silica optical fibers, is a permanent refractive index change in the core induced by visible or UV laser irradiation. The phenomenon has been shown to result from an absorption change at the 240 nm band which is related to Ge-defects in optical fibers. It is useful for grating formation and trimming in PLCs.

Photosensitivity in a planar optical waveguide was also first observed in GeO_2 -doped silica waveguides with Ar^+ laser irradiation[8]. The maximum refractive index change Δn in

PLCs was about 4×10^{-5} , which is much smaller than that in optical fibers taking into account the laser intensity. The change was however found to be used for tuning the optical frequency of a Mach-Zehnder type optical filter because this process can be undertaken after fabrication.

We have studied the effects of irradiating the waveguide from above a UV laser. We obtained a larger Δn of about 8×10^{-5} and a strong polarization dependence (open and closed circles in Fig. 5), which was not observed with Ar⁺ laser irradiation. Moreover, the saturation of Δn was much slower than that in optical fibers. These results indicate that the photosensitivity observed with overhead irradiation in silica waveguides on Si has a strong photoinduced stress-relief component resulting from the substrate interface.

The small Δn with Ar⁺ laser irradiation and stress effects are thought to be due to the small absorption around 240 nm, which was confirmed by measuring UV absorption for a core film formed on a silica substrate (broken line in Fig. 6). To increase the photosensitivity in the PLCs, defects were induced by consolidation in a reducing-atmosphere. The resultant increase in the absorption band at 245 nm is shown as a solid line in Fig. 6. The Δn in the waveguide induced with UV irradiation was greatly increased (rectangles in Fig. 5)[9]. Moreover, a grating has been written with UV irradiation in a waveguide processed with hydrogenation, which also increased the 240 nm absorption band[10].

Acknowledgements

The authors would like to thank M. Nakahara and M. Kawachi for their encouragement and all the members of our laboratory for their contributions.

References

1. M. Kawachi, Opt. Quantum Electron., 22, 391(1990).
2. Y. Hibino, et al., IEEE Photon. Tech. Lett. 1, 349(1989).
3. K. Hatttori, et al., IEEE Photon. Tech. Lett. 3, 882(1991).
4. T. Kitagawa, et al., Electron. Lett., 27, 334(1991).
5. T. Kitagawa, et al., ECOC'92, Berlin, PD II.5(1992).
6. T. Kitagawa, et al., OAA'92, Santa Fe, PD-1(1992).
7. Y. Hibino, et al., Electron. Lett., 28, 1932(1992).
8. Y. Hibino, et al., IEEE Photon. Tech. Lett. 3, 640(1991).
9. Y. Hibino, et al., (to be submitted).
10. G. D. Maxwell, et al., Electron. Lett., 28, 2106(1992).

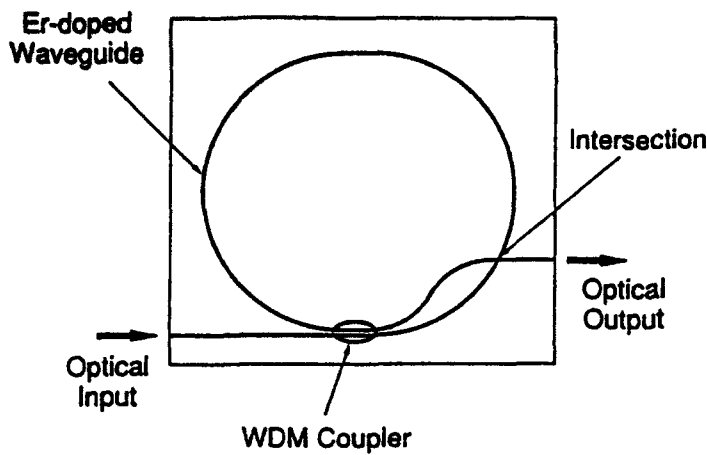


Fig. 1 Configuration of Er-doped silica waveguide ring laser on Si.

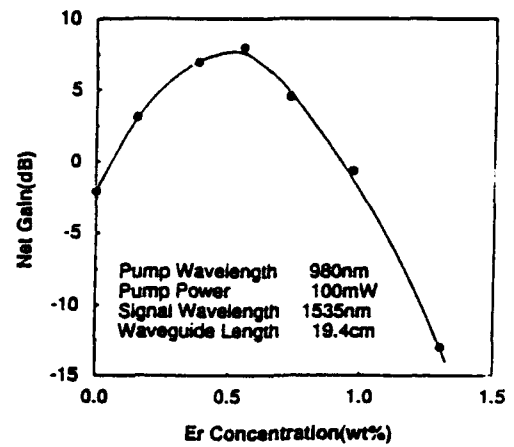


Fig. 2 Er concentration dependence of net gain in Er-doped waveguide amplifier.

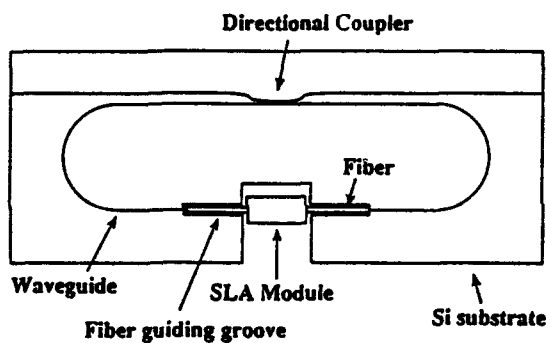


Fig. 3 Configuration of SLA-integrated waveguide ring laser.

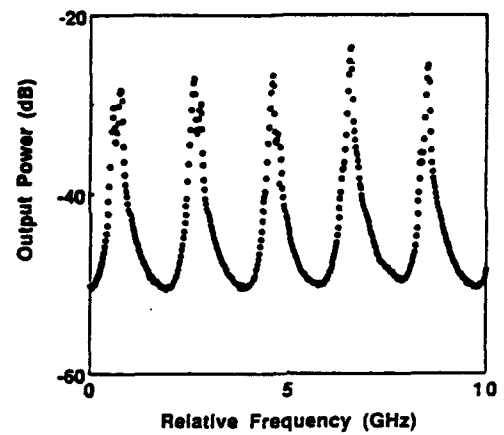


Fig. 4 Lasing spectrum of the SLA-integrated laser.

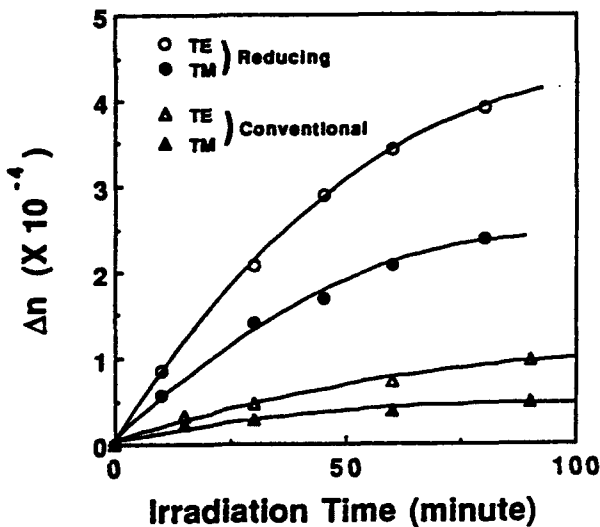


Fig. 5 Photoinduced refractive index changes in PLCs.

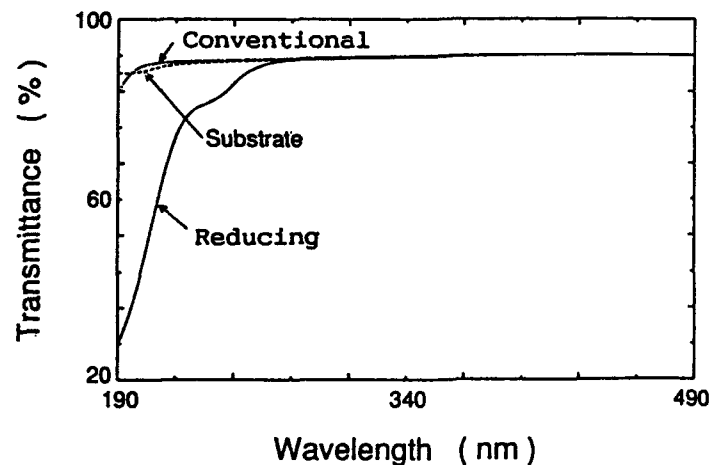


Fig. 6 UV transmittance spectra of FHD films on silica.

Electro-Nanomechanically Tunable Integrated-Optical Bragg Reflectors

W. Lukosz and W. Gabathuler

Optics Laboratory, Swiss Federal Institute of Technology,

8093 Zürich, Switzerland

Phone: (41)-1-377 2810; Fax: (41)-1-372 0630

We report on wavelength-tunable integrated-optical (IO) Bragg reflection actuated by electro-nanomechanically induced effective-refractive-index changes. No electrooptic materials are required; waveguides on silicon are used.

The IO nanomechanical effect

The IO nanomechanical effect works as follows: the width d of the small air gap (with $d \leq \lambda$, where λ is the wavelength) between a nonabsorbing dielectric plate, called "effective-refractive-index-shifting element" E, and a section of the planar or strip waveguide is varied. The evanescent field of the guided wave penetrates through the air gap into E. Therefore, the effective refractive index N depends on d . For suitably designed waveguides, gap-width variations Δd of only a few nanometers induce the effective-refractive-index changes ΔN required for IO device operation.^{1,2} With an element E in the form of a bridge spanned over the waveguide, the gap-width variations Δd are realized by elastic deflection of the bridge under electrostatic forces. Nanomechanically induced intensity modulation and directional switching of guided waves in an IO interferometer has been demonstrated before.^{2,3}

Waveguides and effective-refractive-index-shifting elements

For our experiments at visible wavelengths λ (argon-laser pumped dye laser with Rhodamine 6G dye, $565 \text{ nm} < \lambda < 650 \text{ nm}$), we used planar SiO_2 - TiO_2 waveguides on Si/SiO_2 substrates, i.e., on silicon wafers with

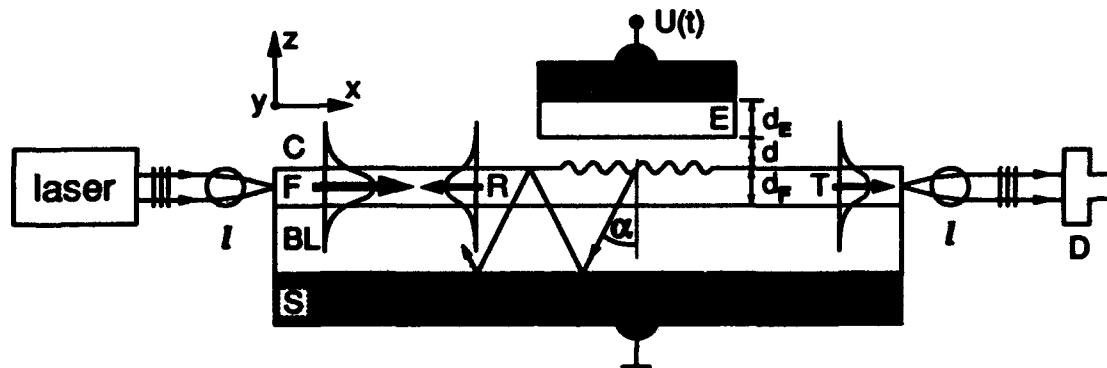


Fig. 1. Schematic of electro-nanomechanically tunable IO Bragg reflector. The surface relief grating with $1/\Lambda = 2400$ lines/mm acts as Bragg reflector and guided-to-leaky mode converter in the diffraction order $m = 2$. Shown are the incident, the reflected (R), and the transmitted (T) guided modes, also a leaky mode in the buffer layer BL and film F, which propagates to the left and radiates into the silicon substrate. S, substrate (silicon wafer); BL, buffer layer (SiO_2); F, waveguiding film (SiO_2 - TiO_2); C, cover (air); E, effective-refractive-index-shifting element (Si/SiO_2); d , air-gap width; l , cylindrical lenses; D, detector; $U(t)$, applied voltage.

thermally grown 3.5- μm -thick SiO_2 buffer layers. The waveguiding $\text{SiO}_2\text{-TiO}_2$ films F with refractive indices of $n_F = 1.75$ and thicknesses $d_F = 170 - 180$ nm were fabricated by dipcoating with the sol-gel process from Liquicoat[®] solutions (Merck, Darmstadt); the firing temperature was 500 $^\circ$ C. The surface relief gratings with $1/\Lambda = 2400$ lines/mm were embossed into the gel film before firing. In the experiments, laser light was endfire-coupled into (and out of) the thin monomode waveguides. Waveguide endfaces of good optical quality were obtained by scribing and cleaving along the (100) crystal plane of the silicon substrate.

The effective-refractive-index-shifting elements E were made of Si/SiO_2 platelets cut from oxidized silicon wafers (of thickness 375 or 500 μm). The evanescent field of the guided wave penetrates only into the nonabsorbing SiO_2 layer of thickness $d_E = 3.5$ μm and of refractive index $n_E = 1.46$, not into the silicon. The air gap was realized by chemically etching a channel into the SiO_2 layer; typically the channel was $\hat{d}_0 = 180$ nm deep, $L_x = 5$ mm long in the x direction, and $L_y = 6$ mm wide in the y direction. These bridges were optical-contact bonded to the planar waveguide. They were spanned transversely over the path of the guided mode (x direction), parallel to the corrugations (y direction) of the surface relief grating (see Fig. 1).

Electrical actuation

A voltage $U(t) = U_0 + \Delta U(t)$ is applied to the condenser formed by the upper conducting silicon part of the bridge and the waveguide substrate (Si). The resulting electrostatic pressure is $p(t) \propto [U(t)]^2 = U_0^2 + 2U_0\Delta U(t)$. By this electrostatic attraction, the gap width is reduced from its initial value \hat{d}_0 to

$$d(t) = d_0 + \Delta d(t) \quad , \quad (1)$$

where d_0 is the median gap width which is adjusted with the d.c. voltage U_0 . The gap-width variations

$$\Delta d(t) = C_p \Delta p(t) \propto C_p U_0 \Delta U(t) \quad , \quad (2)$$

where C_p is the frequency-dependent compliance of the bridge, are linearly proportional to the small a.c. voltage $\Delta U(t)$. By the gap-width variations Δd , the effective refractive index is changed from $N(d_0)$ to $N(d_0) + \Delta N$; the induced effective-refractive-index changes are

$$\Delta N = (\partial N / \partial d)_{d=d_0} \Delta d \quad . \quad (3)$$

For the waveguides used, the calculated sensitivities of the TE_0 mode are $(\partial N_{\text{TE}_0} / \partial d) = (1 - 7) \cdot 10^{-4} \text{ nm}^{-1}$ at median gap widths $d_0 = 10 - 100$ nm; for example, $\Delta N = 5 \cdot 10^{-4}$ is induced by $\Delta d = 1 - 5$ nm.

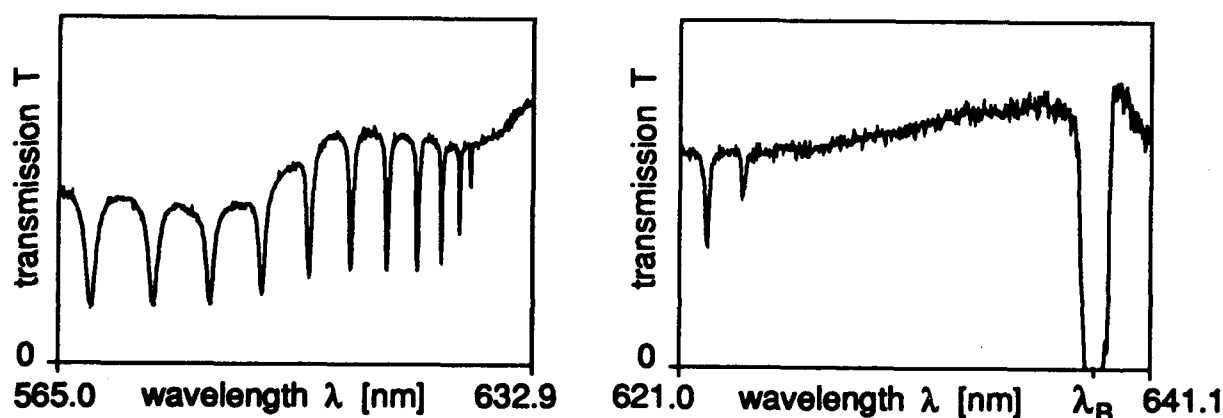


Fig. 2. Wavelength-dependent transmission $T(\lambda)$ of TE_0 mode in waveguide with surface relief grating as shown in Fig. 1. Left: excitation of leaky modes at wavelengths $\lambda_L < \lambda_B$; right: Bragg reflected band around $\lambda_B = 638.7$ nm. Waveguide parameters: $n_F = 1.75$, $d_F = 174$ nm.

Tunable Bragg reflectors

The surface relief grating with an effective-refractive-index-shifting element E over it functions as a wavelength-tunable Bragg reflector. The condition for Bragg reflection is

$$2N\Lambda\sin\Theta = m\lambda_B, \quad (4)$$

where N is the effective refractive index in the grating area, Λ the grating period, $m = 1, 2, \dots$ the diffraction order, and Θ the grazing angle (with respect to the lines of the grating). Figure 1 shows the special case of retroreflection of the incident wave ($\Theta = 90^\circ$). With a nanomechanically induced effective-refractive-index change ΔN , the Bragg reflected wavelength is shifted from λ_B to $\lambda_B + \Delta\lambda_B$, where

$$2(N + \Delta N)\Lambda\sin\Theta = m(\lambda_B + \Delta\lambda_B). \quad (5)$$

The relative shift of the Bragg wavelength is

$$\Delta\lambda_B/\lambda_B = \Delta N/N. \quad (6)$$

Actually, a certain wavelength band $\delta\lambda_B$ around the wavelength λ_B is Bragg reflected; the bandwidth $\delta\lambda_B$ depends on the length and the modulation of the grating (see Fig. 2). This whole stop band is nanomechanically shifted (see Fig. 3); the observed broadening of the stop band is probably caused by an x -dependence of the gap width $d = d(x)$ and, consequently, of $N = N(x)$. Above we implicitly assumed that the gap width d and therefore N are independent of x . According to Eq. (6), the shift $\Delta\lambda_B = 2.1$ nm of the Bragg wavelength $\lambda_B = 638$ nm in the experiment shown in Fig. 3 requires a nanomechanically induced effective-refractive-index change of $\Delta N = 5.0 \cdot 10^{-3}$ since $N_{TE_0} \approx 1.53$.

Bragg reflectors as intensity modulators

We used the nanomechanically tunable Bragg reflector for intensity modulation of the transmitted guided mode (see Fig. 4). The constant wavelength λ was chosen to lie on the slope of the stop band (on the side to longer wavelengths).

The temporal response of the IO nanomechanical device is determined by the dynamics of the mechanical system (bridge) with time constants of the order of microseconds and by the time constant $\tau \approx RC$ (for charging and discharging the condenser C via a resistor R) which can be made as short as a few nanoseconds. However, in the experiment shown in Fig. 4, we had a sub-millisecond time constant τ , due to a high contact resistance R .

From elasticity theory it follows that by a reduction of the thickness D of the bridge, the compliance C_p , which is proportional to D^{-3} , can be greatly increased. Then, the same gap-width variations Δd can be obtained with much smaller applied voltages U_0 and $\Delta U(t)$.

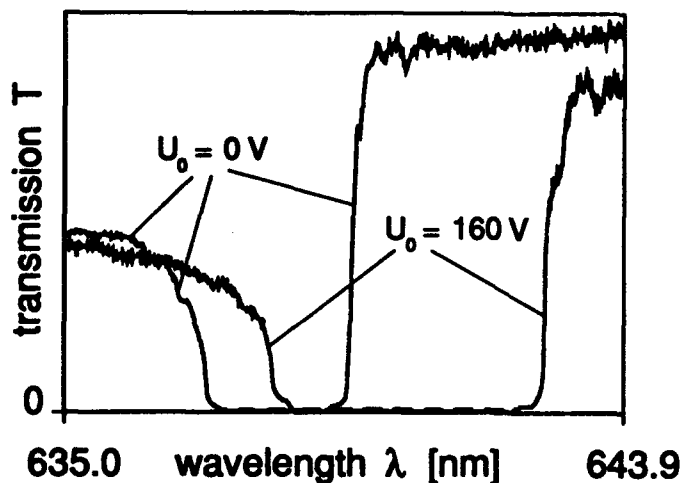


Fig. 3. Electro-nanomechanically shifted Bragg reflection band. Transmission $T(\lambda)$ versus wavelength λ at applied voltages $U_0 = 0$ and $U_0 = 160$ V, respectively. Waveguide parameters: $n_F = 1.74$, $d_F = 180$ nm.

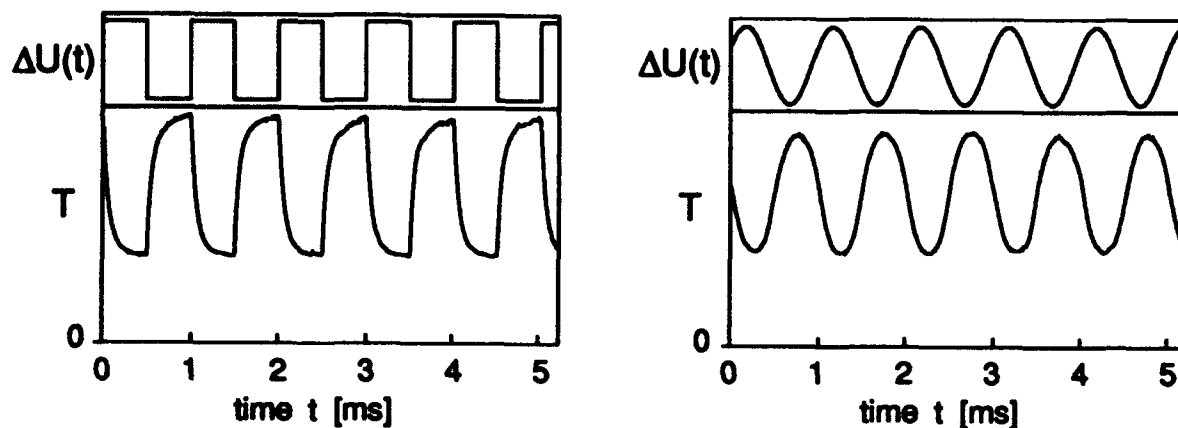


Fig. 4. Electro-nanomechanical intensity-modulation experiments at fixed wavelength $\lambda = 640.1$ nm. Shown is the transmission $T(t)$ in arbitrary units of the TE_0 mode versus time t for sinusoidal and square-wave input voltages $\Delta U(t)$ of frequency 1 kHz. $U_0 = 200$ V; $\Delta U = 20$ V (peak-to-peak). Waveguide as in Fig. 3.

Guided-to-leaky mode conversions

The dips in transmission $T(\lambda)$ at certain wavelengths $\lambda_L < \lambda_B$ shown in Fig. 2 are caused by excitation of leaky modes in the buffer layer BL (plus the thin film F), which are attenuated by radiation into the silicon substrate. The incident mode guided in the film F is converted by diffraction at the surface relief grating into a leaky mode of the same polarization (TE) travelling in the opposite ($-x$) direction (see Fig. 1). The resonance condition is

$$N + N_L = m \lambda_L / \Lambda \quad (7)$$

where N_L (with $n_C < N_L < n(\text{SiO}_2)$) is the effective refractive index or normalized propagation constant of the leaky mode $L = 0, 1, 2, \dots$. In the described experiments with gratings of $1/\Lambda = 2400$ lines/mm, the diffraction order was $m = 2$, the same order as in the Bragg retroreflection of wavelength λ_B . The wavelengths λ_L are nanomechanically tunable. From Eq. (7), we derive for the relative wavelength shift

$$\Delta \lambda_L / \lambda_L = \Delta N / (N + N_L) \quad (8)$$

where ΔN is again given by Eq. (3); we took into account that the effective refractive indices N_L of the leaky modes in the comparatively thick buffer layer are practically not influenced by gap-width changes Δd – in contrast to the effective indices N of the highly confined guided modes in the waveguiding film F.

Conclusions

We demonstrated that tunable IO Bragg reflectors can be actuated electro-nanomechanically. Potential applications are wavelength-tunable filters (and intensity modulators) with response times of microseconds. By a miniaturization of the devices, the necessary driving voltages could be reduced to a few volts; we expect that the necessary IC's and the IO nanomechanical devices could be integrated on the same silicon substrate.

References

1. W. Lukosz, Micro System Technologies '90, 1st Int. Conf. on Micro, Electro, Opto, Mechanic Systems, Berlin, Berlin, 10.-13.9.1990, Ed.: H. Reichl, Springer Verlag Berlin, pp. 725-732, 1990, and Proc. SPIE 1793 (1992) [OE/Fibers '92, Boston, September 1992], in press.
2. W. Lukosz and P. Pliska, *Sensors and Actuators A26*, 337-340 (1991), and *Sensors and Materials* 3, 261-280 (1992).
3. P. Pliska and W. Lukosz, Proc. SPIE 1793 (1992) [OE/Fibers '92, Boston, September 1992], in press.

Integrated-Optic Displacement Sensor Using Linearly Focusing Grating Couplers

S. Ura, M. Shinohara, T. Endoh, T. Suhara and H. Nishihara
Dept. Electronic Eng., Fac. Eng., Osaka University
Yamada-oka 2-1, Suita, Osaka 565, Japan
Tel. +81-6-877-5111 ext. 5007 Fax. +81-6-877-3544

1. Introduction

Integration of optical interferometers for displacement sensing is very attractive because of its high resolution, stability, device compactness, etc. In fact, there have been several reports on integrated-optic vibration sensors [1,2] or displacement/position sensor [3], in which mirror displacement along the beam propagation direction is measured with resolution of sub-micrometer. Besides those sensors, a grating coupler consisting of a double grating has been investigated for measuring a grating scale displacement [4]. In this paper, we propose and demonstrate a new type of integrated-optic sensor device. The proposed sensor is constructed by integrating a slab waveguide, a pair of linearly focusing grating couplers (LFGCs) [5] and a pair of photodiodes (PDs) onto a Si substrate, and is capable of the sensing of the displacement of a grating scale which is moving laterally to the radiated beam from the sensor head.

2. Device Description

A schematic view of the proposed integrated-optic sensor is illustrated in Fig. 1. The waveguide consists of a glass guiding layer and a SiO₂ buffer layer on a Si substrate, and a LFGC pair and a PD pair are monolithically integrated. The guided wave diverging from a butt-coupled laser diode is diffracted by the LFGCs to be two waves in the air. The waves have tilted radiation angles and overlap with each other on the grating scale. The grating scale diffracts both beams to the same direction normal to the scale plane by +1st and -1st order diffraction. The diffracted beams, of which phases vary in the opposite way to each other when the grating scale moves along the grating vector direction, are focused to a line and interfered on the PDs/waveguide. The interference signal is detected by the PDs located between the two LFGCs. Thus the displacement is measured by monitoring the output photocurrent variation. The interference output is insensitive to the grating scale vibration to the other 2-D directions, since the optical path lengths of the two beams are the same and the grating scale has a linear and uniform pattern. If we set previously a phase delay in output photocurrent variation between the two PDs by making interference fringe perpendicular to the focal line, displacement direction can be discriminated by the phase relation.

The LFGC was designed to couple a diverging guided wave to a linearly focused wave with tilted radiation angle in the air. The linearly focusing function results in higher S/N ratio than the case without focusing and larger tolerance than the case using point focusing. The LFGCs were fabricated by the electron-beam (EB) direct writing technique, and the grating pattern equation necessary for EB scanning is written as

$$\Phi_{LF} = \Phi_{DF} - \Phi_{IN} = 2 m \pi + \text{const.} ,$$

$$\Phi_{IN} = k N \sqrt{x^2 + (y + r)^2} ,$$

$$\Phi_{DF} = - k \left\{ \sin \alpha x + \cos \alpha \sqrt{(y - f \sin \theta)^2 + (f \cos \theta)^2} \right\}$$

where $k = 2\pi/\lambda$, λ is wavelength, and N, r, f, α and θ denote mode index, focal lengths and output angles shown in Fig. 2 respectively.

3. Experimental Results

Specifications of the fabricated device are listed in Table I. Fabrication processes are summarized in Fig. 3. A SiO₂ buffer layer was grown on an n-Si substrate by thermal oxidation and patterned for PDs by photolithography. Boron was diffused by using a spin-coated and patterned poly-Boron-film (PBF) to form p-n junctions. A Si-N layer deposited by plasma CVD was patterned by EB writing and RIE to form the LFGC grooves. A #7059 glass guiding layer was RF-sputtered on it. Windows were opened and Al electrodes were fabricated and wire-bonded. A SiO₂ layer on the rear face of the substrate was etched and Au was evaporated for another electrode for PDs. Waveguide end was cleaved and used for exciting a diverging guided wave. Microphotographs of the fabricated LFGCs and PDs are depicted in Fig. 4.

The characteristics of the LFGC were checked at first. The interference fringes, which is generated by two beams radiated by the LFGCs on the plane at the grating scale position, was observed by an objective lens and a CCD 2-D sensor. Fig. 5 shows a photograph of the obtained fringes. It was confirmed that linear and uniform interference fringes with the designed period of 2.3 μm were obtained. A grating scale of 4.6 μm period was set and moved to the direction along grating vector as shown in Fig. 1 while output photocurrents were measured. Fig. 6 shows the dependence of the photocurrents on the displacement. It was confirmed that the photocurrents varied sinusoidally with the period of half of the grating scale period.

4. Conclusion

We have proposed a new integrated-optic displacement sensor using a pair of LFGCs of tilted output angle. The operation principle has been demonstrated experimentally although discrimination of moving direction was not achieved so far. The discrimination is now under study.

References

- [1] M.Izutsu, A.Enokihara, T.Sueta; Electron.Lett., 18, 867 (1982).

- [2] P.Gidon, S.Valette, P.Schweizer; OFS '84, Stuttgart, pap.2.
- [3] S.Ura, T.Suhara, H.Nishihara; Lightwave Technol., 7, 270 (1989).
- [4] B.Geh, A.Dorsel; Appl.Opt., 31, 5241 (1992).
- [5] S.Ura, Y.Furukawa, T.Suhara, H.Nishihara; JOSA A., 7, 1759 (1990).

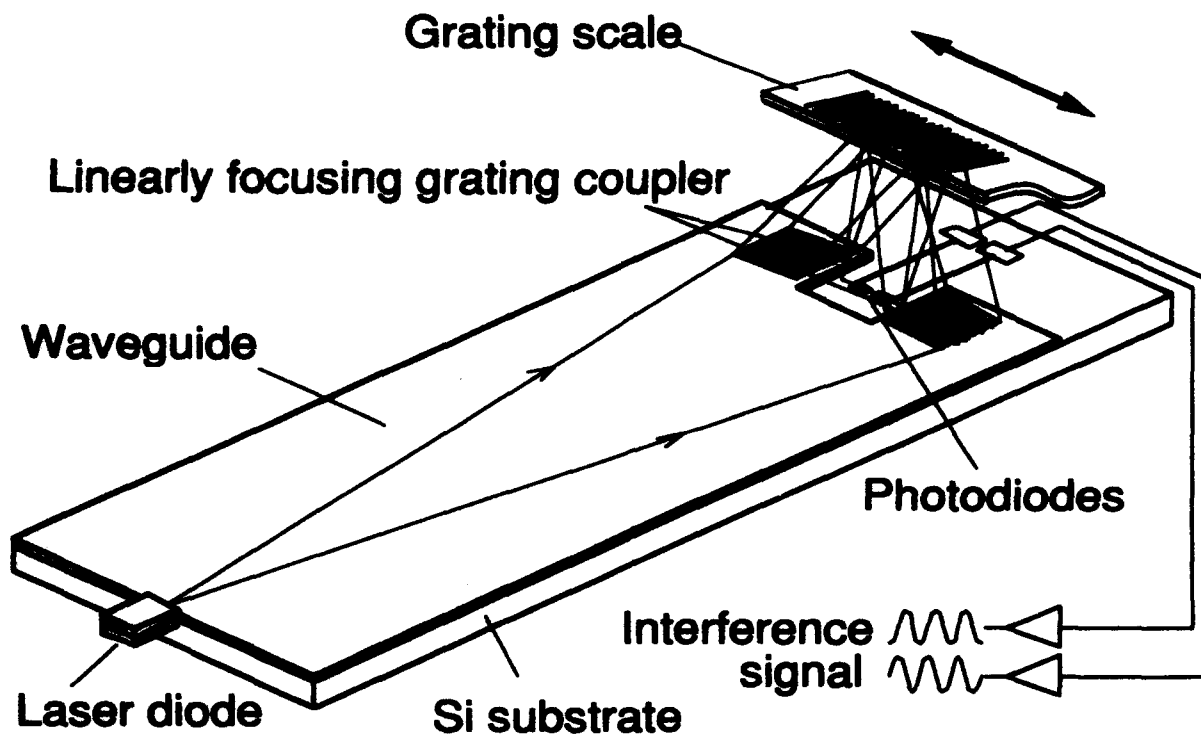


Fig. 1 Schematic view of the proposed integrated-optic displacement sensor.

Table I Specifications of the fabricated device

Laser diode	Wavelength	$\lambda = 0.79 \mu\text{m}$
Waveguide single mode Glass/SiO ₂ /Si	#7059 guide	0.70 μm
	Si-N grating	41 nm
	SiO ₂ buffer	1.78 μm
	Mode index	$N=1.534$
Linearly focusing grating coupler	Aperture	$0.2 \times 0.3 \text{ mm}^2$
	Focal length	$f = 2.8 \text{ mm}$ $r = 10 \text{ mm}$
	Output angle	$\theta = 5 \text{ deg}$
	Tilt angle	$\alpha = 10 \text{ deg}$
	Period	$0.53 - 0.57 \mu\text{m}$
Photodiodes	Element size	$90 \times 66 \mu\text{m}^2$

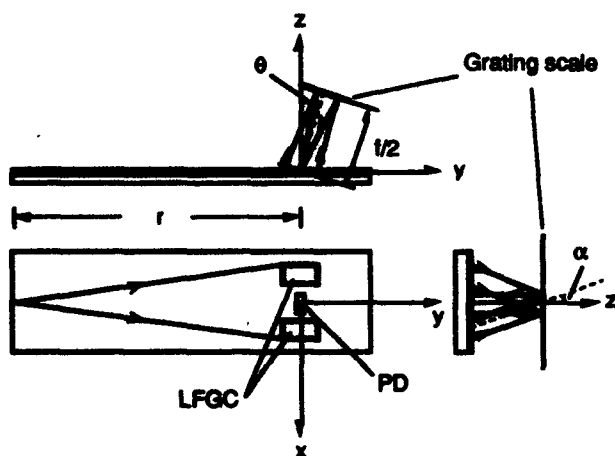


Fig. 2 Configuration of the IC sensor.

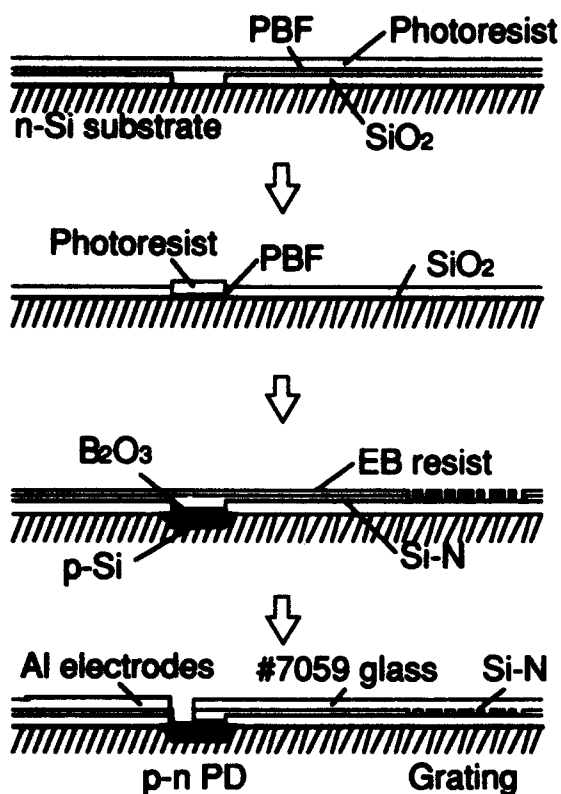


Fig. 3 Fabrication processes.

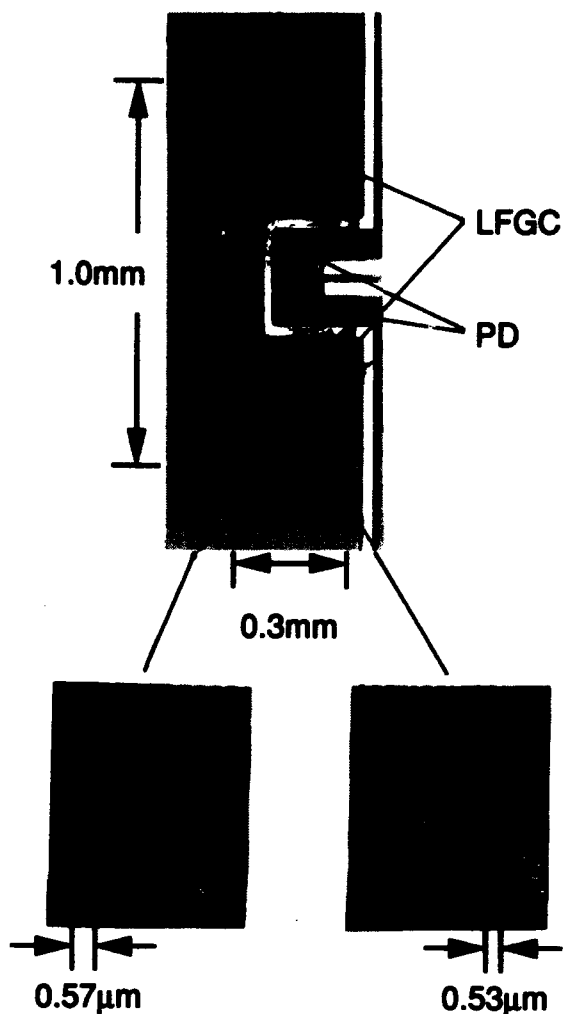


Fig. 4 Microphotographs of the fabricated LFGCs & PDs.

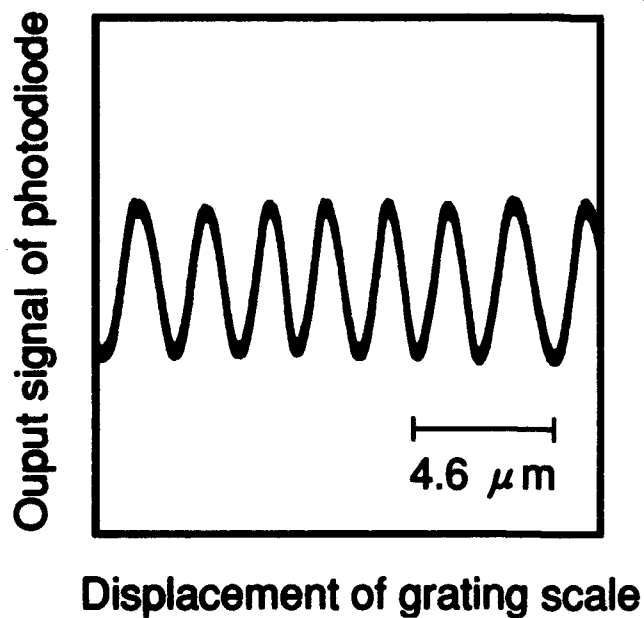


Fig. 6 Dependence of output photocurrent on grating scale displacement.

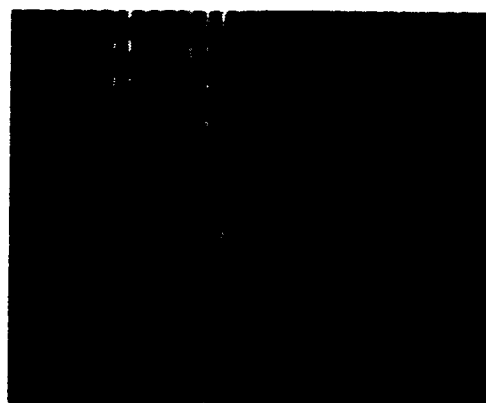


Fig. 5 Photograph of the interference fringes generated by two beams radiated from the LFGC pair.

Direct writing of Volume and Surface Gratings with Sub-micron Periods in Fused Silica.

J. Albert, K. O. Hill, B. Malo, D. C. Johnson
 Communications Research Centre, P.O. BOX 11490, Station "H"
 Ottawa (ONT) CANADA K2H 8S2 [Tel: 613 990 7690]

I. M. Templeton

Institute for Microstructural Sciences, National Research Council, Ottawa (ONT) CANADA
 K1A 0R6

J. L. Brebner

Groupe de Recherche en Physique et Technologie des Couches minces, Département de
 Physique, Université de Montréal, Montréal (QUEBEC) CANADA H3C 3J7

It is well established that ion implantation in silica glass increases the refractive index through compaction of the implanted material¹. Another effect of the implantation is that color centers are created in great numbers, thereby enhancing the photosensitivity of the silica to ultraviolet light². The compaction and color center generation are associated with damage in the material caused by the dissipation of a fraction of the incident ion energy into nuclear processes, the remainder of the energy being dissipated through ionization (i.e. electronic processes). In the work presented here, we demonstrate the use of a Focussed Ion Beam (FIB) facility for the *direct writing* of arbitrary grating patterns with sub-micron pitches. This technique was demonstrated before with an electron beam but only in chalcogenide glass thin films³. For comparison, we also present our results on grating formation in uniformly implanted silica glass by selective photobleaching of the induced color centers with ultraviolet light. Both these techniques may be compatible with the technology of doped silica-on-silicon for optical waveguide fabrication and will allow direct writing of sub-micron pitch grating filters in such photonic integrated circuits.

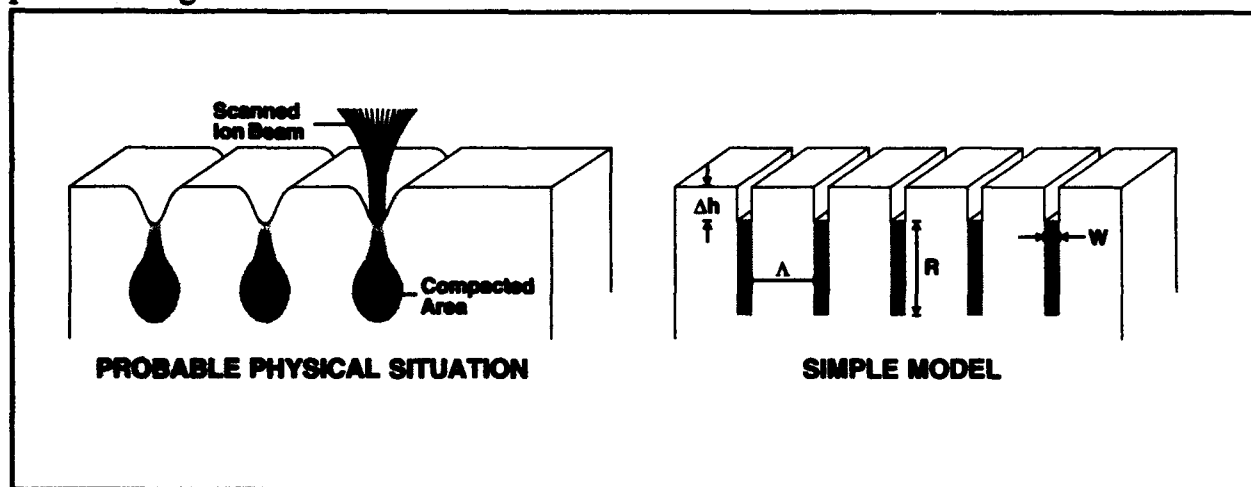


Figure 1 Refractive index grating from FIB implantation and approximate grating model.

In the FIB technique, the substrates used are made of SUPRASIL 2 synthetic fused silica (available from Heraeus Amersil). A thin layer of 20 nm of aluminum was deposited on the top surface and grounded to dissipate the charge from the incoming ions. The FIB system is a 100 kV JEOL 104UHV with a Au-Si-Be liquid metal ion source. For the experiments, Si^{++} or Be^{++}

(200 keV) ions were selected by a EXB filter. In order that the implantation time should not be excessively long, a relatively large aperture was used, giving in each case a beam current of 54 pA with a beam diameter (FWHM) estimated at 0.1 μm . The 1 X 1 mm grating patterns were written as 1250 lines 1 mm long at pitch of 0.72 μm . The writing of single-pass lines consists of a series of overlapping "shots" at 25 nm intervals. A dwell time of 14.8 μs /shot for a 54 pA doubly-charged beam gives 2500 ions/shot, or 10^9 ions/cm. With a beam diameter of 100 nm, this gives a dose of 10^{14} ions/cm². Since the total line length in each grating is 125 cm, the total writing time is 12.3 minutes (or 37 minutes for a dose of 3×10^{14} ions/cm²).

The gratings obtained were visible to the naked eye by shining white light and observing colored fringes coming from the grating areas. The diffraction efficiency in transmission η ($= I_{\text{diff}}/I_{\text{inc}}$) was measured by shining light from a HeNe laser operating at 633 nm through the grating and measuring the power in the diffracted beams. The diffraction angle was 61° corresponding to the FIB design period of 0.72 μm . The difference in optical light path between implanted and non-implanted areas comes from the increased refractive index in the implanted glass and from a surface corrugation directly above the compacted volume where air (refractive index = 1.0) has replaced silica (see Figure 1). To separate the two contributions, distinct measurements are carried out with and without index-matching oil to fill the surface grooves⁴. With the matching liquid the only contribution to the grating efficiency comes from the volume index change. Without the liquid an additional contribution comes from the periodic air gap. Because the two contributions act in opposite directions, filling the grooves increases the efficiency. The diffraction measurement results are listed in Table 1. The expected range of the ions in the material has been obtained from a standard numerical calculation package called TRIM⁵. Also given is the density of stopping energy dissipated into damage processes (E_{dam} divided by the range R). It has been shown that there is a direct link between E_{dam}/R and the compaction observed in silica following ion implantation¹.

TABLE 1

Ion	Dose (ions/cm ²)	Range (R) (nm)	E_{dam} / R (keV/cm ³)	η (air)	η (oil)	Δn	Δh (nm)
Be	1×10^{14}	750	$.24 \times 10^{20}$	2.6×10^{-6}	2.9×10^{-6}	.002	0.2
Be	3×10^{14}	750	$.72 \times 10^{20}$	1.2×10^{-5}	1.4×10^{-5}	.004	0.7
Si	1×10^{14}	320	2.3×10^{20}	2.3×10^{-5}	3.0×10^{-5}	.013	1.2
Si	3×10^{14}	320	7.0×10^{20}	5.5×10^{-5}	8.5×10^{-5}	.022	3.0

It is possible to use the diffraction efficiencies and TRIM parameters in order to estimate the properties of the fabricated gratings. For simplicity (see Figure 1), we model the grating as a square wave with a period Λ , a groove width W , a groove depth Δh , and a uniform volume index change of Δn over the range of the implanted ions R . The lateral extent W of the implanted area is taken as the full width at half maximum of the ion beam (100 nm). With this simplified model, it is possible to relate the diffraction efficiencies, in air and matched in oil, to the grating parameters by the following two formulas:

$$\eta (oil) = \left[\frac{2R\Delta n}{\lambda} \sin\left(\pi \frac{W}{\Lambda}\right) \right]^2$$

$$\eta (air) = \left[\sqrt{\eta(oil)} + \frac{2}{\lambda} \Delta h (n_{air} - n_{silica}) \sin\left(\pi \frac{W}{\Lambda}\right) \right]^2$$

The first equation yields the average index increase in the implanted layer directly while the second equation is sufficient to determine the corrugation height, and from it the average compaction. The results of these calculations are shown in the Table. For the range of implants (0.3-0.7 μm) in the experiment, the surface corrugations and volume changes correspond respectively to average compactions of the order of 1% and refractive index increases of the order of 0.02. For equal doses, the heavier silicon implants yield a larger diffraction efficiency than the beryllium implants (28:9 mass ratio) in spite of the fact that the penetration depth over which the index change occurs is less than half that of the beryllium ion. In order to increase the thickness of the gratings, lighter ions or higher implantation energies are needed. Since the effects observed depend on E_{dose}/R , a higher dose of lighter (less "damaging") ions is needed to yield the same characteristics as heavier ions. The maximum index increase (or compaction) achievable in fused silica from damage processes saturates at about 2%¹, when $E_{\text{dose}} \cong 2 \times 10^{20}$ keV/cm³, and the highest energies available with a Focussed Ion Beam facility limit the maximum range for light ions to about 1 μm in silica. We see from Table 1 that we have reached the maximum achievable index change for the silicon implants. On the other hand, the minimum period obtainable is restricted by the minimum beam width, broadened somewhat by the lateral spreading of the implanted ions in the substrate. Since relatively large doses are needed to produce damage, it will probably be difficult to reduce the line width of a single FIB scan to less than about 100 nm (meaning a grating period of 0.2 μm which is less than half the Bragg period for a reflection filter at 1.3 μm in a silica waveguide). Note that the use of the FIB allows arbitrary grating patterns (including non-periodic) to be written.

A final verification of the grating topology was performed using an Atomic Force Microscope (AFM). Figure 2 shows an AFM picture of the strongest grating (Si, dose = 3×10^{14} cm⁻²). The surface corrugation is clearly seen, with a period of 0.72 μm , which corresponds to the design value and the one obtained from the diffraction experiment. The measured corrugation height is approximately 3 nm and corresponds to the value obtained from Equation 2 and the diffraction efficiency. However, the surface height modulation is far from square, indicating that the compaction is not uniform. Indeed, a complex stress-strain pattern is expected to result from FIB implantation over such a small volume and a more accurate modelling of the index change profile will certainly be very difficult. However, the square wave model seems to yield reasonable "average" values.

By comparison, the other method which we have used to define phase gratings is by using the photosensitivity induced in silica by uniform, high energy ion implantation². Using the same substrates as above, germanium ions have been implanted at a dose of 10^{14} ions/cm², with an energy of 5 MeV. In this case, the damage range extends to almost 4 μm below the

surface, and the index change reaches $+0.015$. More importantly, ultraviolet color centers have been created in the silica, with a strong absorption at a wavelength of 245 nm. Upon exposure of the implanted silica to light whose wavelength is close to the absorption band which in our case is an excimer laser operating at 248 nm, the absorption is bleached and there is a corresponding change in refractive index. We have shown in a previous paper² that the maximum photo-induced index change in this case is a decrease of the order of 2×10^{-3} , over the full range of the implanted ions.



Figure 2 AFM picture of grating surface

While the maximum index modulation is an order of magnitude smaller in this case, the use of an unfocused ion beam to induce the photosensitivity allows the formation of thicker gratings since ion implanters with higher energies are available. Furthermore, direct writing techniques are still possible by scanning a focussed laser beam to define gratings or other patterns in the silica or, for the formation of uniform gratings, UV holography. As a demonstration of this technique, we have written a $4 \mu\text{m}$ pitch, $4 \mu\text{m}$ thick grating in fused silica by exposing a uniformly implanted substrate to the excimer laser light through a metallic shadow mask. The resulting diffraction efficiency of 2×10^{-5} corresponds to an index modulation of 2×10^{-4} . With a more efficient UV writing procedure, the diffraction efficiency could reach 0.1%.

In summary, we have demonstrated two techniques for direct writing of micron-sized refractive index features in planar silica substrates, with immediate applicability to silica-on-silicon waveguide fabrication technology. No photolithography or etching is needed and the resulting refractive index modulation appear mainly in the volume of the glass, with some surface corrugation of the order of a few nanometers.

ACKNOWLEDGEMENTS

The authors wish to thank H. G. Champion for operating the FIB system.

REFERENCES

1. G. W. Arnold, P. Mazzoldi, in Ion beam modification of insulators, Arnold and Mazzoldi (eds.), Elsevier, New York (1987), pp.195-222
2. J. Albert, B. Malo, K. O. Hill, D. C. Johnson, J. L. Brebner, R. Leonelli, Proc. Integrated Photonics Research 1992, p.4-5 and Opt. Lett., Dec. 1 (1992)
3. Y. Handa, T. Suhara, H. Nishihara, J. Koyama, Appl. Opt. **18**, 248 (1979)
4. T. A. Dellin, D. A. Tichenor, E. H. Barsis, J. Appl. Phys. **48**, 1131-1138 (1977)
5. J. F. Ziegler, J. P. Biersack and U. Littmark, The stopping and range of ions in solids, Pergamon Press, New York (1985)

[Redacted]

Semiconductor Device Modeling 2

IWE 11:00am-12:30pm
Mesquite B

Shunji Seki, *Presider*
NTT Opto-Electronics Laboratories, Japan

Electron Waveguides

Supriyo Datta

School of Electrical Engineering

Purdue University

West Lafayette, IN 47907

(317) 494-3511

Progress in nanolithography has made it possible to fabricate electronic devices with feature sizes comparable to the DeBroglie wavelength of electrons. We will discuss our present understanding of such devices, pointing out the similarities and differences between electrons and photons.

Simulations of Space-charge Effects on Quantum-Well Devices using Self-Consistent Solution to the Schrödinger-Poisson Equations

J. J. Chen, A. K. Chan, and C. K. Chui

Department of Electrical Engineering
Texas A&M University
College Station, Texas 77843-3128
Tel. (409)-845-7458

1 Introduction

Space-charge effects play an important role in the dynamics of photonic transition in quantum well devices. The primary effect of space charge causes band-bending resulting a change of the potential profile. Subsequently, the tunneling effect is more pronounced in an infrared detector under a given bias voltage, and the negative resistance region in a double-barrier resonant tunneling structure (DBRTS) also occurs at a higher bias voltage. In this paper, we present a method to obtain the self-consistent solution to the Schrödinger-Poisson equation using the Local Interpolatory Cardinal Spline (LICS). Our results are compared with those without self-consistence using an intersubband infrared detector as an example.

2 Relevant equations

In the effective mass approximation, the envelope function of an electron in a quantum well (QW) is given by the one-particle Schrödinger equation

$$-\frac{\hbar^2}{2} \frac{d}{dz} \frac{1}{m^*(z)} \frac{d}{dz} \psi(z) + V(z)\psi(z) = E\psi(z), \quad (1)$$

where $m^*(z)$ is the effective mass of electrons, and E is the energy of states. $V(z)$ is a combination of a pseudopotential energy $\Delta E_c(z)$ due to offset of the bands, and a net electric potential energy $-qV_E(z)$ from externally applied voltage and space charges. The potential function is written as

$$V(z) = \Delta E_c(z) - qV_E(z). \quad (2)$$

The net electric potential $V_E(z)$ can be obtained by solving the Poisson equation

$$\frac{d}{dz} \left(\epsilon(z) \frac{d}{dz} V_E(z) \right) = -q[N_D^+(z) - n(z)], \quad (3)$$

where $\epsilon(z)$ is the dielectric constant. $N_D^+(z)$ represents the ionised donor concentration, and $n(z)$ is the electron density. Acceptor concentration and hole density are neglected for a n-type modulation-doped quantum well. We assume all donors are ionised (as in most cases of interest), and $N_D^+(z)$ is equal to the donor concentration $N_D(z)$. The electron density $n(z)$ is given by

$$n(z) = \sum_i \frac{m^* K_B T}{\pi \hbar^2} \ln \left[1 + \exp \left(\frac{E_F - E_i}{K_B T} \right) \right] |\psi_i(z)|^2 \quad (4)$$

where K_B is the Boltzmann constant; T is the absolute temperature; E_i and ψ_i are the eigenenergy and eigenfunction of the i^{th} subband; and E_F is the Fermi energy.

The eigenenergy and envelope function, E_i and ψ_i , can be obtained by solving (1) and (3) iteratively. The self-consistent procedure starts with an assumed initial potential $V_E^{(0)}(z)$ for obtaining the eigenfunctions ψ_i and their corresponding eigenenergy E_i by solving (1). $n(z)$ is computed using (4) and a new $V_E^{(n)}(z)$ is obtained by solving the Poisson equation (3). The iterative cycle ends by computing a new potential, $V_{E, \text{new}}^{(n)}(z) = fV_E^{(n)}(z) + (1-f)V_E^{(n-1)}(z)$ where f is the convergence factor ($0 < f < 1$). This process is repeated until the difference in potential from each successive iteration is within a preset value.

3 Numerical Approach

The numerical method used in this paper is based on a variational approach using LICS as basis functions. This method has been used to compute the eigenstates of a quantum well with an arbitrary potential profile[1]. The results agree very well with those published in the literature. Without going through the details, the method is described briefly here.

1. Using a variational approach and the boundary conditions at points of heterointerfaces, we have

$$\left[-\frac{\hbar^2}{2} \delta\psi(z) \frac{1}{m^*(z)} \frac{d}{dz} \psi(z) \right]_{z_0}^{z_N} + \frac{\hbar^2}{2} \int_{z_0}^{z_N} \frac{d}{dz} \delta\psi(z) \frac{1}{m^*(z)} \frac{d}{dz} \psi(z) dz + \int_{z_0}^{z_N} \delta\psi(z) [V(z) - E] \psi(z) dz = 0, \quad (5)$$

where $\delta\psi(z)$ is the first variation of $\psi(z)$ and the region of interest is restricted to a finite interval $z_0 \leq z \leq z_N$.

2. The region $z_0 \leq z \leq z_N$ is divided into N equal segments. The cubic LICS function $\phi(z)$ is used to represent the envelope function $\psi(z)$ in a spline series as:

$$\psi(z) = \sum_{i=0}^N \psi(i) \phi(z-i), \quad (6)$$

where $\psi(i)$ and $\phi(z-i)$ represent $\psi(z_i)$ and $\phi(z-z_i)$ respectively.

3. A general eigen-matrix equation of the form,

$$\bar{A}\bar{C} = E\bar{B}\bar{C},$$

is obtained using (6) in (5), where \bar{C} is the column vector of the coefficients $\psi(i)$ which also equal to the unknown function values at the grid points. The elements of \bar{A} and \bar{B} are given by

$$a_{i,j} = \int_{z_0}^{z_N} \left\{ \frac{\hbar^2}{2} \frac{1}{m^*(z)} \dot{\phi}(z-i) \dot{\phi}(z-j) + V(z) \phi(z-i) \phi(z-j) \right\} dz - \left[\frac{\hbar^2}{2} \frac{1}{m^*(z)} \dot{\phi}(z-i) \phi(z-j) \right]_{z_0}^{z_N}$$

$$b_{i,j} = \int_{z_0}^{z_N} \phi(z-i) \phi(z-j) dz,$$

where $\dot{\phi}(z-i)$ means $\frac{d}{dz} \phi(z-i)$.

The same method is also used to solve the Poisson equation to obtain the electric potential $V_E(z)$ in each cycle of iteration.

4 Examples

A. Modulation-doped heterojunction *GaAs/AlGaAs*

For numerical confirmation, a modulation-doped heterojunction given in [2] is considered. A uniform mesh size of 10\AA is used in the simulation. The full range of calculation is 1200\AA , and the convergence criterion is set at 0.5meV . The choice of convergence factor f depends on the problem being considered. Generally, $f = 0.5$ is appropriate. However, in this example, an adaptive method is used to choose f for each iterative cycle due to the slow convergence at a smooth band edge around the accumulation layer. It takes 10 iterations and one minute of cpu time in VAX 9000 to reach the final result. Two bound states are obtained in this problem. The conduction band edge and the electron density distribution are shown in Fig. 1. The simulated result agrees with that in [2].

B. Intersubband absorption in a modulation-doped rectangular well

It has been shown that a square quantum well can generate a large field induced Stark shift [3] that is useful in high-speed infrared light modulators. Here we assume a two-level (with states 1 and 2) QW system under an applied field F in the z direction. The optical frequency is ω and the polarisation is in the x -direction. The linear absorption coefficient is given by [4]

$$\alpha(\omega) = \omega \sqrt{\frac{\mu}{\epsilon_R}} |M_{21}|^2 \left(\frac{m^* K_B T}{L \pi \hbar^2} \right) \ln \left(\frac{1 + \exp[(E_F - E_1)/K_B T]}{1 + \exp[(E_F - E_2)/K_B T]} \right) \frac{\hbar/\tau}{(E_2 - E_1 - \hbar\omega)^2 + (\hbar/\tau)^2}, \quad (7)$$

where $M_{21} = \langle \psi_2 | qz | \psi_1 \rangle$, L , μ , ϵ_R , c , and τ respectively represent the dipole matrix element, the well width, the permeability of the system, the real part of the permittivity (which is related to the refractive index by $\epsilon_R = n_r^2 \epsilon_0$), the speed of light in free space, and the intersubband relaxation time.

We consider an 80\AA undoped *GaAs* well bounded by a 150\AA thick $Al_{0.4}Ga_{0.6}As$ barrier on each side of the well. The outermost 50\AA of each barrier is considered uniformly doped at $1.0 \times 10^{18} \text{cm}^{-3}$. Assuming room temperature ($T = 300\text{K}$), the refractive index $n_r = 3.2$, and the relaxation time $\tau = 0.14\text{ps}$, the eigenenergy and the corresponding wave function of the QW, the transition energy, and the peak absorption coefficient are obtained by solving the self-consistent coupled equations. The results are shown in Fig. 2. For easy of comparison, the solutions based on a flat band edge are also included in the figures. It can be seen that the transition energy increases with the applied electric field and the peak absorption coefficient decreases. In addition, due to the large band-bending in a highly doped quantum well, the transition energy and peak absorption coefficient are smaller than those in a flat band. In Fig. 2(b), there is an obvious drop in the peak absorption coefficient when the applied electric field is set at 60kV/cm . That result can be explained by the resonant tunneling effect [5] that reduces the screening of electron density and the band-bending. Therefore, the Stark shift is enhanced, but the absorption coefficient is suppressed.

This research project is supported by Texas Higher Education Coordinating Board under Grants No: 32135-70800 and No: 32134-70830.

5 References

1. J.J. Chen, A.K. Chan, and C.K. Chui, "A Local Interpolatory Cardinal Spline Method for the Determination of Eigenstates in Quantum Well Structures with Arbitrary Potential," submitted to IEEE J. of Quantum Electronics.
2. I. Tan, G.L. Snider, L.D. Chang, and E.L. Hu, "A Self-consistent Solution of Schrödinger-Poisson equations using a Nonuniform Mesh," J. Appl. Phys. 68(8), 1990, pp. 4071-4076.
3. A. Harwit and J.S. Harris, jr. "Observation of Stark Shifts in Quantum Well Intersubband Transitions," Appl. Phys. Lett. 50(11), 16 March 1987, pp. 685-687.

4. D. Ahn and S.L. Chuang, "Calculation of Linear and Nonlinear Intersubband Optical Absorptions in a Quantum Well Model with an Applied Electric Field," IEEE J. of Quantum Electronics, QE-23, No. 12, December 1987, pp. 2196-2204.
5. E.J. Roan and S.L. Chuang, "Linear and Nonlinear Intersubband Electroabsorptions in a Modulation-doped Quantum Well," J. Appl. Phys. 69(5), 1 March 1991, pp. 3249-3260.

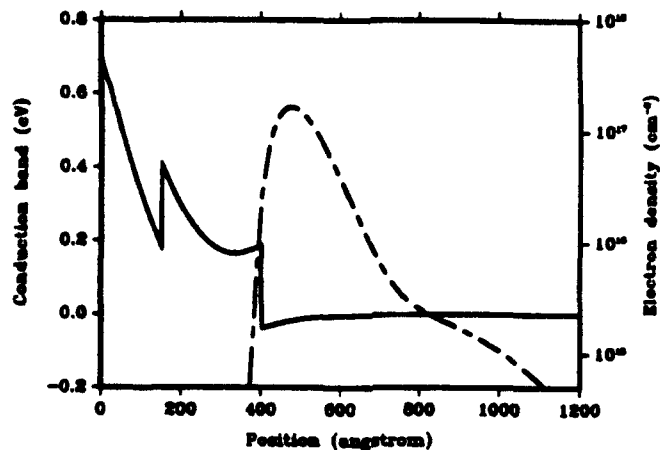


Figure 1: The conduction band edge (solid line) and electron density distribution (dot-dashed line).

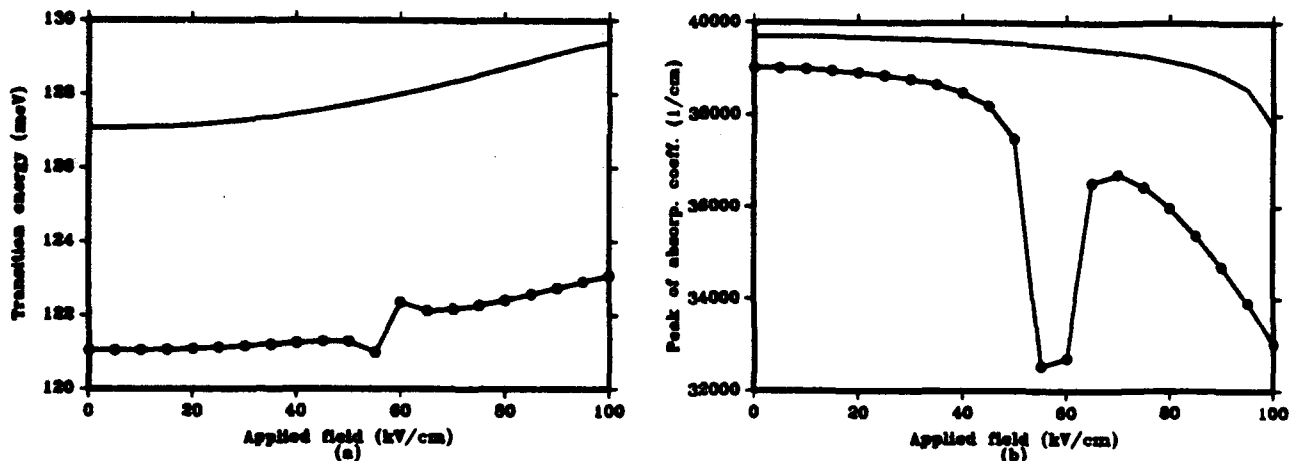


Figure 2: The linear intersubband (a) transition energy and (b) peak absorption coefficient vs. different applied fields. The solid lines with dotted marks are calculated by using a self-consistent method, and lines without dotted marks are calculated based on a flat band.

Time-Domain Simulation of Ultra-Short Pulse Process in Semiconductor Lasers

Wei Yang, Anand Gopinath

Dept. of Elec. Eng., University of Minnesota, Minneapolis, MN 55455

I. Introduction

The propagation of optical signals in a semiconductor laser is governed by the interactions between the photon and carrier densities. These interactions are commonly described by the rate equations in which the photon density is assumed to be evenly distributed in the cavity. This is valid when the signals are of low temporal frequency compared with the photon life time or low spatial frequency compared with the cavity length, which is the case in most applications where the bandwidth is below 20 GHz, due to the large carrier life time. However, semiconductor lasers do have gain spectrums that provide >30,000 GHz of bandwidth and in principle, ultra-short pulses of picosecond width can be generated, such as in the mode-locked semiconductor lasers [1], [2]. At such short time domain, there are several factors must be taken into account: 1) the spatial distribution of the photon and carrier densities, 2) strong non-linear effects as the results of gain/loss saturation, which is primarily responsible for the generation of ultra-short pulses, and 3) modulations of the gain/loss and their bandwidth, or time response, which is very important in shaping the pulse profiles. In this paper we will present our approach by first deriving the rate equation incorporated with the wave equation of the photon density, then discussing the transitional process of the gain/loss, and finally our initial results from GaAs-AlGaAs passive mode-locked laser simulations.

II. Rate Equation

Let us consider the optical fields in the laser medium as a plane wave modulated by a slow varying function $E(x,t)$:

$$e(x,t) = E(x,t)e^{j(kx - \omega t)} \quad (1)$$

where ω and k are the optical frequencies in time and space, $E(x,t)$ may be complex. The wave equation for $e(x,t)$, in a gain or loss medium, is

$$\frac{\partial^2 e(x,t)}{\partial x^2} - \frac{1+j\epsilon}{c^2} \frac{\partial^2 e(x,t)}{\partial t^2} = 0 \quad (2)$$

where c is the group velocity of the wave in the laser medium and the imaginary dielectric constant $j\epsilon$ represents the gain or loss of the medium, take (1) into (2) and neglect all the second derivatives of $E(x,t)$, the photon density $S(x,t) = KE(x,t)E^*(x,t)$ follows

$$\frac{S(x,t)}{\partial x} + \frac{1}{c} \frac{\partial S(x,t)}{\partial t} = k\epsilon S(x,t) = \Gamma g(N) \quad (3)$$

where the phase term is not involved as long as the refractive index is uniform over the whole medium and we do not consider the carrier induced index change. We have used $g(N)$ for the net optical gain, N is the injected carrier density and Γ the optical confinement factor. Equation (3) becomes obvious when we recognize that the right hand side as the photon source term so the equation simply represents the photon or energy conservation. The carrier rate equation takes the common form, if we neglect the spatial inter-diffusion of the carriers:

$$\frac{N(x,t)}{\partial t} = -g(N) + \frac{J(x,t)}{d} - Rnr \quad (4)$$

In the laser cavity, we shall consider two counter-propagating waves E_a and E_b . The interference of these two waves $(E_a + E_b)(E_a + E_b)^*$ leads to spatially distributed photon density $S = S_a + S_b + 2\sqrt{S_a S_b} \cos(kx)$. The interference term is averaged out in a space interval that is much larger than the optical wavelength, but in the strong saturation domains, this term must be taken into account for non-linear effects. The net gain can be expressed approximately as:

$$g(N) = (B(N - N_{th}) - \alpha_{in})S + R_{sp} \quad (5)$$

where N_{th} is the carrier density when the medium becomes transparent, B is a coefficient related to the initial doping of the material.

III. Frequency Dependence of $g(N)$

Due to the intrinsic stimulated emission process, $g(N)$ is a function of optical frequency[3]. In the gain region or $g(N) > 0$, the band width of $g(N)$ is approximately:

$$\Delta f_g = \frac{(E_{fc} - E_{fv})}{h} - f_0 \quad (6)$$

where E_{fc} and E_{fv} are the quasi-Fermi levels for electrons and holes and f_0 is the lasing frequency. So the gain bandwidth is modulated since E_{fc} and E_{fv} change with injected carrier density. For absorption or $g(N) < 0$, we assume that speed of response in the absorption process is only limited by the inter-band transition time. To include these frequency effects in the time domain, we introduce characteristic delay time $\tau = \tau_g = 1/\Delta f_g$ for gain, and $\tau = \tau_a = \tau_r$ for absorption, where τ_r is the band to band transition time, which is on the order of 1ps [4]. Taking the delay effects into account, the rate equation (3) can be modified to be

$$\frac{S(x,t)}{\partial x} + \frac{1}{c} \frac{\partial S(x,t)}{\partial t} = \Gamma g(N) * e^{-t/\tau} \quad (7)$$

where $*$ stands for convolution.

IV. Results and Discussion

Based on the above discussions, numerical simulation has been performed to observe the formation of short pulses in GaAs/AlGaAs lasers. As an example, we studied a laser with gain section length 350 μm and absorber 150 μm side by side, $N_{th} = 1 \times 10^{18} \text{ cm}^{-3}$, $\Gamma = 0.35$, $d = 2000 \text{ \AA}$, internal loss = 20 1/cm, and 95% reflection on both facets are assumed. In the simulation, the cavity is divided into 50 sections and the time steps are 0.11 ps. The pulse generation start to occur when the injection current in the gain section exceeds 90 mA. The pulses have about 1 ps width and 80 GHz repetition frequency, and almost 100% extinction(Fig. 1, 2). The transition time from DC to pulsed mode is typically 1 ns. A slow amplitude modulation of the pulses are observed at about a few MHz. A gradual narrowing of the pulses in the process of forming stable pulsed mode is also noticed. The explanation for the pulsed mode operation in the passive mode-locking laser is that the absorber sharpens up the pulses due to the saturability of the absorber and its very fast response, even though in the gain section the pulses tend to expand due to the smaller

band width, the net effect is that the pulses stabilize at certain width and shape. The repetition frequency is always $c/2L$, where L is the total cavity length. This indicates that the pulsed mode, in frequency domain, is the composition of phase-locked longitudinal modes, which have frequency separations of $c/2L$.

V. Conclusions

We have developed a numerical method to study the short pulses in the laser cavities. Initial results have been obtained showing the expected results. This method is to be modified to study other dynamic processes such as active mode-locking and modulation characteristics.

References

1. M. C. Wu, *et al.*, *Appl. Phys. Lett.*, 57 (8), p759, August 1990
2. S. Sanders, *et al.*, *Appl. Phys. Lett.* 56, No. 4, p331, January 1990
3. K. Y. Lau, *IEEE J. Quantum Electronics*, vol 26, No. 2, p250, February 1990
4. A. Yariv, "Optical Electronics", p474, CBS College Publishing, 1985

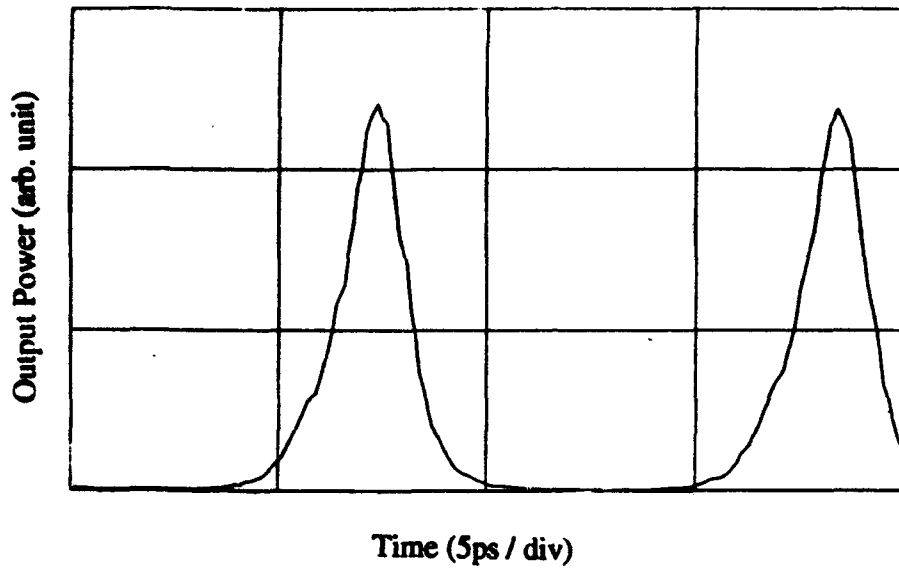


Fig. 1 Stabilized pulse shape 3 ns after turn-on, the time for pulse establishment is about 1 ns in this case.

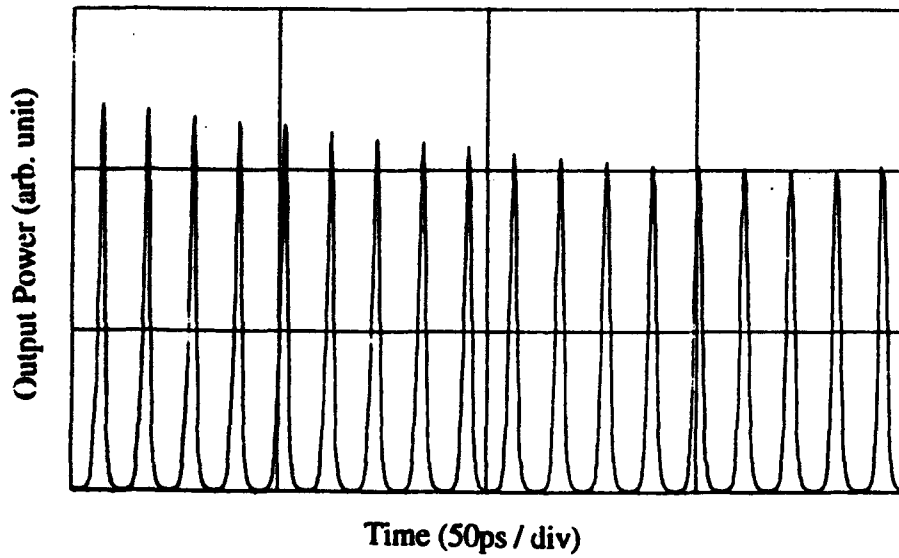


Fig. 2 The train of pulses at 3 ns. The pulse amplitude is subject to a slow modulation.

Modeling Subpicosecond Pulse Evolution in High-Gain Semiconductor Laser Amplifiers

A. Dienes, J. P. Heritage, M. Y. Hong, Y. H. Chang

Department of Electrical & Computer Engineering, University of California, Davis, CA 95616

Recent advances in subpicosecond generation and amplification with semiconductor lasers have shown the necessity of extending and modifying existing theoretical models¹ to include phenomena influencing subpicosecond pulse amplification. To model subpicosecond pulse evolution in semiconductor laser amplifiers (SLA), spectral dependence of both real and imaginary parts of the complex susceptibility (index and gain) within the pulse bandwidth must be included. In addition to the well known gain saturation and selfphase modulation (SPM) due to carrier depletion¹, it is necessary to account for the recently observed rapid gain and phase dynamics which have been attributed to carrier heating². The effects of an instantaneous nonlinear index n_2 must also be included.

We define the pulse envelope by the Fourier transform pair $V(t, z)$ and $V(\omega, z)$. All phase and amplitude changes caused by propagation in the nonlinear medium are included in $V(\omega, z)$ except the carrier phase shift $\beta_0 z$. From the wave equation, using the slowly varying wave approximation, we obtain the propagation equation

$$\frac{\partial V(\omega, z)}{\partial z} = -i \left\{ \frac{\omega}{c} [1 + \chi_m(\omega) + \Gamma \tilde{\chi}(\omega, N, T)]^{1/2} - \beta_0 \right\} V(\omega, z) \quad (1)$$

where the effective mode index $\bar{n} = (1 + \chi_m)^{1/2}$ is frequency dependent due to both material and guide dispersion effects. The transverse dependence has been integrated out to give Γ the confinement factor. The complex susceptibility $\tilde{\chi} = \chi_R + i\chi_I$ represents the contribution of the carriers in the active region. In addition to its frequency dependence, it is also a function of the carrier density N , as well as of the carrier temperature T . Next, we expand real and imaginary parts of both $\tilde{\chi}$ and χ_m in a Taylor series about the pulse center frequency to second order in ω and then transfer into the time domain to obtain

$$\left[\frac{\partial}{\partial z} + \frac{i}{v_g} \frac{\partial}{\partial t} - \frac{i}{2} \beta_2 \frac{\partial^2}{\partial t^2} \right] V(t, z) = \frac{\omega_0 \Gamma}{2c\bar{n}} \left\{ \chi_I(\omega_0) - i\chi_R(\omega_0) \right. \\ \left. - \left[i \frac{\partial \chi_I}{\partial \omega} + \frac{\partial \chi_R}{\partial \omega} \right]_{\omega_0} \frac{\partial}{\partial t} - \frac{1}{2} \left[\frac{\partial^2 \chi_I}{\partial \omega^2} - i \frac{\partial^2 \chi_R}{\partial \omega^2} \right]_{\omega_0} \frac{\partial^2}{\partial t^2} \right\} V(t, z) \quad (2)$$

Here v_g is the group velocity, and β_2 is the group velocity dispersion due to the mode index.

The first and second terms on the right hand side of this equation represent the differential gain and phase change at the pulse center frequency, while the terms that follow describe the frequency dispersion of these quantities. We calculate the susceptibility $\tilde{\chi}$ as a function of ω and of N and T , using greatly simplified assumptions along the line of the theory of Vahala at al³. The calculations are carried out for a range of values of N , T , and on the bases of the resultant curves of $\tilde{\chi}$ vs. ω we find a simple mathematical model for the dependence of each of the terms in the RHS of equation (2) on carrier density and temperature. Fig 1 shows typical curves of the active region gain ($\omega\chi_I/cn$) and of the corresponding index contribution ($\chi_R/2$)

for InGaAsP. On the bases of a series of these curves and rate equation modeling of the nonlinear dynamics of carrier density and temperature, after adding free carrier and two photon absorptions and also the instantaneous nonlinear index effect, we obtain the final form of the pulse propagation equation

$$\left[\frac{\partial}{\partial z} - \frac{i}{2} \beta_2 \frac{\partial^2}{\partial \tau^2} \right] V(\tau, z) = \left\{ \frac{1}{2} g_N(\tau, \omega_0) (1 + i \alpha_N) - \frac{1}{2} \Delta g(\tau, \omega_0) (1 + i \alpha_T) - \gamma_{fc} \right. \\ \left. - i \frac{1}{2} \frac{\partial g(\tau, \omega)}{\partial \omega} \Big|_{\omega_0} \frac{\partial}{\partial \tau} - \frac{1}{4} \frac{\partial^2 g(\tau, \omega)}{\partial \omega^2} \Big|_{\omega_0} \frac{\partial^2}{\partial \tau^2} - \left(\gamma_{2p} + i b_2 \right) |V(\tau, z)|^2 \right\} V(\tau, z). \quad (3)$$

Here, γ_{fc} and γ_{2p} are the free carrier and two photon absorption coefficients, and $b_2 = \omega_0 n_2 / cA$ (A is the effective area). The other terms on the right hand side are given by :

$$g_N(\tau) = g_0 \exp \left[-\frac{1}{W_{s1}} \int_{-\infty}^{\tau} |V(\tau')|^2 d\tau' \right], \quad (4)$$

which describes the well known energy dependent carrier depletion gain saturation¹ (g_0 is the linear gain and W_{s1} is the saturation energy defined in the standard manner).

$$\Delta g_T(\tau) = -\frac{\Delta g_0}{W_{s2}} \int_{-\infty}^{+\infty} u(\tau) e^{-s/\tau_2} \left\{ |V(\tau-s)|^2 + h |V(\tau-s)|^4 \right\} ds, \quad (5)$$

which describes the dynamic gain decrease due to carrier heating. Due to the fast relaxation of the heated carriers to the ambient crystal temperature ($\tau_2 \approx 600$ fs), this function depends on the pulse intensity. Carrier heating is assumed to be due to three causes: stimulated emission, free carrier absorption, and two photon absorption and h is a parameter describing the ratio of the contributions of the third to the first two. The parameter $\Delta g_0 / W_{s2}$ defines the magnitude of the carrier heating caused gain depletion.

The phase changes which (as Figure 1b shows) accompany these gain dynamics are given by the two linewidth enhancement factors

$$\alpha_N = -\frac{\partial \chi_R / \partial N}{\partial \chi_I / \partial N} = -2\beta \frac{\Delta n_N}{\Delta g_N}, \quad \text{and} \quad \alpha_T = -\frac{\partial \chi_R / \partial T}{\partial \chi_I / \partial T} = -2\beta \frac{\Delta n_T}{\Delta g_T}. \quad (6)$$

Equation (3) has no phase dispersion terms. This is because, as can be seen from Fig 1b, the curvature of χ_R is negligibly small. Gain dispersion, however, is not negligible; additionally, it is also a dynamic quantity. The instantaneous value of the two frequency derivatives of the gain can be approximated as linearly related to the net gain $g(\tau) = g_N(\tau) + \Delta g_T(\tau)$.

$$\frac{\partial g}{\partial \omega} = A_1 + B_1 [g_0 - g(\tau)], \quad \text{and} \quad \frac{\partial^2 g}{\partial \omega^2} = A_2 + B_2 [g_0 - g(\tau)] \quad (7)$$

where A_i and B_i are constants determined from the gain vs ω curves.

Equation (3) adds substantial improvements to existing theories.^{1,4} We have verified that the new terms result in modifications that are consistent with recent experimental observations. Second-order gain dispersion acts to restrict the SPM modulated bandwidth (experimentally

observed⁵ but not yet explained) and the carrier heating caused gain depletion and SPM result in behavior that closely mimics the pump and probe results of Ref. 2. The ultimate test of our model, of course, is to fully explain experimental results of high gain subpicosecond pulse evolution.⁵ We used a modified split step Fourier transform method to integrate equation (3) and thus find the pulse evolution in both time and frequency domains. In Figure 2 we show a particular result for a 500 fs duration input pulse under conditions of rather high input pulse energy, which leads to strong saturation due to both carrier depletion and carrier heating. The strong SPM due to both types of saturation results in considerable spectral broadening, while the fast response gain saturation also causes distortion of the pulse shape. For pulses of around 2ps duration or longer both spectral and time domain evolutions were found to be very different. This is due to the diminished importance of the fast carrier heating effects. Qualitatively these results are similar to the experimental observations of Delfeyette et al.⁵ A detailed parametric study is now under way.

References

1. G. P. Agrawal and N. A. Olsson, *IEEE J. Quantum Electr.*, QE-25, 2297 (1989).
2. C. T. Hultgren and E. P. Ippen, *Appl. Phys. Lett.*, 59, 635 (1991).
3. K. Vahala, L. C. Chiu, S. Margalit, and A. Yariv, *Appl. Phys. Lett.*, 42, 631 (1983).
4. A. Uskov, J. Mørk, and J. Mark, *IEEE Photon. Tech. Lett.*, 4, 443 (1992).
5. P. J. Delfeytt, Y. Silberberg, and G. A. Alphonse, *Appl. Phys. Lett.*, 59, 10 (1991).

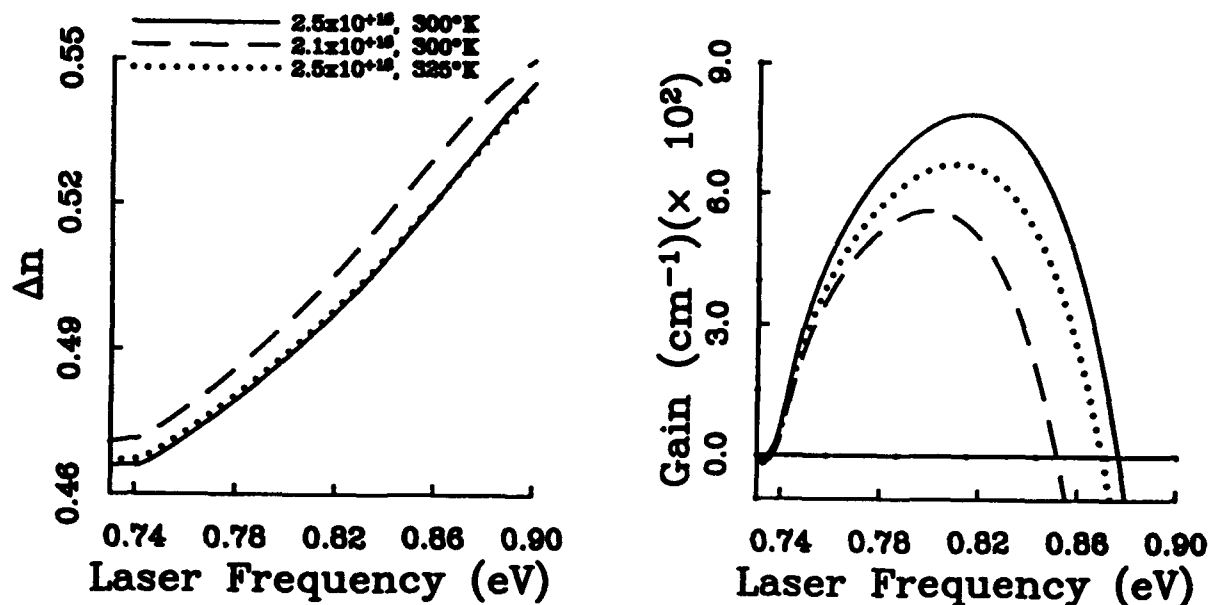


Fig.1. Calculated gain and index contribution due to carriers in InGaAsP at different carrier densities and temperatures.

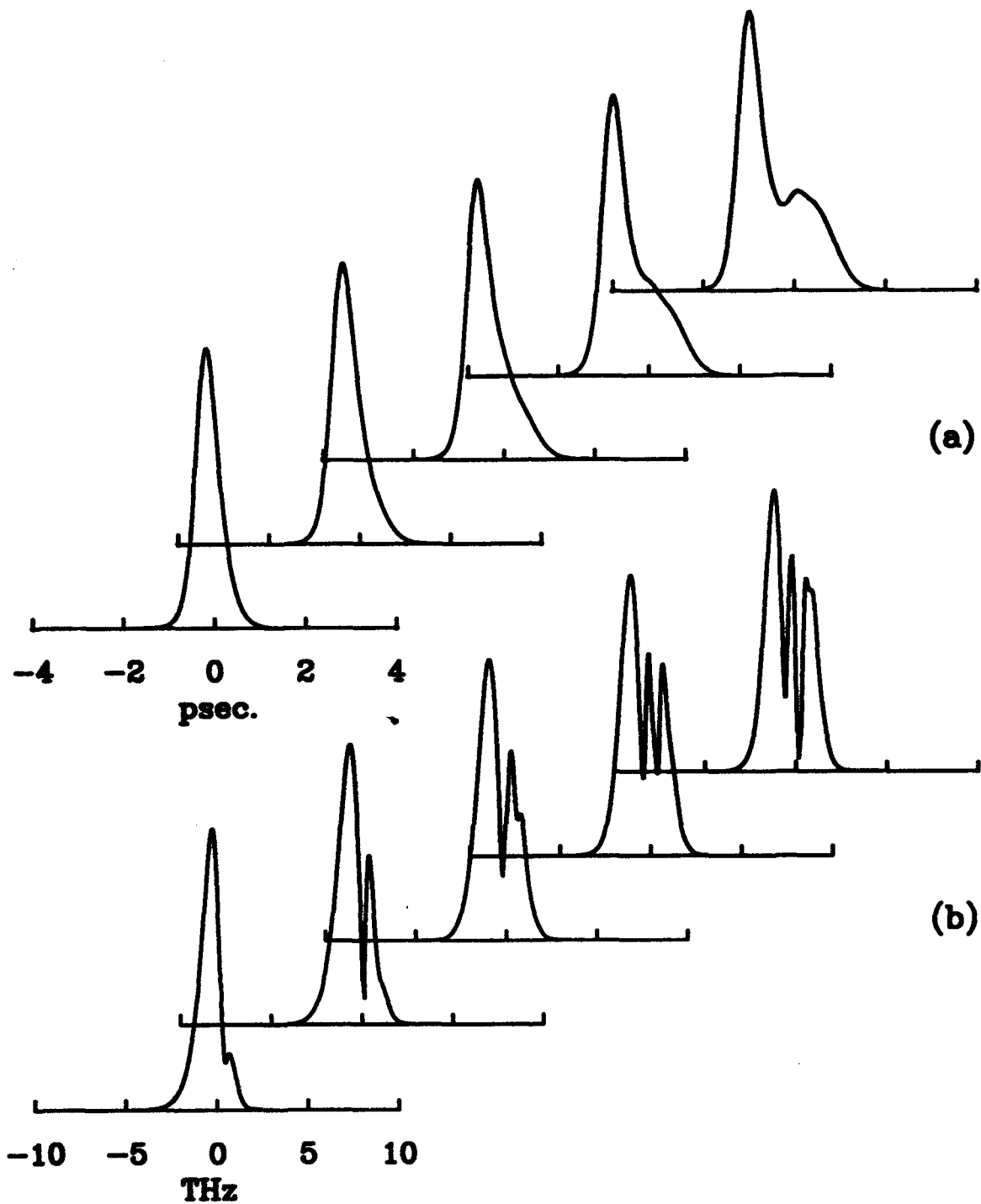


Fig.2. Evolution of a 500 fs input pulse in a 30 DB linear gain InGaAsP amplifier. $\beta_2 = 0.05 \text{ ps}^2/\text{cm}$, $\alpha_N = 3.0$, $\alpha_T = 2.5$, $\gamma_{fs} = 0$, $\gamma_{sp} = 0.15 \text{ cm}^{-1} \text{ w}^{-1}$, $n_2 = -1 \times 10^{-12} \text{ cm}^2/\text{w}$, $W_{in} = 0.7 \text{ pJ}$, $W_{s1} = 5 \text{ pJ}$, $\Delta g/W_{s2} = 750 \text{ cm}^{-1} \text{ pJ}^{-1}$, $A_1 = 0.7 \text{ fs}/\mu\text{m}$, $B_1 = -24 \text{ fs}$, $A_2 = -60 \text{ fs}^2/\mu\text{m}$, $B_2 = 0$.

Lateral and Longitudinal Mode Discrimination in Index-Guided Circular Ring Semiconductor Lasers

R.F. Nabiev, D.Francis, C.J. Chang-Hasnain

Ginzton Lab and Electrical Engineering Department, Stanford University

Stanford, CA 94305-4085

Tel (415) 723-0111, Fax (415) 735-2533

Circular ring semiconductor lasers are promising sources of coherent light for integrated optoelectronics. There have been a number advances in these lasers [1-3]. We believe that the structures with relatively small index step ($\Delta n=0.1-0.2$), for instance ridge-waveguide of buried heterostructure ring lasers, will have better performance characteristics than the devices with deep etching through active region. We present in this paper a WKB analysis of mode structure and thresholds of ridge-waveguide semiconductor lasers, and coupled-mode theory of radially coupled dual ring lasers. We show strong suppression of higher-order lateral modes due to leakage. We show also that radial coupling of concentric two ring lasers results in discrimination of longitudinal modes.

Ridge-waveguide ring laser shown in the Fig. 1 can be described in frames of effective index approximation, with certain profile of refractive index $n(r)$ depending on radius. An electromagnetic field of form $A(r)r^{-1/2} \exp(-iM\phi + i\omega t)$ obeys the equation:

$$\frac{\partial^2 A}{\partial r^2} - k_0^2 \left(\frac{R^2 n_{eff}^2}{r^2} - n^2(r) \right) = 0 \quad (1)$$

where $k_0 = \omega / c$ is the wavevector of photon in a vacuum, R is the outer diameter of the ring, and n_{eff} is the analog of modal refractive index in planar waveguides ($M = 2\pi R n_{eff} / \lambda_0 \gg 1$, λ_0 is the wavelength in a vacuum). The M value characterizes the number of wavelength along the ring. Fig. 2(a) shows intensity distributions of three lowest order modes of the ring waveguide ($R=100 \mu\text{m}$, width of ring is $W=2 \mu\text{m}$, refractive index step is $\Delta n=0.1$). It is clearly seen that the lowest order mode ($N=1$) is shifted to the outer boundary of ring, and the other modes are shifted to the inner part of ring. Fig. 2(b) shows the radial intensity profiles of fundamental modes ($N=1$) of two waveguides of different radii $R=50 \mu\text{m}$ and $100 \mu\text{m}$. The mode profile is more symmetrical for the ring with larger radius because a repulsive potential (the $1/r^2$ term) in the Eq. (2) is flatter inside waveguide region in

this case. The analysis shows that further increasing of the width of ring does not change the profile and the effective refractive index n_{eff} of the fundamental mode.

The bending of the waveguide causes the electromagnetic field to tunnel through potential barrier which, in turn, leads to inherent mode leakage (see solid line for $R=50 \mu\text{m}$, Fig 2(b)). We estimate the losses of modes of ring laser in frames of WKB approximation:

$$\alpha = \frac{n_2}{2R(1 - (n_{\text{eff}}/n_2)^2)^{1/2}} \exp[-2MJ], \quad J = \tanh^{-1} \left[\sqrt{1 - (n_1/n_{\text{eff}})^2} \right] - \sqrt{1 - (n_1/n_{\text{eff}})^2} \quad (3)$$

where n_2 and n_1 are the refractive indices of waveguiding and surrounding regions. Fig. 3 shows the losses of different modes vs. radius of ring (a) and refractive index step for $R=50 \mu\text{m}$ (b). One can see that the losses of the fundamental modes are very small (even for $R=50 \mu\text{m}$, $\alpha=11 \text{ cm}^{-1}$). On the other hand, there is strong discrimination of higher order modes (for $R=50 \mu\text{m}$ and $\Delta n=0.1$, $\alpha(N=2) - \alpha(N=1) = 475 \text{ cm}^{-1}$). Thus, single lateral (radial) mode operation can be achieved more easily in ring lasers than in straight ridge waveguide lasers of same dimensions and equivalent design. This is especially important for laser characteristics above threshold when spatial hole burning of gain profile allows higher order modes to lase.

Y-coupled ring lasers have recently [4] been shown to operate in single longitudinal mode. In our notation it corresponds to specific value of angular number M . We propose here concentric coupled ring laser for still higher longitudinal mode discrimination. Let us consider to concentric ring waveguides of radii R_1 and R_2 . We can represent mode of dual ring as a superposition of the modes of single rings:

$$a_1(\varphi)A_1(r)r^{-1/2} \exp(-iM_1\varphi + i\omega t) + a_2(\varphi)A_2(r)r^{-1/2} \exp(-iM_2\varphi + i\omega t)$$

where radial functions $A_i(r)$ obey the eigenvalue Eq. (1) with the corresponding index profile $n_i(r)$. For angular functions $a_i(\varphi)$ we can write equations:

$$\begin{aligned} \frac{dA_1}{d\varphi} &= i \frac{R_1}{M_1} k_0^2 \kappa_{12} \exp(i\Delta M) \\ \frac{dA_2}{d\varphi} &= i \frac{R_2}{M_2} k_0^2 \kappa_{21} \exp(-i\Delta M) \end{aligned} \quad (2)$$

where $\kappa_{ij} = \int A_i(\varepsilon - \varepsilon_j)A_j r dr$ are coupling coefficients and $\Delta M = M_2 - M_1$. Using round-trip-analysis [5] for this generalized coupled mode theory one can find the thresholds of different

longitudinal (angular) modes. Because of different lengths of rings spacings of their longitudinal modes slightly differ, and the modes of dual ring will have spacing determined by $\Delta M \ll M_1, M_2$. It results in strong longitudinal mode discrimination, which will also be presented at the conference.

Summarizing, ridge-waveguide circular ring laser provide strong lateral mode discrimination at low threshold of fundamental mode. In order to get single frequency operation we propose dual concentric coupled ring lasers.

References:

- [1]. A.F. Jezierski and P.J.R. Laybourn. IEE Proc., 135, 17 (1988).
- [2]. J.P. Hohimer, D.C. Craft, G.R. Hadley, G.A. Vawter, and M.E. Warren. Appl. Phys. Letts., 59, 3360 (1991).
- [3]. H. Han, M.E. Favaro, D.V. Forbes, and J.J. Coleman. IEEE Photonics Technology Letts., 4, 817 (1992).
- [4]. J.P. Hohimer, G.A. Vawter, D.C. Craft, and G.R. Hadley. Appl. Phys. Letts., 61, 1375 (1992).
- [5]. G. Griffel, W.K. Marshall, I. Grave, A. Yariv, R. Nabiev. Optics Letters, 16, 1174 (1991).

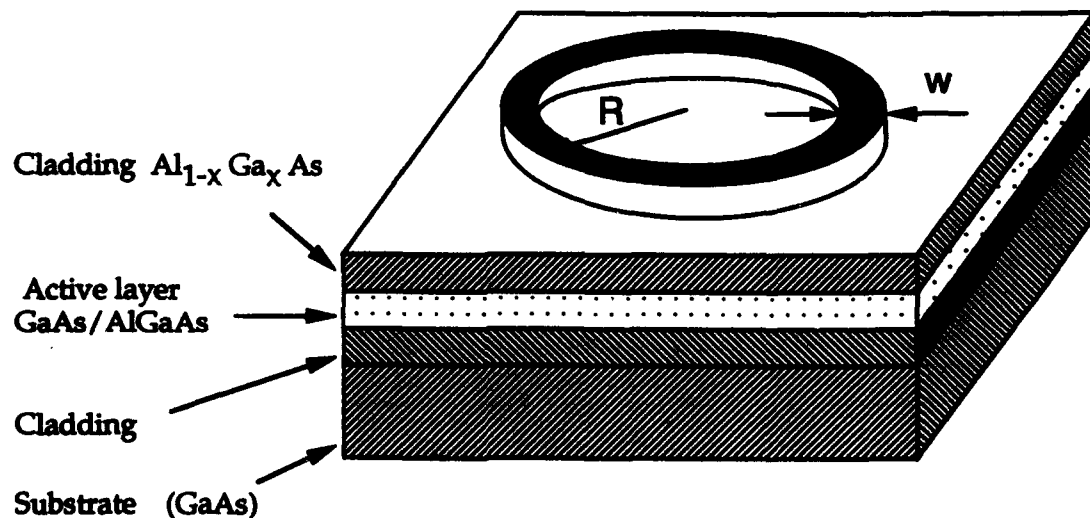


Fig.1. Scketch of ridge-waveguide ring laser.

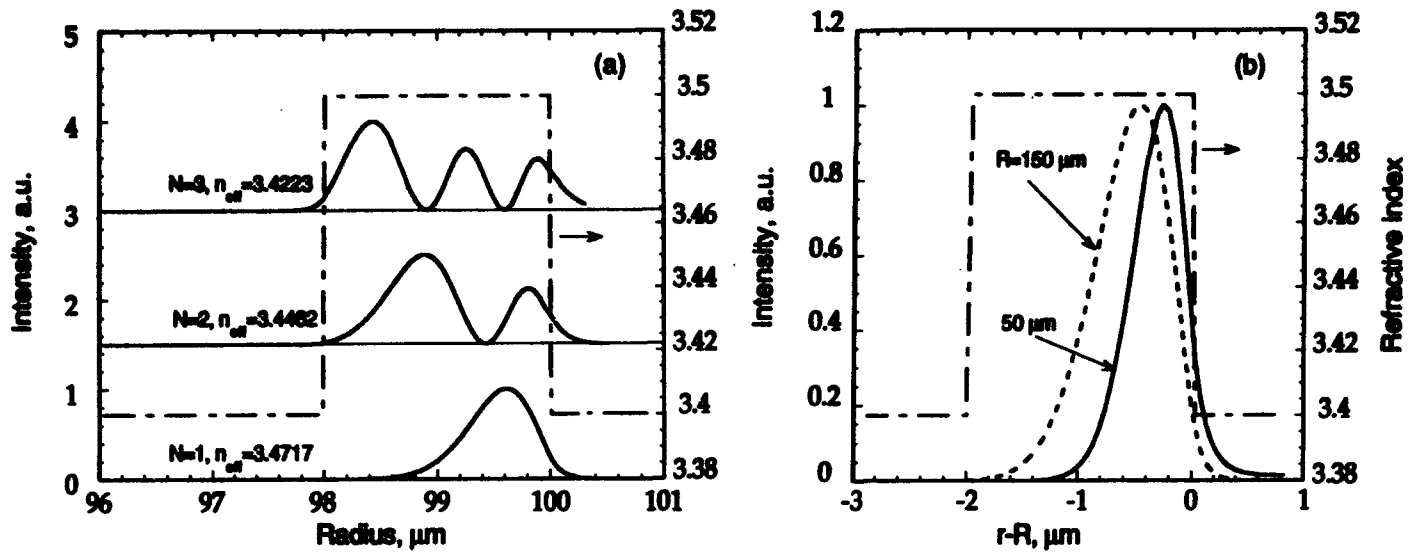


Fig. 2. Intensity distributions of three lowest order modes of the ring waveguide ($R=100\ \mu\text{m}$, width of ring is $W=2\ \mu\text{m}$, refractive index step is $\Delta n=0.1$) (a) and radial intensity profiles of fundamental modes ($N=1$) of two waveguides of different radii $R=50\ \mu\text{m}$ and $100\ \mu\text{m}$ (b).

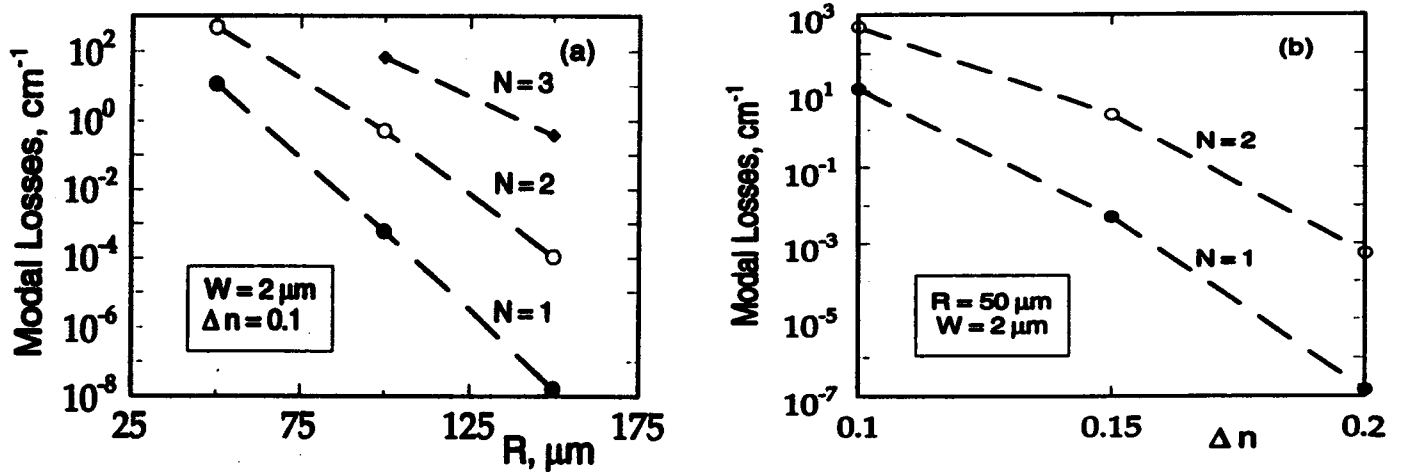


Fig. 3. Losses of lowest-order modes vs. radius of ring for $\Delta n=0.1$ (a) and vs. refractive index step for $R=50\ \mu\text{m}$ (b).



Spatial and Temporal Solitons

IWF 11:00am-12:30pm
Mesquite C/D

Yaron Silberberg, *President*
Bellcore

Varying nonlinearity, waveguides and novel fields

C. Pask and R.A. Sammut

Department of Mathematics, University College

University of New South Wales

Canberra, ACT 2600 Australia (Phone: +61 6 268 8686)

Introduction: Recently two experimental systems have been used to observe nonlinear effects and self-guiding in one transverse dimension. In the first system¹ a beam is broken into a stack of parallel filaments and nonlinear effects are observed across those filaments. This has led to a variety of experiments involving soliton beams and their interactions which are reviewed by Reynaud and Barthelemy.² In the second approach a planar waveguide is used to contain the beam in one transverse dimension (the y -direction) and then nonlinear effects dictate the beam properties in the second transverse dimension (the x -direction)^{3,4}. This is proving to be a valuable experimental system.⁵

The simplest theory⁴ for the planar waveguide system describes the beam using a product of a linear waveguide modal field $\psi_L(y)$ and a solution of the nonlinear Schrödinger equation (NLSE) in the x -direction. This implies that the two dimensions are separated and we have recently shown⁶ that this is an extremely good approximation. However, this does not mean that the two dimensions are fully decoupled. The y -direction field influences the x -direction field by means of an effective nonlinear constant, which is the bulk value of n_2 divided by an effective length. As a consequence, the full three-dimensional propagation problem reduces, under the separability approximation, to a NLSE with the effective nonlinearity.

The model: We consider a symmetric planar waveguide in which the cladding and substrate are linear, but the film is a Kerr-law medium. The beam propagation problem requires us to find the field $E = \Psi(x, y, z)e^{-i\omega t}$ which satisfies the equation

$$\nabla^2 \Psi + k^2 (n_0^2(y)\Psi + \alpha|\Psi|^2\Psi) = 0 \quad (1)$$

where n_0 is the linear refractive index profile, $\alpha = n_f^2 n_2 c \epsilon_0$, n_f is the film index and n_2 is the nonlinear coefficient (measured in m^2/W). If linear guiding dominates in the y direction, we may assume a solution of the form $\Psi = \psi_L(y)/N_2^{1/2} \exp(i\beta_L z) \Phi(x, z)$ where ψ_L is the field of the linear guided mode and $N_m = \int_{-\infty}^{\infty} \psi_L^m(y) dy$. We can then obtain an equation for Φ by averaging over the y direction. That is, we multiply Eqn (1) by $\psi_L(y)/N_2^{1/2}$ and integrate over y to find

$$\frac{\partial^2 \Phi}{\partial z^2} + 2i\beta_L \frac{\partial \Phi}{\partial z} + \frac{\partial^2 \Phi}{\partial x^2} + k^2 \alpha L_{eff}^{-1} |\Phi|^2 \Phi = 0 \quad (2)$$

where $L_{eff} = N_2^2/N_4$ is an effective length.

Since this effective length can vary quite significantly as a function of film width⁶ while β_L remains relatively constant, these equations show that propagation in a one (transverse)-dimensional medium with constant refractive index but a spatially varying nonlinearity can be simulated, both theoretically and experimentally, by using a waveguide whose thickness varies in the transverse direction.

It is possible to envisage a large number of structures being constructed in this way. For example in Figure 1a, a planar waveguide has its thickness decreased along a narrow stripe. The resulting change in L_{eff} leads to an increase in the effective nonlinearity along that stripe. On the other hand an increase in waveguide thickness leads to a decrease in effective nonlinearity as illustrated in Figure 1b. We have thus produced one (transverse)-dimensional structures with constant refractive index but with a step variation in effective nonlinearity. Similarly Figure 1c illustrates the possibility of creating nonlinear couplers while Figure 1d shows that graded nonlinearity profiles can be simulated by tapering the waveguide thickness.

Steady-state solutions for the first three of these structures can be derived analytically in terms of Jacobian elliptic functions^{7,8}. We would not, in general, be able to solve for the last of these profiles analytically but a variational approximation⁹ may be used with very high accuracy.

Example: As an example we focus on one particular case which exhibits particularly intriguing solutions. In the steady-state, $\Phi(x, z) = \psi(x) \exp(i\delta\beta z)$ where ψ satisfies the equation

$$\psi'' + k^2\alpha(x)\psi^3 = \lambda^2\psi. \quad (3)$$

Here primes denote differentiation with respect to x , k is the wavenumber and $\lambda^2 = \beta^2 - \beta_L^2$ where $\beta = \beta_L + \delta\beta$.

In the situation depicted in Figure 1b, two types of symmetric solutions generally occur — one in terms of the Jacobian dn function and the other in terms of the nd function^{7,8}. However if waveguide parameters are chosen such that $\alpha_2 = 2\alpha_1$, a third symmetric solution of the form

$$\begin{aligned} \psi &= (2/\alpha_2)^{1/2} (\lambda/k) & |x| < a \\ &= (2/\alpha_2)^{1/2} (\lambda/k) \operatorname{sech} [\lambda(x \pm a)] & |x| > a \end{aligned} \quad (4)$$

where the + applies in the region $x < a$ and the - applies for $x > a$. This solution has the very unusual property of being constant throughout the central guiding region.

Figure 2 shows the dispersion curves for the three solutions where $\alpha_2 = 2\alpha_1 \simeq 1.3 \times 10^{-11} \text{ m}^2/\text{V}^2$. The inset figures show the field profiles at several points and show, in particular, that all three solutions converge to the same form at a certain power.

The behavior of solutions for other values of the ratio of the two nonlinearities can be quite different. Further examples and a discussion of the stability properties of the solutions will be presented at the conference.

Conclusion: We have shown that when a beam is confined in the y -direction principally by the action of a linear refractive index profile, the nonlinear behavior of the beam in the x -direction is governed by the usual nonlinear Schrödinger equation with parameters modified by the linear waveguide modal properties. Since these parameters can vary quite significantly as a function of film width, this enables us to simulate propagation in a one (transverse)-dimensional medium with constant refractive index but a spatially varying nonlinearity. A variety of interesting nonlinear waveguides may be constructed in this way, some of which have analytical solutions as illustrated here.

This extension of a basic method used in spatial soliton research opens the way for the design of new structures with potential applications in all-optical signal processing.

References

1. A. Barthelemy, S. Maneuf and C. Froehly, "Propagation soliton et autoconfinement de faisceaux laser par non-linéarité optique de Kerr", *Opt. Commun.* 55, 201-206 (1985); S. Maneuf and F. Reynaud, "Quasi-steady state self-trapping of first, second and third order subnanosecond soliton beams", *Opt. Commun.* 66, 325-328 (1988).
2. F. Reynaud and A. Barthelemy, "Soliton beam propagation in nonlinear Kerr media" in *Guided Wave Nonlinear Optics* (ed. D.B. Ostrowsky and R. Reinisch, Kluwer Academic, Dordrecht, 1992).
3. S. Maneuf, R. Desailly and C. Froehly, "Stable self-trapping of laser beams : observation in a nonlinear planar waveguide", *Opt. Commun.* 65, 193-198 (1988).
4. J.S. Aitchison, A.M. Weiner, Y. Silberberg, M.K. Oliver, J.L. Jackel, D.E. Leaird, E.M. Vogel and P.W.E. Smith, "Observation of spatial optical solitons in a nonlinear glass waveguide", *Opt. Lett.* 15, 471-473 (1990).
5. J.A. Aitchison, Y. Silberberg, A.M. Weiner, D.E. Leaird, M.K. Oliver, J.L. Jackel, E.M. Vogel and P.W.E. Smith, "Spatial optical solitons in planar glass waveguides", *J. Opt. Soc. Am. B* 8, 1290-1297 (1991); J.S. Aitchison, A.M. Weiner, Y. Silberberg, D.E. Leaird, M.K. Oliver, J.L. Jackel and P.W.E. Smith, "Experimental observation of spatial soliton interactions", *Opt. Lett.* 16, 15-17 (1991); D.H. Reitze, A.M. Weiner and D.E. Leaird, "High-power femtosecond optical pulse compression by using spatial solitons", *Opt. Lett.* 16, 1409-1411 (1991).
6. R.A.Sammut, C.Pask and Q.Y. Li, "A theoretical study of spatial solitons in planar waveguides", *J.Opt.Soc.Am. B* (in press)
7. P.F.Byrd and M.D.Friedman, "Handbook of elliptic integrals for engineers and scientists" (2nd ed), Springer-Verlag (1971)
8. R.A.Sammut and C.Pask, "Analysis of planar waveguides formed by nonuniform nonlinearity", *Electron. Lett.* (submitted)
9. R.A.Sammut and C.Pask, "Gaussian and equivalent-step-index approximations for nonlinear waveguides", *J.Opt.Soc.Am. B* 8, 395 - 402 (1991); A.W.Snyder, Y.Chen, L.Poladian and D.J.Mitchell, "Fundamental mode of highly nonlinear fibres", *Electron. Lett.* 26, 643 - 644 (1990).

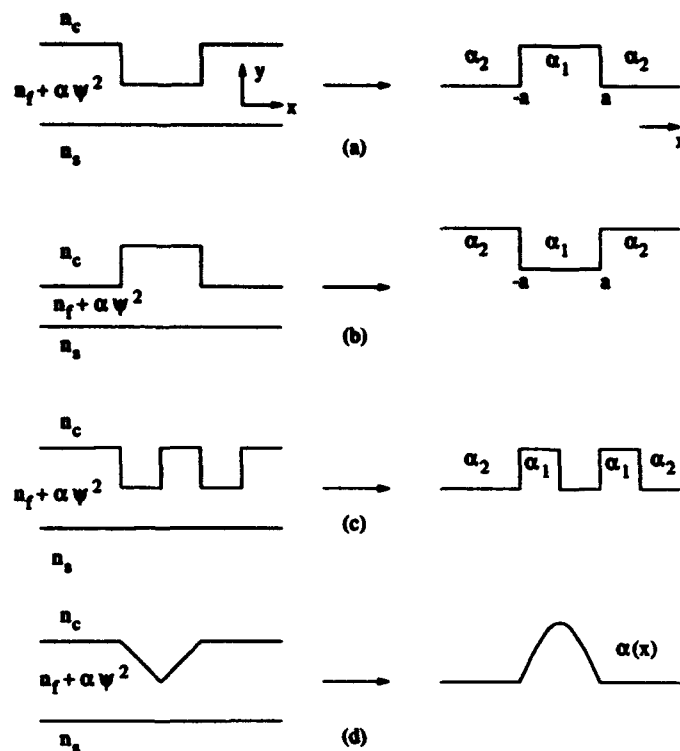


Figure 1 Schematic diagram showing the effective 1-D nonlinearity profiles corresponding to various 2-D geometric structures.

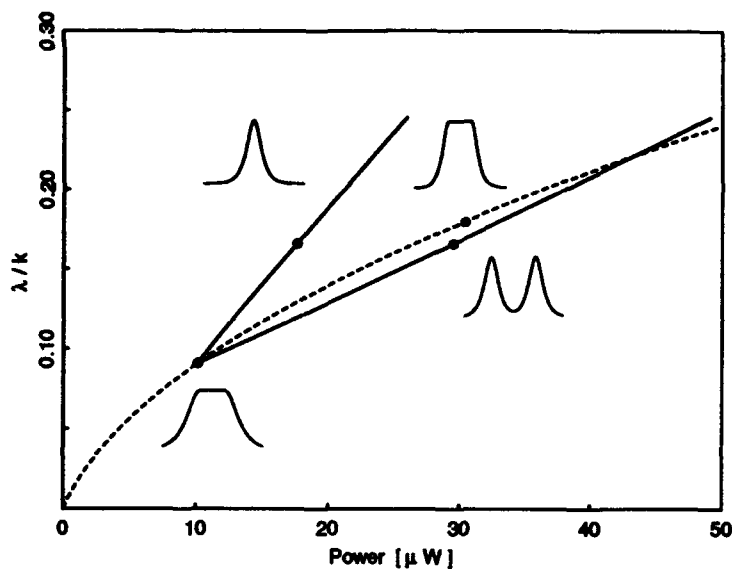


Figure 2 Dispersion curves for the lowest order symmetric solutions of the waveguide shown in Figure 1b. The dashed curve corresponds to the solution described by eqn (4). The inset figures show the field profiles at several powers. $\alpha_2 = 2\alpha_1 \approx 1.3 \times 10^{-11} \text{ m}^2/\text{V}^2$, wavelength is $0.515 \text{ } \mu\text{m}$ and $a = 1 \text{ } \mu\text{m}$.

SPATIAL SOLITON DYNAMICS IN COUPLED PLANAR WAVEGUIDES

A.D. Boardman and K. Xie

Applied Optics Group, Department of Physics
University of Salford, Salford, M5 4WT, U.K.

Tel: (061) 745 5253; FAX: (061) 745 5903

This paper presents the analytical and numerical results of an investigation the dynamics of coupled spatial solitons where the solitons reside, in general, in different planar waveguides. The solitons have the same frequency and polarisation and the waveguides are identical. A very important aspect of the theory, however, is that the nonlinear coupling does not ignore any cross-terms. The omission of many coupling terms, which characterises nearly all published calculations on nonlinear couplers, cannot always be logically justified and this point has attracted some recent attention^{1,2}. In the notation adopted here the stability of the soliton interactions now depends upon three parameters (ν , μ_1 , μ_2). This is an important novel feature here which, when added to an original development of an elegant, mathematical, particle-based approach, permits a far-reaching study of the soliton dynamics to be reported. Traditional Lagrangian variational methods³ are used but we are going to be much more general here, because we do not restrict the number of parameters, as is often done. Two waveguides are used for which the basic coupled equations are

$$\frac{\partial \psi_i}{\partial z} + \frac{\partial^2 \psi_i}{\partial x^2} + 2|\psi_i|^2 \psi_i + 2\nu \psi_j + 2\mu_1(\psi_j^2 \psi_i^* + 2|\psi_j|^2 \psi_i) + 2\mu_2(2|\psi_i|^2 \psi_j + \psi_i^2 \psi_j^* + |\psi_j|^2 \psi_i) = 0$$

where $i = 1$ or 2 with the corresponding $j = 2$ or 1 . $\frac{\omega}{c} \rightarrow 2\beta z$, $\frac{\omega}{c} x \rightarrow x$,

$\left[\frac{4}{3} \chi_1^{(3)} \Gamma^4 \int A_1^4 dy \right]^{\frac{1}{2}} B_1 \rightarrow \sqrt{2} \psi_1$, $\left[\frac{4}{3} \chi_1^{(3)} \Gamma^4 \int A_2^4 dy \right]^{\frac{1}{2}} B_2 \rightarrow \sqrt{2} \psi_2$, $\nu = \frac{(\epsilon_1 - \epsilon_2)}{4} \Gamma^2 \int A_1 A_2 dy$, $\mu_1 = \Gamma^4 \int A_1^2 A_2^2 dy$, $\mu_2 = \Gamma^4 \int A_1^3 A_2 dy = \Gamma^4 \int A_1 A_2^3 dy$. $\epsilon_{1,2}$ are the, respective, dielectric constants of the waveguide and the cladding, $B_{1,2}(x, z)$ are the (x, z) dependent amplitudes of the guided modes propagating along the z -axis, $A_1(y)$, $A_2(y-d)$ are the mode profiles, d is the guides distance between the two, ω is angular frequency, β is the

wavenumber and $\Gamma_1 = \left[1 / \int_{-\infty}^{\infty} A_1^2 dy \right]^{\frac{1}{2}} = \Gamma_2 = \left[1 / \int_{-\infty}^{\infty} A_2^2 dy \right]^{\frac{1}{2}} = \Gamma$ are normalisation

factors. The objective in this short presentation is to concentrate on but one of the properties of the interacting solitons. This is the displacement suffered by two solitons approaching each other. We select cases for which the two beams are equal in magnitude but are either in phase, or $\pm\pi$ out of phase. This is the zero energy exchange regime, within which the beams behave as robust particles. There is nothing new, in general, about any particle representation, because it is a theme that has run through nonlinear physics for a very long time. Nevertheless, various forms exist and we present here a particular development that is designed for spatial solitons. If the solitons engage in weak interactions they, initially, have

the form $\psi_j = \eta_j \operatorname{sech} [\eta_j(x-x_j)] \exp \left\{ \frac{i\xi_j}{2}(x-x_j) + i\theta_j \right\}$ where $x_i = x_{j0} + \xi_i z$ and $\theta_j = \theta_{j0} + [\xi_j^2/4 + \eta_j^2]z$. All the parameters $(\eta_j, \xi_j, x_j, \theta_j)$ in this calculation vary with propagation distance and the Euler-Lagrange equations lead to the definitions $\eta_1 + \eta_2 = 2M$, $\eta_2 x_2 - \eta_1 x_1 = 2M\Delta$, $\eta_2 \xi_2 - \eta_1 \xi_1 = 2M\xi$, $\theta = \theta_2 - \theta_1$, $\eta_2 - \eta_1 = 2N$ and to equations for $\frac{dN}{dz}$, $\frac{d\Delta}{dz}$, $\frac{d\xi}{dz}$ and

$\frac{d\theta}{dz}$. Further normalisation in the form $\frac{\xi}{M} \rightarrow \xi$, $M\Delta \rightarrow \Delta$, $\frac{N}{M} \rightarrow N$, $\frac{\nu}{M^2} \rightarrow \nu$, $M^2 z \rightarrow z$ and $Mx \rightarrow x$ and the soliton coupling leads to important modifications of the single soliton relationships. Δ is the normalised spatial separation of the solitons and for beams with the

same amplitude at $z = 0$, with $(N)_{z=0} = 0$ and $(\theta)_{z=0} = 0$ or $\pm\pi \frac{d\Delta}{dz}$ can be determined analytically and curves can be generated for the complete (ν, μ_1, μ_2) parameter set. From the curvature it can be deduced that ν and μ_2 can create an attractive or a repulsive force (dependent on the relative phase between the soliton beams) but μ_1 always results in an attractive force. For *in-phase* beams ν and μ_2 are positive so all three interaction mechanisms (ν, μ_1, μ_2) contribute to an attractive force. Distinct curves (ξ, Δ) can be differentiated from each other by a critical value $C = C_r$, where C is the integration constant in the equation for ξ^2 , obtained from the variational equations. For $C > C_r$ solitons can follow a path from $-\infty$ to $+\infty$ and their velocity, as $\Delta \rightarrow \pm\infty$ becomes $(d\Delta/dz)_{\pm\infty} = \xi(\pm\infty) = \pm\sqrt{C}$. As the two beams proceeding from $-\infty$ get closer to each other they speed up. Obviously they cross each other at $\Delta = 0$ and, if they survive the collision the speed decreases again towards \sqrt{C} as $+\infty$ is reached. The interaction causes a spatial

$$\text{shift } \delta z = \int_{-\infty}^{\infty} \left[\left(\frac{d\Delta}{dz} \right)^{-1} - \left(\frac{d\Delta}{dz} \Big|_{\infty} \right)^{-1} \right] d\Delta. \text{ If } C = 0, \text{ then } \left(\frac{d\Delta}{dz} \right)_{\pm\infty} = 0 \text{ and solitons}$$

["particles"] can just overcome any attractive force and escape to infinity. Hence, the initial value $\xi_0(\Delta_0)$, corresponding to $C = 0$, and an initial beam separation equal to Δ_0 , is the escape velocity. If $\Delta_0 = 0$ then $\xi = \xi_0(0)$ is the solution of

$$F(\xi) = \frac{\xi^2}{2} - \frac{8}{3} \mu_1 - \frac{4(\nu + \mu_2)\pi\xi/2}{\sinh(\pi\xi/2)} - \frac{\xi^2 + 1}{3} \left[\frac{4\mu_1\pi\xi}{\sinh(\pi\xi)} + \frac{4\mu_2\pi\xi/2}{\sinh(\pi\xi/2)} \right] = 0$$

and it should be recalled that in a wave picture ξ_0 corresponds to the beam propagation angle $\tan(\phi_0) = \xi_0$. For $C < 0$ the soliton beams are trapped in the range $-\Delta_r < \Delta < \Delta_r$, where Δ_r is a solution of

$$(\nu + 2\mu_2) \frac{2\Delta}{\sinh(2\Delta)} + [3\mu_1 - 2\mu_2 \cosh(2\Delta)] \left[\frac{2\Delta \cosh(2\Delta)}{\sinh^3(2\Delta)} - \frac{1}{\sinh^2(2\Delta)} \right] = -\frac{C}{8}$$

As two solitons propagate forward they slow down because of the attractive force. At $\Delta = \Delta_r$ the two beams become parallel and cannot separate any further. They are, therefore, pulled back and cross at $\Delta = 0$, with another attempt to escape. Δ_r , however, is the maximum soliton separation and this periodic, behaviour is characterised by a spatial period

$$4 \int_{\Delta_r}^0 \left[\frac{d\Delta}{dz} \right]^{-1} d\Delta.$$

For beams *out of phase* by $\pm\pi$, $\cos(\theta_0) = -1$ and the parameters $\nu < 0$, $\mu_2 < 0$ cause a repulsive force, while μ_1 causes an attractive one. For realistic cases, $|\mu_1| \leq |\mu_2| < |\nu| \ll 1$ and the net interaction field is repulsive. C is automatically positive, the soliton velocity at

$\pm\infty$ is $\pm\sqrt{C}$ and the critical value of C is $C_r = -8 \left[\nu + \frac{\mu_2}{3} \right] - 8(\mu_1 + \mu_2)$ exists. Thus for $C < C_r$ beams from $\pm\infty$ will 'bounce back', before they "see" each other at the Δ_r given above.

As $C \rightarrow C_r$, Δ_r approaches zero and the value ξ_0 , corresponding to C_r , is called the "touching velocity". The "touching velocity" for a beam incident from ∞ is given by $\frac{d\Delta}{dz} =$

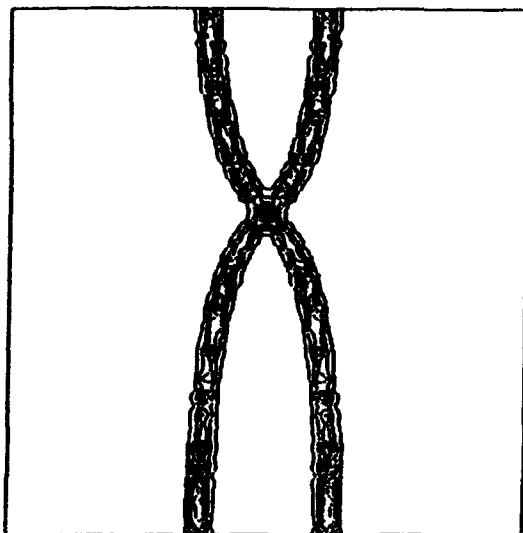
$$\xi_0(\pm\infty) = 2 \sqrt{-2 \left(\nu + \frac{\mu_2}{3} \right) - 2(\mu_1 + \mu_2)}.$$

For angles $\phi > \phi_0 = \tan^{-1}(\xi_0)$ the beams will cross each other but for $\phi < \phi_0$ the beams will be bent back. For $C < C_T$, no solution exists and ξ can never be zero, so beams never become parallel. Suppose two beams that are initially separated at infinity, start to be drawn towards each other as they propagate. In the first phase, they will reduce speed (propagation angle). They will then cross at $\Delta = 0$ with a speed $\xi(0)$ given by $F(\xi(0)) = \frac{C}{2}$.

After the point $\Delta = 0$, the solitons do not usually break and the repulsive force pushes the beam velocity up so that when they finally reach $\pm\infty$ they have a speed equal to the initial value but a shift δz will have occurred.

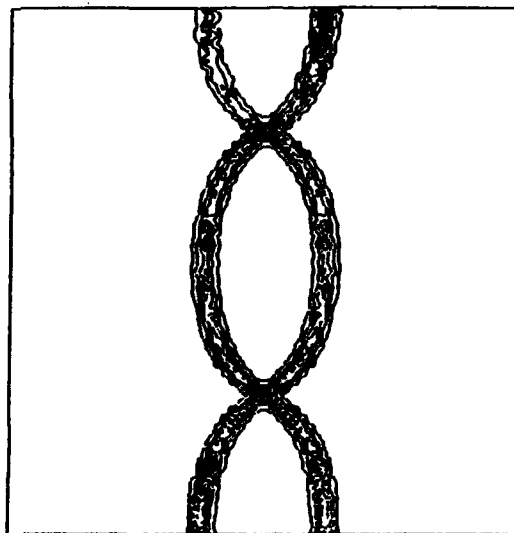
In conclusion we have set up a comprehensive theory of spatial soliton dynamics in coupled waveguides. The nonlinear coupling has been treated rigorously and consistently and analytical results have emerged. Full numerical confirmation of these results will be presented and detailed explorations of the new (ν, μ_1, μ_2) parameter space will be presented. The attached figure, for example, shows that the interaction period is dramatically altered by the inclusion of *all* the self-consistent nonlinear coupling terms. The theory reported here has an important bearing on the type of interaction experiment that can be performed with spatial solitons. Several suggestions for new experiments will be made.

1. C. Mapalagama and R.T. Deck, "Modified Theory of Three-Channel Kerr-Type Nonlinear Directional Coupler". Preprint [University of Toledo] (1992).
2. F.J. Fraile-Pelaez and G. Assanto, "Coupled-Mode Equations for Nonlinear Directional Couplers". Applied Optics, 29, 2216 (1990).
3. A.D. Boardman and K. Xie, Proceedings of the 1992 Nonlinear Optics School, Aalborg University, Denmark [Springer-Verlag].



(a)

Neglecting nonlinear
cross-terms



(b)

Exact theory

Interacting spatial solitons

SELF-TRAPPED, STABLE SOLUTIONS IN NONLINEAR CHANNEL WAVEGUIDES

A.D. Capobianco, B. Costantini, C. De Angelis, G.F. Nalesso, C.G. Somenza

Department of Electronics and Informatics, Università' di Padova
Via Gradenigo, 6/a, 35131 Padova, Italy

Telephone: (+39) 49 828 7660 - Fax: (+39) 49 828 7699

It is well known that a 2-D optical beam propagating along a given direction (say z) in a homogeneous nonlinear medium (HNLM) will either spread out or collapse within a finite distance, depending on whether its power is below or above a critical value, P_c [1]. The next question then is whether or not it is possible to obtain stable, stationary (i.e., z -independent) beams by adding a linearly guiding structure, like for example a channel-waveguide. The linear refractive index has to decrease monotonically as a function of distance from the z axis.

An affirmative answer to this question has been given recently [2]. Indeed, it was proved that planar nonlinear waveguides do propagate self-trapped modes, which are stable below a threshold power equal to the critical power P_c for solitary waves in HNLM. More realistically, we consider now a fully 2-D problem, a channel waveguide (Fig. 1), whose refractive index is assumed to be:

$$n(x,y) = \begin{cases} n_{0e} + n_2 |E|^2 & |x| > c, |y| > c \\ n_{0i} + n_2 |E|^2 & |x| < c, |y| < c \end{cases} \quad (1)$$

where n_2 is the Kerr coefficient of the material.

Under the SVEA approximation, the envelope of the electric field satisfies the 2-D nonhomogeneous nonlinear Schrödinger equation (NLSE)

$$i\partial_z \psi + \partial_{xx} \psi + \partial_{yy} \psi + 2|\psi|^2 \psi + N_0^2(x,y)\psi = 0 \quad (2)$$

where $N_0^2 = \Delta$ inside the square core $|x| < c, |y| < c$, $N_0^2 = 0$ elsewhere.

Equation (2) can be derived from a Lagrangian density [3]:

$$\mathcal{L} = \frac{i}{2} \left(\psi \partial_z \psi^* - \psi^* \partial_z \psi \right) + |\partial_x \psi|^2 + |\partial_y \psi|^2 - |\psi|^4 - N_0^2(x,y) |\psi|^2 = \frac{i}{2} \left(\psi \partial_z \psi^* - \psi^* \partial_z \psi \right) - \mathcal{H} \quad (3)$$

Generalizing the method of Crosignani et al. [4] to the 2-D case, we

introduce a set of trial functions of the form:

$$\psi(x, y, z) = |\psi| \exp \left(i \sum_{n=0}^N \left(a_n(z) x^n + b_n(z) y^n \right) \right) \quad (4)$$

$$\text{with } |\psi|^2 = F(M_{x_n}(z), M_{y_n}(z), x, y) \quad n=0, 1, \dots, N \quad (5)$$

where the M -s are the moments of the function ψ , namely:

$$M_{x_n} = \int_{-\infty}^{+\infty} \int_{-\infty}^{+\infty} x^n |\psi(x, y, z)|^2 dx dy, \quad M_{y_n} = \int_{-\infty}^{+\infty} \int_{-\infty}^{+\infty} y^n |\psi(x, y, z)|^2 dx dy \quad (6)$$

and F is an arbitrary function. As proved in [4], eqn. (2) can be approximated by a set of $4(N+1)$ ordinary differential equations (Hamilton eqns.) which can be obtained by minimizing the reduced Hamiltonian

$$H(a_n, b_n, M_{x_n}, M_{y_n}, z) = \int_{-\infty}^{+\infty} \int_{-\infty}^{+\infty} \mathcal{H} dx dy \quad (7)$$

on the set of trial functions (4,5). M_{x_n} , M_{y_n} turn out to be the conjugate momenta of a_n and b_n , respectively. When applying this procedure to the NL channel waveguide, we simplify the problem as much as possible, without missing its essential physical features, by choosing $N=2$ and trial functions:

$$\psi(x, y, z) = A \operatorname{sech} \left(\frac{\pi(x-x_0)}{\sqrt{12}\alpha} \right) \operatorname{sech} \left(\frac{\pi(y-y_0)}{\sqrt{12}\beta} \right) \exp \left(i \sum_{n=0}^2 (a_n x^n + b_n y^n) \right) \quad (8)$$

where

$$\begin{aligned} x_0 &= M_{x1}/M_0, & y_0 &= M_{y1}/M_0 \\ \alpha^2 &= M_{x2}/M_0 - x_0^2, & \beta^2 &= M_{y2}/M_0 - y_0^2 \end{aligned} \quad (9)$$

represent the coordinates of the center of gravity of the beam and its variance along x and y , respectively. The Hamilton equations are then:

$$\begin{aligned} dM_{x_n}/dz &= - \partial H / \partial a_n, & dM_{y_n}/dz &= - \partial H / \partial b_n \\ da_n/dz &= \partial H / \partial M_{x_n}, & db_n/dz &= \partial H / \partial M_{y_n} \end{aligned} \quad (10)$$

with $n=0, 1, 2$, while H is given by

$$\begin{aligned} H = - M_0 \left\{ \left(\frac{\pi^2}{12} \right) \left(\frac{1}{3\alpha^2} + \frac{1}{3\beta^2} - \frac{M_0}{6\alpha\beta} \right) + a_1^2 + 4a_1 a_2 M_{x1} + 4a_2^2 M_{x2} \right. \\ \left. + b_1^2 + 4b_1 b_2 M_{y1} + b_2^2 M_{y2} \right\} + G(x_0, y_0, \alpha, \beta) \end{aligned} \quad (11.a)$$

and

$$G(x_0, y_0, \alpha, \beta) = (M_0) \frac{\Delta}{4} \left\{ \tanh \left[\frac{\pi}{\sqrt{12}} \left(\frac{(c-x_0)}{\alpha} \right) \right] - \tanh \left[\frac{\pi}{\sqrt{12}} \left(\frac{(-c-x_0)}{\alpha} \right) \right] \right. \\ \left. \left\{ \tanh \left[\frac{\pi}{\sqrt{12}} \left(\frac{(c-y_0)}{\beta} \right) \right] - \tanh \left[\frac{\pi}{\sqrt{12}} \left(\frac{(-c-y_0)}{\beta} \right) \right] \right\} \right. \quad (11.b)$$

As H does not depend on a_0 , b_0 , it is readily seen that $M_{x0} = M_{y0} = M_0$. By definition this is the total power of the beam, a constant of the motion, as expected. Eqns. (10) can be reduced to

$$\frac{d^2 x_0}{dz^2} = - \frac{\partial V(x_0, y_0, \alpha, \beta)}{\partial x_0}, \quad \frac{d^2 y_0}{dz^2} = - \frac{\partial V(x_0, y_0, \alpha, \beta)}{\partial y_0} \quad (12)$$

$$\frac{d^2 \alpha}{dz^2} = - \frac{\partial V(x_0, y_0, \alpha, \beta)}{\partial \alpha}, \quad \frac{d^2 \beta}{dz^2} = - \frac{\partial V(x_0, y_0, \alpha, \beta)}{\partial \beta}$$

where $V(x_0, y_0, \alpha, \beta)$ plays the role of a potential function:

$$V(x_0, y_0, \alpha, \beta) = \left(\frac{\pi^2}{48} \right) \left(\frac{2}{\alpha^2} + \frac{2}{\beta^2} - \frac{M_0}{2\alpha\beta} \right) - \frac{2}{M_0} G(x_0, y_0, \alpha, \beta) \quad (13)$$

The stationary solutions of (12) (self-trapped beams) are those for which the r.h.s. of each of equations (12) vanishes. Taking advantage from spatial symmetries, the result is

$$x_0 = 0, \quad y_0 = 0, \quad \beta = \alpha$$

$$1 - M_0/8 = \frac{3\sqrt{12}}{2\pi^2} (\Delta\alpha) \operatorname{sech}^2 \left(\frac{\pi c}{\sqrt{12}\alpha} \right) \tanh \left(\frac{\pi c}{\sqrt{12}\alpha} \right) \quad (14)$$

Fig. 2 shows α as a function of the beam power M_0 . The second line of (14) indicates that solutions of this type exist only for $M_0 < 8$. For $M_0 = 0$ our solution becomes that of the linear channel waveguide, while as $M_0 \rightarrow 8$, it approaches the solitary wave of the 2-D homogeneous NLSE.

Having succeeded in deriving a potential function for the system, V , we are in a position to investigate stability of these self-trapped modes. Standard procedures indicate that stable solutions exist *if and only if* the matrix of the second derivatives of V is positive definite. Straightforward calculations show that indeed stable self-trapped modes exist for $M_0 < 8$.

In conclusion, the broadening of a 2-D optical beam, which occurs, below a

certain critical power, when it propagates in a homogeneous NL material, can be fully compensated for by introducing a linear channel guiding structure, embedded in a uniform cladding with the same nonlinearity. By using an approximate description of the optical beam in terms of a finite number of generalized coordinates, through a variational approach, we have been able to prove analytically that these self-trapped modes in NL channel waveguides are stable. This result appears to be in contrast with what has been recently reported [5] about the collapse of 2-D spatial solitons in an *unbound* parabolic-index medium. In our own judgement, the physical relevance of our model is much better grounded than that of a medium where the index decrease indefinitely.

This work was supported by CNR (Italian National Research Council) in the framework of the Project "Telecomunicazioni".

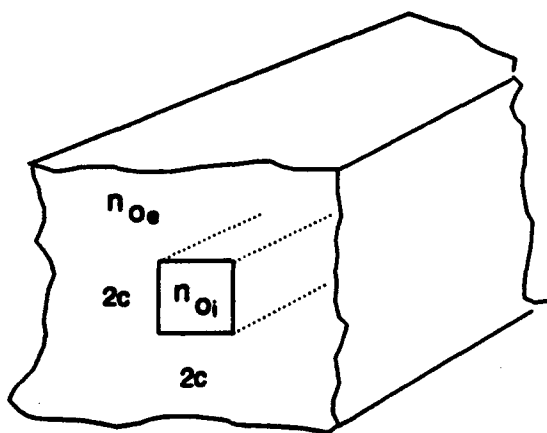


Fig.1
Channel waveguide

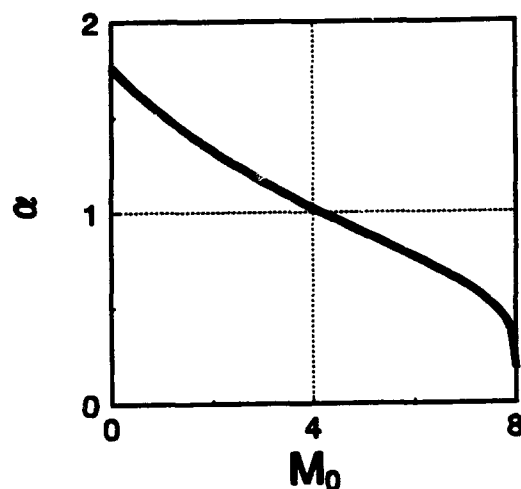


Fig.2
 α versus beam power M_0

REFERENCES

- [1] Rasmussen, J.J., Rypdal, K., *Physica Scripta*, 1986, 33, pp 481-497.
- [2] Aceves A.B., Capobianco A.D., Costantini B., De Angelis C., Nalesso G.F., 'Two dimensional variational analysis of self trapped solutions in planar waveguides' submitted to Optics Letters.
- [3] Anderson D., *Phys. Rev. A*, 1983, 27, pp 3135-3145.
- [4] Crosignani B, Di Porto P, Piazzolla S, *Pure Appl. Opt.*, 1992, 1, pp 7-12
- [5] Manassah J.T., *Optics Letters*, 1992, 17, pp 1259-1261.

Diagrammatic Techniques for the Analysis of Nonlinear Slab Optical Waveguides

Juan P. Torres and Lluís Torner

Polytechnic University of Catalonia

Department of Signal Theory and Communications

P.O. Box 30002, 08080 Barcelona, Spain

Fax: (34) 3 4016801

Tel: (34) 3 4016527

In this paper we report a general procedure to obtain a set of universal diagrams summarizing the properties of the stationary nonlinear waves guided by slab optical waveguides made on intensity-dependent dielectric media. Our goal is to show that a great deal of the information, relative to the stationary properties and stability of the nonlinear waves guided by different structures, can be straightforwardly obtained from the $V - b$ universal diagrams. Here V and b are the well-known normalized waveguide thickness and effective index of guided solutions, respectively. The idea behind a $V - b$ diagram is to partition parameter space into regions of similar waveguiding properties, in such a way that critical points may be easily read off from the plots, without solving the nonlinear wave equation. The critical lines in the diagrams separate regions of forbidden values from those corresponding to different allowed guided waves, both stable and unstable.

The starting point of the procedure is the generalized dispersion relation for nonlinear guided waves derived by Langbein, Lederer and Ponath [1]. We focus on the TE-polarized waves guided by a thin, optically linear film bounded by two identical nonlinear saturable media, with a typical two level nonlinear response. In the nearly Kerr-like case, this waveguide supports a rich set of different guided waves [2], hence it enables us to clearly point out the usefulness of the $V - b$ diagrams. The asymmetric structures containing a single nonlinear bounding medium have been discussed earlier [3].

Our results indicate that, for a wide class of nonlinear permittivities, the allowed and forbidden regions of the $V - b$ plane for stationary guided propagation to occur display a universal pattern, the marginal loci separating different regions being a function of the waveguide asymmetry measures and the saturation measure γ [3]. Allowed bands subdivide into different single and double-valued regions, corresponding to *pure guided waves* (PGW), *bulged guided waves* (BGW) and *surface waves* (SW), according to the classification by Boardman and Egan. The marginal loci separating the allowed from the forbidden bands yield cutoff, power-independent values of the various waveguide parameters for the different kind of waves to exist and, also, the asymptotical values of the normalized effective index for large values of the guided power flow. For instance, when considering waveguide structures with $\gamma > 1$, (this occurs when the optically-induced refractive index change is greater than the difference between the film and cladding linear refractive indices), $b = \gamma$ becomes the maximum allowed value of the normalized effective index for any value of V .

The $V - b$ diagrams for all the guided wave solutions have two sheets, with the lower containing the linear or low-power limit. The upper sheet exhibits two important differences in relation to the plot of the lower one. First, in the upper sheet it does not exist a critical locus corresponding to the linear or low-power limit, but the guided wave power amounts to a finite value at all the cutoff loci. Second, each $V - b$ point belonging to an allowed region of the upper sheet yields (at least) two different field profiles: a symmetric guided wave and an asymmetric one.

When considering a symmetric waveguide there is not cutoff for the TE_0 guided solution. In the ideal Kerr-like case this statement holds as well for the TE_1 solutions, even though the allowed solutions take place only above a power threshold. On the contrary, when the saturation of the optically-induced permittivity is taken into account, there is a (γ -dependent) minimum value of the normalized thickness for a TE_1 solution to be allowed. Concerning the second-order solutions, our results show that, even in the ideal Kerr-like case, there exist a cutoff value of V . In fact, large values of the normalized waveguide thickness are required for the TE_2 solutions coming from the upper sheet of the diagrams to be allowed. Existence of these second-order guided waves in slightly asymmetrical structures has been recently pointed out by Ankiewicz and Tran [4].

In the case of a perfectly symmetrical structure we deal with, a clear stability criterion for the lowest-order solution is available, yielding the locus of marginal stability in the $V - b$ plane. Since the upper sheet of the diagrams is double-valued, it exhibits two critical curves indicating neutral stable waves, which correspond to symmetric and asymmetric waves. The first salient point of the outcoming plots is the existence of a minimum value of the normalized waveguide thickness, which is referred as to V_{cr} , for the unstable waves to be possible. In the Kerr-like case numerical calculations yield $V_{cr} \simeq 2.04$, which is a universal figure. Finally, when considering saturable permittivities, V_{cr} exhibit large shifts towards greater values in relation to the Kerr-like case.

References

- [1] U. Langbein, F. Lederer and H.-E. Ponath, *Opt. Commun.*, vol. 53, pp. 417-420, 1985.
- [2] A. Boardman, P. Egan, F. Lederer, U. Langbein and D. Mihalache, in *Nonlinear Surface Electromagnetic Phenomena.*, H.-E. Ponath and G. I. Stegeman eds., MPCMS vol. 29, chap. II, North-Holland, Amsterdam, 1991.
- [3] L. Torner and J.P. Torres, *IEEE J. Quantum Electron.*, vol. QE-28, pp. 1571-1581, 1992; J.P. Torres and L. Torner, *IEEE J. Quantum Electron.*, vol. QE-28, 1992, in press.
- [4] A. Ankiewicz and H. T. Tran, *J. Mod. Opt.*, vol. 38, pp. 1093-1106, 1991.

Synchronously Pumped Modelocked Erbium Fiber Laser

M.L. Stock*, M.E. Fermann, M.J. Andrejco and Y. Silberberg

Bellcore
331 Newman Springs Rd.
Red Bank, N.J. 07701
Tel. (908) 758 3149
Fax. (908) 758 4372

*Ultrafast Science Laboratory
University of Michigan
Ann Arbor, MI 48109-2099

Synchronous pumping is a well-known technique for the modelocking of lasers with fast relaxation times, which has recently received some renewed attention^[1]. It locks the frequency of the pump to that of the signal and is particularly useful in ultra-fast pump-probe measurement techniques. However, due to the constraints on the relaxation time of the gain medium, it is very difficult to synchronously pump solid-state lasers. A noticeable exception has been demonstrated recently in a Nd:YAG laser, where it was claimed that a gain modulation as low as 10^{-4} can produce pulses in the ≈ 100 psec regime in a special reflection-free cavity^[2]. However, in all cases an accurate control of the respective cavity lengths was required and synchronous pumping attributed only to gain-modulation effects.

Here we demonstrate modelocking by synchronous pumping for the first time in a medium with a msec relaxation time, where pump-induced gain modulation is negligible. We use a long erbium fiber laser as the gain medium, where the long interaction lengths between the pump and the signal allow the exploitation of frequency modulation (FM) via nonlinear cross-phase modulation as the modelocking mechanism^[3]. Equally, the highly dispersive cavity produces a very large locking range and allows an estimate of the fiber dispersion^[4].

The laser system is shown in figure 1. The pump was a frequency-doubled cw modelocked Nd:YLF laser, which provided a train of 50psec pulses at a repetition rate of 75.7MHz at a wavelength of 527nm. The pump light was coupled into a silica fiber laser doped with 4×10^{17} erbium ions/cm³ with a launching efficiency of 50%. The fiber had a length of 9 m, a numerical aperture of NA = 0.14 and a core diameter of 6.8 μ m. From the fiber parameters we calculated the fiber group velocity dispersion as $\beta_2 = -16000$ fsec²/m. The launch end of the fiber was butted to a total reflector at 1.53 μ m and the opposite end was cleaved at an angle

of 15° to reduce back-reflections. A polarizer in conjunction with adjustable fiber loops was used to control the polarization state inside fiber. The cavity was completed with a $100\ \mu\text{m}$ thick un-coated etalon and a 50% output coupler.

For synchronous pumping, the cavity length of the fiber laser was matched to the repetition rate of the pump laser to allow for higher-harmonic modelocking with $n=7$ pulses in the fiber laser cavity. Synchronous modelocking could then be achieved with a minimum launched pump power of 100 mW resulting in a cw modelocked fiber laser output power of 1.6 mW. A photograph of a perfectly synchronized pump and signal is shown in Fig. 2. Typically, the cavity length could be changed by $\pm 25 \pm 5\ \mu\text{m}$ without loss of synchronization. However, cavity-length detuning of this magnitude was accompanied with a spectral shift of $\pm 0.5\ \text{nm}$ as shown in Fig. 3, where the pulse spectra at either end of the tuning range are given. The corresponding pulses had a FWHM width of 900 fsec. The time-bandwidth product is thus 0.30 and the pulses were approximately bandwidth limited. A typical autocorrelation trace is shown in Fig. 4. The pulses were sitting on a 0.1 % pedestal that we estimated to contain about half of the pulse energy. The peak pulse power P in the fiber cavity is then calculated as $P = 23\ \text{W}$.

The large pedestal component may be explained by the large non-linearity of the cavity, which induces significant soliton shaping. The soliton period of the pulses is $\approx 25\ \text{m}$, which is comparable to the cavity round-trip length. However, as is known from the average-soliton model, the generation of pedestal-free pulses requires a soliton period \gg cavity length. The fundamental soliton power in the fiber laser is calculated as 20 W, which compares well with the measurements.

The observed spectral shift $\Delta\omega$ with cavity detuning δL allows an independent estimate of the cavity dispersion. It may be shown⁽⁴⁾ that β_2 is given by

$$\beta_2 = -\frac{\delta L}{Lc\Delta\omega}$$

where c is the velocity of light and L is the fiber length. For a spectral shift of 0.5 nm we thus obtain $\beta_2 = 23000 \pm 6000\ \text{fsec}^2/\text{m}$, which compares well to the estimate given above. The discrepancy may be related to the small bandwidth of the cavity.

The pedestal component observed in the autocorrelation trace could be reduced by a setting of the polarization control to allow passive amplitude modulation. However, in this case synchronization was lost and the pulses appeared at random repetition rates. In a small operating range, however, the repetition rates of the pulses could be controlled, but with unstable pulse amplitudes as shown in Fig. 5.

Clearly, optimum synchronization performance requires an increase of pump-induced with respect to signal-induced phase modulation. In the present configuration modal and chromatic dispersion limit the nonlinear interaction length between the pump and the signal to about 1 m. The corresponding pump-induced phase modulation is thus only $\approx 0.1 \pi$. By using a pump wavelength of 980 nm, interaction lengths of the order of 10 m and pump-induced phase modulations of $\approx \pi$ could be achieved. Such a system is currently under study. In addition, further bandwidth-limiting elements could be incorporated to increase the width of the signal pulses and to decrease signal-induced phase modulation.

In summary we have demonstrated modelocking by synchronous pumping using pump-induced phase instead of gain modulation for the first time. We thus demonstrated synchronous pumping of a gain medium with a msec relaxation time. By resorting to a highly-dispersive cavity a large locking range was achieved and an independent estimate of fiber dispersion obtained. The technique is particularly useful for the synchronization of solid-state waveguide lasers. It allows the generation of pulses with high repetition rates and repetition-rate stabilization.

Acknowledgements

MEF acknowledges financial support from the Alexander von Humboldt Stiftung.

References

1. W.H. Knox and F.A. Beisser, *Opt. Lett.*, 17, 1012 (1992)
2. C.J. Flood, G. Giuliani and H.M. Driel, *Opt. Lett.* 15, 210 (1990).
3. E.J. Greer and K. Smith, *Electron. Lett.* 28, (1992)
4. W.H. Knox, *Opt. Lett.*, 17, 514 (1992)

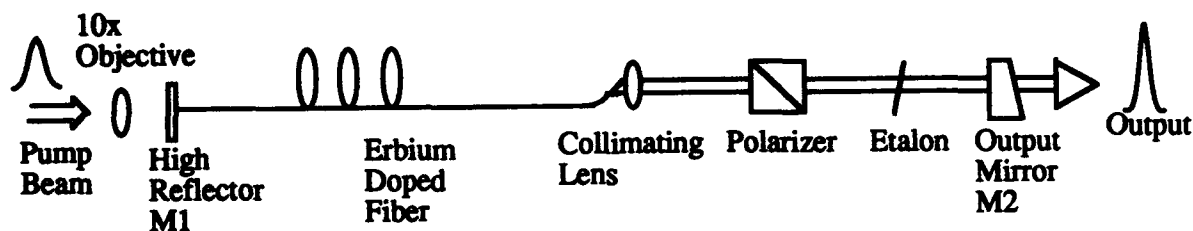


Fig. 1. Cavity design of a synchronously pumped modelocked erbium fiber laser.

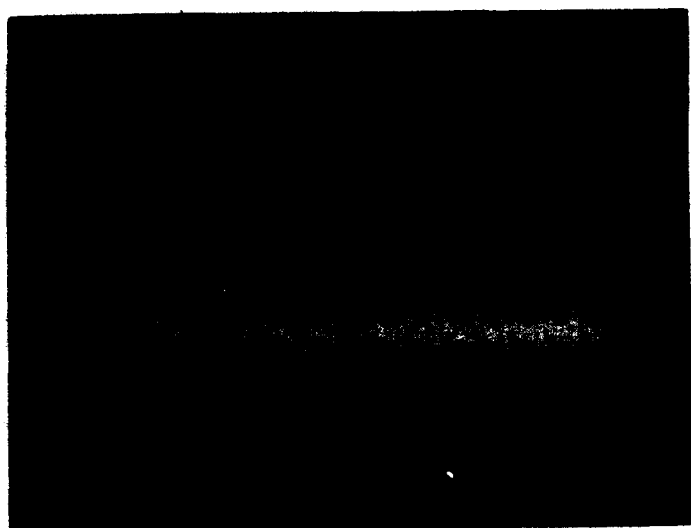


Fig. 2. Photograph of a perfectly synchronized train of signal (large) and pump (small) pulses.

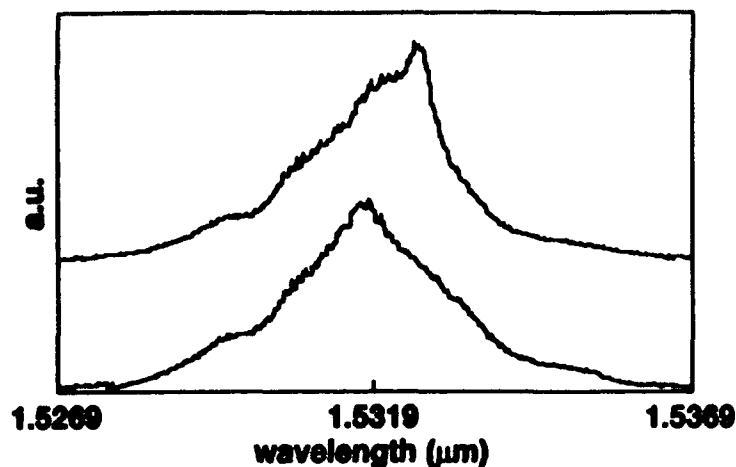


Fig. 3. Generated pulse spectra at either end of the synchronous locking range. A spectral shift of +0.5 nm is observed for a decrease in cavity length by - 25 μm.

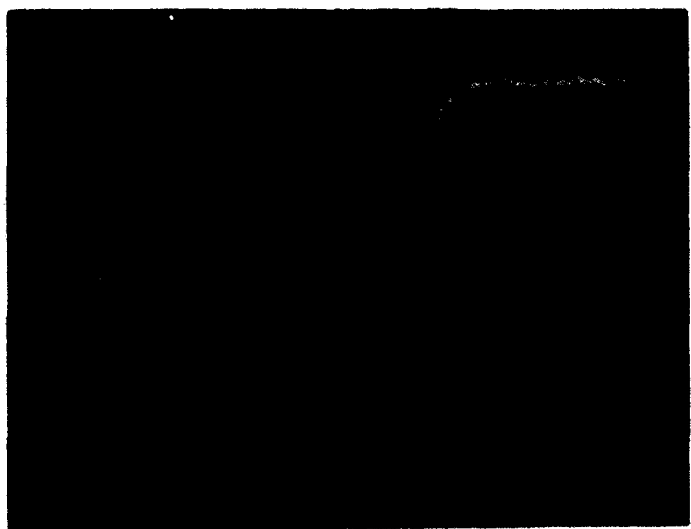


Fig. 4. Typical autocorrelation trace of a generated pulse. The FWHM pulse width is 900 fsec.

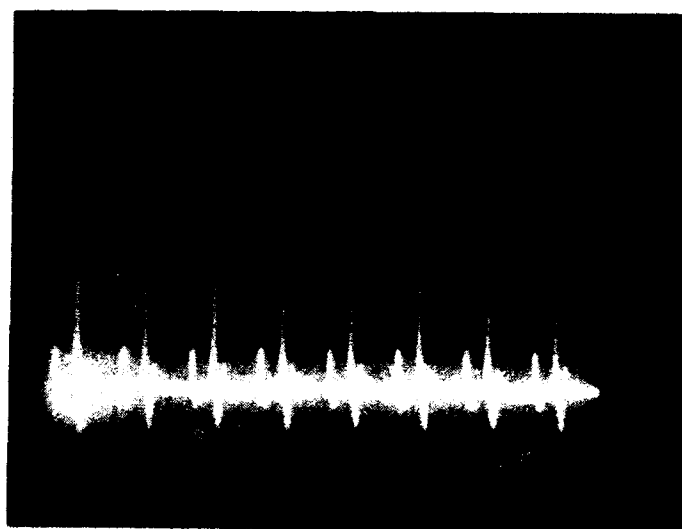


Fig. 5. Photograph of an imperfectly synchronized train of signal (large) and pump (small) pulses.

Generation and Storage of High Repetition Rate Soliton Trains in a Fiber Ring Cavity

M. Haelterman, S. Trillo, and S. Wabnitz

Fondazione Ugo Bordoni, Via B. Castiglione 59, 00142 Roma, Italy

Tel: +396-5480 3206

In order to fully exploit the large bandwidth of optical fibers in future telecommunication systems, the development of soliton sources with repetition rates up to the THz range is required. On the other hand, all-optical signal processing of such high bit rate signals demands the possibility of storing the information contained in an optical pulse train.

Modulational instability (MI) amplifiers and lasers produce ultra-high repetition rate pulse trains, but a non negligible continuous wave (cw) background component seems unavoidable at the output of these sources [1,2]. The generation at high repetition-rate of background free independent soliton trains from a dual frequency pumped fiber with adiabatic amplification or dispersion variation has been proposed [3] and demonstrated [4]. In this work we propose an alternative method for transforming a dual frequency signal into a cw soliton train. The beat signal is injected here into a nonlinear dispersive fiber ring cavity. We show that, under proper conditions on the parameters, MI in the fiber loop generates a single soliton within each semi-period of the beat signal which results in the emission of a periodic train of background-free soliton train. We have also studied the possibility offered by the bistable characteristic of the nonlinear ring cavity for the realization of an optical soliton memory. Mc Donald and Firth proposed that spatial solitary waves could be employed as basic information storage elements in a diffractive nonlinear ring cavity [5] which is equivalent to the synchronously pumped fiber ring considered here. An important limitation to the stable operation of a soliton memory is the interaction between adjacent soliton pulses. In this work, the physical conditions for reducing and even suppressing the interaction forces between adjacent pulse pair in a soliton optical memory are found.

Figure 1 shows the geometry of the proposed setup. The periodic signal $S(t)$ is coupled into the cavity whose round-trip time T_R is assumed to be a multiple of the signal period, say, T_0 . This ensures the synchronization between $S(t)$ and the pulse train formed in the cavity. Under this condition the envelope $U(Z,T)$ of the cavity field is ruled by the map

$$i \partial_z U_n(Z,T) + \frac{1}{2} \partial_{TT}^2 U_n(Z,T) + |U_n(Z,T)|^2 U_n(Z,T) = 0 \quad (1.a)$$

$$U_{n+1}(0,T) = \theta S(T) + \rho^2 U_n(1,T) e^{-i\phi} \quad (1.b)$$

where we introduced a scaling in such a way that the dispersion and the cavity length are equal to unity. θ and ρ are the transmission and reflection coefficient of the couplers, and ϕ is the linear cavity detuning.

Let us consider an input of the form $S(T) = A \sin(2\pi T/T_0)$. In the cw limit ($T_0 \rightarrow \infty$), MI in the cavity leads to the break up of the field envelope into a periodic train of pulses with nonzero background [1,2]. With finite T_0 , a limited number of pulses is formed in each semi-period of the input sinusoidal signal. We found by numerical simulations of the map (1) that one can reduce the period until just a single pulse is left in each semi-period. Fig. 2 shows the intensity profiles of 4 consecutive pulses formed in such conditions. We verified that these pulses are very close to the sech shape of the NLS soliton. Nevertheless, as can be seen on the logarithmic plot (Fig.3), a small pedestal is present in the wings of the generated pulses. As illustrated on curve 3 of Fig. 3, which shows the pulse profile after propagation in a lossless fiber over 35 soliton lengths, this pedestal only has a weak influence on the propagation of the generated pulses. With a transmission $\theta^2 = 0.05$, a fiber loop length of $L = 10$ m, an effective core area of $25 \mu\text{m}^2$, and a dispersion coefficient $D = -10$ ps/nm/km, the example of Figs.3 and 4 corresponds to a train of 670 fsec-solitons at a repetition rate of 118 GHz. The corresponding input peak power is $A^2 = 480$ mW.

For the study of the soliton memory we used a simplified model of the passive nonlinear ring cavity. Moreover, we consider a cw input signal $S(T) = S$. It was shown in Ref.[2] that, under certain conditions, the map (1) can be approximated by the following driven and damped NLS equation

$$i \partial_z U(Z,T) + \frac{1}{2} \partial_{TT}^2 U(Z,T) + |U(Z,T)|^2 U(Z,T) = (\phi - i\theta^2) U(Z,T) + i S \quad (2)$$

Perturbed soliton dynamics in eq.(2) was studied by Nozaki et al. who showed that a stable phase-locked soliton solution may propagate along with a cw background [6]. A unit soliton amplitude is obtained for $\phi = 0.5$ and the solution of Eq. (2) may then be approximated by [6]:

$$U(Z,T) = \text{sech}(T) - 2i S \quad (3)$$

We considered the effects of driving and damping on the interaction between a pair of phase locked solitons with initial temporal separation T_s . The basic mechanism for soliton stability

and independence in the nonlinear ring memory is the existence of a phase-locked soliton attractor which tends to equalize the eigenvalues of a two (and N) soliton bit pattern. The conditions of soliton locking have been derived from standard perturbation analysis of the solution of the driven and damped NLS Eq.(2). The prediction of this analysis is confirmed by the full solution of Eq.(2). Figure (4) shows that, as in Ref.[5], each time slot representing the location of a single bit may be independently addressed by injecting an arbitrary sequence (here 11011110) of solitons into the ring. One verifies the perfect stability of the solitons. Such conditions are obtained with $T_S > 8$. On the other hand, as can be seen, the whole soliton pattern may be erased on a short time scale by turning off the cw beam (in $Z = 260$ on Fig.4).

In conclusion, a method based on dual frequency pumping of a fiber loop was proposed for the generation of high repetition rate trains of independent soliton pulses. The advantage with respect to the cw pumped modulational instability laser is the possibility of cancelling the background and controlling the distance between pulses. The method also compares favourably with dual frequency pumping of a variable dispersion fiber in that a standard fiber of much shorter length may be used. The perturbative and numerical analysis of two soliton interactions in a soliton ring memory showed that the addressing, permanent storage, and erasing of a random sequence of solitons may be achieved.

References:

- [1] M. Nakazawa, K. Suzuki, and H. Haus, Phys. Rev. A 38, 5193 (1988).
- [2] M. Haelterman, S. Trillo, and S. Wabnitz, Opt. Commun. 91, 401 (1992).
- [3] E.M. Dianov, P. V. Mamyshev, A. M. Prokhorov, and S. V. Chernikov, Opt. Lett. 14, 1008 (1989).
- [4] S. V. Chernikov, D. J. Richardson, R. I. Laming, E.M. Dianov, and D. Payne, Electron. Lett. 28, 1210 (1992).
- [5] G. S., Mc Donald, and W. J. Firth, J. Opt. Soc. Am. B 7, 1238 (1990).
- [6] K. Nozaki, and N. Bekki, J. Phys. Soc. Japan 54, 2363 (1991).

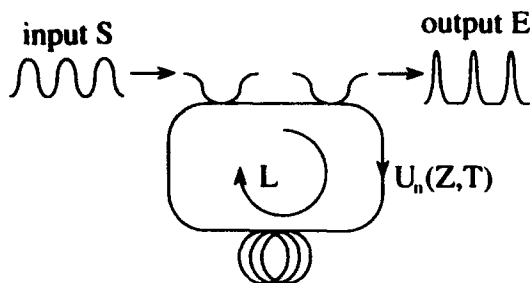


Fig.1 Schematic of the passive nonlinear fiber ring.

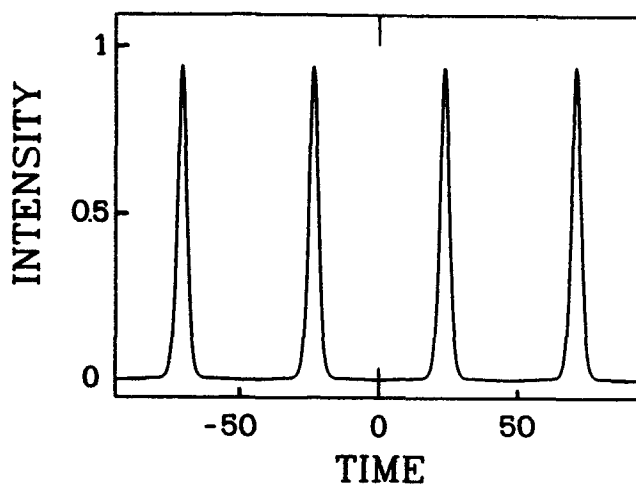


Fig.2 Output pulses from dual-frequency pumped MI laser.

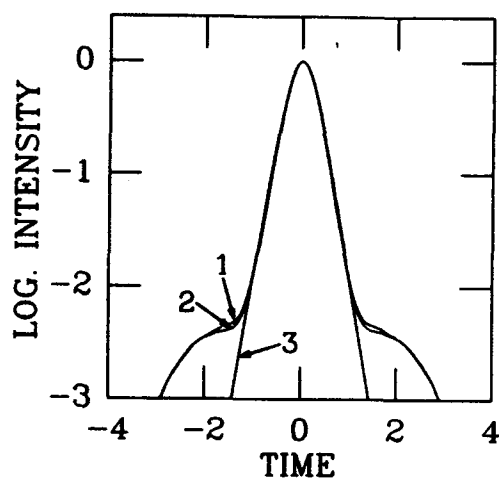


Fig.3

Intensity profile of the pulses in the logarithmic scale. (1) generated pulse shown in Fig.2, (2) the same pulse after propagation over 35 soliton lengths, (3) ideal sech-shaped pulse.

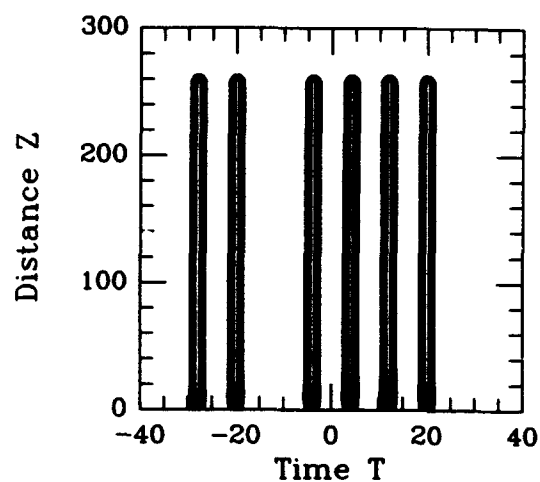


Fig.4

Writing, storage and erasure of the 8 bit soliton pattern (11011110).

KEY TO AUTHORS, PRESIDERS AND PAPERS

Abid, Z. — ITuC1
 Adar, R. — ITuE2
 Ada, R. W. — ITuA6
 Agrawal, Govind Prasad — ITuF
 Agrawal, N. — IWB6
 Alchison, J. S. — ITuD2
 Akhmediev, N. N. — IMB14
 Al-hamyari, K. — ITuD2
 Albert, J. — IMB15, IWD4
 Ando, Takaashi — IMD4
 Andreadekis, N. — IWA2
 Andrejco, M. — IWF5
 Angell, M. J. — IWC5
 Antkiewicz, A. — IMB14
 Arnold, J. M. — ITuD2
 Aronson, Lewis B. — IMB2
 Asakawa, S. — ITuE4
 Ashley, Paul R. — IMC2

Baba, T. — ITuE4
 Babic, Dubravko — IWB1
 Babin, Loic J. M. — IMB18
 Bada, R. — ITuC3, IWB4
 Baldi, P. — ITuH2
 Baran, J. E. — ITuB3
 Basilica, R. P. — ITuA6
 Bassi, P. — ITuH4
 Bava, G. P. — IMB6
 Bellerby, R. — ITuE3
 Benson, T. M. — IMB8
 Betts, G. E. — ITuH3
 Bhat, R. — IWA2
 Blesseaur, H. — ITuI6, IWB4
 Boardman, A. D. — ITuD6, IWF2
 Bonello, R. — IWB4
 Bortz, M. L. — IWC3, IWC5
 Bossi, D. E. — ITuA6
 Botz, D. — ITuF5
 Bowers, John E. — ITuG4, IWB1
 Bozeat, R. J. — IMB8
 Bradshaw, J. — ITuA4
 Brady, David J. — ITuC7
 Brebner, J. L. — IWD4
 Brown-Goebeler, K. — ITuA3
 Bulmer, C. H. — ITuH5
 Burke, S. V. — IMB8
 Burkhardt, H. — IWB4
 Burns, W. K. — ITuH5, ITuH6
 Burrus, C. A. — ITuG5

Campbell, Joseph Charles — IME7, ITuA, IWA5

Caneau, C. — IWA2
 Cannell, G. — ITuE3
 Cao, Hong-li — ITuG6
 Cao, X. F. — IWC2
 Capobianco, A. D. — IWF3
 Carroll, J. E. — IWB4
 Chan, Andrew K. — ITuF3, IWE2
 Chang, T. Y. — ITuA3
 Chang, Y. H. — IWE4
 Chang-Haensain, Constance J. — ITuG, IWE5
 Chaudhuri, S. K. — IMD1
 Chen, J. J. — IWE2
 Chen, Ray T. — IME5
 Chen, S. — ITuH4
 Chen, Yi — ITuA3
 Chien, M.-D. — ITuG5, ITuG7, IWA3
 Chinni, V. R. — ITu3
 Chowdhury, Andalib A. — IWA5
 Chronopoulos, A. — ITuC2

Chu, S. T. — IMD1
 Chui, Charles K. — ITuF3, IWE2
 Chung, Y. K. — IME6
 Chung, Youngchul — ITu4
 Claesse, P. R. — IWB5
 Claiberg, Rolf — ITu7
 Coldren, Larry A. — ITuG6
 Collins, S. D. — IMB19
 Constantini, B. — IWF3
 Cooke, P. W. — ITuG2
 Correc, P. — IWB4
 Cotter, D. — ITuD5
 Curtis, L. — IWA2

d'Alessandro, Antonio — ITuB3
 de Miguel, J. L. — IME4
 Dagli, Nadir — IMC6, ITu4, IWB, IWB3
 Dapkus, P. Daniel — IMB4
 Datta, Supriyo — IWE1
 Davies, J. B. — ITuI6
 Day, S. — ITuE3
 De Angelis, C. — IWF3
 De Micheli, M. P. — ITuH2, ITuH4
 Debernardi, P. — IMB6
 DeFord, J. F. — IMD3
 Deri, Robert J. — IME, ITuC5
 Dienes, A. — IWE4
 Doctor, D. P. — ITuG2
 Dohler, G. H. — ITuA7
 Dong, H. — ITuC2
 Dragone, C. — IME3, ITuB1, IWA3
 Du, Min — ITuF3
 Duan, G. — IWB4

Eldada, L. A. — ITuB2
 Emerson, R. M. — IWC5
 Endoh, T. — IWD3
 Ettinger, R. D. — ITuI6
 Evaldsson, P. A. — ITuG2
 Eyres, L. A. — IWC3, IWC5

Favire, F. — IWA2
 Feit, M. D. — IMD3, ITu2
 Fejer, Martin M. — IWC, IWC3, IWC5
 Fermann, M. E. — IWF5
 Fernandez, F. A. — ITuI6
 Ferreras, A. — IME4
 Fleck, Jr., J. A. — ITuI2
 Forrest, Stephen Ross — IMB, IME6
 Francis, D. — IWE5
 Frateschi, N. C. — IMB4

Gabathuler, W. — IWD2
 Gaiße, Th. — IME3
 Garabedian, R. — IMB19
 Garrett, L. D. — IME7
 Georges, John B. — IWA6
 Gerdes, Johannes — ITuI8
 Gibbons, J. F. — IWC5
 Gnaill, R. P. — IME2
 Gomez-Salas, E. — IME4
 Gonzales, C. — IMB19
 Goorjian, Peter M. — IMD5
 Gopelakrishnan, G.K. — ITuH5, ITuH6
 Gopinath, Anand — IMB13, ITuA5, ITuC, ITuC1, ITuC2, ITuC4, IWE3
 Gossard, Arthur — IMC6
 Gozdz, A. S. — IWA2
 Grant, M. — ITuE3
 Gravert, M. — ITuC6
 Gulden, K. H. — ITuA7

Gustavsson, Mats — ITuA1
 Gutierrez, C. J. — IMC3
 Hadley, G. Ronald — ITu5
 Haeblerman, M. — IWF6
 Haas, J. — ITuC3
 Hamamoto, K. — ITuA2
 Hama, Benno H. M. — IMC1
 Hanaizumi, Osamu — IMB1
 Hansen, P. B. — ITuG5
 Hansmann, S. — IWB4
 Haruna, M. — ITuB5
 Haus, Hermann A. — IMA1, IMC
 Hawkins, Raymond J. — IMA, IMD3, IMD6, ITuC5

Hayes, R. — IWA4
 He, Y.-S. — IME7
 Heiderman, Jean-Luc P. — IMC1
 Henry, Charles H. — ITuE, ITuE2
 Heritage, J. P. — IWE4
 Hernandez-Gil, F. — IME4
 Hess, Karl — IWB2
 Hesselink, Lambertus — IMB2
 Hibino, Yoshinori — IWD1
 Hile, Cheryl V. — ITuF4
 Hill, Kent B. — ITuC7
 Hill, K. O. — IWD4
 Hofer, A. — ITuA7
 Hong, M. Y. — IWE4
 Horsthuis, Winfried H. G. — IMC1
 Hosomatsu, Haruo — ITuG6
 Houde-Walter, Susan N. — IMB9
 Hoyt, J. L. — IWC5
 Huang, T. C. — ITuA4
 Huang, W. P. — IMD1
 Hulse, Charles — IMD7
 Hutchings, D. C. — ITuD2

Iga, K. — ITuG1
 Ilic, I. — IMC3
 Inuzuka, H. — IMB16
 Ironside, C. N. — ITuD2
 Ishikawa, Takuya — ITuG4
 Izumikawa, Manabu — IMB1

Jansen, M. — IMB4
 Janson, Mats — ITuA1
 Javalagi, S. I. — IME7
 Jiang, Wenbin — IWB1
 Johnson, D. C. — IWD4
 Johnson, J. J. — ITuB3
 Johnson, Klein L. — ITuC1, ITuC4
 Jopson, R. M. — ITuG7
 Joseph, Rose M. — IMD5
 Joyner, C. H. — IME3
 Judkins, Justin B. — IMD6

Kalkman, J. S. — IMD3, IMD8
 Kan, S. C. — ITuG3
 Kar-Roy, Arjun — ITuB4
 Kashyap, R. — ITuD5
 Kath, William L. — IMB12, ITuF4
 Kato, T. — ITuB5
 Kawachi, M. — ITuE1
 Kawakami, Shojo — IMB1, IMC4
 Khan, M. Nisa — IMB13, ITuA5
 Kiely, P. A. — ITuG2
 Kiesel, P. — ITuA7
 Kistler, R. C. — ITuE2
 Kitamura, M. — ITuA2
 Kneissl, M. — ITuA7

- Knoesen, Andre — IMB17, IMB19, IMD7
 Krupfer, B — ITuA7
 Koch, Thomas L. — IME2, IWA
 Koerkamp, Marcel M. Klein — IMC1
 Kokubun, Yasuo — ITuE4
 Komatsu, K. — ITuA2
 Koren, U. — IME2, ITuG5, ITuG7, IWA1, IWA3
 Korotky, Steven K. — IWD
 Koza, M. A. — IWA2
 Kramer, Dennis — IMB10
 Kumar, Prem — IMB12
 Kutz, J. Nathan — IMB12
 Kuwahara, Keisuke — IMB1
 Kwong, D.-L. — IME7
- Lallier, Eric — ITuH1, ITuH2
 Lambert, N. — ITuE3
 Lassen, H. E. — IWB4
 Lau, Kam Y. — ITuG3, IWA6
 Laughton, F. — ITuD2
 Leavitt, R. P. — ITuA4
 Lee, T. P. — IWA2
 Levy, M. — IMC3, ITuB2
 Leycuras, A. — ITuH4
 Li, Ruo-Ding — IMB12
 Lin, Cheng-Hui — ITuD3, ITuD4
 Lin, Hao-Hsiung — ITuD3, ITuD4
 Lin, P. S. D. — ITuB2, IWA2
 Lukosz, W. — IWD2
- Madsen, N. K. — IMD3
 Mahalakshmi, V. — IWC6
 Mahoney, D. D. — IWA2
 Majewski, Marian L. — ITuG6
 Maio, B. — IWD4
 Manning, R. J. — ITuD5
 Marsh, J. H. — ITuD2
 Martin, Olivier J. F. — ITu17
 Matin, M. A. — IMB8
 Maziar, Christine M. — IWA5
 Mecozzi, A. — IWB4
 Melchior, Hans — IME1
 Menyuk, C. R. — ITuF1, ITu13
 Mibrod, M. A. — ITuE2
 Miller, B. I. — IME2, ITuG5, ITuG7, IWA3
 Möhlmann, Gustaaf R. — IMC1
 Monnon, G. — ITuH2
 Montrosset, I. — IWB4
 Morthier, G. I. — IWB4
 Mould, Jr., J. — IMD2
 Murtaza, Suhail — IWA5
- Nabiev, R. F. — ITuF5, IWE5
 Nada, Naoki — IWC1
 Nagarajan, Radhakrishnan — ITuG4, IWB1
 Nakano, Hisamatsu — IMD4
 Nakano, Yoshiaki — ITuG6
 Nalesso, G. F. — IWF3
 Narayanan, A. — IWA4
 Newkirk, M. A. — IME2, ITuG5, ITuG7, IWA3
 Ng, W. — IWA4
 Nishihara, H. — ITuB5, IWD3
 Nolting, H.-P. — ITuC3, ITuC6
 Noh, S. — ITuH2
 Noutsios, P. C. — IMB15
- O'Donnell, F. J. — ITuH3
 Ohyama, M. — ITuE4
 Ojeda, C. — IMB11
 Okamoto, K. — ITuE1
 Olesen, H. — IWB4
- Oliver, S. N. — ITuD5
 Osgood, Jr., R. M. — IMC3, ITuB2
 Osterberg, Ulf — ITuF2
 Ostrowsky, D. B. — ITuH2, ITuH4
 Ou, S. S. — IMB4
- Papuchon, M. — ITuH2
 Park, John — IWA6
 Paek, C. — IWF1
 Pathak, B. — IWA2
 Pepeljugin, Petar K. — IWA6
 Pham, J. — ITuA4
 Pollack, Martin A. — IMA2
 Pregla, Reinhold — IMB10, IMD, ITu18
 Presby, Herman M. — IWA3
 Prince, Eric T. — IMC5
 Prinz, G. A. — IMC3
 Pu, Y. — ITuB6
- Rashed, M. Mahub — IWA5
 Ratowsky, R. P. — ITu12
 Ray, K. G. — ITuH3
 Raybon, G. — ITuG5, IWA3
 Reinhart, Franz-Karl — ITu17
 Ren, Z. Y. — IMB5
 Revelli, Joseph F. — IMC5
 Richards, J. D. — IMB17, IMB19
 Riel, P. — ITuA7
 Rodriguez, F. — IME4
 Rosser, S. — ITuE3
 Russell, P. St. J. — ITuD1
- Sacks, R. N. — ITuA6
 Sammut, R. A. — IWF1
 Santos, C. — IMB11
 Sapia, A. — IWB4
 Sargood, S. K. — ITuG2
 Sasaki, T. — IMC4
 Sato, T. — IMC4
 Sauer, N. J. — ITuA3
 Scarmozzino, R. — IMC3, ITuB2
 Schatz, R. — IWB4
 Seki, Shunji — IWB2, IWE
 Shah, V. S. — IWA2
 Shandarov, S. — IMB7
 Shandarov, V. — IMB7
 Shang, C. C. — IMD3
 Shenoy, M. R. — IWC6
 Shinohara, M. — IWD3
 Shiraiishi, K. — IMC4
 Shore, B. W. — IMD3
 Silberberg, Yaron — IWF, IWF5
 Simonis, G. J. — ITuA4
 Smith, David Arthur — ITuB, ITuB3
 Smith, J. S. — ITuA7
 Smith, R. L. — IMB19
 Smith, R. E. — IMB9
 Solgaard, Olav — IWA6
 Someda, C. G. — IWF3
 Song, G. Hugh — ITu11, IWA2
 Sotirelis, Paul — IWB2
 Spencer, R. — IMB19
 Spicer, R. E. — IWA2
 Stead, M. R. — ITuA4
 Stegeman, George I. — IMA3, ITuD, ITuD3, ITuD4
 Stock, M. L. — IWF5
 Stutz, L. W. — IME3
 Subramanian, Prasad — IWB7
 Sugou, S. — ITuA2
 Suhara, T. — IWD3
 Sztafka, G. — ITuC3
- Tada, Kunio — ITuG6
 Taffove, Allen — IMD5
 Takemoto, Hiroyuki — IMB1
 Tartarini, G. — ITuH4
 Tauber, Dan — IWB1
 Taylor, G. W. — ITuG2, IWB5
 Tell, B. — IME2, ITuA3, ITuG5, IWA3
 Templeton, I. M. — IWD4
 Thomas, Mason — IMC6
 Thyagarajan, K. — IWC6
 Tonetti, M. — IMB6
 Tong, F. — ITuB2
 Torner, Lluís — IMB11, IWF4
 Torres, Juan P. — IWF4
 Trillo, S. — IWF6
 Tsai, Chen S. — IMB3, IMB5, ITuB4, ITuB6
 Tsang, C. F. — IWB4
 Tumolillo, Jr., Thomas A. — IMC2
 Tuncer, E. — IME7
- Umegaki, Shinsuke — IWC4
 Ura, S. — IWD3
- Vassilovski, D. — ITuG3
 Verdiell, J. M. — IME2
 Vetoshko, P. M. — ITuD6
 Vey, J.-L. — IWB4
 Villeneuve, Alain — ITuD3, ITuD4
 Volkovoy, V. B. — ITuD6
 Voronko, A. I. — ITuD6
 Vu, T.Q. — IMB3, IMB5
- Wabnitz, S. — IWF6
 Wai, P. K. A. — ITu13
 Waldman, Jonathan — IMC6
 Wang, Gary — IWB1
 Weinert, C. M. — IWB6
 Wetzman, Peter S. — ITuF2
 Wensley, P. — ITuE3
 Wenzel, H. — IWB4
 West, L. C. — IMD2
 Willems, J. — ITuC3
 Wilson, I. — ITuE3
 Winful, Herbert G. — IWB7
 Wojcik, G. — IMD2
 Wolfe, R. — IMC3
 Wright, Ewan M. — ITuC5
 Wu, T. C. — ITuG3
 Wu, X. — ITuA7
- Xie, K. — IWF2
- Yamada, Masahiro — IWC1
 Yamanaka, Takayuki — IWB2
 Yamauchi, Junji — IMD4
 Yang, C. C. — ITuD3, ITuD4
 Yang, J. J. — IMB4
 Yang, Wei — ITuA5, IWE3
 Yap, D. — IWA4
 Yasuda, K. — ITuB5
 Yeh, P. — ITuF5
 Yevick, David O. — ITu1
 Yi, Jong Chang — IWB3
 Yip, Gar Lam — IMB15, IMB18, ITuH
 Yokoyama, Kiyoyuki — IWB2
 Young, M. G. — ITuG5, ITuG7, IWA3
 Young, W. C. — IWA2
 Yu, Mark — ITuH7
- Zah, C. E. — IWA2
 Ziolkowski, Richard W. — IMD6
 Zirngibl, M. — IME3, IWA3
 Zucker, J. E. — ITuA3